



Proceedings of the
**9th Virtual International Conference on
Science, Technology and
Management in Energy**

Editor:
Velimirović, L. Z.

Publishers:
Complex System Research Centre, Niš, Serbia
Mathematical Institute of the Serbian Academy of
Sciences and Arts, Belgrade, Serbia



Serbia, Belgrade, November 23-24, 2023

Editor
Velimirović, L. Z.

eNergetics 2023

9th Virtual International Conference on Science,
Technology and Management in Energy

Proceedings

Publishers

Complex System Research Centre, Niš, Serbia

Mathematical Institute of the Serbian Academy of Sciences and
Arts, Belgrade, Serbia

Serbia, Belgrade, November 23-24, 2023



Proceedings of the
**9th Virtual International Conference
on Science Technology and Management in Energy**

Serbia, Belgrade, November 23-24, 2023

Editors:

Dr. Lazar Z. Velimirović

Technical Editor:

Dr. Petar Vranić

Published by:

Complex System Research Centre, Niš, Serbia

Mathematical Institute of the Serbian Academy of Sciences and Arts, Belgrade,
Serbia

Printed by:

Copy House, Niš, Serbia

Number of copies printed: 100

The publishing year: 2024

Printing of this edition has been financially supported by

The Ministry of Science, Technological Development and Innovation of the Republic
of Serbia

ISBN 978-86-82602-03-3

CIP - Каталогizacija u publikaciji
Narodna biblioteka Srbije, Beograd

620.9(082)(0.034.2)

**VIRTUAL International Conference on Science Technology and Management in Energy
(9 ; 2023 ; Beograd)**

Energetics 2024 [Elektronski izvor] : proceedings / 9th Virtual International Conference on
Science Technology and Management in Energy, Serbia, Belgrade, November 23-24, 2023 ;
editor Velimirović, L.[Lazar] Z. - Niš : Complex System Research Centre ; Belgrade :
Mathematical Institute of the SASA, 2024 (Niš : Copy House). - 1 elektronski optički disk
(DVD) ; 12 cm

Sistemska zahtevi: Nisu navedeni. - Nasl. sa naslovne strane dokumenta. - Tiraž 100. -
Bibliografija uz svaki rad.

ISBN 978-86-82602-03-3 (CSRC)

a) Енергетика -- Зборници

COBISS.SR-ID 139266057

eNergetics 2023

9th Virtual International Conference on Science Technology and Management in Energy

Organizer:

Mathematical Institute of the Serbian Academy of Sciences and Arts,
Belgrade, Serbia

Co-organizers:

- Academy of Sciences and Arts of the Republika Srpska
- Faculty of Mining and Geology, University of Belgrade
- Faculty of Technical Sciences, University St. Climent Ohridski
- Complex System Research Centre COSREC

Supported by:

The Ministry of Science, Technological Development and Innovation of the Republic
of Serbia



Program Committee

Chair:

Dr. Lazar Z. Velimrović, Mathematical Institute of the Serbian Academy of Sciences and Arts, Belgrade, Serbia

Members:

Prof. Dr. Aleksandar Janjić, Faculty of Electronic Engineering, Serbia

Prof. Dr. Detelin Markov, Faculty of Power Engineering and Power Machines, Bulgaria

Prof. Dr. Marko Serafimov, Faculty of Mechanical Engineering, Macedonia

Prof. Dr. Mileta Janjić, Faculty of Mechanical Engineering, Montenegro

Prof. Dr. Zoran Stajić, Faculty of Electronic Engineering, Serbia

Prof. Dr. Miomir Stanković, Mathematical Institute of the Serbian Academy of Sciences and Arts, Serbia

Prof. Dr. Tomislav Sekara, School of Electrical Engineering, Serbia

Prof. Dr. Enver Agić, Public Enterprise Electric Utility of Bosnia and Herzegovina, Bosnia and Herzegovina

Prof. Dr. Niko Majdandžić, Faculty of Mechanical Engineering, Croatia

Prof. Dr. Serkan Abbasoglu, Cyprus International University, Turkey

Prof. Dr. Bojan Srđević, Faculty of Agriculture, Serbia

Dr. Lenin Kanagasabai, PVP Siddhartha Institute of Technology, India

Prof. Dr. Abdelhak Djoudi, National Polytechnic School, Algeria

Dr. Elson Avallone, Federal Institute of Education, Science and Technology of São Paulo, Brazil

Prof. Dr. Zdravko Milovanović, Faculty of Mechanical Engineering, Bosnia and Herzegovina

Prof. Dr. Miloš Jelić, Research and Development Center Alfatec, Serbia

Prof. Dr. Zoran Markov, Faculty of Mechanical Engineering, Macedonia

Dr. Jovan Mikulović, School of Electrical Engineering, Serbia

Dr. Sasa Milić, Institute Nikola Tesla, Serbia

Prof. Dr. Krsto Miljanović, Agromediterranean Faculty, Bosnia and Herzegovina
Prof. Dr. Lana Pantić-Randjelović, Faculty of Sciences and Mathematics, Serbia
Prof. Dr. Krum Todorov, Faculty of Power Engineering and Power Machines,
Bulgaria
Prof. Dr. Dragoljub Mirjanić, Academy of Sciences and Arts of Republic of Srpska,
Bosnia and Herzegovina
Prof. Dr. Tomislav Pavlović, Faculty of Sciences and Mathematics, Serbia
Dr. Howard Njoku, University of Nigeria, Nigeria
Prof. Dr. Zoran Gligorić, Faculty of Mining and Geology, Serbia
Dr. Reza Hamidi, Arkansas Tech University, USA
Prof. Dr. Danijel M. Danković, Faculty of Electronic Engineering, Serbia
Dr. Wassila Issaadi, Faculty of Technology, University of Bejaia, Algeria
Dr. Monica Carvalho, Federal University of Paraíba, Brazil
Dr. Prahaladh Paniyil, Clemson University, USA
Prof. Dr. Milan Rapajić, Faculty of Technical Sciences, Serbia
Dr. Sandra Patricia Castaño Solis, ETS Universidad Politécnica de Madrid, Spain
Dr. Arunava Chatterjee, Meghnad Saha Institute of Technology, India
Prof. Dr. Vesna Karović Maričić, Faculty of mining and geology, Serbia
Dr. Ivana Radonjić Mitić, Faculty of Sciences and Mathematics, Serbia

Organizing Committee

Chair:

Dr. Petar Vranić, Mathematical Institute of the Serbian Academy of Sciences and Arts, Serbia

Members:

Prof. Dr. Miomir Stanković, Mathematical Institute of the Serbian Academy of Sciences and Arts, Serbia

Prof. Dr. Zoran Stajić, Faculty of Electronic Engineering, Serbia

Dr. Lazar Velimirović, Mathematical Institute of the Serbian Academy of Sciences and Arts, Serbia

Dr. Dusan Tatić, Mathematical Institute of the Serbian Academy of Science and Arts, Serbia

Dr. Radmila Janković, Mathematical Institute of the Serbian Academy of Science and Arts, Serbia

Dr. Danijela Protić, Serbian Armed Force, Serbia

Dr. Jelena Velimirović, Mathematical Institute of the Serbian Academy of Sciences and Arts, Serbia

M.Sc. Ivana Veličkovska, Mathematical Institute of the Serbian Academy of Sciences and Arts, Serbia

M.Sc. Vladimir Antić, Serbian Armed Force, Serbia

Table of Contents

The Future Belongs to High Efficiency: Nonflammable Batteries, Wireless Charging, Hydrogen and eFuel Production.....	3
Milan Prokin, Dragana Prokin	
Simulation Study of the Improvement of the Performance of the Drying Unit of the JLE-Jijel Company.....	11
Bessam Toumi, Mohamed Benelhaoues, Ahmed Ghaoui	
Preparation and Characterization of Biochar from Pineapple and Sugarcane Solid Wastes	15
Sidney de Souza Plácido Júnior, Maxwell de Arandas Pimentel, Silvia Layara Floriani Andersen	
Analysis of Voltage-Current Characteristics of Non-Linear Electric Loads.....	23
Bakir Agić, Enver Agić	
Comparison of Traditional and Non-traditional Economic Instruments in Solid Waste Managemnt.....	27
Javad Yahaghi, Alireza Bazargan	
Novel Loco Pilot Training Optimization and Rapid E-learning Inspired Algorithm for Solving the True Power Loss Reduction Problem in Electrical Transmission System.....	33
Lenin Kanagasabai	
Energy and Environmental Management System.....	41
Jelena Malenović-Nikolić	
CuO and CuO/ZnO Nanostructures in Biodiesel Production from Waste Cooking Oil.....	47
Philip Alexandre Araújo Ventura dos Santos, Elvia Leal, Isaac Anderson Alves de Moura, Ana Cristina Figueiredo de Melo Costa, Marta Célia Dantas Silva, Joelda Dantas	

Challenges and Potential Applications of the Renewable Energy for Desalination.....	55
Ammar Zeghloul	
Process Parameter Optimization of Al7SiMg Alloy Casting by Means of Probability-based Multi-objective Optimization.....	61
Mszhengok Zheng, Jie Yu	
Natural Power of Medium Voltage Electric Power Distribution Lines as a Criterion for Optimal Management of the Existing Electric Power Distribution Grid and its Reconstruction.....	65
Suad Halilčević	
Thermodynamic Analysis of a Rankine Cycle Integrated to the Biogas Plant at the Metropolitan Sanitary Landfill of João Pessoa, Northeast Brazil.....	73
Djayr Bispo, Raphael Abrahao, Monica Carvalho	
Predicting Nitrous Oxide Emissions in Ghana using Long Short-term Memory and Gated Recurrent Neural Network.....	81
Benjamin Odoi, Derrick Akoto Boahen, Lewis Brew	
Analyzing Heat Transfer Mechanisms in a Thermodynamic Concentrator.....	89
Loubna Benhabib, Abdellah Benyoucef	
Energetic Properties of Sugar Cane Bagass during Storage in an Ethanol Production Plant.....	95
Rosa Helena César Freire de Souza, Jean Constantino Gomes da Silva, Silvia Layara Floriani Andersen	
CFD Analysis of Flow through a Ribbed Solar Air Heater Plastic Absorber.....	103
David Okenwa, Kalu-Whyte Godson, Howard Njoku	
Coal Price Forecasting Model for Underground Mine and Thermal Power Plant Interaction.....	111
Miloš Gligorić, Saša Jovanović, Zoran Gligorić, Suzana Lutovac	
Thermal Efficiency of a PVC Honeycomb Solar Collector.....	117
Kewyn Ohan Mazer Bueno, Paulo Cesar Mioralli, Paulo Henrique Palota, Pablo Sampaio Gomes Natividade, Sílvio Aparecido Verdério Junior, Elson Avallone	

Ideal and Static Magnetohydrodynamics Computation for Plasma Fusion...	123
Amina Djellouli, Assia Rachida Senoudi	
CFD Evaluation of Fractal-type Structures for Improved Heat Transfer in Heat Exchangers (Part A)	129
Abdulmuttalib A. Muhsen, Natalya Kizilova, Bashar Hassan Attiya	
Quantitative Study of Afforestation Present in Quitaiús de Lavras da Mangabeira/Ceará/Brazil.....	137
Isaac Anderson Alves de Moura, Joelda Dantas, Elvia Leal, Kelly Cristiane Gomes da Silva	
Financial Assessment of Waste to Energy Options for Municipal Solid Waste Management - Tehran Case Study.....	145
Ali Marefa, Alireza Bazargan, Reza Samadi	
Sustainable Location of Solar Plants: An Integrated Bibliometric Approach on Gis-multi-criteria Methods.....	153
Gustavo Gonçalves, Lucia Gaudencio, Rui de Oliveira	
Study of Optimal Injection of Renewable Energy into Distribution Power Grid.....	161
Yao Bokovi, Aka Odoh, Moyème Kabe, Adekunlé Akim Salami	
Structural, Microstructural, Optical, and Electrical Properties of Nickel Doped Tin Oxide Films by PSP Method for Photovoltaic Application.....	167
Roguai Sabrina, Djelloul Abdelkader	
Copper Ferrites and Solar Radiation in the Removal of Rhodamine B: A Bibliometric Approach.....	171
Andrezza Pereira de Matos, Ana Paula Freire de Araújo, Pollyana Caetano Ribeiro Fernandes	
Designing a Social Resilience Index for Electricity Power Systems.....	179
Amir Niroomandfam, Mohammad Hassan Bahmani, Amir Bairami Akhi Jahani, Masood Yahyaei	

Purification of Sewage and Pharmaceutical Wastewater in Urban Areas Using Renewable Dead Biomass.....	187
Esam Saleh, Touzout Feriel, Yous. R., Cherifi H., Salah Hanini	
AC Current Measurement with ARM Microcontroller and Current Transformer CR8349-1500.....	191
Đorđe Lazarević, Uroš Ilić, Jovan Ćirić, Aleksandar Veličković	
Characterization of Watermelon Rind for Energy Purposes.....	199
Mikaely Renaly Carlos da Silva, Silvia Layara Floriani Andersen	
Tube Geometry Influence on Heat Exchanger Efficiency: Part B - Comparative Analysis.....	207
Abdulmuttalib A. Muhsen, Natalya Kizilova, Bashar Hassan Attiya	
Urban Waste as an Energy Source: Dumps Change in Paraíba's Landfills.....	215
Sahyonara Estrela de Lacerda Hussein Mélo, Kelly Cristiane Gomes, Joelda Dantas	
Utilization of the Probabilistic Robust Design in Concurrent Optimization of Machinability and Tool Life in Machining Process.....	221
Maosheng Zheng, Jie Yu	
Fuzzy Logic Control of 5MW Grid Connected Wind Turbine.....	227
Ali Berboucha, Kamel Djermouni, Kaci Ghedamsi, Djamal Aouzellag	
Self-excited Induction Generator for Supporting Grid-isolated Loads in Microgrid with its Techno-economic Analysis.....	235
Arunava Chatterjee	
Environmental Payback of a Solar Photovoltaic System installed in the Brazilian Northeast.....	241
Luiz Felipe Souza Fonseca, Italo Roger Ferreira Moreno Pinheiro da Silva, Luiz Moreira Coelho Junior, Raphael Abrahão, Monica Carvalho	
Neural Networks in Pellet Combustion Control - an Overview of the Group's Research Work in 2022/2023.....	249
Stefan Popović, Dejan Djukić, Sonja Djukić Popović, Milan Gligorijević	

Effect of Temperature on the Absorption of Chrome and Silica-based Solar Absorbing Surfaces.....	255
Mikaely Renaly Carlos da Silva, Kelly Cristiane Gomes	
Exploiting Renewable Energy in Iraq to Conquer the Problem of Electricity Shortage and Mitigate Greenhouse Gas Emissions.....	261
Muthanna M. Al-Hadeethi, Mohd Wazir Bin Mustafa, Abdulmuttalib A. Muhsen	
MHD Mixed Convection and Pressure Drop in an Open Cavity with a Solid-porous Fin.....	269
Brahim Fersadou, Walid Nessab, Khaled Mouaici, Nawal Guerroudj, Henda Kahalerras	
Developing Policy Schemes for Grid-scale Microgrids - A Case Study of the USA.....	277
Mohammad Hassan Bahmani, Amir Niroomandfam, Masood Yahyaei	
Lab-scale Assessment of Biogas Generation using Seaweed in Northeast Brazil.....	285
Mikaely Renaly Carlos da Silva, Sayonara A. Eliziario, João Marcelo Dias Ferreira	
Activation Function Effects on the Power Forecasting of a Photovoltaic Plant	291
Antonio Rivero-Cacho, Alejandro Pulido-Guerra, Víctor Collar-Serradilla, Manuel Botejara-Antúnez, Gonzalo Sánchez-Barroso, Justo García-Sanz-Calcedo	
Ejector Stack Design and Fan Selection for Efficient Flue Gas Discharge: A Computational Fluid Dynamics Study.....	299
Masoud Darbandi, Masoud Fazeli, Behnam Basiriani, Seyyed Mohsen Hosseini, Masoud Allah Dadi	
Calorific Value and Thermogravimetry of Bio-oil from Pyrolysis of Paraíba and Paraná.....	305
Philip Alexandre Araújo Ventura dos Santos, Joelda Dantas, Elvia Leal, Alisson Marcos Fogaça, Flávia de Medeiros Aquino, Andrya Lays Freire Alves	

Numerical Model for Computation of Induced Voltages along Double-circuit Overhead Transmission Lines.....	311
Ivica Jurić-Grgić, Dino Lovrić, Ivan Krolo	
Dynamic Influence of Shapes inside Reformer of Methanol Steam Reaction.....	319
Abaidi Abou Houraira, Madani Brahim	
Exergetic Evaluation and Life Cycle Assessment as Strategies for Sustainability Analysis: Application for Industrial Refrigeration Systems.....	325
Marcos Antônio Oliveira Lima, Alexandre Magno Vieira Gonçalves de Brito, Daniel de Paula Diniz, Fazal Um Min Allah, Raphael Abrahão	
Comparative Study on the Impact of the Nature of Fluids Used in CPV/T-TEG Systems.....	333
Khaled Mouaici, Brahim Fersadou, Walid Nessab, Nawal Guerroudj, Henda Kahalerras	

The Future Belongs to High Efficiency: Nonflammable Batteries, Wireless Charging, Hydrogen and eFuel Production

Milan Prokin¹, Dragana Prokin²

¹University of Belgrade – School of Electrical Engineering, Belgrade, Serbia,

²Academy of Technical and Art Applied Studies, School of Electrical and Computer Engineering, Belgrade, Serbia

^{1,2}National Association of Autonomous and Electric Vehicles, Belgrade, Serbia

¹milan.prokin@naev.rs, ²dragana.prokin@viser.edu.rs

Abstract—Scientists and engineers are divided into separate, sometimes very opposite camps, trying to convince governments, the general public and other scientists that their approach for the future of vehicles is the only possible and worthwhile funding from governments, investment funds and car manufacturers. However, the situation is far from being settled. Namely, in spite of the fact that batteries remain the most sought and promising solution for powering vehicles in the future (until 2035, 2040 or 2050 depending on a country), there are many problems that won't help that plan. Namely, according to the latest studies, there is insufficient quantity of rare chemical elements necessary for manufacturing batteries for both electric vehicles and grid storage to be used for charging during day and discharging during night.

Keywords – nonflammable batteries, wireless charging, hydrogen and eFuel production

I. INTRODUCTION

Battery powered electric vehicles (BEVs) are much heavier than internal combustion engine (ICE) powered vehicles, which will affect both increased road maintenance and construction of multilevel parking lots, so they won't collapse under load. The worst of all is increased pollution by PM2.5 particles from tires and brakes, caused by increased BEV weight, which can't be easily solved by improved technology, even with improved regenerative braking that will decrease

pollution from brakes. Finally, well-known flammability of lithium ion batteries requires use of nonflammable batteries that additionally inherently solve the problem of regenerative braking due to significantly smaller resistance. Therefore, in order to solve all problems with BEVs, high efficiency wireless charging during driving and parking seems the only available solution for decreasing the capacity, weight, size and cost of batteries in electric vehicles.

Hydrogen fuel cell powered electric vehicles have much lower efficiency along the whole chain of hydrogen production, delivery and storage, requiring as much as 4 different hydrogen pressures in production tanks, delivery trucks, hydrogen filling stations and vehicle tanks, in comparison with BEVs requiring power lines and electric vehicle chargers. In order to mitigate efficiency problems with hydrogen and additional emitted water vapor that is much more potent greenhouse gas than carbon dioxide, the best solution is to produce it locally at hydrogen filling stations from captured water vapor from the ambient air (e.g. at 50% humidity) using high efficiency electrolysis powered by green energy, or from captured water vapor from the air (e.g. at 100% humidity) inside evaporative cooling towers of nuclear, coal-fired and geothermal power plants, which is applicable even in land-locked countries, while producing net-zero greenhouse gas effect. Further increase in

efficiency is possible with nonflammable batteries supporting regenerative braking.

The economical and political problem of both aforementioned solutions is that the production of ICE powered vehicles is planned to stop completely, while existing internal combustion engine powered vehicles should cease to be driven due to stopping production of fuels from fossil fuels, which would deprive most drivers from their own vehicles, and destroy economy of scale of their production. However, if we capture carbon dioxide in chimneys or at least from free air, and combine it with hydrogen produced from captured water vapor using green energy, it is possible to produce synthetic fuel, also named eFuel, that can power existing internal combustion engines as pure net-zero vehicles running on green energy, while fuel chemistry will be completely balanced, i.e. water vapor and carbon dioxide captured from the air will be used for production of eFuel, and exactly the same quantities of water vapor and carbon dioxide will be returned back to the air, while only energy consumed in the energy balance of the process will be green energy, which is completely unexpected result. Small nonflammable batteries supporting regenerative braking will additionally decrease eFuel consumption, especially in cities, thus decreasing local air pollution.

There is no need to set in stone a single technology for powering vehicles in the future, since combinations of at least two aforementioned technologies provide much better solutions from the point of view of pollution, efficiency, and cost of vehicles and the cost of “fuel”.

II. MINERALS FOR CLEAN ENERGY

A concerted effort to reach the goals of the Paris Agreement (climate stabilization at “well

below 2°C global temperature rise”, as in the IEA Sustainable Development Scenario [SDS]) would mean quadrupling of mineral requirements for clean energy technologies by 2040. An even faster transition, to hit net-zero globally by 2050, would require six times more mineral resources in 2040 than today [1,2].

An energy system powered by clean energy technologies very much differs from one fuelled by traditional hydrocarbon resources. Building solar photovoltaic (PV) plants, wind farms and electric vehicles (EVs) generally requires more minerals than their fossil fuel based counterparts. A typical BEV requires six times more mineral resources of ICE car, and an onshore wind plant requires nine times more mineral resources than a gas-fired power plant. Since 2010, the average amount of minerals needed for a new unit of power generation capacity has increased 50%.

The types and amounts of mineral resources used vary by used technology. Lithium, nickel, cobalt, manganese and graphite are crucial to battery performance, longevity and energy density (Fig. 1). Rare earth elements are essential for permanent magnets used in wind turbine generators and EV motors. Electricity networks nowadays need a huge amount of copper and aluminum, with copper being in higher demand, while until mid-2010s, the energy sector represented a small part of total demand for most minerals.

In a scenario that meets the Paris Agreement goals, clean energy technologies’ share of total demand rises significantly over the next two decades to over 40% for copper and rare earth elements, 60-70% for nickel and cobalt, and almost 90% for lithium. EVs and battery storage have already displaced consumer electronics to

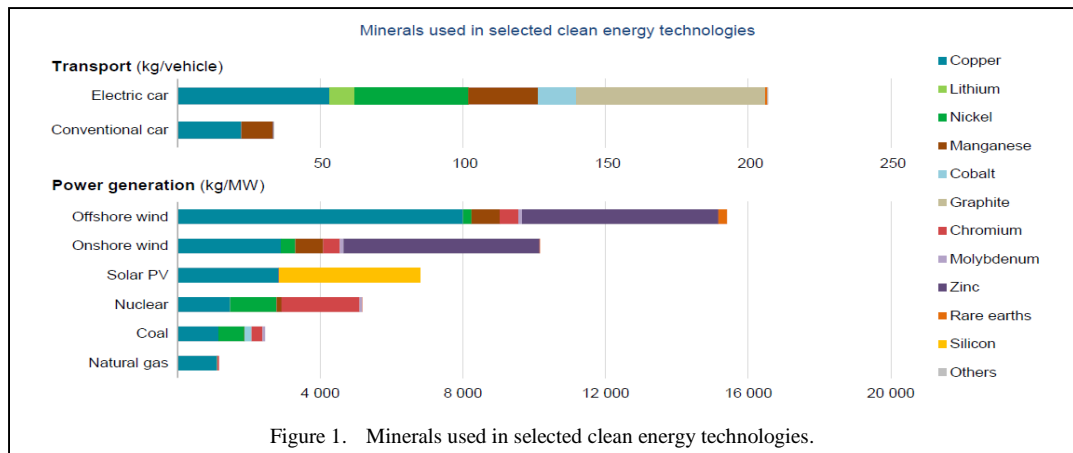


Figure 1. Minerals used in selected clean energy technologies.

become the largest consumer of lithium and are set to take over from stainless steel as the largest end user of nickel by 2040.

Mineral demand for use in EVs and battery storage is a major force, growing at least thirty times to 2040 in climate-driven scenarios. Lithium sees the fastest growth, with demand growing by over 40 times in the SDS by 2040, followed by graphite, cobalt and nickel (around 20-25 times) (Fig. 2). The expansion of electricity networks means that copper demand for power lines more than doubles over the same period.

The rise of low-carbon power generation to meet climate goals also means a tripling of mineral demand from this sector by 2040. Wind generators lead the requirements, especially material-intensive offshore wind. Solar PV follows closely, due to the sheer volume of capacity that is added. Hydropower, biomass and nuclear make only minor contributions given their comparatively low mineral requirements. In other sectors, the rapid growth of hydrogen as an energy carrier underpins major growth in demand for nickel and zirconium for electrolyzers, and for platinum-group metals for fuel cells.

Mineral requirements are subject to large technology and policy uncertainties. For example, cobalt demand could be anything from 6 to 30 times higher than today's levels

depending on assumptions about the evolution of battery chemistry and climate policies. In yet another example, rare earth elements may be required three to seven times more in 2040 than today, depending on the choice of wind turbines and the strength of policy support.

The largest source of demand variability comes from uncertainty around the stringency of climate policies. The big question for suppliers is whether the world is really heading for a scenario consistent with the Paris Agreement. Policy makers have a crucial role in narrowing this uncertainty by making clear their ambitions and turning targets into actions. This will be vital to reduce investment risks and ensure adequate flow of capital to new projects.

III. EXTENDED RANGE ELECTRIC VEHICLE

Extended Range Electric Vehicle (EREV) will consume, on average, less than half of the fuel of a Plug in Hybrid Electric Vehicle (PHEV) in the real world, if overnight charging is assumed, reducing regulated emissions by more than 70% when compared to a [3].

A configuration schemes for both EREV and FCEV are very similar. An EREV is characterized by a powertrain composed by an electric engine, a power converter and an energy storage battery pack, that compound the vehicle propulsion subsystem (Fig. 3).

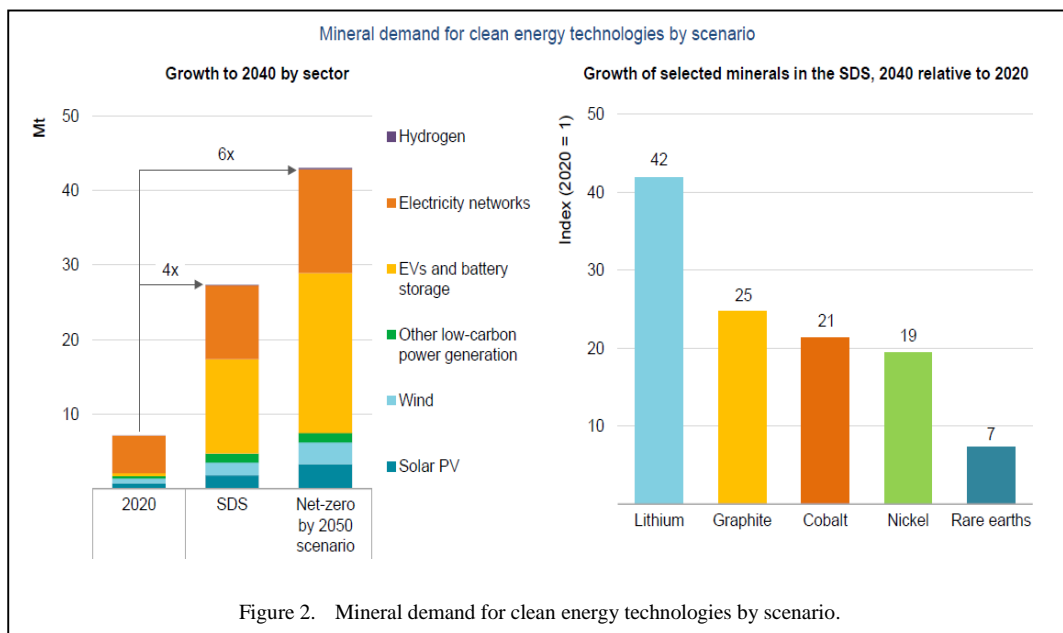


Figure 2. Mineral demand for clean energy technologies by scenario.

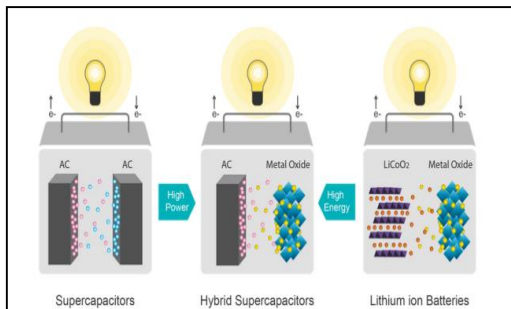


Figure 3. Hybrid supercapacitors are halfway between lithium batteries and carbon supercapacitors.

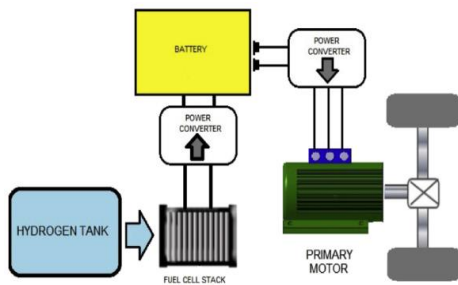


Figure 4. Schematic of an Extended Range Fuel Cell Electric Vehicle (ERFCEV).

It also has a second subsystem, Range Extender (RE), composed by an Internal Combustion Engine (ICE), a fuel tank and an electric generator. That subsystem it is exclusively used to charge the batteries [3].

Fuel Cell Electric Vehicle (FCEV) configuration is very similar to EREV. Like Battery Electric Vehicle (BEV), electricity is used to power an electric engine, but in contrast to other electric vehicles, FCEV produces its primary electricity using the fuel cell powered by hydrogen. FCEV uses the fuel cell as a generator to power what is otherwise BEV (Fig. 4). The power plant has also a small battery pack that helps the fuel cell to boost and also to recover energy during regenerative braking periods. Energy flow is controlled by a Power Electronic Distributor Unit (PDU). According to the arrows inside the box in Fig. 4, when the vehicle is in a transient of hard acceleration, the PDU distributes the power generated from the onboard fuel cell and the battery to cover the power demand. When this transient finishes, the PDU allows the energy flowing from the fuel cell stack to the primary motor through the power converter and, at the same time, the battery could be recharged. The PDU also manages the

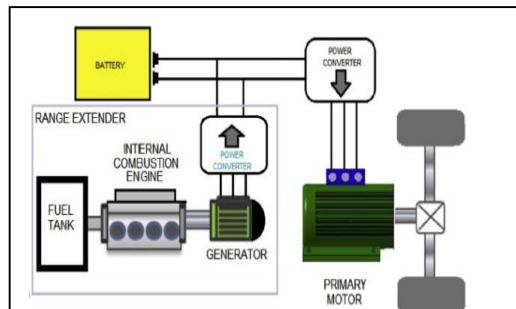


Figure 5. Schematic of an Extended Range Electric Vehicle (EREV).

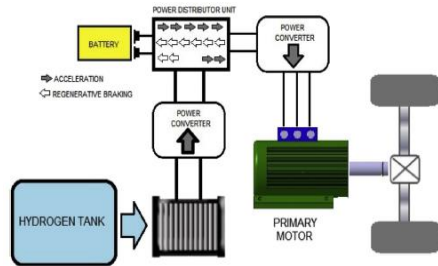


Figure 6. Schematic of a Fuel Cell Electric Vehicle (FCEV).

regenerative braking. This recovered electricity is stored in the battery.

The best batteries for either EREV or FCEV or their combination are nonflammable batteries described in [4-9] as hybrid supercapacitors with one lithium compound and the other graphene electrode (Fig. 5).

It is possible to optimize the design of EREV and FCEV by mixing: Plug-in battery, ER (Extended Range), FC (Fuel cell stack) and EV (Electric Vehicle) (Fig. 6). The aim of ERFCEV is to satisfy the customer specifications defined by today's car user profile in order to cover two specific requirements of vehicle's customers: range and refuel [3].

Onboard hydrogen storage is one of the paramount hurdles that FCEVs are trying to overcome to become competitive with the current fleet of ICE vehicles. Storage options include compressed gas, liquid hydrogen, metal hydrides and carbon nanotubes. All these options are both heavier and larger than gasoline tank counterparts, but they are being further developed to resolve that issue (Fig. 7) [10].

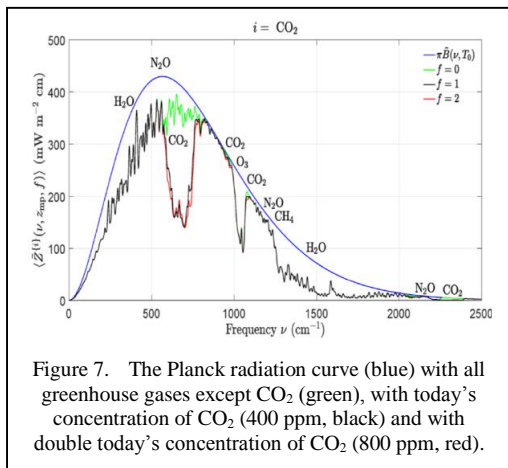


Figure 7. The Planck radiation curve (blue) with all greenhouse gases except CO₂ (green), with today's concentration of CO₂ (400 ppm, black) and with double today's concentration of CO₂ (800 ppm, red).

IV. CO₂ AND TEMPERATURES

CO₂ makes up only about 0.041% of the atmosphere. However, the physics of CO₂ in the atmosphere is complex. If there is one CO₂ molecule and radiation coming up from the Earth hits it at the right frequency, the CO₂ molecule absorbs some radiation, gets into an excited state, nearly immediately decays, reradiates, and sends some of that radiation back to the Earth. It is incorrect to simply add up the heating from many CO₂ molecules. In other words, no matter how many CO₂ molecules there are, they can never reradiate in that frequency range more than a black body would at that temperature. In other word, the radiation at that frequency can saturate.

The smooth blue curve in Fig. 8 is the black body radiation of the Earth at 287 degrees Kelvin, i.e. what the Earth would radiate back to space if the atmosphere had no effect. The greenhouse gases tend to make the actual curve

lower than the black body curve, meaning that the Earth is reabsorbing some of its radiation, heating the planet. The green curve is the radiation with all greenhouse gases except CO₂. The black curve is the radiation with 400 parts per million of CO₂, about today's concentration. The red curve is the radiation with double today's concentration of CO₂ [11].

Water vapor is also a major natural greenhouse gas, but its volatility, i.e., readily evaporating and condensing in response to temperature changes, complicates its role. Increased amount of atmospheric water vapor reinforces the heat absorption by the other greenhouse gases and forms more clouds. Clouds can provide either a positive or a negative feedback by trapping outgoing thermal radiation or reflecting back to space more solar radiation. Roughly 30% of the incoming solar radiation is reflected back to space by the clouds, aerosols, and the surface of the Earth.

There are both technologies and funds to remove all greenhouse gases from the air. However, without them Earth's average temperature would be near 0°F (or -18°C) instead of the much warmer 59°F (15°C) [12].

In 2006, 31,487 scientists, including 9,029 Ph.Ds signed a petition disputing the alarmist climate view (<http://www.petitionproject.org>). The petition was led by Fred Seitz, at that time the president of the National Academy of Science (NAS) in the US. Starting from November 15, 2023 a new organization, Clintel (<https://clintel.org/world-climate-declaration/>) has formed and has put out a similar statement. Already over 1,841 professional scientists from all over the world have signed on, confirming that CO₂ is not a pollutant, but is essential to all life on the Earth. Additional CO₂ in the air has promoted growth in global plant biomass and increase the yields of crops worldwide, thus being also profitable for agriculture. This certainly contradicts the assertion that "the science is settled" [13].

"Using theoretical arguments and statistical tests we find, that the effect of man-made CO₂ emissions does not appear to be strong enough to cause systematic changes in the temperature fluctuations during the last 200 years. Even if recent recorded temperature variations should turn out to deviate from previous variation patterns in a systematic way it is still a difficult

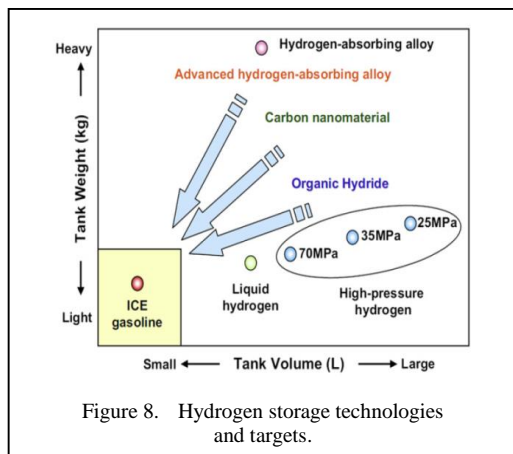


Figure 8. Hydrogen storage technologies and targets.

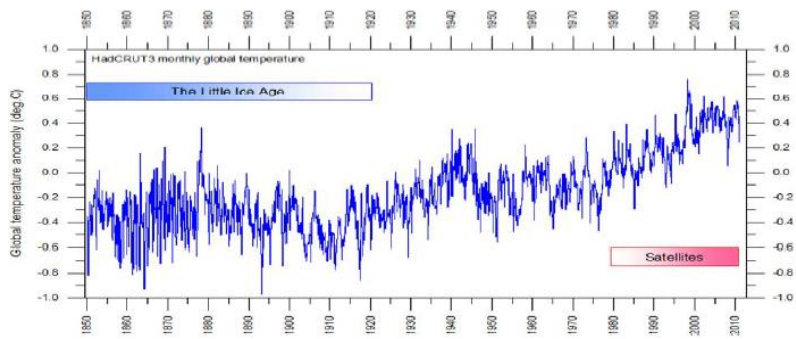


Figure 9. Global air temperatures 1850-2013.

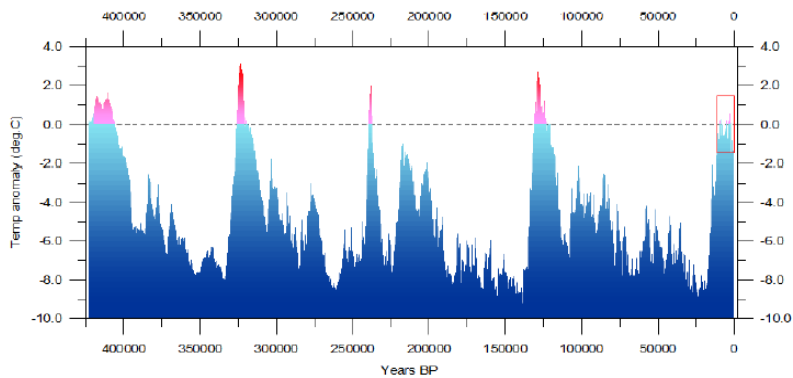


Figure 10. Reconstructed temperatures over last 420,000 year based on the Vostok ice core from the Antarctica.

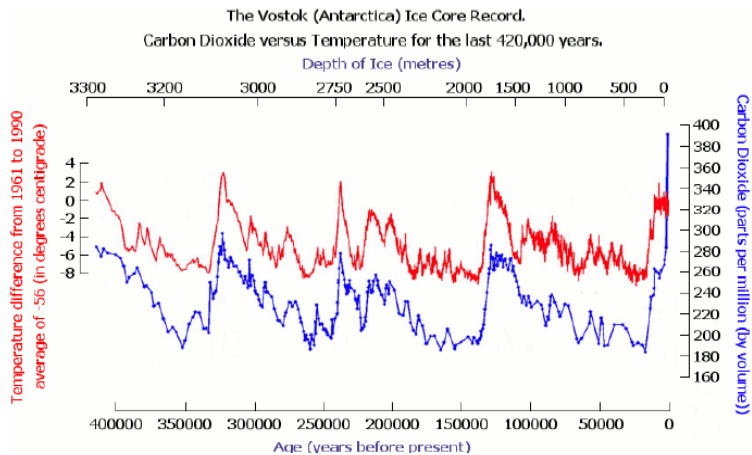
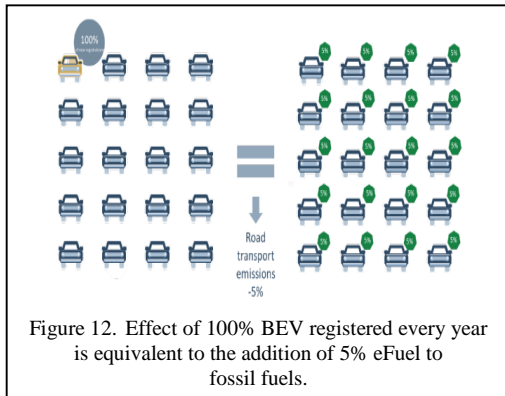


Figure 11. The Vostok (Antarctica) ice core carbon dioxide versus temperature for the last 420,000 years.

challenge to establish how much of this change is due to increasing man-made emissions of carbon dioxide (CO₂) and other greenhouse gases”. It is interesting to notice that we are coming out of fifth ice age during last 420,000 years, but lower global temperature than in previous 4 warm periods. (Fig. 9-11) [13].

In addition to that, measured CO₂ levels are trailing behind temperature increase and not leading, so they are the result and not a cause. Furthermore, if the world keeps using fossil fuel at 10 TW, as it does today, this adds about 2 ppm of CO₂ to the atmosphere per year. In other words it would take 200 years to double the CO₂



concentration and increase the temperature by a degree or two.

The biggest contributor to CO₂ levels in the atmosphere is not human activity but the release of the gas from our planet's oceans, the biggest reservoir of CO₂. Lower temperatures make CO₂ more soluble in water, so CO₂ is absorbed from the atmosphere and dissolves in oceans. Similarly, higher temperatures make CO₂ less soluble, so CO₂ is released into the atmosphere. Warmer temperatures cause more CO₂.

Over the long term, the amount of incoming solar radiation absorbed by the Earth and atmosphere is balanced by the Earth and atmosphere releasing the same amount of outgoing longwave radiation. About half of the incoming solar radiation is absorbed by the Earth's surface. This energy is transferred to the atmosphere by warming the air in contact with the surface (thermals), by evapotranspiration and by longwave radiation that is absorbed by clouds and greenhouse gases. The atmosphere in turn radiates longwave energy back to the Earth as well as out to space (Fig. 12) [14].

V. EFUEL

Liquid fuels allow consumers to achieve refuelling rates of up to 15 MW (calculated at 25 l diesel/min); as such, the refuelling process for a passenger car with an ICE takes just a few minutes [15]. An electric vehicle can achieve a charging rate of between 3.5 kW (single-phase domestic outlet) and 500 kW (ChargePoint Express Plus) depending on the vehicle's equipment (quick charge technology) and the power outlet/charging station. The ultrafast charging option at the top of this range only allows the battery to be charged to 80%. One benefit of the BEV in terms of refuelling is that vehicles can be refuelled during downtime, providing a parking space with a charging station

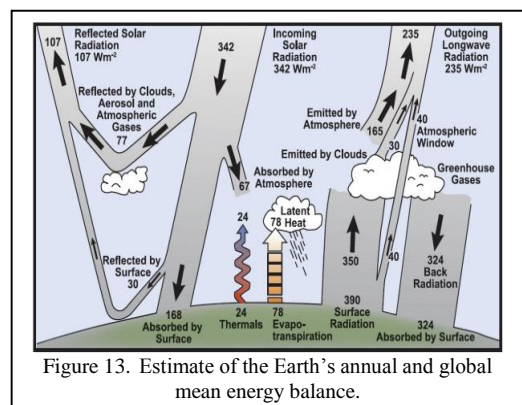
is available. Overall, the liquid energy sources have the advantage in terms of the refuelling time criterion, especially when fuel is required for long-range journeys. However, that advantage can be nullified using wireless BEV charging during driving.

To produce the most suitable and immediately usable synthetic fuels, it is necessary to make investments in conversion plants alongside the generation of electricity from renewable energies. This includes electrolyzers for the production of hydrogen, plants for the extraction of CO₂ and synthesis plants for the production of synthetic liquid fuels or methane. There are various options available as sources of CO₂: biogenic sources, the direct air capture method (the CO₂ is removed from the atmosphere) or from emissions from industrial plants that are difficult to decarbonize for the time being.

New registrations of cars in the European Union usually correspond to a volume that equates to a little more than 5% of the existing fleet. To put it simply, an average registration year of 100% BEV would reduce the emissions of the car fleet by 5% annually (Fig. 13) [16].

Fischer-Tropsch Synthesis (FTS) can be used to produce longer-chain hydrocarbons using H₂ and CO₂ as used in South Africa since 1950s to turn coal into diesel & petrol fuels and chemicals [16]. There are three main paths that could be used to provide a gas for FTS:

- Low-temperature electrolysis and CO/CO₂ extraction from concentrated sources or the ambient air
- High-temperature electrolysis and CO/CO₂ extraction from concentrated sources or the ambient air



- Biomass gasification.

A. *eFuels are Environmentally Friendly [17]*

- eFuels are climate neutral since they don't emit additional greenhouse gases.
- eFuels emit significantly less nitrogen oxide and particulate matter than conventional fuels.

B. *eFuels are Infrastructure Compatible*

- eFuels are compatible with conventional oil heating systems, ICE and turbines.
- eFuels can be distributed via existing infrastructure and be easily available.

C. *eFuels are User-Friendly and Affordable*

- No need for an expensive technologies
- eFuels can be mixed with fossil fuels (drop-in capability from 1–100%).
- eFuels can be produced for 1€/litre.

VI. CONCLUSIONS

The combination of at least 2 out of 4 technologies provides nonflammable battery powered electric vehicle supporting regenerative braking with:

- High efficiency wireless charging during driving and parking as a range extender.
- Hydrogen fuel cells as a range extender.
- An ICE with eFuel as a range extender.

ACKNOWLEDGMENT

This work was partially supported by European Institute of Innovation & Technology Urban Mobility (EIT UM) under grant no. SGA23 23351, as well as Ministry of Education, Science and Technological Development of Republic of Serbia under grant nos. TR32039 and TR32047.

REFERENCES

- [1] World Energy Outlook Special Report (2022 March). *The role of critical minerals in clean energy transitions*. International Energy Agency.
- [2] Herrington, R. (2021). Mining our green future. *Nature Reviews Materials*, 6(6), 456-458.
- [3] Fernández, R. Á., Cilleruelo, F. B., & Martínez, I. V. (2016). A new approach to battery powered electric vehicles: A hydrogen fuel-cell-based range extender system. *International Journal of Hydrogen Energy*, 41(8), 4808-4819.
- [4] Prokin, M., & Prokin, D. (2021, Dec. 16-17). Advanced electric vehicle technologies. In *eNergetics 2021 – 7th Virtual Conference on Science, Technology and Management in Energy* (pp. 325-332).
- [5] Prokin, M., & Prokin, D. (2022, Dec. 15-16). Advanced hydrogen fuel cell vehicle technologies. In *eNergetics 2022 – 8th Virtual Conference on Science, Technology and Management in Energy* (pp. 147-154).
- [6] Liu, S., Ouyang, X., & Zheng, Y. (2016, Aug. 24). Carbon back capacity battery and carbon back capacity battery group. China Patent No. 205751881.
- [7] *Batteries are dead, long live Carbon based Power Capacitors!* Available at: <https://kurt.energy/wp-content/uploads/2019/04/WHITE-PAPER-Carbon-based-power-caps.pdf>
- [8] *Hybrid carbon-based supercapacitor cell specifications*. Available at: <https://kurt.energy/wp-content/uploads/2020/01/Hybrid-C-Supercaps-Datasheet08012020.pdf>
- [9] Zheng, Y., & Zheng, D. (2017, Jul. 11). *New energy automobile charging station based on carbon back capacity battery group*. China Patent No. 206323188.
- [10] Veziroglu, A., & Macario, R. (2011). Fuel cell vehicles: State of the art with economic and environmental concerns. *International Journal of Hydrogen Energy*, 36, 25-43.
- [11] Manheimer, W. (2022). While the Climate Always Has and Always Will Change, There Is no Climate Crisis. *Journal of Sustainable Development*, 15(5).
- [12] Ma, Q. (1998 March) *Greenhouse gases: Refining the role of carbon dioxide*. Goddard Institute for Space Studies, NASA, New York, N.Y.
- [13] Dagsvik, J. K., & Moen, S. H. (2023, Sep.) *To what extent are temperature levels changing due to greenhouse gas emissions?* Statistisk sentralbyrå, Statistics Norway.
- [14] Somerville, R., Le Treut, H., Cubasch, U., Ding, Y., Mauritzen, C., Mokssit, A., ... & Prather, M. (2007). Historical overview of climate change. *Climate change*, 93-127.
- [15] Hobohm, J. et al. (2018 May) *Status and perspectives of liquid energy sources in the energy transition*. A Study by Prognos AG, the Fraunhofer Institute for Environmental, Safety and Energy Technology UMSICHT and the German Biomass Research Centre DBFZ. 161 pages.
- [16] Fritsch, M., Puls, T., Shaefer, T. (2021 March) *Synthetic fuels: potential for Europe*. Institut der Deutschen Wirtschaft, 46 pages.
- [17] eFuel Alliance information brochure. (2023). *eFuel Alliance*, Berlin/Brussels

Simulation Study of the Improvement of the Performance of the Drying Unit of the JLE-Jijel Company

Bessam Toumi¹, Mohamed Benelhaoues², Ahmed Ghaoui³

^{1,2}LMESC-Dpt of Energetics – Faculty of Mechanical and process Engineering/USTHB, Algiers, Algeria

³Department of Mechanics, Jijel University, Algiers, Algeria

¹btoumi@usthb.dz, ²mhenelhaoues@usthb.dz, ³ahmedghaoui04@gmail.com

Abstract—This work aims to enhance the operation and performance of JLE Company's cork granule drying unit by determining the optimal parameters for hot air input through simulations. Thermal balances of the unit were calculated for both actual and simulated operating scenarios, thus enabling the determination of optimal hot air flow rates based on the input temperature. The effects of input parameters, hot air, and cork granules on the convective drying process were studied using Simprosys software. A comparison of energy performance (consumption and thermal efficiency) between the real and simulated cases revealed a significant improvement, with thermal efficiency doubling (approximately 40%) for an average hot air input temperature and tripling (around 60%) for a high temperature.

Keywords - convective rotary dryer, hot air, cork in granules, results and performance, simulation, simprosys

I. INTRODUCTION

Drying is an essential process in many human activities, such as food and industrial activities, and an effective means of preserving agricultural products [1]. Most drying processes rely on rotary dryers. The latter is characterized by great effectiveness [2].

Convection thermal drying uses drying agents (transfers) which are most often superheated water vapor (VES) and hot air (AC) [3].

Jijel Liège Etanchéité (JLE) transforms raw cork into various products (expanded cork, granules...) for different uses. The transformation process includes a thermal drying operation in a hot air convective dryer.

Like any industrial process, the convective dryer of the cork company JLE is the site of significant energy losses, which generates expenses and additional costs for the production of the products of the company JLE.

The objective of this work, as part of our Master's project, is to contribute to the improvement of the thermal efficiency of the drying unit of the JLE company, by studying the influence of certain parameters (of the drying agent and the product to be dried) on the drying process, using the Simprosys simulation software.

II. WORKING PRINCIPLE OF CONTINUOUS CONVECTIVE DRYER

The dryer used in the JLE company is a rotary cylindrical dryer, operating in continuous convective co-current mode, where hot and dry air circulates continuously in contact with wet material (cork granules). The material to be dried is fed into the dryer with a controlled flow rate.

The drying process ensures a transfer of heat (thermal energy) and material (water extraction) in a steady state. In this case, the dryer is considered adiabatic (heat exchange with the

outside neglected). Diagrams of the drying unit and the working principle of the process.

A. Parameters of the Drying Operation

As an example, for studies on the drying of cork into granules, we cite the work [4] that focused on the kinetics of cork drying in granules using a process based on successive DDS expansions.

Also, this process consists of subjecting the cork material in a chamber to a cyclic variation of pressure for temperatures of 50°C, 60°C and 70°C of drying, the cork initially has 15% humidity is dried up to 5.5% humidity in 10min is up to 2% humidity in 40min. This process preserves the cork from any physical deformation [5].

The parameters characterizing the operating conditions of the JLE drying unit, the material to be dried and the drying agent are given respectively in the Tables I and II.

B. Energy Balance of a Rotary Dryer

a) Dryer mass balance

The theoretical mass balance equation for a theoretical installation is written:

$$\text{Material Quantities Received} = \text{Material Quantities Issued}$$

$$\dot{m}_a(Y_s - Y_e) = \dot{m}_m(X_s - X_e) . \quad (1)$$

b) Heat balance of the dryer

The heat balance equation for a theoretical installation is written:

$$\text{Input Energy} = \text{Output Energy}$$

$$\dot{m}_a(h_{as} - h_{ae}) = \dot{m}_m(h_{ms} - h_{me}) . \quad (2)$$

III. RESULTS AND DISCUSSION

A. Study of the Effect of the Inlet Temperature of the Drying Agent

a) Variation in the inlet flow rate of the drying agent

Fig. 1 shows the simulation result of the variation in the inlet mass flow rate of the dryer as a function of the inlet temperature of the dryer for the two material outlet temperatures. Thus, for both curves, it can be seen that the increase in the inlet temperature of hot air causes a sharp decrease in the mass flow rate up to 90°C and then becomes moderate in the rest of the curve.

This shows that convective drying at low air temperatures is more difficult where the enthalpy of the air is lower. Thus, high flow rates are increasing the speed of the drying agent in order to speed up the convective exchange. At high air temperature, the heat exchange is pushed by the high temperature guard between T_{ae} and T_{ms} .

However, the flow values for $T_{ms} = 70^\circ\text{C}$ are slightly larger. This is because part of the heat is used to heat the material at the outlet (Fig. 1).

TABLE I. PARAMETERS OF THE MATERIAL TO BE DRIED.

Type: Solid Particles	Cork granules
Initial Temperature (Inlet) T_{me}	20°C
Final Temperature (Output) T_{ms}	50°C
Average Dry Initial Moisture Content X_{se}	15%
Average final moisture content on a dry basis X_{ss}	2%
Initial Mass Flow of Wet Material G_l	1000 Kg/h
Initial Temperature (Inlet) T_{ae}	150°C
Final Temperature (Output) T_{as}	60°C
Initial Absolute Humidity r_s	0.009 Kg/Kg d'air sec
Initial Volume Flow \dot{m}_v	9000 m ³ /h
Conductivité thermique λ_a	0.026 W/m·K
Dynamic Viscosity μ_a	18.5×10^{-6} Pa s
Density ρ_a	1.205 Kg/m

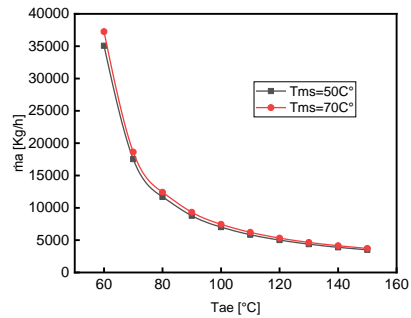


Figure 1. Variation in the mass flow rate of the inlet drying agent as function of its inlet temperature (turbulent regime).

From these two curves, the three phases of drying can be distinguished:

- Medium Temperature Drying (SMT): $70^{\circ}\text{C} < T_{ae} < 82^{\circ}\text{C}$, which requires high air flow, $\dot{m}_a > 14000 \text{ Kg/h}$
- High Temperature Drying (STE): $82^{\circ}\text{C} < T_{ae} < 100^{\circ}\text{C}$, with medium air flow, $14000 \text{ Kg/h} >> 7900 \text{ Kg/h}$
- High Temperature Drying (SHT): $100^{\circ}\text{C} < T_{ae} < 150^{\circ}\text{C}$, where the air flow is low, $< 7900 \text{ Kg/h}$

Also, by comparing the actual and optimal parameters obtained by simulating the drying agent, an optimal air inlet temperature T_{ae} of the order of 90°C is sufficient for the actual air flow at the dryer inlet. This indicates the existence of heat losses in the dryer due to the difference between the actual and optimal temperature.

b) Variation of dryer performance quantities

Fig. 2 illustrates the evolution of specific heat consumption and thermal efficiency as a function of the T_{ae} inlet temperature. The curves show a decrease in the specific heat consumption with the increase in T_{ae} and thus the enthalpy of the drying agent. For temperatures below 100°C , the consumption is very high where part of the heat is served to heat the water to reach its vaporization. As far as efficiency is concerned, it increases with the temperature and therefore with the heat made available for the drying operation.

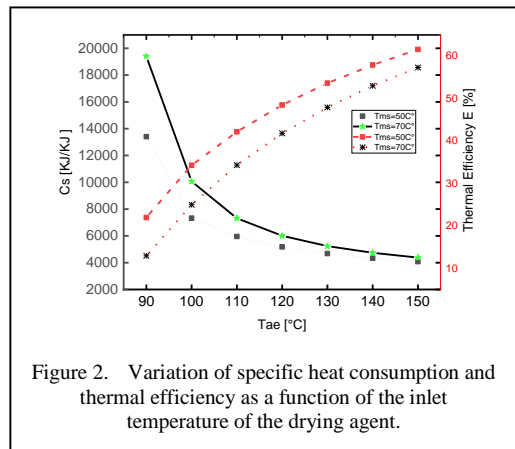


Figure 2. Variation of specific heat consumption and thermal efficiency as a function of the inlet temperature of the drying agent.

B. Determination of the Characteristic Quantities of the Heat Balance

The different values of the characteristic quantities of the drying, i.e. QC, EMC, RCE and η_Q , calculated for optimum parameters of the drying agent (T_{ae} and \dot{m}_a) and for the two cases of material outlet temperatures, are grouped together in Table II.

Note that the best values of the performance quantities are those for $T_{ae} = 150^{\circ}\text{C}$. Indeed, for $T_{ms} = 50^{\circ}\text{C}$, the η_Q is very high (65%) for $T_{ae} = 150^{\circ}\text{C}$, compared to that of $T_{ae} = 90^{\circ}\text{C}$ equal to (40%).

If we compare the values of the performance quantities for the two T_{ms} , they are of the same order, but slightly better for $T_{ms} = 50^{\circ}\text{C}$, which indicates that the optimal process is closer to this case of $T_{ms} = 50^{\circ}\text{C}$.

TABLE II. OPTIMUM HEAT BALANCE CHARACTERISTICS.

Parameters Heat balance	Materials	$T_{ms}=50^{\circ}\text{C}$	Materials	$T_{ms}=70^{\circ}\text{C}$
	$T_{ae}=150^{\circ}\text{C}$ $\dot{m}_a=3500\text{Kg/h}$	$T_{ae}=90^{\circ}\text{C}$ $\dot{m}_a=10500 \text{ Kg/h}$	$T_{ae}=150^{\circ}\text{C}$ $\dot{m}_a=3750 \text{ Kg/h}$	$T_{ae}=90^{\circ}\text{C}$ $\dot{m}_a=11300 \text{ Kg/h}$
Q_C (MJ/h)	457.29	738.69	489.95	794.98
CEM (KJ/Kg d'eau)	3447.2	5568.6	3693.5	5992.9
RCE (Kg vapeur/Kg d'eau)	1.38	2.23	1.48	2.40
η_Q (%)	65.44	40.51	61.07	37.64

For the values of (EMC and RCE), they belong to the performance range ranges of this type of dryer, which confirms the correct choice of the optimal parameters of the drying agent. Bearing in mind that these intervals are: for EMF [3300 to 6500] KJ/Kg of water and for ECR [1.1 to 1.5] Kg of water/Kg of water.

IV. CONCLUSION

The present work is a contribution to the improvement of the energy performance of the cork pellet drying unit of the company Jijel Liège Etanchéité. Indeed, we calculated the heat balance of the convective drying unit and its energy performance parameters, which highlighted the low energy efficiency (about 21%), and therefore the consumption and significant losses present (RCE = 4.28 Kg steam/Kg water).

To improve this performance, we studied, by simulation, the effects of the inlet temperatures of the drying agent and the wet product as well as the humidity of the latter on the drying process, following the variation of certain parameters and characteristics of the drying agent and the product to be dried. Optimum flow rates of the inlet drying agent are obtained as a function of the drying agent temperatures

The effect of the inlet temperature of the drying agent is significant compared to that of the inlet temperature of the product and its moisture content.

The different energy consumption and drying performance parameters achieved under optimal

conditions are significantly better than those of the JLE drying unit. Thus, the thermal efficiency is doubled (~40%) for a T_{ae} temperature = 90°C and tripled (~60%) for a T_{ae} temperature = 150°C.

The calculation of the characteristics of the dryer (RCE and EMC) showed very satisfactory values for the simulated cases and belong to the range of quantities of this type of dryer, unlike those obtained for the actual operation of the drying unit. A considerable improvement in energy performance is achieved with the optimal parameters, which has a positive impact on the drying operation and on the cork processing process.

REFERENCES

- [1] Delelea, M. A., Weiglera, F., & Mellmann, J. (2014). Advances in the Application of Rotary Dryer for Drying of Agricultural Products: A Review. *Drying technology*, 33(5), 541-558.
- [2] Chhabra, R. P. (2017). *CRC Handbook of Thermal Engineering Second Edition*.
- [3] Li, N., Freitas, D. S., Santos, J., Venâncio, A., Noro, J., Su, J., Wang, H., Silva, C., & Cavaco-Paulo, A. (2023). Laccase-Catalyzed Synthesis of Added-Value Polymers from Cork and Grape Extracts. *Journal of Agricultural and Food Chemistry*.
- [4] Abdulla G., Mellok, H., Belghit, A-E. & Allaf, K. (2009). Séchage des produits granulaires par déshydratation par détentes successives (DDS) : Comparaison avec le séchage à air chaud.
- [5] Abdulla, G , Belghit, A-E. & Allaf, K . (2010). Impact of the Instant Controlled Pressure Drop Treatment on Hot Air Drying of Cork Granules (pp 180-185).

Preparation and Characterization of Biochar from Pineapple and Sugarcane Solid Wastes

Sidney de Souza Plácido Júnior¹, Maxwell de Arandas Pimentel²,
Silvia Layara Floriani Andersen³

^{1,2}Postgraduate Program in Renewable Energy - UFPB, João Pessoa - PB, Brazil

³Departament of Renewable Energy Engineering - UFPB, João Pessoa - PB, Brazil

¹sidney.junior@estudante.cear.ufpb.br

Abstract—The growing in energy demand driven by industrial sectors and the increasing of global population has sparked interest in developing new alternatives for energy generation and product conversion. The agroindustrial food production chain presents an environmental problem in the form of excessive agricultural solid waste generation. An environmental mitigation action involves the reuse of these organic materials through pyrolytic processes to produce valuable products like biochar, characterized as a carbonaceous compound with a porous structure. Biochar has numerous promising applications, such as enhancing soil fertilization, carbon sequestration, applied as feedstock for energy production and water filtration. The present paper aims to prepare biochar from solid wastes (pineapple peel and sugarcane bagasse), with the purpose of analyzing the biochar characteristics and verify the potential uses for them. Biochar preparation involved different pyrolysis time for both wastes, (60 and 120 minutes). Higher Heating Value (HHV), Thermogravimetric analysis (TGA) and Fourier-transform infrared spectroscopy (FTIR) were performed. TGA revealed distinct mass loss patterns, indicating the removal of moisture, volatile compounds, and subsequent decomposition of hemicellulose, cellulose, and lignin. Particle size played a crucial role in the thermochemical conversion process due to mass transfer limitations. HHV showed that PP had a higher HHV than SCB, both in raw form and as biochar, making them viable energy sources. FTIR confirmed the presence of characteristic functional groups in biochars, providing insights into their chemical composition. Furthermore, the analyses demonstrated that the biochar exhibits better thermal stability than untreated wastes,

justifying its potential for energy-related applications.

Keywords – biomass, pyrolysis, TGA

I. INTRODUCTION

The growth of the global population and industrial activities has led to a significant increase in the demand for energy. This demand is primarily fulfilled through the utilization of fossil fuels like coal, oil, and natural gas, leading to an increase in atmospheric CO₂ levels. [1].

To reduce dependence on fossil fuels, there is a growing interest in exploring new resources and technologies. In this context, biomass has emerged as a promising alternative due to its abundance and global distribution, making it a carbon-neutral source [2]. The application of biomass and its conversion technologies has gained significant attention due to its potential to convert resources into valuable products through thermochemical, biochemical, and catalytic processes [3].

Among thermochemical processes, pyrolysis stands out for allowing the degradation of biomass in a non-oxidizing atmosphere while minimizing emissions such as NO_x and SO_x [4]. Depending on the temperature conditions, the pyrolysis process is divided into three main types: fast pyrolysis (short period, temperature above 500°C), slow pyrolysis (long period, temperature below 300°C), and moderate pyrolysis (medium time, temperature between 300 and 500°C) [5].

According to [6], fast pyrolysis allows the highest bio-oil yield, serving as raw material for liquid fuels and high-value chemicals, while slow pyrolysis is focused on biochar production. Biochar is defined as an organic material in solid phase with porous characteristics, rich in carbon and obtained through thermochemical processes such as pyrolysis and torrefaction, in the absence of O₂ [5].

Food industries generate a substantial amount of waste, and these residues, referred to as agricultural solid waste, exist in the form of plant materials and organic matter remaining or discarded during cultivation, harvesting, or food processing activities [7].

With the growth of cities and industrial expansion, the availability of land for agricultural production worldwide is decreasing. This decline results in soil fertility reduction and erosion, caused by monoculture practices. In addition to these factors, the intensive use of agrochemicals, such as fertilizers, herbicides, and pesticides, to sustain high levels of productivity, interferes in soil quality [8]. Biochar enhances phytoremediation by fostering a higher microbial population, which effectively breaks down hydrocarbons in contaminated soil [9].

Responsible for contributing annually to the global economy with US \$9 billion, pineapple is a fruit of the *Ananas* genus, cultivated in tropical and subtropical climates [10]. Brazil is the world's largest pineapple producer, with an average annual production of 2.2 million tons, followed by India, Thailand, and Indonesia. It is estimated that by the year 2030, global production will reach an average of 37 million tons annually [11]. Pineapple residues consist of the peel (29-42%), core (9.4-20%), and crown (2.7-5.9%). These waste materials present a challenge for industries due to the expenses associated with their proper disposal. In most developing countries, the residues are buried or burned, causing environmental impacts and wasting the high functional and nutritional value present in this material [12].

Sugarcane is another example of a widely cultivated crop, with a global production exceeding 1.5 billion tons [13]. It is a grass species of the *Saccharum* genus and grows in tropical and subtropical countries [14]. Sugarcane bagasse refers to the fibrous residue left after the extraction of juice for sugar and ethanol production, primarily composed of

cellulose, hemicellulose, lignin, and other minor components. Its average global annual production is estimated to be around 700 million tons [13,15]. Between 2021 and 2022, Brazil produced 585.2 million tons of sugarcane and approximately 16.4 million tons of bagasse [16].

One alternative to mitigate the issues caused by food industry waste and declining fertility in agricultural soils could be the application of biochar in affected areas.

Biochar has a wide range of applications and can be employed as bioadsorbents for the treatment of drinking water and industrial effluents, composting agents, food packaging, carbon electrodes in energy storage supercapacitors, among others [17].

Enhancing soil quality can be achieved by employing natural or organic fertilizers to mitigate negative effects. Biochar emerges as a valuable resource for enhancing soil quality in agricultural fields due to its highly porous structure, enabling it to retain water and nutrients within the soil. This helps prevent nutrient leaching and water runoff, ensuring a consistent supply of essential nutrients for crops. Additionally, the use of biochar has the potential to boost soil fertility and improve nutrient availability [18], such as potassium and sodium, which can be absorbed during plant growth and are essential for various physiological processes [19].

As demonstrated by [20], biochar can be used in the remediation of environmental issues such as global warming, soil infertility, and pollution. This information is supported by [21], which analyzed the effects of increased biochar application rates on water and nutrient retention in soil on an experimental farm in the southwest of the United States. The study found that high rates of biochar application have the potential to improve water and phosphate retention while reducing N₂O emissions in agricultural soils in the desert.

Therefore, the objective of the present paper is to prepare biochar from pineapple peel and sugarcane bagasse, in order to characterize and identify potential applications.

II. METHODS

A. Preparation of Samples

For the present study, two agroindustrial residues were selected: sugarcane bagasse

(SCB) and pineapple peel (PP). PP was obtained from local sellers in the city of João Pessoa, located in the state of Paraíba, Brazil. SCB was acquired through sugarcane processing plant at a local sugarcane mill in the city of Cruz do Espírito Santo, in the state of Paraíba, Brazil.

As a preliminary treatment, both residues were dried in a forced air circulating oven at 105°C for 24 hours, then ground in a knife mill and sieved using mesh sizes of 20 and 100.

The biochar production was conducted in a muffle furnace, with a constant heating rate of 15°C·min⁻¹ and an isotherm at 400°C, one sample for 60 and other for 120 minutes for each biomass.

B. Characterizations

Thermogravimetric analyses (TGA) of the samples (in natura and biochar) were conducted using a TA equipment, model SDT650. TGA analyses were performed using 10 mg, from room temperature to 1000°C under an inert N₂ atmosphere (purity of 99.99%), with a heating rate of 10°C·min⁻¹.

To determine the higher heating value (HHV), an IKA C200 calorimetric bomb was used, following the ASTM D5865M-19 standard.

Fourier Transform Infrared Spectroscopy (FTIR) was performed for biochar samples, using a Shimadzu IR Prestige-21 spectrophotometer, in the range of 4000-400cm⁻¹.

III. RESULTS AND DISCUSSIONS

A. Thermogravimetric Analyses

Thermogravimetric analysis was conducted to observe the thermal behavior of raw samples and their respective biochar. The results are shown in Fig. 1.

Through Fig. 1(a) and Fig. 1(b), it is possible to observe the TG and DTG curves for mesh 20 and mesh 100 pineapple peel and sugarcane bagasse, respectively. It can be observed that the first mass loss, 0.25%·min⁻¹ and 0.79%·min⁻¹ for PP, 0.43%·min⁻¹ and 0.99%·min⁻¹ for SCB, occurs at temperatures below 120°C, which can be attributed to the removal of moisture and light volatile compounds [22]. The removal of moisture content is important because it can decrease the biochar yield by enhancing the transformation of solid carbon into gaseous carbon during the pyrolysis process [23]. During

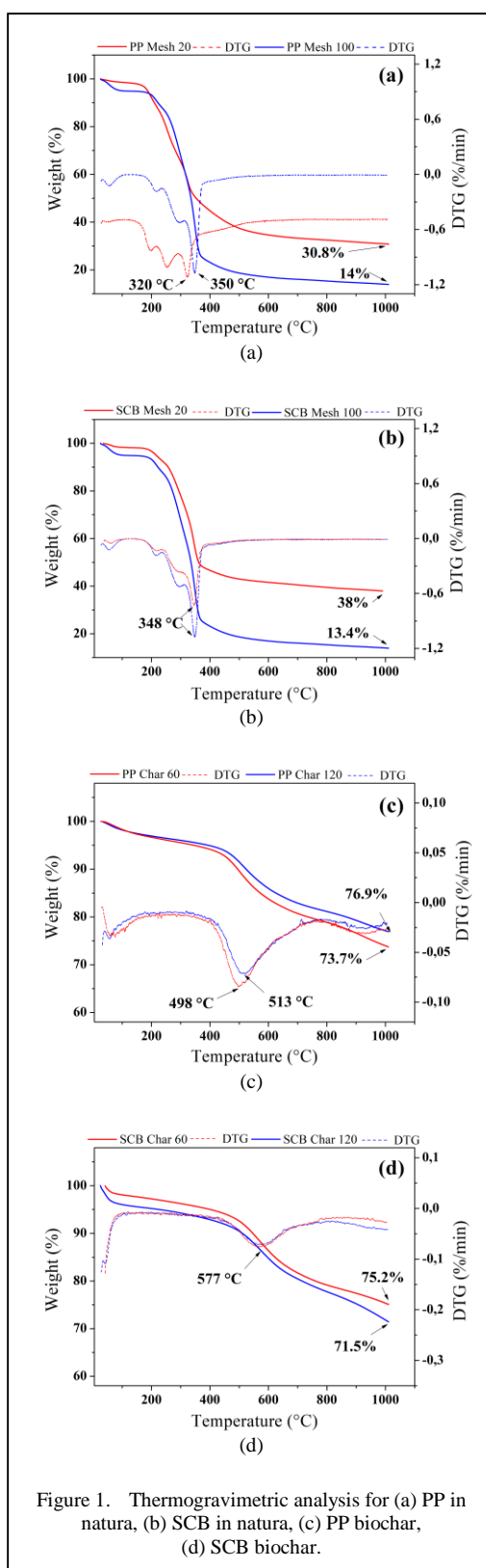


Figure 1. Thermogravimetric analysis for (a) PP in natura, (b) SCB in natura, (c) PP biochar, (d) SCB biochar.

pyrolysis, chemical components decompose, releasing volatile liquid and gaseous fractions, and leaving behind a solid aromatic carbon compound, promoting the creation of biochar [24]. Subsequent mass losses occur at temperatures between 190 and 400°C, with a maximum loss rate of 4.28%·min⁻¹ at 320°C and 4.01%·min⁻¹ at 350°C for PP, 6.54%·min⁻¹ and 9.72%·min⁻¹ at 348°C for SCB. This fact occurs due to the degradation of hemicellulose and cellulose [25]. Finally, at temperatures above 400°C, the residual lignin decomposes, which started degrading around 250°C, along with biomass carbonization [22,25]. The degradation of cellulose and lignin is important because biomass rich in cellulose produces porous graphite biochar, whereas biomass rich in lignin yields fixed carbon-rich biochar with a high specific surface area, forming fine aromatic biochar [26].

Fig. 1(c) and Fig. 1(d) correspond to the biochar TGA analyses. A mass loss of 0.35%·min⁻¹ and 0.30%·min⁻¹ for PP; 1.83%·min⁻¹ and 1.02%·min⁻¹ for SCB can be observed at temperatures below 200 °C, related to the moisture content of the sample [27]. Additionally, at temperatures ranging from 400 to 600°C, there is a mass loss of 0.76%·min⁻¹ and 0.65%·min⁻¹ for PP; 0.69%·min⁻¹ and 0.64%·min⁻¹ for SCB. According to [27], this loss is attributed to the decomposition of organic material present in the biochar. In total, there were mass losses in the PP biochar at 60 and 120 minutes, respectively, of 26.3% and 23.1%. As for the SCB biochar, there were losses of 24.8% and 28.5%.

The shape and size of biomass particles affect the surface area for heat and mass transfer. Therefore, raw materials with different shapes and sizes can have different conversion efficiencies [28]. As seen in Fig. 1(a) and Fig. 1(b), particle size played a crucial role in the thermochemical conversion process. Thus, biomass with a large particle size, had a less mass loss compared to the small particle size biomass under the same conditions, due to mass transfer limitation [29].

B. Higher Heating Value (HHV)

HHV can be described as the heat released when one unit of fuel mass is burned completely. Therefore, a fuel with high HHV will produce higher energy output [30].

TABLE I. HIGHER HEATING VALUE.

Biomass	HHV (MJ·kg ⁻¹)
PP in natura	19.23
SCB in natura	18.71
PP Biochar 60	28.32
PP Biochar 120	29.09
SCB Biochar 60	25.68
SCB Biochar 120	26.72

Table I shows the results for the HHV of all analyzed samples.

Comparing the raw biomass materials, it can be observed that the HHV of PP is higher than that of SCB. This fact can be confirmed by [31,32], who found HHV values for PP and SCB to be 21.44% and 18.29%, respectively. Such difference occurs due to the chemical composition of the biomasses, as well as the climate and soil conditions [28].

From Table I, it is also possible to compare the values between the raw biomasses and their respective biochars. Therefore, it can be observed that the HHV values underwent a change after the pyrolysis process. The HHV for PP was increased from 19.23MJ·kg⁻¹ to 28.32MJ·kg⁻¹ after 60 minutes and to 29.09MJ·kg⁻¹ after 120 minutes. Similarly, SCB had its HHV altered, increasing from 18.71MJ·kg⁻¹ to 25.68MJ·kg⁻¹ after 60 minutes and to 26.72MJ·kg⁻¹ after 120 minutes.

This increase occurs due to the removal of volatile components, such as water and low molecular weight organic compounds, through the pyrolysis process, leaving only the biochar [33]. As a result, the biochar has a higher carbon concentration and fewer impurities, increasing HHV [33]. Since the ranges of HHV for coal are between 25 and 35MJ·kg⁻¹, and the biochars in this study have values within this range, they can be considered viable options for use as energy sources [34].

C. Fourier Transform Infrared Spectroscopy

FTIR analyses were conducted to identify relevant information about the chemical composition of biochars, observing the interaction between substances and electromagnetic radiation in the infrared range [35].

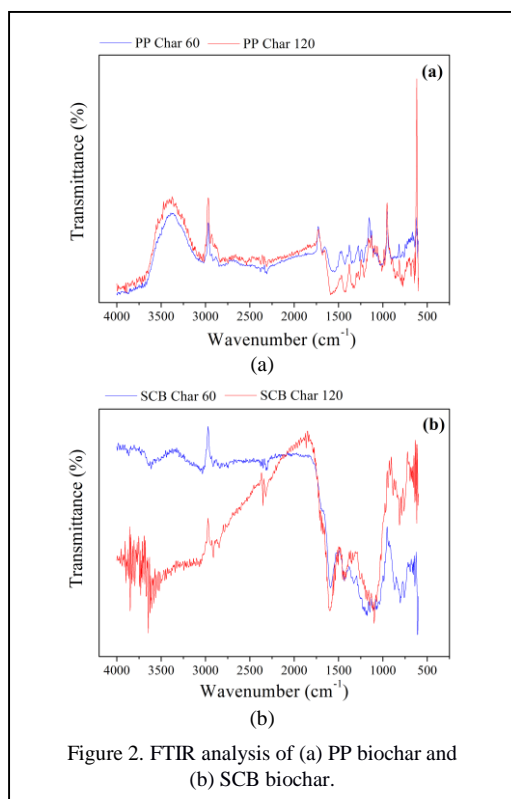


Figure 2. FTIR analysis of (a) PP biochar and (b) SCB biochar.

Fig. 2(a) displays the FTIR analysis for PP. It shows a peak in the range between 3500 and 3000 cm^{-1} in both samples. This peak corresponds to the O-H stretching vibrations of water, hemicellulose, cellulose, and lignin [35]. Another peak is observed near 3000 cm^{-1} , corresponding to the C-H vibrations of polysaccharides and lignin [36]. At approximately 2300 cm^{-1} , there is another peak due to the occurrence of C-O bonds [37]. Between 1750 and 1600 cm^{-1} , two peaks are visible, related to the stretching of unconjugated carbonyl and carbonyl conjugated with an aromatic ring, respectively [38]. The region below 1500 cm^{-1} contains multiple peaks, attributed to the asymmetric deformation of C-H in methoxyl (1420 cm^{-1}), C-H deformation in hemicellulose and cellulose (1350 cm^{-1}), CH_2 wagging in crystalline cellulose (1100 cm^{-1}), and amorphous cellulose (900 cm^{-1}) [28,36].

Fig. 2(b) represents the FTIR analysis for SCB biochar. Similar to Fig. 2(a), the peak between 3500 and 3000 cm^{-1} corresponds to the C-H vibrations of polysaccharides and lignin [36]. Between 2900 and 2800 cm^{-1} , due to the C-H bond vibration, corresponding to polysaccharides and lignin [38]. A peak between

1642 and 1600 cm^{-1} occurs due to the C-C bond vibrations, corresponding to lignin [39]. Similar to PP, the major concentration of peaks occurs in the region below 1500 cm^{-1} and is primarily related to the deformation vibration of the C-H bond corresponding to polysaccharides and lignin (1400 cm^{-1}); vibration of C-O-C ester bonds corresponding to polysaccharides (1250 cm^{-1}); due to the vibration of C-O-C bonds corresponding to polysaccharides (1160 cm^{-1}); due to the vibration of the C-OH bond corresponding to polysaccharides and lignin (1050 cm^{-1}); and between 830 and 873 cm^{-1} , due to the vibration of the C-H bond corresponding to polysaccharides and lignin [39].

This paper is a preliminary assessment, and further studies are needed for a deeper understanding and application of biochar derived from PP and SCB. These include assessing the morphological structure of the produced biochar, analyzing the behavior of biochar at different heating rates, and evaluating the chemical composition of the produced biochar.

IV. CONCLUSION

This piece of work evaluates the potential of producing biochar from pineapple peel and sugarcane bagasse using pyrolysis processes.

The study aimed to analyze the pyrolysis process and explore the possible applications of the biochars. Thermogravimetric analyses illustrated the thermal behavior of the raw samples and their respective biochar, indicating that the initial decrease below 120 $^{\circ}\text{C}$ was due to moisture and volatile compound evaporation, followed by subsequent losses between 190 and 400 $^{\circ}\text{C}$ attributed to hemicellulose and cellulose degradation. Lignin decomposition occurred above 400 $^{\circ}\text{C}$, aligning with biomass carbonization. For the biochar TGA, it was possible to observe a small amount of mass loss, varying between 23 and 29%. Furthermore, biomass with larger particles sizes had different mass loss due to limitations in mass transfer.

The biochar exhibited better thermal stability than untreated wastes, making it suitable for energy-related applications. The biochar also had higher HHV than the raw materials, indicating their potential as energy sources. The comparison of raw biomass materials revealed that PP has a higher HHV than SCB. Furthermore, the pyrolysis process led to a significant increase in HHV values for both PP

and SCB. Consequently, the biochars produced, with HHV values within the coal range of 25 to 35MJ·kg⁻¹, demonstrate their potential as viable energy sources.

Additionally, Fourier transform infrared spectroscopy offered insights into the biochar's chemical composition, revealing the presence of functional groups like O-H, C-H and C-O bonds.

In conclusion, this research suggests that biochar derived from pineapple peel and sugarcane bagasse holds promise for various applications, including combustion and environmental remediation. The use of agricultural waste for biochar production contributes to a circular bioeconomy, offering a sustainable solution for waste management.

ACKNOWLEDGMENT

This work was funded by Public Call n. 03 Produtividade em Pesquisa PROPESQ/PRPG/UFPB/PVK-13605-2020.

REFERENCES

- [1] Ighalo, J. O. et al. (2023). Biochar from coconut residues: An overview of production, properties, and applications. *Industrial Crops and Products*, 204, 117300.
- [2] de Almeida, S. G. C., Tarelho, L. A. C., Hauschild, T., Costa, M. A. M., & Dussán, K. J. (2022). Biochar production from sugarcane biomass using slow pyrolysis: Characterization of the solid fraction. *Chemical Engineering and Processing - Process Intensification*, 179.
- [3] Yaman, E., & Özbay, N. (2023). Effect of different pre-treatment techniques on thermogravimetric characteristics and kinetics of lignocellulosic biomass pyrolysis. *Journal of the Energy Institute*, 111.
- [4] Tan, S. et al. (2023). Utilization of current pyrolysis technology to convert biomass and manure waste into biochar for soil remediation: A review. *Science of the Total Environment*, 864, 160990.
- [5] Ghodake, G. S. et al. (2021). Review on biomass feedstocks, pyrolysis mechanism and physicochemical properties of biochar: State-of-the-art framework to speed up vision of circular bioeconomy. *Journal of Cleaner Production*, 297, 126645.
- [6] Zhang, H. et al. (2023). Biomass directional pyrolysis based on element economy to produce high-quality fuels, chemicals, carbon materials – A review. *Biotechnology Advances*, 69, 108262–108262.
- [7] Potnuri, R. et al. (2023). A review on analysis of biochar produced from microwave-assisted pyrolysis of agricultural waste biomass. *Journal of Analytical and Applied Pyrolysis*, 173.
- [8] Mng'ong'o, M. E., Ojija, F., & Aloo, B. N. (2023). The role of Rhizobia toward food production, food and soil security through microbial agro-input utilization in developing countries. *Case Studies in Chemical and Environmental Engineering*, 8.
- [9] Van Nguyen, T. T. et al. (2022). Valorization of agriculture waste biomass as biochar: As first-rate biosorbent for remediation of contaminated soil. *Chemosphere*, 307.
- [10] Nath, P. C. et al. (2023). Recent advances in valorization of pineapple (Ananas comosus) processing waste by-products: A step towards circular bioeconomy. *Trends in Food Science & Technology*.
- [11] Tran, T. V. et al. (2023). A critical review on pineapple (Ananas comosus) wastes for water treatment, challenges and future prospects towards circular economy. *Science of the Total Environment*, 856, 158817.
- [12] Paz-Arteaga, S. L. et al. (2023). Bioprocessing of pineapple waste for sustainable production of bioactive compounds using solid-state fermentation. *Innovative Food Science and Emerging Technologies*, 85.
- [13] Singh Rawat, S., & Sharma, A. (2023). Sugarcane bagasse ash—The future composite material: A literature review. *Materials Today: Proceedings*.
- [14] Wani, A. K., Rahayu, F., Fauziah, L., & Suhara, C. (2023). Advances in safe processing of sugarcane and bagasse for the generation of biofuels and bioactive compounds. *Journal of Agriculture and Food Research*, 12.
- [15] Iwuozor, K. O. et al. (2022). A Review on the thermochemical conversion of sugarcane bagasse into biochar. *Cleaner Materials*, 6, 100162.
- [16] Fioranelli, A., & Bizzo, W. A. (2023). Generation of surplus electricity in sugarcane mills from sugarcane bagasse and straw: Challenges, failures and opportunities. *Renewable and Sustainable Energy Reviews*, 186, 113647.
- [17] Mishra, R. K., & Mohanty, K. (2023). A review of the next-generation biochar production from waste biomass for material applications. *Science of the Total Environment*, 167171–167171.
- [18] He, X., Yang, Y., Huang, B., Wang, Z., & Wang, M. (2023). An overview of characteristic factors of biochar as a soil improvement tool in rice growth- A review. *Environmental Research*, 117794.
- [19] Lyra, G. P., Borrachero, M. V., Soriano, L., Payá, J., & Rossignolo, J. A. (2021). Comparison of original and washed pure sugar cane bagasse ashes as supplementary cementing materials. *Construction and Building Materials*, 272.
- [20] Singh, P. et al. (2023). A review on biochar composites for soil remediation applications: Comprehensive solution to contemporary challenges. *Journal of Environmental Chemical Engineering*, 11(5), 110635–110635.
- [21] Høglund, S. R., Rathke, S. J., Fidel, R. B., & Blankinship, J. C. (2023). Contrasting effects of biochar application rate in an alkaline desert cropland soil. *Journal of Arid Environments*, 215.
- [22] Escalante, J. et al. (2022). Pyrolysis of lignocellulosic, algal, plastic, and other biomass wastes for biofuel production and circular bioeconomy: A review of thermogravimetric analysis (TGA) approach. *Renewable and Sustainable Energy Reviews*, 169.
- [23] Wang, N., Chen, Q., Zhang, C., Dong, Z., & Xu, Q. (2022). Improvement in the physicochemical characteristics of biochar derived from solid digestate

- of food waste with different moisture contents. *Science of the Total Environment*, 819, 153100.
- [24] Boraah, N., Chakma, S., & Kaushal, P. (2023). Optimum features of wood-based biochars: A characterization study. *Journal of Environmental Chemical Engineering*, 11(3), 109976–109976.
- [25] Santos, V. O. et al. (2020). Pyrolysis of acai seed biomass: Kinetics and thermodynamic parameters using thermogravimetric analysis. *Bioresource Technology Reports*, 12.
- [26] Sahoo, S. S., Vijay, V. K., Chandra, R., & Kumar, H. (2021). Production and characterization of biochar produced from slow pyrolysis of pigeon pea stalk and bamboo. *Cleaner Engineering and Technology*, 3, 100101.
- [27] Stylianou, M. et al. (2023). Tomato waste biochar in the framework of circular economy. *Science of the Total Environment*, 871.
- [28] Cai, J. et al. (2017). Review of physicochemical properties and analytical characterization of lignocellulosic biomass. *Renewable and Sustainable Energy Reviews*, 76, 309–322.
- [29] Consuegra, A. S. A. (2013). Kinetics of gasification of orange magass and wood sawing with CO₂. [Thesis, Federal University of Santa Catarina]. RIUFSC – Internal Repository of Federal University of Santa Catarina. <http://repositorio.ufsc.br/handle/123456789/103529> - In portuguese.
- [30] Veza, I. et al. (2022). Improved prediction accuracy of biomass heating value using proximate analysis with various ANN training algorithms. *Results in Engineering*, 16, 100688.
- [31] Azaare, L., Commeh, M. K., Smith, A. M., & Kemausuor, F. (2021). Co-hydrothermal carbonization of pineapple and watermelon peels: Effects of process parameters on hydrochar yield and energy content. *Bioresource Technology Reports*, 15, 100720.
- [32] Costa, M. A. M., Schiavon, N. C. B., Felizardo, M. P., Souza, A. J. D., & Dussán, K. J. (2023). Emission analysis of sugarcane bagasse combustion in a burner pilot. *Sustainable Chemistry and Pharmacy*, 32, 101028.
- [33] Onyenwoke, C., Tabil, L. G., Mupondwa, E., Cree, D., & Adapa, P. (2023). Effect of Torrefaction on the Physicochemical Properties of White Spruce Sawdust for Biofuel Production. *Fuels*, 4(1), 111–131.
- [34] Mohit, A., & Remya, N. (2023). Optimization of biochar production from greywater grown polyculture microalgae using microwave pyrolysis. *Bioresource Technology*, 388, 129666.
- [35] Toscano, G. et al. (2022). FTIR spectroscopy for determination of the raw materials used in wood pellet production. *Fuel*, 313.
- [36] Traoré, M., Kaal, J., & Martínez Cortizas, A. (2018). Differentiation between pine woods according to species and growing location using FTIR-ATR. *Wood Science and Technology*, 52(2), 487–504.
- [37] Lingegowda, D. C., Komal Kumar, J., Devi Prasad, A. G., Zarei, M., & Gopal, S. (2013). FTIR spectroscopic studies on cleome gynandra-comparative analysis of functional group before and after extraction. *Romanian Journal of Biophysics*, 22, 137-149.
- [38] Andersen, S. L. F. et al. (2019). Improving enzymatic saccharification of Eucalyptus grandis branches by ozone pretreatment. *Wood Science and Technology*, 53(1), 49–69.
- [39] Rodier, L., Bilba, K., Onésippe, C., & Arsène, M. A. (2019). Utilization of bio-chars from sugarcane bagasse pyrolysis in cement-based composites. *Industrial Crops and Products*, 141.

Analysis of Voltage-Current Characteristics of Non-Linear Electric Loads

Bakir Agić¹, Enver Agić²

¹Faculty of Electrical engineering, University of Tuzla, Tuzla, Bosnia and Herzegovina

²PIM University Banja Luka, Banja Luka, Bosnia and Herzegovina

¹bakir.agic@outlook.com, ²enveragic99@gmail.com

Abstract—The paper considers analysis of voltage-current characteristics of non-linear electric loads on PC (personal computer). Using electrical equipment: power analyzer MI 7111, regulation transformer (220/400V, 1.25kVA, 5A), PC (220V, 300W) and software tool, analysis of resistor current is done.

Keywords – analysis, load current, PC, harmonics

I. INTRODUCTION

The following electrical equipment was used for the analysis:

- Power analyzer MI 7111
- Regulation transformer (220/400V, 1.25kVA, 5A)
- PC (220V, 300W)

For the scheme in Fig. 1, the waveforms of the current and voltage of the personal computer were recorded, then an analysis of the harmonic

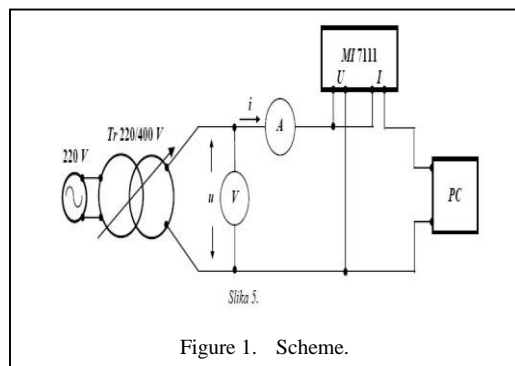


Figure 1. Scheme.

components of the current of the personal computer and the corresponding voltage was performed. The values of the harmonic components up to the 10th harmonic were analyzed and the total harmonic distortion of the current waveform of the personal computer was calculated [1].

II. MEASUREMENT ANALYSIS

A. Voltage-Current Characteristics of Personal Computer PC and Corresponding Harmonic Analysis of PC Current

Rectifiers, as the most commonly used energy electronic converters, are one of the main sources of higher harmonics. The switching mode of operation results in a constant change in the configuration of the active part of the rectifier. This leads to the fact that the waveform of the grid current of the rectifier is composed of segments and is non-sinusoidal.

The flow of non-sinusoidal current causes a voltage drop on the grid impedance, which leads to a distortion of the basic sinusoidal voltage.

At the same time, on the consumer's side, the voltage waveform consists of parts of a sinusoid, that is, in addition to the direct component, there are also alternating components - higher (even) harmonics [2].

Standard PCs contain single-phase rectifiers in the power supply section and are required to generate stable DC voltages, to be as simple as possible in construction and with high reliability. For these reasons, they are usually

diode rectifiers with a filter capacitor on the DC side or, more recently, DC switching power supplies, which also have a capacitor at the output.

In case of need for a different voltage level or a more stable voltage, a linear or switching power supply is connected behind the capacitor. However, in both cases, this rectifier distorts the mains current, and partly the voltage.

Distortion is the result of topping up the capacitor in periods when the mains voltage is higher than the DC voltage, that is, the voltage on the capacitor [3].

Using the power analyzer MI 7111, the following characteristics were obtained, and after connecting the elements of the electric circuit as in Fig. 2.

Fig. 2. shows the oscillogram of the current waveform, as well as the current spectrum in Fig. 3 of a standard PC with a built-in single-phase rectifier. It is easy to see the moment of charging the capacitor with a current pulse,

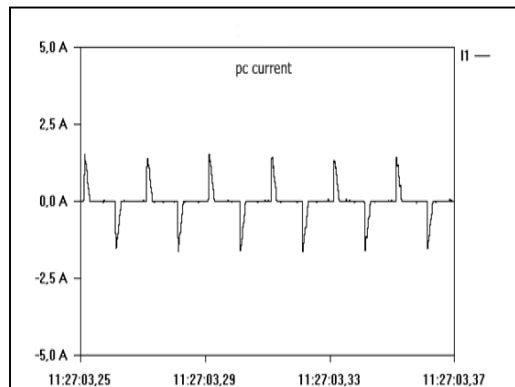


Figure 2. PC current analysis.

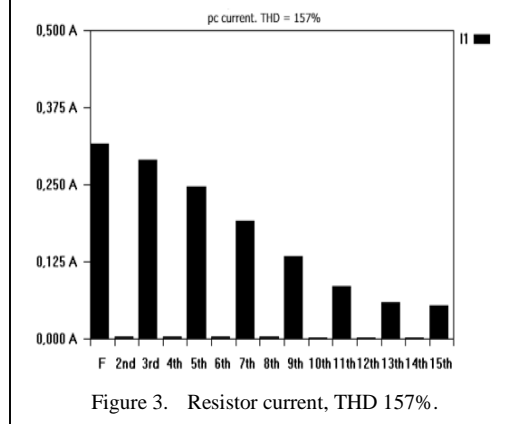


Figure 3. Resistor current, THD 157%.

which is accompanied by a slight distortion (flattening) of the voltage.

TABLE I. HARMONICS VALUES.

Harmonic	Current (A)	Deviation from fundamental (%)
Fundamental	0.320	-
Third	0.280	90
Fifth	0.245	78
Seventh	0.190	60
Ninth	0.130	41

Odd harmonics are dominant in the spectrum, although even harmonics also exist, but in a much smaller amount. Given that they are far more pronounced than in the previous cases, the estimated values of these harmonics from Fig. 3 are presented in a Table I.

Computer current measurements showed that the current waveform is highly distorted due to its non-linear operation, THDI is 132.5%, with the presence of the third, fifth, seventh and other odd harmonics up to the recorded fifteenth. The total harmonic distortion of the personal computer current waveform is:

$$\begin{aligned}
 THDI_{\%} &= \sqrt{\sum_{n=2}^{10} \frac{I_n^2}{I_1^2}} \times 100\% = \\
 &= \sqrt{\frac{I_2^2 + I_3^2 + \dots + I_{10}^2}{I_1^2}} \times 100\% = \\
 &= 1.325 \times 100\% = 132.5\%
 \end{aligned} \quad (1)$$

B. Voltage-Current Characteristics of the Fluorescent Lamp and the Corresponding Harmonic Analysis of the Current of the Lamp

Fluorescent lamps work on the principle of electric discharge in gases. On this occasion, an electric arc is created in the gas, which causes a negative impact on the quality of the voltage. Based on the measurement results, it can be concluded that the presence of higher harmonics of the current of fluorescent lamps is much less compared to their presence in computers, THDI = 60%.

However, as fluorescent lamps are used in large numbers in administrative buildings, shopping centers and educational institutions, it is expected that their negative effect on the level of current and voltage harmonics in the transformer stations that supply them will be significant (Fig. 4).

TABLE II. HARMONICS VALUES FOR LAMP.

Harmonic	Current (A)	Deviation from fundamental (%)
Fundamental	58	-
Second	0.95	-
Third	24	42
Fourth	0.7	-
Fifth	16	27
Sixth	0.7	-
Seventh	12.5	22
Eighth	1.4	-
Ninth	8	15
Tenth	1	-

In Fig. 5, we see the influence of the fluorescent lamp on the voltage waveform, i.e. influence of higher harmonic components on the voltage waveform.

On the spectrum of the voltage waveform, Fig. 6, apart from the fundamental one, all the odd harmonics in the descending order (third to fifteenth) dominate, whose values are found in Table II.

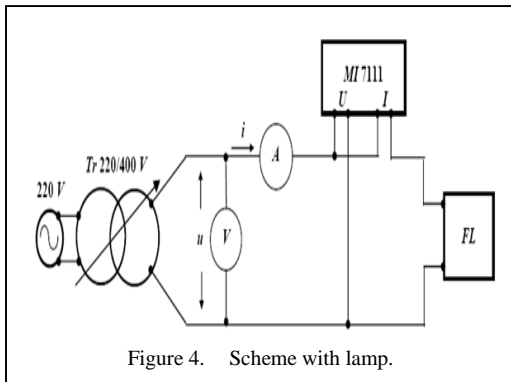


Figure 4. Scheme with lamp.

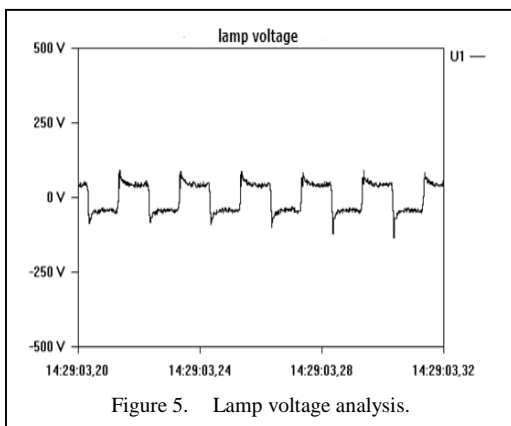


Figure 5. Lamp voltage analysis.

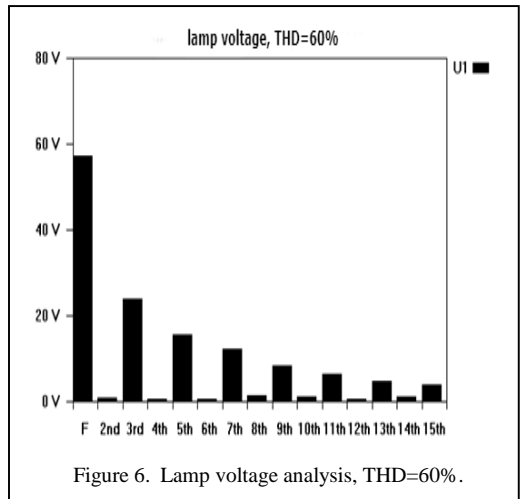


Figure 6. Lamp voltage analysis, THD=60%.

Total harmonic distortion of the lamp current waveform:

$$\begin{aligned}
 THDI_{\%} &= \sqrt{\sum_{n=2}^{10} \frac{I_n^2}{I_1^2}} \times 100\% = \\
 &= \sqrt{\frac{I_2^2 + I_3^2 + \dots + I_{10}^2}{I_1^2}} \times 100\% = \quad (2) \\
 &= 0.472 \times 100\% = 47,2\%
 \end{aligned}$$

III. CONCLUSION

The waveforms and characteristic values of the currents of individual non-linear receivers given in these exercises confirm the presence of higher harmonics. Ignoring now the classic sources of harmonics (transformers, induction furnaces, etc.), considering the constant increase in the representation of non-linear receivers in various electrical devices, etc. and with the tendency of further increase, they also become a significant source of higher harmonics in the network.

It can be assumed what the deviations of current waveforms, voltage drop values are, i.e. the presence of harmonics in the low-voltage distribution network (because this is where we have the largest number of these consumers).

With the introduction of normative acts in our country related to the presence of current harmonics, which are similar to the existing international IEEE standard, it will be necessary to revise them for the connection of individual devices or to consider the possibilities of installation harmonic filters in individual transformer stations.

In addition, it is necessary to carry out measurements at various places, i.e. transformer stations located at the end nodes of the medium voltage distribution network and those that supply specific non-linear consumers. The results of these measurements can be used for the purposes of planning and expanding the distribution network, and especially for managing the distribution network.

REFERENCES

- [1] Power Quality Laboratory exercises, PDS Tuzla. (2006) (p. 5, 9)
- [2] Power Analyzer MI 7111 – Users guide (p. 2)
- [3] Gerald Heydt (1994). *Electric power quality. Second edition.* Stars in Circle Pub (p. 23)

Comparison of Traditional and Non-traditional Economic Instruments in Solid Waste Management

Javad Yahaghi¹, Alireza Bazargan²

^{1,2}School of Environment, College of Engineering, University of Tehran, Iran

¹javad.yahaghi@ut.ac.ir, ²alirezabazargan@ut.ac.ir

Abstract—The generation of solid waste is experiencing a significant increase due to the rapid rate of urbanization, population growth, and consumerism. This surge in waste production presents both challenges and opportunities. Effectively managing these wastes requires a complex approach that takes into account environmental, economic, and social factors. One of the key challenges in solid waste management (SWM) is ensuring that waste is managed in a way that minimizes its negative impact on the environment while also being economically sustainable. This necessitates the use of economic instruments, which play a crucial role in optimizing SWM systems and facilitating the transition towards a circular economy. This article provides a concise overview of economic instruments in SWM, with particular emphasis on comparing traditional and non-traditional approaches. Traditional economic instruments, such as command-and-control systems or landfill tipping fees, typically focus on managing waste at the disposal stage. On the other hand, non-traditional economic instruments like deposit-refund schemes are designed to promote waste reduction, recycling, and resource recovery by altering financial incentives. It is important to note that no single instrument can be universally applied to all aspects of SWM. However, by combining various instruments strategically, it is possible to strike a balance between waste generation and the provision of effective services. In conclusion, economic instruments offer valuable tools for building SWM systems while promoting sustainability. By understanding the differences between traditional and non-traditional approaches and considering their advantages and disadvantages, policymakers can make informed decisions about which instruments are most suitable for their specific context.

Keywords - waste management, economic instruments, circular economy, sustainability

I. INTRODUCTION

This Solid waste generation is experiencing both challenges and opportunities. The generation of solid waste is increasingly growing as a result of rapid rate of urbanization, population growth and consumerism, hence raising concern about environmental impacts such as Green House Gas (GHG) emissions [1] and leachate production [2]. According to World Bank's estimation, "without urgent action, global waste will increase by 70 percent by 2050" [3]. This issue in combination with scarce land resource in urban areas, and difficulties associated with collection, treatment, and disposal of waste, have posed problems for decision-makers to handle ever-increasing volumes of waste generated.

Solid waste materials can range from household garbage and industrial waste to construction debris and hazardous materials. Managing these wastes in an effective manner is a complex task that involves a blend of environmental, economic, and social considerations. One of the fundamental challenges in solid waste management (SWM) is ensuring that waste is handled in a manner that minimizes its adverse impact on the environment while also being economically sustainable.

Therefore, it is important to understand the essential role of economics in SWM and how to optimize SWM systems using various economic instruments that play a significant role in shaping the sustainability of waste management

practices. Economic SWM instruments are tools used to influence the behavior of individuals, businesses, and governments regarding the generation, disposal, and recycling of waste [4].

In this article, a brief review has been done on economic instrument in solid SWM with focus on the comparison of traditional and non-traditional economic instruments used in this field. Economic instruments play a pivotal role in driving the transition of solid waste management towards a circular economy. By integrating economic incentives and disincentives, governments and businesses can encourage responsible waste handling and recycling practices while discouraging wasteful disposal.

II. SOLID WASTE GENERATION

Population growth and increase in income are two highly influencing factor in increasing waste generation. However, it is statistically proven that the amount of solid waste generated grows in linear proportion to the population (elastic relationship), but in less than proportion to the income of households (inelastic relationship) [5]. According to the abovementioned statement, the demand for waste services also increases proportionally with population but does not increase proportionally with respect to income.

In a more general perspective, the generation of solid waste is closely related to the Gross Domestic Production (GDP) of countries [6],

e.g., countries with more per capita GDP commonly produce more per capita solid waste. This is also approved by the latest report of World Bank Group (WBG) on estimating the global generation of solid waste and quantifying the contribution of different regions in solid waste production [7] (Fig. 1 and Table I).

It is noteworthy that more than about two-thirds of this amount of MSW is being landfilled or openly dumped, with less than 20% being recycled or composted, as shown in Fig 2 [7]. The statistics shown in the Fig. 1 and Table I represent just MSW, but there are other types of solid waste including industrial waste, agricultural waste, construction and demolition waste, hazardous waste, medical waste, and electronic waste. Waste generation data have shown that the amount of industrial waste generated by industrial activities may be several times higher than the MSW generated in some countries [7].

To provide a foundation for understanding economic instruments, it is crucial to recognize the significance of the waste hierarchy, which prioritizes waste management actions in the following order: reduce, reuse, recycle, recover (energy), and dispose [8]. By reducing and reusing materials, recycling and recovering energy from waste, and only disposing of waste, when necessary, the environmental impact can be minimized while valuable resources are conserved.

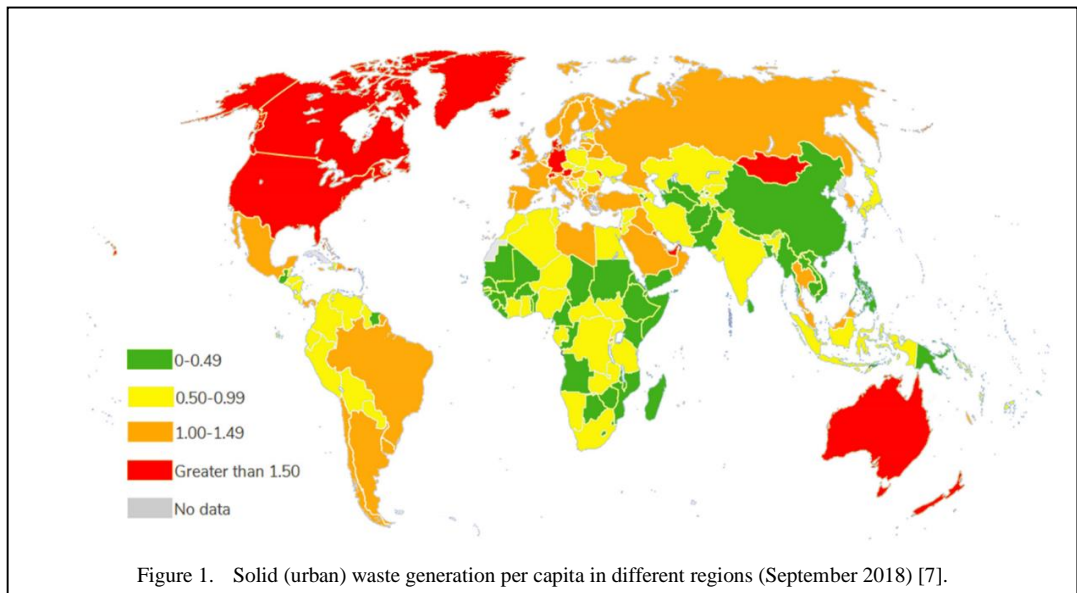


TABLE I. AMOUNT AND SHARE OF SOLID (URBAN) WASTE GENERATION, BY REGION (SEPTEMBER 2018) [7].

Region	Amount of waste generated (Mt/year)	Percent of region from total
East Asia and Pacific	468	23%
Europe and Central Asia	392	20%
South Asia	334	17%
North America	289	14%
Latin America and the Caribbean	231	11%
Sub-Saharan Africa	174	9%
Middle East and North Africa	129	6%

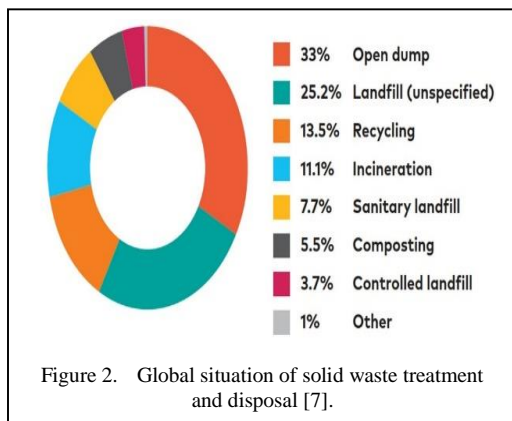


Figure 2. Global situation of solid waste treatment and disposal [7].

III. ECONOMIC INSTRUMENTS IN SOLID WASTE MANAGEMENT

In solid waste management systems, society can be divided to receiver and provider of services. Based on this division, the behavior of each party depends on their property right. Exclusivity (beside Transferability and Enforceability) which is among basic features of a desirable and efficient property right structure, means to return all responsibilities (benefits and costs) accrued as a result of their behavior, only and only to the same person [9]. Whenever part of the society (individuals or entities) does not have to be responsible for consequences of their action, there would be an “Externality”. The ideal purpose of economic instruments is to internalize the externality by means of creating economic incentives, in order to move towards the top of waste hierarchy pyramid, in accordance with the following goals [4]:

- Reducing the generation of waste;

- Reducing hazardous waste generation;
- Discrete and special handling of hazardous waste and not to blend them with other waste resource;
- Encourage reuse, recycle and recovery over disposal of waste;
- Economic optimization of collection, transportation, treatment and disposal of solid waste.
- Minimizing negative environmental impacts associated with above steps
- Providing revenues for covering costs of solid waste management

There is an intimate correlation between economic instruments and the polluter-pays-principle (PPP), the basis of which is to make consumers and producers responsible for paying costs associated with waste management services, resource consumption, and pollution control. According to this principle, the polluter is responsible for all environmental costs, including internal and external, thereby eliminating all subsidies related to resource use, production, and waste management.

Economic instruments in solid waste management can be categorized into traditional and non-traditional economic instruments. The general approach in traditional instruments is to prevent polluters from polluting environment by means of penalties and providing a monetary supply for waste disposal expenditures [4,10], while the manner of non-traditional instruments (generally market-based approaches) is to create more economic incentive for polluters not to pollute the environment or to treat the pollution themselves (Table II). In the following section, each economic instrument is briefly explained under this categorization.

A. Traditional Economic Instruments

As represented in Table II, traditional economic instruments include command-and-control, landfill tipping fee, landfilling/incineration taxes or charges and subsidy reduction which mainly focus on partially reflecting waste services costs on waste producers through penalties and providing a monetary supply for waste disposal expenditures.

1) *Command-and-Control standards*: The traditional approach of environmental policy

(including waste management) has mainly relied on the application of command-and-control regulatory standards. This approach involves setting an environmental standard (target) that is enforced by the authority, and penalizing any polluter who fails to meet that standard [4]. However, applying command-and-control standards to solid waste is a little challenging, because online monitoring systems for tracking waste production is rare, and require some technological and legislative infrastructures before its implementation. Therefore, implementing this approach for solid waste requires a detailed monitoring system to prevent waste generators from law-evasion.

2) *Landfilling/incineration charges*: Landfilling or incineration charges refer to fees or costs associated with disposing of waste in landfills or through incineration. These charges are typically imposed to cover the expenses of managing and processing waste by these methods. When talking about industrial wastes, charges are applied to waste-producing industries; but in case of MSW, they are not imposed to waste generators, but to waste collector parties. Despite being effective in some cases, this approach often results in inefficiencies and insufficient financial resources for addressing emerging waste management issues [10]. Some researchers have argued based on evidence that charges for disposal have been shown to increase illegal disposal [11]. Therefore, it is better to levy charges directly to waste generators through, for example, unit-pricing schemes [12]. A case study in Canada showed that unit-based waste disposal scheme resulted in increasing the recycling rate, but it needs continuous enforcement for better efficacy [12].

3) *Landfilling/incineration taxes*: Taxes are like charges which impose the costs of waste disposal on the producers, but there is a difference between a tax and a charge with respect to how revenues are allocated. In fact, tax's revenues go into the general budget, while a charge's revenues are specifically used to finance environmental measures. A case study conducted on incineration practices in Belgium revealed that incremental increases in incineration taxes can be effective in reducing landfill usage, but their success hinges on considering prevailing market conditions [13].

4) *Subsidy reduction*: Solid waste services include many hidden subsidies, where central

TABLE II. ECONOMIC INSTRUMENTS CATEGORIZATION BASED ON TRADITIONAL AND NON-TRADITIONAL [4,6,10].

Traditional economic instruments	Non-traditional economic instruments
Command -and-control standards	Subsidies/ Tax incentives
Landfill tipping fee	Grants/ Funds
Landfilling/Incineration charges	Environmental liability law
Landfilling/Incineration taxes	Developments rights
Subsidy reductions	Trade-off arrangements
	Deposit-refund scheme
	Take-back systems
	Performance disclosure

governments subsidize loans, provide seconded staff, exempt municipalities from customs duties on equipment, and provide land for disposal sites [4]. Moreover, some municipalities or local governments provide free or low-cost services for industries to collect and dispose of their industrial waste. Eliminating these subsidies, for example through encouraging private sector participation in delivering solid waste services, can influence the behavior of waste generators by increasing the cost of waste generation.

B. Non-traditional Economic Instruments

Non-traditional economic instruments, on the other hand, are designed to promote waste reduction, recycling, and resource recovery. The incentives of non-traditional instruments may be financial or non-financial, but both encourage parties toward more sustainable approaches. As represented in Table II, deposit-refund scheme, tax credits and market-based mechanisms like cap-and-trade schemes for waste disposal or emissions linked to waste, are some examples of non-traditional economic instruments.

1) *Subsidies/Tax incentives*: There is an opportunity to consider subsidies on raw materials for businesses who implement recycling action on their waste or any change in the product or production process towards minimum discharge. Furthermore, tax credits can be granted to businesses or individuals who actively engage in waste reduction or recycling practices. This could involve tax incentives for using eco-friendly packaging, investing in recycling technologies, or employing waste reduction strategies [14]. By providing financial

benefits through subsidies and tax credits, governments encourage industries and individuals to opt for environmentally friendly practices, ultimately diverting waste from landfills and incineration by making recycling and waste reduction more economically advantageous.

2) *Environmental liability law*: Environmental liability law acts exactly on the basis of the polluter-pays-principle. The purpose of liability laws has traditionally been to cover the damages to people and property when they are at fault. Extended Producer Responsibility (EPR) and Pay-as-You-Throw (PAYT) schemes are examples of environmental liability laws. EPR programs require manufacturers to take responsibility for the entire lifecycle of their products, including post-consumer disposal or recycling [15] promoting design for recycling and incentivizing the recovery of valuable materials. PAYT systems directly tie waste generation and disposal costs to producers, where households or businesses are charged based on the amount of waste they produce, incentivizing reduced waste generation and encouraging recycling [12].

3) *Grants/Funds*: Allocating grants and funds in order to stimulate research on waste reduction or recycling methods and technologies could act as a leading economic instrument towards a more sustainable waste management system [4]. These financial resources support researchers, innovators, and institutions in conducting in-depth studies, experiments, and the development of cutting-edge technologies aimed at reducing, reusing, and recycling waste. Funds allocated for such research encourage the exploration of sustainable alternatives, fostering the discovery of more efficient, cost-effective, and environmentally friendly methods for waste management.

4) *Development and property rights*: This instrument is mostly applied when there is a contaminated site or a contaminating (or hazardous) waste stream which is produced as the byproduct of an industrial process. Based on development and property rights enacted, the owner of the industrial process does not have the right to develop new production line/units unless it implements more environmentally friendly methods for disposing or recycling its waste stream [4]. Moreover, there are examples of giving the ownership of a contaminated site to whomever can treat the contamination. This

instrument can provide attractive incentives for recycling or more environmentally friendly methods of waste management.

5) *Trade-off systems*: Although trade-off arrangements have been applied in air emission (particularly greenhouse gases emissions) under the cap-and-trade system; there is also a possibility to apply this system to SWM area with focus on landfilling of waste, which can create a market for tradable permits. Landfill Allowance Trading Scheme (LATS) is an example of trade-off arrangements which was enacted in 2005 in England to enforce diverting the biodegradable municipal waste from landfills [16]. Result of the mentioned system showed that through a 6-year implementation of scheme, the volume of landfilled waste experienced a 20% reduction from about 60% to under 40%.

6) *Deposit-refund scheme*: Deposit-refund scheme (DRS) can be tailored to specific categories of waste, primarily those capable of retaining their integrity after use, having high value for recycling, and easily recyclable [4]. Beverage containers (particularly glass, aluminum and PET) used batteries (specially lead-acid batteries), tires and consumer electronics are some examples of waste streams that can be well managed through this instrument [17]. Combined taxation and rebates are offered when products or their packaging are returned to be recycled or disposed of appropriately under a deposit-refund scheme. DRS functions by requiring initial deposits to be paid upon purchase, with a refund offered upon the return of products or packages.

7) *Performance disclosure*: Since waste production is an indispensable part of daily human life, this instrument has limits when being applied for MSW systems. However, disclosure of the performance of some businesses and industrial units in producing (hazardous) waste or polluting environment, and consequences associated with that, may heavily influence the consumer's decision to not purchase products from a polluter [4]. Considering the market and sale volume of product-oriented industries, this instrument can push waste generators toward more environmentally friendly management of their wastes.

Some instruments are easier to implement while other involve complexities, but this should not create an either-or situation. Moreover, there

is not a unique description for all countries, hence best combination of useful instruments should be applied to achieve the most sustainability.

IV. CONCLUSION

One of the primary challenges in the management of solid waste (SWM) lies in the need to effectively reduce its adverse environmental impact while ensuring economic sustainability. Economic tools and strategies are crucial in guiding the behavior of stakeholders within the solid waste system towards sustainability by delineating property rights for all parties involved. In this context, traditional economic instruments primarily aim on discouraging waste landfilling by increasing the cost of the disposal stage for waste producers, simultaneously generating revenue to defray the expenses associated with waste management. In contrast, non-traditional instruments predominantly incentivize waste reduction, recovery, or recycling by shifting financial incentives towards these stages in the waste management hierarchy. The feasibility and implementation of various economic instruments may vary, with some being more straightforward to put in place, while others may necessitate the development of new infrastructure. It is essential to recognize that no single instrument can be universally applied to all facets of SWM. Instead, the harmonious equilibrium between regulatory controls and economic instruments in each country will depend on local conditions and preferences.

REFERENCES

- [1] Yaashikaa, P. R., Kumar, P. S., Nhung, T. C., Hemavathy, R. V., Jawahar, M. J., Neshanthini, J. P., & Rangasamy, G. (2022). A review on landfill system for municipal solid wastes: Insight into leachate, gas emissions, environmental and economic analysis. *Chemosphere*, 136627.
- [2] Yahaghi, J., & Bazargan, A. (2022). The synergetic effects of radio-frequency electromagnetic field and pH adjustment on landfill leachate microbial inactivation. *Process Safety and Environmental Protection*, 167, 516–526.
- [3] World Bank (2022). Trends in Solid Waste Management. What a Waste 2.0: A Global Snapshot of Solid Waste Management to 2050. Available at: https://datatopics.worldbank.org/what-a-waste/trends_in_solid_waste_management.html
- [4] Cointreau, S., & Hornig, C. (2003). Global review of economic instruments for solid waste management in Latin America. Regional Policy Dialogue, Inter-American Development Bank, Washington DC.
- [5] van Beukering, P., Kuik, O., & Oosterhuis, F. (2014). The economics of recycling. In *Handbook of Recycling* (pp. 479–489). Elsevier.
- [6] Matheson, T. (2022). Disposal is not free: Fiscal instruments to internalize the environmental costs of solid waste. *International Tax and Public Finance*, 1–27.
- [7] Silpa Kaza, Lisa Yao, Perinaz Bhada-Tata, and F. V. W. (2018). *What a Waste 2.0: A Global Snapshot of Solid Waste Management to 2050*.
- [8] Wilson, D. C. (2023). Learning from the past to plan for the future: An historical review of the evolution of waste and resource management 1970–2020 and reflections on priorities 2020–2030–The perspective of an involved witness. *Waste Management & Research*, 0734242X231178025.
- [9] Tietenberg, T., & Lewis, L. (2018). *Environmental and natural resource economics*. Routledge.
- [10] Pearce, D. W., & Turner, R. K. (1993). Market-based approaches to solid waste management. *Resources, Conservation and Recycling*, 8(1–2), 63–90.
- [11] Fullerton, D., & Kinnaman, T. C. (1994). Household demand for garbage and recycling collection with the start of a price per bag. *NBER Working Paper Series (USA)*.
- [12] Lakhan, C. (2015). Evaluating the effects of unit based waste disposal schemes on the collection of household recyclables in Ontario, Canada. *Resources, Conservation and Recycling*, 95, 38–45.
- [13] De Weerd, L., Sasao, T., Compernelle, T., Van Passel, S., & De Jaeger, S. (2020). The effect of waste incineration taxation on industrial plastic waste generation: A panel analysis. *Resources, Conservation and Recycling*, 157, 104717.
- [14] Sparks, K. (1998). *Tax Credits: An incentive for recycling*. Resource Recycling Magazine. Available at: [Http://Www. Epa. Gov/Wastes/Conserve/Tools/Rmd/Docs/Taxcred. Pdf](http://www.epa.gov/Wastes/Conserve/Tools/Rmd/Docs/Taxcred.Pdf).
- [15] Runkel, M. (2003). Product durability and extended producer responsibility in solid waste management. *Environmental and Resource Economics*, 24, 161–182.
- [16] Calaf-Forn, M., Roca, J., & Puig-Ventosa, I. (2014). Cap and trade schemes on waste management: A case study of the Landfill Allowance Trading Scheme (LATS) in England. *Waste Management*, 34(5), 919–928.
- [17] Walls, M. (2011). Deposit-refund systems in practice and theory. *Resources for the Future Discussion Paper*, 11–47.

Novel Loco Pilot Training Optimization and Rapid E-learning Inspired Algorithm for Solving the True Power Loss Reduction Problem in Electrical Transmission System

Lenin Kanagasabai¹

¹Prasad V. Potluri Siddhartha Institute of Technology, Andhra Pradesh, India

¹gklenin@gmail.com

Abstract—This paper proposes Loco Pilot Training Inspired (LPT) optimization algorithm and Rapid E-Learning inspired (RLO) optimization algorithm for solving the True power loss reduction problem. LPT optimization algorithm is mathematically designed based on the realistic training of loco pilot. In the procedure, Training, self- learning and simulation based acquisition of knowledge are three segments designed. In the simulation based acquisition of knowledge segment, the trainees will develop their skills through a simulator about the functioning of systems and how to handle the conditions when accident occurs. Rapid e-learning is, fundamentally, a quicker procedure of planning and developing virtual based learning. Instead of outlay many weeks for designing a subject or course, rapid e-learning permits makers to construct modules within few days. The students learning form E-content will be Operational at generating noble results. They can learn everywhere which is not limited by habitation or period. Validity of Loco Pilot Training Inspired (LPT) optimization algorithm and Rapid E-Learning inspired (RLO) optimization algorithm verified in 23 Benchmarking functions, IEEE 30, 354 systems.

Keywords - Loco pilot training, rapid e- learning, true power

I. INTRODUCTION

Plentiful methods are applied consecutively to solve the in True power loss reduction problem

in electrical transmission system. In this paper Loco Pilot Training Inspired (LPT) optimization algorithm and Rapid E- Learning inspired (RLO) optimization algorithm are applied to solve the True power loss reduction problem. LPT optimization algorithm is mathematically designed based on the realistic training of loco pilot. Indian railway system is in fourth place in the globe and Loco Pilots are responsible of operating the trains in the predefined route line. Loco Pilot Training Inspired (LPT) optimization algorithm is mathematically designed based on the realistic training of loco pilot. Indian railway system is in fourth place in the globe and Loco Pilots are responsible of operating the trains in the predefined route line. In order to become a Loco Pilot in Indian railway, candidate's necessity to possess an Industrial Training Institute (ITI) degree and should pass the examination conducted by Railway Recruitment Board Assistant Locomotive Pilot (RRB ALP). Loco Pilots are competent experts who comprehend the machine learning and engines of train functionality. Loco pilots are mainly accountable for the safety of the passengers. In Indian railways Loco Pilot are positioned as Assistant Pilot, in Express trains, in goods train, passenger trains, Shunting purposes, etc., In the proposed Mathematical design of LPT three segments are there: Training, self- learning and simulation based acquisition of knowledge. In Railway Recruitment Board Assistant

Locomotive Pilot (RRB ALP) the trainees has to undergo the training for 151 days. This period of training in RRB ALP define the exploration impact in the procedure. In the process of learning the students has be in balanced mode and there should be cognitive, collective growth and their emotional requirements need to be fulfilled. Rapid e-learning is, fundamentally, a quicker procedure of planning and developing virtual based learning. Instead of outlay many weeks for designing a subject or course, rapid e-learning permits makers to construct modules within few days. The students learning form E-content will be Operational at generating noble results. They can learn everywhere which is not limited by habitation or period. Number of individuals or groups can be learnt without any sort of limitations. Validity Loco Pilot Training Inspired (LPT) optimization algorithm and Rapid E-Learning inspired (RLO) optimization algorithm are verified in 23 Benchmarking functions, IEEE 30, 354 systems.

II. PROBLEM FORMULATION

Objective function of Electrical Power Loss Reduction Problem is demarcated as:

$$\begin{aligned} \min \tilde{F}(\bar{g}, \bar{h}), \\ M(\bar{g}, \bar{h}) = 0, \\ N(\bar{g}, \bar{h}) = 0. \end{aligned} \quad (1)$$

Control (\bar{g}) and dependent (\bar{h}) vectors are defined as:

$$g = [VLG_1, \dots, VLG_{N_G}; QC_1, \dots, \dots, QC_{N_C}; T_1, \dots, T_{N_T}] \quad (2)$$

$$h = [PG_{slack}; VL_1, \dots, VL_{N_{Load}}; QG_1, \dots, QG_{N_G}; SL_1, \dots, SL_{N_T}] \quad (3)$$

$Q_C \rightarrow$ Reactive power compensator

$T \rightarrow$ Transformer tap

$V_G \rightarrow$ Generator voltage

$PG_{slack} \rightarrow$ Slack generator

$V_L \rightarrow$ Voltage in transmission lines

$Q_G \rightarrow$ Reactive power generator

Fitness functions are defined as follows:

$$F_1 = P_{min} = \min \left[\sum_m^{N_{TL}} G_m [V_i^2 + V_j^2 - 2 \times V_j \cos \theta_{ij}] \right],$$

$$F_2 = \min \left[\sum_{i=1}^{N_{LB}} |V_{Lk} - V_{Lk}^{desired}|^2 + \sum_{i=1}^{N_G} |Q_{GK} - Q_{GK}^{Lim}|^2 \right],$$

$$F_3 = \text{Minimize } L_{maximum},$$

$$S_L \rightarrow \text{Apparent power},$$

$$L_{max} = \max [L_j]; j = 1; N_{LB},$$

$$\begin{cases} L_j = 1 - \sum_{i=1}^{N_{PV}} F_{ji} \frac{V_i}{V_j}, \\ F_{ji} = -[Y_1]^{-1} [Y_2] \end{cases} \quad (4)$$

$$L_{max} = \max \left[1 - [Y_1]^{-1} [Y_2] \times \frac{V_i}{V_j} \right].$$

Parity constraints:

$$0 = \begin{bmatrix} P_{Gi} - P_{Di} - V_i \sum_{j \in N_B} V_j \\ G_{ij} \cos[\theta_i - \theta_j] + B_{ij} \sin[\theta_i - \theta_j] \end{bmatrix}, \quad (5)$$

$$0 = \begin{bmatrix} Q_{Gi} - Q_{Di} - V_i \sum_{j \in N_B} V_j \\ G_{ij} \sin[\theta_i - \theta_j] + B_{ij} \cos[\theta_i - \theta_j] \end{bmatrix}, \quad (6)$$

N_B is the number of buses,

$P_G, Q_G \rightarrow$ real and reactive power,

$G_{ij}, B_{ij} \rightarrow$ mutual conductance and susceptance,

$P_D, Q_D \rightarrow$ real and reactive load.

Disparity constraints:

$$P_{Gsl}^{min} \leq P_{Gsl} \leq P_{Gsl}^{max}. \quad (7)$$

Reactive power generation (Q_{Gi}):

$$Q_{Gi}^{min} \leq Q_{Gi} \leq Q_{Gi}^{max}, i \in N_G. \quad (8)$$

Load bus voltage (V_{Li}):

$$V_{Li}^{min} \leq V_{Li} \leq V_{Li}^{max}, i \in N_L. \quad (9)$$

Transformers tap setting (T_i):

$$T_i^{min} \leq T_i \leq T_i^{max}, i \in N_T. \quad (10)$$

Switchable reactive power compensations (Q_{Ci}):

$$Q_C^{min} \leq Q_C \leq Q_C^{max}, i \in N_C, \quad (11)$$

$$|SL_i| \leq S_{L_i}^{max}, i \in N_{TL}. \quad (12)$$

Generator bus voltage (V_{Gi}):

$$V_{Gi}^{min} \leq V_{Gi} \leq V_{Gi}^{max}, i \in N_G. \quad (13)$$

$$\begin{aligned} \text{Multi objective fitness (MOF)} &= \\ &= F_1 + r_i F_2 + u F_3 = \\ &[\sum_{i=1}^{N_L} x_v [V_{Li} - V_{Li}^{min}]^2 + \\ &+ \sum_{i=1}^{N_G} r_g [Q_{Gi} - Q_{Gi}^{min}]^2] + r_f F_3 \end{aligned} \quad (14)$$

$$\begin{aligned} V_{Li}^{minimum} &= \\ &= \begin{cases} V_{Li}^{max}, V_{Li} > V_{Li}^{max}, \\ V_{Li}^{min}, V_{Li} < V_{Li}^{min} \end{cases}, \end{aligned} \quad (15)$$

$$\begin{aligned} Q_{Gi}^{minimum} &= \\ &= \begin{cases} Q_{Gi}^{max}, Q_{Gi} > Q_{Gi}^{max}, \\ Q_{Gi}^{min}, Q_{Gi} < Q_{Gi}^{min} \end{cases}. \end{aligned} \quad (16)$$

III. LOCO PILOT TRAINING INSPIRED OPTIMIZATION ALGORITHM

Loco Pilot Training Inspired (LPT) optimization algorithm is mathematically designed based on the realistic training of loco pilot. Indian railway system is in fourth place in the globe and Loco Pilots are responsible of operating the trains in the predefined route line. In order to become a Loco Pilot in Indian railway

candidate's necessity to possess an Industrial Training Institute (ITI) degree and should pass the examination conducted by Railway Recruitment Board Assistant Locomotive Pilot (RRB ALP) [1] (Fig. 1). Loco Pilots are competent experts who comprehend the machine learning and engines of train functionality.

Loco pilots are mainly accountable for the safety of the passengers. In Indian railways Loco Pilot are positioned as Assistant Pilot, in Express trains, in goods train, passenger trains, Shunting purposes, etc., In the proposed Mathematical design of LPT three segments are there: Training, self-learning and simulation based acquisition of knowledge. In the training segment the selected candidates or trainees will undergo rigorous training and the trainees should undergo both single and dual traction training programs conducted by RRB ALP for 151 days. In the self-learning with eagerness the trainees will learn through self-study and communications with other trainees. In the simulation based acquisition of knowledge segment, the trainees will develop their skills through a simulator about the functioning of systems and how to handle the conditions when accident occurs. Population in LPT is engendered as follows:

$$L = \begin{bmatrix} L_1 \\ \vdots \\ L_i \\ \vdots \\ L_N \end{bmatrix}_{N \times m} = \begin{bmatrix} L_{1,1} & \cdots & L_{1,m} \\ \vdots & \ddots & \vdots \\ L_{N,1} & \cdots & L_{N,m} \end{bmatrix}_{N \times m}, \quad (17)$$

$L \rightarrow$ matrix of population,

$N, m \rightarrow$ number and variables of population.

Capriciously initial positions are engendered in the examination region:

$$l_{i,j} = lb_j + Rand \times (ub_j - lb_j), \quad (18)$$

$Rand \in [0,1],$

$i = 1,2,3,\dots,N,$

$j = 1,2,3,\dots,m,$

$ub_j, lb_j \rightarrow$ max and min limits .

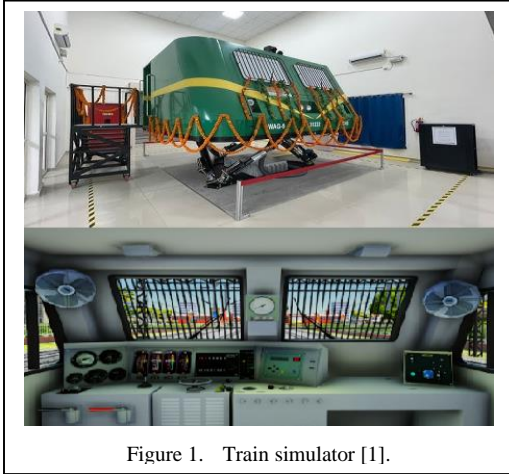


Figure 1. Train simulator [1].

Rate of Objective function is premeditated as:

$$U = \begin{bmatrix} U_1 \\ \vdots \\ U_i \\ \vdots \\ U_N \end{bmatrix}_{N \times 1} = \begin{bmatrix} U(L_1) \\ \vdots \\ U(L_i) \\ \vdots \\ U(L_N) \end{bmatrix}_{N \times 1}, \quad (19)$$

$U \rightarrow$ Rate of Objective function .

In Railway Recruitment Board Assistant Locomotive Pilot (RRB ALP) the trainees has to undergo the training for 151 days. This period of training in RRB ALP define the exploration impact in the procedure.

$$TP_i = \{L_k | k \in \{1,2,\dots,N\} \wedge \wedge U_k < U_i\} U\{L_{best}\}, \quad (20)$$

$TP_i \rightarrow$ Training period,

$L_{best} \rightarrow$ population best trainee.

In RRB ALP the trainee will learn about function and operations sequentially.

$$L_{i,j}^{p1} = l_{i,j} + Rand \times (TP_{i,j}^s - P \cdot l_{i,j}), \quad (21)$$

$L_{i,j}^{p1} \rightarrow$ ith trainee location ,

$Rand \in [0,1]$,

$TP_{i,j}^s \rightarrow$ training span ,

$P \in \{1,2\}$.

If the fresh locations objective functional rate is advanced than preceding one, then exchange will be completed.

$$L_i = \begin{cases} L_i^{p1}, U_i^{p1} < U_i \\ L_i, Else \end{cases}, \quad (22)$$

$U_i^{p1} \rightarrow$ objective function new rate .

In the second segment; self-learning with eagerness, the trainees will learn through self-study and communication with other trainees.

$$L_{i,j}^{p2} = \begin{cases} l_{i,j} + Rand \times (l_{i,i,j} - P \times l_{i,j}), U_{li} < U_i \\ l_{i,j} + Rand \times (l_{i,j} - P \times l_{i,i,j}), Else \end{cases} \quad (23)$$

$$L_i = \begin{cases} L_i^{p2}, U_i^{p2} < U_i \\ L_i, Else \end{cases}, \quad (24)$$

$L_{i,j}^{p2} \rightarrow$ ith trainee new position ,

$l_{i,i,j} \rightarrow$ communication with other trainees.

In the third section; simulation based acquisition of knowledge segment, the trainees will develop their skills through a simulator about the functioning of systems and how to handle the conditions when accident occurs.

$$L_{i,j}^{p3} = l_{i,j} + \frac{lb_j + Rand \times (ub_j - lb_j)}{t}, \quad (25)$$

$L_{i,j}^{p3} \rightarrow$ ith trainee location ,

$i = 1,2,3,\dots,N$,

$j = 1,2,3,\dots,m$,

$t = 1,2,3,\dots,T$.

$$L_i = \begin{cases} L_i^{p3}, U_i^{p3} < U_i \\ L_i, Else \end{cases}. \quad (26)$$

- a. Start
- b. Create the population
- c. For $t = 1$ to T
- d. For $i = 1$ to N
- e. Employ the training segment
- f. $TP_i = \{L_k | k \in \{1,2,\dots,N\} \wedge U_k < U_i\} U\{L_{best}\}$
- g. $L_{i,j}^{p1} = l_{i,j} + Rand \times (TP_{i,j}^s - P \times l_{i,j})$
- h. $L_i = \begin{cases} L_i^{p1}, U_i^{p1} < U_i \\ L_i, Else \end{cases}$
- i. Perform the self-learning segment
- j. $L_{i,j}^{p2} = \begin{cases} l_{i,j} + Rand \times (l_{i,i,j} - P \times l_{i,j}), U_{li} < U_i \\ l_{i,j} + Rand \times (l_{i,j} - P \times l_{i,i,j}), Else \end{cases}$
- k. $L_i = \begin{cases} L_i^{p2}, U_i^{p2} < U_i \\ L_i, Else \end{cases}$
- l. Apply the simulator based learning segment
- m. $L_{i,j}^{p3} = l_{i,j} + \frac{lb_j + Rand \times (ub_j - lb_j)}{t}$
- n. $L_i = \begin{cases} L_i^{p3}, U_i^{p3} < U_i \\ L_i, Else \end{cases}$
- o. End for
- p. $t = t + 1$
- q. Output the L_{best}
- r. End

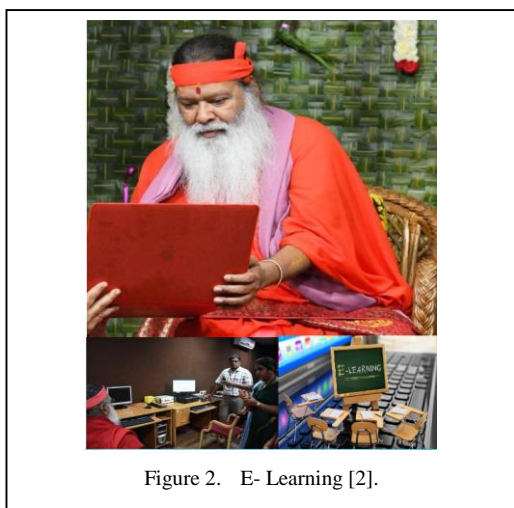


Figure 2. E- Learning [2].

IV. RAPID E- LEARNING INSPIRED OPTIMIZATION ALGORITHM

Rapid E-Learning inspired (RLO) optimization algorithm is mathematically designed based on the quick learning of students [2]. In the process of learning the students has be in balanced mode and there should be cognitive, collective growth and their emotional requirements need to be fulfilled. Rapid e-learning is, fundamentally, a quicker procedure of planning and developing virtual based learning. Instead of outlay many weeks for designing a subject or course; Pontiff SGS verifying the Rapid E-Learning content (Fig. 2) and rapid e-learning permits makers to construct modules within few days. The students learning form E-content will be Operational at generating noble results. They can learn everywhere which is not limited by habitation or period. Number of individuals or groups can be learnt without any sort of limitations. Depend on the needs of the students time to time the E-content can be updated and it will be fulfill the requirement of the students. This mode of E-learning will be self-paced, cost effective, efficient utilization of time and it's adaptable for learning. Arts, science, technology, religion studies etc., anything can be learned from the E-learning. The students are the members of the population and their target is learning from the E-content.

Population randomly engendered in the search region:

$$Z_i = \min + (\max - \min) \times NP \times D , \quad (27)$$

$Z_i \rightarrow E - learning \text{ content} ,$

$\max, \min \rightarrow \text{limits} ,$

$NP \rightarrow \text{population number} ,$

$D \rightarrow \text{dimension} .$

In Rapid E-learning procedure the students will learn quickly with flexibility in learning and its scientifically described as:

$$Z_{new} = \begin{cases} Z_{new} & \text{if } R < VR_0 \\ \text{Random Else} & \end{cases} , \quad (28)$$

$R \in [0,1] ,$

$VR_0 \rightarrow \text{valuation rate operator} .$

Rendering to the rapidness of learning, the student will cover the E-content and learning will be in quick pace. The target of learning will be accomplished once the student completely covers the E-content during learning.

$$Z_{new} = z + R \times A_R \times (T_P \times R_R - T \times P_R), \quad (29)$$

$R \in [0,1] ,$

$A_R \rightarrow \text{accomplishment rate} ,$

$A_R \in [0.1,1] ,$

$T_P \rightarrow \text{Target in learning} ,$

$R_R \rightarrow \text{Rapidness rate of learning} ,$

$R_R \in [0.68,0.3] ,$

$T \rightarrow \text{Target} ,$

$P_R \rightarrow \text{rapidness rate of covering the content} ,$

$P_R \in [0,1] .$

When the student fail to understand the E-content or unable to learn or unable to cover the complete content of learning then the fail condition will be reached. This condition is mathematically formulated as:

$$Z_i^{k+1} = \begin{cases} MT_P & \text{if } F(Z) < F(Z_{new}) \\ T = 0, \text{Else} & \end{cases} , \quad (30)$$

$MT_P \rightarrow \text{Modernized Target position} ,$

$F(Z) \rightarrow \text{Fitness value of learning} ,$

$F(Z_{new}) \rightarrow \text{Fitness value of covered level of content} .$

- a. Start
- b. Engender the population
- c. $Z_i = \min + (\max - \min) \times NP \times D$
- d. Define the Target
- e. Initialize the Rapid E-learning process
- f. *if* $R < VR_O$, *then*
- g. Modernize the rate of learning
- h. $Z_{new} = \begin{cases} Z_{new} & \text{if } R < VR_O \\ \text{Random} & \text{Else} \end{cases}$
- i. Else
- j. Rationalize the Learning process
- k. Compute the fitness rate
- l. $Z_{new} = Z + R \times A_R \times (T_P \times R_R - T \times P_R)$
- m. *if* $F(Z) < F(Z_{new})$, *then*
- n. Modernize the content coverage
- o. Streamline the target of learning
- p. Else
- q. $Target = 0$
- r. $n = n + 1$
- s. Output the best solution
- t. End

V. RESULTS

Loco Pilot Training Inspired (LPT) optimization algorithm and Rapid E- Learning inspired (RLO) optimization are validated in corroborated in 23 benchmark functions (Main 7-Unimodal, succeeding 6-Multimodal, concluding 10-fixed-dimension multimodal) [3], Table I show the results of LPT, RLO in 23 benchmark functions.

TABLE I. RESULT OF LPT, RLO IN BENCHMARK FUNCTIONS.

Benchmark Function	ADASSA [3].	EESSA [3].	LPT	RLO
1	6.38×10^{-12}	6.96×10^{-9}	6.31×10^{-12}	6.31×10^{-12}
2	3.08×10^{-7}	5.48×10^{-6}	3.02×10^{-7}	3.02×10^{-7}
3	2.53×10^{-1}	4.35×10^{-10}	2.51×10^{-1}	2.51×10^{-1}
4	6.71×10^{-7}	1.19×10^{-5}	6.69×10^{-7}	6.69×10^{-7}
5	4.110208	4.11726	4.110202	4.110202
6	3.19×10^{-10}	4.50×10^{-10}	3.18×10^{-10}	3.18×10^{-10}
7	2.23×10^{-5}	0.002002	2.21×10^{-5}	2.21×10^{-5}
8	-2877.61	-3052.87	-2872.60	-2872.60
9	1.01×10^{-12}	22.85084	1.00×10^{-12}	1.00×10^{-12}
10	4.79×10^{-7}	0.810233	4.72×10^{-7}	4.72×10^{-7}
11	5.91×10^{-12}	0.33718	5.90×10^{-12}	5.90×10^{-12}
12	2.56×10^{-12}	0.051897	2.53×10^{-12}	2.53×10^{-12}
13	0.000366	0.001099	0.000362	0.000362
14	0.998004	0.998004	0.998003	0.998003
15	0.000307	0.000829	0.000301	0.000301
16	-1.03163	-1.03163	-1.03161	-1.03161
17	0.397887	0.397887	0.397884	0.397884
18	3	3	3	3
19	-3.86278	-3.86278	-3.86274	-3.86274
20	-3.23084	-3.21497	-3.23073	-3.23073
21	-10.1532	-8.80506	-10.1531	-10.1531
22	-10.0486	-8.46635	-10.0484	-10.0484
23	-10.5364	-9.28557	-10.5362	-10.5362

Loco Pilot Training Inspired (LPT) optimization algorithm and Rapid E- Learning inspired (RLO) optimization are validated in IEEE 30 bus system [4]. Table II shows the True power loss (TES (MW)), Energy irregularity (EIR (PU)) and Equilibrium (ETM (PU)). Fig. 3 give the evaluation.

Loco Pilot Training Inspired (LPT) optimization algorithm and Rapid E- Learning inspired (RLO) optimization are validated in IEEE 354 bus test system [12]. Table III and Fig. 4 shows assessment.

TABLE II. ESTIMATION OF RESULTS (IEEE30 BUS).

Method	TES(MW)	EIR(PU)	ETM(PU)
PURVC [5]	4.6862	0.1354	0.1271
TQTLBO [6]	4.5777	0.0913	0.1180
EEFS [7]	4.5135	0.0896	0.1252
IS [8]	4.5284	0.0891	0.1245
PUDE [9]	4.6482	0.0802	0.1004
CTFWO [10]	4.9448	0.1212	0.1232
IMPA [11]	4.5677	0.1250	0.1135
LPT	4.4909	0.0832	0.1338
RLO	4.4906	0.0829	0.1343

TABLE III. ASSESSMENT OF OUTCOME (IEEE354 BUS).

Method	TES(MW)	EIR(PU)
PURISAI [13]	337.374	0.4978
EPURSAII [13]	338.715	0.5117
EESA [13]	339.325	0.5216
TUICLSO [14]	341.001	0.5354
EDPSO [14]	341.123	0.6395
LPT	336.128	0.4421
RLO	336.108	0.4418

Table IV and Fig. 5 show the time taken by LPT, RLO.

TABLE IV. TIME TAKEN BY LPT, RLO.

METHOD	30 BUS T(S)	354 BUS T(S)
LPT	19.08	81.82
RLO	18.91	80.97

VI. RESULTS

Loco Pilot Training Inspired (LPT) optimization algorithm and Rapid E- Learning inspired (RLO) optimization solved the problem competently. In LPT In the training segment the selected candidates or trainees will undergo rigorous training and the trainees should undergo both single and dual traction training programs conducted by Railway Recruitment Board Assistant Locomotive Pilot for 151 days. In the self-learning with eagerness the trainees will learn through self-study and communications with other trainees. In the simulation based acquisition of knowledge

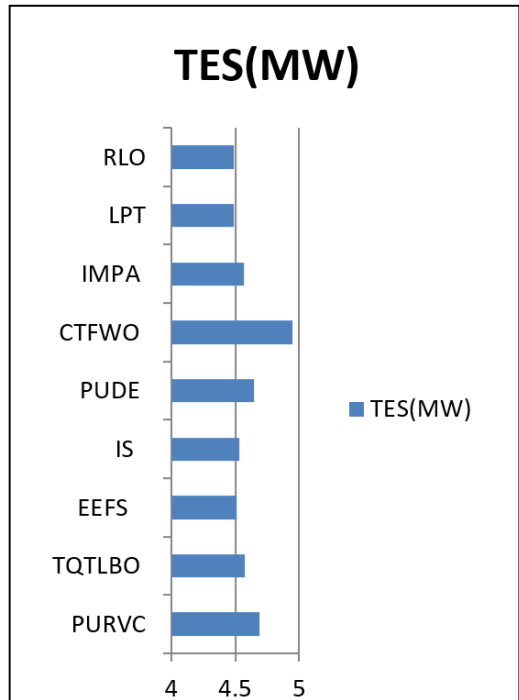


Figure 3. TES (MW) valuation (IEEE30 BUS).

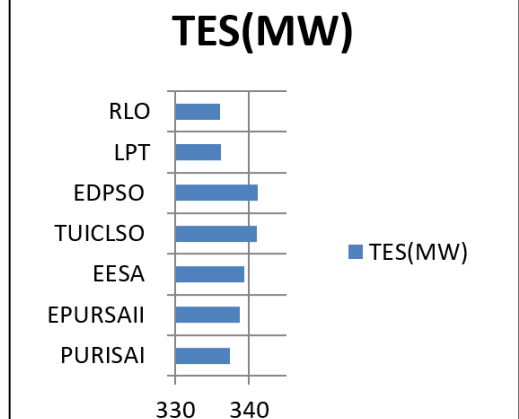


Figure 4. TES (MW) valuation (IEEE354 BUS).

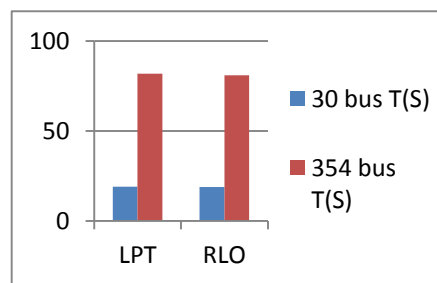


Figure 5. Time taken by LPT, RLO.

segment, the trainees will develop their skills through a simulator about the functioning of systems and how to handle the conditions when accident occurs. Simulation based acquisition of knowledge segment. The students learning form E-content will be Operational at generating noble results. They can learn everywhere which is not limited by habitation or period. Number of individuals or groups can be learnt without any sort of limitations. Depend on the needs of the students time to time the E-content can be updated and it will be fulfil the requirement of the students. This mode of E-learning will be self-paced, cost effective, efficient utilization of time and it's adaptable for learning. Validity of Loco Pilot Training Inspired (LPT) optimization algorithm and Rapid E- Learning inspired (RLO) optimization algorithm are verified in 23 Benchmarking functions, IEEE 30, 354 systems.

In future Loco Pilot Training Inspired (LPT) optimization algorithm and Rapid E- Learning inspired (RLO) optimization algorithm can be applied in the area of medical diagnosis and image processing.

REFERENCES

- [1] Rikku, R., & Chakrabarty, N.(2013). Training needs analysis: A case study of loco pilots. *Procedia - Social and Behavioral Sciences*, 104(1), 1105-1111.
- [2] Ameen, A., & Banu, A. (2023). E-learning on semantic web. In A. Kumar, G. Ghinea, & S. Merugu (Eds.), *Proceedings of the 2nd International Conference on Cognitive and Intelligent Computing. ICCIC 2022*. Cognitive Science and Technology. Springer, Singapore.
- [3] Tudose, A. M., Piciroaga, I. I., Sidea, D. O., & Bulac, C. (2021). Solving single and multi-objective optimal reactive power dispatch problem using an improved salp swarm algorithm. *Energies*, 14(1), 1-20.
- [4] Illinois Center for a Smarter Electric Grid (ICSEG). (n.d.). *IEEE 30-Bus System*. Available at: <https://icseg.iti.illinois.edu/ieee-30-bussystem/>
- [5] Mandal, R. (2013). Optimal reactive power dispatch using quasi-oppositional teaching learning based optimization. *International Journal of Electrical Power & Energy Systems*, 53, 123–134.
- [6] Mouassa, B. S. (2017). Ant lion optimizer for solving optimal reactive power dispatch problem in power systems. *Engineering Science and Technology, an International Journal*, 20(3), 885–895.
- [7] Tran. (2019). Finding optimal reactive power dispatch solutions by using a novel improved stochastic fractal search optimization algorithm. *Telecommunication Computing Electronics and Control*, 17(5), 2517–2526.
- [8] Duong, T. L., Duong, M. Q., Phan, V.-D., & Nguyen, T. T. (2020). Optimal reactive power flow for large-scale power systems using an effective metaheuristic algorithm. *Hindawi Journal of Electrical and Computer Engineering*, 1(1), 6382507, 1-11.
- [9] Kumar, P. G. A., Jeyanthi, P. A., & Devaraj, D. (2022). Hybrid CAC-DE in optimal reactive power dispatch (ORPD) for renewable energy cost reduction. *Sustainable Computing: Informatics and Systems*, 35(1), 100688, 1-18.
- [10] Abd-El Wahab, A. M., Kamel, S., Hassan, M. H., Mosaad, M. I., & Abdul Fattah, T. A. (2022). Optimal reactive power dispatch using a chaotic turbulent flow of water-based optimization algorithm. *Mathematics*, 10(3), 346-360.
- [11] Khan, N. H., Jamal, R., Ebeed, M., Kamel, S., Zeinoddini-Meymand, H., & Zawbaa, H. M. (2022). Adopting scenario-based approach to solve optimal reactive power dispatch problem with integration of wind and solar energy using improved marine predator algorithm. *Ain Shams Engineering Journal*, 13(1), 101726, 1-15.
- [12] PSTCA. (2023). *Power systems test case archive*. University of Washington. Available at: <http://www.ee.washington.edu/research/pstca/>
- [13] Mouassa, S., & Bouktir, T. (2018). Multi-objective ant lion optimization algorithm to solve large-scale multi-objective optimal reactive power dispatch problem. *COMPEL: The International Journal for Computation and Mathematics in Electrical and Electronic Engineering*, 35(1), 350-372.
- [14] Nagarajan, K., Parvathy, A. R. (2020). Multi-objective optimal reactive power dispatch using Levy interior search algorithm. *International Journal on Electrical Engineering and Informatics*, 12(1), 547-570.

Energy and Environmental Management System

Jelena Malenović-Nikolić¹

¹Faculty of Occupational Safety, Niš, Serbia

¹malenovicfznr@gmail.com

Abstract—Defining energy and environmental policies, while respecting the basic principles of sustainable development, forms the basis for creating a modern energy and environmental management system. Engineering aspects of energy management indicate the possibility of reducing energy consumption and preserving the quality of air, water, and soil. It is necessary to hire professional energy managers and consistently adhere to regulations in the field of energy and environmental protection. The application of alternative energy sources and the rational use of fossil fuels can have significant benefits in terms of energy economics and the management of advanced power systems. Monitoring the parameters of energy transformations is also significant from the perspective of managing energy risks associated with energy supply and distribution. The organization of energy and environmental management systems, based on the implementation of legal norms and modern energy management principles, has positive effects on eliminating system inefficiencies, as presented in this paper.

Keywords – energy and environmental policies, energy efficiency, energy risk

I. ORGANIZATION OF ENERGY AND ENVIRONMENTAL MANAGEMENT SYSTEMS

Improving the process of organizing energy transformation management and mitigating environmental impacts is a very important task for energy managers. The level of energy efficiency is significantly low compared to the expectations of the EU and the standards of developed countries. The management system [1] should be created with the aim of integrating the basic principles of sustainable energy development.

National regulations in the field of energy and environmental protection adhere to the requirements that are part of EU regulations, but this has not yielded the expected results. There are numerous problems in the implementation and practical application. The adopted directives are either not fully or not at all implemented in practice within energy and environmental management systems. Serbia needs to address numerous issues related to inefficient energy consumption and distribution, as well as the emission of pollutants, if there is a serious intention to join the EU. The government has allocated financial resources for the promotion and implementation of modern regulations, but misappropriation has led to the formation of an institutional organization that does not yield significant results.

Organizational systems have already been designed, but practical implementation is yet to produce the expected results. It is necessary to consider the size of fines and compare them with the average European financial penalties, as pollutant emissions occur in the same geographical area. Exceeding the limit values is not a rare occurrence in the energy sector, and cross-border emissions represent a serious problem for Serbia, a country that mainly relies on fossil fuels for energy supply.

Organizing energy and environmental management systems [2] should be based on compliance with international regulations, implementation of modern technologies, and efficient energy use, but accompanied by the definition of a mechanism for applying the proposed solutions. The assessment of the degree of organization of energy and environmental management systems (Fig. 1) depends on the degree of efficiency of enforcement of the Law

on Environmental Protection [3], the Law on Energy [4], the Law on Energy Efficiency and Rational Use of Energy [5], the Law on the Use of Renewable Energy Sources [6], and the Law on Inspection Supervision [7].

It is a prerequisite for the functioning of the energy and environmental management system to respect the principles of compliance, implementation, and effective enforcement of current national and adopted international regulations.

Serbia, as a country striving for EU membership, needs to fulfill the same goals as other members, since it creates energy and environmental policies based on the same principles.

Organizational problems in the functioning of energy and environmental management systems lead to a disruption of economic stability and environmental quality, to increased corruption, and to inappropriate management practices.

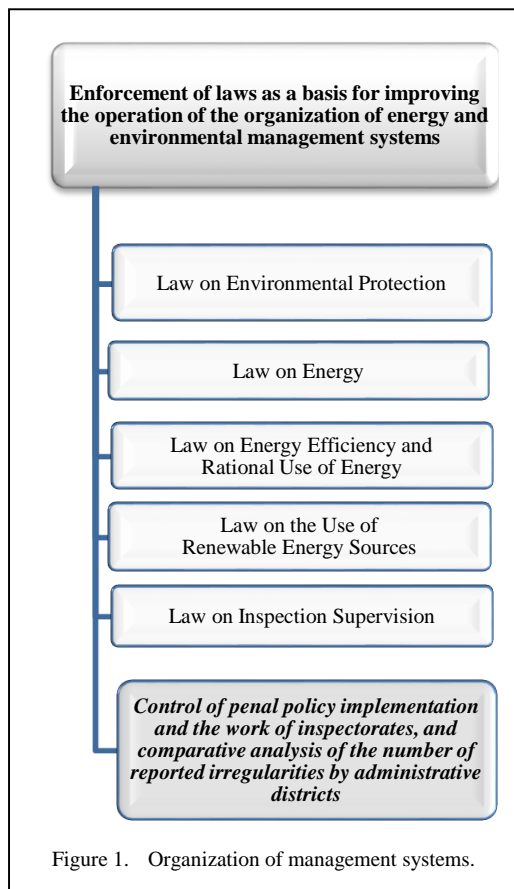


Figure 1. Organization of management systems.

Developed countries overcome organizational problems by increasing the level of responsibility for the implementation of adopted laws, energy, and environmental policies, for all organizational modes of state administration. It is necessary to ensure the efficient functioning of the judiciary system when assessing the task performance of competent authorities. Timely information sharing with the public about current energy and environmental issues aids in finding specific solutions.

The implementation of environmental protection activities is most often neglected due to the lack of financial resources, which contradicts the current legislative regulation. There is a real need for problem resolution by public prosecutors, whose special expertise would be based on multidisciplinary knowledge in numerous environmental fields, as is the case in developed countries.

II. ESTABLISHING A REAL BASIS FOR ENERGY AND ENVIRONMENTAL SYSTEM MANAGEMENT

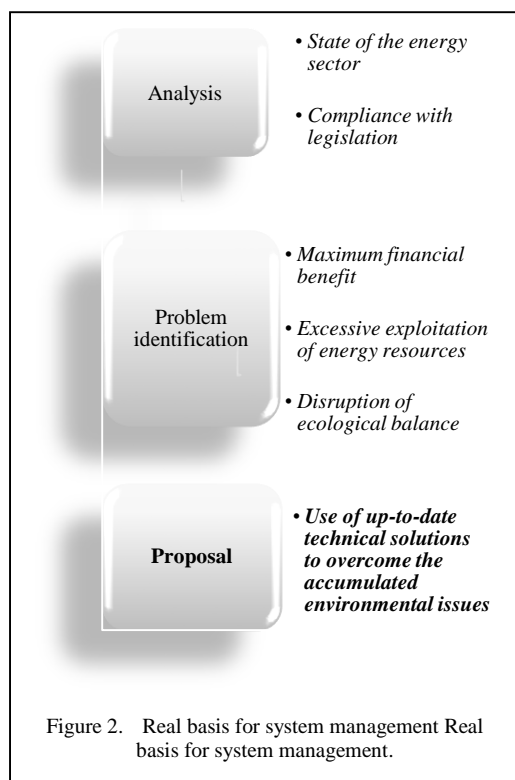
Managing the energy and environmental system in a modern and efficient manner provides an opportunity to exercise the constitutionally guaranteed right of people to live in a healthy environment. Rational use of non-renewable energy reserves, together with reduced use of fossil fuels and the degradation of air, water, and soil quality, can form a real basis for management. Problems arise when the pursuit of maximum economic benefits and the neglect of cross-border environmental pollution are placed ahead of the aforementioned model.

Achieving maximum economic benefits while preserving environmental quality is a guideline that leads to the achievement of the principles of sustainable energy development. A management system created in such a manner also provides a basis for managing the quality of water and air at the national and international levels.

Long-term investment in energy efficiency may ensure the provision of financial resources for solving potential and neglected environmental problems.

Problems arise when significant financial resources are required for the reclamation and remediation of land endangered by municipal, industrial, and radioactive waste.

The principle of energy production cost rationalization, mitigation of the consequences of energy reserve exploitation, and environmental degradation is not unattainable at the current level of development. The management system is largely disrupted by the implementation of the principle of maximum financial benefit, which was adhered to in previous decades. The expectation of the improvement of the energy and environmental management system should have a realistic basis (Fig. 2), which primarily involves solving accumulated environmental issues using additional financial resources. Failures related to the implementation of one of the basic principles of sustainable development, ‘the polluter pays’, are the main cause of the instability of the energy and environmental management system. The disrupted structure in the functioning of the management system can only be corrected through strict enforcement of legally prescribed norms and compliance with adopted regulations, without delay and acceptance of financial justifications. The management systems of modern states do not operate based on justifications but on the application of technical solutions to overcome existing problems of natural balance disruption and to meet the energy demands.



Support for the EU processes of energy source diversification, and assurance of supply security, energy efficiency, and decarbonization of the economy is carried out in cooperation with the Government of Serbia, so an improvement in the energy sector management system is to be expected.

III. FUNCTIONING OF ENERGY AND ENVIRONMENTAL MANAGEMENT SYSTEMS

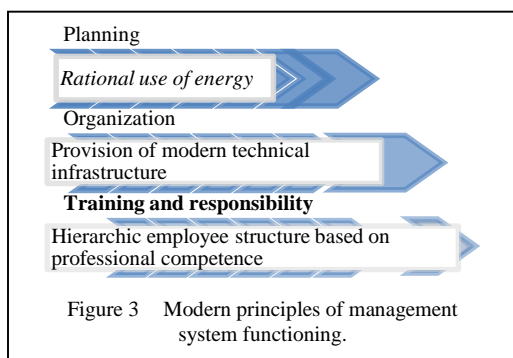
The Sector for Energy Efficiency and Renewable Energy Sources of the Ministry of Mining and Energy of the Republic of Serbia conducts strategic planning and coordination of the development of energy sectors at the national and local levels. It also prepares a professional foundation for drafting laws and proposals for sub-legal acts, harmonizing domestic regulations with EU regulations, drafting technical regulations in this field, as well as analyzing the effects of implementing these regulations [4]. It also plays a significant role in monitoring the impact of climate change in the energy sector, as well as in the implementation of environmental protection procedures.

Energy and environmental system management based on modern functioning principles (Fig. 3) involves the rational use of energy while preserving the quality of life, providing the necessary technical infrastructure, and creating a rational hierarchical structure of human resources based on professional competence and appropriate education.

Operation of the energy sector in line with modern management principles (Fig. 3), accompanied by the implementation of international standards ISO 50000, pertaining to energy management, and ISO 14000, pertaining to environmental quality management, shows promise.

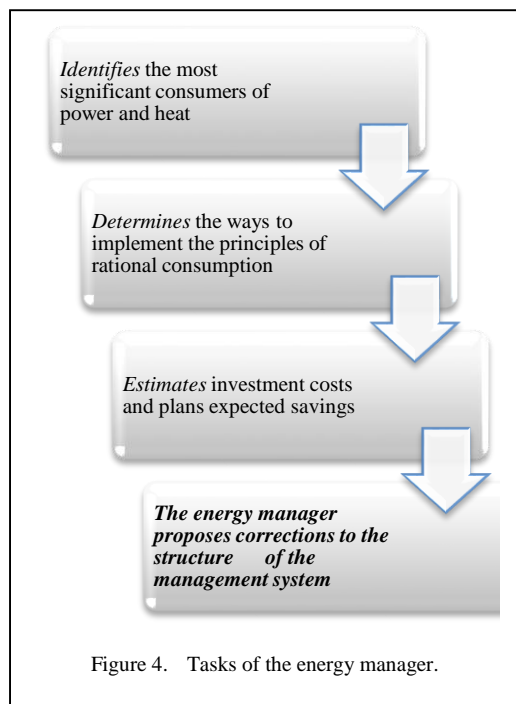
The Ministry of Environmental Protection performs tasks related to environmental protection and the functioning of the environmental protection and improvement system.

Cooperation with the Ministry of Mining and Energy is necessary in terms of availability of information to the representatives of the public, and in terms of solving problems of cross-border cooperation and air and water pollution [3], which is feasible through adherence to the aforementioned principles of management system functioning.



Adherence to the guidelines of the Law on Energy Efficiency and Rational Use of Energy [5] provides guidelines and proposes procedures on which the management system should be based. The Law emphasizes the importance of choosing an energy manager (Fig. 4), who should have a significant role in determining the rationality of energy transformations based on collected data on energy flows and financial investments. The energy manager should also plan financial investments in measurement devices for power metering, procurement of an information system for analyzing the collected data, improvement of the energy characteristics of buildings, and implementation of a modern management system.

Executing such complex tasks is possible only if care is taken to hire a highly qualified



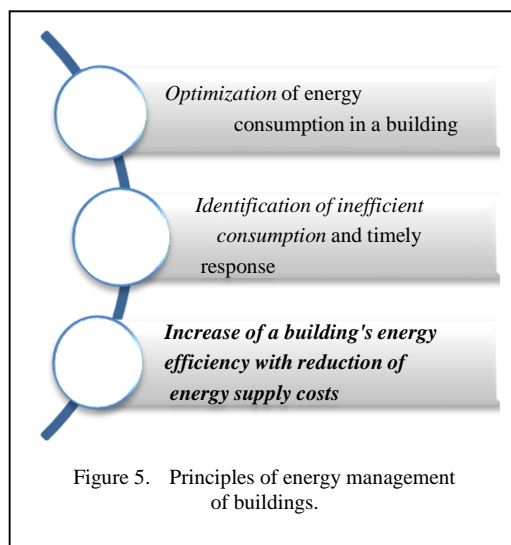
energy manager who is familiar with the basics of energy consumption systems, heat loss calculations, the operation of heating and cooling systems, and estimation of investment costs, and who possesses decision-making abilities, knowledge of organizational structure, computer skills, is able to use software applications, takes initiative, possesses communication skills, and is willing to improve their skillset [5,8]. An energy manager, if possessing the said characteristics and knowledge, can improve the structure of the energy management system based on the available infrastructure capacities and additional financial resources, effectively manage the implementation of the energy efficiency plan, participate in energy accounting, and monitor the management system.

The energy balance of the Republic of Serbia indicates the level of rationality in the use of energy, energy efficiency, and the use of renewable energy sources.

IV. ENERGY MANAGEMENT OF BUILDINGS

Managing the energy of a building, as one of the crucial tasks of an energy manager, is aimed towards integrated application of conventional and alternative energy sources to ensure the functioning of sustainable energy supply principles (Fig. 5). A multidisciplinary approach to problem-solving requires the collaboration of an energy manager with experts in the fields of mechanical engineering, civil engineering, architecture, and environmental protection.

As a result of successful collaboration of experts in various fields, the goal is to organize the energy management of a building and create



realistic energy efficiency plans based on advanced models of meeting energy needs, with rational use of non-renewable energy sources.

V. CONCLUSION

Organization of the energy and environmental management system, with implied adherence to the principles of rational use of energy resources and the preservation of air, water, and soil quality, is realistically achievable. This requires involving professional personnel, adopting a multidisciplinary approach, staying abreast of modern technical solutions, and complying with the legal requirements.

ACKNOWLEDGMENT

This paper was supported by the Ministry of Development and Innovation of the Republic of Serbia under the grant no. 451-03-47/2023-01/200148.

REFERENCES

[1] Arimura, T.H., Hibiki, A., & Katayama, H. (2008). Is a voluntary approach an effective environmental

policy instrument?: A case for environmental management systems. *Journal of Environmental Economics and Management*, 55(3), 281–295.

- [2] Zobel, T., 2016. The impact of ISO 14001 on corporate environmental performance: a study of Swedish manufacturing firms. *Journal of Environmental Planning and Management*, 59(4), 587–606.
- [3] *Law on Environmental Protection*, “Official Gazette of the RS”, no. 135/2004, 36/2009, 36/2009 – other law, 72/2009 – other law, 43/2011 – Constitutional Court decision, 14/2016, 76/2018, 95/2018 – other law, and 95/2018 – other law.
- [4] *Law on Energy*, “Official Gazette of the RS”, no. 145/2014, 95/2018 – other law, 40/2021, 35/2023 - other law and 62/2023, 2023.
- [5] *Law on Energy Efficiency and Rational Use of Energy*, “Official Gazette of the RS”, no. 40, 22 April, 2021, 2021.
- [6] *Law on the Use of Renewable Energy Sources*, “Official Gazette of the RS”, no. 40 from 22 April, 2021, no. 35 from 29 April, 2023, “Official Gazette of the RS”, no. 25/2013 and 40/2021 – other law.
- [7] *Law on Inspection Supervision*, “Official Gazette of the RS”, no. 36/2015, 44/2018 – other law and 95/2018, 2018.
- Rulebook on Energy Manager Training and Examinations*, “Official Gazette of the RS”, no. 117/2022, 2022.

CuO and CuO/ZnO Nanostructures in Biodiesel Production from Waste Cooking Oil

Philip Alexandre Araújo Ventura dos Santos¹, Elvia Leal², Isaac Anderson Alves de Moura³, Ana Cristina Figueiredo de Melo Costa⁴, Marta Célia Dantas Silva⁵, Joelda Dantas⁶

^{1,3,4,5,6}Federal University of Paraíba, João Pessoa - PB, Brazil

²Federal University of Campina Grande, Campina Grande - PB, Brazil

¹philip.santos@cear.ufpb.br, ⁶joelda.dantas@cear.ufpb.br

Abstract—Biodiesel is a clean biofuel as it is derived from biomass and is considered a renewable energy source. The raw materials can be based on oilseeds, animal fats and leftover frying oil. This potential also extends to the research and development of catalysts that can help increase the yield and speed of chemical reactions in production. Among them, the esterification reaction is used to obtain biodiesel. Thus, this work aimed to initially use the catalysts with 100% CuO and that with 80% CuO plus the addition of 20% ZnO as test parameters to produce biodiesel from waste cooking oil. The catalysts were synthesized by combustion reactions and characterized by X-ray diffraction (XRD), infrared spectroscopy (FTIR) and thermogravimetric analysis (TG). After the characterization of the catalyst, the remaining frying oil was converted into biodiesel by esterification. Finally, the catalyst efficiency was verified by gas chromatography analysis and the residue was converted into biodiesel converting 17.95% for the sample with CuO and 80.4% for the sample with CuO80/ZnO20. The results of structural and thermal characterization indicate that the metal oxides used as catalysts have sufficient performance for biodiesel production.

Keywords - biodiesel, residual oil, oxides, combustion

I. INTRODUCTION

Discussions on fuel consumption and/or CO₂ emissions pose serious challenges for reducing greenhouse gases (GHG) and achieving peak neutralization of toxic emissions. Limited

reserves of fossil fuels, such as oil, and global warming caused by excessive carbon dioxide (CO₂) emissions have stimulated demand for alternative and sustainable energy sources around the world, indicating a growing interest in the transition to alternative fuels. Renewable, sustainable and environmentally friendly. With this in mind, it is important to consider the economic and market forces that influence the adoption rates of energy technologies [1].

Biodiesel, which is an alternative to fossil fuel, is an important source of sustainable energy and has therefore received considerable attention in global energy crisis scenarios. Biodiesel has been gaining popularity and prominence for its advantages such as being able to be produced from vegetable oils, animal fats and a wide variety of wastes, emerging as a viable solution. Biodiesel is a renewable fuel obtained commercially from a chemical process called transesterification. Through this process, the triacylglycerides present in oils and fats react with a primary alcohol, methanol or ethanol, generating two products, the ester and crude glycerin, in the presence of a catalyst [2].

Large amounts of food waste are produced worldwide through agricultural processing, food transportation and storage as well as daily human consumption. The valorization of food waste into a spectrum of marketable products represents a promising strategy to deal with waste while addressing the objectives of a sustainable development, i.e. food security, environmental

protection and energy efficiency [1]. Among the widely produced food waste is oil from frying processes. In the specialized literature there are relevant studies using this source as a raw material in the production of biodiesel [3,4].

A catalyst is used to accelerate the transesterification or esterification reaction to produce biodiesel. A homogeneous catalyst is found in the same phase as the reactants, in liquid form, and there are two different types of homogeneous catalysts, acidic and alkaline. The difficulty of recovering homogeneous catalysts, either acid or alkaline, means that reuse in a new reaction does not happen, thus losing the catalyst, and thus causing the cost of its replacement and the high cost of water for washing biodiesel, demonstrating a great economic disadvantage [5].

In order to reduce costs, new technologies are being developed using heterogeneous catalysis. This type of catalyst has both acidic and basic properties. This group includes simple oxides, impregnated oxides, supported oxides, mixed oxides, laminar double hydroxides, inorganic complexes, among others. For industries producing biodiesel on a large scale, heterogeneous catalysts will help reduce biodiesel production costs, as they avoid wasting wastewater on washing the biodiesel. A very important advantage is that the catalyst and biodiesel can be easily separated by the Biodiesel. The process is simple, filterable, recyclable and reusable in other transesterification or esterification reactions in the future; thus avoiding the waste of catalyst [6].

CuO has acidic properties and low reduction temperature, as well as a low cost compared to other metal oxide nanoparticles, which favors heterogeneous catalysis applications. This attribute is directly related to the fact that the CuO compound is a semiconductor of the type p having a characteristic of donating electrons since transition metals have their valence shell filled [7].

Nano-structured materials are increasingly being used in studies, due to their magnetic, electrical, mechanical, optical and chemical properties. Among these, zinc oxide is very promising, mainly because it presents physical-chemical characteristics, which allow this material to be used as a catalyst [8].

In this context, there are still few studies on the efficiency of the esterification reaction for the

production of biodiesel from frying oil using heterogeneous catalysts obtained from combustion reactions, so this work aims to provide results that are satisfactory for developing this type of technology. Among the viable alternatives of heterogeneous catalysts and efficient methods for obtaining them, this work was aimed at synthesizing copper oxide (CuO) and zinc oxide (ZnO) through the combustion reaction for use in the production of biodiesel, using as raw material residual cooking oil. Therefore, it is expected to contribute to the sum of studies involving efficient chemical methods, economically viable and sustainable products, to be used by academia and industry.

II. METHODOLOGICAL PROCESSES

A. Synthesis of CuO

To obtain nano-structured copper oxide (CuO), copper II trihydrate nitrate ($\text{Cu}(\text{NO}_3)_2 \cdot 3\text{H}_2\text{O}$) as the oxidizing material and urea $\text{CO}(\text{NH}_2)_2$ as the fuel, in the following proportions: 120.3 grams of copper II nitrate Trihydrate and 48.87 grams of urea. The solution of copper II nitrate trihydrate and urea was prepared and mixed homogeneously in a container.

The CuO catalyst was synthesized using the combustion reaction method, which is based on the theory of propellants and explosives [9]. The container containing the solution was placed over a ceramic furnace with an internal electric heating element, and the zinc nitrate and urea sample was heated until it ignited. The duration of the flame and the time for the combustion reaction to occur were measured using a pyrometer, and the color of the flame was recorded using a digital camera. Due to the release of gases from the combustion process, the procedure was carried out in an exhaust hood.

The reaction product was manually deagglomerated with the aid of a mortar and pestle, then sieved through a 325-mesh and taken for characterization (X-ray diffraction (XRD), infrared spectroscopy (FTIR) and thermogravimetric analysis (TG)).

B. Synthesis of ZnO

The reaction to obtain zinc oxide (ZnO) was similar to that carried out for CuO. To obtain nano-structured ZnO, zinc nitrate hexahydrate ($\text{Zn}(\text{NO}_3)_2 \cdot 6\text{H}_2\text{O}$) was used as the oxidizing material and urea ($\text{Zn}(\text{NO}_3)_2 \cdot 6\text{H}_2\text{O}$) as the fuel,

in the following proportions: 113.48 grams of zinc nitrate hexahydrate and 38.09 grams of urea.

Similarly, to the preparation of CuO, the method used to prepare the ZnO catalyst was combustion synthesis. The container containing the solution was placed over a ceramic furnace with an internal electric heating element, and the sample of zinc nitrate and urea was heated. The combustion reaction took place in a chapel due to the gases released. The ZnO was deagglomerated using a mortar and pestle, then passed through a 325-mesh sieve and sent for characterization.

After obtaining the copper and zinc oxides, ZnO was added to the CuO in the proportion of 20% ZnO and 80% CuO, which was called CuO80/ZnO20, and the sample with 100% CuO, which was called CuO100, was used for comparison purposes. Both samples were used to carry out heterogeneous catalysis in the production of biodiesel from used cooking oil.

C. Synthesis of Biodiesel

The synthesis of biodiesel was carried out from the esterification reaction, using residual frying oil, which was raw material from pastry shops located in the city of João Pessoa/PB, also methyl alcohol with 99.8% purity, in addition to the CuO and ZnO samples with the addition of ZnO as heterogeneous catalysts.

The frying oil was passed through filter paper in order to remove suspended materials that could compromise esterification. After the filtration process, 30 g of oil was separated for use in esterification. The tests were carried out in a stainless steel reactor with a capacity of 100 mL, which contains a borosilicate beaker, in a pressurized condition and composed of a thermocouple inlet duct and coupled to a glycerin manometer. The system was stirred and heated by a magnetic stirring plate. The reaction temperature was 180°C, the alcohol:oil ratio was 15:1, the catalyst:solution ratio was 3:100 and the reaction time was 1 hour. The product obtained in the esterification reaction was transferred to a separating funnel where it remained until the separation of ester and water was observed. It was also washed with distilled water to remove impurities.

After the washing was completed, the reaction product was centrifuged for 30 minutes at 9000 RPM's in order to separate remaining water and/or catalyst residues that could still be present in the biodiesel. After this step, the reaction product was packed in amber tubes to be

stored at a temperature between 6 and 10°C, and separated aliquots in 1.5 mL eppendorf, for analysis by gas chromatography.

III. RESULTS AND DISCUSSION

The combustion flame time and temperature are essential parameters that influence the transition of reactants into products in the course of the combustion reaction synthesis process. The flame temperature varies from material to material, the characteristic of the reagent, the purity and the amount used, will impact the reaction speed, and, consequently, the temperature and the combustion flame time, which will determine the structural and morphological characteristic of the final product [10].

Table I shows the values obtained during the combustion synthesis of CuO and ZnO, respectively. The flame time, time for combustion reaction to occur, ignition temperature, flame temperature and flame color were measured and observed.

In general, it was observed that the time taken for the CuO combustion reaction to occur was shorter than the time taken for the ZnO combustion reaction to occur. In addition, the maximum reaction temperature was higher for

TABLE I. PARAMETERS OBTAINED IN THE SYNTHESIS BY COMBUSTION REACTION TO OBTAIN CuO AND ZnO NANOSTRUCTURES.

Parameters	CuO	ZnO
Time for combustion reaction to occur, minute	10	20
Maximum synthesis temperature, °C	801	541
Flame time, second	2	2
Flame color	green	yellow

CuO, so its heat of formation was higher than the heat of formation of ZnO.

Regarding the flame color parameter, it was possible to observe during the progress of the combustion reactions, a change in the color of the flame, from yellow in the ZnO reaction to greenish in the CuO reaction. Therefore, considering that in the color spectrum the energy varies inversely proportional to the wavelength, so that in the range of the visible spectrum, which varies from 400 nm and 700 nm, the colors transit between violet and red, then, based on this theory, it is that the violet color generates greater energy than the red color. If the ratio of energy released in terms of heat is realized, a red flame will be less hot than a violet flame, so it is possible to conclude that green is hotter than yellow because it has a shorter wavelength, and consequently will generate more energy [5,6].

The diffractograms and the X-ray diffraction pattern of the CuO100 and CuO80/ZnO20 samples are illustrated in Figs. 1 and 2, which shows the peaks referring to CuO and ZnO, corroborating the research disseminated in the specialized literature and indicating that the synthesis used to obtain these metal oxide samples was successful.

All diffraction peaks are well defined, indicating the formation of crystalline phase with a high long-range organization. The presence of two CuO phases can also be observed, which may possibly have resulted from the combustion process [6].

The X-ray diffraction plots show the characteristic peaks that indicate the formation of the crystal structure of CuO, as shown in Fig. 1. The main 2θ angles referring to this oxide were 32.4° ; 35.5° ; 38.7° ; 48.8° and 66.2° [7,11].

The formation of the crystal structure of ZnO present in the CuO80/ZnO20 sample was observed, as shown in Fig. 2. It was possible to observe the formation of the characteristic patterns of ZnO, and the main 2θ angles for this sample were 31.85° ; 34.55° ; 36.36° ; 47.5° ; 56.6° ; 62.9° and 69.0° [8,12].

The X-ray diffraction confirmed the formation of nanoparticles for both samples used as catalysts. Table II lists the crystallinity percentage and crystallite size of the samples.

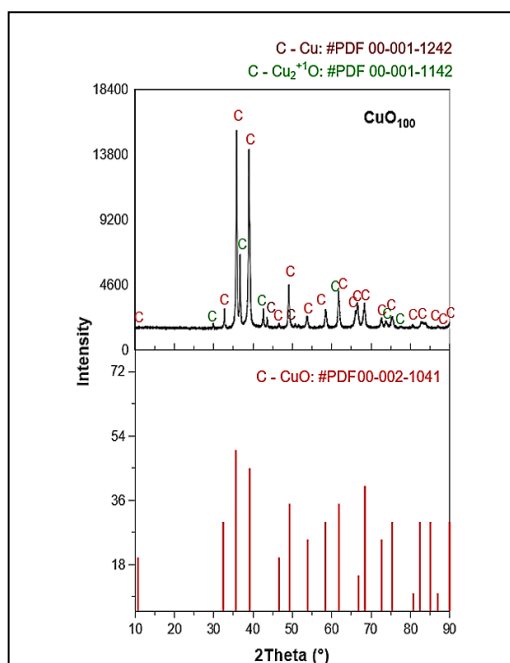


Figure 1. DRX diffractograms of the samples: CuO100.

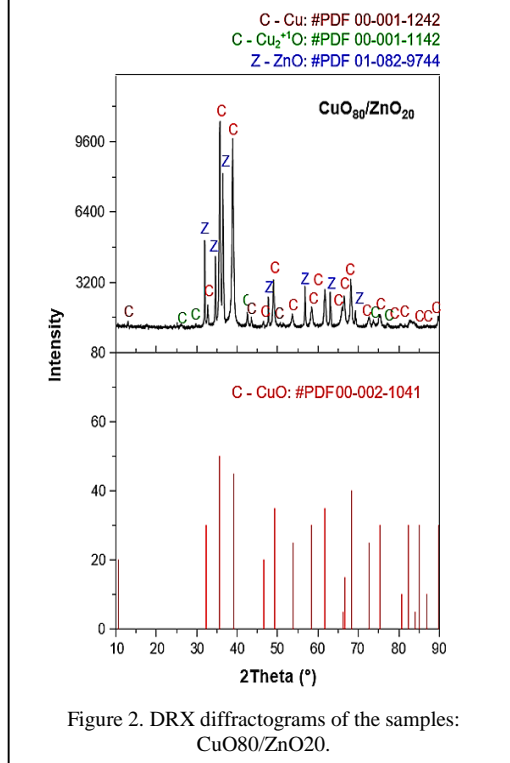


Figure 2. DRX diffractograms of the samples: CuO80/ZnO20.

TABLE II. RESULT OF THE CRYSTALLINITY OF THE CATALYSTS.

Sample	Crystallinity (%)	Crystallite size (nm) ⁽¹⁾
CuO100	83.6	30.95
CuO80/ZnO20	83.3	30.22

(1) Nanometers

In general, smaller changes in crystallite size were observed, ranging from 30.22 to 30.95 nm. therefore, nanoscale crystallites can be obtained without additional sintering, confirming the efficiency of the combustion reaction method for the synthesis of these materials.

The efficiency of this method in obtaining powders with nano characteristics, with grain sizes ranging from 12 to 45 nanometers, was also demonstrated through combustion reactions [13].

As for the crystallinity of the samples, it was also observed that due to the structural organization and periodicity of the crystals within the network, they show values close to 82.8% to 83.6%. In all cases, the combustion reaction process proved to be an excellent technique for obtaining nanoscale catalysts.

These results were confirmed by the characteristic bands obtained by FTIR. Figs. 3 and 4 show the vibrational spectra in the infrared region with the absorption conditions.

It can be observed in Fig. 3 a vibration in the range of 500-603 cm^{-1} , this occurs due to the presence of CuO. These bands confirm the formation of the phase [14,15].

It was also observed in the spectra referring to the two synthesized samples, the presence of a band in a band above 3500 cm^{-1} , characteristic of O-H-O bonds, attributed to the presence of water in the samples, which may come from surface adsorption by the humidity of the atmospheric air and also due to the KBr used in the preparation for analysis, which has a great facility to absorb moisture [16].

It was also observed that, in addition to the O-H-O bands, there is the presence of the O-H group in a band located around 1500 cm^{-1} that can be attributed to the vibrations referring, respectively, to the stretching and folding of the hydroxyls of the water molecules adsorbed on

the surface, thus proving the presence of water [6].

Fig. 4 shows the infrared spectroscopy of the CuO80/ZnO20 sample, with the absorbance conditions. Similarly to the CuO100 sample, the CuO80/ZnO20 sample shows vibrations in the range of 450-550 cm^{-1} , confirming the presence of the CuO molecule. The bands around 400-650 cm^{-1} are attributed to the stretching of ZnO, showing the formation of this phase [17–19]. Bands observed between 1250 cm^{-1} and 2400 cm^{-1} are attributed to the stretching of

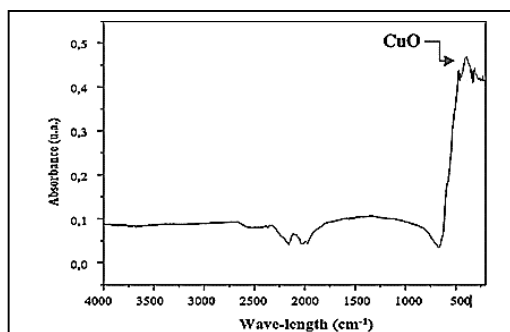


Figure 3. Infrared spectroscopy of the CuO100 sample in the absorbance condition.

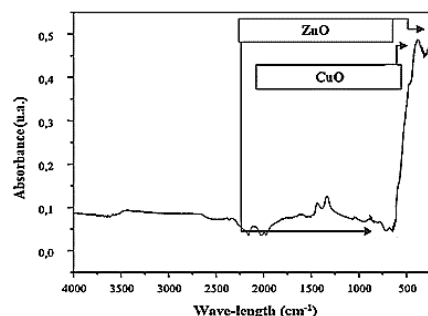


Figure 4. Infrared spectroscopy of the CuO80/ZnO20 sample under absorbance condition.

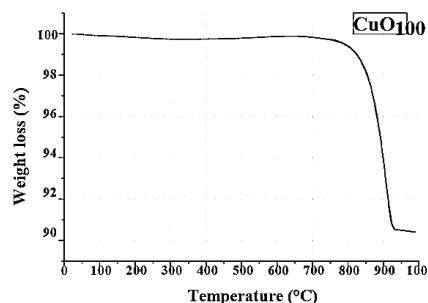


Figure 5. Curve obtained in the thermal analysis of the CuO100 sample.

the C-C, C=O, C-O of aromatics in the ring and the strain deformation NH₂ bonds and the bands observed in the regions near 3420 cm⁻¹ and 3800 cm⁻¹ are from the stretching of the OH group [20–22].

It can be stated that the CuO100 sample presented a good thermal stability, losing 1% of its mass until reaching the temperature of 700°C to 900°C, where from this point there is a decomposition of copper oxide, which provides a loss of 8,5% of the mass of the sample represented in Fig. 5. Showing excellent thermal stability, as in [23,24].

Fig. 6 shows the thermal analysis of CuO80/ZnO20. The material has excellent thermal stability with a mass loss of 1% in the range of 50°C to 300°C and a mass loss of 7% in the range of 700°C to 900°C. The temperature range from 50°C to 250°C corresponds to the continuous evaporation of solvents, including water [25,26].

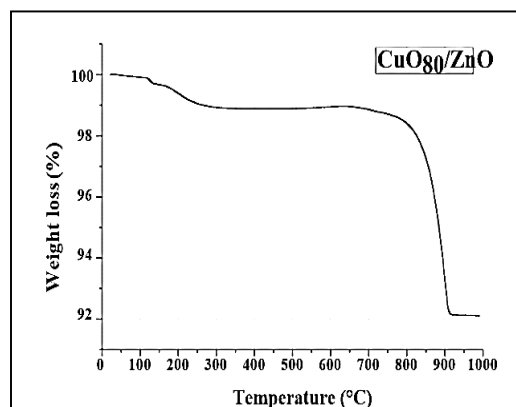


Figure 6. Curve obtained from the thermal analysis of the CuO80/ZnO20 sample.

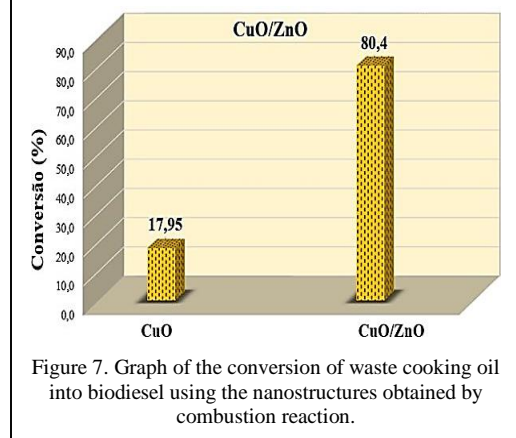


Figure 7. Graph of the conversion of waste cooking oil into biodiesel using the nanostructures obtained by combustion reaction.

IV. ANALYSIS OF THE CONVERSION OF WASTE COOKING OIL INTO BIODIESEL

The process of conversion of waste frying oil into ester was carried out through the esterification process via the methyl route. Fig. 7 shows the results obtained by using the CuO100 and CuO80/ZnO20 samples tested as catalysts.

It was observed that the CuO100 sample obtained 17.95% conversion, this can possibly be attributed to the presence of few active or accessible chemical sites, not reaching the minimum kinergy to initiate a more satisfactory chemical reaction, causing part of the catalyst to not participate effectively during the reaction, even though it is reported that this type of material has a considered surface area, a characteristic that is important to act as a good catalyst [5].

On the other hand, a significant increase in the conversion rate was observed when ZnO is mixed with CuO. The CuO80/ZnO20 sample showed a positive conversion of waste cooking oil into biodiesel, reaching 80.4%. This result is due to the addition of ZnO in the CuO sample, which possibly increased the presence of active chemical sites for the occurrence of catalysis. Recent work [27] basic surface sites, which makes them very efficient in catalytic processes.

According to the results obtained, it can be concluded that the use of ZnO added to CuO contributes to significant conversion of waste oil into methyl esters, and that the production of this important biofuel was successful for the initial tests under the reaction conditions adopted and tested. However, optimization studies of the independent variables are being developed in order to obtain higher conversion rates in biodiesel, until reaching the minimum limit regulated by the National Agency of Petroleum, Natural Gas and Biofuels (ANP).

V. CONCLUSION

Heterogeneous catalysis presents advantages in the reduction of processes in the production of biodiesel and has a reduction of costs in the industry, however, it needs the development of technologies to improve the techniques for obtaining heterogeneous catalysts, and the combustion reaction is an excellent alternative to produce suitable nanostructures. The presence of ZnO concentration added to CuO improved the conversion rate by 62.45%, probably due to the increased presence of active chemical sites that favor heterogeneous catalysis. The objective of

the work was achieved, since the nanostructures of metal oxides obtained by combustion reaction and used as catalysts, presented relevant characteristics evidenced by characterization techniques. Moreover, the conversion of used cooking oil into biodiesel, 80.4%, was very expressive for the initial tests under the adopted conditions, showing that the addition of a dopant can benefit the catalytic reaction and revealing promising results for its use in biodiesel production. In view of this, the expectation is to contribute to obtaining nanostructured materials with suitable characteristics for application in the production of biodiesel by the use of residual raw material, and thus promote sustainability and a considered cost benefit, providing the maintenance of a healthy environment. Future work is being focused on providing more suitable reaction conditions to increase the conversion rate to biodiesel up to at least 96.5%, as governed by the ANP.

The nanoparticles studied can be used in other studies as battery components, photocatalyzers and impurity removers, among other research. Feasibility studies will be developed to prove the reduction in costs with the heterogeneous catalysis process.

ACKNOWLEDGEMENTS

The authors thank PNP/CAPE/CNPq, process number (88882.317968/2019-01), and PNP/FAPE/SQ/PB (N°1990/2022, Edital N°17/2022), beneficiary program (24001015072P9-Renewable Energy), for the financial support for financial support.

The authors acknowledge the financial support of the Postgraduate Research Grant, grant 16/2022, Paraíba State Research Foundation (FAPE/SQ), Program 22210.12.573.5011.1998, line 3390.18 of the Source 500.

REFERENCES

[1] Karakurt, I. & Aydin, G. (2023). Development of regression models to forecast the CO₂ emissions from fossil fuels in the BRICS and MINT countries. *Energy*, 263, 125650.

[2] Dantas, J., Leal, E., Comejo, D.R., Kiminami, R.H.G.A., & Costa, A.C.F.M. (2020). Biodiesel production evaluating the use and reuse of magnetic nanocatalysts Ni_{0.5}Zn_{0.5}Fe₂O₄ synthesized in pilot-scale. *Arabian Journal of Chemistry*, 13(1), 3026–3042.

[3] Bhonsle, A.K., Singh, J., Trivedi, J., & Atray, N. (2022). Comparative LCA studies of biodiesel produced from used cooking oil using conventional

and novel room temperature processes. *Bioresource Technology Reports*, 18, 101072.

- [4] Dantas, J., Leal, E., Mapossa, A.B., Pontes, J.R.M., Freitas, N.L., Fernandes, P.C.R., et al. (2021). Biodiesel production on bench scale from different sources of waste oils by using NiZn magnetic heterogeneous nanocatalyst. *International Journal of Energy Research*, 45(7), 10924–10945.
- [5] Dantas, J., Leal, E., Mapossa, A.B., Comejo, D.R., & Costa, A.C.F.M. (2017). Magnetic nanocatalysts of Ni_{0.5}Zn_{0.5}Fe₂O₄ doped with Cu and performance evaluation in transesterification reaction for biodiesel production. *Fuel*, 191, 463–471.
- [6] Dantas, J., Leal, E., Mapossa, A.B., Silva, A.S., & Costa, A.C.F.D.M. (2016). Synthesis, characterization and catalytic performance of mixed nanoferrites subjected to transesterification and esterification reactions via methyl and ethyl routes for biodiesel. *Matéria (Rio de Janeiro)*, 21(4), 1080–1093.
- [7] Amirsoleimani, A.R., Siampour, H., Abbasian, S., Rad, G.B., Moshaii, A., & Zaradshan, Z. (2023) Copper oxide nanocolumns for high-sensitive non-enzymatic glucose sensing. *Sensing and Bio-Sensing Research*, 42, 100589.
- [8] Selvaraj, B., Karnam, J.B., & Rayappan, J.B.B. (2023). Effect of chromium dopant on electrospun zinc oxide nanostructure: A room temperature ethanol sensor. *Ceramics International*, 49(23), 37106–37117.
- [9] Jain, S.R., Adiga, K.C., and Pai Verneker, V.R. (1981). A new approach to thermochemical calculations of condensed fuel-oxidizer mixtures. *Combustion and Flame*, 40, 71–79.
- [10] Dantas, J., Leal, E., and Costa, A.C.F. de M. (2021). *Ceramic nanomaterials by combustion reaction*. 1st ed. Poisson.
- [11] Gnatenko, Yu.P., Bukivskij, P.M., Gamernyk, R.V., Yevdokymenko, V.Yu., Opanasyuk, A.S., Bukivskii, A.P., et al. (2023) Study of optical and photoelectric properties of copper oxide films. *Materials Chemistry and Physics*, 307, 128175.
- [12] Salem, M., Ghannam, H., Almohammed, A., Salem, J., Rashid Bouazzi, I., Massoudi, I., et al. (2023). Improved photoelectrochemical sensitivity of Al-doped ZnO nanostructure prepared by co-precipitation and spin-coating techniques. *Materials Letters*, 352, 135085.
- [13] Leal, E., Dantas, J., Santos, P.T.A.D., Bicalho, S.M.D.C.M., Kiminami, R.H.G.A., Da Silva, M.R., et al. (2018). Effect of the surface treatment on the structural, morphological, magnetic and biological properties of MFe₂O₄ iron spinels (M = Cu, Ni, Co, Mn and Fe). *Applied Surface Science*, 455, 635–645.
- [14] Qamar, H., Rehman, S., Chauhan, D.K., Tiwari, A.K., & Upmanyu, V. (2020). Green Synthesis, Characterization and Antimicrobial Activity of Copper Oxide Nanomaterial Derived from Momordica charantia. *International Journal of Nanomedicine*, 15, 2541–2553.
- [15] Yang, N., Guo, H., Cao, C., Wang, X., Song, X., Wang, W., et al. (2021). Infection microenvironment-activated nanoparticles for NIR-II photoacoustic imaging-guided photothermal/chemodynamic synergistic anti-infective therapy. *Biomaterials*, 275, 120918.

- [16] Noor, T., Pervaiz, S., Iqbal, N., Nasir, H., Zaman, N., Sharif, M., et al. (2020). Nanocomposites of NiO/CuO Based MOF with rGO: An Efficient and Robust Electrocatalyst for Methanol Oxidation Reaction in DMFC. *Nanomaterials*, 10(8), 1601.
- [17] Munawar, T., Iqbal, F., Yasmeen, S., Mahmood, K., & Hussain, A. (2020). Multi metal oxide NiO-CdO-ZnO nanocomposite—synthesis, structural, optical, electrical properties and enhanced sunlight driven photocatalytic activity. *Ceramics International*, 46(2), 2421–2437.
- [18] Ahmad, M., Rehman, W., Khan, M.M., Qureshi, M.T., Gul, A., Haq, S., et al. (2021). Phyto-genic fabrication of ZnO and gold decorated ZnO nanoparticles for photocatalytic degradation of Rhodamine B. *Journal of Environmental Chemical Engineering*, 9(1), 104725.
- [19] Faisal, S., Jan, H., Shah, S.A., Shah, S., Khan, A., Akbar, M.T., et al. (2021). Green Synthesis of Zinc Oxide (ZnO) Nanoparticles Using Aqueous Fruit Extracts of Myristica fragrans: Their Characterizations and Biological and Environmental Applications. *ACS Omega*, 6(14), 9709–9722.
- [20] Karthik, K.V., Raghu, A.V., Reddy, K.R., Ravishankar, R., Sangeeta, M., Shetti, N.P., et al. (2022). Green synthesis of Cu-doped ZnO nanoparticles and its application for the photocatalytic degradation of hazardous organic pollutants. *Chemosphere*, 287, 132081.
- [21] Panchal, P., Paul, D.R., Sharma, A., Choudhary, P., Meena, P., & Nehra, S.P. (2020). Biogenic mediated Ag/ZnO nanocomposites for photocatalytic and antibacterial activities towards disinfection of water. *Journal of Colloid and Interface Science*, 563, 370–380.
- [22] Muthuvel, A., Jothibas, M., & Manoharan, C. (2020). Effect of chemically synthesis compared to biosynthesized ZnO-NPs using Solanum nigrum leaf extract and their photocatalytic, antibacterial and in-vitro antioxidant activity. *Journal of Environmental Chemical Engineering*, 8(2), 103705.
- [23] Veisi, H. (2021). Biosynthesis of CuO nanoparticles using aqueous extract of herbal tea (*Stachys Lavandulifolia*) flowers and evaluation of its catalytic activity. *Scientific Reports*.
- [24] Cherubin, M.R., Carvalho, J.L.N., Cerri, C.E.P., Nogueira, L.A.H., Souza, G.M., & Cantarella, H. (2021). Land Use and Management Effects on Sustainable Sugarcane-Derived Bioenergy. *Land*, 10(1), 72.
- [25] Nagarani, S., Sasikala, G., Yuvaraj, M., Kumar, R.D., Balachandran, S., & Kumar, M. (2022). ZnO-CuO nanoparticles enameled on reduced graphene nanosheets as electrode materials for supercapacitors applications. *Journal of Energy Storage*, 52, 104969.
- [26] Yadav, R., Chundawat, T.S., Surolia, P.K., & Vaya, D. (2022). Photocatalytic degradation of textile dyes using β -CD-CuO/ZnO nanocomposite. *Journal of Physics and Chemistry of Solids*, 165, 110691.
- [27] Baskar, G. & Soumiya, S. (2016). Production of biodiesel from castor oil using iron (II) doped zinc oxide nanocatalyst. *Renewable Energy*, 98, 101–107.

Challenges and Potential Applications of the Renewable Energy for Desalination

Ammar Zeghloul¹

¹Laboratory of Fundamental and Applied Sciences (LSFA), Polytechnic National School, BP 182, El Harrach, Algiers 16200, Algeria

¹ammar.zeghloul@g.enp.edu.dz

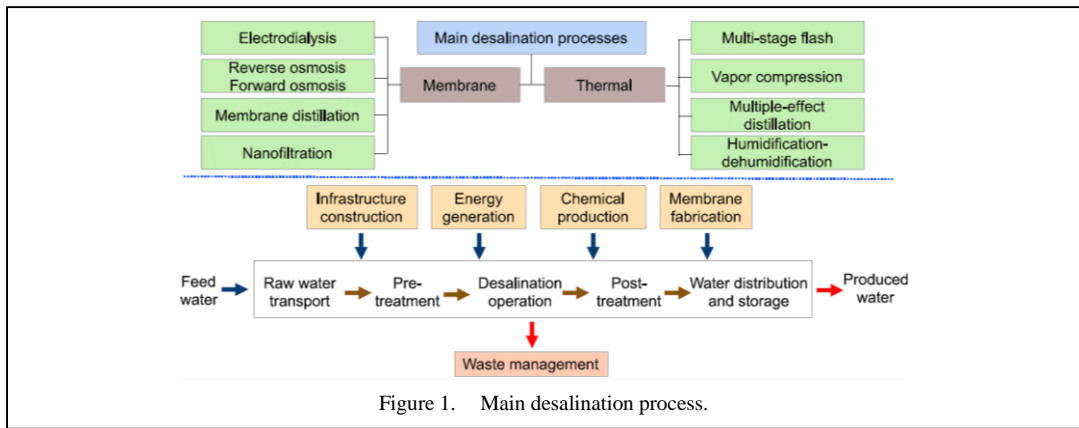
Abstract—The countries in the world are quickly rising in population while having relatively limited access to freshwater resources. Because many nations have ready access to saline water, saltwater desalination is offered as a viable solution to this problem. However, desalination procedures have a high energy consumption, which is usually fulfilled by fossil-fuel-powered power plants. Desalination capacity has dramatically increased over the previous decade as a result of excellent scientific advancements in desalination technology, particularly in RO infrastructure, resulting in a significant reduction in the expense of water from desalination and growing water demand. Other factors, like as grants or local promotions, may cause a significant variation in generated water costs across different locations and facilities, despite investment and operational costs. In the present work, several proposals have been made to identify future research routes and reduce water final costs. Current improvements that have resulted in a substantial drop in both cost and energy usage include the utilization of integrated systems that utilize renewable energy sources, breakthroughs in material and process design, and increased unit capacity. The advent of cutting-edge desalination technology in the future may have a significant impact on the computation of cost disparities.

Keywords – reverse osmosis, renewable energy, water, desalination, hybrid systems

I. INTRODUCTION

Global population expansion, along with increased industrial and agricultural activity, has ultimately resulted in the depletion and pollution of fresh water supplies [1]. While fresh water

supplies are depleted, alternate water supply solutions must be identified and implemented. Seawater may be used for human consumption as well as industrial and agricultural applications. However, seawater can be desalted and delivered in huge amounts, desalination has become a significant technique in addressing the problem of fresh water shortage. Although it offers a stable water supply to many locations throughout the world, seawater desalination is a mature technology that contributes to a higher level of life. The standard desalination procedure for creating freshwater from saltwater is shown in Fig. 1. In overall, desalination of seawater needs the construction of a plant for desalination as well as pipeline transportation facilities for water transfer from a coastal area to the interior. A saltwater desalination plant is being built along the seashore to treat seawater and create freshwater for human use. Seawater's salty content is decreased to make it safe for people to drink. Pumping, water distribution, and the movement of saltwater via membranes in the microfiltration and reverse osmosis processes all need energy generation. Chemical components are necessary for a variety of processes such as disinfection, chlorine removal, membrane cleaning, mineralization, and potabilization [2-4]. The growing importance and quick spread of desalination technology has also generated concerns about the long-term availability of fresh water. Land use change, repercussions on the marine environment, energy usage, and noise pollution were all possible environmental consequences of desalination technology. In light of this, a suitable solution including



environmental impact measurements into the desalination process is required. Desalination is a high-energy process, with the bulk of desalination facilities relying on fossil fuels as their primary energy source [5]. For a variety of reasons, this is no longer a viable choice. One of the most important causes is the serious environmental consequences and toxic emissions caused by fossil fuels [6].

The purpose of this paper is to examine efficiently drive desalination operations. In part 2, the discussion begins with a summary of the primary desalination processes, with an emphasis on well-established technologies such as reverse osmosis as the benchmark membrane desalination technique. The benchmark thermal desalination techniques have been multistage flash distillation MSF and multi-effect distillation MED. In section 3, the present study provides a much broader view on the cost analysis of desalination systems, analyzes several issues related with the economic feasibility of desalination, and considers future challenges and opportunities for cost-competitive desalination.

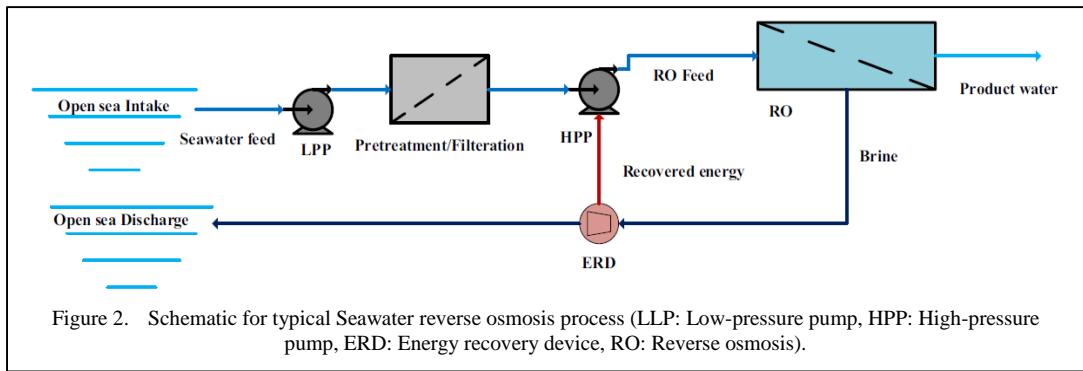
II. DESALINATION PROCESSES

A broad variety of desalination techniques have been created, each one having its own driving force and operating principles [7]. As a result, several categories may be used to categorize such processes. Based on their operational principles, desalination systems are classified as thermal, membrane, or other processes. Thermal treatments use heat or drainage to create freshwater separation in combination with phase change. In its most basic concepts, thermal processes imitate the natural water cycle, in which solar thermal energy causes water evaporation from enormous amounts of

water such as seas and oceans, subsequently followed by condensation and precipitation. Examples of thermally-driven desalination processes involve multistage flash distillation (MSF), multi-effect distillation (MED), thermal vapor compression (TVC), membrane distillation (MD), adsorption desalination (AD), humidification/dehumidification (HDH), and freeze desalination (FD). Mechanically-driven desalination methods use pressure to separate water molecules across a semi-permeable tight membrane. Reverse osmosis (RO), nanofiltration (NF), and pressure-assisted osmosis (PAO) are all examples of osmosis. On the other hand, like in mechanical vapor compressions (MVC), the pressure can be reduced to increase water vaporization.

A. Reverse Osmosis (RO)

RO is the most widely used desalination process worldwide, meaning that saline water is pressurized and pushed to flow through a narrow semi-permeable membrane that limits the flow of solutes and permeates water. The saline water is pressed to a value greater than the osmotic pressure in order to extract product water via the RO membrane, leaving behind a higher concentration stream known as brine, reject, or concentrate, which is charged back to the sea. The operating pressure for seawater reverse osmosis (SWRO) is normally between 50 and 70 bars, which must be greater than the brine stream's osmotic pressure. At the moment, the most common membrane types are cellulose acetate/triacetate (CA/CTA) or thin-film composite membrane (TFC), which is composed mostly of a polyamide active layer atop a polysulfone support layer. As shown in Fig. 2, a typical SWRO plant includes intake, pretreatment, high-pressure pumps, RO modules, an energy recovery device (ERD), and product



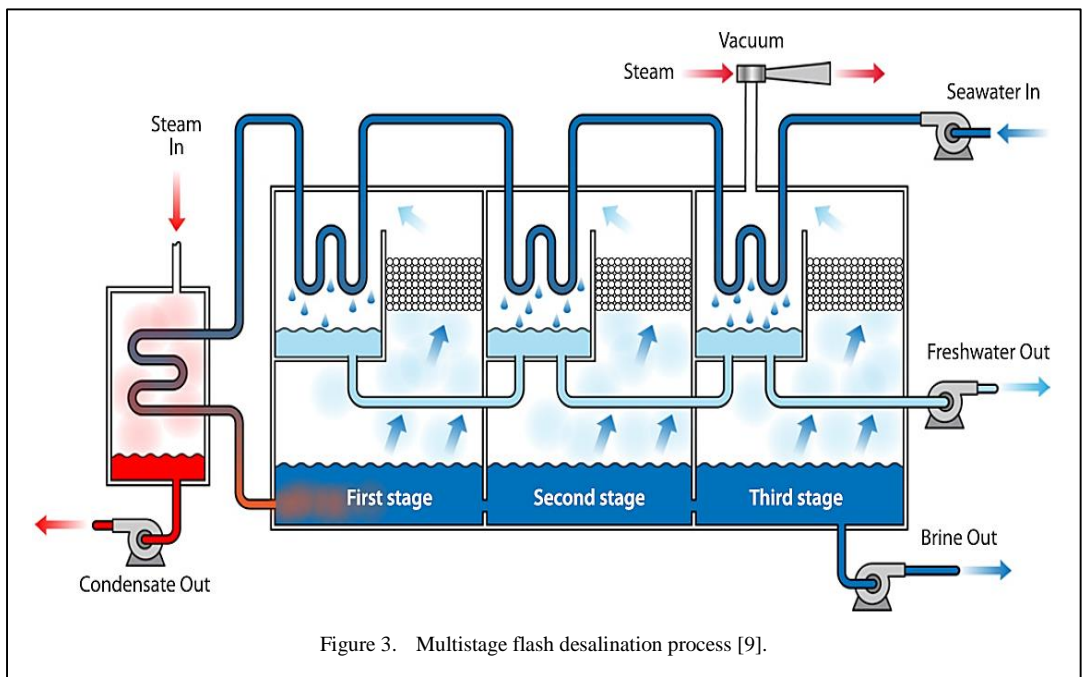
post-treatment to make it acceptable for certain home or industrial uses.

B. Multistage Flash (MSF)

The MSF method was invented in the 1950s, making it one of the first desalination procedures [8]. MSF, as shown in Fig. 3, is made up of multistage chambers, each of which is kept at a lower pressure than the one before it by a steam ejector. The procedure begins by raising the temperature of the salty water. The heated feedwater is then fed to the first chamber or stage, where it partially evaporates owing to the reduced pressure. The vapor produced is condensed as the feedwater is preheated over tubes situated at the top of each step. To enhance water productivity and energy efficiency, the procedure is done several times. Most modern commercial MSF facilities have 10 to 30 steps,

with a temperature reduction of 2 degrees Celsius every stage. Multi-Effect Distillation (MED)

MED was the first desalination process developed during the late 1800s, and it dominated the desalination industry until MSF appeared in the 1950s. Because they both rely on evaporating feedwater, the principles of MED and MSF are identical. In MED, as shown in Fig. 4, the inlet seawater is sprayed over evaporating tubes heated with steam. The evaporation tubes and seawater sprayers are housed in vacuum vessels known as “Effects” [8]. After being sprayed over the evaporating tubes, the seawater evaporated, leaving the initial effect. The evaporated water from the first effect, i.e., steam, is then utilized to heat the second effect, in which the steam is cooled and condensed before being gathered as pure freshwater product.



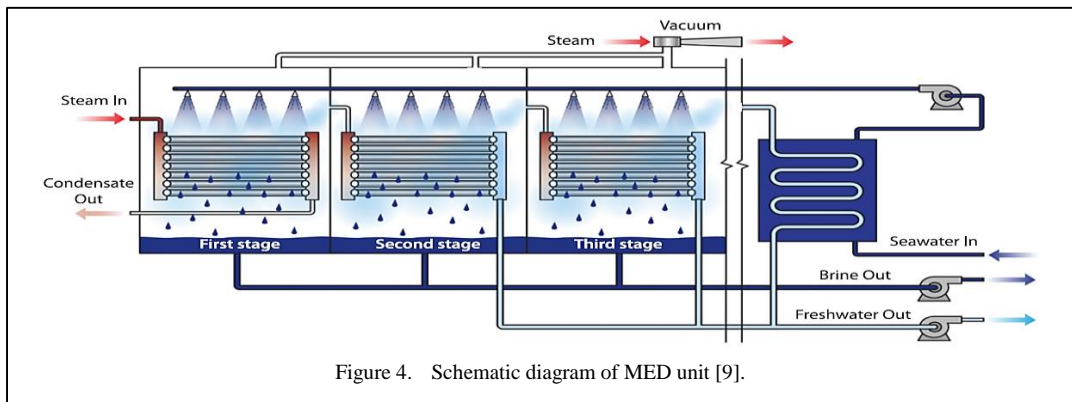


Figure 4. Schematic diagram of MED unit [9].

C. Other Desalination Processes

Thermal desalination employing MSF and MED procedures dominated the desalination business from the 1950s through the 1980s, when RO membrane desalination began to take off, eventually dominating the market having a market share of 70% [10]. The primary motivations for designing new desalination processes have always been to reduce costs, primarily by decreasing energy consumption, and to accommodate a wide range of feedwater quality. However, most of these procedures are still at the lab or pilot size due to technical and technological obstacles that are impeding their large-scale application.

III. COST TRENDS IN DESALINATION

One of the key causes for the low precision in estimating water costs for the same works is the use of different approaches by different project delivery companies. The entire expected price of desalinated water may be established with high accuracy if the major elements influencing the supply costs, such as laws and

regulations, energy costs, technology employed, capacity of the plant, and level of salt, are recognized in advance. Certain elements, such as political and financial risks and subsidies, caused significant variances in project bidding; nevertheless, their impact is limited.

Desalination costs have consistently been reduced in recent decades, with water costs approaching $\$0.5/\text{m}^3$ for wide-range RO facilities and less than $\$1/\text{m}^3$ for MSF [7]. Regarding the amount and quality of water vary by location, estimating the cost of brackish water is difficult [11]. However, Given the reduced salinity rate, requiring a smaller pressure and a higher recuperation rate, salty water is often less expensive when using the RO procedure. Fig. 5 depicts the cost of generated water in terms of plant capacity with economies of scale [12]. On a $30,000 \text{ m}^3/\text{day}$ reference capacity, the costs of RO, MED, and MD are 0.69 , 1.48 , and $\$1.72/\text{m}^3$, respectively. These findings show that, in compared to RO, a steam-powered plant is not economically feasible, as it is expected due to a lack of waste heat on-site.

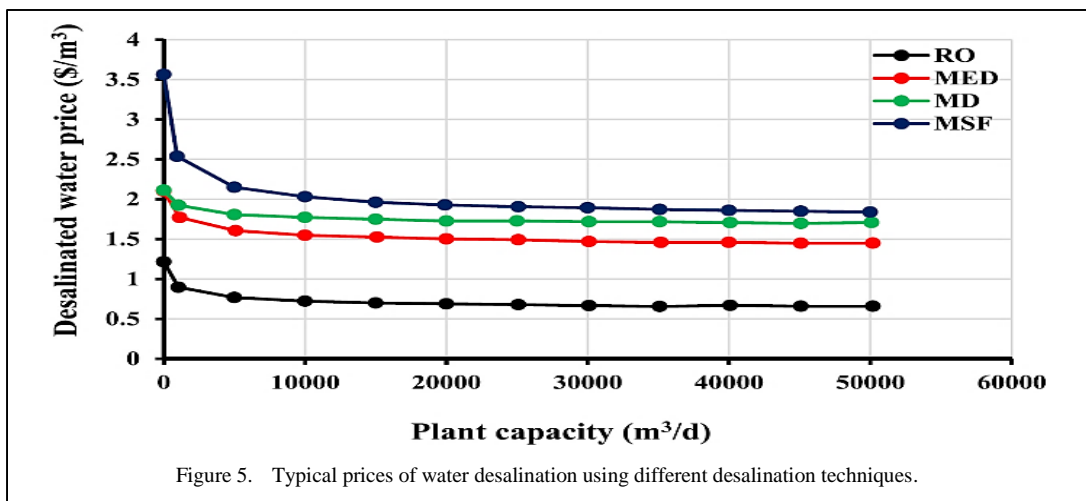


Figure 5. Typical prices of water desalination using different desalination techniques.

IV. CONCLUSIONS

Desalination is being used in many parts of world to help alleviate water constraint. Desalination has been a critical water source since it can supply a significant quantity of high-quality water in big quantities. Apart from ensuring freshwater supply, it is generally recognized that the desalination process has a variety of environmental consequences, including land use changes, marine ecosystem deterioration, and air and sea pollution. Desalination has a significant impact because of the large quantity of energy it consumes, which in turn accelerates climate change. When supplied by fossil fuels, high carbon emissions ensue. As a result, the environmental impacts of desalination technology should be included into long-term planning choices.

Desalinated water capital and operating expenditures, that involve the type of agreement for delivery and the quantity of energy consumed, and plant capacity, are the primary considerations used by decision-makers to pick the best desalination process. However, because there are multiple elements that influence the ultimate cost of desalinated water, quoted cost information is sometimes contradictory for different processes or equipment of the same size. Cost reduction trends are occurring in all desalination methods, particularly over the previous decade, with RO technology experiencing the greatest decline.

REFERENCES

- [1] Hanafiah, M. M., Leuven, R. S. E. W., Sommerwerk, N., Tockner, K., & Huijbregts, M. A. J. (2013). Including the Introduction of Exotic Species in Life Cycle Impact Assessment: The Case of Inland Shipping. *Environmental Science & Technology*, 47(24), 13934–13940.
- [2] Lee, S. H., Jung, H. J., Lee, S. J., Theerthagiri, J., Kim, T. H., & Choi, M. Y. (2020). Selective synthesis of Au and graphitic carbon-encapsulated nanoparticles by pulsed laser ablation in solvents: Catalytic Au and acid-resistant nanoparticles. *Applied Surface Science*, 506, 145006.
- [3] Senthil, Raja Arumugam, Khan, A., Pan, J., Osman, S., Yang, V., Kumar, T. R., & Liu, X. (2020). A facile single-pot synthesis of visible-light-driven AgBr/Ag₂CO₃ composite as efficient photocatalytic material for water purification. *Colloids and Surfaces A: Physicochemical and Engineering Aspects*, 586, 124183.
- [4] Senthil, R A, Theerthagiri, J., Selvi, A., & Madhavan, J. (2017). Synthesis and characterization of low-cost g-C₃N₄/TiO₂ composite with enhanced photocatalytic performance under visible-light irradiation. *Optical Materials*, 64, 533–539.
- [5] Sharaf Eldean, M. A., & Soliman, A. M. (2017). A novel study of using oil refinery plants waste gases for thermal desalination and electric power generation: Energy, exergy & cost evaluations. *Applied Energy*, 195, 453–477.
- [6] Elsaid, K., Kamil, M., Sayed, E. T., Abdelkareem, M. A., Wilberforce, T., & Olabi, A. (2020). Environmental impact of desalination technologies: A review. *Science of The Total Environment*, 748, 141528.
- [7] Ghaffour, N., Missimer, T. M., & Amy, G. L. (2013). Technical review and evaluation of the economics of water desalination: Current and future challenges for better water supply sustainability. *Desalination*, 309, 197–207.
- [8] Husain, A., Al-Gobaisi, D. M. K., Hasan, A., Kesou, A., Kurdali, A., & Podesta, S. (1993). Modelling, simulation, optimization and control of multistage flashing (MSF) desalination plants Part II: Optimization and control. *Desalination*, 92(1), 43–55.
- [9] Al-Karaghoul, A., & Kazmerski, L. L. (2013). Energy consumption and water production cost of conventional and renewable-energy-powered desalination processes. *Renewable and Sustainable Energy Reviews*, 24, 343–356.
- [10] Jones, E., Qadir, M., van Vliet, M. T. H., Smakhtin, V., & Kang, S. (2019). The state of desalination and brine production: A global outlook. *Science of The Total Environment*, 657, 1343–1356.
- [11] Arras, W., Ghaffour, N., & Hamou, A. (2009). Performance evaluation of BWRO desalination plant — A case study. *Desalination*, 235(1), 170–178.
- [12] Kesieme, U. K., Milne, N., Aral, H., Cheng, C. Y., & Duke, M. (2013). Economic analysis of desalination technologies in the context of carbon pricing, and opportunities for membrane distillation. *Desalination*, 323, 66–74.

Process Parameter Optimization of Al7SiMg Alloy Casting by Means of Probability-based Multi-objective Optimization

Mszhengok Zheng¹, Jie Yu²

¹School of Chem. Eng., Northwest University, Xi'an, 710069, China

²School of Life Sci. & Tech., Northwest University, Xi'an, 710069, China

¹mszhengok@aliyun.com, ²yujie@nwu.edu.cn

Abstract—Manufacturing industry is the paving stone of the development of society. As a result of globalization, the improvement of quality of products with reduced cost is the constant issue, which can be obtained by optimum design of processing parameters. In this paper, the process parameter optimization of Al7SiMg alloy casting is conducted by means of probability - based multi - objective optimization (PMOO). The Taguchi experimental design and quantitative evaluation of optimized responses (attributes, or objectives) of Al7SiMg alloy casting process and the determination of their weighting factors in the spirit of PMOO are employed. The casting process parameters, pouring temperature, amount of degasser, holding time, type of mold, are optimized. The application of proper multi-objective optimization in industry field will benefit to its quality improvement with reduced cost.

Keywords - process parameter, optimization, PMOO, weight factor

I. INTRODUCTION

Al-Si alloys are the widely used aluminium alloys, which have been used in broad range, especially in transport field owing to their excellent castability, corrosion resistance and high specific strength (strength – to - weight ratio) [1].

Recently, the improvement of quality of castings with reducing cost is considered to be of great significance. If the casting process is properly managed, the quality of castings can be

simultaneously maintained with reducing cost, thus the optimization of process parameters should be done so as to perform an appropriate manufacturing activity.

In general, Taguchi method has been used to conduct the design of experiment. However, the theoretical analysis of optimization is puzzled for multi –objective problem [2,3].

Some “additive algorithms” or Pareto method are often used to deal with the optimization problem with multiple objectives [2-4]. However, these “additive algorithms” contain uncertainties of subjective elements for weighting factors and denominators of normalization of performance utility; Pareto method can only give a set solution instead of exact optimal solution [2-4].

Currently, probability-based multi-objective optimization (PMOO) is proposed to conduct the simultaneous optimization of multiple objectives in a system [3,4].

In fact, the intrinsic intention of multi-objective optimization (optimization) is the “simultaneously optimization” of multiple objectives. The multiple objectives in the optimization are within a system actually, so the optimization of these multiple objectives is actually the optimization of a system, which is the integral optimization of the system.

From the perspective of probability theory, it is the “product” of the probability of each

objective (attribute) and the “intersection” of each objective in set theory. Furthermore, the probability theory method can be adopted to deal with the issue of optimization problem with multiple objectives. The new concept of “preferable probability” was introduced [3,4]. The objectives (attributes) of candidate schemes in the optimization are preliminarily divided into two basic types, i.e., beneficial attribute and beneficial (cost) attribute, and a quantitative evaluation method of assessment of the partial preferable probability corresponding is established with a linear correlation [3,4]. In probability theory, the “simultaneously optimization” of multiple objectives is treated as “multiple events appearing at the same time”. Therefore, the total preference probability of each candidate scheme is the product of all partial preferable probabilities of the candidate scheme so as to deal with the integral optimization of the system. Finally, the total preference probability of each candidate scheme is the unique and decisive indicator of the scheme to win the competition in this optimization. The process is shown in Fig. 1 [3,4].

In Fig. 1, P_{ij} reflects the partial preferable probability of the j -th performance utility index of the i -th alternative X_{ij} ; n is the total number of alternatives; m represents the total number of objective utility; \bar{X}_j is the arithmetic value of the j -th objective utility index within the involved alternatives; X_{max} and X_{min} reflect the maximum and minimum values of the j -th performance utility index respectively; α_j and β_j are the normalization factor of the j -th utility index X_{ij} of beneficial and unbeneficial indicators respectively; P_i is the total preferable probability of the i -th alternative [3,4].

In fact, there exist obvious differences between the new method and previous approaches, which are mainly reflected in the fact that the “probability-based multi-objective optimization” is with both viewpoint of system theory and methodology. According to the viewpoint of system theory, “the optimum point of multi-objective optimization” is the “optimal point of system”, and thus this optimum point of system can be obtained by using probability theory. However, all previous approaches of multi-objective optimization are short of viewpoint while only with algorithms, which did not define the optimum point of “multi-objective optimization” indeed.

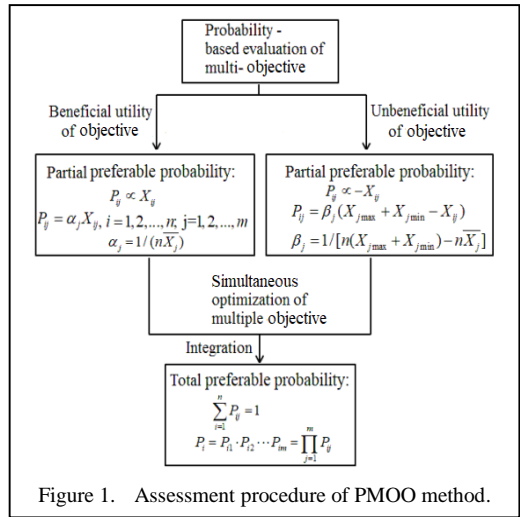


Figure 1. Assessment procedure of PMOO method.

In this paper, parameter optimization of Al7SiMg alloy casting is taken as an example to illuminate the application of probability - based multi - objective optimization in material manufacturing process.

II. APPLICATION OF PROBABILITY - BASED MULTI-OBJECTIVE OPTIMIZATION IN PARAMETER OPTIMIZATION OF AL7SiMG ALLOY CASTING

Viquar Mohiuddin et al once studied the parameter optimization of A356 aluminum alloy (Al7%SiMg) casting process [1]. Here it is restudied by means of PMOO. The chemical composition of A356 alloy used in the study is: Si-7.42%, Cu-0.005%, Mg-0.568%, Fe-0.22%, Zn-0.019%, Mn-0.003%, Sn-0.002%, Ti-0.007%, Pb-0.012%, Ni-0.001%, Al-remainder [1].

Three quality attributes (objectives), i.e., density of casting (d), ultimate tensile strength (UTS) and elongation to fracture (ϵ_f), are involved as the evaluating indicators of the quality of the castings; there are four input independent parameters to be optimized, i.e., pouring temperature (PT), degasser amount (DA), holding time (HT), and mold type (MT) [1]. Table I shows the casting processes parameters and the results of the attributes with $L_9(3^4)$. In Table I, the mold type (MT) including 1, 2 and 3 indicate the sodium silicate, dry, and air-set sand moulds, respectively.

TABLE I. EXPERIMENTAL CASTING PROCESSES PARAMETERS AND THE RESULTS OF THE ATTRIBUTES WITH $L_9(3^4)$.

Trial no.	Casting process parameters			
	PT (°C)	DA (%)	HT (min)	MT
1	690	0.5	2	1
2	690	1.0	4	2
3	690	1.5	6	3
4	720	0.5	4	3
5	720	1.0	6	1
6	720	1.5	2	2
7	750	0.5	6	2
8	750	1.0	2	3
9	750	1.5	4	1
Casting quality attributes				
	d (ton/m ³)	UTS (MPa)	ϵ_f (%)	
1	2.565	90.1215	5.02	
2	2.651	90.028	4.9	
3	2.611	56.163	3.08	
4	2.564	89.723	3.36	
5	2.622	84.047	3.5	
6	2.612	55.9515	3.25	
7	2.555	91.837	3.39	
8	2.627	90.453	4.8	
9	2.600	49.205	2.67	

A. Assessment of Partial Preferable Probability

In the assessment of optimization by means of PMOO [3,4], the attributes of density of casting (d), ultimate tensile strength (UTS) and elongation to fracture (ϵ_f) are all belong to beneficial type of utility indicators obviously. The assessment results of partial preferable probabilities for d , UTS and ϵ_f are shown in Table II.

TABLE II. ASSESSMENT RESULTS OF PARTIAL PREFERABLE PROBABILITIES FOR d , UTS AND ϵ_f .

Trial no.	Partial preferable probability		
	P_d	P_{UTS}	P_{ϵ_f}
1	0.1096	0.1292	0.1478
2	0.1133	0.1291	0.1442
3	0.1115	0.0805	0.0907
4	0.1095	0.1286	0.0989
5	0.1120	0.1205	0.1030
6	0.1116	0.0802	0.0957
7	0.1092	0.1317	0.0998
8	0.1122	0.1297	0.1413
9	0.1111	0.0705	0.0786

B. Assessment of Weight Factor of Attribute

According to probability-based multi-objective optimization [3], the weight factor w_j of attribute is assessed as following according to its variability,

$$w_j = C_j / (\sum_{j=1}^m C_j), \quad (1)$$

$$C_j = \left[\sum_{i=1}^n (P_{ij} - \frac{1}{n})^2 / n \right]^{0.5}. \quad (2)$$

In Eqs. (1) and (2), m is the number of the optimized attributes (objectives), n is the number of the schemes, and P_{ij} is the partial preferable probability of j -th attribute of i -th scheme. The assessment results of weight factor w_i for d , UTS and ϵ_f are shown in Table III.

TABLE III. ASSESSMENT RESULTS OF WEIGHT FACTOR w_j FOR d , UTS AND ϵ_f .

	Attribute		
	d	UTS	ϵ_f
c_i	0.00132	0.02438	0.02452
w_i	0.02633	0.48545	0.48822

C. Assessment of Total Probability - based Multi - Objective Optimization

The assessment of total preferable probability by means of probability - based multi - objective optimization with the weight factors shown in Table III are conducted accordingly, which is shown in Table IV. Table IV shows that the experiment scheme No.1 is with the highest total preferable probability, which can be selected as the optimized scheme at the 1st glance.

TABLE IV. ASSESSMENT RESULTS OF TOTAL PREFERABLE PROBABILITY BY MEANS OF PMOO.

Trial no.	Assessment result	
	Total preferable probability P_i	Rank
1	0.1374	1
2	0.1358	2
3	0.0861	8
4	0.1127	5
5	0.1114	6
6	0.0882	7
7	0.1144	4
8	0.1347	3
9	0.0753	9

D. Range Analysis of Total Preferable Probability by Means of Probability - based Multi - objective Optimization

Range analysis can be conducted for the total preferable probability P_i , which is shown in Table V.

Table V indicates that the impact order of controlling input variables is, $HT > DA > PT > MT$, and the optimum configuration is $PT_1DA_2HT_1MT_2$, i.e., pouring temperature (PT) is 690° , degasser amount (DA) is 1%, holding time (HT) is 2 min, and mold type (MT) is dry mould.

Viqar Mohiuddin et al employed signal noise ratio to assess their experimental results, their study gave an optimal configuration from the respect of density is $PT_1DA_2HT_2MT_2$, while another optimal configuration from the viewpoint of “Quality Index” is $PT_1DA_2HT_1MT_2$ [1]. Obviously, this is a dual-result from every response instead of unique optimum status as a whole for the problem from overall viewpoint.

TABLE V. RANGE ANALYSIS RESULT OF THE TOTAL PREFERABLE PROBABILITY BY MEANS OF PROBABILITY - BASED MULTI - OBJECTIVE OPTIMIZATION.

Level	Input parameter			
	PT	DA	HT	MT
1	0.1197	0.1215	0.1201	0.1080
2	0.1041	0.1273	0.1079	0.1128
3	0.1081	0.0832	0.0658	0.1111
Range	0.0157	0.0441	0.0543	0.0048
Impact order	3	2	1	4
Optimum conf.	1	2	1	2

III. CONCLUSION

Above study indicates that process parameter optimization of alloy casting can be conducted properly by means of probability-based multi-objective optimization (PMOO); the determination of weighting factors of attributes can be performed in the spirit of PMOO appropriately. PMOO is an overall optimization for a problem as a whole.

The benefits of the application of proper multi-objective optimization in manufacturing industry will involve many areas due to its improvement of quality of products with reduced cost, such as in economic, social and environmental protection respects, etc.

The directions of future work on this topic might contain explorations of more rational methodology of multi-objective optimization and application in engineering from theoretical respect and practical side.

REFERENCES

- [1] Viqar Mohiuddin, M., Krishnaiah, A., Ferhathullah Hussainy, S., & Laxminarayana, P. (2016). Influence of process parameters on quality of Al7SiMg alloy casting using statistical techniques, *Materials Today: Proceedings*, 3, 3726–3733.
- [2] Truong, N. X., Ašonja, A., & Trung, D. D. (2023). Enhancing Handheld Polishing Machine Selection: An Integrated Approach of Marcos Methods and Weight Determination Techniques, *Applied Engineering Letters*, 8(3), 131-138.
- [3] Zheng, M., Yu, J., Teng, H., Cui, Y., & Wang, Y. (2023). *Probability-Based Multi-objective Optimization for Material Selection*. 2nd ed., Springer, Singapore.
- [4] Zheng, M., Wang, Y., & Teng, H. (2021). A new “intersection” method for multi-objective optimization in material selection. *Technicki Glasnik*, 15(4), 562-568.

Natural Power of Medium Voltage Electric Power Distribution Lines as a Criterion for Optimal Management of the Existing Electric Power Distribution Grid and its Reconstruction

Suad Halilčević¹

¹University of Tuzla, Tuzla, Bosnia and Herzegovina

¹suad.halilcevic@untz.ba

Abstract—In this paper, natural power of electric power distribution lines is analyzed as a criterion for optimal control and reconstruction of the electric power distribution grid. Natural power is directly connected with the natural impedance (characteristic impedance) of the electric power distribution line. The benefits arising from the electric power distribution lines loaded by their natural power are reflected in voltage equality along the power lines, the absence of a phase shift between the voltage and current vectors and their own reactive power compensation. However, the natural power values of electric power distribution lines in distribution grids are below the economic, and in particular below the thermally limited power transmission which is the basis of all types of analyzes in the electric power distribution grids. The management of the distribution grid by establishing the electric power flows as close as possible to the artificially adjusted values of the natural power of these electric power distribution lines leads to all the benefits of operation in such states, that is, to optimal operation. The Euclidean distance is used as a measure of the optimum load of the electric power distribution lines, which calculates deviations of the actual power flows from those of the natural flows. Additional equipment in the form of capacitor and inductive batteries distributed along the distribution lines can adjust the natural impedance in such a way that the power flows corresponding to the permissible operating temperature of the

distribution lines are closer to the natural power flows.

Keywords – electric power distribution lines, natural power, economical power, heat-limited power

I. NATURAL POWER, ECONOMIC POWER AND POWER LIMITED BY THE THERMAL CAPACITY OF ELECTRIC POWER DISTRIBUTION LINES

Natural power is one of the most important characteristics of every system and process. Natural power is well explained in the themes of the transmission part of the electric power system [1], however, in practice it is not as often used as a criterion for managing the transmission grid. The maximum load carrying capacity of a transmission electric power line (expressed by the surge impedance limit (SIL)), depending on the length of the line, is found on the St. Clair curve [2]. SIL is based on characteristic impedance of transmission electric power line without energy losses (long electric power line).

Even worse situation regarding natural power is in the electric power distribution grids. There, different methods of optimum control of power flows are used, but none use the aspect of natural power of distribution power lines. In these procedures of optimal distribution grid

management, minimal losses, reliability and safety of power supply to the consumer are set as objective functions [3]. These optimization procedures use constraints when searching for objective functions (target functions) related to the allowed range of voltage changes, allowed current load on power lines and reduced number of changes in the configuration of the distribution grid. Optimization methods are based on linear [4] and nonlinear programming [5] (deterministic procedures) and heuristic procedures [6,7].

The natural power of electric power distribution line (EPDL) depends on the constructive characteristics of the line, the properties of the environment in which it exists and the material from which it is made. These characteristics are ohmic resistance (r), inductive resistance ($j\omega L$), susceptance ($j\omega C$) and conductance (g). Conductance in distribution systems is neglected because in the conditions of operation of the distribution grid the conductance has a very low value.

In transmission electric power lines, because of the much lower value of the r than the inductive one, r can be neglected in the serial branch of the transmission power line model. Equalizing the reactive power of the capacitive type ($-V_{LN}^2(j\omega C)$) and the reactive power of the inductive type ($I_L^2(j\omega L)$) gives a surge impedance Eq. (1):

$$Z_0 = \sqrt{\frac{L}{C}} = \sqrt{\frac{X}{Y}} . \quad (1)$$

Such operating regime, the equivalency of capacitive and inductive reactive power means that the reactive energy on the power line is zero, $Q = 0$ and that the impact of L and C on the power line is eliminated. It remains only r and if such a power line is closed with an ohmic load r , then we are talking about the load of that electric power line with the surge impedance load with all its benefits of transmission characterized by ohmic electric power load. In reality, at the end of the transmission electric power line there is an electric power load of different characteristics, including the inductive and capacitive character of the load, which makes the deviations from the operating regime $Q = 0$.

In EPDLs, the situation regarding natural power is somewhat more complicated because the analysis of surge impedance should take into account the ohmic resistance r , that is, a complex

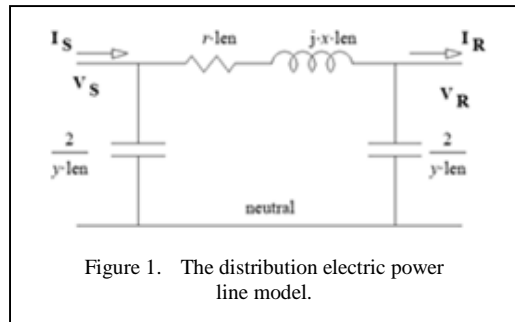


Figure 1. The distribution electric power line model.

surge impedance version should be considered, which in this case is called a characteristic impedance Z_c Eq. (2) and is equal to:

$$Z_c = \sqrt{\frac{r+j\omega L}{g+j\omega c}} = \sqrt{\frac{r+jx}{g+jb}} . \quad (2)$$

An EPDL model is given in Fig. 1 (in electric power distribution grids, EPDLs are shorter than the threshold length to which these lines can be considered short, up to 70 km, and a model of such EPDLs is shown in Fig. 1).

Medium voltage distribution grids (10 kV, 20 kV, 35 kV) are performed with overhead electric power lines (with Al-steel conductors) and underground power cables isolated with pvc insulation. In the case of medium voltage distribution grids the r is greater than X or approximately equal to X (as opposed to the transmission grids where $X \gg r$). Thus, each EPDL of the distribution grid should be described by the location, the type of conductor material, the type of insulation material and cross-section. All of this affects the value of the characteristic impedance.

In today's practice of electric power distribution grid management, a goal function is set that reflects the minimum electrical losses, maximum reliability and safety of the operation of the grid, with limitations of electric current value per EPDL and limits per voltage. Voltage limits are determined by the Distribution System Operator's grid code, and electric current limits are related to the rated current load (depending on the impedance characteristics and the manner of formation of the conductor and the place of laying of the power line - overhead or underground) and the short-circuit current. On average, this concept of using EPDLs is based on the current density J_0 from 2.5 to 4.14 A/mm² (calculated on the base of data given in the catalogues of EPDLs producers).

This is one possible criterion for the management of EPDLs and their loads. However, in addition to this possible load on the EPDLs (practically related to the permissible thermal load), the EPDLs can be operated on the basis of the so called economic impedance, which by its value is very close to the characteristic impedance of the overhead power lines. The economic impedance of an EPDL is determined by the total cost of that line consisting of the parts determined by the cross-section of the conductor(s), the value of the voltage and the part that is independent of either the cross-section of the conductor or the operating voltage at which that conductor operates (that is to say, the costs relating directly to the choice of route, maintenance and safety). However, for the economic impedance of an EPDL to be accurate, the impedance of the transformer through which the electricity is fed to the considered EPDL must also be taken into account. That means that under our conditions, the economic impedance Z_e of the overhead electric power lines varies between 110 and 500 ω . For short electric power transmission (length less than 70 km), economic load P_e of EPDL is given with Eq. (3):

$$P_e = \frac{U^2}{Z_e} . \quad (3)$$

The economic load on the EPDL is above its natural load, which is equal to Eq. (4):

$$P_{nat} = \frac{U^2}{Z_c} . \quad (4)$$

As such, the economic electric current density of distribution power lines $J_0 \approx 1.1$ A/mm² is defined; e.g. for Al/Fe lines J_0 is about 1 A/mm², for Al and Cu power cables $J_0 \approx 1.4$ A/mm² - depending on the price of electricity. Economic values of the electric current density should be seen through the prism of the electrical energy price (euro/kWh). If the price of electricity is high, higher electricity losses caused by higher load on distribution power lines will cause higher financial losses. In such cases, the EPDLs should be loaded with a lower electric current density. That is, the economic density of electric current is a function of operating costs caused by the cross-section of conductors and joule losses.

The economic impedance of the electric power cable is fairly constant and is significantly

below the characteristic impedance of the cable itself (50 Ω). This means that, from an economic point of view, electric power cables can be loaded more than overhead EPDLs of the same voltage.

The third possible criterion for managing the distribution grid is the criterion of the characteristic impedance of the EPDL and its natural power. It is characterized by an average current density J_0 of about 0.6 A/mm².

Thus, the distribution system operator has at its disposal three management concepts, depending on the type of impedance used and the power criteria related to it: economic, thermal or natural. The current practice is based on the criterion of the permissible thermal load of distribution power lines, as it stands in all catalogs of manufacturers of conduits (overhead power lines and underground power cables). Why is the criterion of economic power not used? Why is the criterion of natural power not used? The answer is the consequence of insufficient utilization of the capacity of conduits (of a certain cross-section) from the aspect of electric power load and its heat available capacity.

II. CALCULATION OF NATURAL IMPEDANCE OF MEDIUM VOLTAGE ELECTRIC POWER DISTRIBUTION LINES

Using Eq. (2), after ignoring g , the absolute value of the characteristic impedance of the distribution line represented by the model in Fig. 1 is written (by calculating the square root of the complex number according to [8]):

$$Z_c = \pm \left(\sqrt{\frac{z+x}{2b}} - j \sqrt{\frac{z-x}{2b}} \right) , \quad (5)$$

with an absolute value of Z_c equal to:

$$|Z_c| = \sqrt{\frac{|z|}{2b}} , \quad (6)$$

where $|z| = \sqrt{x^2 + r^2}$.

The characteristic impedance argument is:

$$Arg(Z_c) = arctg \left(\sqrt{\frac{z-x}{z+x}} \right) . \quad (7)$$

Eqs. (6) and (7) indicate the directions of action in the distribution grid to reduce the characteristic impedance and increase the natural power as close as possible to the thermally

limited electric power, if this is the criterion of maximum utilization of the existing distribution grid.

Taking into account the technical-technological and economic resources of existing power distribution grids in South East Europe, a better approach is to act on susceptance b , instead of inductive reactance x . Therefore, compensation of distribution power lines using shunt capacitors of a certain capacity is a good solution for bringing EPDLs into the new natural state of electric power distribution. Further analysis is needed to determine the benefits and costs arising from distributed reactive power compensation on the EPDL or from compensation at the ends of the EPDL [9]. The capacitive operating regime of distribution lines should also be taken into account when dealing with the compensation of EPDLs. Namely, there are medium voltage EPDLs (20 and 35 kV) that are very poorly loaded at some time intervals that inject the reactive power of the capacitive type into the distribution line, raising at its ends the voltage. Therefore, when the compensation of medium-voltage EPDLs is analyzed, in the analysis of efficient use of EPDLs, in addition to the capacitor type of compensators (shunt capacitors), also inductive type of compensators (shunt coils) should be considered.

Therefore, in the studies of the distribution grid, the natural power P_{nat} of each distribution line should be calculated based on its characteristic impedance Z_c . Comparison of this power with the power of the EPDL which is limited by the thermal capacity of that distribution line, it is possible to take measures of appropriate compensation of the distribution line by using Eq. (6). There are a number of different cross sections of Al-steel overhead EPDLs that are described by their nominal electric current determined by the permissible increase in the temperature of the materials of which the distribution line is made. Some of the most common applied EPDLs are of cross-sections of 50 mm², 70 mm², and 95 mm² with allowed rated currents in the amount of 170 A, 290 A, and 350 A, respectively, (Source: Tim cable company catalog). This corresponds to a thermally limited electric current density of about 3.7 A/mm². For the mentioned cross sections, the natural electric current densities for 10 kV EPDLs would be in the range of 0.11 to 0.66 A/mm², and for 20 kV the natural electric current density would be in the range of 0.22 to 1.3 A/mm².

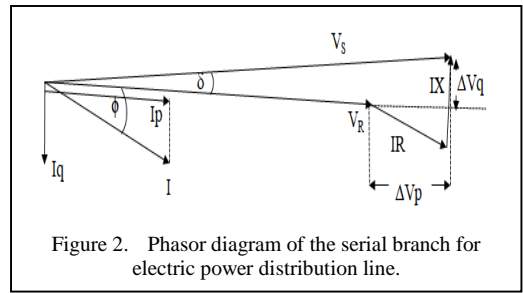


Figure 2. Phasor diagram of the serial branch for electric power distribution line.

Thus, the electric current densities according to economic, natural and thermally limited load criteria are 1.1 A/mm², 0.6 A/mm² and 3.7 A/mm², respectively.

Thus, the distribution system operator has at its disposal three aspects of distribution grid management based on economic, natural and heat-limited distribution of electric power. Thus, in [10], it is shown that the thermally limited electric power distribution through the EPDLs is about four times higher than the economic one, and about 10 times higher than the natural power distribution of the 10 kV EPDL. Thermally limited electric power distribution through the 35 kV EPDLs is about four times higher than the economic power based electric power distribution and seven times higher than the natural power based electric power distribution. Directions of action for $L-C$ compensation of medium voltage EPDLs can be seen from the Fig. 2 (without the transverse branch b).

Longitude and transversal voltage drops are given in Eqs. (8) and (9):

$$\Delta V_p = \frac{PR+QX}{V}, \quad (8)$$

$$\Delta V_q = \frac{XP-RQ}{V}. \quad (9)$$

The reduction or elimination of voltage drop ΔV_q on the reactive part of the impedance of EPDL reduces the angle of transmission of electrical power through the distribution line, approaching that transmission of electrical power as if it were transmission over a resistor (joule's electrical resistance r). The Q reduction also reduces the second component (ΔV_p) of the voltage drop. In this case, the applied procedure of optimal power flows in distribution grid will give better results than in the case of optimization of uncompensated EPDLs.

With natural power flows in the distribution network, a minimum power (energy) loss is

realized. The minimum energy loss in the network is the goal of each optimization procedure. The action to be taken in this respect concerns the investment in L/C compensation, which is the lack of a proposed way to optimize the distribution network. An economic analysis is needed to assess the feasibility of an investment in L/C compensation of medium voltage EPDLs. However, bringing natural power to the level of thermally limited power of EPDLs, along with the mentioned benefits of natural power flows, maximizes the capacity of EPDLs. L/C compensation would become an integral part of the hardware of 110/35 kV, 35/10 kV and 110/20 kV power transformer stations.

What makes this method of optimizing the distribution network acceptable is the simplicity of calculation. Depending on the power flows on each of the distribution lines, the required range of inductance and capacitor of L/C compensation is easily calculated, which will, through several degrees of the values of L and C, bring the natural impedance of EPDL to the impedance that determines the thermally limited power of transmission.

Euclidean distance $d(P_{nat}, P_{actual})$ [10] is introduced as a measure of the deviation of actual power flows through EPDLs from natural power flows:

$$d(P_{nat}, P_{actual}) = \sqrt{\sum_{i=1}^{8760} \sum_{l=1}^N (P_{nat} - P_{actual})^2}, \quad (10)$$

where P_{nat} is the natural power and P_{actual} is the actual power through the considered EPDL for a given hour. N is the number of EPDLs.

Euclidean distance is a measure of optimal operation of the distribution grid. The smaller Euclidean distance, the closer the distribution grid is to the optimal mode (the ideal case would be $d = 0$).

III. EXAMPLE OF A PART OF THE ELECTRIC POWER DISTRIBUTION GRID IN TUZLA CANTON

A part of the electric power distribution grid in Tuzla Canton is analyzed from the aspect of three possible load states of the distribution grid presented in the previous part of this paper. The analysis was performed using PowerCad [11]. Several 10 kV EPDLs were analyzed. Relations between economic, natural and thermally limited impedance, and with related economic, natural

and thermally limited electric power transmission through EPDLs of various cross-sections, are based on the input data of producers of overhead EPDLs.

In this paper, overhead EPDLs with cross-sections of 50 and 70 mm² are presented in Table I.

The average value of natural power for analyzed 10 kV EPDLs is about 290 kW. Compared to the maximum allowable transmission of electric power from the point of the allowable thermal load of the EPDLs, it is 2.7 times lower transmission of electric power. The maximum allowable electrical power according to the thermal criterion is 1.8 times higher than the economic criterion of the transmission of electric power.

The results of the power flow calculation and associated voltage drops show that on some 10 kV EPDLs a larger voltage drop occurs even in conditions of low load of these distribution lines (Table I). This voltage drop is caused by the withdrawal of reactive energy from the power grid to magnetize the iron core of the transformer (10/0.4 kV/kV) at the end of such distribution lines.

Therefore, in such cases, it is necessary to have installed shunt capacitors at the ends of 10 kV lines that would take on the supply of reactive power to the transformer 10/0.4 kV/kV. This would relieve the distribution power line from the flow of the reactive electric current component. The elimination of reactive power from the EPDL through the compensation system (using shunt capacitors) is beneficial for both the transversal and longitudinal part of the voltage drop (Fig. 2).

The Euclidean distance for the sixteen considered 10 kV EPDLs is amounted to 1371 kW without capacitive compensation. When the measures of capacitive compensation are applied, the Euclidean distance has been decreased to 341 kW. The measures of reconfiguration of distribution grid has not been applied. These measures based on the redirection of the power flows through the EPDLs could bring the all distribution grid closer to the optimal mode of operation.

The same type of analysis can be performed for 35 kV EPDLs. With them the situation is a bit more complicated, because 35 kV electric power cables produce 0.125 MVar/km of reactive

TABLE I. ELECTRIC POWER FLOW RESULTS OF THE PART OF THE ELECTRIC POWER DISTRIBUTION GRID GRAČANICA.

Distribution lines	dU [%]	P [MW]	Q [MVA _r]	S _{max} [MVA]	Percentage of utilized electric power distribution line capacity (according to the thermal criterion of load)
10(20)-Bazen Ibrić	-10.52	0.0031	0.0101	0.16	7%
10(20)-Benprom	-10.47	0.0014	0.0401	1.00	4%
10(20)-Benprom	-10.47	0.1650	0.0165	1.00	17%
10(20)-Brđani	-14.12	0.1190	0.0436	0.16	79%
10(20)-Dobrnjići	-14.15	0.0340	0.0171	0.16	24%
10-Džafići	-14.36	0.0543	0.0208	0.10	58%
10-Džamija	-12.06	0.1390	0.0507	0.16	92%
10-G.Orahovica	-14.25	0.0944	0.0355	0.16	63%
10-Hotilj	-12.11	0.0282	0.0132	0.10	31%
10(20)-Husamovići	-14.53	0.0257	0.0121	0.10	28%
10-Makovci	-12.06	0.0082	0.0053	0.05	20%
10(20)-Mujići 2	-14.15	0.0509	0.0197	0.10	55%
10-Ravkići	-14.59	0.1160	0.0420	0.10	123%
10-Rijeka 1	-12.33	0.1740	0.0633	0.16	116%
10-Rijeka 2	-12.85	0.1370	0.0498	0.16	91%
10(20)-Rijeka 3	-13.04	0.0771	0.0301	0.16	52%

power. On such EPDLs, it is necessary to analyze the parallel connection of capacitors and reactors to the distribution line, which would operate in accordance with the inductive or capacitive operating regime of such distribution lines.

Voltage changes using dynamic shunt compensation response in capacitive and inductive mode (L/C compensation) are shown in Fig. 3 for the 35 kV EPDL. The L/C compensation used is based on 120 kVA_r of power of the capacitors and reactors placed in the middle of the considered distribution line.

At the 35 kV electric power distribution cable there was an average hourly loss of reactive power of 205 VAR and active power of 95 VA. Thus, the reactive power loss is much greater than the active power loss, especially in low-loaded distribution power lines. In one year, the analyzed distribution cable lost 1.94 MVA_hr of reactive power and 0.98 MWh of active power without L/C compensation.

By using L/C compensation, the annual loss of reactive energy is 1.13 MVA_hr, i.e. 41.75% less compared to the state of the distribution cable without L/C compensation. The simulation was performed in PowerCad with central L/C

compensation set to the center of the electric power distribution cable.

By compensating the medium-voltage EPDLs with shunt capacitors and reactors of

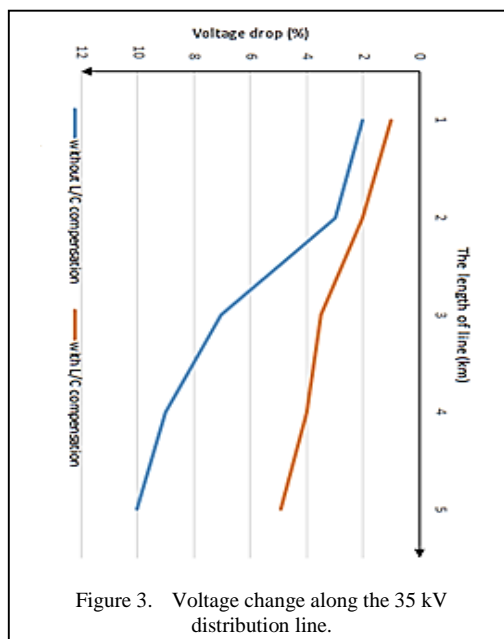


Figure 3. Voltage change along the 35 kV distribution line.

different capacity and inductance values (in accordance with the characteristics of the EPDLs and their operation regimes), the characteristic impedance can be reduced to a level that would allow the value of natural power to be only a few percent below the value of heat limited electric power. This would restore the voltage at these lines to the range of allowed voltage values. At the same time, electricity consumers would be protected from excessive voltages in the event of a low load on the distribution power line to which they are connected (when the voltage increases above the rated voltage).

IV. CONCLUSION

The model of the medium voltage EPDL, by means of which the characteristic impedance is calculated, i.e. its amplitude and argument, is presented in the paper. The obtained equations point to a way of reducing the characteristic impedance and increasing the natural power according to the heat-limited power of the EPDL. In order to achieve this goal, the paper presents the possibilities of L/C compensation of distribution lines. Furthermore, an economic analysis should be carried out to demonstrate the cost-effectiveness of this type of intervention in the structure of the distribution grid. Also, by introducing L/C compensation of EPDLs, it is necessary to conduct an analysis with respect to possible increase/decrease of single-phase to ground fault currents in relation to the potential of the ground system and the way of treating the neutral point in medium voltage substations. Extensions and improvements of the proposed approach to optimize the distribution network should be directed towards the combination of the proposed approach with the network reconfiguration in the context of the switch-off and switch-on of individual EPDLs with the aim of ensuring natural power flows through the distribution network.

The concept of introducing natural power into the operation of EPDLs and the distribution grid can become an integral part of the operation of smart, self-healing and flexible grids.

REFERENCES

- [1] Dutta Roy S. C. (2010). Some Little-Known Facts About Transmission Lines and Some New Results. *IEEE Transactions on Education*, 53(4), 556-561.
- [2] Martin, H., Hamacher, T., Deetjen, T. A., & Webber, M. E. (2017, June). Reduced transmission grid representation using the St. Clair curve applied to the electric reliability council of Texas. In *2017 14th International Conference on the European Energy Market (EEM)* (pp. 1-5). IEEE.
- [3] Tomoiagă B., Chindriș M., Sumper A., Sudria-Andreu A., & Villafafila-Robles R. (2013). Pareto Optimal Reconfiguration of Power Distribution Systems Using a Genetic Algorithm Based on NSGA-II. *Energies*, 6, 1439-1455.
- [4] Boyd, S., & Vandenberghe, L. (2009). *Convex optimization*. Cambridge University Press.
- [5] Molzahn, D. K., Dörfler, F., Sandberg, H., Low, S. H., Chakrabarti, S., Baldick, R., & Lavaei, J. (2017). A survey of distributed optimization and control algorithms for electric power systems. *IEEE Transactions on Smart Grid*, 8(6), 2941–2962.
- [6] Akbulut L., Tezcan S. S., & Coşgun A. (2020). Analysis of Electrical Distribution Grid Voltage Configuration with Mixed Integer Linear Programming Algorithm and Genetic Algorithm Regarding Energy Cost. *Electrica*, 20(2), 124-132.
- [7] İsmail Alperen Ö., Baimakhanov O., Saukhimov A., & Ceylan O. (2022). A Heuristic Methods-Based Power Distribution System Optimization Toolbox. *Algorithms*, 15(1), 14.
- [8] Rabinowitz S. (1993). How to find the square root of a complex number. *Mathematics and Informatics Quarterly*, 3, 54-56.
- [9] Guo, W., & Tian, M. (2022, June). Analysis of reactive power compensation of railway 20kV primary through line. In *Journal of Physics: Conference Series* (Vol. 2290, No. 1, p. 012006). IOP Publishing.
- [10] Liberti L., & Lavor C. (2017). *Euclidean Distance Geometry - An Introduction*. Springer Cham.
- [11] Electrical Engineering Design Software (2023). *Power CAD*. Available at: <https://www.powercad.com.au>

Thermodynamic Analysis of a Rankine Cycle Integrated to the Biogas Plant at the Metropolitan Sanitary Landfill of João Pessoa, Northeast Brazil

Djayr Bispo¹, Raphael Abrahao², Monica Carvalho³

¹Postgraduate Program in Mechanical Engineering, Technology Center, Federal University of Paraíba, João Pessoa, Brazil

^{2,3}Department of Renewable Energy Engineering, Center for Alternative and Renewable Energy, Federal University of Paraíba, João Pessoa, Brazil

¹djayrbispo@gmail.com, ²raphael@cear.ufpb.br, ³monica@cear.ufpb.br

Abstract—The present study shows a thermodynamic analysis and simulation of the integration of a Rankine cycle to a real biogas plant. The plant uses internal combustion engines and is located in the Metropolitan Sanitary Landfill of João Pessoa, Northeast Brazil. Urban solid waste is treated at the landfill, and undergoes a process of biochemical decomposition through anaerobic digestion of its particles. The plant is responsible for the proper treatment of biogas, and also for its use. All biogas is used through a first thermodynamic process, through internal combustion engines. This work proposes the integration of a Rankine cycle to the plant, to reuse the exhaust gases in a second thermodynamic process. In addition to the basic Rankine cycle, two more arrangements for the cycle were analyzed in sensitivity analyzes for comparative purposes. The data used in this work were collected in technical visits to the plant at the Metropolitan Sanitary Landfill of João Pessoa, in consultations with manufacturers' manuals, and review of the scientific literature. For thermodynamic modeling, the Engineering Equation Solver software was used. The results show that the integration of a Rankine cycle to the current biogas plant increases the generation of electric energy. This proposal can be adapted to different realities on a global scale, allowing a more rational use and guaranteeing the maximum thermodynamic potential of natural resources.

Keywords - exhaust gases, steam turbine, energy efficiency, sustainability

I. INTRODUCTION

The Rankine cycle is characterized as one of the most important ways of transforming thermal energy into mechanical and/or electrical energy. This cycle is normally implemented in nuclear and coal-fired power plants, but it can also be implemented in several other ways, such as in agro-industrial activities that use sugarcane bagasse as a raw material for generating electricity. The process is done by burning this renewable source of energy, using the heat from the exhaust gases in steam turbines [1], or in combined cycles that use this heat in a first thermodynamic process, for reuse in a Rankine cycle in a second process. Combined cycles are quite common in plants that use cogeneration technology, which is characterized by obtaining two or more forms of energy from a single source [2].

The main components of a Rankine cycle are: condenser, pump, vaporizer (or boiler), and turbine, in addition to the working fluid [3]. The working fluid can be water (conventional) or organic fluids. When the working fluid of the cycle is of the organic type, the cycle is called Organic Rankine Cycle (ORC). Organic fluids have a low enthalpy of evaporation, and are generally used at lower temperatures and

pressures, often offering better energy yields, as in the case of solar, geothermal, and biomass products [4]. Thus, there is a wide variety of organic fluids for application in an ORC, such as R113, R123, R134a, isobutane, R12 and R22 [5-7]. Some important characteristics for a good working fluid are low toxicity, good material compatibility and fluid stability limits, in addition to low flammability, adhesion and encrustation.

There are ways to ensure better performance in a Rankine cycle, such as reheating and regeneration [8,9]. This is made possible by modifications to the basic components of the cycle. The Rankine cycle with reheating is an essential process to decrease the moisture content of steam at the turbine outlet. The reheating pressure is selected to increase cycle efficiency. However, there is a risk of overheating, especially in low-pressure stages at the turbine outlet [10]. The regenerative Rankine cycle is characterized by the presence of a water feeder, which receives the fluid that leaves the condenser, and is reheated by the steam that leaves the high-pressure turbine. This process increases the temperature of the circulating fluid, which consequently increases the thermodynamic efficiency of the cycle. However, sometimes this can make the process complex, with low financial returns [11].

With regard to feeding the Rankine cycle or ORC, due to environmental concerns, the trend is for renewable fuels to gain more and more space (e.g., biomass, biogas) [12]. In [13] authors presented a systematic review of the different ways of using biogas resulting from organic matter, where biogas can be used in different proposals through thermodynamic cycles for the production of electrical and thermal energy. Often, in addition to the financial advantages [14], there are environmental advantages [15].

In the work by [16], there was a technical and financial feasibility analysis of the use of Metropolitan Sanitary Landfill of João Pessoa (MSLJP) biogas to generate electricity, together with the use of thermal energy to evaporate the leachate (cogeneration). In this case, the landfill manages to generate 11,277.28 t/year of biogas at its peak production, which will occur in the year of closure of its activities, in 2028. Cogeneration was technically feasible with the Jenbacher 620 GS-BL engine, generating electricity to meet the needs of landfill activities and sell the surplus to the electricity utility. The

total economic balance, over the useful life of the landfill, is just over R\$ 29 million plus, considering all the possibilities for using the biogas mentioned above.

The objective of the present study was to develop and simulate a thermodynamic model for the integration of a Rankine cycle to the MSLJP biogas plant. The proposal is based on the use of exhaust gases from internal combustion engines at the plant. Sensitivity analyzes were also carried out to verify the impact of strategies to increase efficiency: reheating and regeneration.

II. MATERIAL AND METHODS

A. Study Case

In the city of João Pessoa, the final destination of all waste collected is MSLJP. The solid urban waste (also known as manure solid waste, by the acronym MSW) produced is collected by the Municipal Special Authority for Urban Cleaning (EMLUR) of João Pessoa [17]. In this way, urban cleaning services are the sole and exclusive responsibility of EMLUR. In addition to João Pessoa, the MSLJP receives waste from other cities that are part of an inter-municipal consortium. The cities are: Cabedelo, Conde, Santa Rita, Bayeux, Pedras de Fogo, Mamanguape, Marcação, Caaporã and Baía da Traição [18]. To meet all the demand for waste collected in these municipalities, the MSLJP was designed with 24 cells (each with a final volume of 450,000 m³), installed in an area of 100 hectares, with a useful life of approximately 25 years [19]. The landfill receives an average of 2,400 tons/day of MSW, had its activities started in 2003, and is approximately 19 km from the commercial center of the city of João Pessoa [18].

The MSW collected, treated and deposited in the landfill undergo a biochemical decomposition process [20,21] transforming a large part of the organic matter into biogas. The biogas plant was installed to start the distribution of renewable energy in the electrical grid. Initially, the project was installed with 4.2 MW of power, producing around 30,000 MWh of electricity per year [22]. The biogas plant of the MSLJP has four Jenbacher JMS 420 engines. Here, it is proposed the integration of a basic Rankine cycle to the existing biogas plant, where the exhaust gases coming out of the engines go directly to a recovery boiler. Fig. 1 illustrates the proposed system.

The working fluid in the boiler is water, which is fed by a pump that draws water from a reservoir located in the plant. In this way, the exhaust gases, when in contact with the pipes, which contain water inside, effect steam, and the steam feeds the turbine, generating work. There is a generator coupled to the turbine, which converts mechanical energy into electrical energy. Through the system's condensation process, the fluid in the liquid phase is sent to a condenser, which in turn recovers part of the water and is sent back to the cycle.

Points 1, 2, 3, 4, 5, 6 and 7 identified in Figs. 1-3 are used in the thermodynamic analysis of the plant. Eq. (1) represents general approval for the First Law of Thermodynamics (FLT).

$$\left(\frac{dE}{dt}\right) = \dot{Q} - \dot{W} + \sum \dot{m}_{in} h_{in}^T - \sum \dot{m}_{out} h_{out}^T \quad (1)$$

The time rate of change of energy contained in the control volume at a given instant is represented by the term $\left(\frac{dE}{dt}\right)$, \dot{Q} represents the net heat rate (kW), \dot{W} is the net work rate (kW), \dot{m} refers to the mass flow rate (kg/s), h^T is the total enthalpy, which includes kinetic and potential energy components (kJ/kg).

In this study, the following considerations were made: steady state, there is no head loss in the pipes, and kinetic and potential energy variations were disregarded. Table I shows the application of the FLT for each control volume of Fig. 1, where \dot{Q}_{boiler} is the heat transfer rate in the boiler, \dot{W}_T is the turbine power, $\dot{Q}_{condenser}$ is the heat transfer rate in the condenser.

The total energy yield of the Rankine cycle integrated into the MSLJP biogas plant can be calculated by Eq. (2), which, in turn, depends on

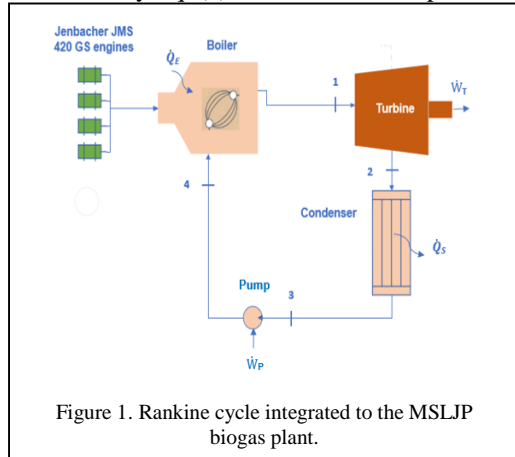


Figure 1. Rankine cycle integrated to the MSLJP biogas plant.

the resolution of Eq. (3) (for a basic Rankine cycle and for a regenerative Rankine cycle).

$$\eta = \frac{W_{total}}{\dot{Q}_{boiler}} \quad (2)$$

$$W_{total} = \dot{W}_T - \dot{W}_{pump} \quad (3)$$

Thermodynamic simulations were modeled and solved using the software Engineering Equation Solver (EES) [23]. The EES software has been used as a programming tool to analyze and simplify the energy balance of thermodynamic plants. Its basic function is to solve a set of algebraic problems, including non-linear equations, differential equations and equations with complex variables [24]. Here, an isentropic efficiency of 90% is assumed for the pump and turbine.

Table II shows the data obtained for the plant's engines. For the integration of a Rankine cycle to the plant, the data of interest are those referring to the exhaust gases of the engines after the combustion process. Data based on [25].

For dimensioning the thermodynamic plant outlined in Figs. 1-3, the equipment must meet the actual demands of the plant. Considering that there are four engines, the total mass flow is 31.696 kg/h. Thus, the heat recovery boiler needs to work with gases at approximately 465°C and with this mass flow rate.

TABLE I. ENERGY BALANCE OF EACH BASIC RANKINE CYCLE DEVICE.

Device	Energy balance
Boiler	$\frac{\dot{Q}_{boiler}}{\dot{m}} = h_1 - h_4$
Turbine	$\frac{\dot{W}_T}{\dot{m}} = h_1 - h_2$
Pump	$\frac{\dot{W}_{pump}}{\dot{m}} = h_4 - h_3$
Condenser	$\frac{\dot{Q}_{condenser}}{\dot{m}} = h_2 - h_3$

TABLE II. ENGINE EXHAUST GAS DATA.

Properties	Data
Exhaust temperature	465°C
Exhaust mass flow	7.924 kg/h

B. Sensitivity Analyses

This section analyzes the impact of strategies aimed at increasing the efficiency of the Rankine cycle. The sensitivity analysis was based on [26].

For the case of the Rankine cycle with reheating, following Fig. 2, the steam expands through a turbine in the first stage (process 1-2), up to a pressure value between the boiler and condenser pressures. After reheating occurs, the steam is expanded to a second stage (process 2-3), feeding the second turbine. After converting mechanical energy into electrical energy, the fluid is routed to the condenser (process 3-4). After condensation, the water is transferred back to the cycle through a suction pump.

In this case, Eq. (3) is replaced by Eq. (4), which represents the cycle Rankine with reheating.

$$\dot{W}_{total} = \dot{W}_{T1} + \dot{W}_{T2} - \dot{W}_{pump}. \quad (4)$$

Table III represents the application of the FLT for each control volume studied referring to Fig. 2. \dot{W}_{T1} and \dot{W}_{T2} respectively represent the power in turbines 1 and 2.

In the case of the Rankine regenerative cycle, following Fig. 3, the influence is carried out by means of a feed water heater. Steam enters the first stage turbine at state 1 and expands to state 2, where a full flow distribution is drawn to the feedwater heater. The rest of the steam expands through the turbine in the second stage to state 3. This part is condensed into a saturated liquid at state 4. It is then pumped up to the draw pressure and introduced into the heater at state 5. A single mixed stream exits the heater at state 6.

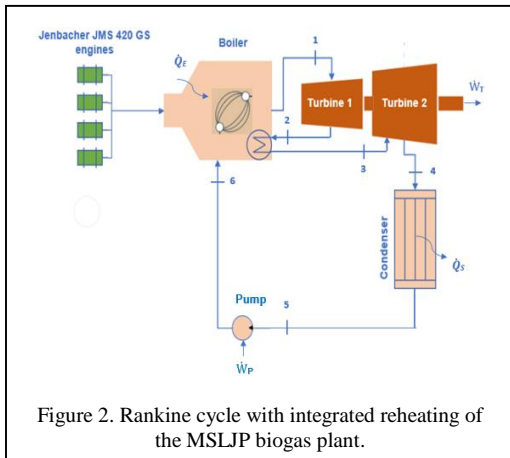


Figure 2. Rankine cycle with integrated reheating of the MSLJP biogas plant.

And finally, the liquid is pumped to state 7, and contacts the boiler, resulting in state 1 conditions.

Table IV represents the application of the FLT for each control volume studied referring to Fig. 3. The generation of the total flow extracted in state 2 is determined by y (represented by applying the Fig. 3 principles of conservation of mass and energy to the control volume surrounding the feedwater heater).

III. RESULTS AND DISCUSSION

Table V shows the values of pressure (P), enthalpy (h), entropy (s), specific volume (v) and temperature (T) for each point of the system represented in Fig. 1, considering the isentropic efficiencies of the turbine and the pump. Table VI shows the results of the energy balance (FLT). According to Table VI, \dot{W}_{net} represents the total power of the cycle. That is, the turbine power

TABLE III. ENERGY BALANCE OF EACH RANKINE CYCLE DEVICE WITH REHEATING.

Device	Energy balance
Boiler	$\frac{\dot{Q}_{boiler}}{\dot{m}} = (h1 - h6) + (h3 - h2)$
Turbine 1	$\frac{\dot{W}_{T1}}{\dot{m}} = h1 - h2$
Turbine 2	$\frac{\dot{W}_{T2}}{\dot{m}} = h3 - h4$
Pump	$\frac{\dot{W}_{pump}}{\dot{m}} = h6 - h5$
Condenser	$\frac{\dot{Q}_{condenser}}{\dot{m}} = h4 - h5$

TABLE IV. ENERGY BALANCE OF EACH REGENERATIVE RANKINE CYCLE DEVICE.

Device	Energy balance
Boiler	$\frac{\dot{Q}_{boiler}}{\dot{m}} = h1 - h7$
-	$y = (h6 - h5)/(h2 - h5)$
Turbine	$\frac{\dot{W}_T}{\dot{m}} = h3 - h4$
Pump	$\frac{\dot{Q}_{pump}}{\dot{m}} = (h7 - h6) + (1 - y) \times (h5 - h4)$
Condenser	$\frac{\dot{Q}_{condenser}}{\dot{m}} = (1 - y) \times (h3 - h4)$

TABLE V. THERMODYNAMIC PROPERTIES FOR EACH POINT OF THE BASIC RANKINE CYCLE.

Flow	P (kPa)*	h (kJ/kg)	s (kJ/kg.K)	v (m ³ /kg)	T (°C)
1	8000	3310.0	6.608	-	465
2	8	2191.0	-	-	-
3	8	173.9	0.5925	0.0010	-
4	8000	182.8	-	-	-

*[26] [27].

TABLE VI. RESULTS FOR THE ENERGY BALANCE OF BASIC RANKINE CYCLE EQUIPMENT.

$\frac{\dot{Q}_{boiler}}{\dot{m}}$ (kJ/kg)	$\frac{\dot{Q}_{pump}}{\dot{m}}$ (kJ/kg)	$\frac{\dot{W}_T}{\dot{m}}$ (kJ/kg)	$\frac{\dot{W}_{net}}{\dot{m}}$ (kJ/kg)	η (%)
3128	8.955	1119	1110	35.5

minus the pump power. And η represents the energy efficiency of the cycle considering the isentropic losses of the system.

Table VII shows the values of pressure (P), enthalpy (h), entropy (s), specific volume (v) and temperature (T) for each point of the system represented in Fig. 2, considering the isentropic efficiencies of the turbine and the pump. Table VIII shows the results of the energy balance (FLT). \dot{W}_{T1} and \dot{W}_{T2} respectively represent the power of turbines 1 and 2, \dot{W}_{net} represents the total power of the cycle. Given by the sum of the power of the two turbines, minus the power of the pump. And η represents the energy efficiency of the cycle considering the isentropic losses of the system.

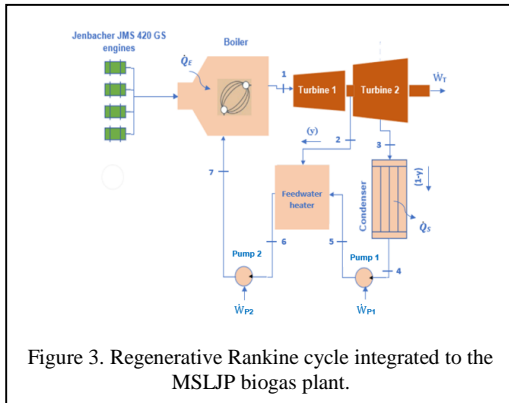


Figure 3. Regenerative Rankine cycle integrated to the MSLJP biogas plant.

TABLE VII. THERMODYNAMIC PROPERTIES FOR EACH RANKINE CYCLE POINT WITH REHEATING.

Flow	P (kPa)*	h (kJ/kg)	s (kJ/kg.K)	v (m ³ /kg)	T (°C)
1	8000	3310.0	6.608	-	465
2	700	2778.0	-	-	-
3	700	3353.0	7.757	-	440
4	8	2521.0	-	-	-
5	8	173.9	0.5925	0.0010	-
6	8000	182.8	-	-	-

*[26] [27].

TABLE VIII. RESULTS FOR THE ENERGY BALANCE OF RANKINE CYCLE EQUIPMENT WITH REHEATING.

$\frac{\dot{Q}_{boiler}}{\dot{m}}$ (kJ/kg)	$\frac{\dot{Q}_{pump}}{\dot{m}}$ (kJ/kg)	$\frac{\dot{W}_{T1}}{\dot{m}}$ and $\frac{\dot{W}_{T2}}{\dot{m}}$ (kJ/kg)	$\frac{\dot{W}_{net}}{\dot{m}}$ (kJ/kg)	η (%)
3702	8.955	1364.2	1355	36.61

Table IX shows the values of pressure (P), enthalpy (h), entropy (s), specific volume (v) and temperature (T) for each point of the system represented in Fig. 3, considering the isentropic efficiencies of the turbine and the pump. Table X shows the results of the energy balance (FLT). \dot{W}_{net} represents the total power of the cycle. That is, the power of the turbines minus the power of the pumps, and η represents the energy efficiency of the cycle considering the isentropic losses of the system. For the state at point 2, the superheated steam saturation temperature is approximately 165°C (referring to P2=700 kPa) [26]. Therefore, a temperature higher than this value, 220°C, was estimated for calculation purposes.

TABLE IX. THERMODYNAMIC PROPERTIES FOR EACH POINT OF THE REGENERATIVE RANKINE CYCLE.

Flow	P (kPa)*	h (kJ/kg)	s (kJ/kg.K)	v (m ³ /kg)	T (°C)
1	8000	3310.0	6.608	-	465
2	700	2778.0	6.976	-	220
3	8	2242.0	-	-	-
4	8	173.9	0.5925	0.0010	-
5	700	174.6	0.5925	-	-
6	700	697.4	1.993	0.0011	-
7	8000	706.3	-	-	-

*[26] [27].

TABLE X. RESULTS FOR THE ENERGY BALANCE OF REGENERATIVE RANKINE CYCLE EQUIPMENT.

$\frac{\dot{Q}_{boiler}}{\dot{m}}$ (kJ/kg)	$\frac{\dot{Q}_{pump}}{\dot{m}}$ (kJ/kg)	$\frac{\dot{W}_T}{\dot{m}}$ (kJ/kg)	$\frac{\dot{W}_{net}}{\dot{m}}$ (kJ/kg)	γ	η (%)
2605	9.606	960	951	0.2008	36.5

Knowing that the exhaust gases coming from the four engines of the plant offer 31.696 kg/h of post-combustion biogas, the ideal Rankine cycle manages to produce $\dot{W}_{net} = 78.18 \text{ kWh/day}$, while the Rankine cycles with reheating and efficiency effect 95.44 and 66.97 kWh/day, respectively. As the focus of the work concerns only the production of electrical energy, the Rankine regenerative cycle presented lower results than the others (with regard to net power). However, for thermal energy this cycle has better conservation, considering that the enthalpies at points 6 and 7 are greater than the enthalpies at points 6 and 5 (reheating) and 4 and 3 (basic) of the other cycles.

Table XI shows an estimate for the amount of electrical energy produced for the three Rankine cycles presented in this work. It was considered, for calculation purposes, that the engines work 8 hours a day, during 365 days per year. For the Rankine cycle with reheating, the power of the two turbines were summed. The last column on the right of Table XI represents the sum of the electric energy produced by the plant plus the integration of the respective cycles. It is known that the potential for production of electricity by the MSLJP plant represents 30.000 MWh annually [22], and a useful life with the supply of biogas until the year 2042 [16].

TABLE XI. ELECTRICITY PRODUCTION ESTIMATE FOR EACH STUDIED CYCLE.

Cycle	\dot{W}_T (kWh/ year)	$\dot{W}_{T(PLANT)} + \dot{W}_T$ (MWh/year)	$\dot{W}_{T(PLANT)} + \dot{W}_T$ (MWh/ lifespan)
Real power plant (without the integration of a Rankine cycle)	-	30.000	600.000
Basic Rankine cycle	28.537	30.029	600.571
Rankine cycle with reheating	34.836	30.035	600.697
Regenerative Rankine cycle	25.444	30.026	600.449

The results shown in Table XI represent values where all the fuel needed for production comes from landfill biogas, a renewable source of energy. According to the values obtained by the simulation carried out in the EES, the Rankine cycle with reheating was the one that obtained the highest production of electric energy among all the analyzed ones. In addition to having better energy yield. Therefore, it would be most recommended for integration into the MSLJP biogas plant.

There are other positive experiences of using landfill biogas for energy schemes. In [28] authors carried out a technical and economic evaluation of combined cycle plants powered by landfill biogas in Monterrey, Mexico. The proposal, in addition to increasing energy efficiency, brings environmental benefits through the reduction of greenhouse gas (GHG) emissions, with emphasis on recycling reusable products (glass, metal, paper and plastic). The standard combined cycle is characterized by the integration of internal combustion engine (ICE) with ORC. The method with the best financial, economic and environmental return was to integrate only one ORC module with 1.5 MW_e of production capacity to 16 ICE modules. Thus, the electricity generation capacity of 16.94 MW_e would increase to 18.44 MW_e (an increase of 8.9%), generating 11.24 GWh/year of electricity. The financial return would be recovered in less than eight years (when electricity prices are higher than 0.09 US\$/kWh), and after that there would be a profit, enabling the sale of generated and stored energy. Furthermore, the new plant would avoid the emission of 4,159 MT of CO₂ per year. In [14] authors evaluated the potential for biogas generation in a landfill located in Seville, Spain. According to the authors, a Jenbacher JMS 420 engine was identified as having better integration with the availability of the study biogas. In addition, the use of the resulting heat provided by the engine's post-combustion process to accelerate the leachate evaporation, reducing the risks of slurry surplus, was also evaluated. The study shows that the captured biogas capacity is approximately 65,000 tons in 30 years.

The contribution of this work compared to the study by [16], is that the possibility of coupling a Rankine cycle to reuse the exhaust gases of post-combustion biogas was analyzed. This considered four Jenbacher JMS 420 model engines (real situation of the plant), during the work of [16] considered only a Jenbacher

JMS 620 model engine (hypothetical situation). Finally, it is observed that there is still plenty of space for works with this proposal in the current scientific literature. The use of landfill biogas for energy purposes and environmental mitigation proves to be an excellent opportunity to meet global electricity demands and diversify the portfolio of the global energy matrix. The integration of a Rankine cycle to ICE plants is a strategy to take advantage of available natural resources, as well as to mitigate the environmental impacts derived from GHG emissions.

In Brazil, there are already other plants that use landfill biogas for energy purposes. In the municipality of Sabará, Minas Gerais, there is a plant with the capacity to produce 46.000 MWh of electricity per year, and avoid the emission of about 380.000 tons of CO₂ into the atmosphere [29]. In Jaboatão dos Guararapes, Pernambuco, the company's largest and most productive plant in Brazil is located, with eight engines and a total production of 96.500 MWh per year of electricity [30].

As a suggestion for future studies, it is expected that the same sensitivity analysis applied in this work can be expanded to landfill plants that work with more than four engines in the energy use of biogas. Therefore, the amount of supply of exhaust gases will probably be greater, consequently increasing the electrical energy potential of the system. Furthermore, studies focusing on other energy sources can also make use of the models proposed in this work. An economic analysis, followed by an environmental analysis, can also be made for proposed Rankine cycles integrated into the MSLJP biogas plant, to verify feasibility and cost-effectiveness. With the economic analysis, it is possible to know the payback of the project to integrate the Rankine cycles into the plant. Regarding environmental analysis, it is possible to quantify the mitigation of impacts on the environment. Therefore, it will be possible to know the real feasibility of implementing this work at ICE biogas plants.

IV. CONCLUSION

This work shows the importance of using renewable energy sources and their energy integration as a viable solution to ensure environmental, energy and economic benefits.

The biogas resulting from biochemical processes in sanitary landfills can be used in

processes of internal combustion engines, as is the case of the biogas plant in the Metropolitan Sanitary Landfill of João Pessoa.

Sensitivity thermodynamic analysis was performed for three different thermodynamic arrangements, for comparative purposes. The first was a basic Rankine cycle. The second represented a Rankine cycle with reheating. The third is a regenerative Rankine cycle. The values calculated for each cycle show yields of approximately: 35.5%, 36.61% and 36.5% respectively. With regard to the cycle with the highest production of electrical energy, the Rankine cycle with reheating showed the best results. When the additional electricity resulting from the integration of the Rankine cycle with reheating is added to the potential of the MSLJP biogas plant, the value would increase from 30.000.00 MWh/year to around 30.034.84 MWh/year. The Rankine cycle with reheating alone can produce about 696.714 MWh of electricity over its entire useful life, corresponding to the year in which the MSLJP activities ended, in 2042. The use of these exhaust gases increases the energy efficiency of the general process, and allows for an increase in electricity exports. This additional electricity can contribute to increased financial benefits, and has the potential to contribute to the mitigation of greenhouse gas emissions.

This study can be readapted to other present realities, proving that the more sustainable use of natural resources can be an extremely interesting solution to increase electricity production and minimize damage to the environment.

ACKNOWLEDGMENTS

The present work was carried out with support from the Brazilian National Council for Scientific and Technological Development (CNPq) (projects 308753/2021-6 and 309452/2021-0).

REFERENCES

- [1] Dantas, G. A., Legey, L. F., & Mazzone, A. (2013). Energy from sugarcane bagasse in Brazil: An assessment of the productivity and cost of different technological routes. *Renewable and Sustainable Energy Reviews*, 21, 356-364.
- [2] Colonna, P., Casati, E., Trapp, C., Mathijssen, T., Larjola, J., Turunen-Saaresti, T., & Uusitalo, A. (2015). Organic Rankine cycle power systems: from the concept to current technology, applications, and an outlook to the future. *Journal of Engineering for Gas Turbines and Power*, 137(10), 100801.

- [3] Tchanche, B. F., Lambrinos, G., Frangoudakis, A., & Papadakis, G. (2011). Low-grade heat conversion into power using organic Rankine cycles—A review of various applications. *Renewable and Sustainable Energy Reviews*, 15(8), 3963-3979.
- [4] Mago, P. J., Chamra, L. M., Srinivasan, K., & Somayaji, C. (2008). An examination of regenerative organic Rankine cycles using dry fluids. *Applied thermal engineering*, 28(8-9), 998-1007.
- [5] Vijayaraghavan, S., & Goswami, D. Y. (2005). Organic working fluids for a combined power and cooling cycle.
- [6] Drescher, U., & Brüggemann, D. (2007). Fluid selection for the Organic Rankine Cycle (ORC) in biomass power and heat plants. *Applied thermal engineering*, 27(1), 223-228.
- [7] Quoilin, S., Van Den Broek, M., Declaye, S., Dewallef, P., & Lemort, V. (2013). Techno-economic survey of Organic Rankine Cycle (ORC) systems. *Renewable and sustainable energy reviews*, 22, 168-186.
- [8] Li, G. (2016). Organic Rankine cycle performance evaluation and thermoeconomic assessment with various applications part I: Energy and exergy performance evaluation. *Renewable and Sustainable Energy Reviews*, 53, 477-499.
- [9] Li, G. (2016). Organic Rankine cycle performance evaluation and thermoeconomic assessment with various applications part II: Economic assessment aspect. *Renewable and Sustainable Energy Reviews*, 64, 490-505.
- [10] Hemadri, V. B., & Subbarao, P. M. V. (2021). Thermal integration of reheated organic Rankine cycle (RH-ORC) with gas turbine exhaust for maximum power recovery. *Thermal Science and Engineering Progress*, 23, 100876.
- [11] Anvari, S., Jafarmadar, S., & Khalilarya, S. (2016). Proposal of a combined heat and power plant hybridized with regeneration organic Rankine cycle: Energy-Exergy evaluation. *Energy Conversion and Management*, 122, 357-365.
- [12] Ghaffarpour, Z., Mahmoudi, M., Mosaffa, A. H., & Farshi, L. G. (2018). Thermoeconomic assessment of a novel integrated biomass based power generation system including gas turbine cycle, solid oxide fuel cell and Rankine cycle. *Energy conversion and management*, 161, 1-12.
- [13] Junior, D. A. B., Abrahão, R., & Carvalho, M. (2021). O uso de biogás de matéria orgânica para fins energéticos e mitigação ambiental: uma revisão sistemática. *Revista Multidisciplinar de Educação e Meio Ambiente*, 2(3), 93-93.
- [14] Chacartegui, R., Carvalho, M., Abrahão, R., & Becerra, J. (2015). Analysis of a CHP plant in a municipal solid waste landfill in the South of Spain. *Applied Thermal Engineering*, 91, 706-717.
- [15] Palacio, J. C. E., et al. (2019). Municipal solid waste management and energy recovery. In *Energy Conversion-Current Technologies and Future Trends*. IntechOpen.
- [16] Nascimento, D. P., Menezes, V. L., Carvalho, M., & Chacartegui, R. (2019). Energy analysis of products and processes in a sanitary landfill. *IET Renewable Power Generation*, 13(7), 1063-1075.
- [17] Legislação Municipal De João Pessoa/PB, 1991. “Lei N° 6811, de 04 de novembro de 1991”. Available at: <https://leismunicipais.com.br/a1/pb/j/joao-pessoa/lei-ordinaria/1991/6811/6811/lei-ordinaria-n-6811-1991-al-tera-a-natureza-juridica-da-empresa-municipal-de-limpeza-urbana-emlur-e-determina-outras-providencias-correlatas-e-complementares>. Access: 09 out. 2023.
- [18] EMLUR, 2021. “Seplan e Emlur acompanham estudos para aumentar vida útil do aterro sanitário”. Available at: <https://www.joao Pessoa.pb.gov.br/noticias/secretarias-e-orgaos/seplan-e-emlur-acompanham-estudos-para-aumentar-vida-util-do-aterro-sanitario/>. Access: 09 out. 2023.
- [19] Silva, G. A., Morais Jr, J. A., & Rocha, E. R. (2016). Proposta de procedimento operacional padrão para o teste do Potencial Bioquímico do Metano aplicado a resíduos sólidos urbanos. *Engenharia Sanitaria e Ambiental*, 21, 11-16.
- [20] Walker, L., Charles, W., & Cord-Ruwisch, R. (2009). Comparison of static, in-vessel composting of MSW with thermophilic anaerobic digestion and combinations of the two processes. *Bioresource technology*, 100(16), 3799-3807.
- [21] Peralta-Yahya, P. P., Zhang, F., Del Cardayre, S. B., & Keasling, J. D. (2012). Microbial engineering for the production of advanced biofuels. *Nature*, 488(7411), 320-328.
- [22] ASJA, 2019. “João Pessoa: uma nova planta de biogás da asja no Brasil”. Available at: <https://www.asja.energy/pt-br/noticias/joao-pessoa-uma-nova-planta-de-biogas-da-asja-no-brasil/>. Access: 09 out. 2023.
- [23] EES: *Engineering Equation Solver*, 2022. Available at: <https://fchartsoftware.com/ees/>. Access: 09 out. 2023.
- [24] Ghodbane, M., & HUSSEIN, A. K. (2021). Performance analysis of a solar-driven ejector air conditioning system under El-Oued climatic conditions, Algeria. *Journal of Thermal Engineering*, 7(1), 172-189.
- [25] Jenbacher Gas Engines, 2012. “Technical Description Genset-Container. JMS 420 GS-LL”. Available at: <https://vdocuments.mx/j420-gs-ll-container.html>. Access: 09 out. 2023.
- [26] Moran M. J., Shapiro H. N., Boettner D. D., Bailey M. B., 2014. “Princípios de Termodinâmica para Engenharia”, LTC publishing company: 7ª edition, Rio de Janeiro.
- [27] Tran, H., & Vakkilainen, E. K. (2008). The kraft chemical recovery process. *Tappi Kraft Pulping Short Course*, 1-8.
- [28] Saravia, J. R., Galaz, J. R. V., Villena, A. C., & Ortiz, J. N. (2012). Technical and economical evaluation of landfill-biogas fired combined cycle plants. *Distributed Generation & Alternative Energy Journal*, 27(3), 7-25.
- [29] ASJA, 2017. “Asja continua a crescer no Brasil: Inaugurada nova planta de biogás”. Available at: <https://www.asja.energy/pt-br/noticias/asja-continua-crescer-no-brasil-inaugurada-nova-planta-de-biogas/>. Access: 09 out. 2023.
- [30] ASJA, 2019. “A planta de biogás de Jaboatão, Brazil, entra em operação”. Available at: <https://www.asja.energy/pt-br/noticias/a-planta-de-biogas-de-jaboatao-brazil-entra-em-operacao/>. Access: 09 out. 2023.

Predicting Nitrous Oxide Emissions in Ghana using Long Short-term Memory and Gated Recurrent Neural Network

Benjamin Odoi¹, Derrick Akoto Boahen², Lewis Brew³

^{1,2,3}University of Mines and Technology, Tarkwa, Ghana

¹bodoi@umat.edu.gh, ²derekboahen@gmail.com, ³lbrew@umat.edu.gh

Abstract—The rapid release of Nitrous Oxide (N₂O) into space and its devastating effects on the environment has raised serious concerns among governmental agencies and researchers worldwide, prompting the need for urgent action. This research explores the predictive capabilities of Long Short-Term Memory (LSTM) and Gated Recurrent Neural Network (GRU) models in forecasting N₂O emissions in Ghana. Leveraging data from the World Bank spanning the years 1990 to 2020, the study examines emissions in the Energy sector. The primary objectives were to develop LSTM and GRU models that could accurately predict N₂O emissions from the Energy sector in Ghana, and to select the best model. To which LSTM performed relatively better than the GRU model. The findings demonstrate the effectiveness of LSTM and GRU models in capturing the intricate temporal patterns and dependencies within the data, outperforming conventional time-series forecasting methods. By dissecting emissions into distinct sectors, granular insights into the sources and drivers of N₂O emissions in Ghana are provided. The research not only contributes to the burgeoning field of greenhouse gas emissions prediction but also offers practical implications for environmental policymakers and stakeholders. The sectoral analysis aids in the development of targeted strategies for emission reduction and sustainable environmental management in Ghana. As nations strive to meet their climate commitments, understanding and accurately forecasting emissions dynamics become paramount, and this study adds a valuable tool to this effort.

Keywords – nitrous oxide emissions, energy sector, long short-term memory, gated recurrent neural network, pattern

I. INTRODUCTION

The ongoing increase in temperature on our planet is deeply concerning, and it can be traced back to the root cause of global warming. This process begins when the sun's energy reaches Earth, with about 30% of it being reflected back into space by clouds, water particles, reflective surfaces, and the ocean surface. The remaining energy is absorbed by the land, air, and seas [1], which in turn heats up the planet's surface and atmosphere, making life possible. As the Earth warms up, the solar energy is radiated back out into space through thermal radiation and infrared rays, which cools the planet down [2]. However, some of this energy is reabsorbed by greenhouse gases like nitrous oxide (N₂O), carbon dioxide (CO₂), water vapor, ozone, methane (CH₄), and others, which trap the heat and radiate it back to the Earth's surface, causing further warming.

Nitrous oxide is a significant anthropogenic greenhouse gas that has garnered attention for its potential to mitigate global warming. It is also recognized as the most important ozone-depleting substance in the stratosphere [3]. Ranking as the third most prevalent greenhouse gas after carbon dioxide and methane, N₂O has steadily increased in atmospheric concentration since the 1990s, with an atmospheric life of 121 years and a global warming potential 300 times that of CO₂ over a 100-year period [4].

In 2016, total national greenhouse gas emissions in Ghana were 42.2 MtCO₂e, with N₂O ranking as the second largest greenhouse gas at about 18.3%. N₂O is a stable substance that can influence global atmospheric concentrations for several decades [5], making it a significant concern for climate change [6].

Despite its ability to absorb infrared light, N₂O has a major effect on Earth's radiation budget and can contribute significantly to greenhouse gas emissions. Additionally, it is the leading ozone-depleting agent currently released. Therefore, legislation to restrict N₂O emissions could help protect the climate and recover ozone.

This research aims to analyze historical data on N₂O emissions in Ghana from 1990 to 2020 and make future predictions up to 2025 using LSTM and GRU models to help the Ghanaian government implement policies and strategies to limit N₂O emissions within the country.

II. SOME RELATED LITERATURE

The following are some related works considered under this study.

Reference [7] introduced Long Short-term Memory (LSTM), a novel recurrent neural network architecture that can learn to store information over extended time intervals. The paper compares LSTM with other recurrent neural network algorithms and shows that LSTM leads to many more successful runs and learns much faster.

Reference [8] introduces the concept of encoder-decoder neural architectures and discusses their properties. While not focused solely on GRUs, it provides foundational insights into sequence-to-sequence models, which can be helpful for understanding GRU-based sequence modeling.

The article by [9] presents a method called Learning to Forget, which is a continual prediction with LSTM. The paper shows that LSTM can learn to forget irrelevant information and store relevant information over extended time intervals.

Reference [10] present an empirical evaluation of Gated Recurrent Neural Networks (GRUs) on sequence modeling tasks. It discusses how GRUs improve over traditional recurrent networks and provides insights into their effectiveness in capturing long-range dependencies in sequences.

Reference [11] present a bidirectional LSTM architecture for frame-wise phoneme classification. The paper shows that bidirectional LSTM outperforms other neural network architectures for this task.

Reference [12] also introduces the concept of "Clockwork RNNs", an extension of traditional RNNs that can process different parts of a sequence at different timescales. Although not specifically about GRUs, this concept offers inspiration for time-dependent modeling using gated structures.

Reference [13] reports on sequence-to-sequence learning with neural networks. The research gives insight into machine translation, image captioning, and other sequence to sequence tasks using LSTM.

Reference [14] explore memory-efficient neural networks for time series modeling. It discusses techniques that can complement the capabilities of GRUs, contributing to the understanding of memory-efficient modeling.

The survey in [15] provides a comprehensive overview of various recurrent neural network architectures, including GRUs. It discusses their training techniques and applications, which aids in understanding the broader context of GRUs in sequence modeling.

Reference [16], though not solely about GRUs, this influential paper introduces the Transformer architecture, which uses self-attention mechanisms. Understanding attention mechanisms can be valuable when considering the capabilities of GRUs in capturing sequence relationships.

Reference [17] propose a Depth-Gated LSTM, a modification to the traditional LSTM architecture that enhances performance on natural language processing tasks by improving depth learning.

In this paper, Karpathy and Li present a visualization technique to understand the behavior of recurrent neural networks, including LSTM, providing insights into their internal representations [18].

Reference [19] apply LSTM-based generative models to zero-shot learning from noisy texts, showcasing the versatility of LSTM in various machine learning tasks.

In this empirical evaluation study [20], the performance of various recurrent and

convolutional networks, including GRUs, for sequence modeling are compared. It provides insights into the strengths and weaknesses of GRUs in relation to other architectures.

III. METHODS USED

This chapter provides an exhaustive methodology for predicting nitrous oxide emissions in Ghana using Gated Recurrent Neural Networks.

A. Background: Recurrent Neural Network

An extension of the conventional feed-forward neural network is the recurrent neural network (RNN), which has the capability to process input sequences of varying lengths. The RNN accomplishes this by utilizing a recurrent hidden state, where the activation at each time step is influenced by the previous time step's activation. More formally, given a sequence $x = (x_1, x_2, \dots, x_T)$, the RNN updates its recurrent hidden state by h_t :

$$h_t = \begin{cases} 0, & t = 0 \\ \varphi(h_{t-1}, x_t), & \text{otherwise} \end{cases}, \quad (1)$$

where φ is a nonlinear function such as composition of a logistic sigmoid with an affine transformation. Optionally, the RNN may have an output $y = (y_1, y_2, \dots, y_T)$ which may again be of variable length. Traditionally, the update of the recurrent hidden state in Eq. (1) is implemented as:

$$h_t = g(Wx_t + Uh_{t-1}), \quad (2)$$

where g is a smooth, bounded function such as a logistic sigmoid function or a hyperbolic tangent function.

A generative RNN can produce a probability distribution for the next element in a sequence based on its current state h_t . This type of generative model can also represent sequences of varying lengths by using a unique output symbol to indicate the end of the sequence. The probability of the sequence can be broken down into smaller parts:

$$p(x_1, \dots, x_T) = p(x_1)p(x_2 | x_1) \times p(x_3 | x_1, x_2) \cdots p(x_T | x_1, \dots, x_{T-1}), \quad (3)$$

where the last element is a special end-of-sequence value. We model each conditional probability distribution with:

$$p(x_t | x_1, \dots, x_{t-1}) = g(h_t), \quad (4)$$

where h_t is from Eq. (1). Such generative RNNs are the subject of this research.

Unfortunately, [21] have observed that training RNNs to capture long-term dependencies is challenging due to the tendency for gradients to either vanish (most of the time) or explode (rarely but with severe consequences). This difficulty is not only due to the variations in gradient magnitudes but also because the effect of long-term dependencies is hidden by the effect of short-term dependencies, which are exponentially smaller with respect to sequence length. To address this issue, researchers have pursued two dominant approaches. The first approach involves developing better learning algorithms than simple stochastic gradient descent, such as clipped gradient or second-order methods (see, e.g., [22-24]).

The second approach, which is the focus of this research, involves designing more sophisticated activation functions, such as those consisting of affine transformations followed by simple element-wise nonlinearities using gating units. One such activation function is the Long Short-Term Memory (LSTM) unit, which was proposed by [7] (Fig. 1). Another type of recurrent unit, the Gated Recurrent Unit (GRU), was recently proposed by [10]. RNNs using either of these recurrent units have been shown to perform well in tasks requiring the capture of long-term dependencies.

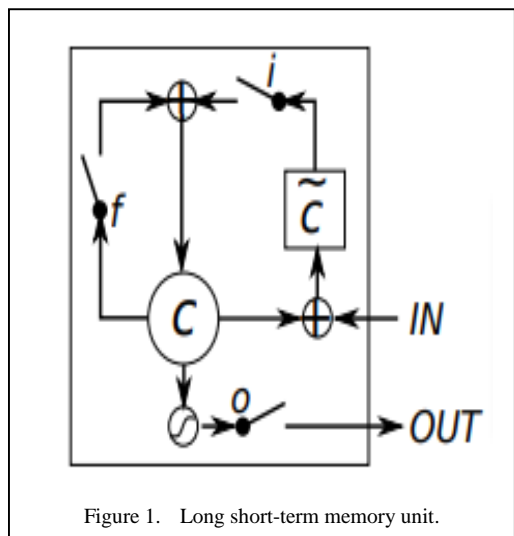
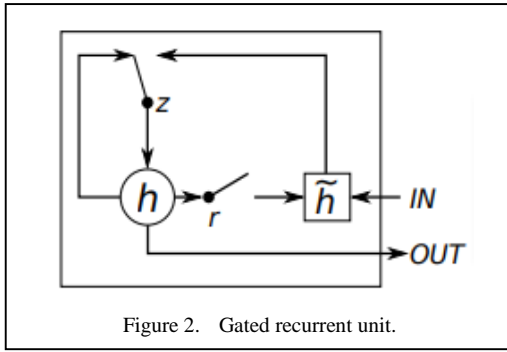


Figure 1. Long short-term memory unit.



In the diagram above, i , f and o are the input, forget and output gates, respectively. c and \tilde{c} denote the memory cell and the new memory cell content. In Fig. 2 r and z are the reset and update gates, and h and \tilde{h} are the activation and the candidate activation.

B. Gated Recurrent Neural Networks

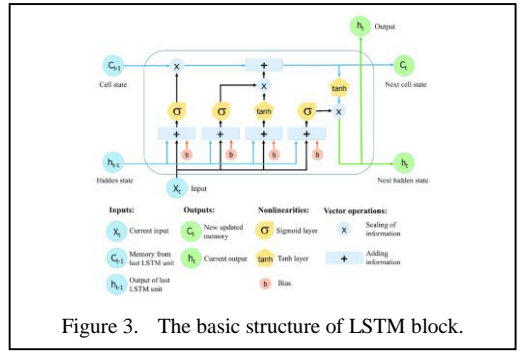
In this research, we are interested in implementing those recently proposed recurrent units (LSTM unit and GRU) for climate change prediction. Before the analysis, we first describe each of those recurrent units in this section.

1) Long short-term memory

The LSTM unit is a more complex form of the recurrent neural network (RNN) structure that was developed in 1997 to tackle the issue of gradient vanishing or exploding encountered by RNN. This was achieved by incorporating supplementary interactions per cell [7].

The LSTM network is a modified version of RNN that incorporates a gating mechanism and replaces RNN nodes with memory blocks. These memory blocks not only include a memory cell to store temporal states, but also feature adaptive multiplicative units known as gates that regulate information flow within the block [25]. By default, LSTM can learn long-term dependencies and retain information for extended periods. [26] note that the 18 LSTM model has a chain structure, but the repeating module follows a distinct chain structure with four interacting layers and a unique communication method. The structure of the LSTM neural network is depicted in Fig. 3.

The cell state and hidden state are the two states that are transmitted to the next cell. The cell state, which is the primary data flow, allows the data to progress forward with minimal changes, although some linear transformations may occur. The sigmoid gates regulate the addition or removal of data from the cell state



[25]. The memory cell, which acts as a state information accumulator in the LSTM network, features three gate types: forget, input, and output gates. These gates maintain and modify the cell state. The LSTM network can determine which cells to restrict or promote and what information to retain or discard based on the previous state, current memory, and current input. This occurs during the training process [27].

The current cell state is updated by the input gate, which determines the amount of new information to be added. The forget gate regulates the amount of information to be discarded from the previous cell state, preventing unbounded growth of internal cell values [25]. The output gate filters the new state to determine which information from the memory (cell state) will be used as output information [28]. To construct an LSTM network, unnecessary information is identified and excluded from the cell state using the sigmoid function. This function takes the output of the last LSTM unit h_{t-1} at time $t - 1$ and the current input X_t at time t to determine which part of the old output should be eliminated, known as the forget gate f_t , where f_t is a vector ranging from 0 to 1, corresponding to each number in the cell state C_{t-1} .

$$f_t = \sigma(W_f[h_{t-1}t - 1, X_t]) + b_f. \quad (5)$$

Thus, σ represents the sigmoid function, while W_f and b_f represent the weight matrices and bias of the forget gate, respectively. The input gate is responsible for determining and storing information from the new input X_t , in the cell state, as well as updating the cell state. It comprises of two components: the sigmoid layer and the tanh layer. The sigmoid layer determines whether the new information should be updated or ignored (0 or 1), while the tanh function assigns weight to the values that have passed, determining their level of importance (-1 to 1).

These two values are multiplied to update the new cell state, which is then added to the old memory C_{t-1} resulting in C_t ,

$$i_t = \tanh(W_i[h_{t-1}, X_t] + b_i), \quad (6)$$

$$C_t = \tanh(W_c[h_{t-1}, X_t] + b_c), \quad (7)$$

where C_{t-1} and C_t are the cell states at time $t-1$ and t . Also, W and b are the weight matrices and bias respectively of the cell state. The final step involves the output gate, which serves to filter the cell state and compute the required data. The filtered version of the output values, h_t , is determined by the output cell state, O_t . To achieve this, a sigmoid layer is employed to select the relevant sections of the cell state for output. The resulting output of the sigmoid 2 gate, O_t , is then multiplied by the new values generated by the tanh layer from the cell state, C_t , which fall within the range of -1 to 1.

$$O_t = \tanh(W_o[h_{t-1}, X_t] + b_o), \quad (8)$$

$$h_t = O_t \cdot \tanh(C_t), \quad (9)$$

W_o and b_o are the weight matrices and bias, respectively, of the output gate.

2) Gated recurrent unit

Reference [10] proposed Gated Recurrent Units, a simplified version of LSTM that improves network performance and requires less training time. The GRU cell operates similarly to the LSTM cell, but it uses one hidden state that combines forget and input gates into a single update gate. Additionally, the GRU cell merges the cell state and hidden state into one state, resulting in half the total number of gates compared to LSTM (update and reset gates).

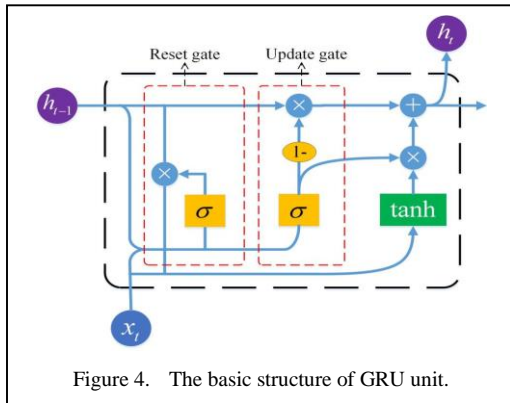


Figure 4. The basic structure of GRU unit.

As a result, GRU has become a popular and simplified variant of the LSTM cell. The following equation updates the hidden state of the GRU cell:

$$h_t = (1 - z_t) \times h_{t-1} + z_t \times \tilde{h}_t. \quad (10)$$

The update gate is computed by the following equation, which decides how much of the GRU unit get updated:

$$z_t = \sigma(W_z \times [h_{t-1}, x_t]). \quad (11)$$

The reset gate is computed very similar to the update gate, it is given by the following equation:

$$r_t = \sigma(W_r \times [h_{t-1}, x_t]). \quad (12)$$

The new remember gate is generated by applying hyperbolic tan function to the reset gate, which is described by the following function:

$$\tilde{h}_t = \tanh(W \times [r_t \times h_{t-1}, x_t]). \quad (13)$$

IV. DATA ANALYSIS AND RESULTS

A. Introduction

This section entails the research analysis conducted using secondary data collected from the World Bank. The data covers the period from 1990 to 2020.

B. Data Sample

Table I shows a sample of the dataset on N_2O emissions in the energy sector while Fig. 5 shows a line plot of the data-points over the years.

TABLE I. DATA SAMPLE ON N_2O EMISSIONS.

Date	Emission	Date	Emission
1991	180.2	1998	227.4
1992	181.5	1999	245.1
1993	192.7	2000	256.1
1994	197.7	2001	217.1
1995	204.2	2002	208.1
1996	212.5	2003	210.5
1997	221	2004	196

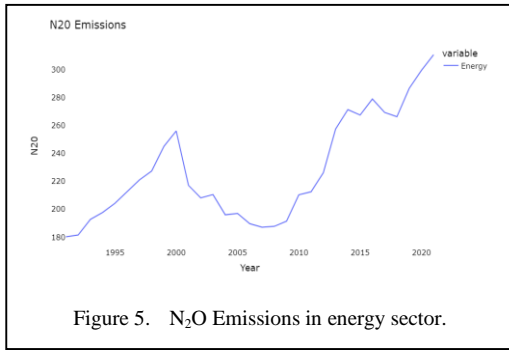


Figure 5. N₂O Emissions in energy sector.

It can be deduced from Fig. 5 above that the Energy sector saw a significant downward trend in N₂O emissions from the period of 1999-2005, after which it has seen not much decline for more than a decade.

C. Preliminary Analysis of Data

Table II presents the descriptive statistics of the data. The table shows the mean, standard deviation, minimum, and maximum values for the variable considered:

TABLE II. DESCRIPTIVE STATISTICS OF THE DATA.

Variable	Mean	Standard Deviation	Min. Value	Max. Value
Energy	227.70	38.10	180.20	310.80

D. Model Prediction

Fig. 6 shows both LSTM and GRU model forecasts for the next 5 years in the Energy sector. From the data below, it is observed that the period of 1990-1997 saw a significant upward trend in N₂O emissions owing to several probable factors. The basic factor to be considered for such observations in the data is poor regulatory policies by the state to control the use of energy resources in the country.

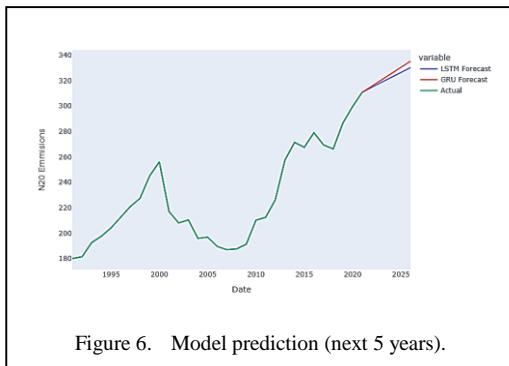


Figure 6. Model prediction (next 5 years).

Another factor could be low technological know-how or lack of technological equipment to aid companies in the sector with the necessary capability to tap into cleaner sources of energy for public consumption. High and steady rising demand for energy resources at the time could also be considered. From the period of 1997-1999, the data saw a constant demand in energy resources because of restrictions in the Energy sector at the time.

In a paper released by the Bureau of Democracy, Human Rights, and Labor on January 30th 1998 of the US Department of State which covers the Ghana Country Reports on Human Right Practices 1997, President Jerry John Rawlings, incumbent president of Ghana at the time, founder of the National Democratic Congress (NDC) in 1992 was re-elected into office in 1997 with 57% of the votes resulting from the December 1996 general elections.

Under the auspices of the NDC government, Act 541, which is the Energy Commission Act 1997 was legislated to form a body that could regulate the use of energy resources in the country. This leads to the observation in the data after 1999 where it sees a serious downward trend in N₂O emissions from the sector to the period of 2005.

As observed from the data, there is a general pattern in the period of 2014-2016 mimicking the 1997-1999 period, after which both the LSTM and GRU models predict an upward trend in N₂O emissions after 2020 for the next 5 years. Here, the GRU model predicts a much higher trend than LSTM.

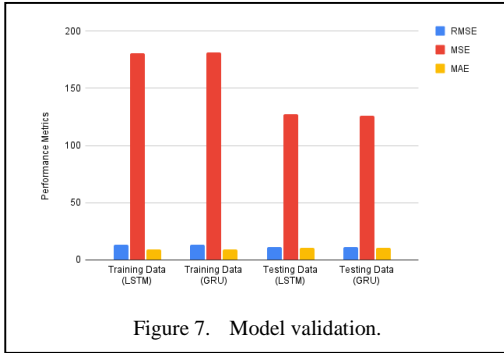
E. Model Validation

The model validation involves the use of various performance metrics to evaluate the predicted values against the actual data. Here, Root Mean Squared Error (RMSE) which quantifies the magnitude of the error, Mean Squared Error (MSE) which measures the average squared difference, Mean Absolute Error (MAE) which evaluates the average absolute difference between the predicted values and the actual values in the model were employed (Table III).

In Fig. 7 below, LSTM model performed better with the training dataset since the error metrics were relatively lower than the GRU model while GRU rather performed better than LSTM with the testing dataset.

TABLE III. PERFORMANCE METRICS.

	RMSE	MSE	MAE
Training Data (LSTM)	13.435436	180.510966	9.050326
Training Data (GRU)	13.467509	181.373814	9.054179
Testing Data (LSTM)	11.284701	127.344496	10.684333
Testing Data (GRU)	11.212475	125.719601	10.593684



V. CONCLUSION AND RECOMMENDATION

A. Conclusion

Based on the model validation with the performance metrics, it is shown that the LSTM model performed significantly better with the training dataset from the Energy sector, since the error metrics were lower than the GRU model. Hence, LSTM is a relatively better model for N₂O predictions in Ghana than GRU.

B. Recommendation

In order to better nitrous oxide emission prediction from the Energy sector of Ghana, it is recommended that other deep learning models in the likes of Facebook Prophet etc., be employed in comparison with LSTM to determine the best model.

ACKNOWLEDGMENT

We acknowledge the technical help of Master Seth Antanah of University of Mines and Technology (UMaT), Tarkwa-Ghana.

REFERENCES

- [1] Jacobson, M. Z. (2020). *100% clean, renewable energy and storage for everything*. Cambridge University Press.
- [2] Eppelbaum, L., Kutasov, I., & Pilchin, A. (2014). *Applied geothermics* (p. 267). Springer, Berlin Heidelberg

- [3] Ravishankara, A. R., Daniel, J. S., & Portmann, R. W. (2009). Nitrous oxide (N₂O): the dominant ozone-depleting substance emitted in the 21st century. *Science*, 326(5949), 123-125.
- [4] Griffis, T. J., Chen, Z., Baker, J. M., Wood, J. D., Millet, D. B., Lee, X., ... & Turner, P. A. (2017). Nitrous oxide emissions are enhanced in a warmer and wetter world. *Proceedings of the National Academy of Sciences*, 114(45), 12081-12085.
- [5] Ogeya, M., Nyambane, A., & Wanjiru, H. (2018). *Technical report: Nordic Green to Scale for countries: Unlocking the potential of climate solutions in Kenya and Ethiopia*. Nordic Council of Ministers.
- [6] Tiemeyer, B., Albiac Borrás, E., Augustin, J., Bechtold, M., Beetz, S., Beyer, C., ... & Zeitz, J. (2016). High emissions of greenhouse gases from grasslands on peat and other organic soils. *Global change biology*, 22(12), 4134-4149.
- [7] Hochreiter, S., & Schmidhuber, J. (1997). Long short-term memory. *Neural computation*, 9(8), 1735-1780.
- [8] Cho, K., Van Merriënboer, B., Bahdanau, D., & Bengio, Y. (2014). On the properties of neural machine translation: Encoder-decoder approaches. *arXiv preprint arXiv:1409.1259*.
- [9] Gers, F. A., Schmidhuber, J., & Cummins, F. (2000). Learning to forget: Continual prediction with LSTM. *Neural computation*, 12(10), 2451-2471.
- [10] Chung, J., Gulcehre, C., Cho, K., & Bengio, Y. (2014). Empirical evaluation of gated recurrent neural networks on sequence modeling. *arXiv preprint arXiv:1412.3555*.
- [11] Graves, A., & Schmidhuber, J. (2005). Framewise phoneme classification with bidirectional LSTM and other neural network architectures. *Neural networks*, 18(5-6), 602-610.
- [12] Koutnik, J., Greff, K., Gomez, F., & Schmidhuber, J. (2014, June). A clockwork rnn. In *International conference on machine learning* (pp. 1863-1871). PMLR.
- [13] Sutskever, I., Vinyals, O., & Le, Q. V. (2014). Sequence to sequence learning with neural networks. *Advances in neural information processing systems*, 27.
- [14] Wang, X., Girshick, R., Gupta, A., & He, K. (2018). Non-local neural networks. In *Proceedings of the IEEE conference on computer vision and pattern recognition* (pp. 7794-7803).
- [15] Sankar, A., Wu, Y., Gou, L., Zhang, W., & Yang, H. (2020, January). Dysat: Deep neural representation learning on dynamic graphs via self-attention networks. In *Proceedings of the 13th international conference on web search and data mining* (pp. 519-527).
- [16] Vaswani, A., Shazeer, N., Parmar, N., Uszkoreit, J., Jones, L., Gomez, A. N., ... & Polosukhin, I. (2017). Attention is all you need. *Advances in neural information processing systems*, 30.
- [17] Knight, K., Nenkova, A., & Rambow, O. (2016, June). Proceedings of the 2016 Conference of the North American Chapter of the Association for Computational Linguistics: Human Language Technologies. In *Proceedings of the 2016 Conference of the North American Chapter of the Association for*

- [18] Karpathy, A. (2017). Convolutional neural networks for visual recognition. *Notes accompany the Stanford CS class CS231*.
- [19] Zhu, Y., Elhoseiny, M., Liu, B., Peng, X., & Elgammal, A. (2018). A generative adversarial approach for zero-shot learning from noisy texts. In *Proceedings of the IEEE conference on computer vision and pattern recognition* (pp. 1004-1013).
- [20] Bai, S., Kolter, J. Z., & Koltun, V. (2018). An empirical evaluation of generic convolutional and recurrent networks for sequence modeling. *arXiv preprint arXiv:1803.01271*, 2.
- [21] Bengio, Y., Simard, P., & Frasconi, P. (1994). Learning long-term dependencies with gradient descent is difficult. *IEEE transactions on neural networks*, 5(2), 157-166.
- [22] Bengio, Y., Léonard, N., & Courville, A. (2013). Estimating or propagating gradients through stochastic neurons for conditional computation. *arXiv preprint arXiv:1308.3432*.
- [23] Pascanu, R., Mikolov, T., & Bengio, Y. (2013, May). On the difficulty of training recurrent neural networks. In *International conference on machine learning* (pp. 1310-1318). Pmlr.
- [24] Martens, J., & Sutskever, I. (2011). Learning recurrent neural networks with hessian-free optimization. In *Proceedings of the 28th international conference on machine learning (ICML-11)* (pp. 1033-1040).
- [25] Liu, G., & Guo, J. (2019). Bidirectional LSTM with attention mechanism and convolutional layer for text classification. *Neurocomputing*, 337, 325-338.
- [26] Le, X. H., Ho, H. V., Lee, G., & Jung, S. (2019). Application of long short-term memory (LSTM) neural network for flood forecasting. *Water*, 11(7), 1387.
- [27] Altan, A., Karasu, S., & Zio, E. (2021). A new hybrid model for wind speed forecasting combining long short-term memory neural network, decomposition methods and grey wolf optimizer. *Applied Soft Computing*, 100, 106996.
- [28] Fischer, T., & Krauss, C. (2018). Deep learning with long short-term memory networks for financial market predictions. *European journal of operational research*, 270(2), 654-669.

Analyzing Heat Transfer Mechanisms in a Thermodynamic Concentrator

Loubna Benhabib¹, Abdellah Benyoucef²

^{1,2}URMER Laboratory, Aboubekr Belkaid University, Tlemcen, Algeria

¹loubna.benhabib@univ-tlemcen.dz, ²abdellah.benyoucef@utbm.fr

Abstract—The development of solar concentrator technology has just reached a very significant level. Using reflectors to concentrate the sun's rays on the absorber dramatically reduces the size of the absorber, reducing heat loss and increasing its efficiency at high temperatures. Another advantage of this system is that the reflectors are significantly less expensive, per unit area, than the flat collectors. To determine the performances of a cylindrical-parabolic concentrator, mathematical modeling of the heat balance on the absorber, the coolant, and the glass envelope was established using Matlab. The system of equations obtained is solved by the finite difference method. The results for a typical day are the variation in the temperature of the heat transfer fluid, the absorber tube, and the glass envelope. Thus, we examine the effect of the wind speed, flow rate on the temperature distribution of the coolant at the outlet. However, for a mass flow rate of the fluid of 0.1 kg / s, the outlet temperature of the fluid is 85 °C with a thermal efficiency of 73%. Excluding the energy absorbed by the absorber tube is 75% of the solar intensity received on the reflector.

Keywords – solar concentrator, thermodynamic system, simulation

I. INTRODUCTION

Renewable energies have experienced the first phase of development during the oil shocks of 1973 and 1978. Then a period of decline after the counter-shock of 1986, before regaining a new lease of life in 1998 following the signing of the Kyoto protocol, which predicts, in particular, a 5.2% drop in greenhouse gas emissions from wealthy countries over the period 2002-2012 compared to 1990 [1].

Solar energy can be used to generate power using concentrated solar systems. It is based on

spherical, parabolic or Fresnel lens-based mirror concentrators [2], which have the principle of focusing the incident solar radiation in a point or a line. The conversion efficiency is high, and Temperature can easily surpass 500°C. These technologies offer a natural alternative to the consumption of fossil resources with a low environmental impact and a high potential for cost reduction, as well as the possibility of hybridization of these facilities, by utilizing direct solar radiation, which is considered the primary resource and is very significant on a planetary scale [3]. When it comes to the specific challenges of electricity generation, transmission, and distribution, alternative sources, as opposed to conventional ones, can be a feasible answer. In areas where electrical energy delivery is unreliable, including alternative energy generation sources, such as solar, can be a viable choice [4].

Several studies have been conducted to anticipate, analyze, and estimate the performance of parabolic trough collectors under a variety of weather conditions and configurations. A comprehensive review is presented, that examines various models and simulation approaches of PTCs. This study constitutes a complementary application contribution to parabolic trough concentrators [5]. According to the literature a detailed heat transfer solar receiver model has been performed [6]. The proposed models are based on the detailed analysis of one-dimensional or two-dimensional heat transfer processes assumed by trough collectors. Other researchers [7] performed precise two-dimensional digital heat transfer of PTC using synthetic oil Therminol VPI as heat transfer fluid (HTF). They came up with two software

options based on the properties of the solar PTC they were using. The first was written in Matlab and was used to calculate the annual solar energy collected on the absorber pipe using several tracking modes that were available in the area. Because (EES) automatically detects all unknowns and groups of equations for the most efficient solutions, the second program code is written using a simultaneous equation solving software (EES) to evaluate the performance of the heat collector element (HCE) [8].

In the current approach, a simulation program will be developed under Matlab to deal with the different modes of heat transfer in the concentrator absorber by determining the evolution of the system's temperature. Different parameters are studied to explain their importance in the temperature variation. The results taken are for a sunny day of June 21 in the region of Tlemcen, north-western Algeria, and water as the heat transfer fluid.

II. MATERIALS AND METHODS

The absorber was the essential element in the composition of the cylindrical-parabolic concentrator, whose role is to absorb the incident solar radiation for its conversion into heat before transmitted to the heat transfer fluid. We report in Fig. 1 the diagram of the process explaining the heat flow exchanged between components. However, the heat exchange coefficients are considered as known while considering the following assumptions:

- The transfer by conduction between the absorber and the glass is considered negligible.
- The flow of the incompressible fluid is in a one-dimensional direction.

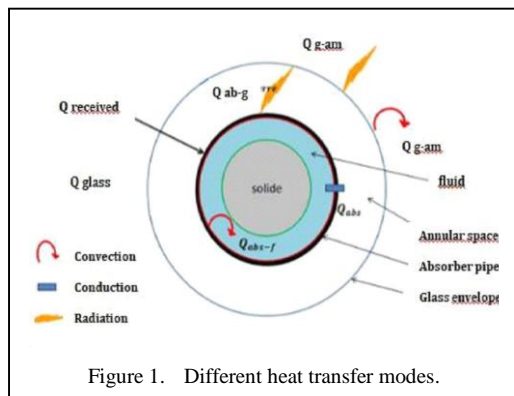


Figure 1. Different heat transfer modes.

A. Incident Radiation

Our study will focus on the equations of direct incident solar irradiance, as it is the resource of concentrating systems [9]. Modeling is done on a horizontal plane using two models. The data considered for the simulation in the Mediterranean countries provide from the site of Tlemcen city having the following coordinates Latitude 34.53° , Altitude 806m, Longitude 1.33° [10]

Direct solar radiation is calculated according to the Capderou model, and the expression gives it:

$$I_d = I_0 \times \varepsilon_0 \times \sin h_s \times \exp(-T_L \times m_a \times \delta_R) \quad (1)$$

where ε_0 represents the earth-sun distance correction, it is expressed as follows [11]:

$$\varepsilon_0 = 1 + 0.034 \times \cos\left(\frac{360}{365} \times (N - 2)\right) \quad (2)$$

With h_s is the sun elevation angle, N is the number of days, and is the constant solar (1367 W/m^2).

The atmospheric mass m_a , as well as the Rayleigh thickness δ_R , is given by [11,12]:

$$m_a = [\sin(h_s) + 9.4 \times 10^{-4} \times (\sin(h_s) + 0.0678)^{-1.253}]^{-1} \quad (3)$$

$$\delta_R^{-1} = 6.6296 + (1.7513 \times m_a) - (0.1202 \times m_a^2) + (0.0065 \times m_a^3) - (0.00013 \times m_a^4) \quad (4)$$

Or the Linke factor T_L is given by the expression [13]:

$$T_L = T_0 + T_1 + T_2 \quad (5)$$

where:

$$T_0 = (2.4 - 0.9 \times \sin\varphi) + 0.1 \times (2 + \sin\varphi) - (0.2 \times z) - (1.22 + 0.14 \times A_{he}) \times (1 - \sin(h_s)) \quad (6)$$

$$T_1 = 0.89^z \quad (7)$$

$$T_2 = [0.9 + (0.4 \times A_{he})] \times 0.63^z \quad (8)$$

With z is altitude, φ is latitude and winter-summer alternation.

However, the expression of the energy absorbed by the absorber is given by the expression [14]:

$$q_{abs} = \frac{A_0 \times I_d \times \alpha_0 \times \rho_0 \times \gamma \times K}{A_0} = L \times W. \quad (9)$$

The transmission-absorption coefficient α_0 is given according to the following expression [15]:

$$\alpha_0 = \frac{\alpha_{ab} \times \tau_g}{1 - (1 - \alpha_{ab}) \times (1 - \tau_g)}. \quad (10)$$

As for the modified angle of incidence is given by [16]:

$$K = 1 - 3.84 \times 10^{-5} \times (\theta) - 143 \times 10^{-6} \times (\theta)^2. \quad (11)$$

B. Heat Balance

The incident solar energy absorbed is not entirely transmitted to the heat transfer fluid. Some are dissipated in the form of thermal losses between the absorber and the glass envelope. Fig. 2 shows several heat transfer analyses between collector components and between the collector receiver and its surrounding environment.

- For the glass envelope:

$$A_g \times \rho_g \times C_{pg} \times dT/dt = q_{abs,g} + q_{int} - q_{ext}. \quad (12)$$

- For the absorber pipe:

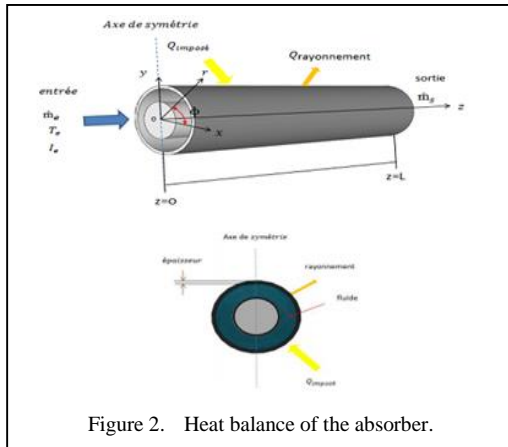


Figure 2. Heat balance of the absorber.

$$A_{ab} \times \rho_{ab} \times C_{pab} \times dT/dt = q_{abs} + q_{int} - q_u. \quad (13)$$

- For the fluid:

$$A_f \times \rho_f \times C_{pf} + \dot{m} \times C_p \times dT/dx = q_u. \quad (14)$$

Whose:

$$q_{abs,g} = A_0 \times I_d \times \alpha_g \times \rho_0 \times \gamma \times K. \quad (15)$$

The boundary condition: $T_{g,0} = T_{am}$; $T_{ab,0} = T_{a,e}$; $T_{f,0} = T_e$ (T_{am} is the ambient temperature).

C. The Heat Transfer Coefficients

1) Heat transfer between glass envelope and atmosphere

Convection and radiation are two transfer techniques for transferring heat from the glass enclosure to the atmosphere; convection requires wind.

The coefficient of radiation is given by [17]:

$$h_{r(ext)} = \varepsilon_g \times \sigma \times \left((T_{sky} + 273.15)^2 + (T_g + 273.15)^2 \right) \times (T_{sky} + T_g + 546.3). \quad (16)$$

With the expression of the sky temperature [18]:

$$T_{sky} = 0.0552 T_{am}^{1.5}. \quad (17)$$

Then the coefficient of convection is given by [19]:

$$h_{c(ext)} = \frac{\lambda_a}{D_{ge}} \times \left[0.6 + 3.87 \times \left[\frac{Ra_a}{1 + \left(\frac{0.559}{Pr_a} \right)^{9/16}} \right]^{1/6} \right]^2. \quad (18)$$

2) Heat transfer between the absorber and the glass envelope

Convection and radiation are the two ways of heat transmission. The annulus pressure affects the convection mechanism. Temperature variations between the outer absorber surface and the inner glass surface cause radiation.

With the expression of the sky temperature [20]:

$$h_{r(int)} = \varepsilon_{int} \times \sigma \times \left((T_{ab} + 273.15)^2 + (T_g + 273.15)^2 \right) \times (19) \times (T_{ab} + T_g + 546.3)$$

with

$$\varepsilon_{int} = \frac{1}{\left(\frac{1}{\varepsilon_{ab}} + \frac{1-\varepsilon_g}{\varepsilon_g} \right) \times \left(\frac{D_{abe}}{D_{gi}} \right)}. \quad (20)$$

Then the coefficient of convection is given by:

$$h_{c(int)} = \frac{2\lambda_{eff}}{D_{abe} \times \ln\left(\frac{D_{gi}}{D_{abe}}\right)}. \quad (21)$$

With:

$$\lambda_{eff} = 0.386 \times \lambda_a \times \left(\frac{Pr_a}{Pr_a + 0.861} \right)^{1/4} \times (Ra_c)^{1/4}, \quad (22)$$

$$Ra_c = \frac{\left(\ln\left(\frac{D_{gi}}{D_{abe}}\right) \right)^4}{L_{eff}^3 \times \left(D_{abe}^{-3/5} + D_{gi}^{-3/5} \right)^5} \times Ra_{eff}, \quad (23)$$

$$L_{eff} = \frac{D_{gi} - D_{abe}}{2}, \quad (24)$$

$$Ra_{eff} = Gr_a \times Pr_a. \quad (25)$$

3) Heat transfer between the fluid and the absorber

The flow type affects convective heat transfer from the inside surface of the absorber pipe to the fluid. We consider the case of turbulent flow [21] and is given by:

$$h_u = \frac{\lambda_f \times Nu_f}{D_{abi}}. \quad (26)$$

With:

$$Nu_f = \frac{\left(\frac{L}{8} \right) \times (Re_f - 1000)}{1 + 12.7 \times \sqrt{\frac{L}{8} \times (Pr_f^{2/3} - 1)}} \times \frac{\left(1 + \left(\frac{D_{abi}}{L} \right)^{2/3} \right) \times Pr_f}{1 + 12.7 \times \sqrt{\frac{L}{8} \times (Pr_f^{2/3} - 1)}} \times \left(\frac{Pr_f}{Pr_{ab}} \right)^{0.11}. \quad (27)$$

Knowing that:

$$f = (1.84 \times \log(Re_f) - 1.64)^{-2} \text{ for } D_{abi} < L, \text{ and;}$$

$$f = (1.8 \times \log(Re_f) - 1.5)^{-2} \text{ for } D_{abi} > L.$$

The physical proprieties of fluid (water) are considering variants.

III. SOLUTION PROCEDURE, RESULTS AND DISCUSSION

Matlab did the programming of these equations. We used the finite difference method to solve these equations. The process consists of giving a value of the variable and recalculating this variable with the equation, and finally, we compare the two deals. Depending on the desired precision, if the difference between the two calculated and proposed values is less than the fixed accuracy, this value is taken. Otherwise, the second value is taken, and the calculations are repeated until the difference between these two values becomes inferior to precision.

The characteristics of the solar PTC are mentioned in Table I.

TABLE I. CHARACTERISTICS OF THE SIMULATED PTC.

Absorber length (L)	7.8m
Collector width (W)	5m
Focal length (f)	1.84m
The absorber external diameter (D_{abe})	0.07m
The absorber internal diameter of (D_{abi})	0.066m
The glass external diameter (D_{ge})	0.115m
The glass internal diameter (D_{gi})	0.109m
Thermal conductivity of the absorber (λ_{ab})	54W/mK
Thermal conductivity of the glass (λ_v)	1.2W/mK
Absorption of the absorber (α_{ab})	0.906
Glass transmissivity (τ_g)	0.95
Transmissivity-absorbance factor (α_o)	0.864
Emissivity of glass	0.86
Reflection of reflector	0.93
Interception factor)	0.92

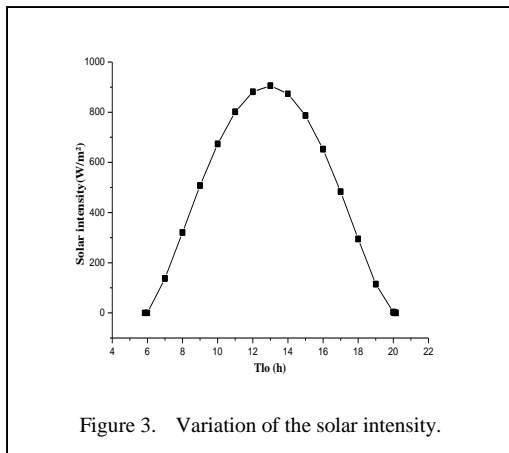


Figure 3. Variation of the solar intensity.

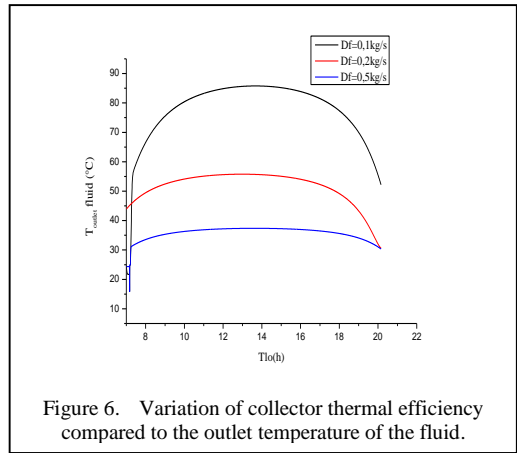


Figure 6. Variation of collector thermal efficiency compared to the outlet temperature of the fluid.

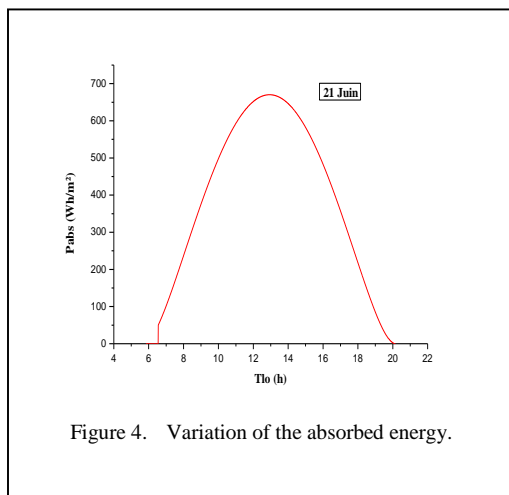


Figure 4. Variation of the absorbed energy.

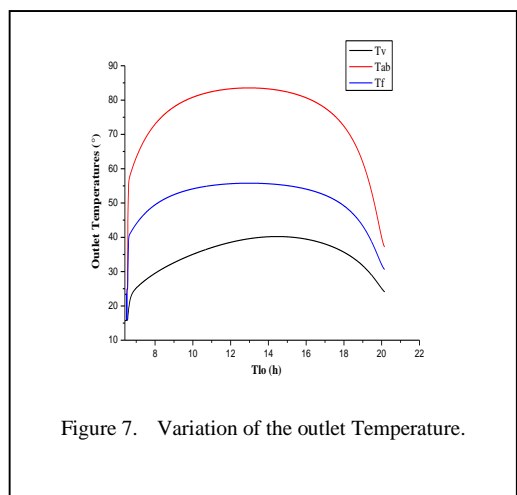


Figure 7. Variation of the outlet Temperature.

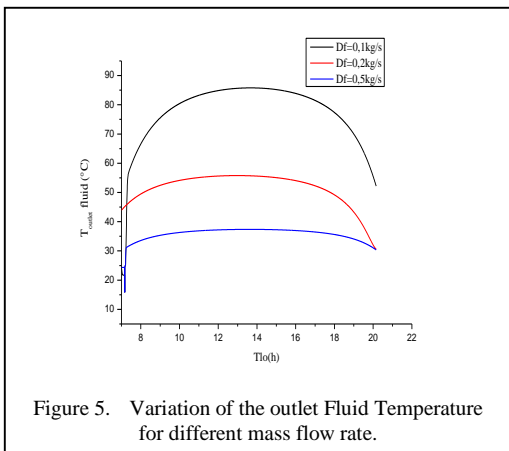


Figure 5. Variation of the outlet Fluid Temperature for different mass flow rate.

Following the use of the Capderou model for the calculation of the solar intensity and based on a solar tracking system for our solar system, we notice that the solar intensity at the level of the

Tlemcen region and for a day sunny, reaches 900W/m^2 as shown in Fig. 3.

Moreover, the solar power absorbed by the absorber tube reached 680W/m^2 , Fig. 4, which explains the existence of heat losses between the glass envelope and the absorber tube.

These losses cause a decrease in the rate of energy absorbed, which is of the order of 75%.

Moreover, Fig. 5 shows the variation in the outlet temperatures of the fluid, absorber and glass envelope. It is noted that the fluid outlet temperature is 55°C for a mass flow rate of 0.2Kg/s . On the other hand, according to Fig. 6, it is deduced that the outlet temperature of the fluid varies as a function of the mass flow rate or the temperature increases by decreasing the latter.

In what follows Fig. 7, shows the variation of the thermal efficiency as a function of the

temperature of the collector which is equal to 73%.

This efficiency helps to control the reliability of our system since it is the ratio between the useful flux and the power absorbed through the absorber tube. We note that the thermal efficiency is close to the experimental, whose value is 73.68% in the air in the annular space and validated by SNL. This difference only has to let us think of the existence of thermal losses.

IV. CONCLUSION

Our study relates to the study of the various existing heat transfers for a PTC sensor. For this, a mathematical simulation in Matlab language is carried out to solve the nonlinear equations. Our results are based on the study of outlet temperatures and influencing parameters.

Among those proposed the mass flow rate of the fluid shows an important parameter introducing into the variation of the outlet temperature or we have seen that the water outlet temperature reaches a value of 85°C for a flow rate of 0.1 kg/s. however, the energy absorbed is 75% relative to the solar intensity received on the reflector. Concerning the thermal efficiency which explains the rate of the useful flux linked to the heat transfer fluid, it is 73% for our system under the conditions of the Tlemcen region for a sunny day. In contrast, the wind speed turned out to be negligible.

In addition, the sun tracking system is essential and necessary for the operation of the PTC as it only uses direct solar radiation.

REFERENCES

- [1] Jones, R. W., Bascomb, J. D., Kosiewicz, C. E., Lazarus, G. S., McFarland, R. D., & Wray, W. O. (1982). *Passive solar design handbook. Volume 3: Passive solar design analysis*, 3.
- [2] Ogilvie, K. (2003). *L'abc des technologies de l'énergie renouvelable*, Pollution Probe. Canada.
- [3] Forristall, R. (2003). *Heat transfer analysis and modeling of a parabolic trough solar receiver implemented in engineering equation solver* (No. NREL/TP-550-34169). National Renewable Energy Lab., Golden, CO.(US).
- [4] Keou, C. J. N., Njomo, D., Sambou, V., Finiavana, A. A., & Tidiane, A. D. (2017). Two-dimension numerical simulation of parabolic trough solar collector: Far north region of Cameroon. *Energy and Power Engineering*, 9(3), 147-169.
- [5] Benhabib, L., Belaid, Z. H., & Benyoucef, A. (2021). Theoretical study and Modeling of a Parabolic trough Solar Concentrator. *Algerian Journal of Materials Chemistry*, 4, 7-14.
- [6] Ferriere, A., & Flamant, G. (2004). *Captation, transformation et conversion de l'énergie solaire par les technologies à concentration*. IMPCNRS, Centre du Four Solaire, BP5, 66125.
- [7] <http://www.infoclimat.fr>
- [8] Capderou, M. (1987). *Theoretical and experimental models, Solar atlas of Algeria*. University Publications Office.
- [9] Kasten, F. (1996). The Linke turbidity factor based on improved values of the integral Rayleigh optical thickness. *Solar energy*, 56(3), 239-244.
- [10] Capderou, M. (1987). *Atlas Solaire de l'Algérie, modèles théoriques et expérimentaux*. Vol. 1, T1, Office des Publications Universitaires, Algérie.
- [11] Duffie, J. A., & Beckman, W. A. (1991). *Solar engineering of thermal processes*. John Wiley & Sons. Inc. New York.
- [12] Quoilin, S. (2007). *Concentrator solar power plants (in French), faculty of applied Sciences*. University of Liège.
- [13] Kalogirou, S. A. (2004). Solar thermal collectors and applications. *Progress in energy and combustion science*, 30(3), 231-295.
- [14] Duffie, J. A., & Beckman, W. A. (2013). *Solar engineering of thermal processes*. John Wiley & Sons.
- [15] García-Valladares, O., & Velázquez, N. (2009). Numerical simulation of parabolic trough solar collector: Improvement using counter flow concentric circular heat exchangers. *International journal of heat and mass transfer*, 52(3-4), 597-609.
- [16] Agagna, B., Smaili, A., & Behar, O. (2018). An improved model for predicting the performance of parabolic trough solar collectors. *International Journal of Energy Research*, 42(14), 4512-4521.
- [17] Ratzel, A. C., Hickox, C. E., & Gartling, D. K. (1979). Techniques for reducing thermal conduction and natural convection heat losses in annular receiver geometries.
- [18] Gnielinski, V. (2013). On heat transfer in tubes. *International Journal of Heat and Mass Transfer*, 63, 134-140.

Energetic Properties of Sugar Cane Bagass during Storage in an Ethanol Production Plant

Rosa Helena César Freire de Souza¹, Jean Constantino Gomes da Silva²,
Silvia Layara Floriani Andersen³

^{1,3}Federal University of Paraíba, João Pessoa, Brazil

²State University of Campinas, São Paulo, Brazil

¹rosinhacesar@gmail.com, ²jeancgs@unicamp.br, ³silvia@cear.ufpb.br

Abstract—The sale of energy by the sugar and alcohol sector is increasingly prominent in the Brazilian electricity matrix, and its presence as a product in the industry grows annually. A large part of this energy is generated from the burning of bagasse resulting from the crushing of sugar cane, and the surplus is sent to storage yards without any technique or planning. As a result, millions of tons of bagasse are degraded, affecting its characteristics. This work aims to monitor and compare variations in the energetic properties of sugarcane bagasse during the 6-month storage period. The research methods involve physical-chemical and thermal characterizations of the samples during this period. The results demonstrate a yard with varying dimensions and temperatures, as well as the values of ash, volatile material, fixed carbon and humidity, which ranged from 15.05% to 79.90% and influenced the size of biomass particles by up to 43%. The calorific value of the bagasse from the conveyor belt was 17.46 ± 0.19 to 19.37 ± 1.98 MJ·kg⁻¹, very similar to that found in the storage yard of 17.50 ± 0.33 to 19.62 ± 0.73 MJ·kg⁻¹. In thermogravimetric analyses, the thermal degradation of hemicellulose, cellulose and lignin are clearly evident. Therefore, this study highlights the importance of bagasse characteristics for the storage process, which is influenced by climate and the environment in which it is stored.

Keywords - sugar cane bagasse, storage, energetic properties

I. INTRODUCTION

Brazil is one of the most important agricultural countries in the world, and in recent

decades, sugarcane has emerged as one of its primary agricultural raw materials for various sustainable products. The Brazilian sugar and alcohol sector plays a crucial role in the national economy, standing as the world's largest producer of sugar cane. In the 2022/2023 harvest, it was responsible for producing 610.1 million tons of cane destined for the sugar and ethanol production [1]. This market has enormous potential for expansion, especially given the alarming increase in greenhouse gas emissions since the beginning of the industrial revolution. This scenario highlights the need to diversify energy sources. According to data from the Climate Observatory's Greenhouse Gas Emission Estimation System (SEEG), Brazil emitted 2.42 billion tons of CO₂ in 2021, which made the country responsible for the biggest increase in the emission of greenhouse gases in 20 years, as reported during COP-27, the UN climate conference [2].

However, over the years, the sugar and alcohol industry has undergone significant transformations, aiming to improve its production processes to reduce costs, while also demonstrating a growing concern for the environmental impacts generated by its activities [3]. The industrial processing of sugar cane generates a series of by-products and waste, such as bagasse, straw, vinasse and filter cake. It's crucial to highlight that the recovery and use of this waste represent a significant opportunity for the development of new products across various application, in addition to contributing to

the environment preservation. This approach aligns with the growing trend of the circular economy, which aims to minimize waste and maximize the utilization of available resources [4].

According to [5], bagasse is a fibrous lignocellulosic residue generated during the sugarcane juice extraction process. A portion of it is normally used as fuel boilers, while the remainder is sent to the storage yard. Energy production through bagasse cogeneration is an efficient enterprise capable of meeting quarter of the energy demand in the world's major sugarcane producing countries [6]. Furthermore, in Brazil, renewable sources represented 78.1% of the domestic electricity supply, of which energy from sugarcane biomass was 16.4% in 2021. This percentage is extremely important for the energy matrix Brazilian because the harvest period at the plants coincides with periods in which the generation capacity of Brazilian hydroelectric plants goes through a decline due to the reduction in water levels [7,8]. However, it is crucial to thoroughly understand the characteristics of the sugarcane bagasse before use as it exhibits different attributes, resulting in energy values ranging from 17 to 20MJ·kg⁻¹ depending on its nature and stored form [9,10].

Storage is essential due to the seasonality of production and the interest in using bagasse for energy cogeneration. Currently, there are no adequate techniques or planning for its storage, leading to a direct impact on its energy potential over time, resulting in waste over 1.500.000 tons annually [11;12]. In this context, the objective of this is to evaluate variations in the physical-chemical and thermal properties of sugarcane bagasse over storage period, with the following specific objectives: Monitor changes in the storage during 2 months and their potential impact on the energetic characteristics of sugarcane bagasse.

II. THEORETICAL REFERENCE

Sugarcane, belonging to the genus *Saccharum* of the Poaceae family, is a semi-evergreen plant known for its significant accumulation of sucrose in its stems [13]. Introduced to Brazil in 1532, sugar cane found extremely favorable climatic, soil, temperature, and relief conditions [14]. Thus, sugarcane cultivation quickly became fundamental in the production of sugar destined for export to Europe [15].

The expansion of sugarcane cultivation has been rapid and consistent over the decades. This success is due not only to the natural adaptability of sugarcane but also to the positive outcomes of the genetic improvement program. These programs have introduced increasingly productive sugarcane varieties, resistant to biotic and abiotic stresses, and adapted to different growing environments, such as energy cane [15]. It is estimated that in the 2022/2023 harvest in Brazil, 572.874,9 thousand tons of sugar cane will be produced, with each ton yielding around 280 kg of bagasse [15,16]. Globally, around 448-540 million metric tons of this cellulosic agro-industrial by-product are generated annually, more than sufficient for the industry's self-sufficiency, for the electricity generation, for the sale of surplus and for storage in the yard [16].

According [17], freshly ground bagasse has a composition of approximately 50% moisture, 45% lignocellulosic fibers, 2 to 3% insoluble solids, in addition to soluble solids. This material consists mainly of cellulose (40–50%), hemicellulose (20–35%) and lignin (10–30%), responsible for its high energy content [16].

However, the energy use of bagasse come with disadvantages, such as high moisture content, high oxygen content, hygroscopic nature, low calorific value and heterogeneous properties [16,18]. In this context, storage conditions require attention and care, as poor storage can lead to factors that contribute to inefficient use over time. It is essential to ensure that the bagasse is stored properly so that it can be used efficiently in future applications.

In most Brazilian plants there is a storage yard where a tractor spreads the bagasse on top of the pile, which can be around 300m long, 100m wide and 40m high [17,19]. In these yards, one of the major consequences is the deterioration of the external layer, which protects the internal layers, generating losses and changes in the chemical composition of the biomass during different storage times. Similar changes occur with bagasse stored in indoor and outdoor buildings for several months before use [20]. The variety of shapes and particle sizes interfere with surface and volumetric areas, affecting processes of heat and mass transfer such as decomposition [21].

One of the challenges is the size of the fibers, as smaller ones are more likely to remain airborne during typical food storage operations. bagasse than other fibers. Furthermore, it fills the

voids between larger particles of bagasse making the stock less porous. The larger ones, on the other hand, retain a lot of water, making the bagasse more humid [21]. According to [19], dust, groundwater infiltration, spontaneous combustion and leachate generation are possible impacts that bagasse stocks can cause to the environment and neighboring communities.

Bagasse characterization techniques include proximate and thermal analyses. In proximate analyses, moisture content is a crucial parameter in the characterization of biomass energy production [22]. Volatile material is the main constituent of biomass in bulk, which is based on the amount of condensable and non-condensable vapor released in the process of heating a fuel [22,23]. Ash in large quantities is harmful to the calorific value of biomass. Finally, the fixed carbon content is calculated by the difference between the total percentage of the sample and the ash and volatile materials content [23].

In thermal analyses, the calorific value is served as an indicator of the chemically bound energy and in the combustion process it is converted into thermal energy [22]. The calorific value can be represented in two ways: higher and lower. On the other hand, thermogravimetry, according to [23], monitors the variation in the mass of the sample as a function of time and temperature.

III. MATERIAL AND METHODS

The material used in this study was sugarcane bagasse, sourced from a distillery located in the city of Pedras de Fogo, Paraíba. The bagasse was stored in the yard and obtained on the day of collection, following the grinding process of a distillery producing anhydrous, hydrated, and neutral ethanol.

The bagasse yard's dimensions were assessed every two months during the 22/23 harvest, taking into account its length, width, and height. AutoCAD® 2023 software was employed for visualization and design purposes. Daily bagasse samples were collected from the conveyor belt at the existing collection point in the plant for moisture analysis. Sampling points within the storage yard were determined post-sizing to encompass the entire area and its layers. Samples were collected at a minimum depth of 30cm from the surface to ensure the absence of any contaminants in the raw material [13]. Temperature readings at each point were

recorded during collection using the SBC Solution digital thermometer, model FY-10.

Moisture content was determined using a moisture balance (Moisture Analyzer, MF-50) with the sample in its wet state. Before conducting immediate analysis, the sample was air-dried in an oven with circulation for one hour at 105°C, then crushed in an industrial blender. Subsequently, it was sieved through a 100 mesh sieve. Ash content and volatile material content were determined, on a dry basis, following the ASTM E1755-01 and ASTM E872-82 standards, respectively.

The results obtained were used to determine the fixed carbon content (dry basis), by difference, in accordance with the ABNT/NBR 8112 standard. The higher calorific value of the sample was determined using the IKA calorimetric bomb (model C 200) following the ASTM D5865 methodology.

Thermogravimetric analyzes were performed on a Discovery SDT 650 simultaneous thermogravimetric analyzer from TA Instruments. The samples, weighing approximately 10mg, were subjected to a heating rate of 10°C/min, in an N₂ atmosphere (99.99% purity) with a constant flow of 100 mL/min, from room temperature to 1000°C and leaving in isotherm for 30 minutes.

All previously mentioned analyses were carried out in triplicate.

IV. RESULTS AND DISCUSSION

According to [12], the storage of sugarcane bagasse often lacks techniques or planning, leading to various stages of biomass degradation. It is noted that, in October 2022, the disposal of bagasse in the storage area did not occupy its entire length. However, in December 2022 and February 2023, the courtyard underwent modifications, increasing both in height and

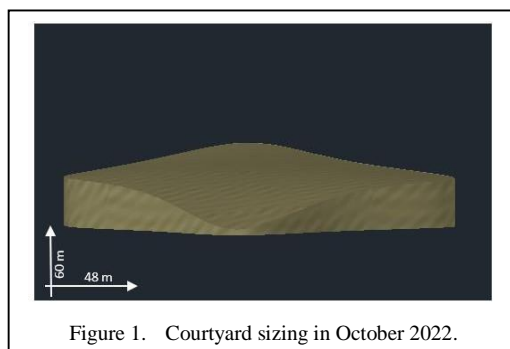


Figure 1. Courtyard sizing in October 2022.

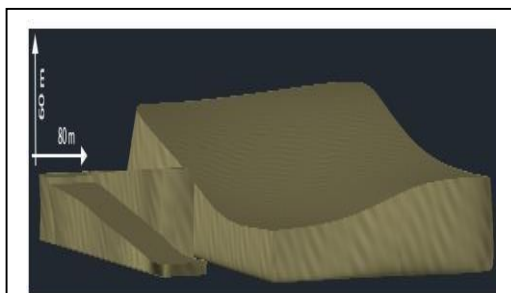


Figure 2. Courtyard sizing in December 2022.

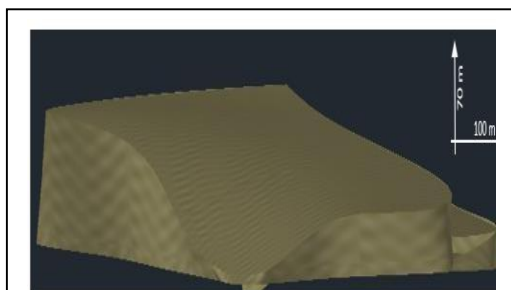


Figure 3. Courtyard sizing in February 2023.

length (Figs. 1-3). This change in height resulted in the formation of two main layers at the ends (upper and lower). This division was extremely important, as after December 2022, access to the upper layer became unfeasible due to the height and instability of the yard.

Based on these dimensions, sampling points were defined allowing the entire storage area to be covered as shown in Table I with the average temperatures at each point. According to [24], the temperature of the bagasse stock is normally in the range of 50 to 65°C, which is consistent with the values found in almost all points of the stock analyzed. However, point 1 did not reach a high temperature, as it is constantly in motion and lacks successive layers

TABLE I. AVERAGE TEMPERATURE AT EACH SAMPLING POINT.

Sampling point	Average temperature of each point (°C)
1	35.6
2	56.2
2.1	46.3
3	57.2
3.1	47.0
4	53.7
4.1	49.1
5	59.3

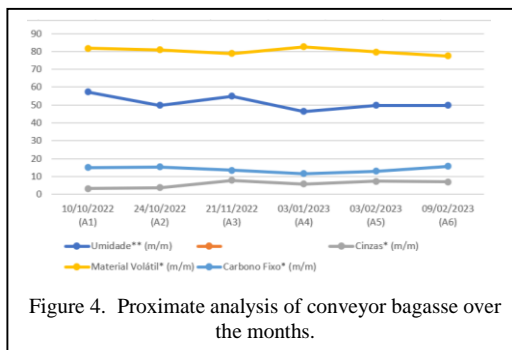


Figure 4. Proximate analysis of conveyor bagasse over the months.

of bagasse overlapping. This constant movement did not allow heat to accumulate in the same way as it happens in other parts of the stock, where the bagasse is deposited for longer and creates thermal layers. For this reason, point 1 showed a lower tendency for temperature compared to other points in the stock.

High temperatures are a cause for concern, as spontaneous combustion in stocks can occur within the range of 60 to 65°C. This occurrence is the result of the combination of temperature, not only the environment but also microbiological reactions, and moisture content, which cause the release of energy from the latent heat of condensation and heat of absorption [24]. According to [25], storage temperature had an impact of 34.7% on the diversity of microorganisms, while storage time had an even greater influence, corresponding to 73.7% of the observed effect. Upon entering the storage yard, this bagasse (Fig. 4) underwent changes at all sampling points, with humidity values ranging from 15.05% ± 0.45 to 79.82% ± 1.37.

This wide variation in humidity can result in different impacts on stored bagasse and the thermal efficiency of burning. In comparison to the study by [12], where moisture levels varied from 72.9% to 80.5% at different collection points in the bagasse storage yard, the hydrophilic nature of bagasse contributes to an increase in humidity over the months. On sunny days, the water content decreases, while on rainy days, it increases [22].

This characteristic is especially evident in point 1, which had no layers, allowing for more efficient drying of the bagasse in the sun. During the rainy season, there was an increase in humidity. On the other hand, point 3.1 did not show the same behavior, showing only a slight increase between months and a large compaction between layers. Therefore, water had difficulty penetrating deeper layers, resulting in lower

humidity in this region. This compaction occurs due to the weight of the bagasse layers, which is a characteristic present in all parts of the yard. However, at other points, rainwater hits more frequently and can penetrate better between the layers, making the bagasse looser and moister.

In this study, ash content reached up to 7.82% in bagasse from the conveyor belt and 9.48% in samples from the yard. This variation demonstrates that the content of mineral impurities, such as silica, can vary significantly. The presence of silica can come from both absorption by sugarcane roots and residual sand. Furthermore, ash also contains small amounts of metallic oxides that can influence the properties of the ash and, consequently, the combustion and energy generation process.

Studies have shown that manual harvesting results in higher levels of mineral impurities compared to mechanized harvesting, with variations from 91.06% to 56.86%. In the literature, the ash content of sugarcane bagasse can vary widely, with studies reporting values between 0.2 and 6.6% or represented as a percentage of sugarcane weight, varying from 0.14 to 3.21% [26].

The point that presented one of the highest ash contents was point 1, which was expected due to the movement of the harvesting machine (Michigan). Points 2.1, 3.1 and 4.1 also had high values at some point, due to the fact already reported as well as being exposed to mineral impurities carried by the wind. On the other hand, point 4 presented the lowest percentages of ash, which may be a result of the constant use of this area to feed the boiler. The levels of volatile material found in the bagasse from the conveyor belt varied between 77.43 and 82.58%.

This result was close to the value reported by [9], which was 81.90%. According to this author, this data reflects the thermal decomposition behavior of bagasse, which favors ignition and presents an intense release of volatile particles. However, it also has low thermal resistance, which results in a shorter burn time.

The volatile content material values at the collected points ranged from 71.78% to 80.82%. These results are quite similar to those obtained in the study of [12], which reported values of 61.39% to 89% for the content of volatile material at different collection points in the bagasse storage yard.

The fixed carbon content presented values at the collection points between 11.34 and 20.23%, and a smaller variation in the conveyor bagasse of 11.61 to 15.62%, which is close to that found by [27] of 12.04 to 16.4% and [28], 14.95%. However, [9] found an even greater variation in their work from 10.42 to 38.19%. These values end up being quite diverse, being influenced by the percentage of volatile material and ash. Knowing that the higher the fixed carbon content, the higher the combustion rate, since carbon is the main fuel element with hydrogen and sulfur [12].

The higher calorific value of the bagasse from the mat varied, with sample A1 presenting the highest value with $19.37 \pm 1.98 \text{MJ}\cdot\text{kg}^{-1}$ and sample A4 the lowest with $17.46 \pm 0.19 \text{MJ}\cdot\text{kg}^{-1}$. These results are a consequence, respectively, of a lower ash content and a higher fixed carbon content, maintaining an approximate volatile material content. It is important to highlight that the values found are higher than those found by [29], which was $16.87 \text{MJ}\cdot\text{kg}^{-1}$, and are very similar to the results obtained by [30], which had an average of $18.16 \text{MJ}\cdot\text{kg}^{-1}$. The calorific value tends to decrease as the storage time increases. Therefore, it ends up suffering more and more from the action of the storage environment and the climate. Just as there is an intensification of the actions of microorganisms in the energetic components of the bagasse.

The calorific value tends to decrease as the storage time increases. Therefore, it ends up suffering more and more from the action of the storage environment and the climate. Just as there is an intensification of the actions of microorganisms in the energetic components of the bagasse. Therefore, as time passes, the bagasse is degraded and loses its ability to generate energy, becoming a huge waste, not calculated internally, for the industry. According [31], bagasse can only be stored for a maximum of 10 weeks, limiting its further use during the non-grinding period.

It was noted that each month, there were variations in the calorific value, except in the months of January and February 2023. This stability may be related to the results of the proximate analyzes (Fig. 4). Regarding the higher calorific value obtained during the collected points over the months, it varied from 17.50 ± 0.33 to $19.62 \pm 0.73 \text{MJ}\cdot\text{kg}^{-1}$. According to [17], in the courtyard the calorific value was $12.68 \text{MJ}\cdot\text{kg}^{-1}$. In turn, the results obtained

by [12] ranged from 17.55 to 23.07MJ·kg⁻¹, being more like the present study.

As it is a mixture of bagasse that was influenced by the weather and the storage environment, a significant oscillation in the higher calorific value was expected, but there was none. However, point 3.1 showed the smallest fluctuation between months, which was a result of compression. This result is important data for better management of the yard in the search for stability over the months, enabling operational viability to be worked on through different levels of storage compaction.

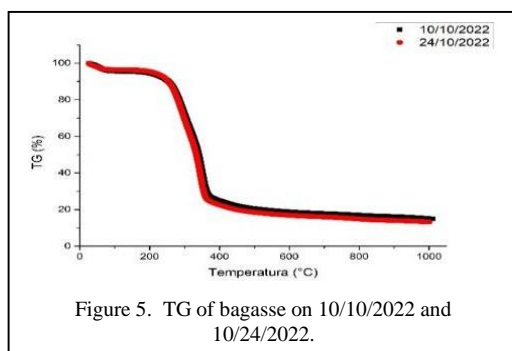


Figure 5. TG of bagasse on 10/10/2022 and 10/24/2022.

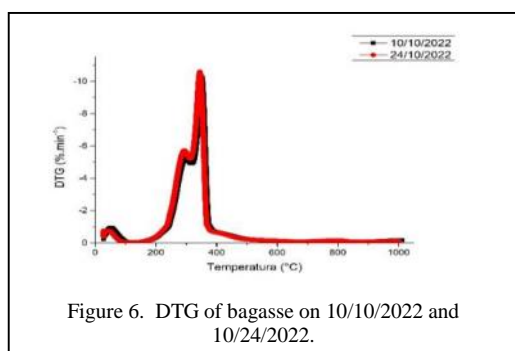


Figure 6. DTG of bagasse on 10/10/2022 and 10/24/2022.

TABLE II. DIFFERENCES IN TEMPERATURE AND MASS LOSS OF DTG ON 10/10/2022 AND 10/24/2022.

Samples	Temperature (°C)	
	10/10/2022 (A1)	24/10/2022 (A2)
1° Peak	55.83	50.41
2° Peak	297.35	303.79
3° Peak	350.13	354.63
4° Peak	419.12	415.04
Samples	Mass Loss (%)	
	10/10/2022 (A1)	24/10/2022 (A2)
1° Peak	4	3
2° Peak	38	39
3° Peak	25	28
4° Peak	5	4

Figs. 5 and 6 presents the TG and DTG curves of the bagasse pyrolysis from the conveyor belt on 10/10/2022 in comparison with the bagasse from point 2 on 10/24/2022 during the month's biomass was being stored. Therefore, the TG and DTG curves are very similar with small differences in temperatures and mass losses highlighted in Table II.

In the results obtained, thermogravimetry (TG) revealed the variation in the mass percentage of the bagasse with the increase in temperature, both for the bagasse from the conveyor belt and for point 2. In these cases, it was observed that the percentage of mass reduction increased sharply after reaching temperatures of 150°C and 200°C, stabilizing above 600°C. The DTG curve, which represents the mass variation per minute, revealed that samples A1 and A2 presented four distinct mass reduction peaks: the first was at 55.83 and 50.41°C, suggesting that they had a percentage of approximate humidity between the bagasse, which comprised a temperature range from 30 to around 95°C with mass losses of 4 and 3%.

Similar mass losses were in the second point also with 38% and 39%, with a peak at 297.38°C and 303.79°C comprising all the hemicellulose because of its low thermal stability, easily volatilizing a part of the cellulose [32]. Which has its greatest decomposition in the third peak which was at 350.13°C and 354.63°C, it is visible in Fig. 6 that it is greater in A2 as it presents a mass loss of 29%. Lignin, which has its maximum loss with the fourth peak, which was 419.12°C and 415.04°C with a mass loss of 5 and 4%.

In the study of [33], DTG showed four points of mass loss, very similar to the results found: the first peak was at 73°C, the second at 330°C, the third at 383°C and the fourth at 444°C, with mass losses of 2%, 41%, 30% and 9%, respectively.

V. CONCLUSION

The changes observed in the bagasse storage yard over the course of the harvest are essential to understand the dynamics of bagasse storage. This understanding is instrumental in effective implementation of management practices, ensuring the preservation of the material quality and optimizing bioenergy generation in the sugar and alcohol plant. The characteristics of the bagasse on the conveyor belt are very important, because from them, with the influence of the environment, climate and form of storage, the

bagasse that is in the yard will undergo changes with a tendency to increase humidity and ash, as well as a decrease in volatile materials and fixed carbon.

The calorific value, compared to the bagasse from the conveyor belt, decreased over time in the storage yard, but this decrease was not as significant, especially in point 3.1. It presented the lowest PCS fluctuation with 18.76MJ·kg⁻¹ in November 2022 and 18.52 MJ·kg⁻¹ in March 2023. This consistency is attributed to the compaction and lower moisture levels in the bagasse in this specific point.

Moisture content of the bagasse increased over time at other points, a consequence of outdoor storage. Furthermore, the ash content fluctuated at each collected point, underscoring the significance of considering factors like sampling point locations, bagasse movement, and exposure to mineral impurities when interpreting analysis results. The percentage of volatile material also suffered fluctuations, but to a lesser extent. This indicates a limited degradation of the biomass in the layer after 30 cm depth. On the other hand, fixed carbon had greater fluctuations, as it depends on ash and volatile material.

Thermogravimetric analyzes between samples from the yard and bagasse from the conveyor belt were similar. This indicates that for a difference in mass loss, the sample needs to spend more time in the storage yard.

ACKNOWLEDGMENT

This work was funded by the public call n. 03 productivities research propesq/prpg/ufpb proposal code: pvk-13605-2020.

REFERENCES

- [1] Conab. (2023). *Sugarcane production reaches 610.1 million tons in the 2022/23 harvest with an improvement in crop productivity*. Available at: <https://www.conab.gov.br/ultimasnoticias/4977producao-de-cana-quega-a-610-1milhoesdetoneladas-na-safra-2022-23-commelhora-naprodutividade-nas-lavouras>.
- [2] Isa. (2022). *Brazil arrives at COP27 amid record greenhouse gas emissions*. Available at: <https://www.socioambiental.org/noticiassocioambientais/brasil-quega-na-cop27-emmeio-recorde-deemissoes-de-gases-de-efeito>.
- [3] Cardoso, T. F., Watanabe, M. D. B., Souza, A., Chagas, M. F., Cavalet, O., Morais, E. R., Nogueira, L. A. H., Leal, M. R. L. V., Braunbeck, O. A., Cortez, L. A. B., & Bonomi, A. (2019). A regional approach to determine economic, environmental and social impacts of different sugarcane production systems in Brazil. *Biomass and Bioenergy*, 120, 9-20.
- [4] Teixeira, F. S., Vidigal, S. S. M. P., Pimentel, L. L., Costa, P. T., Pintado, M. E., & Alcalá, L. M. R. (2021). Bioactive Sugarcane Lipids in a Circular Economy Context. *Foods*, 10(5).
- [5] Gomes, M. G. (2019). *Biogas production from sugarcane bagasse after pre-treatment with diluted citric acid*. Available at: <https://repositorio.ufu.br/bitstream/123456789/27087/1/Produ%C3%A7%C3%A3o%20Biog%C3%A1s%20Baga%C3%A7o%20.pdf>.
- [6] Arshad, M., & Ahmed, S. (2016). Cogeneration through bagasse: A renewable strategy to meet the future energy needs. *Renewable and Sustainable Energy Reviews*, 54, 732-737.
- [7] Ben. (2022). *Balance Energetic Nacional*. Available at: <https://www.epe.gov.br/sites/pt/publicacoes/dadosabertos/publicacoes/Arquivos/publicacao-675/topico-638/BEN2022.pdf>.
- [8] Hofsetz, K., & Silva, M. P. (2012). Brazilian sugarcane bagasse: Energy and non-energy consumption. *Biomass and Bioenergy*, 46, 564-573.
- [9] Grotto, C. G. L., Costa, A. M. F., Colares, C. J. G., & Pereira, D. H. (2021). *Characterization of sugarcane bagasse biomass with energetic views*. Available at: <https://www.sciencegate.app/document/10.29069/for-science.2021v9n1.e928>.
- [10] Anukan, A., Mamphweli, S., Reddy, P., Meyer, E., & Okoh, O. (2016). Pre-processing of sugarcane bagasse for gasification in a downdraft biomass gasifier system: A comprehensive review. *Renewable and Sustainable Energy Reviews*, 66, 775-801.
- [11] Salehi, F. A., Abdoli, M. A., Shokouhmand, H., & Jafari, H. R. (2012). Techno-economic assessment for energy generation using bagasse: case study. *Energy Research*, 37(8), 982-990.
- [12] Correia, M. A. C., Seye, O., Silva, A. M. P., & Silva, R. L. (2020). Characteristics and energy potential of sugarcane bagasse stored uncovered for a prolonged period. *Rama*, 13(1).
- [13] Ripoli, M. L. C., & Ripoli, T. C. C. (2006). Planters in the sugarcane fields. *Cultivate Machines*, 6(55), 16-19.
- [14] Rodrigues, G. S. S. C., & Ross, J. L. S. (2020). The trajectory of sugarcane in Brazil: geographic, historical and environmental perspectives. *Edufu*.
- [15] Cangussu, N., Chaves, P., Rocha, W., & Maia, L. (2021). Particleboard panels made with sugarcane bagasse waste: an exploratory study. *Environmental sustainability and remediation*.
- [16] Torgbo, S., Quan, V., & Sukyai, P. (2021). *Cellulosic value-added products from sugarcane bagasse*. Springer Nature.
- [17] Santos, M. L., Lima, O. J., Nassar, E. J., Ciuffi, K. J., & Calefi, P. S. (2011). Study of sugarcane bagasse storage conditions by thermal analysis. *New Chemistry*, 34, 507-511.
- [18] Manatura, K. (2020). Inert torrefaction of sugarcane bagasse to improve its fuel properties. *Case Studies in Thermal Engineering*, 19.
- [19] Rainey, T. J., O'hara, I. M., Mann, A. P., Bakir, C. H., & Plaza, F. (2013). Effect of depithing on the safety and environmental aspects of bagasse stockpiling. *Process Safety and Environmental Protection*, 91(5), 378-385.

- [20] Posom, J., Phuphaphud, A., Saengprachatanarug, K., Maraphum, K., Saijan, S., Pongkan, K., & Srimai, K. (2022). Real-time measuring energy characteristics of cane bagasse using NIR spectroscopy. *Sensing and Bio-Sensing Research*, 38.
- [21] Pérez, A. A. D., Palacio, J. C. E., Venturini, O. J., Reyes, A. M. M., Orozco, D. J. R., Lora, E. E. S., & Olmo, O. A. A. (2018). Thermodynamic and economic evaluation of reheat and regeneration alternatives in cogeneration systems of the Brazilian sugarcane and alcohol sector. *Energy*, 152, 247-262.
- [22] Basu, P. B. E. (2010). Experimental study on fluidization of biomass, inert particles, and biomass/sand. University of North Texas.
- [23] Mousa, E., Wang, C., Riesbeck, J., & Larsson, M. (2016). Biomass applications in iron and steel industry: An overview of challenges and opportunities. *Renewable and Sustainable Energy Reviews*, 65, 1247-1266.
- [24] Pattamasuwan, A., Phaeon, N., Chapanya, P., Sriroth, K., Wongrat, W., & Vanichsiratana, W. (2020). Spontaneous Combustion Tendency in Bagasse Stockpiles: Biotic and Abiotic Responses Relation. *Sugar Tech*.
- [25] Peng, N., Yao, Z., Wang, Z., Huang, J., Khan, M. T., Chen, B., & Zhang, M. (2021). Fungal deterioration of the bagasse storage from the harvested sugarcane. *Biotechnology for Biofuels*.
- [26] Marcondes, L. A., & Bueno, S. M. (2019). *Sugarcane dry cleaning process*. Available at: file:///C:/Users/rosin/Downloads/220Texto%20do%20Artigo-710-1-1020191028pdf
- [27] Nunes, J. V. S., Nogueira, K. M. V., Vidal, M. S., Malveira, J. Q., & Rios, M. A. S. (2017). *Analysis of the viability of sugarcane bagasse (saccharum spp) for the production of briquettes*. Available at: https://www.confea.org.br/sites/default/files/antigos/contecc2017/agronomia/3_advdbsspapdb.pdf.
- [28] Santos, S. F. (2020). Using bagasse from the sugarcane industry as an addition to the renewable energy matrix. Universidade de Ribeirão Preto.
- [29] Girão, L. E. B. (2016). *Sugarcane bagasse: investigation of calorific value and energy potential*. Available at: https://repositorio.ufc.br/bitstream/riufc/35111/1/2016_tcc_lebgirao.pdf.
- [30] Lizcano, J. V. (2015). *Calorific value, energy and ash of drip-irrigated sugarcane biomass, for different varieties, blades and maturation processes*. Available at: https://www.teses.usp.br/teses/disponiveis/11/11152/tde17092015161201/publico/JonathanVasquez_Lizcano_versao_revisada.pdf.
- [31] Valix, M., Katyla, S., & Cheung, W. H. Combustion of thermochemically torrefied sugar cane bagasse (2017). *Bioresource Technology*, 223, 202-209.
- [32] Melles, V. (2018). *Roasting sugarcane bagasse for energy purposes*. Available at: <https://repositorio.unesp.br/bitstream/handle/11449/203740/000924872.pdf?sequence=1&isAllowed=y>.
- [33] Belini, G. B. (2018). *Thermogravimetry applied to characterize biomass*. Available at: <https://repositorio.ufscar.br/bitstream/handle/ufscar/9855/Disserta%C3%A7%C3%A3o%20Gabriela%20Bertoni%20Belini.pdf?sequence=1&isAllowed=y>.

CFD Analysis of Flow through a Ribbed Solar Air Heater Plastic Absorber

David Okenwa¹, Kalu-Whyte Godson², Howard Njoku³

^{1,2,3}Department of Mechanical Engineering, University of Nigeria, Nsukka, Nigeria

^{1,2,3}Sustainable Energy Engineering Research Group (SEERG), Department of Mechanical Engineering, University of Nigeria, Nsukka

¹chidinma.okenwa.247917@unn.edu.ng, ³howard.njoku@unn.edu.ng

Abstract—Solar Air Heaters are excellent for harnessing the sun's thermal power for warming houses and drying agricultural produce. This project extended the knowledge of plastic absorbers' thermal performance and suitability for SAHs by numerically studying a ribbed PVC absorber. The absorber was modelled in SolidWorks 2019 and studied numerically using Ansys Fluent 2021 R2. The study showed the ribbed PVC absorber (80.12%) to have higher efficiency than the aluminum absorber (67.75%) - this was because the aluminum absorber lost heat to the surrounding air faster than the PVC absorber in the absence of insulation. One challenge of using PVC and, indeed, most plastic absorbers highlighted by this numerical study is the lower continuous operating temperatures of plastics (60°C for PVC) which can be exceeded by the solar insolation on hot days.

Keywords – solar air heater, computational fluid dynamics, plastic absorber

I. INTRODUCTION

Climate change, widely regarded as the most important challenge of our generation, is fueled by greenhouse gases for which energy production and use account for 73 per cent [1]. This is why efforts to decarbonize energy and switch to more renewable sources are highly encouraged, including decarbonizing heating, which accounted for 50 per cent of energy use in 2021 [2].

Solar air heaters (SAH) convert the radiation from the sun into useful thermal energy in air. The heated air can then be used for space

heating, crop drying and other processes that involve low and moderate air temperatures. The components of a SAH include; an absorber plate, glazing, insulation, frame/enclosure and flow passages. Some of its components can be seen in the diagram of a SAH shown in Fig. 1. Solar air heaters have lower efficiencies because of the small specific heat capacity of air (1.005kJ/kg·K compared to that of water-4.18kJ/kg·K-for example). This has motivated scientists and researchers to develop various ways of enhancing the thermal efficiencies of solar air heaters by modifying the different components.

Researchers study the modifications using experimental or numerical methods or both. Experimental methods, if done accurately, are more accurate but can be time-consuming and capital-intensive. Numerical analysis involves a simulation of the SAH in a computer. It is best to conduct a numerical analysis first and then construct only the best design.

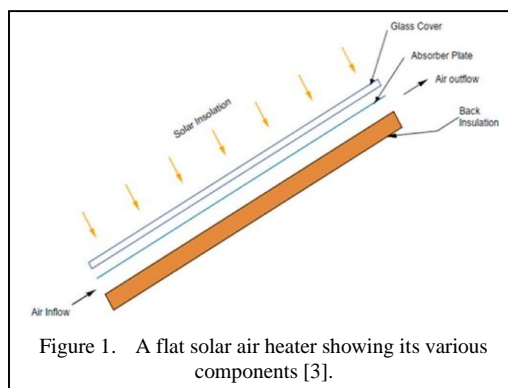


Figure 1. A flat solar air heater showing its various components [3].

Ribs, also called artificial roughness, on absorber plates help improve the efficiency of SAHs by breaking the laminar flow of the flowing air, making it more turbulent and encouraging the mixing of fluids across layers. Reference [4] studied the thermal enhancement of an inverted-t-shaped ribbed solar air heater and got a maximum Nusselt number enhancement of 2.747 and maximum friction factor enhancement of 3.404. The maximum THPP obtained was 1.87 at a Reynolds number of 15.000. A THPP greater than one indicates that there is some improvement of efficiency over the flat plate SAH. Reference [5] carried out an experimental and numerical study of SAH with reversed L-shaped ribs and got an optimum THPP of 1.9. The results of CFD analysis were in good agreement with experimental results and standard theoretical approaches.

Although these innovative modifications would effectively enhance thermohydraulic efficiencies of SAHs, the sophisticated designs would also greatly increase the cost and difficulty of production [6]. Besides being cost-effective, plastic SAHs are lightweight and more resistant to corrosion. Plastic SAHs are solar air heaters whose absorber, glazing or both are plastic. Reference [7] performed a comparative study between metal Transparent Solar Collectors (mTSC) and plastic Transparent Solar Collectors (pTSC) for brooding livestock and poultry. The plastic TSC gave a maximum temperature increase of 25.4°C and an average temperature increase of $8.1 \pm 4.2^\circ\text{C}$. Although the metal TSC gave a slightly higher temperature rise, Reference [7] opined that the cheaper plastic TSC would be cost-effective for large-scale agricultural use. The plastic TSC's absorber was made of a thick black flexible PVC sheet. Reference [6] designed and investigated a flexible SAH made of warp-knitted spacer fabric composite with polyester monofilament. They had a maximum temperature rise of 21.2°C. They concluded that the flexible SAH not only has lower manufacturing cost and higher thermal efficiency than traditional SAH but can also serve in industrial applications involving low to medium temperatures. They also observed that as the length of the SAH increased, its outlet temperature increased but the thermal efficiency decreased.

The scantiness of the studies on plastic solar air heaters compared to traditional metal solar air heaters reveals a gap that researchers need to fill up. Again, all literature review with

numerical evaluations imposed a constant heat flux solar irradiation. This is not obtainable in real life as the sun rises in the morning, peaks around noon and falls in the evening in a sinusoidal pattern. This work intends to numerically investigate the performance of a ribbed PVC solar air heater absorber, compare its performance to that of a similarly shaped absorber made of conventional aluminum and investigate the limitations of using plastics as absorbers. The ribbed plastic SAH was evaluated using a sinusoidal heat flux boundary condition which is closer to real life.

II. NUMERICAL SETUP

A. Geometry

The CFD simulation was run on Ansys Fluent 2021 release 2. Further analysis and graphing were carried out using Microsoft Excel. The ribbed plastic absorber shown in Figs. 2-5 was designed using SolidWorks 2019. A labelled plane and lines were added to the design to aid the display of results.

Temperature graphs and contours were plotted along the lines shown in Figs. 5 and 6.

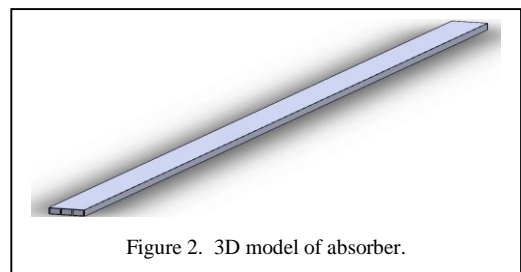


Figure 2. 3D model of absorber.

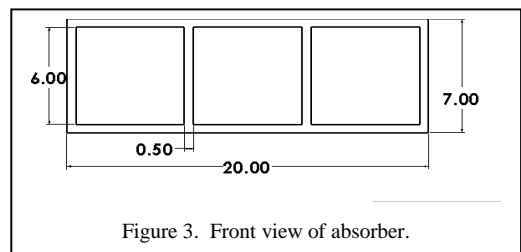


Figure 3. Front view of absorber.

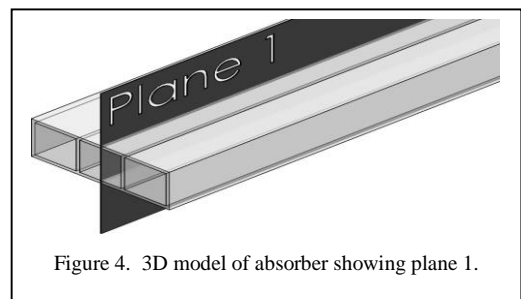


Figure 4. 3D model of absorber showing plane 1.

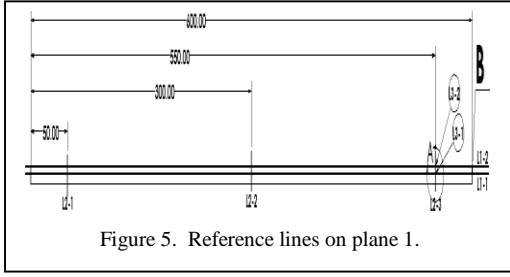


Figure 5. Reference lines on plane 1.

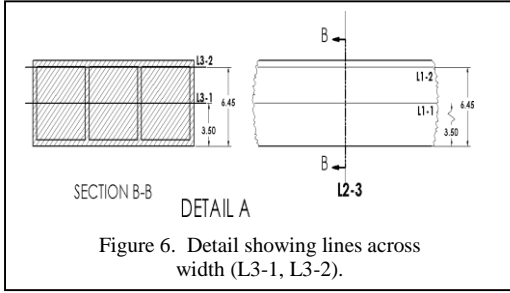


Figure 6. Detail showing lines across width (L3-1, L3-2).

B. Meshing

After designing the computational domain in SolidWorks, it was imported into ANSYS Fluent and meshed in the ANSYS Fluent Mesher. Simple mesh was used, and the size of the elements was 0.5mm, the smallest thickness in the absorber. The meshed domain is shown in Fig. 6.

A grid independence test was carried out to determine the appropriate mesh size. The number of mesh elements was increased from ~500,000 to ~700,000 in five steps. The temperature at the end of length line L1-1 (point B, Fig. 5) was gotten from ANSYS. The temperature at point B changed significantly at the beginning of the mesh element variation but only minimally around 672.000 and mesh size of 0.5mm. It had a maximum change of $\pm 1.1\%$ at around 672.000 elements. These results summarized in Table I show that the simulations were independent of the grid sizes.

TABLE I. GRID INDEPENDENCE TEST.

S/N	Mesh Size (mm)	Mesh Elements	Temp at Point B (K)	% Change in Temp
1	0.55	524.771	338	-
2	0.53	549.020	314.5	-7.0
3	0.51	659.120	350	11.3
4	0.5	672.000	352	0.6
5	0.485	697.668	348	-1.1

Governing Equations

Three fundamental fluid mechanics equations guide the entire CFD analysis: the continuity equation, momentum equation and energy equation. These equations in differential form for 3D incompressible flow as presented by [8] are shown below.

- Continuity:

$$\frac{\partial u}{\partial x} + \frac{\partial v}{\partial y} + \frac{\partial w}{\partial z} = 0. \quad (1)$$

- Momentum:

- X component:

$$\rho \left(\frac{\partial u}{\partial t} + u \frac{\partial u}{\partial x} + v \frac{\partial u}{\partial y} + w \frac{\partial u}{\partial z} \right) = -\frac{\partial P}{\partial x} + \rho g_x + \mu \left(\frac{\partial^2 u}{\partial x^2} + \frac{\partial^2 u}{\partial y^2} + \frac{\partial^2 u}{\partial z^2} \right). \quad (2)$$

- Y component:

$$\rho \left(\frac{\partial v}{\partial t} + u \frac{\partial v}{\partial x} + v \frac{\partial v}{\partial y} + w \frac{\partial v}{\partial z} \right) = -\frac{\partial P}{\partial y} + \rho g_y + \mu \left(\frac{\partial^2 v}{\partial x^2} + \frac{\partial^2 v}{\partial y^2} + \frac{\partial^2 v}{\partial z^2} \right). \quad (3)$$

- Z component:

$$\rho \left(\frac{\partial w}{\partial t} + u \frac{\partial w}{\partial x} + v \frac{\partial w}{\partial y} + w \frac{\partial w}{\partial z} \right) = -\frac{\partial P}{\partial z} + \rho g_z + \mu \left(\frac{\partial^2 w}{\partial x^2} + \frac{\partial^2 w}{\partial y^2} + \frac{\partial^2 w}{\partial z^2} \right). \quad (4)$$

- Energy:

$$\rho \frac{Du}{Dt} = k \left(\frac{\partial^2 T}{\partial x^2} + \frac{\partial^2 T}{\partial y^2} + \frac{\partial^2 T}{\partial z^2} \right) + \left[2\mu \left(\frac{\partial u}{\partial x} \right)^2 + \left(\frac{\partial v}{\partial y} \right)^2 + \left(\frac{\partial w}{\partial z} \right)^2 + \frac{1}{2} \left(\frac{\partial u}{\partial y} + \frac{\partial v}{\partial x} \right)^2 + \frac{1}{2} \left(\frac{\partial v}{\partial z} + \frac{\partial w}{\partial y} \right)^2 + \frac{1}{2} \left(\frac{\partial u}{\partial z} + \frac{\partial w}{\partial x} \right)^2 \right]. \quad (5)$$

where: x, y, z are the cartesian coordinates; u, v, w are the velocity components (m/s); t is the time (s); P is the pressure (N/m^2), ρ is the density (kg/m^3); μ is the viscosity (kg/(ms)); and k is the thermal conductivity (W/mK).

C. Boundary Conditions

The initial and boundary conditions used are listed below. A laminar air flow with Reynolds number, R_e , of 1000 was simulated. All walls were set to no slip.

Inlet: Pressure = 1atm, Temperature = 300K;

Outlet: $\frac{\partial u}{\partial x} = 0$.

Top wall: $\dot{q} = \frac{\dot{q}_{max}}{2} \sin\left(\frac{2\pi}{t_{max}}t + \frac{3\pi}{2}\right) + \frac{\dot{q}_{max}}{2}$.
This gives a sinusoidal variation from $\dot{q} = 0$ to $\dot{q}_{max} = 1000\text{W/m}^2$ as shown in Fig. 7. t_{max} = total simulation time (12 hours), t = instantaneous time.

Bottom wall: $h = 3.913 \text{ W/m}^2 \cdot \text{K}$;

Side walls: $h = 12.6123 \text{ W/m}^2 \cdot \text{K}$;

Front PVC Face: $h = 0 \text{ W/m}^2 \cdot \text{K}$;

Back PVC Face: $h = 14.381 \text{ W/m}^2 \cdot \text{K}$.

Where \dot{q} = heat flux (W/m^2); and h = convective heat transfer coefficient ($\text{W/m}^2 \cdot \text{K}$)

Convective heat transfer coefficient, h , at various external surfaces were evaluated using correlations presented by [9].

Nusselt number correlation for natural convection:

$$Nu_u = 0.68 + \frac{0.97R_a^{1/4}}{[1+(0.492/P_r)^{9/16}]^{4/9}}, \quad (6)$$

(for vertical walls)

$$Nu_u = 0.68R_a^{1/4}, \quad (7)$$

(for horizontal walls)

where R_a is the Rayleigh number (calculated) and P_r is the Prantl number.

Rayleigh number, R_a , for both wall types:

$$R_a = \frac{g\beta(T_s - T_\infty)L^3}{\nu\alpha}, \quad (8)$$

where T_s is the temperature of surface (K), T_∞ is the free air temperature (K), L is the characteristic length (m), ν is the kinematic viscosity (m^2/s), α is the thermal diffusivity (m^2/s) and β is the volumetric thermal expansion coefficient (K^{-1}). $\beta = 1/T$.

Characteristic length, L :

$$L = \text{height, } h(\text{in vertical walls}). \quad (9)$$

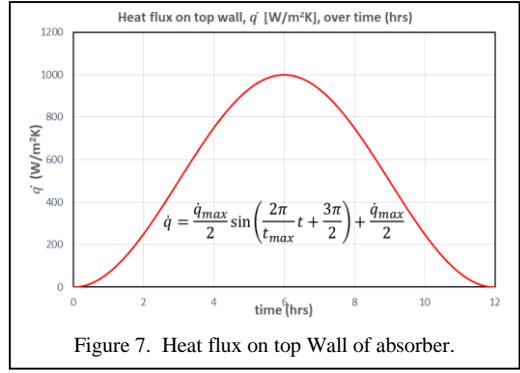


Figure 7. Heat flux on top Wall of absorber.

$$L = A_s/P_s, \quad (\text{for horizontal walls}), \quad (10)$$

where A_s =Area of surface (m^2) and P_s =perimeter of surface (m). We then get h using the relation:

$$Nu_u = \frac{hL}{k}, \quad (11)$$

where k = thermal conductivity of the surface ($\text{W/m}^2 \cdot \text{K}$).

• Transient Setup

Time step size = 60s;

Number of time steps = 720;

Total time, $t = 43.200\text{s}$ (12 hours);

Maximum iteration per time step = 10.

D. Materials and Properties

The fluid used was air and the absorber was made of polyvinyl chloride (PVC) and aluminum. Table II shows the properties of the materials used.

TABLE II. PROPERTIES OF MATERIALS USED.

S/N	Property	PVC	Air	Aluminum
1	Density (g/cm ³)	1.45	1.225	2.719
2	Thermal cond. (W/m.k)	0.28	0.0242	202.4
3	Specific heat (J/kg°C)	1170	1006.43	871
4	Viscosity (kg/(ms))	-	1.7894 × 10 ⁻⁵	-
5	Operating temp. (°C)	60	-	150
6	Melting temp. (°C)	100-260	-	660.3

E. Efficiency Evaluation

Thermal Performance measures how efficiently the collector transforms incident solar radiation to internal energy of the flowing air. It is the ratio of useful energy gained by flowing air (Q_{useful}) to the total amount of energy supplied

by solar irradiation (Q_{solar}). Thermal efficiency η_{th} is given by:

$$\eta_t = \frac{Q_{useful}}{Q_{solar}}$$

$$Q_{useful} = C_p \dot{m} \int_{t_0}^{t_{max}} (T_0 - T_i) dt$$

$$Q_{solar} = A \int_{t_0}^{t_{max}} \left(\frac{\dot{q}_{max}}{2} \sin\left(\frac{2\pi}{t_{max}} t + \frac{3\pi}{2}\right) + \frac{\dot{q}_{max}}{2} \right) dt \quad (12)$$

III. RESULTS AND DISCUSSION

A CFD analysis of laminar flow through ribbed plastic PVC and aluminum absorbers was carried out. A sinusoidal heat flux with maximum flux of 1000 W/m² was imposed on the top absorber surface to mirror the behavior of solar radiation variation from dawn to dusk (12-hour period from 6 am to 6 pm). The results are presented here. Figs. 8-11 shows temperature plots along reference lines and planes in the PVC absorber. Figs. 12-15 shows corresponding plots in the aluminum absorber. Fig. 16 shows the average rise in air temperature over the 12-hour period.

From the temperature plots along the lengths (Fig. 8 and Fig. 12), as expected, there is a steady rise in air temperature along the length. The height plot along the centre line, L2-2 shows a significant difference in temperatures between

the top and lower walls for PVC (Fig. 9): the upper wall and the air close to it are significantly hotter than the lower wall and air close to it. However, this difference is not noticeable in aluminum absorber (Fig. 13). The upper and

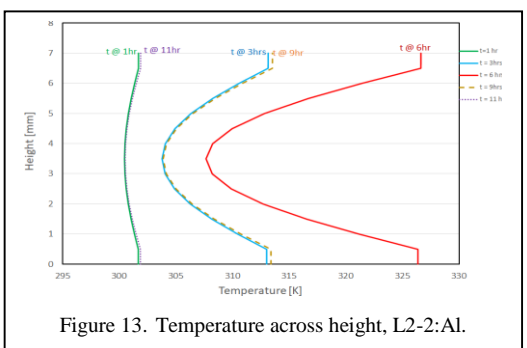
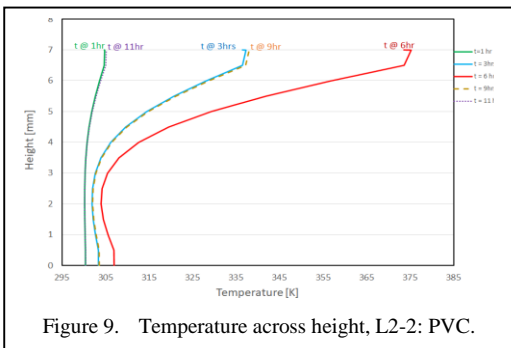
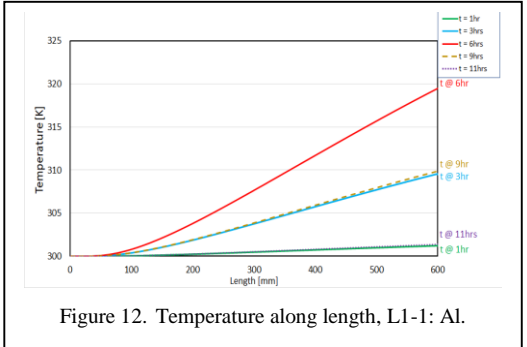
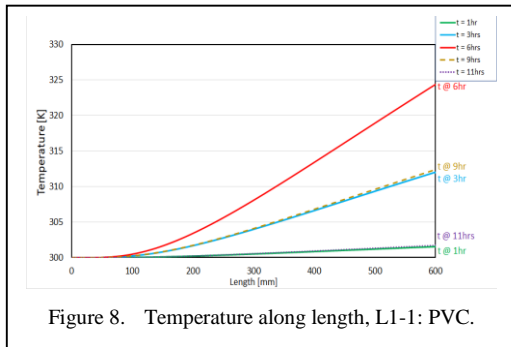
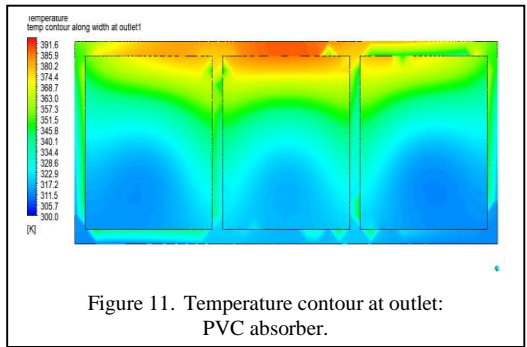
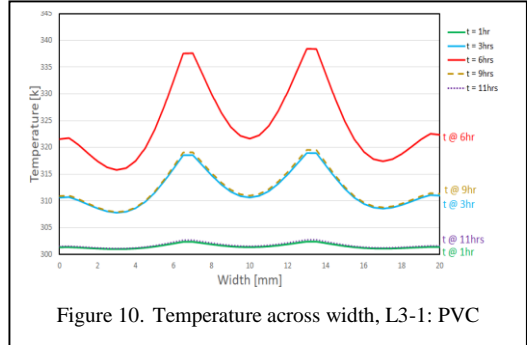


TABLE III. KEY RESULTS OF SIMULATION.

Config uration	Material	Max Temp in Absorber		Efficiency (%)
		K	°C	
C1	PVC	391.5	118.5	80.42
C2	Aluminum	333.2	60.2	67.75

lower ribs were almost at the same temperature for the aluminum absorber.

This is because of the high thermal conductivity of aluminum (202.4W/m·K) compared to PVC (0.28W/m·K). Notwithstanding, from Fig. 10, it can be seen that the air through the PVC absorber experiences higher temperature rise than that through the aluminum absorber. Two things can explain this. Firstly, since the PVC does not lose heat easily, its temperature builds up, ultimately resulting in heat being passed to the flowing air from a higher temperature absorber. The second strengthens the first; aluminum loses heat to the surrounding air much faster than PVC leading to higher heat loss. This can be seen in the lower thermal efficiencies for Aluminum compared to PVC calculated using (12) and summarized in Table III. Thus, aluminum absorbers have a higher need for insulators than PVC absorbers.

The temperature contour in the outlet face shows that a maximum temperature of 391.5K (118.5°C) is present in the PVC absorber (Fig. 11). This is more than the operating temperature for PVCs (333K or 60°C). This is one shortcoming of PVCs and will be addressed in a later subsection. The aluminum absorber reaches a maximum temperature of 333.2K (60.2°C) which can be easily handled by aluminum which has an operating temperature around 453K or 180°C.

A. Maximum Operating Temperatures of Plastic Absorbers

The maximum operating temperature of absorbers is the temperature at which they can operate for extended periods and still maintain their stability. The maximum operating temperature of PVC is 60°C and it experienced a peak temperature of 118.5°C at a maximum solar insolation of 1000 W/m². This, however, doesn't write off the suitability of PVCs and plastics as absorbers as the maximum temperature occurs only around the peak insolation. This doesn't last for too long.

Also, the advantages of using plastic absorbers can be harnessed by using other

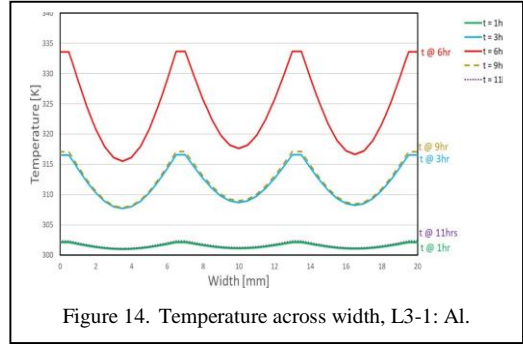


Figure 14. Temperature across width, L3-1: Al.

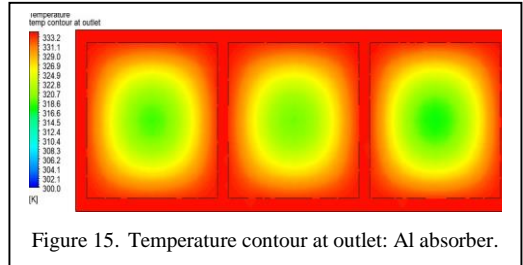


Figure 15. Temperature contour at outlet: Al absorber.

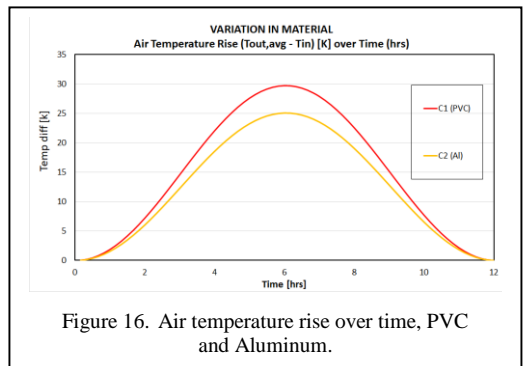


Figure 16. Air temperature rise over time, PVC and Aluminum.

plastics with higher operating temperatures such as Polytetrafluoroethylene (PTFE), 260°C; Polyetherimide (PEI), 170°C; or Polyether ether ketone (PEEK) up to 310°C [10].

IV. CONCLUSION

A solar air heater ribbed plastic PVC absorber was numerically studied in this work. Its performance was compared to that of an aluminum absorber under similar conditions. Notably, it was seen that the PVC absorber had higher efficiencies than the aluminum absorber. This might be because it lost less heat to the surrounding. The air through the PVC absorber also experienced higher temperature rise than that through the aluminum absorber. This might be because the temperature of the PVC absorber builds up and transfers heat to the flowing air from a higher temperature. Although the absorber had high efficiencies, it has the

limitation of temperature resistance. Its maximum operating temperature limits the conditions under which it can operate for a longer time and that limit was surpassed during the simulation.

The authors recommend that further work be done on solar air heaters with plastic absorbers in the following areas:

1. Economic implications of using plastic absorbers versus metallic absorbers;
2. Thermal performance of other plastics with high operating temperatures;
3. Studying the effect of different configurations of fins and ribs on the thermal and thermo-hydraulic performance of plastic absorbers be studied.

REFERENCES

- [1] World Resources Institute. (2016). *World greenhouse gas emissions, 2016*. Available at <https://www.wri.org/data/world-greenhouse-gas-emissions-2016>.
- [2] International Energy Agency. (2022). *Heating - fuels and technologies*. Available at <https://www.iea.org/fuels-and-technologies/heating>.
- [3] Nidhul, K., Yadav, A. K., Anish, S., & Kumar, S. (2021). Critical review of ribbed solar air heater and performance evaluation of various V-rib configuration. *Renewable and Sustainable Energy Reviews, 142*, 110871.
- [4] Mahanand, Y., & Senapati, J. R. (2020). Thermal enhancement study of a transverse inverted-T shaped ribbed solar air heater. *International Communications in Heat and Mass Transfer, 119*, 104922.
- [5] Gawande, V. B., Dhoble, A. S., Zodpe, D. B., & Chamoli, S. (2016). Experimental and CFD investigation of convection heat transfer in solar air heater with reverse L-shaped ribs. *Solar Energy, 131*, 275-295.
- [6] Zhu, J., Jia, H., Cheng, X., Huang, X., Liu, X., & Guo, J. (2019). The design and performance evaluation of a high-efficient flexible solar air heater based on transparent spacer fabric composite. *Solar Energy Materials and Solar Cells, 201*, 110089.
- [7] Poole, M. R., Shah, S. B., Grimes, J. L., Boyette, M. D., & Stikeleather, L. F. (2018). Evaluation of a novel, low-cost plastic solar air heater for turkey brooding. *Energy for Sustainable Development, 45*, 1-10.
- [8] Yunus, A. C. (2010). *Fluid Mechanics: Fundamentals And Applications (Si Units)*. Tata McGraw Hill Education Private Limited.
- [9] Incropera, F. P., & DeWitt, D. P. *Fundamentals of Heat and Mass Transfer*, John Wiley and Sons, New York, 1990.
- [10] Global Solar Atlas (2022). *Global solar atlas*. Available at: <https://globalsolaratlas.info/map?s=6.852123,7.36496&m=site&c=6.924723,7.324104,11>.
- [11] Fast Radius (2020). *Top 5 heat-resistant plastic*. Available at: <https://www.fastradius.com/resources/top-5-heat-resistant-plastics/>.

Coal Price Forecasting Model for Underground Mine and Thermal Power Plant Interaction

Miloš Gligorić¹, Saša Jovanović², Zoran Gligorić³, Suzana Lutovac⁴

^{1,3,4}University of Belgrade, Faculty of Mining and Geology, Belgrade, Serbia

²University of Priština in Kosovska Mitrovica, Faculty of Technical Sciences, Kosovska Mitrovica, Serbia

¹milos.gligoric@rgf.bg.ac.rs, ²sasa.m.jovanovic@pr.ac.rs, ³suzana.lutovac@rgf.bg.ac.rs,

⁴zoran.gligoric@rgf.bg.ac.rs

Abstract—Constant fluctuations of coal prices on the market significantly affect the stable and sustainable operation of the thermal power plant. Creating a mechanism to predict the future value of the coal price is of great importance for every mining company and mining engineer. This paper presents a combination of fuzzy C-mean clustering algorithm and first-order autoregressive time series AR (1) model for coal price forecasting. The fuzzy C-means clustering algorithm (FCM) is used for transforming the original time series into seven possible states. The first-order autoregressive time series AR (1) model is applied to forecast the obtained states per monthly span. The model is based on monitoring of coal price of the past 228 months. Mean absolute percentage error (MAPE) between original and predicted time series is 7.27% indicating the high efficiency of the developed model.

Keywords - coal price, time series, forecasting model, thermal power plant, energy supply

I. INTRODUCTION

Coal is still one of the most popular products at the world market that used for obtaining electricity, heat or some other type of energy. Process of combustion of any type of coal takes place in facilities known as thermal power plants. Each thermal power plant primarily depends on a stable and secure supply of coal. However, variations of coal prices at market have a huge impact on supplying the thermal power plant and providing a fully functioning relationship

between underground coal mine and thermal power plant.

Many authors are deal with a problem of coal price forecasting using different methods. There is a hybrid forecasting model of coal price based on ARIMA (AutoRegressive Integrated Moving Average) and SVM (Support Vector Machine) model [1]. Combination of VMD (Variational Mode Decomposition), LSTM (Long Short-Term Memory) and SVR (Support Vector Regression) method are used for predicting the coal price [2]. Also, VAR (Vector AutoRegression) model [3] and VARMA (Vector AutoRegressive Moving Average) model [4] are applied to forecast coal price. An integrating model based on ISSA (Improved Sparrow Search Algorithm) and LSSVR (Least Squares Support Vector Regression) algorithm is developed to predict coal price [5].

The main aim of this study is to analyse the short – term forecast of the coal price. The paper integrates two approaches, FCM and AR (1) to create forecasting model. FCM is used to transform actual coal price time series into one of the seven initial states while AR (1) estimates the values of predicted and forecasted states.

The rest of the paper is organized as follows. Section 1 is referred on Introduction and shortly literature review. Fuzzy C-means clustering algorithm (FCM) is presented in Section 2 while the first-order autoregressive time series AR (1) model for coal price forecasting is briefly

described in Section 3. Section 4 is related to detailed Numerical example of the developed forecasting model. At last, concluding remarks and future research are discussed in Section 5.

II. THE FUZZY C-MEANS CLUSTERING ALGORITHM (FCM)

To make much easier and accurately prediction process of the original time series, fuzzy C-means clustering algorithm (FCM) is applied. The main idea is to transform the original time series into seven possible states. It means that one of the seven possible states should be assigned to each value of the original time series. After that, new time series containing only a certain state (initial state) are formed and subjected to autoregressive analysis. The FCM is based on minimizing following function [6]:

$$J = \sum_{j=1}^k \sum_{i=1}^N u_{i,j}^m \times d_{ij}, \quad (1)$$

subject to:

$$\sum_{j=1}^k u_{i,j} = 1, \quad i = 1, \dots, N, \quad (2)$$

where: $u_{i,j}$ represents the membership function (degree of belongingness) between monitored time series Y_i and cluster centers C_j ;

d_{ij} presents the squared Euclidean distance between monitored time series Y_i and cluster centers C_j ;

k is the number of clusters;

N is the total number of data in monitored time series;

m is the fuzzifier parameter (adopted 2).

The main steps of FCM methodology are as follows:

Step 1. Select an integer number of cluster centers C_j ($j = 1, 2, \dots, k$) and threshold value ε (very small positive number, $\varepsilon = 0,0001$); set the fuzzifier parameter m ($m = 2$).

Step 2. Sort up the cluster centers from the smallest to largest.

Step 3. Calculate squared Euclidean distances d_{ij} , $i = 1, \dots, N$ and $j = 1, \dots, k$. Calculate and update the membership functions $u_{i,j}$ by the following equation:

$$u_{i,j} = \frac{1}{\frac{1}{d_{ij}^2} \times \sum_{l=1}^k \left(\frac{1}{d_{il}^2}\right)^{\frac{1}{m-1}}}, \quad (3)$$

where d_{il} presents the squared Euclidean distance between monitored time series Y_i and cluster centers C_l ($l = 1, 2, \dots, k$).

Step 4. Calculate the center for each cluster to determine a new set of cluster centers by the following equation:

$$C_j(t) = \frac{\sum_{i=1}^N u_{i,j}^m Y_i}{\sum_{i=1}^N u_{i,j}^m}, \quad (4)$$

where t is the iteration number.

Step 5. If $|C_j(t) - C_j(t-1)| < \varepsilon$ then stop. Otherwise go to Step 2.

III. THE FIRST-ORDER AUTOREGRESSIVE TIME SERIES AR (1) MODEL

Since the new time series of defined states (initial states) are created instead of original time series, the prediction process of coal price is much simpler. For that purpose, the first-order autoregressive time series AR Eq. (1) model is implemented. Briefly description of this method is given below. The AR Eq. (1) model where 1 indicates the order of autoregression is defined as follows [7-8]:

$$Y_{(t)} = c + \varphi_1 \times Y_{(t-1)} + \varepsilon_{(t)}, \quad (5)$$

where:

$Y_{(t)}$ is the value of the coal price time series at time t ;

c represents the intercept at the vertical axis (y-axis);

φ_1 presents the slope coefficient;

$Y_{(t-1)}$ is the value of the coal price time series at time $t-1$;

$\varepsilon_{(t)}$ represents the error term (residual term);

t is a monitored monthly span, $t = 1, 2, \dots, T$.

By using ordinary least square method, the intercept and slope coefficient are estimated to predict the initial states of the original coal price time series as follows:

$$Y_{(t)}^p = c^p + \varphi_1^p \times Y_{(t-1)}^p, \quad (6)$$

where:

$Y_{(t)}^p$ is predicted value of the coal price time series at time t ;

c^p represents the estimated value of the intercept;

φ_1^p presents the estimated value of the slope coefficient;

$Y_{(t-1)}^p$ is predicted value of the coal price time series at time $t - 1$.

In the same way, the forecasting process is determined by the following equation:

$$Y_{(t+1)}^f = c^p + \varphi_1^p \times Y_{(t)}^f, \quad (7)$$

where:

$Y_{(t+1)}^f$ is forecasted value of the coal price time series at time $t + 1$;

$Y_{(t)}^f$ is forecasted value of the coal price time series at time t .

IV. NUMERICAL EXAMPLE

To test the developed model, we have monitored the values of coal price from January 2004 to December 2022, or the total of 228 months (19 years). The model testing can be divided into two phases. The first phase represents the prediction process which takes into consideration all 228 months of the actual coal prices. The second phase is referred on forecasting process which forecasts the next 36 months of the coal prices in the future. Original values of the coal price time series are presented in Table I.

Using fuzzy C-means clustering algorithm (Eqs. 1 to 5), the original values of the coal price time series is transformed into one of the possible seven states. The initial states of the original coal price time series are shown in Table II.

The original coal price time series and transformed coal price time series are graphically illustrated in Fig. 1. Based on the first-order autoregressive time series AR Eq. (1), the prediction process, Eq. (6), of the initial states is carried out. On the same way, the forecasting process, Eq. (7), of the initial states in the future is realized. In Table III, obtained values of predicted states of the original coal price time series is shown while Table IV presents the forecasted states (from January 2023 to

December 2025). Graphical representation of the initial states and predicted states of the original coal price time series as well as forecasted states in the future is demonstrated in Fig. 2. To make simpler prediction and forecasting process, the rounding of all obtained values (predicted and forecasted) is performed for easy comparison with the initial states of the original coal price time series.

TABLE I. ORIGINAL VALUES OF THE COAL PRICE TIME SERIES [9].

Date	Price \$/t
Jan-04	37.75
Feb-04	41.75
Mar-04	48.94
Apr-04	53.25
May-04	56.44
Jun-04	59.55
Jul-04	61.38
Aug-04	59.25
Sep-04	55.38
Oct-04	56.63
Nov-04	52.83
Dec-04	52.25
Jan-05	53.05
Feb-05	49.9
Mar-05	50.93
Apr-05	51.25
May-05	51.31
Jun-05	51
Jul-05	50.9
Aug-05	49.13
Sep-05	45.25
Oct-05	42.46
Nov-05	38.06
Dec-05	38.23
...	...
Jan-22	196.95
Feb-22	219.78
Mar-22	314.04
Apr-22	310.85
May-22	371.86
Jun-22	374.08
Jul-22	402.2
Aug-22	406.97
Sep-22	430.81
Oct-22	389.79
Nov-22	342.16
Dec-22	379.23

TABLE II. INITIAL STATES OF THE ORIGINAL COAL PRICE TIME SERIES.

Date	Price \$/t	Initial state
Jan-04	37.75	1
Feb-04	41.75	1
Mar-04	48.94	1
Apr-04	53.25	1
May-04	56.44	1
Jun-04	59.55	1
Jul-04	61.38	2
Aug-04	59.25	1
Sep-04	55.38	1
Oct-04	56.63	1
Nov-04	52.83	1
Dec-04	52.25	1
Jan-05	53.05	1
Feb-05	49.9	1
Mar-05	50.93	1
Apr-05	51.25	1
May-05	51.31	1
Jun-05	51	1
Jul-05	50.9	1
Aug-05	49.13	1
Sep-05	45.25	1
Oct-05	42.46	1
Nov-05	38.06	1
Dec-05	38.23	1
...
Jan-22	196.95	6
Feb-22	219.78	6
Mar-22	314.04	7
Apr-22	310.85	7
May-22	371.86	7
Jun-22	374.08	7
Jul-22	402.2	7
Aug-22	406.97	7
Sep-22	430.81	7
Oct-22	389.79	7
Nov-22	342.16	7
Dec-22	379.23	7

TABLE III. PREDICTED STATES OF THE ORIGINAL COAL PRICE TIME SERIES.

Date	Initial state	Predicted state
Jan-04	1	
Feb-04	1	1
Mar-04	1	1
Apr-04	1	1
May-04	1	1
Jun-04	1	1
Jul-04	2	1
Aug-04	1	2
Sep-04	1	1
Oct-04	1	1
Nov-04	1	1
Dec-04	1	1
Jan-05	1	1
Feb-05	1	1
Mar-05	1	1
Apr-05	1	1
May-05	1	1
Jun-05	1	1
Jul-05	1	1
Aug-05	1	1
Sep-05	1	1
Oct-05	1	1
Nov-05	1	1
Dec-05	1	1
...
Jan-22	6	5
Feb-22	6	6
Mar-22	7	6
Apr-22	7	7
May-22	7	7
Jun-22	7	7
Jul-22	7	7
Aug-22	7	7
Sep-22	7	7
Oct-22	7	7
Nov-22	7	7
Dec-22	7	7

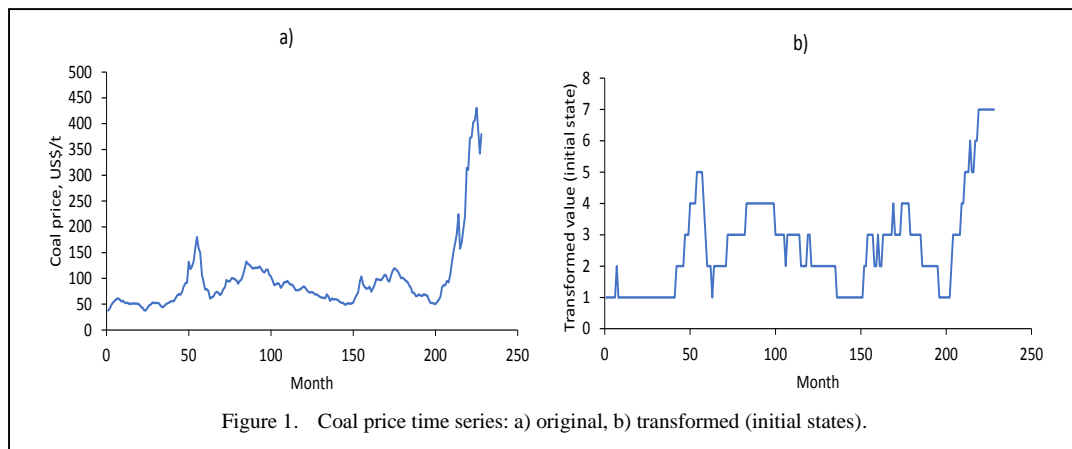


Figure 1. Coal price time series: a) original, b) transformed (initial states).

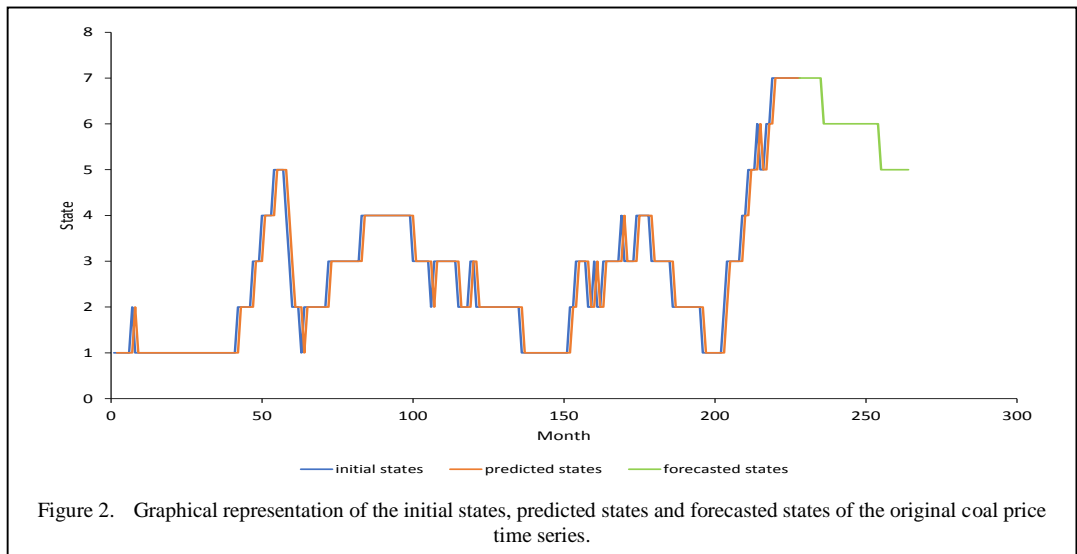


Figure 2. Graphical representation of the initial states, predicted states and forecasted states of the original coal price time series.

TABLE IV. FORECASTED STATES OF THE COAL PRICE TIME SERIES.

Date	Forecasted state
Jan-23	7
Feb-23	7
Mar-23	7
Apr-23	7
May-23	7
Jun-23	7
Jul-23	7
Aug-23	6
Sep-23	6
Oct-23	6
Nov-23	6
Dec-23	6
Jan-24	6
Feb-24	6
Mar-24	6
Apr-24	6
May-24	6
Jun-24	6
Jul-24	6
Aug-24	6
Sep-24	6
Oct-24	6
Nov-24	6
Dec-24	6
Jan-25	6
Feb-25	6
Mar-25	5
Apr-25	5
May-25	5
Jun-25	5
Jul-25	5
Aug-25	5
Sep-25	5
Oct-25	5
Nov-25	5
Dec-25	5

As it can be seen from Table III, Table IV and Fig. 2 obtained values of predicted states are very similar to initial states of the monitored time series. The accuracy of developed forecasting model is evaluated by well-known Mean Absolute Percentage Error (MAPE). Comparing initial and predicted states, MAPE with a 7.27% indicates a high effectiveness and performance of the developed forecasting model.

V. CONCLUSION

Having in mind that the coal is one of the most important energy sources for producing the electricity, continuous supply of thermal power plant with coal is the key task for mining engineers. The economic factor, in a first-row coal price, represents the most dominant aspect in providing sustainable thermal power plant supply chain.

This paper combines two methods, fuzzy C-means clustering algorithm and first-order autoregressive time series AR Eq. (1) model, to forecast the coal price. From the obtained results, it can be concluded that our developed forecasting model presents a reliable base for strategic production planning in underground coal mines. MAPE with a 7.27% confirms that the model is absolutely applicable and suitable for making forecasting model of any mineral commodity. Also, this paper provides a great assistance to underground coal mine management to do business and to overcome the risks in the future.

Future research can be focused on including the fuzzy or interval values of the monitored time

series data to increase the uncertainty of the input parameters. Also, the combination of existing AR Eq. (1) forecasting model with some of the popular forecasting methodologies such as ARIMA, SVM or LSSVR algorithm is another way to extend our developed model.

REFERENCES

- [1] Zheng, Y., Yuan, K., & Dai, L. (2021). Research on Coal Price Forecast based on ARIMA and SVM combination Model. In *E3S Web of Conferences* (Vol. 257, p. 02008). EDP Sciences.
- [2] Zhang, K., Cao, H., Thé, J., & Yu, H. (2022). A hybrid model for multi-step coal price forecasting using decomposition technique and deep learning algorithms. *Applied Energy*, 306, 118011.
- [3] Guo, X., Shi, J., & Ren, D. (2016). Coal price forecasting and structural analysis in China. *Discrete Dynamics in Nature and Society*, 2016.
- [4] Warsono, W., Russel, E., Wamiliana, W., Widiarti, W., & Usman, M. (2019). Modeling and forecasting by the vector autoregressive moving average model for export of coal and oil data (case study from Indonesia over the years 2002-2017). *International Journal of Energy Economics and Policy*, 9(4), 240-247.
- [5] Cao, B., Wang, S., Bai, R., Zhao, B., Li, Q., Lv, M., & Liu, G. (2023). Boundary optimization of inclined coal seam open-pit mine based on the ISSA–LSSVR coal price prediction method. *Scientific Reports*, 13(1), 1-22.
- [6] Chang, C. T., Lai, J. Z., & Jeng, M. D. (2011). A fuzzy k-means clustering algorithm using cluster center displacement. *Journal of Information Science and Engineering*, 27(3), 995-1009.
- [7] Jafarova, H. A., & Aliyeva, R. T. (2022). The use of autoregressive process AR (1) in the analysis of some finance indices. *Informatics and Control Problems*, 42(1), 19-25.
- [8] *Time-series analysis*, Available at: <https://www.cnblogs.com/fangwenyu/p/4265367.html> Accessed on: October 18, 2023.
- [9] *Coal, Australian thermal coal*, Available at: <https://www.indexmundi.com/commodities/?commodity=coal-australian> Accessed on: October 18, 2023.

Thermal Efficiency of a PVC Honeycomb Solar Collector

Kewyn Ohan Mazer Bueno¹, Paulo Cesar Mioralli², Paulo Henrique Palota³, Pablo Sampaio Gomes Natividade⁴, Sílvio Aparecido Verdério Junior⁵, Elson Avallone⁶

¹Student in the Control and Automation Engineering at the Federal Institute of Science and Technology of São Paulo, Catanduva-SP, Brazil

^{2,3,4,6}Lecturer in the Control and Automation Engineering course at the Federal Institute of Science and Technology of São Paulo, Catanduva-SP, Brazil

⁵Lecturer in the Mechanical Engineering course at the Federal Institute of Science and Technology of São Paulo, Araraquara-SP, Brazil

¹k.bueno@aluno.ifsp.edu.br, ²mioralli@ifsp.edu.br, ³palota@ifsp.edu.br, ⁴pablo.sgn@ifsp.edu.br, ⁵verderio@ifsp.edu.br, ⁶elson.avallone@ifsp.edu.br

Abstract—The use of solar collectors for water heating represents a significant economic and technological development throughout the world, generating a significant reduction in electricity consumption. A PVC lining honeycomb plate was converted into a solar collector, and its thermal efficiency was then analyzed. Using DS18B20 sensors, the cold water inlet, hot water outlet and ambient temperatures were measured. Direct incident and reflected radiation from the ground were measured using two thermal radiometers, with the same inclination as the solar collector, one facing upwards and the other downwards. The volumetric flow was measured using a YF-S401 sensor connected to a water pump, keeping the flow constant. The average thermal efficiency of the PVC collector was 39.16%, being able to work as a hybrid system to support electric showers. It can be built by the user himself and utilized to heat water for low-income families, which is a promising result for a low-investment equipment element, compared to commercial solar collectors (FPC).

Keywords – solar collector, prototype, PVC, thermal efficiency

NOMENCLATURE

Symbol	Specification	Unit
A	Front and rear collector area	[m ²]
<i>cp</i>	Specific heat of water at constant pressure	[J/kg·K]
<i>G_{dir}</i>	Incident solar heat flow	[W/m ²]
<i>G_{ref}</i>	Solar reflected heat flow	[W/m ²]
<i>ṁ</i>	Mass flow	[kg/s]
<i>T_h</i>	Hot water temperature	[°C]
<i>T_c</i>	Cold water temperature	[°C]
<i>T_∞</i>	Ambient temperature	[°C]
<i>Q̇_a</i>	Absorbed heat rate by the collector	[W]
<i>Q̇_i</i>	Incident heat rate by the collector	[W]
<i>Q̇_{sup}</i>	Incident heat rate on the upper surface of the collector	[W]
<i>Q̇_{inf}</i>	Incident heat rate on the lower surface of the collector	[W]
<i>α</i>	Solar collector inclination	[°]
<i>η</i>	Thermal efficiency of the solar collector	[dimensionless]

I. INTRODUCTION

Brazil leads the renewable energy market in Latin America in solar water heating and has great potential for growth in this technology due to its simplicity and high economic viability. Among the renewable energy sources used until the end of 2015, investments were distributed between 2.3% in nuclear energy and 19.3% in all

other renewable energies, demonstrating great solar, wind and geothermal energy potential [1]. At the end of 2009, thermal energy storage capacity was approximately 600 MW and at the end of 2013 a total of 3.6 GW [2]. In 2016, production capacity increased to 456 GW, distributed across 652 million m² of installed collectors [3]. In the study of [4], the main use of solar energy is restricted to domestic water heating using solar collectors, as it has a low environmental impact and a significant reduction in the use of conventional energy sources. Reducing family electricity demand leads to social improvement, environmental preservation, the possibility of creating jobs and financial savings, in addition to a significant reduction in greenhouse gas emissions. The International Conference Rio +20 [5] reports on the construction of sustainable cities, including the rational use of energy, with effective control by public authorities. The residential sector has an average consumption of 24% of the total electricity consumed [3]. The use of a hybrid system consisting of solar collectors linked to electric showers allows a 10% reduction in electricity costs [6]. General Electric published a report stating that the use of renewable energy can quickly change the trajectory of climate change. The generation and distribution of renewable energy must provide an economically viable, renewable and reliable energy matrix and the most effective way is diversification [7]. As Brazil's energy matrix is mostly hydroelectric, the use of solar energy for residential water heating corresponds to savings of 70% in electricity consumption [8] and the application of new technologies makes it possible to reduce fossil fuels for generation and electrical energy distribution [9]. The Flat Plate Collector (FPC) is used in moderate heating situations, taking advantage of solar radiation, with little maintenance, widely applied in water heating in buildings and various industrial processes. The goal of this study is to build a PVC honeycomb solar collector and measure its thermal efficiency.

II. METHODOLOGY

The solar collector studied was built with a PVC (Polyvinyl Chloride) honeycomb plate, whose internal channels provide water circulation, with better heat distribution (Fig. 1).

PVC tubes with slots are fixed to the ends of the linen with high-resistance PVC glue and epoxy resin, as shown in Fig. 2.

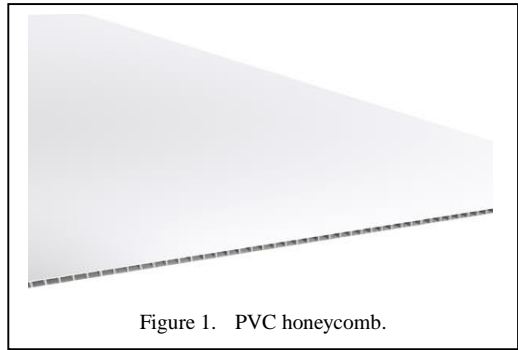


Figure 1. PVC honeycomb.

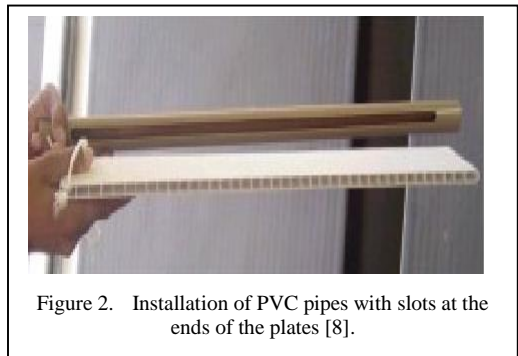


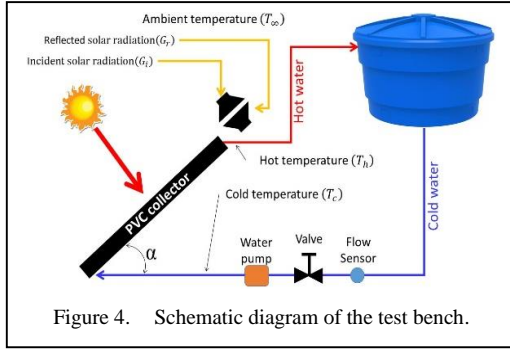
Figure 2. Installation of PVC pipes with slots at the ends of the plates [8].



Figure 3. Complete assembly.

The solar collector was coated with high absorptivity matte black paint, used to manufacture commercial solar collectors. The complete assembly is shown in Fig. 3.

The angle α in Fig. 4 is determined according to Technical Standard ABNT-NBR 15569 [10], [11] and [12] with an inclination of the local



latitude of 21°8'16" south plus 10°. Water is pumped between the PVC collector and the reservoir, (Fig. 4), maintaining a constant flow.

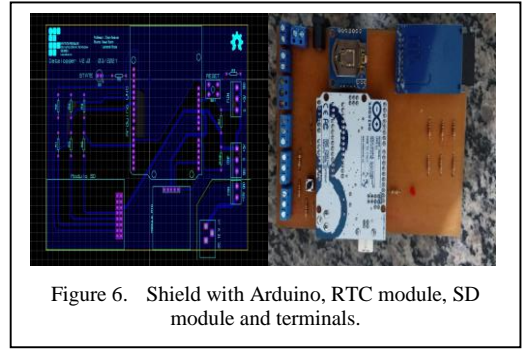
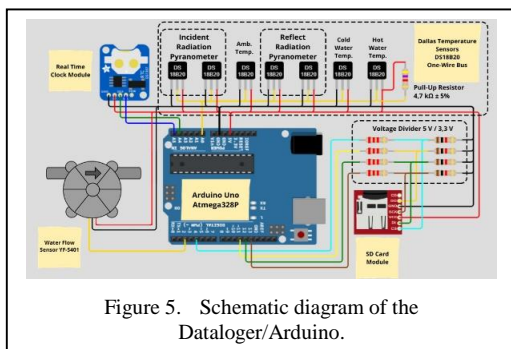
The electric pump flow adjustment is carried out through the manual valve and monitored by the Arduino serial monitor [13].

The temperatures of hot water (T_h) and cold water (T_c) are measured with DS18B20 encapsulated sensors [14] and installed in the PVC connections at the hot water outlet and cold water inlet, respectively. The ambient temperature is measured with the same sensor (DS18B20) installed in a tube open at both ends, thermally isolated and with forced ventilation.

The radiation incident from the sun and reflected from the ground are measured using thermal radiometers constructed according to [15–19] and installed with the same inclination as the angle α .

To measure the volumetric flow, a YF-S401 sensor [20] was used, calibrated on a test bench, and the results were converted into mass flow. The circuit flow was set at 0.017 kg/s by the valve in Fig. 4 and visualized by the Arduino serial monitor.

The electronic circuit diagram developed for this work is shown in Fig. 5. A similar assembly was developed by [21].



The shield with the Arduino, RTC module, SD module and terminals is shown in Fig. 6.

A. Mathematical Formulation

To evaluate the heat flow absorbed by the solar collector, the summarized First Law of Thermodynamics was used, presented in Eq. (1) [10,22,23].

$$\dot{Q}_a = \dot{m} \times cp \times (T_h - T_c), \quad (1)$$

where, \dot{Q}_a is the heat flow absorbed by water [W], \dot{m} the mass flow rate of water [kg/s], cp the specific heat of water at constant pressure with a value fixed at 4186 J/kg·K, T_h the temperature at the hot water outlet [°C], T_c the temperature at the cold water inlet [°C] and specific mass of water $\rho = 1000 \text{ kg/m}^3$.

The total solar flux incident on the collector \dot{Q}_i is determined by adding the heat flux on the upper surface $\dot{Q}_{sup} = G_{dir} \times A$ and the heat flux on the lower surface $\dot{Q}_{inf} = G_{ref} \times A$ presented in Eq. (2).

$$\dot{Q}_i = \dot{Q}_{sup} + \dot{Q}_{inf}, \quad (2)$$

where the direct (G_{dir}) and reflected (G_{ref}) radiation are measured using the radiometer developed by [21] and A is the upper and lower area ($A = 0.7381 \text{ m}^2$) of the collector with dimensions 0,613 x 1,204 m. The PVC solar collector does not have the glass cover and protective box, found in commercial collectors, solar intensity is measured both by direct incidence and reflected by the ground, that is, the total available heat flux is determined by the already defined Eq. (2).

To determine the thermal efficiency of the PVC collector, Eq. (3) is used.

$$\eta = \frac{\dot{Q}_a}{\dot{Q}_i} \times 100, \quad (3)$$

where η is the thermal efficiency of the collector in percentage.

III. RESULTS AND DISCUSSION

Fig. 7 shows the temperature profiles of cold water inlet, hot water outlet and ambient temperature. The cold, hot and ambient temperatures measured in forced circulation are, respectively, the cold water inlet, lower region of the collector, hot water outlet, upper region and ambient temperature. The oscillations in Figs. 7 and 9 refer to the passage of clouds in the experiment region.

The two radiometers, installed with inclination angle α , shown in Fig. 8 measure direct solar radiation and that reflected from the ground, respectively.

The incident and reflected transient radiations are shown in Fig. 9, where the oscillations indicate clouds.

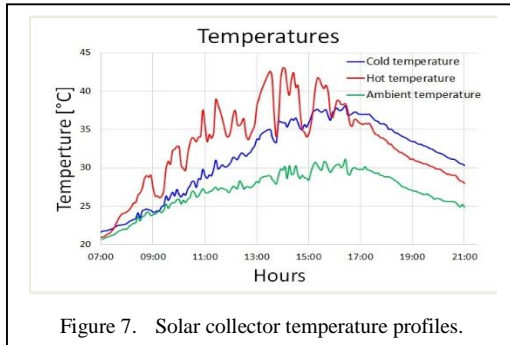


Figure 7. Solar collector temperature profiles.



Figure 8. Radiometers for incident and reflected radiation.

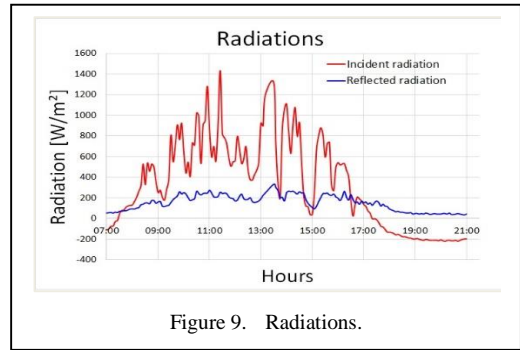


Figure 9. Radiations.

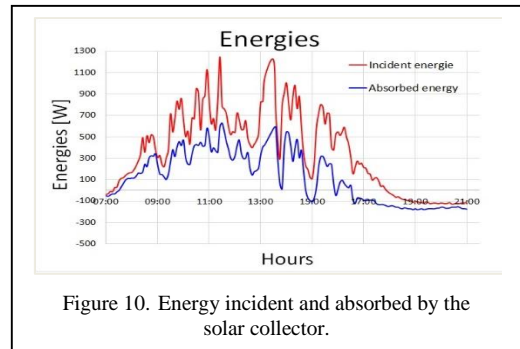


Figure 10. Energy incident and absorbed by the solar collector.

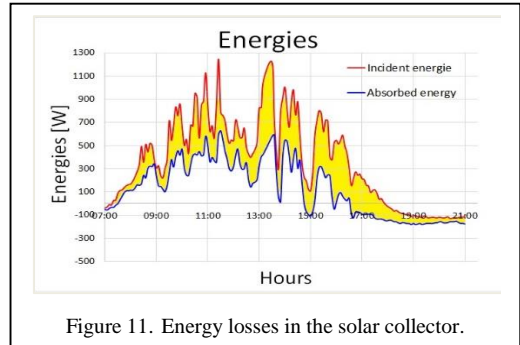


Figure 11. Energy losses in the solar collector.

The incident and absorbed energies are shown in Fig. 10. The interesting about this graph is the interval between energies, representing the losses in the solar collector, with an average of 298.33 W.

Fig. 11 better presents the collector losses, highlighted in yellow.

The transient efficiency of the solar collector is shown in Fig. 12. The sudden drop at 15:00 refers to the passage of many clouds over the experiment site, also visualized in the radiation graph in Fig. 9.

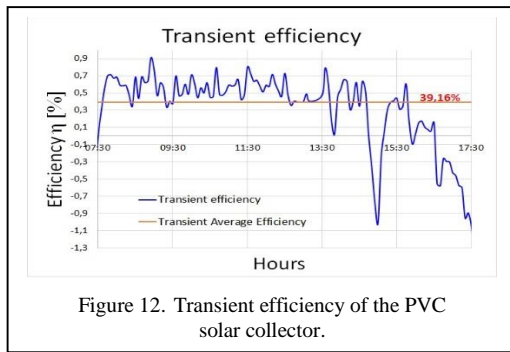


Figure 12. Transient efficiency of the PVC solar collector.

Fig. 12 also shows the average value of 39.16% in PVC collector efficiency.

IV. CONCLUSION

The build PVC solar collector has an average efficiency of 39.16% with a maximum temperature of 42.94 °C. Commercial flat plate solar collector (FPC), which are built with copper or aluminum piping with fins for greater absorption of solar heat flow installed in a metal box covered with a glass, have an average efficiency of 60% [10]. The efficiency of the PVC collector has an interesting result, as it is a cheap project. The application of this solar heater collector makes it possible to use it for low-income families and even with a not-so-high efficiency, it can be used as a hybrid system, to support electric showers with a dimer to control the electric resistance, which could reduce electric power bill. Another important factor is that the solar collector is a do-it-if yourself with easy-to-find materials and simple assembly, eliminating the use of metal welding. The system proposed for this work uses a single water tank, for both hot and cold water, using stratified thermal separation. As a result, low-income families will not have to spend with another reservoir for storing hot water. As it is cheap equipment, acceptance is inevitable. Therefore, the PVC collector is a great option, with a maximum cost of US\$ 30.00. The PVC solar collector works best in regions close to the equator due to greater solar incidence. Even with relatively higher temperatures than in the northern hemisphere, there are still low temperatures, such as below the Tropic of Capricorn. In addition, the poorest regions are located close to the equator, and this equipment can bring a reduction in electricity bills.

ACKNOWLEDGMENT

To the Federal Institute of Education, Science and Technology of São Paulo, Campus

Catanduva-SP for the constant support and encouragement.

REFERENCES

- [1] Zervos, A., & Lins, C. (2017). Renewable energy policy network for the 21st century. *REN21 Renewables Global Status Report*.
- [2] Van der Hoeven, M. (2014). Technology roadmap: Solar Thermal Electricity. *International Energy Agency (IEA), Paris, France, Tech. Rep.*
- [3] Pereira, Ê. B., Martins, F. R., Gonçalves, A. R., Costa, R. S., LIMA, F., RÜTHER, R., ... & SOUZA, J. (2017). Atlas brasileiro de energia solar. 2ª. *Instituto Nacional de Pesquisas Espaciais (INPE), São José dos Campos*.
- [4] Netz, B., Davidson, O. R., Bosch, P. R., Dave, R., & Meyer, L. A. (2007). Climate change 2007: Mitigation. Contribution of Working Group III to the Fourth Assessment Report of the Intergovernmental Panel on Climate Change. Summary for Policymakers.
- [5] United Nations. (2012). *A Rio+20 e a Construção de Cidades Sustentáveis—A Rio+20 e a Construção de Cidades Sustentáveis*. Available at: <http://www.un.org.br/rio20/cidades.pdf>
- [6] Oliveira, A., Jordão, R., Resende, R., Caputo, R., & da Silva, R. (2015). Projeto de Residência com melhor aproveitamento energético—Residential project with better energy use. *O Setor Elétrico*, 109. Available at: <https://www.osetoreletrico.com.br/edicoes-eletronicas>
- [7] Winoker, S. (2021). *GE Announces Plans to Form Three Public Companies*. *General Electric*. Available at: <https://www.ge.com/news/reports/ge-announces-plans-to-form-three-public-companies>
- [8] ASBC. (2001). *Sociedade do Sol*. ASBC. Available at: <http://www.cds.unb.br/obmts>
- [9] EPE. (2016). Nota técnica DEA 13/15—Demanda de Energia 2050. *Empresa de Pesquisa Energética (EPE)*. Available at: <https://www.epe.gov.br/sites-pt/publicacoes-dados-abertos/publicacoes/PublicacoesArquivos/publicacao-227/topico-458/DEA%2013-15%20Demanda%20de%20Energia%202050.pdf>
- [10] Kalogirou, S. A. (2009). *Solar Energy Engineering (1a, Vol. 1)*. British Library Cataloguing-in-Publication.
- [11] NBR 15569: Sistema de aquecimento solar de água em circuito direto—Projeto e instalação—Direct circuit solar water heating system—Design and installation, NBR 15569, 18 (2008).
- [12] NBR 15569. (2021). Sistema de aquecimento solar de água em circuito direto—Requisitos de projeto e instalação. Associação Brasileira de Normas Técnicas. Available at: <https://www.normas.com.br/visualizar/abnt-nbr-nm/27001/nbr15569-sistema-de-aquecimento-solar-de-agua-em-circuito-direto-requisitos-de-proje-to-e-instalaca>
- [13] Arduino. (2015). Arduino UNO. Arduino. Available at: <https://www.arduino.cc/en/Main/ArduinoBoardUno>
- [14] Maxim. (2012). DS18B20 Dallas Semiconductor. Dallas Semiconductor. Available at: www.maximintegrated.com
- [15] Avallone, E., Mioralli, P. C., Scalon, V. L., Padilha, A., & Oliveira, S. D. R. (2018). Thermal pyranometer

- using the open hardware arduino platform. *International Journal of Thermodynamics*, 21(1), 1-5.
- [16] Avallone, E., Pansanato, C., Faro, Á. N., Silva, D. I. A. da, Silva, J. W. da, Gonçalves, G. B., Ito, M. C., Garcia, R. P., & Mioralli, P. C. (2021). Radiômetro Solar de Baixo Custo Usando a Plataforma Aberta Arduino. In Em H. A. Holzmann & J. Dallamuta, *Coleção desafios das engenharias: Engenharia mecânica* (1o ed, p. 79–91). Atena Editora.
- [17] Garcia, R. P., Avallone, E., Pansanato, C., Gonçalves, G. B., Ito, M. C., & Scalon, V. L. (2018). Thermal radiometer using LM35 analog sensors, connecting to an Arduino Board. In *Proceedings of ENCIT 2018*, 1, 1–8.
- [18] Pansanato, C., Gonçalves, G. B., Ito, M. C., Scalon, V. L., Avallone, E., & Garcia, R. P. (2018). Low cost thermal pyranometer using Dallas DS18B20 sensor and Arduino. In *Proceedings of ENCIT 2018*, 1–8.
- [19] Scalon, V. L., Avallone, E., Pansanato, C., & Ito, M. (2017). Development of a low cost pyranometer for solar radiation measurements.
- [20] DFRobot Electronic Product. ([s.d.]). Flow sensor—YF-S401-1/8". Recuperado 1o de dezembro de 2018, Available at: https://www.dfrobot.com/wiki/index.php/Water_Flow_Sensor_-_1/8%22_SKU:_SEN0216
- [21] Avallone, E., Mioralli, P. C., Scalon, V. L., & Padilha, A. (2016, August). Thermal pyranometer using the arduino platform for data acquisition. In *Contemporary Problems of Thermal Engineering*. 1, (pp. 303–311).
- [22] Duffie, J. A., & Beckman, W. A. (2013). *Solar engineering of thermal processes*. John Wiley & Sons.
- [23] Struckmann, F. (2008). Analysis of a flat-plate solar collector. Heat and Mass Transport, Project Report, 2008MVK160.

Ideal and Static Magnetohydrodynamics Computation for Plasma Fusion

Amina Djellouli¹, Assia Rachida Senoudi²

¹Laboratory of Theoretical Physics, Abou Bekr Belkaid University, Tlemcen, Algeria

²Department of Physics, Abou Bekr Belkaid University, Tlemcen, Algeria

djellouliamina13@gmail.com¹, arsenoudi@gmail.com²

Abstract—In this work, we applied the finite elements method to nuclear fusion research. To explore its applicability, we used with a time-independent of plasma equilibrium problem and solved the Grad Shafranov (GS) equation. Comparisons between analytical and numerical results confirm the validity and accuracy of our calculations.

Keywords - ideal static equilibrium, magnetohydrodynamic, Grad Shafranov equation, finit element method, FreeFEM tools

I. INTRODUCTION

The fusion plasma in thermonuclear reactor is an electrically conducting fluid or gas consisting in complete or partial charged particles. The highly ionized plasma is an excellent conductor at high temperatures, and can be controlled by powerful magnetic fields [1]. The equilibrium of the plasma fusion confined inside the tokamak reactor could be formulated by the magnetohydrodynamic equations (MHD) and defines the beginning state to understand MHD instabilities phenomena [2]. Numerical computation of the equilibrium is of primary importance in the science of Tokamak fusion. From the point of view of Tokamak operation, equilibrium codes are essential for designing the geometry of new fusion machines; these codes can set up discharge scenarios and verify their feasibility.

Requiring the axisymmetric for the plasma, ideal and stationary MHD results in GS equation, which is an elliptical and nonlinear partial differential equation established in a cylindrical

plane (r,z) . The poloidal magnetic flux ψ consists in the unknown scalar function in GS equation [1]. The second hand of GS equation represents the current source so-called toroidal current density and depends strongly on the flux. Spatial configurations of plasma at equilibrium state are given through its isofluxes of ψ [3]. The determination of ψ is necessary to calculate physical quantities of the plasma fusion as the total current source, the safety factor. These quantities are all defined by surface integral formulas which require the perfect knowledge of the plasma boundary. However, the problem consisted in an unbounded domain with a non-linearity due to the current density profile in the unknown plasma domain, and the computational challenge of our code is to solve non-linear elliptic problem with non-linear source terms vanishing outside the unknown free boundary of the plasma.

Two kinds of numerical tools generally based on the finite element methods (FEM), ones are fixed boundary, where the plasma domain is chosen as a hypothetical rectangle [4] or elliptical coordinate equations describing the plasma boundary and having parameters values according to experimental data [5]; the seconds are free boundary methods [6]. The FEM is usually used for MHD, modeling the plasma on very short timescales, however there are limits within which the finite element method could encounter difficulties in capturing the complexity of the fusion processes. The computation of the plasma domain itself poses a real problem, the magnetic field lines can be

unclosed and a magnetic diverter is often placed in the Tokamak cavity at a geometric point called a fixed point.

In this work, we propose to compute the plasma border from the analytical solution of GS equation and the problem becomes an interior Dirichlet value. This paper is organized as follows, in Section II, is given a background of theoretical study leading to the GS equation. We present the analytical solution in a particular case, when the current source does not depend on ψ [7-12], it is called the Soloviev equilibrium. In Section III, we developed the steps used in our FEM computation and consisting on the following algorithm:

- Giving the analytical solution of the GS equation for Soloviev's equilibrium.
- Computing the last closed flux line from the analytical solution and considering it as the plasma's border.
- Implementing the FEM in writing C++ code using FreeFEM++ software [13].
- Calculating and plotting the isofluxes of magnetic flux function ψ , this will show the profile of plasma equilibrium.

In Section IV, we presented the methodology of the FEM and in Section V, we presented the configuration of plasma equilibrium obtained numerically for two different current density. Error calculation has been also performed. Finally, we give the effect of the current source on the plasma profiles.

II. THEORETICAL BACKGROUND

A. Plasma Equilibrium:

Theoretical model in ideal and static case of MHD [1,2] consists in following system of equations:

$$\vec{\nabla}P = \vec{j} \wedge \vec{B}, \quad (1)$$

$$\vec{\nabla} \cdot \vec{B} = 0, \quad (2)$$

$$\mu_0 \vec{j} = \vec{\nabla} \wedge \vec{B}, \quad (3)$$

where, μ_0 is the magnetic permeability of free space, \vec{B} is the magnetic field, \vec{j} and P are the current density and the pressure of the confined plasma, respectively.

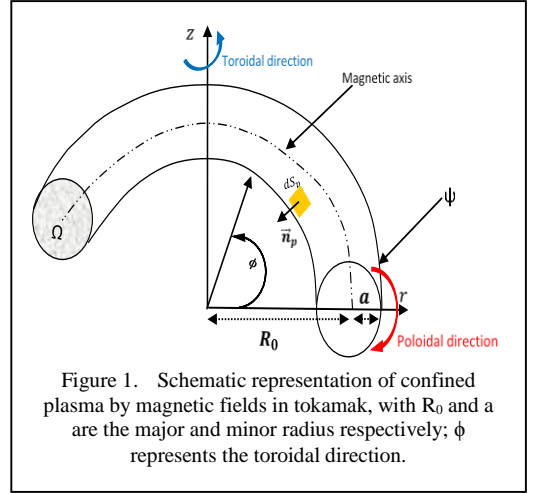


Figure 1. Schematic representation of confined plasma by magnetic fields in tokamak, with R_0 and a are the major and minor radius respectively; ϕ represents the toroidal direction.

The geometry of plasma (see Fig. 1) is described in cylindrical coordinates (r, z, ϕ) . Assuming the axisymmetric in plasma, the magnetic field \vec{B} can be expressed as:

$$\vec{B} = \vec{\nabla} \wedge (\psi \vec{\nabla} \phi) + F \vec{\nabla} \phi. \quad (4)$$

In Eq. (4), ψ , the poloidal flux, and the function $F(\psi) = -Ip(\psi)/2\pi$, the total poloidal current. The function ψ satisfies the GS equation in plane section (r, z) ,

$$-r \frac{\partial}{\partial r} \left(\frac{1}{r} \frac{\partial \psi}{\partial r} \right) - \frac{\partial^2 \psi}{\partial z^2} = F \frac{\partial F}{\partial \psi} + \mu_0 r^2 \frac{\partial P}{\partial \psi}. \quad (5)$$

The second hand of Eq. (5) represents the toroidal current density J_ϕ . Both of pressure P and F are function of ψ .

III. THE PLASMA COMPUTATIONAL BOUNDARY

A. Analytical Solution of GS Equation:

Soloviev's plasma equilibrium is a particular case when J_ϕ does not depend on ψ , this implies:

$$\mu_0 \frac{\partial P}{\partial \psi} = c_1, \quad F \frac{\partial F}{\partial \psi} = c_2 R_0^2. \quad (6)$$

Analytical solution of Eq. (6) [5] is the sum of homogeneous ψ_h and particular ψ_p solutions:

$$\psi(r, z) = \psi_h(r, z) + \psi_p(r, z), \quad (7)$$

$$\psi_h(r, z) = -\frac{1}{2}(c_0 r^2 + c_2 R_0^2) \cdot z^2, \quad (8)$$

$$\psi_p(r, z) = -\frac{1}{8}(c_1 - c_0)(r^2 - R_0^2)^2 + \psi_0, \quad (9)$$

where, R_0 represents plasma major radius. The two constants c_1 and c_2 are adjusted to meet the equilibrium constraints, and ψ_0 , is the value of the flux at the major radius.

The analytical solution in Eqs. (7)-(9) verifies the equality $\psi(r, z = z_B) = \psi_B$ with ψ_B , the value of magnetic flux on the plasma's border chosen as the last closed magnetic surface. The previous analytical solution is valid when the pressure has this form, $P(\psi) = c_1(\psi - \psi_B)/\mu_0$.

For usual tokamak devices [5], the constants c_0 and c_1 are expressed as:

$$c_0 = \frac{8\psi_0}{R_0^4} \alpha^2, \quad c_1 = \frac{8\psi_0}{R_0^4} (\alpha^2 + 1). \quad (10)$$

In Eq. (10), the parameter α determines the shape of equilibrium flux surface.

B. Computation of Plasma Boundary

From Eq. (5), it is easy to show that plasma boundary $\partial\Omega$ for Soloviev's equilibrium, can be analytically found and written as:

$$\partial\Omega = \left\{ z_B = \mp \sqrt{\frac{2(\psi_0 - \psi_B) - \frac{1}{4}(c_1 - c_0)(r^2 - R_0^2)^2}{c_2 R_0^2 + c_0 r^2}} \right\}, \quad (11)$$

$$r \in [R_1, R_2] > 0. \quad (12)$$

The values of radial borders R_1 and R_2 of $\partial\Omega$ are computed from the equality given in Eqs. (11) and (12) when putting $z_B = 0$:

$$R_{1,2} = \left(R_0^2 \mp \left(\frac{8(\psi_0 - \psi_B)}{(c_1 - c_0)} \right)^{\frac{1}{2}} \right)^{\frac{1}{2}}. \quad (13)$$

The inequality $\psi_0 > \psi_B > 0$ guaranteed the closure of the Isoflux.

IV. VARIATIONAL FORM OF GS EQUATION

One important step to solve the partial differential equation with FEM is to transform the problem to a weak problem with an integral form. After development we have found the integral form of GS equation given in Eq. (5) as:

$$\begin{aligned} & \iint_{\Omega} \vec{\nabla} \psi \vec{\nabla} \varphi dS + \iint_{\Omega} \frac{1}{r} \frac{\partial \psi}{\partial r} \varphi dS = \\ & = \iint_{\Omega} \left(F \frac{\partial F}{\partial \psi} + \mu_0 \frac{\partial P}{\partial \psi} r^2 \right) \varphi dS, \quad (14) \end{aligned}$$

with ∇ the gradient operator in (r, z) coordinates system, φ , an arbitrary function relative to ψ , Ω , the computational domain of the delimited plasma and dS , the surface element of Ω . The Dirichlet boundary condition on the $\partial\Omega$ is fixed to be $\psi = \psi_B$.

After the subdivision of the computational plasma domain by triangular elements, the integral form given in Eq. (14) is calculated in each element of the mesh domain and all the quantities are assembled in global matrix. The linear matrix system could be easily resolved by standard direct or iterative numerical methods.

Global relative error in Hilbert space [13] is:

$$E = \sqrt{\frac{\int_{\Omega} (\psi_{exact} - \psi)^2 d\Omega}{\int_{\Omega} \psi_{exact}^2 d\Omega}}. \quad (15)$$

V. RESULTS AND DISCUSSION

Using FreeFEM++ software [13], we performed a code in C++, where the domain of the plasma, delimited by the border $\partial\Omega$ is well defined and the integral form in Eq. (14) is implemented.

We choose the data of international thermonuclear experimental reactor (ITER) [14]: $R_0 = 6.2$ m, for testing we put, the values of $c_2 = 0$, $\psi_0 = 0.5$ Wb, $\alpha = 1$ and $\psi_B = 0.05$ Wb.

To check the proposed FEM fixed boundary solver, Fig. 2 reports on the same graph both the isofluxes ψ in the (r, z) plane by FEM and analytical solution in Eq. (5). This graphic shows an excellent agreement. Also, the relative global error computed from Eq. (10) is of value $= 7 \times 10^{-3}\%$ and corresponding to number of triangular mesh elements $= 1.2 \times 10^6$.

The Fig. 3 shows the variation of poloidal flux function ψ as function of the radial position r ; along the r -axis ($r, z=0$); As we can see the analytical and numerical solution are identical and we observe a good agreement between them and the absolute error does not exceed the value of 10^{-3} corresponding to number of triangular mesh elements $= 10^5$.

In the Fig. 4, we report the evolution of the important physical quantities in our study as function of radial direction; first graph represents the profile of the plasma pressure and the second one represents the poloidal component of the magnetic field. As we can see the pressure and poloidal magnetic field has the opposite profile and in center of plasma the values of pressure are

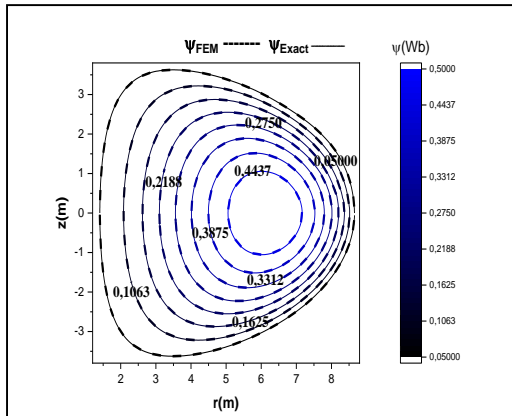


Figure 2. Plasma equilibrium with Dshape profile. Both Numerical FEM and analytical isofluxes of poloidal magnetic function ψ of ITER for $c_2=0$.

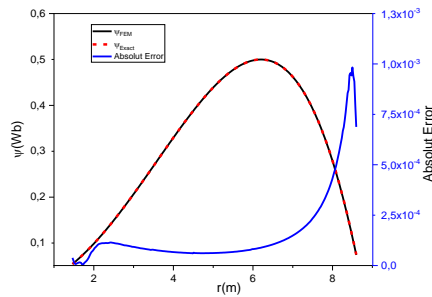


Figure 3. Numerical FEM, analytical isofluxes of Ψ and computed error, upon radial distance r (m), along.

in high value, unlike the poloidal component of magnetic field it's vanishes to zero and then increase when the radial position increase.

The second case which we studied is when $c_2 \neq 0$ and we see the effect of the parameters contained in the term source, on the plasma configuration. For this, we have taken the same values of ITER reactor, and we found another plasma profile for $c_2=0.01$. The Fig. 5 shows both numerical and analytical solution. As we can see the function F through the parameter c_2 has a great effect on the plasma equilibrium shape, indeed for weak value of c_2 , we can see that the plasma configuration changes completely.

VI. CONCLUSIONS

In this paper, we carried out a computational solution of the GS equation by using the FEM fixed boundary solver of the plasma equilibrium and FreeFEM++ software. The isofluxes of the poloidal magnetic flux function gives the spatial

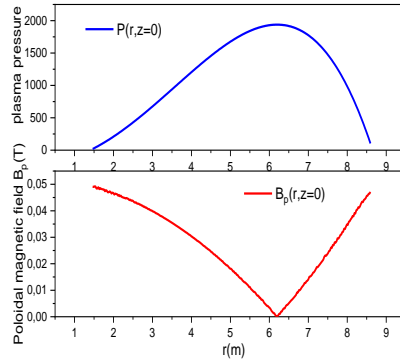


Figure 4. Pressure and poloidal component of magnetic field as function of radial distance (at $z=0$).

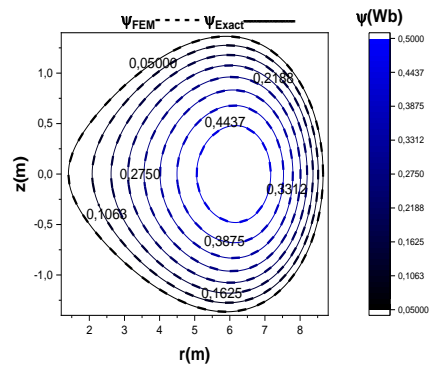


Figure 5. Numerical FEM and analytical isofluxes of poloidal function for $c_2=0.01$.

configuration of the plasma equilibrium. Since the plasma boundary was correctly calculated, no particular difficulty was encountered in reaching agreement between the analytical and numerical results. A global relative error of the order of $10^{-4}\%$ demonstrated a very good agreement. We study also the effect of parameter c_2 which is related to toroidal function F and we have shown that a slight increase in c_2 from 0, the plasma can lose its equilibrium configuration initially Dshape in agree with the tokamak machine geometry. The incoming study will be focused on the plasma equilibrium with FEM free boundary.

REFERENCES:

- [1] Zheng, L. (2015). Advanced Tokamak Stability Theory. Chapter 1. In *IOP Concise Physics*. Morgan & Claypool Publishers.
- [2] Miyamoto, K. (2005). *Plasma physics and controlled nuclear fusion*. Springer Series on atomic, optical, and plasma physics. Berlin Heidelberg N.Y.

- [3] Stephen J. (2010). *Computational methods in plasma physics*. Chapman & Hall/CRC Computational Science Series (pp. 93–95).
- [4] Tezer-Sezgein, S. H. A. (2008). Numerical solution of grad shafranov equation for the distribution of magnetic flux in nuclear fusion devices. *Turkish J. Eng. Env. Sci.* 32, 265–275.
- [5] Han, K. S. Park, B. H. & Aydemir, A. Y. (2017). Computational magnetohydrodynamics using the deal. In *II Finite Element Library, M&C 2017-International Conference on Mathematics & Computational Methods Applied to Nuclear Science & Engineering*, Jeju, Korea, April 16–20.
- [6] Takeda, T. & Tokudas S. (1991). Computation of MHD equilibrium of tokamak plasma. *J. of Comp. physics* 93, 1–107.
- [7] Lopez J. E. et al. (2019). Fixed boundary Grad-Shafranov solver using finite difference method in non homogeneous mesh grid. *J. Phys., conf. Serbia.* 1159, 012017.
- [8] Soloviev, L. S. (1967). The theory of hydrodynamic stability of toroidal plasma configurations. *Sov. Phys. JETP* 26, 400.
- [9] Djellouli, A. & Senoudi, A. R. (2021). Fixed-boundary grad shafranov solver using finite element method with FreeFem++ Tools. In *7th virtual int. conf. on sciences tech. and manag. in energy mathematical institute of Serbia Academy*. (pp. 161-165), ISBN: 978-86-80593-73-9. December 16–17.
- [10] Nath, D. et al. (2015). Computation of fixed boundary tokamak equilibria using a method based on approximate particular solutions. *Comput. and Math. with Applications*, 70, 1220–1233.
- [11] Mc Carthy, P. J. (1999). Analytical solutions to the Grad-Shafranov equation for tokamak equilibrium with dissimilar source functions. *Physics of Plasma*, 6, (9), 3554–3560.
- [12] Ludwig, G. O. (1994). Direct variational solutions to the Grad-Schlüter-Shafranov equation. *Plasma Phys. Control. Fusion* 37, 633646.
- [13] Hecht, F. FreeFem++. Third Edition, Version 3.56-2. Laboratoire Jacques-Louis Lions, University of Pierre et Marie Curie, Paris. Available at: <http://www.freefem.org/ff++>.
- [14] Lecture1. (2011). Introduction to ITER AP 4990y Seminar Columbia University Spring. Available at: http://sites.apam.columbia.edu/courses/apph4990y_ITER/ITER-Lecture-1.pdf

CFD Evaluation of Fractal-type Structures for Improved Heat Transfer in Heat Exchangers (Part A)

Abdulmuttalib A. Muhsen¹, Natalya Kizilova², Bashar Hassan Attiya³

^{1,2}Warsaw University of Technology, Warsaw, Poland

¹Haditha Hydropower Station, Ministry of Electricity, Haditha, Iraq

³Imam Ja'afar Al-Sadiq University, Kirkuk, Iraq

¹abdulmuttalib.muhsen.dokt@pw.edu.pl

Abstract—The optimization of heat transfer rates is of utmost importance in a wide range of industrial applications, leading to ongoing endeavors aimed at improving the efficiency of heat transfer processes. In the present context, researchers have shown considerable interest in the application of fractal-type structures. In contrast to conventional pipelines, fractal-type structures have exhibited enhanced heat transfer performance despite their larger surface area. The present study investigates the cooling efficiency of various fractal-type structures and performs a comparative analysis utilizing Computational Fluid Dynamics (CFD) techniques. The temperature data obtained from the output of the computational fluid dynamics (CFD) analysis is then utilized in the governing equations for heat transfer to assess the thermal and hydraulic resistance. This research makes a valuable contribution to the current investigation of heat transfer techniques, providing insights into the potential of fractal-type structures for enhancing heat transfer processes.

Keywords - fractal-type structures, computational fluid dynamics, thermal resistance

I. INTRODUCTION

Heat exchangers are applied widely in energy production, electronics, heat recovery, air-conditioning, and many other fields. When it comes to increasing heat transfer between the solid and liquid phases, fractal fin's structure, which are abound in nature [1-3], plays a key role. In addition, the fractal fin structure has a significant impact on heat transmission

performance. Solid-liquid phase-change heat transfer is greatly affected by structural parameters such as length ratio, width ratio, bifurcation level, and bifurcation angle. Consequently, a number of researchers are devoted to improving the fractal fins' structural parameters. The impacts of fractal fin length ratio and width index on solid-liquid phase change heat transfer were studied in [4-8]. Under specified circumstances, the ideal length-to-width ratio and width index were found to be approximately 1 and 0.7.

The term extended surface is commonly used to depict an important special case involving heat transfer by conduction within a solid and heat transfer by convection (and/or radiation) from the boundaries of the solid. Until now, we have considered heat transfer from the boundaries of a solid to be in the same direction as heat transfer by conduction in the solid. In contrast, for an extended surface, the direction of heat transfer from the boundaries is perpendicular to the principal direction of heat transfer in the solid. Although there are many different situations that involve such combined conduction-convection effects, the most frequent application is one in which an extended surface is used specifically to enhance heat transfer between a solid and an adjoining fluid. Such an extended surface is termed a fin [9]. Three techniques were used to investigate the heat transfer increase in fractal type pipelines in [10]. These techniques were analytical, numerical, and experimental. Results from these methods showed that the fractal heat

exchanger had a higher heat transfer to overall volume ratio than a conventional tube-in-tube heat exchanger. An analytical heat transfer analysis was done to a quadratic Koch Island fractal heat exchanger, and it was found that heat transfer increases with every application of the fractal, at least doubling at every fractal iteration. The prediction was validated numerically. Although the size of the heat exchanger increases significantly. The experimental results showed an increase in heat transfer, and it was higher than ones obtained as numerical results. The cause of this higher value were other factors such as the heat transfer coefficients that were also contributing to the heat transfer increase.

In [11] a validated and verified model of a double-pipe heat exchanger to evaluate the effectiveness of double-pipe heat exchangers inspired by the first three iterations of the Koch snowflake fractal pattern is used. The fractal heat exchangers will be compared to a traditional double-pipe heat exchanger operating under similar conditions. It was concluded that the use of the Koch snowflake design is that an increase in surface area can be achieved without impacting package volume. Thus, heat exchangers with fractal designs have significantly higher surface areas per unit package volume when compared with traditional heat exchangers. The increase in surface area associated with each fractal iteration resulted in higher overall heat transfer coefficients and heat transfer rates. Also, the effectiveness of the fractal heat exchangers was greater than that of the traditional heat exchanger regardless of iteration. The effectiveness increased with the increase in the number of iterations.

A triangular finned heat sink provides a faster cooling rate than other finned heat sinks at different Reynolds numbers. In descending order, triangle, square, rectangle, hexagon, and circular finned heat sinks perform better in heat transfer. The circle finned heat sink has the lowest pressure drop, followed by the hexagon, rectangle, square, and triangle. In terms of heat transfer and pressure drop, square and triangular finned heat sinks function similarly. In every scenario, staggered designs outperform inline geometries by about 4%. Circular fins perform best when the pressure drop, and pumping power are modest. Triangular pin-fins provide the best performance at higher values [12].

In [13], a comparison of heat transfer between smooth tube, tube with extended surface

of six longitudinal fins, tube with extended surface of Koch snowflake of second generation, and tube with extended surface with the Cesaro curve of second generation was done by creating a CAD design then carrying out finite element analyses FEA with ANSYS is given. It was found that the tube with extended surface of the Cesaro curve increased the heat transfer from the inside of the tube to its surroundings; this is because the contact area of the external fluids increased, and the tube's geometry facilitated the turbulence that favors the early change of the internal and external temperatures of the tube. Although the tube with the extended surface with the Koch snowflake did not surpass the heat transfer of a tube with the extended surface of longitudinal fins, it would be useful when a faster heat transfer is required. The main work of this paper is to establish the fractal pipes of heat exchangers models and study the effect of fins with different fractal-type structures on the heat transfer performance. With the material volume as the constraint condition, the output temperature determine by CFD were used in the governing heat transfer equation to determine the thermal resistance and hydraulic resistance in different types of fractal fin heat exchangers are analyzed. We aim to assess the performance benefits of three fractal-type fin structures in a circular tube heat exchanger. As this study main focus is on comparing the effectiveness of different fractal designs, this study did not include circular tube without fins results. This choice is deliberate to isolate and evaluate the proposed fractal-type structures' heat transfer efficiency effects. A forthcoming paper (Part B) will analyze and report the circular tube data without fins to compare and understand how fractal fins improve heat exchanger performance.

II. METHODOLOGY

A. Governing Equations

Fractal structures can be optimized by a balance between thermal resistance (Z_{th}) and hydraulic resistance (Z_h).

$$Z_{th} = \frac{T_{in} - T_{out}}{J_{th}}, \quad (1)$$

$$Z_h = \frac{P_{in} - P_{out}}{\dot{m}}, \quad (2)$$

where T_{in} , T_{out} and P_{in} , P_{out} are inlet and outlet temperature and pressure, J_{th} and \dot{m} are the heat and mass fluxes.

B. Dimensions of Pipelines

1) T-shaped fractal pipeline

TABLE I. T-SHAPED FRACTAL PIPELINE DIMENSIONS.

Length of pipe	1900 mm
Inside diameter of pipe (d)	16 mm
Volume of pipe (SolidWorks)	293286.77 mm ³
Mass of pipe	2346.3 gram

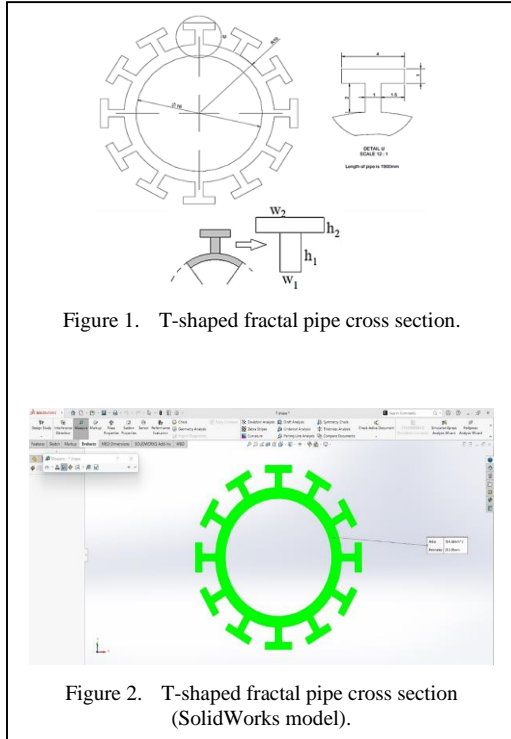


Figure 1. T-shaped fractal pipe cross section.

Figure 2. T-shaped fractal pipe cross section (SolidWorks model).

2) Y-shaped fractal pipeline

TABLE II. Y-SHAPED FRACTAL PIPELINE DIMENSIONS.

Length of pipe	1900 mm
Inside diameter of pipe (d)	16 mm
Volume of pipe (SolidWorks)	293286.77 mm ³
Mass of pipe	2346.3 gram
Details of T-fractal fin	
w_2	4mm
h_2	1mm
w_1	1mm
h_1	2mm

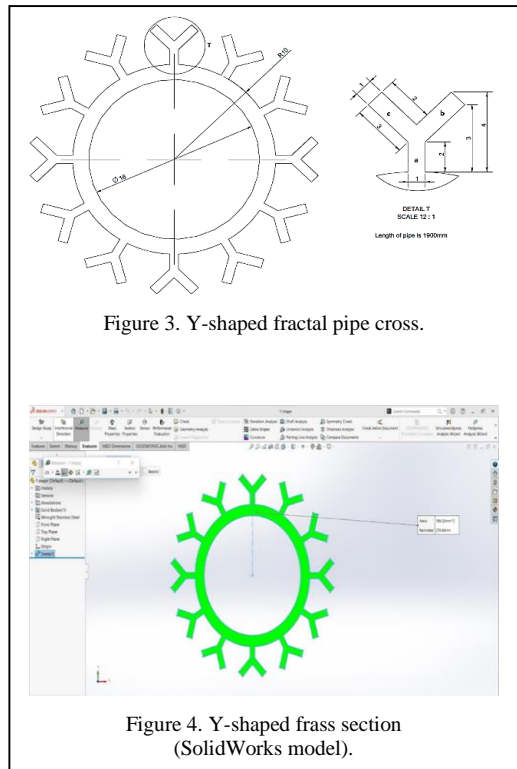


Figure 3. Y-shaped fractal pipe cross.

Figure 4. Y-shaped frass section (SolidWorks model).

3) Koch shaped fractal pipeline

TABLE III. KOCH SHAPED FRACTAL PIPELINE DIMENSIONS.

Length of pipe	1900 mm
Inside diameter of pipe (d)	16 mm
Volume of pipe (SolidWorks)	293916.57 mm ³
Mass of pipe	2351.33 gram

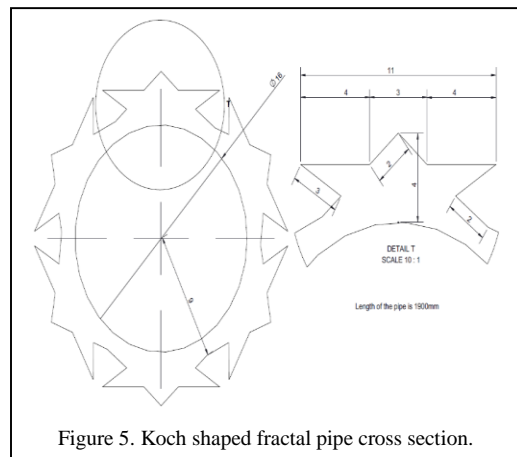


Figure 5. Koch shaped fractal pipe cross section.

C. Geometry

The geometry of different fractal type pipeline structures was created in SolidWorks for performing CFD Analysis using ANSYS.

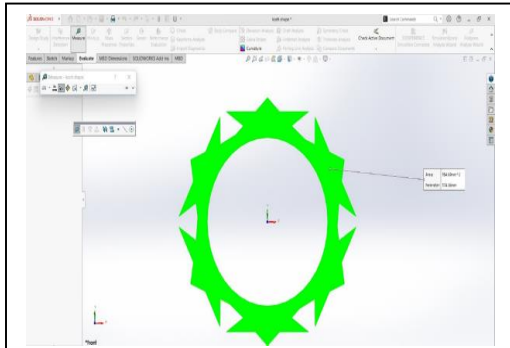


Figure 6. Koch shaped fractal pipe cross section (SolidWorks model).

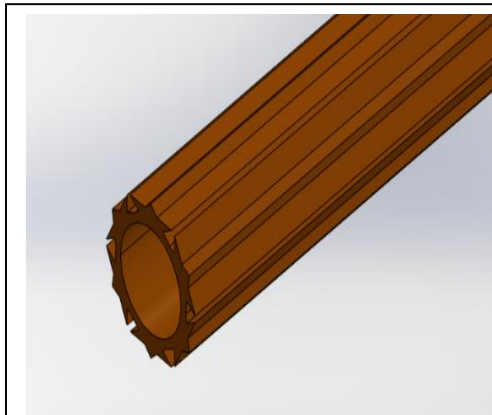


Figure 7. Koch shaped fractal pipeline.

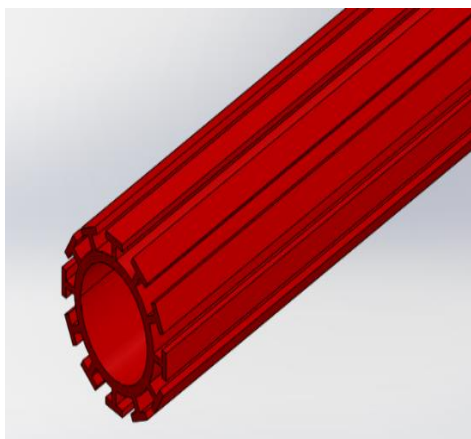


Figure 8. T-shaped fractal pipeline.

III. SIMULATION

The generated mesh models for each fractal type pipeline were done in such a way that the accuracy of results would be satisfactory.

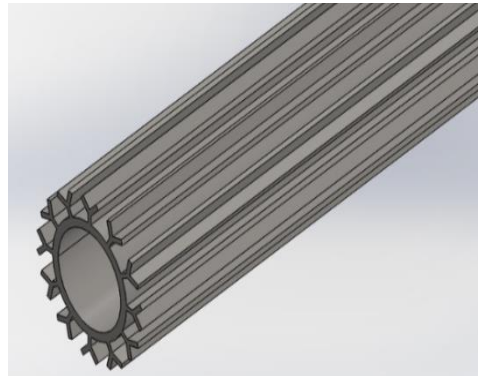


Figure 9. Y-shaped fractal pipeline.

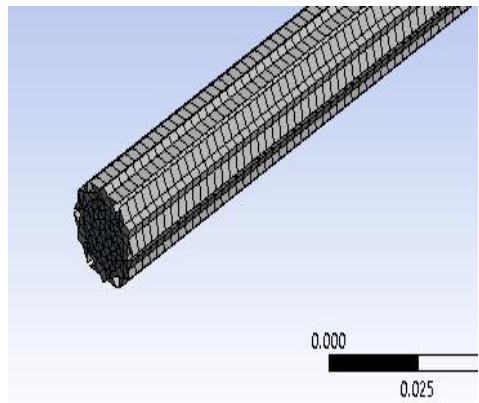


Figure 10. Koch pipeline mesh model.

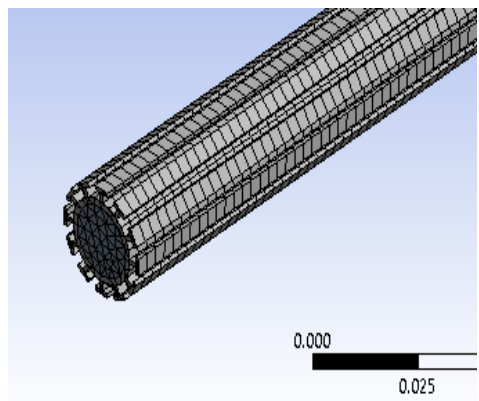


Figure 11. T-shaped pipeline mesh model.

IV. CALCULATIONS

A. Nomenclature

T_{in} = Inlet Temperature

T_{out} = Outlet Temperature (simulation)

k = Thermal conductivity (For copper $k = 398 \frac{W}{m \cdot K}$)

J_{th} = total Heat Flux = $k\Delta T$

\dot{m} = Mass flow rate =

= ρAv , P_{in} = Inlet Pressure)

Z_{th} = Thermal resistance

Z_h = Hydraulic resistance

L_e = Thermal entry length

Re = Reynolds number = $\frac{\rho v d}{\mu}$

ρ = Density of fluid

(for water $\rho = 1000 \frac{kg}{m^3}$)

v = Inlet velocity

A = Cross sectional area = $\frac{\pi \cdot d^2}{4}$

(where d is diameter of smooth pipe)

B. Inlet Conditions

TABLE IV. INLET CONDITIONS FOR ALL PIPELINES.

Inlet Temperature (K)	Inlet Velocity (m/s)	Inlet Pressure (bar)
373	0.0063	2.5

C. T-shaped Fractal Pipeline

$$\begin{aligned} \text{Thermal resistance} &= \\ &= Z_{th} = \frac{T_{in} - T_{out}}{J_{th}} \end{aligned} \quad (3)$$

$$T_{in} = 373 \text{ K}$$

$$T_{out} = 349.068 \text{ K (from probe at outlet)}, \quad (4)$$

$$J_{th} = k\Delta T$$

where k is thermal conductivity of copper (398 W/mK).

$$\begin{aligned} J_{th} &= (398) \times (373 - 349.068) \\ &= 9524.9 \text{ W/m} \end{aligned} \quad (5)$$

$$Z_{th} = \frac{373 - 349.068}{9524.9} = 2.51E - 03, \quad (6)$$

$$\begin{aligned} \text{Hydraulic Resistance} &= Z_h = \frac{P_{in}}{\dot{m}} \\ \dot{m} &= \rho Av \end{aligned} \quad (7)$$

$$A = \frac{\pi d^2}{4} = \frac{\pi(0.016)^2}{4} = 2.01E - 04 \text{ m}^2$$

$$\begin{aligned} \dot{m} &= 1000 \times (2.01E - 04) \times 0.0063 = \\ &= 1.26E - 03 \text{ kg/sec}, \end{aligned}$$

$$Z_h = \frac{P_{in}}{\dot{m}} = \frac{0.25 \text{ (in MPa)}}{1.26E - 03} = 198.4, \quad (8)$$

$$Re = \frac{\rho v d}{\mu} = \frac{1000 \cdot 0.0063 \cdot 0.016}{1E - 03} = 100.8.$$

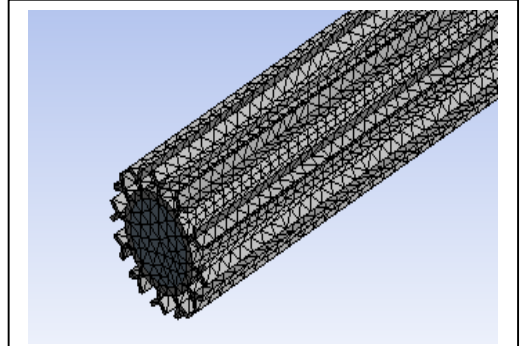


Figure 12. Y-shape pipeline mesh model.

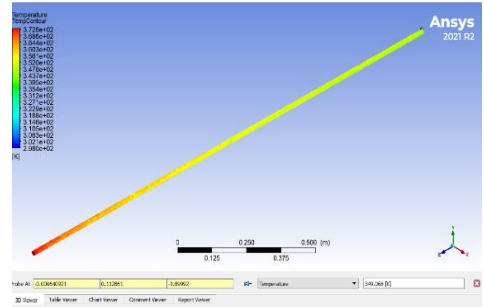


Figure 13. Temperature contours of T-shaped fractal pipeline.

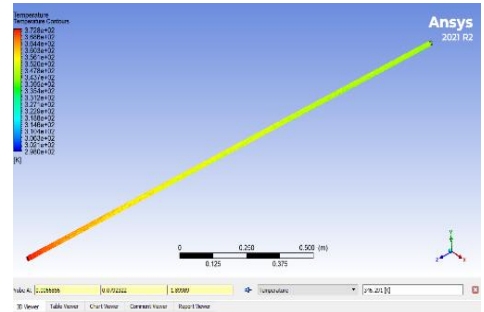


Figure 14. Temperature contours of Y-shaped fractal pipeline.

Since $Re < 2300$ then the flow is laminar. Now finding out thermal entry length (L_e):

$$L_e = 0.06Re \cdot d = 0.06 \cdot 100.8 \cdot 0.016 = 0.0967m \quad (9)$$

D. Y-shaped Fractal Pipeline

$$J_{th} = (398) \cdot (373 - 346.291) = 10630.182 W/m \quad (10)$$

$$Z_{th} = \frac{373-346.291}{10630.182} = 2.51E - 03 \quad (11)$$

$$\text{Hydraulic Resistance} = Z_h = \frac{P_{in}}{\dot{m}}, \quad \dot{m} = \rho Av, \quad (12)$$

$$A = \frac{\pi d^2}{4} = \frac{\pi(0.016)^2}{4} = 2.01E - 04m^2,$$

$$\dot{m} = 1000 \cdot (2.01E - 04) \times 0.0063 = 1.26E - \frac{03kg}{sec},$$

$$Z_h = \frac{P_{in}}{\dot{m}} = \frac{0.25 (in MPa)}{1.26E-03} = 198.4, \quad (13)$$

$$Re = \frac{\rho v d}{\mu} = \frac{1000 \cdot 0.0063 \cdot 0.016}{1E-03} = 100.8.$$

Since $Re < 2300$ then the flow is laminar. Now finding out thermal entry length (L_e):

$$L_e = 0.06Re \cdot d = 0.06 \times 100.8 \times 0.016 = 0.0967m \quad (14)$$

E. Koch Shaped Fractal Pipeline

$$J_{th} = (398) \times (373 - 348.074) = 9920.548 W/m \quad (15)$$

$$Z_{th} = \frac{373-348.074}{9920.548} = 2.51E - 03 \quad (16)$$

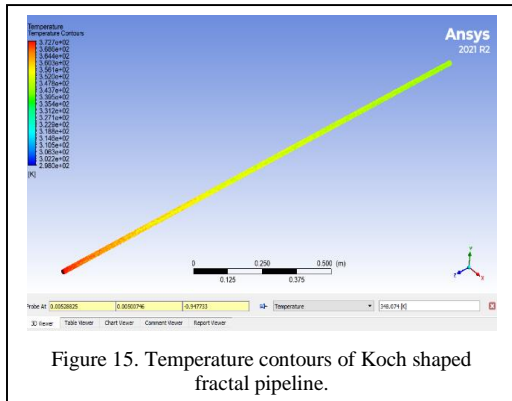


Figure 15. Temperature contours of Koch shaped fractal pipeline.

$$\text{Hydraulic Resistance} = Z_h = \frac{P_{in}}{\dot{m}}, \quad \dot{m} = \rho Av, \quad (17)$$

$$A = \frac{\pi d^2}{4} = \frac{\pi(0.016)^2}{4} = 2.01E - 04m^2.$$

$$\dot{m} = 1000 \cdot (2.01E - 04) \times 0.0063 = 1.26E - \frac{03kg}{sec},$$

$$Z_h = \frac{P_{in}}{\dot{m}} = \frac{0.25 (in MPa)}{1.26E-03} = 198.4, \quad (18)$$

$$Re = \frac{\rho v d}{\mu} = \frac{1000 \cdot 0.0063 \cdot 0.016}{1E-03} = 100.8.$$

Since $Re < 2300$ then the flow is laminar. Now finding out thermal entry length (L_e):

$$L_e = 0.06Re \cdot d = 0.06 \times 100.8 \times 0.016 = 0.0967m \quad (19)$$

V. RESULTS

The results of hydraulic resistance remained the same in all cases and thermal resistance did not change much in all the cases although the outlet temperature was decreased the most in case of Y-shaped fractal under identical conditions.

TABLE V. KOCH SHAPED RESULTS.

Outlet Temp. (K)	Hydraulic Resistance	Thermal resistance	Thermal length
348.074	198.4	2.5E-03	0.09677

TABLE VI. T-SHAPED RESULTS.

Outlet Temp. (K)	Hydraulic Resistance	Thermal resistance	Thermal length
349.068	198.4	2.5E-03	0.09677

TABLE VII. Y-SHAPED RESULTS.

Outlet Temp. (K)	Hydraulic Resistance	Thermal resistance	Thermal length
346.291	198.4	2.51E-03	0.09677

The heat flux for each pipeline can give a general description of heat transfer ability. The heat flux was measured by means of ANSYS.

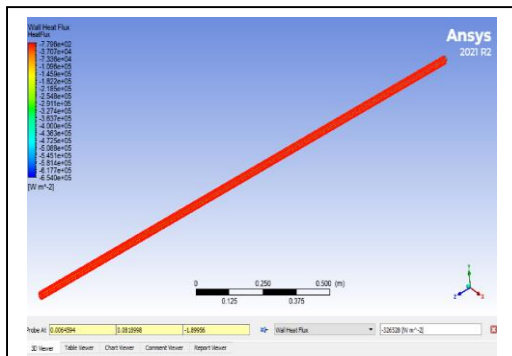


Figure 16. Heat flux across T-shaped pipeline.

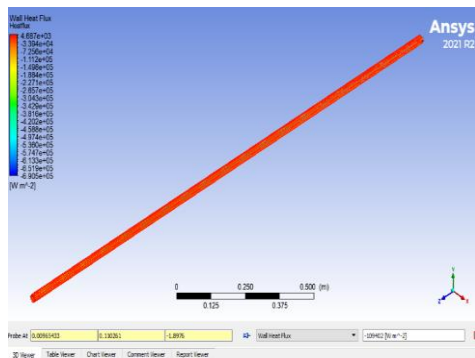


Figure 17. Heat flux across Y-shaped pipeline.

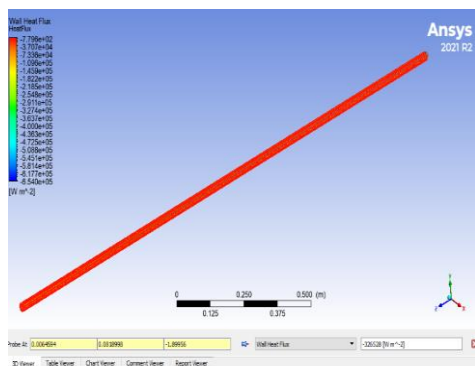


Figure 18. Heat flux across Koch shaped pipeline.

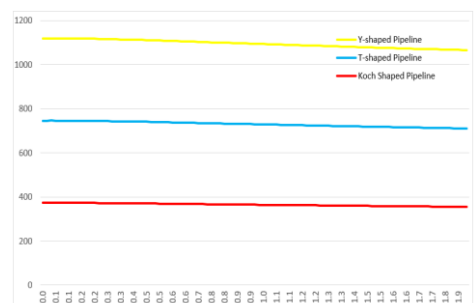


Figure 19. Temperature plot of fractal pipelines.

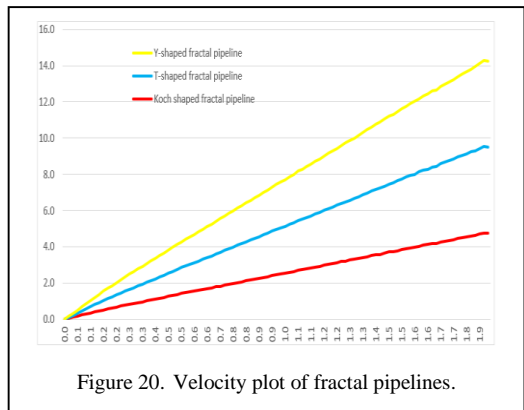


Figure 20. Velocity plot of fractal pipelines.

VI. CONCLUSION

Heat exchangers are formed by tubes with extended surfaces that improve the transfer of heat between two media (e.g., a solid and a liquid in motion), the heat exchanger is an important device in almost all mechanical industries as in the case of process industries it is a key element.

This paper involves the study of different fractal type pipelines under same conditions in order to provide a comparison on how much cooling effect can occur in each case. The hydraulic and thermal resistance remained approximately the same in all cases. T-shaped 12 fins fractal had the highest output temperature and is the least efficient cooling fractal. The most efficient is Y-shaped 12 fin fractal as it decreased the most temperature.

Also, this study showed that it is possible both to integrate fractal geometries into the field of mechanical engineering, specifically in the area of heat transfer, and to make viable designs with the support of Computer-aided design CAD. Likewise, the results of this study serve as foundations to continue the research in this area, oriented toward the application of devices that exchange heat at industrial, automotive, and household levels, such as heaters, boilers, and radiators; and with the goal of offering to the market new devices able to handle the high temperature in short times.

REFERENCES

- [1] Cioczek-Georges, R., & Mandelbrot, B. B. (1996). Alternative micropulses and fractional Brownian motion. *Stochastic processes and their applications*, 64(2), 143-152.
- [2] Mandelbrot, B. B. (1992). Plane DLA is not self-similar; is it a fractal that becomes increasingly

- compact as it grows?. *Physica A: Statistical Mechanics and its Applications*, 191(1-4), 95-107.
- [3] Muhsen, A. A., & Kizilova, N. (2022). The Advanced Cooling System of Generator for Hydropower Plant. *changes*, 8, 10.
- [4] Xu, P., Yu, B., Yun, M., & Zou, M. (2006). Heat conduction in fractal tree-like branched networks. *International Journal of Heat and Mass Transfer*, 49(19-20), 3746-3751.
- [5] Peng, Y., Zhu, X., Cao, B., Luo, Y., & Zhou, W. (2019). Heat transfer and permeability of the tree-like branching networks. *International Journal of Heat and Mass Transfer*, 129, 801-811.
- [6] Pu, L., Xu, L., Zhang, S., & Li, Y. (2019). Optimization of ground heat exchanger using microencapsulated phase change material slurry based on tree-shaped structure. *Applied energy*, 240, 860-869.
- [7] Zhang, C., Li, J., & Chen, Y. (2020). Improving the energy discharging performance of a latent heat storage (LHS) unit using fractal-tree-shaped fins. *Applied Energy*, 259, 114102.
- [8] Yu, C., Wu, S., Huang, Y., Yao, F., & Liu, X. (2020). Charging performance optimization of a latent heat storage unit with fractal tree-like fins. *Journal of Energy Storage*, 30, 101498.
- [9] Incropera, F. P., Dewitt, D. P., Bergman, T. L., & Lavine, A. S. (2002). *Fundamentals of heat and mass transfer*. John Wiley & Sons. Inc., Hoboken, NJ., 981p.
- [10] Meyer, J. P., & Van Der Vyver, H. (2005). Heat transfer characteristics of a quadratic Koch island fractal heat exchanger. *Heat transfer engineering*, 26(9), 22-29.
- [11] Gomez, A. (2017). Thermal Performance of a Double-Pipe Heat Exchanger with a Koch Snowflake Fractal Design. Electronic Theses and Dissertations.
- [12] Arjun, K. S., & Kumar, R. (2018). Optimization of micro pin-fin heat sink with staggered arrangement. *Thermal Science*, 22(6 Part B), 2919-2931.
- Llano-Sánchez, L. E., Domínguez-Cajeli, D. M., & Ruiz-Cárdenas, L. C. (2018). Thermal transfer analysis of tubes with extended surface with fractal design. *Revista Facultad de Ingeniería*, 27(47), 31-37.

Quantitative Study of Afforestation Present in Quitaiús de Lavras da Mangabeira/Ceará/Brazil

Isaac Anderson Alves de Moura¹, Joelda Dantas², Elvia Leal³,
Kelly Cristiane Gomes da Silva⁴

^{1,2,4}Federal University of Paraíba (UFPB), João Pessoa, Brazil

³Federal University of Campina Grande (UFCG), Campina Grande, Brazil

¹isaacmoura@cear.ufpb.br, ²joelda.dantas@cear.ufpb.br, ³elvialeal@gmail.com,

⁴gomes@cear.ufpb.br

Abstract—Knowing the types of tree species is essential in urban planning, especially in arid/semi-arid regions. Efficient planning avoids or minimizes risks to soil and society, because as plantations become increasingly important sources of wood and fiber, they also cause significant hydrological impacts. Considering the problem, a quantitative survey of plant species found in the afforestation of the district of Quitaiús, municipality of Lavras da Mangabeira, Ceará/Brazil, was carried out. An inventory was produced in all streets, squares and public buildings. It was recorded 368 individuals, distributed across 11 species, *Azadiractha indica* (176 individuals - 47.83%) and *Ficus benjamina* (154 individuals - 41.85%) as being the most abundant, and corresponding to 89.68% of the total trees. *Senna siamea* (4.89%), *Terminalia catappa* (1.63%), *Tamarindus indica* (0.82%), *Delonix regia* (0.27%) and *Prosopis juliflora* (0.27%), were also inventoried, totaling 359 individuals of exotic origin (97.56%). Native species represented 2.44% of the total species, totaling 9 individuals, with *Ziziphus joazeiro* (1.36%) and *Paubrasilia echinata* (0.54%) being the most represented. Considering that Quitaiús has an estimated population of 5,500 inhabitants, these results reveal a low number of trees. Furthermore, there is a prevalence of exotic species that interfere with the region's ecosystem, reflecting urban afforestation carried out without planning. The findings of this case provide new directions on afforestation management in the Brazilian Northeast, potentially leading to the future introduction of species that contribute more effectively to nutrient retention, mediating soil properties and microbial activities, and

consequently, managing knowledge and changes in use of the urban.

Keywords – urban trees, exotic species, planning, diversity, semi-arid regions

I. INTRODUCTION

Since the era of the industrial revolution, the increase in atmospheric carbon dioxide (CO₂) and global warming have been universally recognized as undeniable facts [1]. Therefore, investigating vegetation productivity and its interannual variability is of great benefit for understanding the underlying mechanism of carbon balances between atmospheric CO₂ concentration and terrestrial ecosystem carbon sequestration through land-atmosphere exchanges [2].

The relationship between humans and nature has been changing in a way that these changes create an imbalance concerning population growth and cities. Human activity in the environment is limited due to space constraints. In most cities, irregular settlements, large constructions, widening of streets, avenues, shopping centers, among others, end up altering the appearance and eliminating green areas necessary to conserve the quality of the environment and promote the well-being of the population. Thus, the protection of natural resources such as water, soil, fauna, flora, and landscape aspects becomes essential [3].

In relation to urban afforestation, it can be said that it is the set of trees located on the urban

perimeter of a city. Although there is the erroneous perception that urban afforestation is only that planted by public bodies, the concept also includes native forests remaining in the urban perimeter, as well as trees from components of the anthropic landscape, such as trees in gardens and domestic orchards [4].

Urban afforestation is characterized by the planting of trees in squares, parks, on sidewalks and in boulevards, nowadays constituting one of the most relevant activities in urban management, and should be part of urban plans, projects and programs in cities. Urban afforestation integrates the natural environment, thus forming part of the natural heritage [5]. Studies report that vegetation is an irreplaceable element that participates in several essential processes on Earth, including hydrological regulation [6].

The preservation of urban vegetation plays a fundamental role in promoting sustainable development, making cities more livable, healthy and resilient. It is interconnected with several United Nations Sustainable Development Goals (SDGs - 11, 15, 13, 3 and 2, in this order of importance) as it affects not only the environment, but also the quality of life of people living in urban areas.

According to [7], the presence of vegetation in a city is fundamental, bringing quality of life to its inhabitants. Afforestation provides shade, reduces noise pollution and temperature, releases oxygen into the atmosphere, increases air humidity and absorbs carbon dioxide, the main agent of the greenhouse effect. Despite the intensification of afforestation in the city, in certain areas a climatological and socio-environmental study is necessary.

Under the terms of the Federal Constitution (art. 30 and art. 182) and the City Statute (Law 10.257/01), it is up to the municipality to create, preserve and protect green areas and also the afforestation system, both as part of its policy of urban development. Municipal action must occur through specific laws, specific to each municipality, in order to meet local interests, but without contradicting the determinations and guidelines of federal and state laws [8].

The benefits are numerous, but greater awareness is needed on the part of city political authorities. One of the ways to guarantee green areas in urban centers is to establish the organization of open spaces, and have them

ensured by public authorities the creation and maintenance of urban parks to meet different environmental, social, recreational and contemplative purposes [9].

For better planning of urban environments, it is important to pay attention to the population's perception of the environment, as through these studies it is possible to obtain important information for the sustainable management of cities, including regarding their afforestation [10]. The lack of initiatives aimed at guiding the increase in urban afforestation, planned according to the desired ecosystem services, adapted to local specificities and current needs, means that urban afforestation is still seen as a merely aesthetic element in the urban landscape. However, to achieve these objectives, a greater understanding of local specificities is necessary to develop proposals adapted to these realities [11].

Community involvement in urban planning, especially in decisions related to afforestation, is essential to guarantee the success and sustainability of initiatives. For example, public meetings and consultations; participation in workshops and events; inclusion of practical activities, such as tree planting, to promote active participation; implementation of awareness campaigns about the importance of urban trees and the ecosystem services they provide; highlight the specific benefits of diverse and native species. Furthermore, promoting partnerships with local organizations, educational initiatives, and school programs, integration of school curricula that address the importance of afforestation and encourage student participation in tree planting projects. Also, environmental education events focusing on the organization of environmental education events in schools, parks or community centers, involving the presentation of lectures, expert panels and practical demonstrations. Furthermore, promote the creation of volunteer programs that allow the community to actively participate in the planting and maintenance of urban trees.

To understand the afforestation of a city, it is necessary to carry out a survey to evaluate the situation and, through the results obtained, verify the possible solutions for each location [12]. According to [13], access and dissemination of information, specifically dealing with research in the area of afforestation, is currently gaining greater visibility due to the

environmental and well-being benefits it provides in the urban environment. In this scenario, scientific journals play a fundamental role, as they contribute to the dissemination of the state of the art of research, allowing the construction of a regional scenario on urban and/or institutional afforestation, in relation to the content of the research, including methodological contributions.

It can be emphasized that, in addition to the benefits provided to humans, such as shading and temperature reduction, afforestation can also perform an important ecological function, such as maintaining the biological characteristics of the location. To this end, plant species that occur naturally in each region must be valued. Furthermore, urban afforestation has an important ecological function in providing housing and food for fauna, which helps to maintain and preserve the region's characteristic species.

Taking into account the importance of knowing the characteristics of the vegetation that makes up the afforestation of a municipality or district, to promote planning with public management and maintenance actions, in the present work a quantitative diagnosis of the urban afforestation existing in the district of Quitaiús, municipality of Lavras da Mangabeira-CE, Brazil.

II. METHODOLOGY

The study was carried out in the district of Quitaiús, municipality of Lavras da Mangabeira, in the State of Ceará, which has an estimated population of 550000 inhabitants, located in the Vale do Riacho do Rosário, in the hinterland of the upper Jaguaribe; mesoregion: south-central Ceará; microregion: Lavras da Mangabeira. The locality has soil irrigated by water from the Cariri springs, 24 km from its headquarters Lavras da Mangabeira and approximately 60 km from Juazeiro do Norte.

The methodology adopted for the quantitative survey was the Census, which the literature on forest inventory describes as suitable for small forested areas or areas with a small number of individuals, given that measuring many individuals (trees) constitutes an activity with a significant time and cost investment [14]. Therefore, all tree individuals, excluding palm trees, found on streets, squares, and public facilities in the district in question were quantified and identified.

In the on-site data collection, a form was used to record information about the street, neighborhood, collection date, number of existing trees, their common name, total tree height, and diameter at breast height (DBH). The materials used for the collection included a measuring tape and a graduated rod for measuring tree height and DBH.

To identify the species, the samples were classified by visual comparison with cataloged species. As a parameter for inclusion of individuals in the study, all individuals included in the urban afforestation that had a minimum height of 1.50 m and a minimum DBH of 3 cm were analyzed.

Regarding the phytogeography of species (exotic or native), it was considered that those that are exotic are those that occur in an area outside their historically known natural limit, as a result of accidental or intentional dispersal due to human activities. In relation to natives, conceptually, they are those whose presence occurs naturally in a given region. As such, to classify the phytogeography of the species, information from [15,16] was used as a parameter.

III. RESULTS AND DISCUSSION

In general, the results obtained in this study demonstrate that the Quitaiús district of Ceará has a low floristic diversity, when compared to cities in other Brazilian states. A total of 368 trees were quantified, distributed across 11 species, resulting in an approximate ratio of 1 tree for every 15 inhabitants in the district, similar to the findings by [17] in the city of Serra Talhada –Pernambuco, with a ratio of 1 tree for every 12 inhabitants. In the municipality of Buriticupo – Maranhão, the authors [18] quantified 544 individuals from 33 different species using the same methodology employed in this study, the tree census.

Out of the individuals quantified in the urban tree cover of the district in Ceará, 154 (41.85%) were *Ficus benjamina*, and 176 (47.83%) were *Azadiractha indica* (Fig. 1), together accounting for 89.68% of the total trees, indicating arboreal homogeneity. Visually, these species are quite common in the urban tree cover of northeastern cities.

Reference [15] found that in the city of Lavras da Mangabeira in Ceará, there is a predominance of the species *Ficus benjamina*,

corresponding to 42.42% of the individuals in the afforestation, and in the municipality of Altamira in Pará, the same species accounts for 24.7% of the population [19].

Regarding the species *Azadirachta indica*, it is predominant in urban afforestation in the squares of the municipality of Paulistana in Piauí and in the neighborhood of São Bento, municipality of Parnaíba in the same Brazilian state [20,21].

It is noteworthy that the values of the two species found in the Quitaiús district were above the technical recommendations for urban afforestation, where according to [22], no species should represent more than 10% of the number of trees in a city.

The other exotic species that make up the afforestation of Quitaiús were: *Senna siamea* (4.89%), *Terminalia catappa* (1.63%), *Tamarindus indica* (0.82%), *Delonix regia* (0.27%) and *Prosopis juliflora* (0.27%), totaling 359 individuals, corresponding to 97.56%. This predominance of individuals of exotic species over native ones was also observed in works such as that of [15], in which they identified 95.4% of exotic species for the city of Lavras da Mangabeira-CE, and also by [24] with 61.9% of the trees in the city of Cerro Corá in the state of Rio Grande do Norte; highlighting that this is not a situation exclusive to the district in question.

The native species identified represented only 2.44% of the total afforestation, distributed in 4 species, totaling 9 individuals, *Ziziphus joazeiro* (1.36%) (Fig. 2), *Paubrasilia echinata* (0.54%), *Peltophorum dubium* (0.27%) and *Talipariti tiliaceum* (0.27%) (Table I). These



Figure 1. *Azadirachta indica* A. Juss: exotic species most found in the urban forestry of the Quitaiús district in Lavras da Mangabeira-CE, Brazil.

Source: [23].

data show a very low number of native species in the tree composition of the Quitaiús district. A similar finding was reported by [17] in the city of Serra Talhada in the state of Pernambuco, accounting for only 2%.

It is necessary to highlight that the introduction of exotic species into afforestation without prior study can result in damaging local problems. According to [25] the tradition of using exotic species in the afforestation of streets, squares and parks devalues the rich biodiversity of municipalities and mischaracterizes the natural composition, favoring the development of a culture increasingly distanced from the surrounding natural environment.

Thus, in general, different Brazilian cities use a similar set of exotic species in public tree planting. It is important to highlight that the planting of these exotic species occurs due to the fact that they present rapid growth, regular stems when well-managed, large and dense canopies, providing shading, serving as a viable alternative in urban terms, despite the negative consequences, mainly on birdlife and the other species.

The exotic species observed in the Quitaiús afforestation have specificities, such as toxic properties, making them a natural repellent for fauna and flora, which can cause damage to microbial species present in the soil, implicating the functions performed by microorganisms that they are related to the various ecosystem activities, which manifest themselves in ecosystem services, compromising the quality and fertility of the soil in the long term. The presence of a diverse and active microbiota



Figure 2. *Ziziphus joazeiro* Mart: native species most found in the urban forestry of the Quitaiús district in Lavras da Mangabeira-CE, Brazil. Source: [23].

plays important roles in nutrient cycling and plant health. It is important to mention that some

TABLE I. QUANTITATIVE RELATIONSHIP OF SPECIES IN THE URBAN ARBORIZATION OF THE QUITAIÚS DISTRICT IN LAVRAS DA MANGABEIRA-CE, BRAZIL.

Common name	Scientific name	N°	%	Origin
Algarrobo	<i>Prosopis juliflora</i> (Sw.) DC.	1	0.27	Exotic
Pará cotton	<i>Talipariti tiliaceum</i> (L.) Fryxell	1	0.27	Native
Canafístula	<i>Peltophorum dubium</i> (Spreng.) Taub.	1	0.27	Native
Acacia	<i>Senna siamea</i> (Lam.) H. S. Irwin&Barneby	18	4.89	Exotic
Castanhola	<i>Terminalia catappa</i> L.	6	1.63	Exotic
Flamboyant	<i>Delonix regia</i> (Hook.) Raf.	1	0.27	Exotic
Ficus	<i>Ficus benjamina</i> L.	154	41.85	Exotic
Juazeiro	<i>Ziziphus joazeiro</i> Mart.	5	1.36	Native
Indian neem	<i>Azadirachta indica</i> A. Juss	176	47.83	Exotic
Pau Brasil	<i>Paubrasilia echinata</i> (Lam.) Gagnon, H.C. Lima & G.P. Lewis	2	0.54	Native
Tamarind	<i>Tamarindus indica</i> L.	3	0.82	Exotic
Total	11 species	368	100.00	-

exotic species may have different water consumption patterns than native species. This can affect the availability of water in the soil, with possible impacts on water retention and local hydrological cycles.

The species composition of urban trees plays a crucial role in the provision of ecosystem services. Native species are generally more adapted to local conditions, which can increase their resistance to specific pests, diseases and

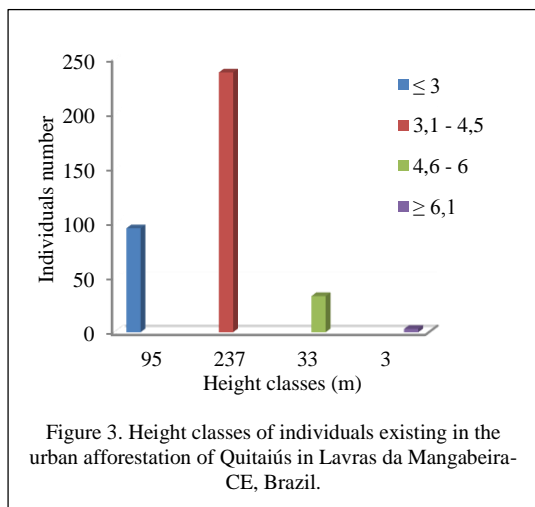
climate conditions. Alien species may have difficulty adapting, which may limit their effectiveness in providing ecosystem services. However, the exotic species observed in the inventory, such as Neem and Ficus, are adapted and perform important functions such as air purification, formation of visual and/or sound barriers, beautification of the city, among others. However, some species pose structural problems due to the expansion of their roots, and do not contribute to local biodiversity, as they are not likely to attract and sustain wildlife within urbanization.

The Neem tree (*Azadirachta indica*), for instance, has been widely used in recent years for urban tree planting due to its cultivation and rapid growth, meeting the demands of people who need shading in a short period. However, some issues related to this species often go unnoticed. *Azadirachta indica* is highly aggressive in terms of territorial invasion, posing potential problems to the environment.

Concern about the introduction of the *Azadirachta indica* species and its consequences has sparked some actions, according to [26] this can be seen in the Environmental Pact of the Inhamuns Region (Parisc), which expresses the mobilization against the proliferation of *Azadirachta indica* planting in municipalities in this region, given the environmental damage already observed in that region. The author also stated that planting actions for this species will cause great damage to the environment and the biome in the near future, based on five justifications: the species feeds on soil microorganisms, it is a natural repellent of disastrous proportions for fauna and flora, it has extraordinary reproductive power that is already out of control, making it an invasive tree. Furthermore, it acts as a natural abortifacient, causing damage to the region [26].

Regarding the total height of the trees, only 24 individuals (6.52%) exhibited a height greater than 5 m, as depicted in Fig. 3, indicating the recent planting of trees in the area, a result also observed by [15].

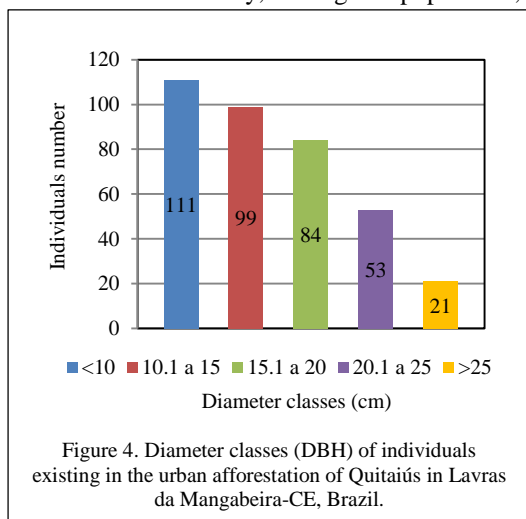
Regarding the diameter at breast height (DBH), the afforestation of Quitaiús is mostly composed of trees with low development in woody biomass. Around 30.2% of the trees (111 individuals) had DBH less than or equal to 10 cm; 26.9% (99 individuals) had DBH between 10.1 and 15 cm; 22.8% (84 individuals) had a DBH size between 15.1 and 20cm; 14.4%



(53 individuals) had DBH in the range of 20.1 to 25cm; and, only 5.7% (21 individuals) reached a DBH greater than 25cm Fig. 4.

Similar data were observed by [15] in the city of Lavras da Mangabeira-CE where afforestation presented only 3.5% of trees with a DBH greater than 25cm. In the neighborhood of São Benedito, Parnaíba-PI, the majority of individuals sampled had DBH greater than 0.48 m [20], results superior to those found in this study.

Therefore, the data as a whole showed that the district's afforestation presents a predominance of individuals with stem development below 10cm in diameter, and height between 3.1 and 4.5m, with an abundance of two species. To better understand this situation, a more specific study is necessary, which aims to identify, among the population,



the real reasons for planting such species and the period of action.

IV. CONCLUSIONS

The afforestation of Quitaiús presents little diversity of species, compared to other municipalities in the same state and other Brazilian states, with a concentration of individuals of the exotic species, *Azadirachta indica* and *Ficus benjamina*, with the majority of specimens being between 3.1 and 4.5m.

After field research, it was realized that the trees were planted without scientific knowledge, considering that residents only took into consideration species that have rapid growth and the ability to provide shade. Thus, a large number of *Azadirachta indica* were identified as part of the district's afforestation, which could harm the local flora and fauna.

The monitoring and monitoring of activities related to urban afforestation do not take place effectively in the municipality of Lavras da Mangabeira, the Urban Afforestation Plan, which is the responsibility of each municipality and which legitimizes and describes the actions related to management, implementation, planting, maintenance and monitoring of trees, is a document unknown to the community, making it difficult to access information and support decisions, such as carrying out plant extraction, planting, among other determining factors. The implementation of a monitoring system to evaluate the success of planting and make adjustments aimed at improvement is a necessary activity for the success of effective afforestation in view of its environmental functions.

There are great challenges in carrying out adequate afforestation, factors such as water scarcity can limit the growth of trees, and these are points that require efforts, although some practices have already been carried out in the Brazilian semi-arid region, such as capturing and storing water rain, efficient irrigation and water availability. However, the choice of adapted native species, selection of species resistant to water and thermal stress, carrying out planting practices that promote native biodiversity, avoiding invasive species that can compete with native ones, are important practices that must take place before any execution arboreal. It is important to encourage the active participation of local communities and public bodies, from planning to implementation,

ensuring that projects meet local needs and promote ongoing ownership and care.

Choosing tree and plant species adapted to the specific conditions of the region, including physiologically plants with drought tolerance, heat resistance and the ability to thrive in poor soils, implementing soil management practices such as adding organic matter to improve soil structure and moisture retention. Therefore, greater attention must be paid to working with native trees, in addition to accentuating the floristic heterogeneity of urban afforestation, highlighting afforestation with native plants. Species such as Pau Brasil (*Paubrasilia echinata* (Lam.) Gagnon, H.C. Lima & G.P.Lewis), Canafístula (*Peltophorum dubium* Spreng.) and Brasileirinho (*Erythrina indica-picta* L. B. & M.) can be introduced, contributing to the diversity and origin of local species.

ACKNOWLEDGMENTS

The authors are grateful to PNPd/FAPESQ/PB (Nº1990/2022, Edital Nº17/2022) for the financial support, beneficiary Postgraduate Program in Renewable Energies (PPGER/CEAR) and to the Thin Film Synthesis and Characterization Laboratory (LabFilm).

REFERENCES

- [1] Cai, W., Ng, B., Wang, G., & Santoso, A. (2022). Increased ENSO sea surface temperature variability under four IPCC emission scenarios. *Nature Climate Change*, (12), 3.
- [2] Tian, F., Zhu, Z., Cao, S., Zhao, W., Li, M., & Wu, J. (2024). Satellite-observed increasing coupling between vegetation productivity and greenness in the semiarid Loess Plateau of China is not captured by process-based models. *Science of The Total Environment*, (906), 167664.
- [3] Bezerra, R. C. L., Golçalves, M. I. P., Melo, J. P. P., Galvão, M. N. C., Silva, C. T. R., & Feitosa, J. R. M. (2011). Educação Ambiental. *URCA*.
- [4] Araújo, S. V. (2012). Conceitos de arborização urbana: *webartigos*. Disponível em: <http://www.webartigos.com/artigos/conceitos-de-arborizacao-urbana/99622/>.
- [5] Tozzi, R. H. B. B. (2017). A tutela jurídica da arborização urbana. *Âmbito Jurídico*, (159), 1.
- [6] Qiu, D., Xu, R., Wu, C., Mu, X., Zhao, G., & Gao, P. (2022). Vegetation restoration improves soil hydrological properties by regulating soil physicochemical properties in the Loess Plateau, China. *Journal of Hydrology*, (609), 127730.
- [7] Giudice, D. S., & Jesus, V. L. S. de. (2021). Arborização urbana no Município de Paulo Afonso - Bahia: algumas sugestões de manejo. *Brazilian Journal of Development*, (7), 12889-12912.
- [8] Companhia Energética de Minas Gerais. (2011). Manual de arborização. Belo Horizonte: Cemig / Fundação Biodiversitas, 112. Disponível em: <https://www.cemig.com.br/wp-content/uploads/2020/10/manual-arborizacao-cemig-biodiversitas.pdf>.
- [9] Silva, L. R., Meunier, I. M. J., & Freitas, Â. M. M. (2007). Riqueza e densidade de árvores, arvoretas e palmeiras em parques urbanos de Recife, Pernambuco, Brasil. *Revista da Sociedade Brasileira de Arborização Urbana*, (2), 4.
- [10] Cabral, P. I. D. (2013). Arborização urbana: Problemas e Benefícios. *Revista Especialize*, (1), 6.
- [11] Duarte, T. E. P. N., Angeoletto, F., Richard, E., Vacchiano, M. C., Leandro, D. S., Bohrer, J. F. C., Leite, L. B., & Santos, J. W. M. C. (2017). Arborização Urbana no Brasil: Um Reflexo de Injustiça Ambiental. *Terr@Plural*, (11), 291-303.
- [12] Assunção, K. C., Luz, P. B., Neves, L. G., & Sobrinho, S. P. (2014). Levantamento Quantitativo da Arborização de Praças da Cidade de Cáceres/MT. *Revista da Sociedade Brasileira de Arborização Urbana*, (9), 123-132.
- [13] Lima, J. R., & Filho, L. S. O. (2020). Publicações sobre arborização urbana na região nordeste, Brasil. *Revista da Sociedade Brasileira de Arborização Urbana*, (15), 56-69.
- [14] Soares, C. P. B., Neto, F. P., & Souza, A. L. (2007). Dendrometria e Inventário Florestal. *Ed. UFV*, 276.
- [15] Calixto Júnior, S. L., Santana, G. M., & Filho, J. A. L. (2009). Análise Quantitativa da arborização urbana de Lavas da Mangabeira, CE Nordeste do Brasil. *Revista da Sociedade Brasileira de Arborização Urbana*, (4), 99-109.
- [16] Araújo, Y. R. V., & Moreira, Z. C. G. (2015). Composição florística, fitogeografia e diversidade da arborização urbana implantada em 2011-2013: uma análise da cidade de João Pessoa, PB, BR. *Revista Científica Eletrônica de Engenharia Florestal*, (25), 1.
- [17] Lundgren, W. J. C., Silva, L. F., & Almeida, A. Q. de. (2013). Influência das espécies exóticas arbóreas urbanas na área de cobertura da cidade de Serra Talhada – PE. *Revista da Sociedade Brasileira de Arborização Urbana*, (8), 96- 107.
- [18] Sousa, L. A., Cajaiaba, R. L., Martins, J. S. C., Colácio, D. S., Sousa, E. S., & Pereira, K. S. (2019). Levantamento quali-quantitativo da arborização urbana no município de Buriticupu, MA. *Revista da Sociedade Brasileira de Arborização Urbana*, (14), 42-52.
- [19] Parry, M. M., Silva, M. M. Sena, I. S., & Oliveira, F. P. M. (2012). Composição florística da arborização da cidade de Altamira, Pará. *Revista da Sociedade Brasileira de Arborização Urbana*, (7), 143-158.
- [20] Silva, A. A. R., Veras, C. H. G., Machado, J. C., Sousa, J. F., Leal, M. A. S., Silva, M. J., & Mendes, M. R. A. (2018). Diagnóstico da arborização do bairro São Bento, município de Parnaíba, Piauí. *Revista da Sociedade Brasileira de Arborização Urbana*, (13), 29-40.
- [21] Silva, I. C., & Ribeiro, V. T. (2017). Arborização urbana na cidade de Paulistana-PI: uma análise das praças públicas. *Revista da Sociedade Brasileira de Arborização Urbana*, (12), 79-91.
- [22] Meunier, I. (2005). Planejamento para uma boa arborização municipal. *Nordeste Rural*. Disponível em: <http://www.nordesteural.com.br/nordesteural/mater.asp?newsId=2071>.

- [23] Silva, T. (2015). *Plantas do semiárido nordestino, e suas importâncias. Raízes do sertão*. Disponível em: <http://tuica-silva.wixsite.com/raizes-do-sertao/plantas>.
- [24] Silveira, L. P., Freire, M. S., Andrade, F. M. V., Vasconcelos, W. S., Maracajá, P. B., & Sousa, D. F. M. (2013). A. Diagnóstico visual da arborização tombada do município de Cerro Corá, RN, Brasil. *Revista Brasileira de Gestão Ambiental*, (7), 16-19.
- [25] Leão, T. C. C., Almeida, W. R., Dechoum, & M., Ziller, S. R. (2011). *Espécies Exóticas Invasoras no Nordeste do Brasil: Contextualização, Manejo e Políticas Públicas*. Centro de Pesquisas Ambientais do Nordeste e Instituto Hórus de Desenvolvimento e Conservação Ambiental.
- [26] Moura, J. (2013). *Ambientalistas alertam contra cultivo do Nim. Diário do Nordeste*. Disponível em: <http://diariodonordeste.verdesmares.com.br/cadernos/regional/ambientalistas-alertam-contra-cultivo-do-nim-1.243149>.

Financial Assessment of Waste to Energy Options for Municipal Solid Waste Management - Tehran Case Study

Ali Marefa¹, Alireza Bazargan², Reza Samadi³

¹Faculty of Environment, University of Tehran, Iran

^{2,3}Department of Environmental Management, Science and Research Branch, Islamic Azad University, Tehran, Iran

¹ali.marefat@ut.ac.ir, ²alireza.bazargan@ut.ac.ir, ³samadireza@yahoo.com

Abstract—The production of large amounts of municipal solid waste (MSW) has become a serious challenge for municipalities around the world. This is especially true for metropolises like Tehran, which produces a staggering 4800 to 6800 tons of MSW every day. In order to effectively manage this waste and also contribute to the renewable energy sector, utilization of waste-to-energy (WtE) technologies has emerged as a solution. The objective of this study is to evaluate the viability of WtE investments in Tehran. Several WtE options are considered, including the collection of landfill gas (LFG), anaerobic digestion (AD), and incineration (INC). The financial profitability of these options is assessed using various indicators such as Net Present Value (NPV), Internal Rate of Return (IRR), Levelized Cost of Energy (LCOE), and payback period. The analysis reveals that Tehran's urban wastes have the potential to generate approximately 84 MW, 30 MW, and 27 MW of electricity through INC, AD, and LFG technologies, respectively. However, the financial model shows that incineration plants have high capital and operation & maintenance expenditures, making energy production from them economically unviable under the current electricity power purchase agreement. In order to make the NPV positive for waste incinerators, a gate fee of at least US\$ 0.014 must be considered in the financial models. On the other hand, the financial model identifies LFG as the most economical technique for converting MSW to energy, with a faster payback period compared to other technologies. Additionally, a sensitivity

analysis is conducted to determine the main factors affecting the financial profitability of WtE plants. The discount rate and tariff sale are found to be highly influential factors in the outputs of the financial model. Furthermore, it is observed that the energy conversion efficiency (η) of WtE plants has a negative effect on profitability. Overall, this study highlights that careful financial analysis and consideration of various factors are crucial in determining the economic viability of WtE investments.

Keywords - waste to energy, landfill gas, incineration, anaerobic digestion

I. INTRODUCTION

In response to rapid growth of population and increase in municipal solid waste (MSW) production, waste to energy (WtE) technologies have been widely utilized in developed countries [1,2]. WtE technologies help both solve challenges of waste dumping and provide a new source of renewable energy [3]. In addition, WtE plants contribute to global warming mitigation and reduction of fossil fuel dependence [2,3]. More importantly, WtE plants offer a solution for managing non-recyclable wastes [4]. Numerous researchers have considered the WtE as a subcategory of renewable energies [5-7]. Furthermore, WtE approaches have been recognized as an appropriate alternative to fossil fuels which have the potential to offer up to 52TWh of green

electricity by 2050 [8]. Selection of an appropriate WtE technology depends on many factors such as waste composition, climatic conditions, population, and geographical conditions [9]. WtE approaches can be divided into physical, biological and thermal methods. Through physical method, MSW is converted into refuse derived fuel (RDF). Thermal or incineration (INC) WtE approach includes combustion, gasification and pyrolysis methods. Incineration is a reliable form of WtE which is widely used in developed as well as developing countries such as Bangladesh, India and Sri Lanka [10]. The recovery of landfill gas (LFG) and anaerobic digestion (AD) are the most common biological approaches of WtE systems and will lead to biogas production which is mainly composed of methane and carbon dioxide [11,12].

In Iran, WtE technologies have not yet gained widespread adoption. Given the trend of waste generation growth, it is important to assess the feasibility of WtE technologies utilization in the country. This paper aims to evaluate economic

viability of the most common WtE systems namely LFG, AD and INC in Tehran city. The analysis will be conducted based on financial indicators, i.e. internal rate of return (IRR), net present value (NPV), payback period (PBP), discounted payback period (DPBP), levelized cost of electricity (LCOE) and levelized cost of waste (LCOW). Finally, sensitivity analysis will be done on the created financial model in order to identify the main affecting factors in profitability of a WtE system.

II. METHODS

A. MSW in Tehran

The Tehran metropolis, with an area of 700 square kilometers and a population of about 12,000,000 is the capital and the largest city in Iran. The daily average generation of MSW is more than 4800 tons [5]. It is very important to know the physical composition of the waste in order to design the methods and technologies used for its treatment [13]. Table I represents the physical composition, amount, and lower calorific value of MSW in Tehran.

TABLE I. COMPOSITION, AMOUNT AND LOWER CALORIFIC VALUE OF MSW IN TEHRAN.

Waste type	Glass	Wood	Plastic	Textiles	Paper and Cardboard	Food and yard waste	Metals	Inert	Total
Composition (%)	2	5.5	8.9	3.3	5	74.5	2/5	2	100
Quantity (ton)	96	86	427	158	240	3576	120	2	4800
LCV (Kj/Kg)	-290	15000	25000	13000	12000	3000	-290	18000	

B. Estimation of Energy Outputs

To estimate the quantitative electrical energy generation from INC, AD and LFG, a series of calculations should be performed. In this regard, the electrical energy production was estimated in the following formulas:

$$E_{INC}(KWh/year) = \frac{LHV_{waste} \times M \times \eta_{INC}}{3.6}, \quad (1)$$

where LHV_{waste} , M and 3.6 are lower heating value of MSW (MJ/Kg), the amount of MSW that could be utilized for incineration (tons/yr), and conversion factor from MJ to KWh, respectively. Conversion efficiency (η_{INC}) is taken for incineration and as 25% [14].

$$E_{AD} \left(\frac{KWh}{year} \right) = \frac{LHV_{CH_4} \times M \times V_{CH_4} \times \eta_{AD}}{3.6}, \quad (2)$$

where LHV_{CH_4} , M , V_{CH_4} , and 3.6 are lower heating value of methane (= 37.2 MJ/m³), the amount of feedstock which is fed into the digester (tons/yr), the content of methane in the biogas (m³/ton), and conversion factor from MJ to KWh, respectively. Conversion efficiency (η) is taken as 26% for an anaerobic digester [3].

$$E_{LFG}(KWh/year) = \frac{LHV_{CH_4} \times Q_C \times \eta_{LFG}}{3.6}, \quad (3)$$

where LHV , Q_C and 3.6 are lower heating value of methane (= 37.2 MJ/m³), average methane collected (m³/year) and conversion factor from MJ to KWh, respectively. In this study, conversion efficiency (η) is taken as 33% for a LFG system [15].

C. Estimation of Lower Heating Value of MSW

The basis for energy production using incineration is LHV or calorific values of different components of MSW. Table I and Eq. (4) are used to calculate lower heating value of Tehran MSW. Where LHV_i and W_i are calorific value and weight percentage of each fraction of MSW, respectively:

$$LHV_{total} = \sum(LHV_i) \times (W_i) . \quad (4)$$

D. Financial Model

A financial model was developed in order to compare economic viability of INC, AD and LFG technologies in Tehran MSW management. In addition, the financial feasibility of a WtE plant in Tehran using the above-mentioned technologies is investigated through a set of financial indicators, i.e. NPV, IRR, PBP, DPBP, LCOE and LCOW. The following equations and definitions are used to calculate the financial indicators. NPV is the equivalent of all cash inflows and outflows during the lifetime of a project at the present time.

$$NPV = 1 + \frac{\sum_{t=0}^n OPEX_t}{(1+r)^t} . \quad (5)$$

The value of discounted rate that makes NPV equal to zero is IRR. PBP is the required number of years to recover investment costs. However, DPBP is the years required to recover discounted investment costs. LCOE demonstrates the minimum price at which electricity must be sold to reach breakeven point at the end of project life.

$$LCOE = \frac{I_0 + \sum_{t=0}^n \frac{OPEX_t}{(1+r)^t}}{\sum_{t=0}^n \frac{E_t}{(1+r)^t}} . \quad (6)$$

Similarly, LCOW demonstrates the unit cost of the treated waste during the operational life of the WtE facilities.

$$LCOW = \frac{I_0 + \sum_{t=0}^n \frac{OPEX_t}{(1+r)^t}}{\sum_{t=0}^n \frac{W_t}{(1+r)^t}} , \quad (7)$$

where:

I_0 - The initial investment cost;

$OPEX_t$ - The operation & maintenance costs in year t ;

r - The discounted rate;

E_t - The total energy produced in year t (MWh);

W_t - The amount of total waste treated in year t .

E. Financial Assumptions

The following is used to facilitate the financial analysis. The numbers utilized in this paper are mostly derived from the studies done by International Renewable Energy Agency (IRENA) and the reports published in the literature pertinent to Iran.

1. Operational life: The paper considers 18 years of economic life for AD and LFG technologies, starting from year 2026, and 17 years of economic life for INC technology, starting from year 2027.
2. Construction phase: The design and construction phase are assumed to take 3 years for INC and 2 years for AD and LFG technologies.
3. Capacity factor: The paper assumes 85% capacity factor.
4. Transportation cost: the analysis begins after the waste is delivered to WtE plants and the study does not regard waste transportation cost.
5. Environmental benefits: This paper does not consider environmental benefits of a WtE plant such as greenhouse gas mitigation or land saving.
6. Electricity sale tariff: According to the government legislation, the base sale tariff for power plants using waste as feed is 5 Cent /Kwh.
7. Annual increase in electricity sales tariff: According to the government legislation, based on average annual increase in the exchange rate and the inflation rate, the sale tariff increases by 24.5% annually.
8. Discounted rate: This paper assumes discounted rate equal to bank interest rate in Iran i.e. 20%.
9. Capital Expenditure (CAPEX): The average CAPEX cost for WtE technologies using INC, AD and LFG is assumed to be 7000 USD/KW, 5000 USD/KW and 2500 USD/KW, respectively.
10. Operation and Maintenance Expenditure (OPEX): This paper assumes that OPEX

accounts for 4% of total CAPEX cost for all technologies [16].

F. Technical Assumptions

Different generation rate of methane is reported for LFG and AD technologies depending on MSW composition, ambient temperature, nutrients, rainfall and so on [14]. The methane generation rate for LFG technology is reported ranging from 25 to 200 Nm³ t⁻¹ [17]. However, this rate for AD technology is reported ranging from 67.5 to 122 Nm³ t⁻¹ [18]. In this study the value of 50 Nm³ t⁻¹ is adopted for both technologies. In regard to input feedstocks, it must be mentioned that only organic fraction of Tehran MSW (putrescible waste and paper) must be utilized for AD and LFG technologies.

III. RESULTS AND DISCUSSION

According to equations 1 to 3, INC, AD and LFG plants capacity are 85 MW, 27 MW and 21 MW, respectively. However, as will be shown, power generation would not lead to more profitability. Table II, III and IV represent initial

investment costs, annual operational and maintenance costs, and annual incomes. As shown, the highest initial investment cost belongs to INC technology with about USD 600 million. On the other hand, the lowest initial investment cost belongs to LFG technology with about USD 68 million. The initial investment cost required for AD technology is about USD 104 million. In addition, the annual operational and maintenance costs for INC, AD and LFG are about USD 23 million, USD 4 million and USD 2.6 million, respectively. The present value of electricity sale for INC, LFG and AD is estimated to be USD 612 million, USD 194 million and USD 153 million. By comparing AD and LFG technologies, it could be concluded that LFG is better in treatment of biodegradable MSW, because both CAPEX and OPEX are lower, and electricity generation is higher [15]. However, to more confidently compare the financial profitability of WtE technologies, it is necessary to evaluate other financial indicators [19,20].

TABLE II. CASH FLOW FINANCIAL MODEL OF INC TECHNOLOGY.

Discounted Cumulative cash flow	Cumulative cash flow	Cash flow	Electricity income	OPEX	CAPEX	Year
(US\$)						
-195.708,333	-195.708,333	-195.708,333			195.708,333	2024
-358.798,611	-391.416,667	-195.708,333			195.708,333	2025
-494.707,176	-587.125,000	-195.708,333			195.708,333	2026
-490.704,278	-580.207,992	6.917,008	30.402,008	23.485,000		2027
-483.845,083	-565.984,766	14.223,226	37.708,226	23.485,000		2028
-474.487,253	-542.699,491	23.285,276	46.770,276	23.485,000		2029
-462.924,861	-508.174,371	34.525,119	58.010,119	23.485,000		2030
-449.398,855	-459.708,247	48.466,125	71.951,125	23.485,000		2031
-434.105,777	-393.950,811	65.757,436	89.242,436	23.485,000		2032
-417.205,019	-306.746,611	87.204,199	110.689,199	23.485,000		2033
-398.824,867	-192.941,558	113.805,054	137.290,054	23.485,000		2034
-379.067,535	-46.142,926	146.798,632	170.283,632	23.485,000		2035
-358.013,349	141.578,309	187.721,235	211.206,235	23.485,000		2036
-335.724,236	380.056,676	238.478,367	261.963,367	23.485,000		2037
-312.246,619	681.490,141	301.433,465	324.918,465	23.485,000		2038
-287.613,827	1.061,008,089	379.517,947	403.002,947	23.485,000		2039
-261.848,102	1.537,375,800	476.367,711	499.852,711	23.485,000		2040
-234.962,253	2.133,868,232	596.492,433	619.977,433	23.485,000		2041
-206.961,042	2.879,353,788	745.485,556	768.970,556	23.485,000		2042
-177.842,326	3.809,638,530	930.284,741	953.769,741	23.485,000		2043

TABLE III. CASH FLOW FINANCIAL MODEL OF AD TECHNOLOGY.

Discounted Cumulative cash flow	Cumulative cash flow	Cash flow	Electricity income	OPEX	CAPEX	Year
(US\$)						
-52.887,731	-52.887,731	-52.887,731			52.887,731	2024
-96.960,841	-105.775,463	-52.887,731			52.887,731	2025
-95.016,196	-102.415,117	3.360,346	7.591,365	4.231,019		2026
-92.556,665	-97.230,412	5.184,705	9.415,723	4.231,019		2027
-89.632,378	-89.782,918	7.447,494	11.678,512	4.231,019		2028
-86.285,038	-79.528,842	10.254,077	14.485,095	4.231,019		2029
-82.549,149	-65.793,704	13.735,138	17.966,157	4.231,019		2030
-78.453,067	-47.740,935	18.052,769	22.283,788	4.231,019		2031
-74.019,891	-24.332,921	23.408,014	27.639,033	4.231,019		2032
-69.268,212	5.717,312	30.050,233	34.281,251	4.231,019		2033
-64.212,762	44.006,024	38.288,711	42.519,730	4.231,019		2034
-58.864,951	92.513,087	48.507,063	52.738,081	4.231,019		2035
-53.233,329	153.694,178	61.181,091	65.412,110	4.231,019		2036
-47.323,980	230.595,122	76.900,945	81.131,963	4.231,019		2037
-41.140,847	326.993,720	96.398,597	100.629,616	4.231,019		2038
-34.686,016	447.575,650	120.581,930	124.812,949	4.231,019		2039
-27.959,948	598.152,658	150.577,008	154.808,026	4.231,019		2040
-20.961,683	785.933,167	187.780,509	192.011,528	4.231,019		2041
-13.689,006	1.019,857,931	233.924,765	238.155,783	4.231,019		2042
-6.138,586	1.311,016,350	291.158,419	295.389,437	4.231,019		2043

TABLE IV. CASH FLOW FINANCIAL MODEL OF LFG TECHNOLOGY.

Discounted Cumulative cash flow	Cumulative cash flow	Cash flow	Electricity income	OPEX	CAPEX	Year
(US\$)						
-33.563,368	-33.563,368	-33.563,368			33.563,368	2024
-61.532,841	-67.126,736	-33.563,368			33.563,368	2025
-57.510,779	-60.176,612	6.950,124	9.635,194	2.685,069		2026
-53.042,387	-50.910,955	9.265,656	11.950,726	2.685,069		2027
-48.164,535	-38.773,298	12.137,658	14.822,727	2.685,069		2028
-42.906,684	-23.073,439	15.699,859	18.384,928	2.685,069		2029
-37.292,083	-2.955,310	20.118,129	22.803,199	2.685,069		2030
-33.640,798	12.744,549	15.699,859	18.384,928	2.685,069		2031
-29.741,770	32.862,678	20.118,129	22.803,199	2.685,069		2032
-25.607,518	58.460,878	25.598,199	28.283,269	2.685,069		2033
-21.247,507	90.856,119	32.395,241	35.080,311	2.685,069		2034
-16.668,628	131.681,869	40.825,750	43.510,819	2.685,069		2035
-11.875,587	182.964,149	51.282,280	53.967,349	2.685,069		2036
-6.871,241	247.215,875	64.251,726	66.936,796	2.685,069		2037
-1.656,865	327.553,867	80.337,993	83.023,062	2.685,069		2038
3.767,616	427.843,982	100.290,115	102.975,184	2.685,069		2039
9.403,445	552.881,117	125.037,135	127.722,205	2.685,069		2040
15.252,876	708.612,483	155.731,366	158.416,435	2.685,069		2041
21.319,048	902.414,524	193.802,041	196.487,110	2.685,069		2042
27.605,875	1.143,436,393	241.021,869	243.706,939	2.685,069		2043

Table V presents the results of financial indicators for each studied WtE technology. For incineration, IRR and NPV considering the current tariff of electricity sale are 16% and USD -148,201,938, respectively. Therefore, incineration technology is not economically profitable to recover energy. Furthermore, LCOE and LCOW reveal that energy recovery and waste treatment using INC technology is extremely expensive [21,22]. On the other hand, Table V approves that with current electricity sale tariff, using AD and LFG technologies is a cost-effective way to recover energy and treat the organic fraction of Tehran MSW. In addition, based on the values of LCOE and LCOW in

Table V, it appears that LFG technology offers the cheapest way for energy recovery and waste treatment. However, as mentioned, LFG and AD technologies can only treat the organic fraction of MSW. Meanwhile, to economically justify INC technology, different values of gate fee will be assessed. Table VI present the results of financial indicators under different value of gate fee. Thus, INC technology will be economically justified with the current tariff of electricity sale, if USD 0.01 per kilogram of waste is paid as gate fee. However, considering DPBP indicator (19 years), it does not seem that investment in incineration waste projects is attractive.

TABLE V. THE FINANCIAL INDICATORS FOR DIFFERENT WTE TECHNOLOGIES.

Financial indicator	INC	AD	LFG
NPV (USD)	-148.201,938	11.330,012	74.630,738,24
IRR (%)	16	21	31
PBP (Years)	9	9	5
DPBP (Years)	-	18	11
LCOE (USD/KWh)	0.20	0.14	0.07
LCOW (USD/ton)	84.6	19.1	12.1

TABLE VI. ECONOMIC ASSESSMENT OF INC TECHNOLOGY UNDER DIFFERENT VALUE OF GATE FEE.

Gate fee (USD)	IRR (%)	NPV (USD)	PBP	DPBP
0.005	18	-59.088,785,84	8	-
0.007	20	-14.532,209,59	7	-
0.01	21	30.024,366,66	7	19
0.12	22	74.580,942,91	7	18

A. Sensitivity Analysis

Sensitivity analysis identifies the effective input parameters on profitability of a project [23]. In this paper, the input parameters selected for analysis are electricity tariff sale, discount rate, facility waste capacity, CAPEX and OPEX. For the analysis, these parameters will be changed by $\pm 10\%$ to re-compute NPV of WtE technologies. Table VII demonstrates the

influence of increasing the selected input parameters on the NPV of WtE technologies. According to Table VII, VIII and IX, the NPV of all WtE technologies has a positive relationship with the increase in electricity tariff, while an inverse relationship is observed when discount rate and CAPEX. Changes in facility waste capacity and OPEX have minimal impact on the NPV, but the NPV is highly sensitive to the discount rate.

TABLE VII. EFFECT OF INPUT PARAMETERS CHANGE ON INCINERATION PLANT NPV (CONSIDERING USD 0.01 AS GATE FEE).

Input parameters	-10% decrease	No change	+10% increase	sensitivity
Electricity tariff sale	-2.870,173	30.024,366	62.918,907	high
Discounted rate	131.395,323	30.024,366	-45.094,367	very high
Facility waste capacity	27.021,929	30.024,366	33.026,803	low
CAPEX	77.739,100	30.024,366	-17.690,367	high
OPEX	36.513,502	30.024,366	23.535,230	low

TABLE VIII. EFFECT OF INPUT PARAMETERS CHANGE ON ANAEROBIC DIGESTION PLANT NPV.

Input parameters	-10% decrease	No change	+10% increase	sensitivity
Electricity tariff sale	703,018	11.330,012	21.957,006	high
Discount rate	32.519,762	11.330,012	-4.531,470	very high
Facility waste capacity	10.197,011	11.330,012	12.463,013	low
CAPEX	20.824,005	11.330,012	1.836,019	high
OPEX	12.743,935	11.330,012	9.916,090	low

TABLE IX. EFFECT OF INPUT PARAMETERS CHANGE ON LANDFILL GAS EXTRACTION PLANT NPV.

Input parameters	-10% decrease	No change	+10% increase	sensitivity
Electricity tariff sale	61.142,630	74.630,738	88.118,846	high
Discounted rate	103.991,942	74.630,738	52.280,692	very high
Facility waste capacity	67.167,664	74.630,738	82.093,812	low
CAPEX	80.655,772	74.630,738	68.605,704	high
OPEX	75.528,035	74.630,738	73.733,441	low

IV. CONCLUSION

Despite the fact that WtE plants offer a unique opportunity to recover green energy and at the same time treat waste hygienically, there is a serious limitation in their application in Iran. The results reveal that waste incineration technology is not economically justified due to extremely high investment cost and also operational and maintenance costs. In addition, calculations demonstrate that the treatment cost using incineration technology would require more than USD 86 per ton of waste. On the other hand, considering the conditions considered in this study, the extraction of landfill gas provides a unique and cost-effective solution to address putrescible wastes management. The calculation of levelized cost of energy shows that the generation cost of each kilowatt hour of electricity with landfill gas would be only ϕ 7.

REFERENCES

- [1] Hu, Y., Cheng, H., & Tao, S. (2018). The growing importance of waste-to-energy (WTE) incineration in China's anthropogenic mercury emissions: Emission inventories and reduction strategies. *Renewable and Sustainable Energy Reviews*, 97, 119-137.
- [2] Zhang, D., Huang, G., Xu, Y., & Gong, Q. (2015). Waste-to-energy in China: Key challenges and opportunities. *Energies*, 8(12), 14182-14196.
- [3] Kumar, S., & Ankaram, S. (2019). Waste-to-energy model/tool presentation. In *Current developments in biotechnology and bioengineering* (pp. 239-258): Elsevier.
- [4] Awasthi, M. K., Sarsaiya, S., Chen, H., Wang, Q., Wang, M., Awasthi, S. K., ... Zhang, Z. (2019). Global status of waste-to-energy technology. In *Current developments in biotechnology and bioengineering* (pp. 31-52), Elsevier.
- [5] Takuma, M., Kaihara, Y. U. U. J. I., & YAMADA, A. (2004). Contribution of waste to energy technology to global warming. *Technical Review*, 41(4).
- [6] Ferdan, T., Pavlas, M., Nevrlý, V., Šomplák, R., & Stehlík, P. (2018). Greenhouse gas emissions from thermal treatment of non-recyclable municipal waste. *Frontiers of Chemical Science and Engineering*, 12, 815-8317.
- [7] Anonas, S. D. S., Eugenio, F. D. T., Flores, B.-H. F., Balite, P. H. M., Tomacruz, J. G. T., Limjuco, L. A., & Ocon, J. D. (2023). From Waste to Renewable Energy: A Policy Review on Waste-to-Energy in the Philippines. *Sustainability*, 15(17), 12963.
- [8] Kothari, R., Tyagi, V. V., & Pathak, A. (2010). Waste-to-energy: A way from renewable energy sources to sustainable development. *Renewable and Sustainable Energy Reviews*, 14(9), 3164-3170.
- [9] Moya, D., Aldás, C., López, G., & Kaparaju, P. (2017). Municipal solid waste as a valuable renewable energy resource: a worldwide opportunity of energy recovery by using Waste-To-Energy Technologies. *Energy Procedia*, 134, 286-295.
- [10] Kaur, A., Bharti, R., & Sharma, R. (2021). Municipal solid waste as a source of energy. *Materials Today: Proceedings*.
- [11] Alzate, S., Restrepo-Cuevas, B., & Jaramillo-Duque, Á. (2019). Municipal solid waste as a source of electric power generation in Colombia: A techno-economic evaluation under different scenarios. *Resources*, 8(1), 51.
- [12] Andriani, D., & Atmaja, T. D. (2019). The potentials of landfill gas production: a review on municipal solid waste management in Indonesia. *Journal of Material Cycles and Waste Management*, 21, 1572-1586.
- [13] Rezaei, M., Ghobadian, B., Samadi, S. H., & Karimi, S. (2018). Electric power generation from municipal solid waste: A techno-economic assessment under different scenarios in Iran. *Energy*, 152, 46-5615.

- [14] Dionisi, D., Bolaji, I., Nabbanda, D., & Silva, I. M. (2018). Calculation of the potential production of methane and chemicals using anaerobic digestion. *Biofuels, Bioproducts and Biorefining*, 12(5), 788-801.
- [15] Gómez, A., Zubizarreta, J., Rodrigues, M., Dopazo, C., & Fueyo, N. (2010). Potential and cost of electricity generation from human and animal waste in Spain. *Renewable Energy*, 35(2), 498-505.
- [16] Ayodele, T., Ogunjuyigbe, A., & Alao, M. (2017). Life cycle assessment of waste-to-energy (WtE) technologies for electricity generation using municipal solid waste in Nigeria. *Applied energy*, 201, 200-218.
- [17] Nikolina, S. (2016). International renewable energy agency (IRENA).
- [18] Themelis, N. J., & Ulloa, P. A. (2007). Methane generation in landfills. *Renewable Energy*, 32(7), 1243-1257
- [19] Capela, I., Rodrigues, A., Silva, F., Nadais, H., & Arroja, L. (2008). Impact of industrial sludge and cattle manure on anaerobic digestion of the OFMSW under mesophilic conditions. *Biomass and Bioenergy*, 32(3), 245-251.
- [20] Abushammala, M. F., & Qazi, W. A. (2021). Financial feasibility of waste-to-energy technologies for municipal solid waste management in Muscat, Sultanate of Oman. *Clean Technologies and Environmental Policy*, 23(7), 2011-2023.
- [21] Hadidi, L. A., & Omer, M. M. (2017). A financial feasibility model of gasification and anaerobic digestion waste-to-energy (WtE) plants in Saudi Arabia. *Waste management*, 59, 90-101. 23.
- [22] Makarichi, L., Jutidamrongphan, W., & Techato, K.-a. (2018). The evolution of waste-to-energy incineration: A review. *Renewable and Sustainable Energy Reviews*, 91, 812-821.
- [23] Udomsri, S., Martin, A. R., & Fransson, T. H. (2010). Economic assessment and energy model scenarios of municipal solid waste incineration and gas turbine hybrid dual-fueled cycles in Thailand. *Waste management*, 30(7), 1414-1422.

Sustainable Location of Solar Plants: An Integrated Bibliometric Approach on Gis-multi-criteria Methods

Gustavo Gonçalves¹, Lucia Gaudencio², Rui de Oliveira³

^{1,3}State University of Paraíba, Campina Grande, Brazil

²Federal University of Campina Grande, Campina Grande, Brazil

¹gustavo.leite.goncalves@aluno.uepb.edu.br, ²lucia.gaudencio@ufcg.edu.br,

³ruideoliveira@servidor.uepb.edu.br

Abstract—The application of solar plants has been implemented, not only for energy generation but also to reduce carbon emissions and mitigate climate change. Adequate geographic location is crucial for optimizing project efficiency and must balance technical, economic, environmental and social factors. The use of geographic information systems proves to be useful in this planning stage, however, as it is a multifaceted process and involves weighted criteria, its integration with multi-criteria methodologies makes it possible to assign weights to criteria and evaluate alternatives in a controlled manner. This manuscript describes bibliometric approach research to analyze solar plant location planning studies based on GIS-Multicriteria methods. Data on titles, keywords, authors, countries and relevant journals were collected and analyzed, identifying a growing trend in publications from 2013 onwards, where some articles stood out in terms of number of citations, as well as being concentrated in some high-impact journals. In short, the methodological model studied has established itself as an effective approach for choosing locations for the installation and operation of solar plants in a sustainable and efficient manner.

Keywords – photovoltaics, GIS, energy planning, renewable energy, systematic review

I. INTRODUCTION

Currently, the search for sustainable energy sources is a global priority. Solar energy is considered one of the most promising solutions to reduce carbon emissions and address climate change. The installation of large-scale

photovoltaic plants is becoming popular in several countries. However, having satisfactory solar indices is no guarantee of success for these projects. It's essential to find geographically suitable locations to optimize energy generation, reduce operational costs, and minimize environmental impacts.

The process of choosing sites for these plants is challenging and involves various considerations. It's crucial to balance technical, economic, environmental, and social aspects, seeking efficiency in all areas and acceptance from the local community. This complexity involves different specifications, such as proximity to electrical infrastructures, terrain topography, preservation areas, conservation of natural resources, and impacts on local socio-economic activities, as well as addressing stakeholders' concerns [1].

To assist in this planning, the integration of Geographic Information Systems (GIS) has proven increasingly effective. This system allows for storing, retrieving, manipulating, analyzing, and mapping geographic data, following cartographic rules to facilitate interpretation [2]. GIS considers ambiguities, uncertainties, and complex concepts, resulting in a comprehensive evaluation of the potential of each area [3].

Although a valuable tool for exploring geographic information, GIS alone doesn't solve problems with multiple factors, as determining suitable areas for photovoltaic plants is

subjective and based on weighted criteria [4,5]. To address this issue, the GIS-Multicriteria combination emerges as an ideal methodology to solve it [4,6]. This approach allows for the assignment of weights to different criteria and the evaluation of location alternatives in a holistic and informed manner, ensuring well-founded decisions. Multicriteria decision-making is an analytical tool used to choose among alternatives from a set of possibilities. It compares different criteria according to their characteristic properties to identify the best areas for solar plant installation. This combination integrates spatial information and criterion weights based on a weighted analysis among solar resources, topography, infrastructure, natural social, economic aspects, among others [2].

The integration of these approaches enables a more accurate and comprehensive analysis, facilitating the identification of locations that meet a wide range of desirable criteria. In the transition to a more sustainable and fair energy matrix, the strategic selection of sites for solar plants plays a crucial role in the viability and success of these ventures. Thus, the aim was to conduct a bibliometric analysis of studies on solar plant site planning based on GIS-Multicriteria methods, reviewing the main criteria used in the literature.

II. METHODOLOGY

The methodological procedure employed in this article consisted of elaborating a bibliometric analysis to assess the developmental models of the research line, collaborations, correlations, as well as their spatiotemporal distribution [7]. Subsequently, network and content analyses were employed to describe, interpret, and review the content of the selected documents, meeting specific reliability and validation criteria [8]. The methodological development stages are described in Fig. 1.

Initially, an exploratory analysis was carried out to determine the problem to be investigated, in addition to defining the object of study. Subsequently, papers focusing on the technical location of solar power plants based on multiple sustainability indicator criteria integrated with geoprocessing tools were speculatively probed. Based on this survey, the main terms adopted in the literature were identified and categorized into three groups of keyword descriptors: 1) Photovoltaic energy, solar energy, photovoltaic, solar, solar farm, solar plant, solar power farm,

solar power plant; 2) Multicriteria analysis, multicriteria decision, multicriteria analysis method, multicriteria model, multicriteria evaluation, multicriteria prioritization, multicriteria theory; 3) Geographic information systems, GIS, spatial data analysis, GIS applications, spatial analysis, remote sensing, geographical mapping, GIS modeling.

Once the terms were established, two searches were conducted, taking into account the prior preparation of the databases. Information collection took place in July 2023, on the Web of Science (WOS) and Scopus (SC) platforms, two of the most well-known and widely used databases in the global academic sphere [9]. In both, the search was initiated by entering the groups of descriptors in specific search fields, activating the "All Fields" option. The "OR" argument was used among the terms, returning results associated with any of the inserted expressions. Among the fields, the "AND" argument was used, obliging the connection between all three groups. As a result, the action yielded 106 articles in WOS and 117 in SC.

The following phase involved applying inclusion and exclusion criteria for study selection. Initially, only scientific and review articles were selected, while all other types of materials, as well as duplicates between the databases, were excluded, totaling 149 manuscripts. The union between the files provided by WOS and SC and the removal of duplicate items were executed using the open-source software RStudio version R-4.3.1 [10].

Subsequently, the titles and abstracts of these publications were read, aiming to select sustainability indicator applications for GIS-multicriteria location of photovoltaic plants. Simultaneously, other articles were excluded based on the following criteria: (i) the studied energy sources were different from photovoltaic, (ii) they addressed small-scale solar applications, (iii) the purposes of energy conversion were other than distributed electric generation, or (iv) they diverged from the theme entirely. After this stage, 93 texts remained, which were subjected to bibliometrics.

Quantitative and qualitative balances formed the basis for a better understanding of the topic. The investigation of the chronological line of publications and citations were carried out with the aid of Excel software version 2307 [11].

With support from VOSviewer software

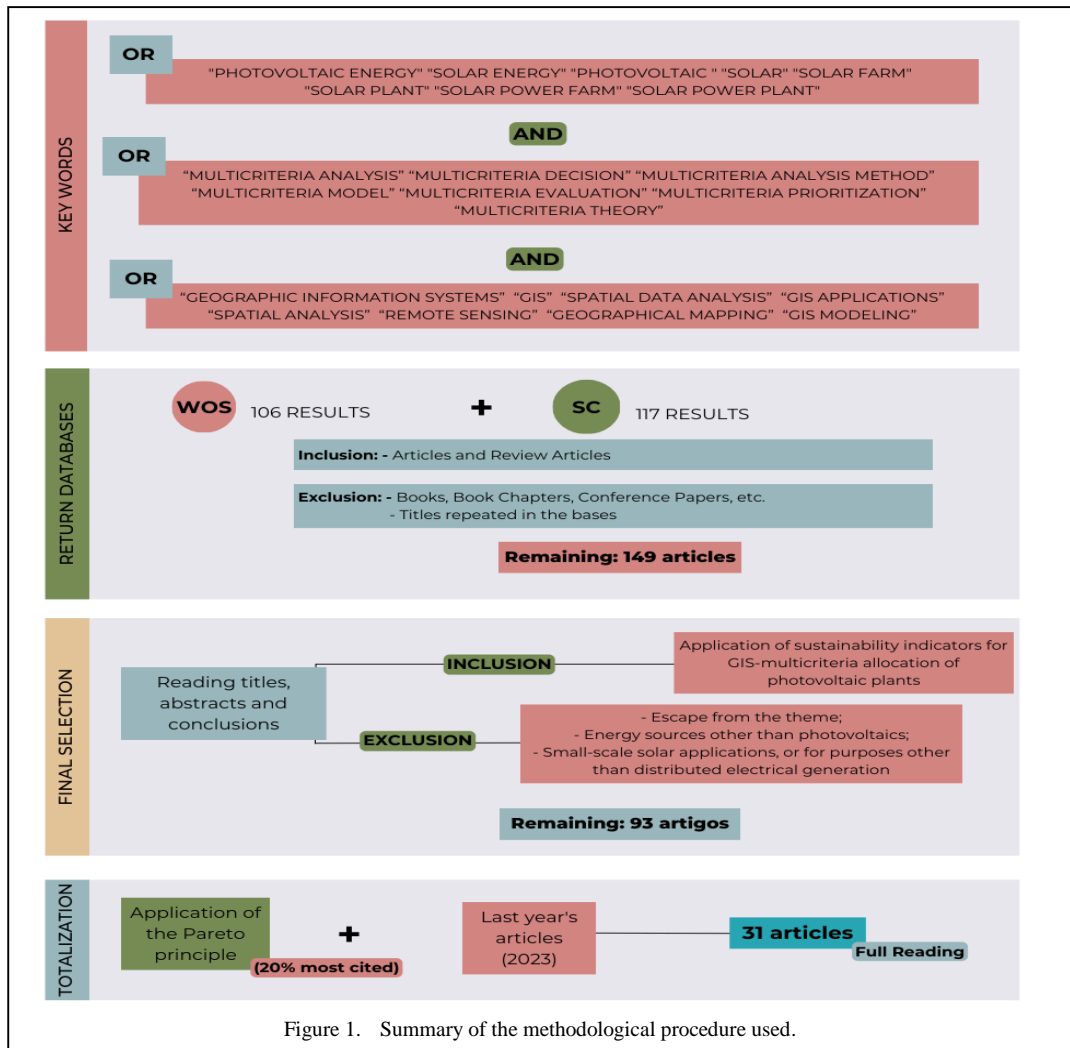


Figure 1. Summary of the methodological procedure used.

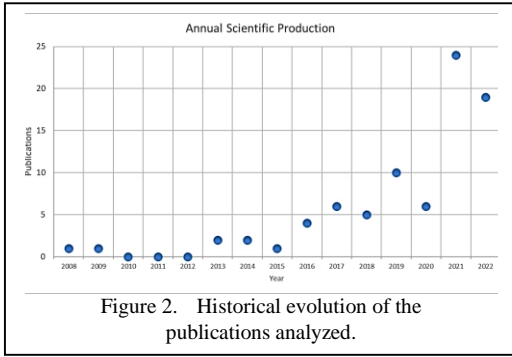
version 1.6.19, the clustering analysis of keywords identified and graphically represented 14 words with a minimum occurrence of 20 times [12]. Finally, using the open-source tool Biblioshiny [13], data on keyword recurrence, authors, articles, most relevant journals, production quantities by country, and a topic analysis on the addressed subjects were extracted and illustrated. It was decided not to illustrate data from the year 2023, as it does not match the reality of the year, since the search was carried out in July 2023.

As the number of remaining papers exceeds 40, the Pareto principle was applied. With this methodology, it is expected that extracting the 20% most cited articles will retain 80% of the most important information on the subject [14]. Therefore, the 19 most cited articles were separated, in addition to the addition of the 12

articles dated from the year of writing of this manuscript (2023), to reveal the most recent information on the subject. Finally, 31 files remained for full reading and comprehensive analysis of the historical evolution of the topic, covering the number of publications, number of citations, most cited articles, influential journals, keywords, interrelationships between topics and trends in density and centrality. This assessment will also include an analysis of the most prominent countries in publications related to the subject, offering a global perspective on scientific contributions.

III. RESULTS AND DISCUSSION

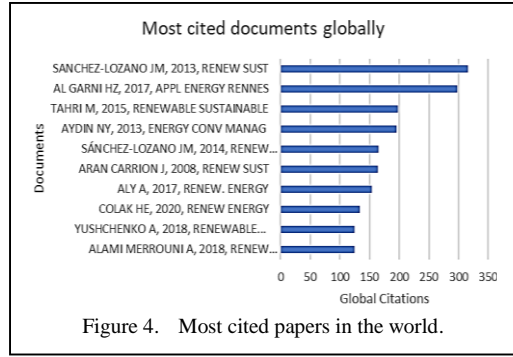
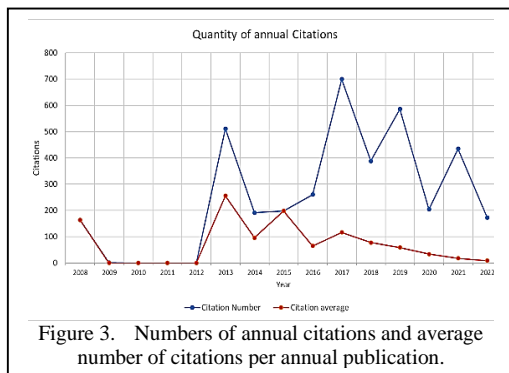
According to the compiled data, the research topic dates back to the last 15 years, commencing in 2008 and displaying a gradual increase in publications, particularly from 2013, with some



years showing substantial growth (2017, 2019, 2021) and others moderate growth (2020, 2022, 2023). The period between 2010 and 2012 reflects varying levels of activity, including years with no publications. Despite a considerable rise until 2021, which became the peak year with 24 publications, this number decreased in 2022 and 2023. Fig. 2 illustrates this temporal distribution.

The first published manuscript, authored by [15], addresses the optimal siting of grid-connected photovoltaic power plants, considering criteria classified into: environment, orography, location, and climate. The selection process was regulated using a model combining multicriteria analysis, Analytic Hierarchy Process (AHP), with GIS technology [15]. In one of the most recent publications, [3] evaluated the TOPSIS as a multicriteria method, also based on GIS and for the same purpose, considering both fuzzy and non-fuzzy principles and based on economic, geographical, climatic, infrastructural, and demographic criteria.

The overall increase in the number of published papers over the years is also reflected in an increase in citations. However, this trend is not linear and varies from year to year, with some years concentrating notable citation values in contrast to others with few or none. Furthermore, there is no direct correlation between the number

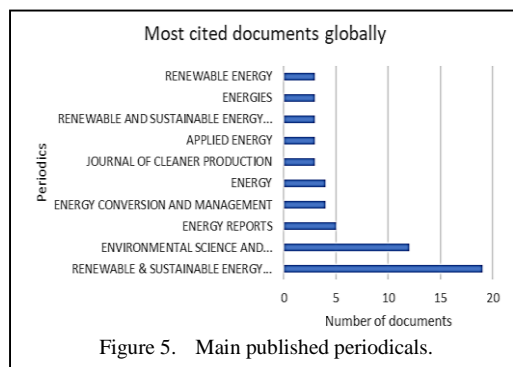


of published articles and the number of citations found, as presented in Fig. 3.

Years 2008, 2013, 2014, 2015, and 2017 especially had a considerably high average of citations, suggesting that articles published during these periods had a significant impact on the scientific community, reflecting their quality. Through Fig. 4, it is observed that some articles have a large number of citations, causing a significant increase in their respective annual averages. Texts from 2022 and 2023 had a relatively low average number of citations, possibly influenced by the number of published papers or their impact.

As depicted, certain manuscripts stood out in terms of their influence. Some examples include: [6] and [16], with 396 and 165 citations, respectively; [17] with 198; [18] with 195; and [15], previously mentioned and yielding 164 references, likely due to its pioneering role.

Despite the limited number of publications on the topic, the high number of citations, even from a few main papers, indicates the content's significant relevance and impact. In support of the material's quality, there was a high standard in the journals in which they were published. As shown in Fig. 5, some sources were responsible for nearly half of the publications. Journals such



as Renewable Energy, Energies, Renewable and Sustainable Energy Reviews, Applied Energy, Journal of Cleaner Production, and Energy together represent 47 publications. In affirming this assertion, the impact factors associated with these journals are highlighted, where, except for “Energies,” the second most recurring with an index of 3.2, the rest fall within the range of 8.7 to 15.9, considered high. The impact factor reflects the average of received citations in a year and the number of articles published in the journal in the two previous years [19]. In addition to these numbers, at the national level, it was noted that these same journals are classified as A1, except “Energies,” classified as A2, in the Qualis Capes quadrennium 2017-2020, a Brazilian system for journal evaluation, considered of high impact, further reflecting the content’s quality [20].

Another important point to highlight is the synthesized information obtained from the analysis of interrelations between the research and its contents. Fig. 6 and 7 provide a visual representation of the most frequent keywords, relations, and semantic patterns, emphasizing key concepts, predominant topics, and contextual associations between specific terms. Most expressions and flows observed translate into the theme of GIS-Multicriteria decision-making for siting photovoltaic power plants. Examples of this pattern can be observed in articles on the selection of the ideal location for photovoltaic solar energy plants using GIS and AHP, through a case study in the Malatya province, Turkey, authored by [21], and the sustainable location of solar energy installations in the Mediterranean, also using a GIS-AHP approach, by [22].

In support of the presented rationale, through the outlined topic graph in Fig. 8, it is possible to gauge the levels of centrality and density of the field of study. According to the explanation by [23], the increase along the horizontal axis indicates the measure of centrality, hence the importance of the topic. The strength between the word links is indicated by their density, which increases along the vertical axis and portrays the

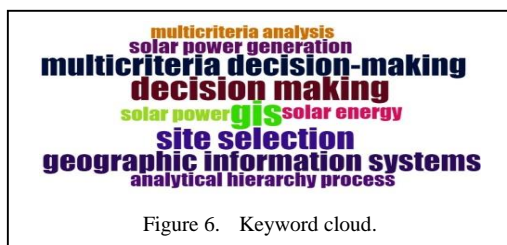


Figure 6. Keyword cloud.

coherence and completeness of the research issues. Finally, the size of each domain is proportional to the number of articles containing the respective keywords [23].

The first quadrant is the central core, composed of the driving themes underlying the study area, indicating a high degree of development, as it is at the apex of the axis growth. In this case, there is an interrelation between the terms expressing a logic related to the application of GIS tools for decision-making under the effects of photovoltaic generation. This observation, along with the considerable size of the graph domain, reaffirms the primary idea developed in this study, as well as highlighting the importance and relevance of the subject.

In the second quadrant, two issues were obtained, characterized as fewer central themes than the previous one but have a considerable internal connection strength, attesting to their maturity as independent research. These singular proportion niches provide insights into investment analysis and cost-benefit using artificial intelligence and information systems as support for multicriteria decision-making.

The third quadrant highlights a marginal area of research with low articulation force within and outside its themes. The listed term on the evaluation of photovoltaic farm siting portrays a superficial research situation, with few relationships. Associated with the fourth quadrant, with low relevance but significant internal connections, the multicriteria decision-making for location selection based on GIS demonstrates a support that relates to other research fields.

Countries with better solar potentials naturally have greater interest in the efficient use of these resources, where geography plays a crucial role in the viability of plants and the use of GIS tools to optimize their locations. Regarding the distribution of publications among countries, it is not uniform, as seen in Fig. 9. While some countries like Iran, Turkey, and Spain have relatively high publication numbers, others have much lower amounts. This fact may reflect differences in developmental stages and access to research resources, as well as national energy policies. Iran, with 12 publications, demonstrates considerable interest in using GIS tools to select sustainable areas for solar plants, possibly related to an interest in diversifying its energy matrix and utilizing sunny weather. With 11 published, Turkey also seems to drive the

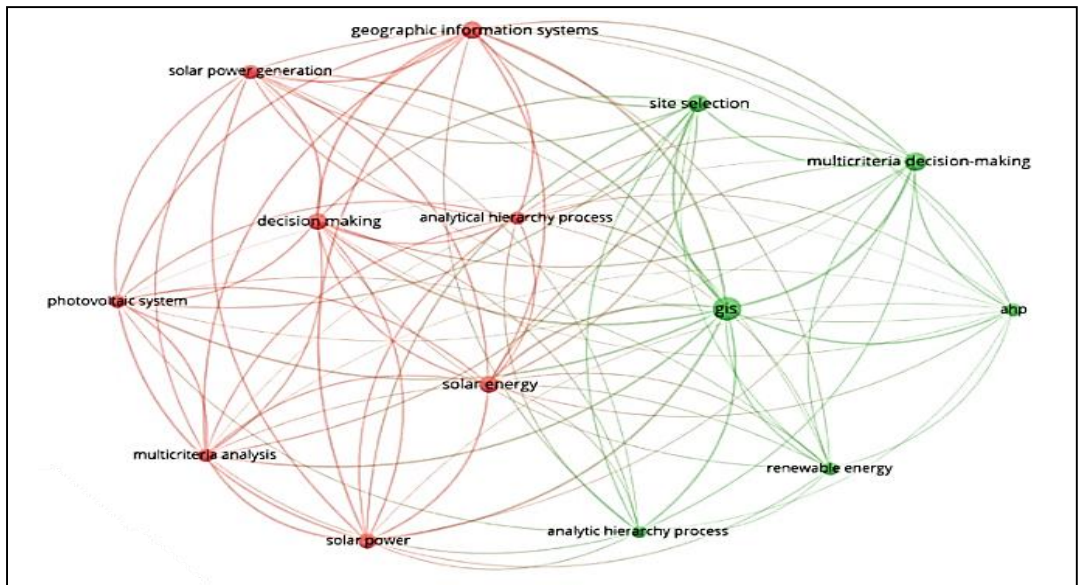


Figure 7. Keyword Cluster Chart.

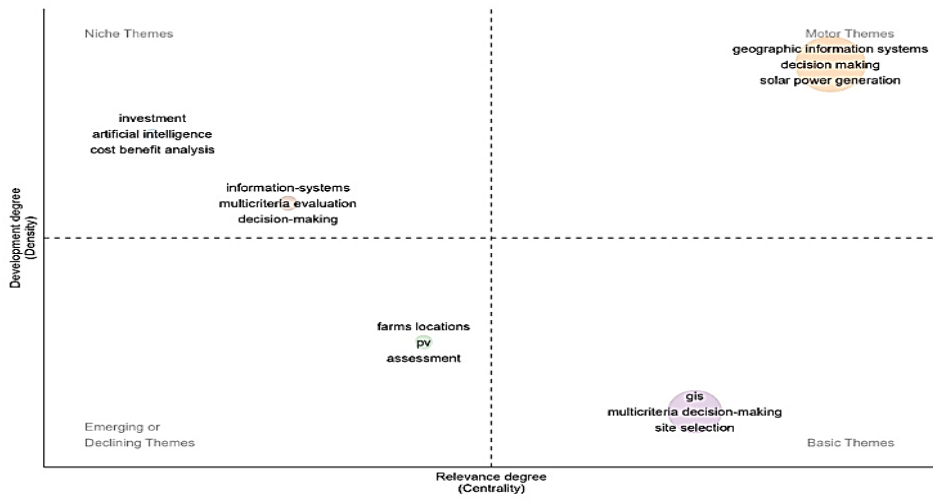


Figure 8. Field of Study Topic Chart.

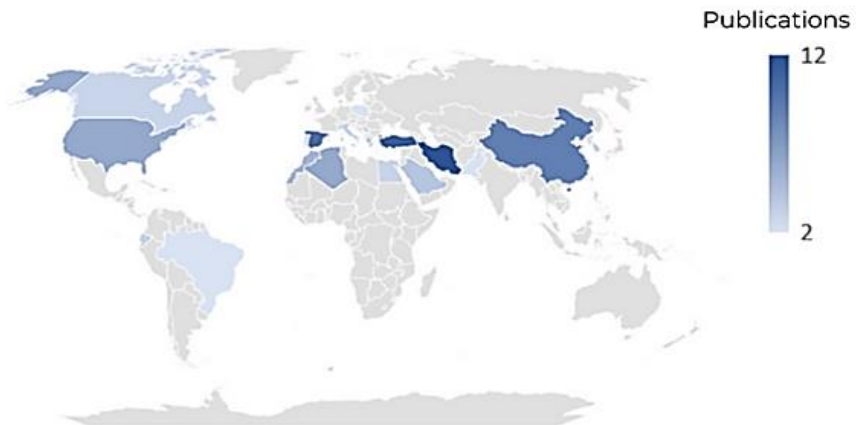


Figure 9. Spatial distribution of publications.

in its matrix.

The share of renewable energies in its matrix Spain and China, still in the top rankings (10 and 9 articles respectively), reflect initiatives in renewable energies, exploring ways to optimize the location of solar plants to maximize energy efficiency and significant investments in solar technology and research in these countries. Additionally, other highlighted countries, including Algeria, Saudi Arabia, and Morocco, known for strong oil dependence, show interest in solar plants and sustainability, indicating an intention to diversify their energy sources and reduce vulnerability to fossil fuel prices.

It's noticeable that some countries have fewer publications compared to others, even those with good solar indices, like Brazil, Ecuador, and Egypt. These countries may not focus on academic research on solar plants based on GIS tools, but rather direct their efforts into implementing solar projects, attracting investments, or other practical aspects. However, these low counts also represent opportunities to advance the use of GIS technologies in energy decisions.

IV. CONCLUSIONS

In summary, the analysis covered compiled data from the last 15 years, revealing a significant yet unstable evolution in research on the selection of sites for photovoltaic plants using a GIS-Multicriteria approach. The trends make it clear that this approach has emerged as an effective method to assess project viability. From pioneering article to the most recent approaches, researchers have been dedicated to improving these methodologies to consider environmental, economic, and geographical criteria in selecting the best locations.

Although there isn't a large number of publications, some papers stand out due to a considerable number of citations, pointing to their lasting impact in the scientific community. The selection of journals for publication also reflects the quality of the content, with several articles published in highly relevant journals. In summary, the combination of multicriteria parameters and GIS has established itself as an effective method, with relevant and impactful studies that have contributed to the understanding and sustainable and efficient Selection: Highlight all author and affiliation lines.

ACKNOWLEDGMENT

This work was carried out with the support of the Coordination for the Improvement of Higher Education Personnel – Brazil (CAPES) – Financing Code 001.

REFERENCES

- [1] Bohra, S. S., & Anvari-Moghaddam, A. (2021). A comprehensive review on applications of multicriteria decision-making methods in power and energy systems. *International Journal of Energy Research*, 46(4), 4088-4118.
- [2] Villacreses, G., Jijón, D., Nicolalde, J. F., Martínez-Gómez, J., & Betancourt, F. (2022). Multicriteria Decision Analysis of Suitable Location for Wind and Photovoltaic Power Plants on the Galápagos Islands. *Energies*, 16(1), 29.
- [3] Hooshangi, N., Gharakhanlou, N. M., & Razin, S. R. G. (2023). Evaluation of potential sites in Iran to localize solar farms using a GIS-based Fermatean Fuzzy TOPSIS. *Journal of Cleaner Production*, 384, 135481.
- [4] Almasad, A., Pavlak, G., Alquthami, T., & Kumara, S. (2023). Site suitability analysis for implementing solar PV power plants using GIS and fuzzy MCDM based approach. *Solar Energy*, 249, 642-650.
- [5] Rekik, S., Alimi, S. E. (2023). Optimal wind-solar site selection using a GIS-AHP based approach: a case of Tunisia. *Energy Conversion and Management: X*, 18, 100355.
- [6] Sánchez-Lozano, J. M., Teruel-Solano, J., Soto-Elvira, P. L., García-Cascales, M. S. (2013). Geographical Information Systems (GIS) and Multi-Criteria Decision Making (MCDM) methods for the evaluation of solar farms locations: case study in south-eastern Spain. *Renewable and Sustainable Energy Reviews*, 24, 544-556.
- [7] Van Raan, A. (2019). Measuring Science: basic principles and application of advanced bibliometrics. In *Springer Handbook of Science and Technology Indicators* (pp. 237-280). Elsevier BV.
- [8] Hannigan, T. R., Haans, R. F. J., Vakili, K., Tchalian, H. V., Glaser, V. L., Wang, M. S., Kaplan, S., & Jennings, P. D. (2019). Topic Modeling in Management Research: rendering new theory from textual data. *Academy of Management Annals*, 13(2), 586-632.
- [9] Zhu, J., & Liu, W. (2020). A tale of two databases: the use of Web of Science and Scopus in academic papers. *Scientometrics*, 123(1), 321-335.
- [10] POSIT. (2023). *Rstudio Desktop*. Available in: <https://posit.co/download/rstudio-desktop/>.
- [11] Microsoft. (2023). *Microsoft Excel*. Available in: <https://www.microsoft.com/pt-br/microsoft-365/excel>
- [12] Van Eck, N. J., & Waltman, L. (2023). *Leiden University's Centre for Science and Technology Studies*. VOSviewer.
- [13] Bibliometrix. (2023). *Biblioshiny*. Available in: <https://www.bibliometrix.org/home/index.php/layout/biblioshiny>.
- [14] Thamaraiselvi, M., Lakshmi, S., Manthiramoorthi, M., Thirumagal, A. (2020). *Application of bibliometrics*

- laws in scientometric journal publications during 2010 - 2019: a scientometric analysis.*
- [15] Arán-Carrion, J., Ramos-Ridao, A. F., Aznar-Dols, F., Hernández, E. A., & Espín-Estrella, A. (2009). A multicriteria evaluation model to optimally place grid-connected photovoltaic power plants. *Renewable Energy and Power Quality Journal*, 1(07), 712-715.
- [16] Sánchez-Lozano, J. M., Antunes, C. H., García-Cascales, M. S., Dias, L. C. (2014). GIS-based photovoltaic solar farms site selection using ELECTRE-TRI: evaluating the case for Torre Pacheco, Murcia, southeast of Spain. *Renewable Energy*, 66, 478-494.
- [17] Tahri, M., Hakdaoui, M., & Maanan, M. (2015). The evaluation of solar farm locations applying Geographic Information System and Multi-Criteria Decision-Making methods: case study in southern Morocco. *Renewable and Sustainable Energy Reviews*, 51, 1354-1362.
- [18] Aydin, N. Y., Kentel, E., & Duzgun, H. S. (2013). GIS-based site selection methodology for hybrid *Renewable Energy* systems: a case study from western Turkey. *Energy Conversion and Management*, 70, 90-106.
- [19] Clarivate Analytics. (2023). *Impact Factor*. Available in: <https://clarivate.com/webofsciencegroup/essays/impact-factor/>.
- [20] CAPES - Coordination for the Improvement of Higher Education Personnel. (2023). *Ministry of Education. Qualis Periódicos*. Available in: <https://sucupira.capes.gov.br/sucupira/public/consultas/coleta/veiculoPublicacaoQualis/listaConsultaGeralPeriodicos.jsf>.
- [21] Colak, H. E., Memisoglu, T., & Gercek, Y. (2020). Optimal site selection for solar photovoltaic (PV) power plants using GIS and AHP: a case study of Malatya Province, Turkey. *Renewable Energy*, 149, 565-576.
- [22] Giamalaki, M., & Tsoutsos, T. (2019). Sustainable siting of solar power installations in the Mediterranean using a GIS/AHP approach. *Renewable Energy*, 141, 64-75.
- [23] Wei, Z., Liu, H., Tao, X., Pan, K., Huang, R., Ji, W., & Wang, J. (2023). Insights into the application of machine learning in industrial risk assessment: a bibliometric mapping analysis. *Sustainability*, 15(8), 6965.

Study of Optimal Injection of Renewable Energy into Distribution Power Grid

Yao Bokovi¹, Aka Odoh², Moyème Kabe³, Adekunlé Akim Salami⁴

^{1,2,4}Departement de Génie Electrique, Laboratoire de Recherche en Sciences de l'Ingénieur (LARSI), Ecole Polytechnique de Lomé (EPL), Lome, Togo

^{1,2,3,4}Centre d'Excellence Régional pour la Maîtrise de l'Electricité (CERME), University de Lome (UL), Lome, Togo

¹bokoviyao@gmail.com, ²odohdieudonne1@gmail.com, ³danielkabe2@gmail.com, ⁴akim_salami@yahoo.fr

Abstract—The integration of renewable sources into the power grid has currently become an essential necessity for these technical and economic advantages and to preserve the environment. However, a rate of integration of these renewable energies, in an uncontrolled manner, into existing power grid, could have harmful effects on the latter, hence the need to find a way to avoid these problems. In this work, studies are carried out to, firstly, show that the integration of decentralized sources in an uncontrolled manner has harmful effects on the host power grid, in particular overvoltages which disrupt the protection equipment and finally, secondly, a study is made for the integration of decentralized sources in an optimal way and this by searching for the best location and the adequate power to inject. The method used in this work is based on several steps including the correct choice of the voltage at the connection point, the calculation of the grid reception capacity which corresponds to the maximum power of Distributed Source DS to be injected, the limit of the rate harmonics in the power grid guaranteeing the quality of the energy supplied and finally the search for the location of the DS connection. This study is applied on the standard IEEE 14 node power grid under the Power World Simulator software and also on the IEEE 15 node radial power grid under Simulink/Matlab. The application of this method made it possible to show, as results, the importance of injections of renewable energies into the power grid such as the correction of voltage drops and the filling of energy deficits.

Keywords - renewable energies, power grid, injections, reception capacity

I. INTRODUCTION

The integration of renewable sources into the distribution power grid has currently become an unavoidable necessity not only for its technical, economic [1] and environmental advantages but also for the problems it generates, mainly [2,3] overvoltage problems and network stability. Several studies have been carried out showing the contribution to reducing the energy deficit by injecting photovoltaic energy onto the distribution power grid [4,5]. Impact studies have also been carried out on the use of FACTS devices in the integration of renewable sources into distribution power grids [6].

The objective of this study is to inject photovoltaic solar renewable energies into the MV distribution power grid without major incidents while guaranteeing the security of the latter.

The method used in this work is based on several steps including the correct choice of the voltage at the identified connection point, the calculation of the network reception capacity in terms of the maximum power of the Distributed Source (SD to be injected there, the limit the harmonic rate in the power grid by guaranteeing the quality of the energy supplied and finally the search for the location of the SD connection by controlling the voltage profile.

After the introduction, the methods and materials used in this paper are first presented by the modeling and simulation of the power distribution grid by SIMULINK/MATLAB with the case of the IEEE 15 BUS RADIAL network. Then the results obtained are shown and finally followed by discussion and conclusion.

II. THE METHOD

The method used is based on five steps including:

- modeling of the power grid studied;
- calculation of power flow;
- connection of the PV generator;
- calculating the reception capacity;
- voltage profile control at power grid nodes and evaluation of harmonic distortion rate correction.

A. Modeling of Power Grid Studied

Fig. 1 shows the IEEE 15 Bus Radial network modeled with Simulink under MATLAB for the study.

B. Correction Power Flow Calculation

The study of power flow is an essential step in any serious analysis of a power grid. Indeed, it

makes it possible to calculate the quantities of a power grid in balanced steady state, namely the modules and phases of the voltages at any point of the grid.

From these, we can calculate the currents in the transmission lines, the active and reactive powers transmitted and the power losses caused during the transport of electrical energy. This analysis is very important for the studies, planning and operation of a power grid [7].

C. Connecting the PV Generator

Fig. 2 shows the connection of the PV generator to the IEEE 15 Bus Radial power grid.

D. Calculation of Reception Capacity

The reception capacity at a given node of a power grid (Fig. 3) is the maximum connection power which respects at any time the voltage and current constraints on the entire power grid considered. Under the deterministic approach to producer connection studies, the maximum connection power P_{racmax} at a node k corresponds to the maximum power that can still be injected into this node when the existing production is maximum and the existing consumption is minimum on the departure considered.

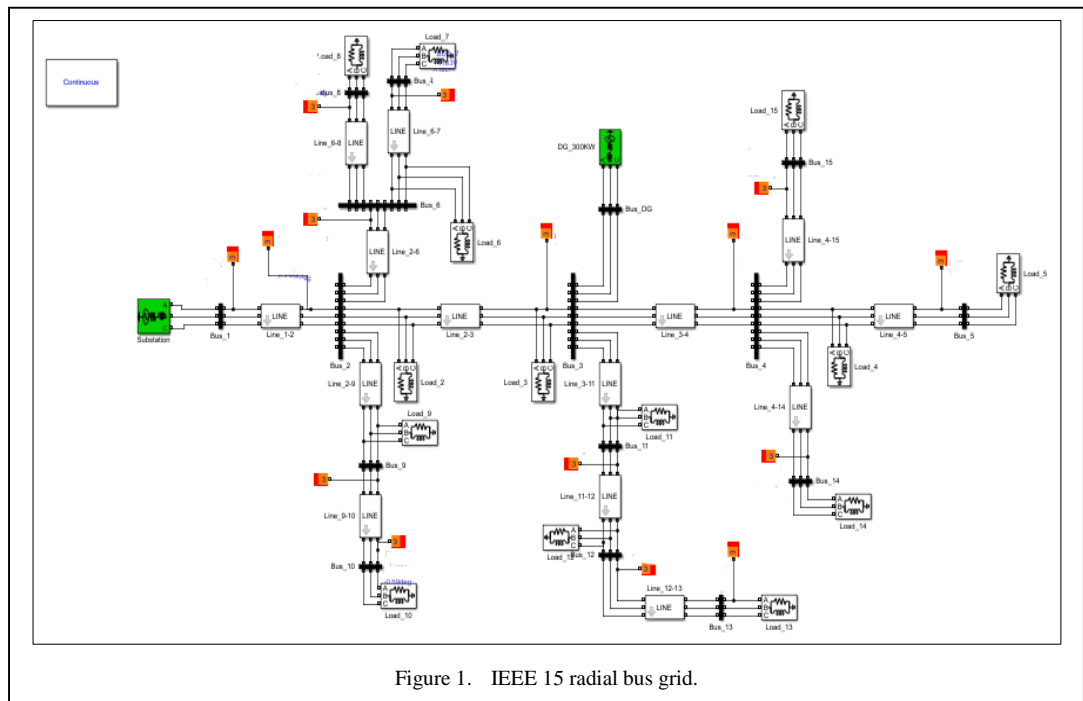


Figure 1. IEEE 15 radial bus grid.

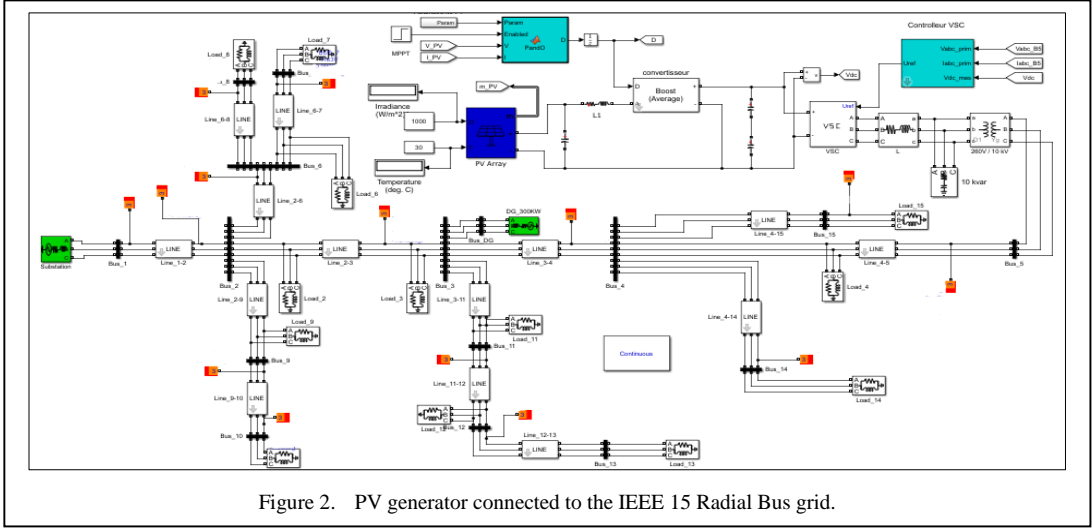


Figure 2. PV generator connected to the IEEE 15 Radial Bus grid.

It is calculated by the Eq. (1) [3,8]:

$$P_{raccmax} = \frac{U_{max}^2 - U_0^2 + (2\varepsilon - \varepsilon^2)(RP_{cmin} + XQ_{cmin})}{2\varepsilon(R + Xtang(\varphi))} \quad (1)$$

with $\varepsilon = l/L$,

- L , R and X : length, resistance and reactance of the departure;
- P_{cmin} and Q_{cmin} : the minimum active and reactive powers consumed on departure;
- $Tan(\varphi)$: the production tangent associated with $P_{raccmax}$ at distance 1;
- U_0 : the secondary voltage of the upstream transformer;
- U_{max} : the maximum allowable voltage at the distance l from the substation.

E. Voltage Profile Check at Network Nodes and Harmonic Distortion Rate Evaluation

This is a crucial step in the process of determining the optimal power to be injected into the network without disruption for the latter. It ensures the quality of the energy supplied.

Harmonic currents are due to the presence of non-linear electrical charges in an electrical grid. Due to the impedances of the network, these harmonic currents are the cause of the appearance of voltage harmonics which then

affect other customers of the distribution power grid.

III. MATERIALS

A. Simulink/MATLAB

Simulink is a functional diagram environment intended for multi-domain simulation and the Model-Based Design modeling approach. It is integrated with MATLAB, which allows MATLAB algorithms to be incorporated into models and the results of simulations to be exported to MATLAB to complete analyzes [9]. It was used in this work for power flow calculations and analyzes of harmonic distortion rates in the power grid.

B. Power Grid Studied

The IEEE 15 BUS RADIAL network is used, consisting of 02 generators, 14 electrical lines and 11 loads. Node 01 is taken as the reference node and all phase angles have an initial value of 0.0° .

The data from this test power grid made up of 15 nodes are summarized in Tables I and II.

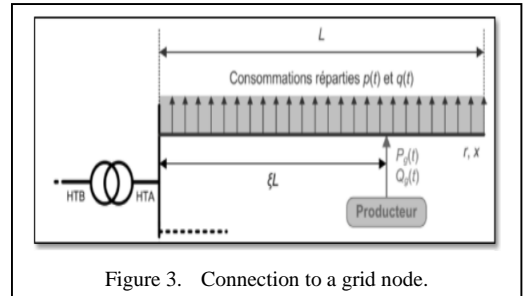


Figure 3. Connection to a grid node.

TABLE I. IEEE 15 RADIAL BUS POWER GRID DATA.

	V_{ref} (pu)	V_{angle}	P_{gen} (MW)	Q_{gen} (MVar)	P_{Load} (MW)	Q_{Load} (MVar)
BUS_1	1.0200	0	0	0	0	0
BUS_2	1.0000	0	0	0	0.0441	0.0450
BUS_3	1.0000	0	0.0700	0.0714	0.0003	0
BUS_4	1.0000	0	0	0	0.1400	0.1428
BUS_5	1.0000	0	0	0	0.0441	0.0450
BUS_6	1.0000	0	0	0	0.1400	0.1428
BUS_7	1.0000	0	0	0	0.0700	0.0714
BUS_8	1.0000	0	0	0	0.1400	0.1428
BUS_9	1.0000	0	0	0	0.0700	0.0714
BUS_10	1.0000	0	0	0	0.0441	0.0450
BUS_11	1.0000	0	0	0	0.0700	0.0714
BUS_12	1.0000	0	0	0	0.0441	0.0450
BUS_13	1.0000	0	0	0	0.1400	0.1428
BUS_14	1.0000	0	0	0	0.1400	0.1428

TABLE II. IEEE 15 LINES POWER GRID DATA.

From BUS	To BUS	R (en ohm)	X (en ohm)
1	2	1.35309	0.0035107
2	3	1.17024	0.0030363
2	8	2.55727	0.0045754
2	9	2.01317	0.0036019
3	4	0.84111	0.0021823
3	11	1.79553	0.0032125
4	5	1.53248	0.0027258
4	14	2.23081	0.0039913
4	15	1.19702	0.0021417
6	7	1.0882	0.0019470
6	8	1.25143	0.0022390
9	10	1.68671	0.0030178
11	12	2.44845	0.0043807
12	13	2.01317	0.0036019

IV. RESULTS AND DISCUSSIONS

A. Results

The power grid being modeled using Simulink (Fig. 1), an analysis of the power flow was carried out in order to obtain the state of the grid data before moving on to connecting the PV generator to the latter as shown in Fig. 2.

Initially, the network parameters are summarized in Table III.

Two scenarios were studied in this work by injecting renewable energy into two locations to assess the impacts of each.

In each scenario, the network capacity is calculated at the indicated node where the quality of the energy supplied has also been evaluated by checking the voltage profile and the harmonic distortion rate.

TABLE III. CHARACTERISTICS OF THE NETWORK STUDIED.

Start length L	10 km
Nominal voltage One	10 KV
U_o voltage set point	1.02A or 10.2 KV
U_{max} maximum permissible voltage (taking into account an uncertainty margin of 1%)	1.03A or 10.3KV
Maximum active power consumption on the depart P^*_{max}	1.26 MW
Minimum active power consumption on the $P^*_{cmindepart}$	0.2 P^*_{max} or 0.252 MW
Minimum reactive power consumption on the $Q^*_{cmindepart}$	0.4 P^*_{cmin} or 0.1 MVar

Case 1: $\varepsilon=1$ (BUS 5)

Here the connection is made at the end of the main spoiler (to bus 5), knowing that the PV generators do not produce reactive power ($\text{tang}(\varphi)=0$). The capacity of the power grid for using Eq. (1) and the data in Table III, is:

$$P_{raccmax} = \frac{10300^2 - 10200^2 + (2-1^2)}{2 \times 2.2} \times \frac{(2.2 \times 0.25 \times 10^6 + 0.9 \times 0.1 \times 10^6)}{2 \times 2.2} \quad (2)$$

$$P_{raccmax} = 0.6114 \text{ MW} . \quad (3)$$

- Evaluation of the quality of the energy to be injected into the network

In this study, we performed several simulations to evaluate the maximum power of the PV generator that can be connected to the grid, at the same time we evaluated the quality of the energy for each case. The results found are presented in Table IV.

TABLE IV. SIMULATION RESULTS WITH END-OF-LINE PV GENERATOR.

	Injected power (MW)	Network voltage at connection point (pu)	THD (%)	The quality of energy
1	0.2	0.995	2.54	Good
2	0.4	0.998	2.93	Good
3	0.6	1	3.2	Good

- Interpreting

For the case of $\varepsilon = 1$, the connection of the PV generator does not affect the energy quality, the harmonic rate remains below the acceptable limit. The maximum capacity of the PV generator to connect to the network is 0.6114 MW, thus 0.6114 MVA.

Case 2: $\varepsilon = 0.5$ (BUS 3)

Here the connection is made to bus 3 of the main altère.

- The capacity of the network

Using Eq. (1) and the data in Table III, the capacity becomes $P_{raccmax} = 1.15 \text{ MW}$.

- Evaluation of the quality of the energy to be injected

Table V shows the results found after simulation.

TABLE V. SIMULATION RESULTS WITH PV GENERATOR ON BUS 3.

	Injected power (MW)	Network voltage at connection point (pu)	THD (%)	The quality of energy
1	0.8	1	4.12	Good
2	0.9	1	5.01	Bad
3	1	1	5.27	Bad
4	1.15	1.13	5.53	Bad

- Interpreting

We notice that the more the nominal power of the PV generator increases, the more the rate harmonics exceeds the threshold set by the standard and an overvoltage begins to be observed on the injection bus (BUS 3). The maximum capacity of the PV generator depends on the distance which separates it from the source. For this case, the maximum power to be injected into the network is 1 MW, provided that harmonic filtering means are provided.

B. Discussion

From this study it can be seen that the closer we get to the main source, the greater the reception capacity of the power grid becomes. This makes it possible to make an optimal choice of the location of the PV generator depending on the availability of sunshine.

We also note that as the power to be injected increases, the rate of harmonic distortion increases as well as the risk of overvoltage, hence the need to make progressive injections to better assess the behavior of the grid according to these connections.

V. CONCLUSION

Over time, the demand for electrical energy continues to grow, which requires an increase in production to meet the strong demand from consumers. The insertion of distributed productions into distribution networks is today an established and recognized advance. Because of this strong integration of energies news based on renewable resources, electricity networks are undergoing disturbances of several parameters and especially of tension. The operating plan classic distribution networks has been called into question. Indeed the arrival of its energies has not fact that increases the risk of imbalance because of their unpredictable characteristics due to meteorological phenomena.

The introduction of productions distributed to the networks is done at the level of the networks of distribution because of their low production rates compared to production plants classics and for its participation in tension adjustment. Their connections cause several impacts on all aspects of an electrical network, such as protection, frequency, as well as voltage. The impacts affect several aspects of tension such as stability, its hold, etc.

REFERENCES

- [1] Boubekeur, M., & Argilos, A. (2023). Integration of renewable energy sources in Algeria, Realisation and perspective. *Modern Economic and Sustainable Development*, 6(1), 71-83.
- [2] Gougui, A. *Study and experimentation of a hybrid system photovoltaic/hydrogen for system integration electric* (Doctoral dissertation, Université de Ouargla-Kasdi Merbah).
- [3] Soukaina, N. (2017). *Impact de l'intégration des énergies renouvelables au réseau de distribution HTA*.
- [4] Djeddi, S. (2023). How do renewable energies contribute to the development of the agricultural sector in Algeria?. *Revue des Réformes Economiques et Intégration En Economie Mondiale*, 71(17).
- [5] Gahou, J. H. (2017). Etude de L'Impact de L'Injection de L'Energie D'Une Centrale Photovoltaïque de 60 MVA sur le Réseau Electrique de la Sbee de la Ville de Natitingou.
- [6] Madiha, M. (2012). Etude de la stabilité d'une ferme éolienne connectée à un réseau électrique avec des dispositifs FACTS. *Mémoire de Magister, Université FERHAT Abbas—Setif*.
- [7] http://espace.etsmtl.ca/id/eprint/2245/1/AMOR_Wael.pdf
- [8] Pham, T. T. H. (2006). *Impacts of dispersed generation on the management of critical infrastructures of electrical power system*.
- [9] Lahatry, N. (2017). *Nal_Espa_Mast2_2017.pdf*.

Structural, Microstructural, Optical, and Electrical Properties of Nickel Doped Tin Oxide Films by PSP Method for Photovoltaic Application

Roguai Sabrina¹, Djelloul Abdelkader²

^{1,2}Department of Science of Matter, Abbes Laghrour University, khenchela, Algeria

¹rog.sabrina@yahoo.fr

Abstract—In this study, we used a pneumatic spray pyrolysis technique at 450°C to deposit Sn1 - xNi_xO₂ thin films 0.0 ≤ x ≤ 0.10 on glass substrates. The influence of doping content on the films structural and optical was investigated. Structural characterization by X-ray diffraction indicated that the rutile phase of SnO₂ is present in all thin films, and crystallite sizes are estimated to be in the range of 27–47nm. The optical bandgap energy increases from 3.83 to 4.01 eV as the dopant content increases according to the Burstein-Moss effect. Resistivity is affected by doping and the thickness of thin films. The lowest resistivity of 1.32x10⁻²cm and the maximum conductivity of 75cm⁻¹ was found at a Ni content of 2%.

Keywords - thin films, PSP method, X-ray diffraction, optical properties, electrical properties

I. INTRODUCTION

As a result of their unique structural (suitable textured morphology), electrical (relatively low resistivity, on the order of 10-15Ωsq⁻¹), and optical (high optical transmittance) characteristics, transparent semiconductor oxide (TCO) thin films have been the subject of intense research for several years [1,2]. These materials are very important from a technological point of view, and their applications are extremely diverse; they are found in sectors such as electronics [3], silicon solar cells [4], optoelectronics [1] and photovoltaic conversion [4]. Tin oxide is one of these chemicals (SnO₂).

In this work, thin films of pure and Ni doped SnO₂ films are deposited by pneumatic spray pyrolysis (PSP) technique onto glass substrates at 450°C for 30min. This technique has several advantages, such as the possibility of using high purity precursors, the ease of deposition on large surfaces and complex shaped substrates, and all this at low temperatures and low cost [5]. The general principle of this technique is based on the vaporization and the projection of a solution of various reactive compounds, using an atomizer, on a heated substrate. The temperature of the substrate allows the activation of the chemical reaction between the compounds. The experiment can be carried out in air, and can be prepared in a chamber (or in a reaction chamber) under a vacuum reaction chamber with a vacuum of about 50Torr. The description of the film formation by the spray pyrolysis method can be summarized as follows: (1) Formation of droplets at the nozzle outlet. (2) Decomposition of the precursor solution on the surface of the heated substrate by pyrolysis reaction [6]. In general, the systems used to produce a spray stream fall into two categories: Pneumatic spray (PSP) technique: in this case, it is the effect of the pressure of the carrier gas that causes the liquid to be sprayed in fine droplets. Ultrasonic spray technique: in this case, the atomization of the liquid is produced by ultrasonic waves. Several studies have been using pneumatic spray pyrolysis technique [7]. The effects of the doping on structure and optical properties are discussed.

II. MATERIALS AND METHOD

A. Film Preparation

In this the thin films of pure and nickel-doped tin oxide at 2 at%, 5 at%, and 10 at% of Ni were prepared by pneumatic spray pyrolysis on a glass substrate, using tin chloride dehydrate content [SnCl₂-2H₂O] (purity: 99.99%) as a precursor, and nickel chloride [Ni] (purity: 90.00%) as a doping source. The sputtering solution was prepared from a mixture of tin chloride [SnCl₄, 2H₂O] (Fulka 99.9%) (0.6g) dissolved in 10ml of distilled water (resistivity = 18.2 MXcm) and 10 ml of methanol (CH₃OH) (Merck 99.5%) with a source of nickel (NiCl₂-6H₂O) (Fulka 99.9%) for different doping concentrations (2, 5 and 10 at%). This solution was agitated for 1h using a heated magnetic stirrer at room temperature. The thin films are deposited onto microscope cover glass substrates (30×12×1.2mm³) unheated at 450°C.

B. Characterization Techniques

The structure of the films is characterized by X-ray diffraction (Rigaku Ultima IV equipped with Cu-K α radiation, 0.15418nm). The optical properties are determined by measuring the transmittance of the films using a SpectroScan 80D spectrophotometer UV-vis in the 190–1100nm spectral range.

III. RESULTS AND DISCUSSION

A. Structure And Microstructure Analysis

The XRD spectra of SnO₂, Sn_{1-x}Ni_xO₂ [0.0 ≤ x ≤ 0.10] thin films, obtained by the pneumatic pyrolysis technique, is shown in Fig. 1 this shows that all the films crystallize into a rutile-like tetragonal structure of SnO₂ according to JCPDS card no: 77-0452, by the presence of peaks with directions (110), (101), (200), (211), (310) and (301) [8]. Moreover, the

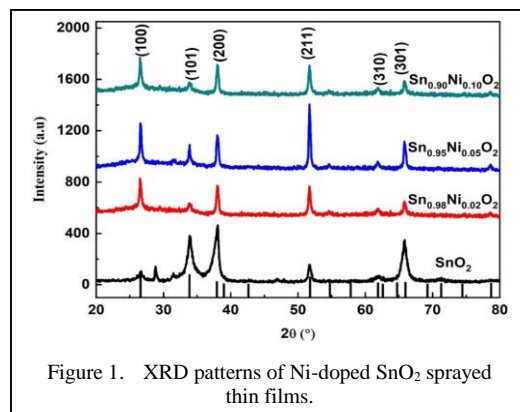


Figure 1. XRD patterns of Ni-doped SnO₂ sprayed thin films.

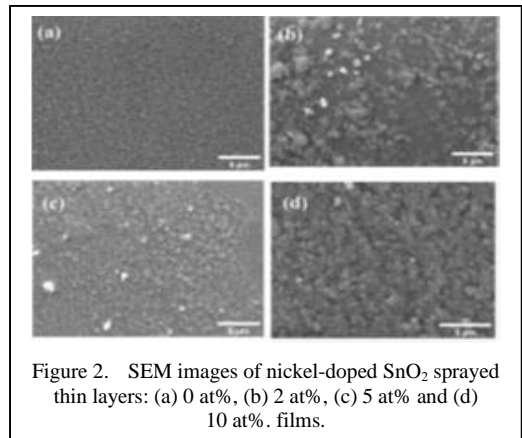


Figure 2. SEM images of nickel-doped SnO₂ sprayed thin layers: (a) 0 at%, (b) 2 at%, (c) 5 at% and (d) 10 at% . films.

XRD spectra confirm the absence of another diffraction peak related to metal clusters and/or oxide impurity phases such as NiO, NiO₂, which confirm the insertion of Ni into the SnO₂ lattice.

B. Structure And Microstructure Analysis

In Fig. 2 we performed microstructural studies of pure and nickel-doped SnO₂ thin films to highlight some effects due to the change in doping content. Scanning electron microscopy (SEM) micrographs of the surface of Sn_{1-x}Ni_xO₂ layers (x = 0.02, 0.05, 0.10) are shown in Fig. 3, respectively. The SEM observations showed that the Ni-SnO₂ layers have tightly packed regular grains with an almost smooth grain surface, fine and small grain size distribution, with no pin-holes and fissures.

C. Optical Analysis

Fig. 3 shows the variation of the transmittance as a function of the wavelength in the range [190–1100 nm] for the undoped and Ni-doped SnO₂ samples prepared at different contents (2, 5 and 10 at%). It can seem that all the layers show good optical transparency in the visible range, with a transmission value that varies between 76 and 82% in the visible range after doping. This result shows that Ni doping improves the optical properties that have an important role in photovoltaic devices [9,10]. It is also noted that the 10 at% Ni-doped layer has the highest transparency in the visible range. In addition, the transmission edge shifts to lower wavelengths (blue shift) with the doping, resulting an increase in the optical bandgap energy is noticed at values of 3.83, 3.98, 3.99, and 4.01 eV for the SnO₂, Sn_{0.98}Ni_{0.02}O₂, Sn_{0.95}Ni_{0.05}O₂, and Sn_{0.90}Ni_{0.10}O₂ thin films, respectively. This increase can be explained by the distortions caused in the

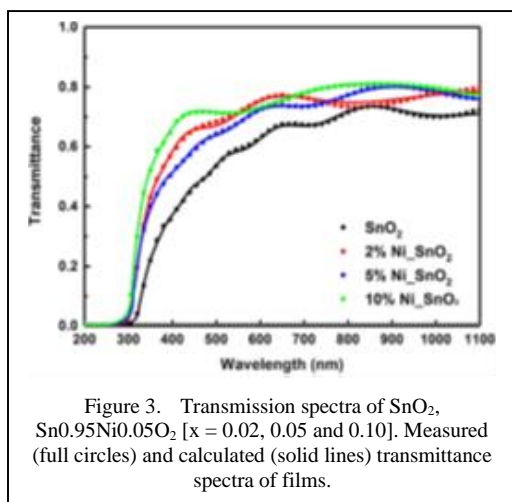


Figure 3. Transmission spectra of SnO_2 , $\text{Sn}_{0.95}\text{Ni}_{0.05}\text{O}_2$ [$x = 0.02, 0.05$ and 0.10]. Measured (full circles) and calculated (solid lines) transmittance spectra of films.

crystallographic lattice of SnO_2 . It can also be found that the introduction of more Ni gives an increase in the optical bandgap energy. This increase is often reported in the literature and is referred to as the Burstein-Moss effect [11]. This can be due to the increase in the number of charge carriers (electrons) from the donor Ni^{2+} ions that are incorporated into the substitutional or interstitial locations of the Sn_{4+} cation. This rise in the optical bandgap energy values confirms the incorporation of Ni^{2+} ions into the SnO_2 host lattice, which is in agreement with the XRD results.

D. Electrical Properties

The electrical properties of SnO_2 thin films are of considerable interest, especially with respect to the applications envisaged in the optoelectrical field. We recall that our main objective is to improve and optimize the electrical conductivity of the films while maintaining high optical transparency with doping [12,13]. The effect of nickel doping on the resistivity of SnO_2 : Ni films are presented in Table I. To further test the homogeneity of our samples, we measured the square resistance at different points as presented in Table I.

The resistivity and conductivity values of the films are grouped in Table I. It is noticed that the conductivity (resistivity) increases (decreases) by 64, 75, 32, and 40 $\Omega\cdot\text{cm}^{-1}$, (by 1.56, 1.32, 3.12, and 2.50 $\times 10^{-2}\Omega\cdot\text{cm}$) with the content of doping (0%, 2%, 5%, and 10 at%) respectively. In other words, the decrease in resistivity (increase in conductivity) as a function of doping content is probably due to the decrease in thickness of the thin films prepared.

TABLE I. ELECTRICAL PROPERTIES OF THE SnO_2 , $\text{Sn}_{1-x}\text{Ni}_x\text{O}_2$ [$x = 0.00, 0.02, 0.05$, AND 0.10] FILMS.

Samples	Resistance, Ω	Resistivity ($\times 10^{-2}$), $\Omega\cdot\text{cm}$	Conductivity, $\Omega^{-1}\cdot\text{cm}^{-1}$
SnO_2	220	1.56	64
2%Ni- SnO_2	380	1.32	75
5%Ni- SnO_2	600	3.12	32
10%Ni- SnO_2	500	2.50	40

The lowest resistivity was found in the case of the 2 at% Ni film ($\rho_{\text{min}} = 0.132\Omega\cdot\text{cm}$). This decrease in resistivity is possibly due to the replacement of the Sn^{4+} cation by cations from doping (Ni^{2+} ion) in substitutional or interstitial locations. The presence of a small percentage of Ni^{2+} ions relative to Sn^{4+} ions is desirable to accentuate the decrease in resistivity.

Such behavior can be interpreted by the increase of defects, introducing the formation of intermediate states in the bandgap [14,15]. This result found is in very good agreement with the optical properties, more precisely with the interpretation proposed in the decrease of transmittance, have interpreted a similar decrease in SnO_2 thin films doped with Ni with the increase in crystallite size and, consequently, a reduction in the size of grain boundaries. From the results, it is also noticed that there is an increase in resistivity at 5 at% Ni content. It can be assumed that an increase in electrical resistivity is attributed to the decrease in charge carrier mobility.

IV. CONCLUSION

This study consisted of the elaboration and characterization of SnO_2 , $\text{Sn}_{1-x}\text{Ni}_x\text{O}_2$ [$x = 2,5$ and 10at%] thin films deposited by the pneumatic spray pyrolysis technique in order to study the influence of nickel doping on the different structural, microstructural and optical properties of the films obtained. The results of the XRD characterization show that all the films are polycrystalline with a tetragonal structure of the rutile type. The increase in the concentration of the Ni dopant clearly causes an increase in the intensity of the peaks. All the Ni-doped SnO_2 films showed a preferential growth trend along the (200) direction. The average crystallite size varied between 27 and 47nm. SEM revealed a

smooth surface. The UV–visible spectrophotometer analysis represents an important feature in evaluating the quality of the deposited films. The average transmittance was found to be around 76–82% with the presence of an interference fringe. In the visible range, which indicates that our films are homogeneous and smooth, in other words, the values of optical bandgap energy obtained from our films are in the range of 3.83–4.01eV. The electrical characteristics of the films show that the resistivity increases as the concentration of Ni dopants in the solution increase, moreover, the minimum resistivity of 1.32 $10^{-2}\Omega\cdot\text{cm}$ is obtained for the 2 at% Ni-doped SnO₂ thin films.

ACKNOWLEDGMENT

The authors would like to thank the National Project Research (PRFU) and LASPI2A Laboratory of Khenchela University (Algeria).

REFERENCES

- [1] Roguai, S., & Djelloul A.(2022). Structural and optical analysis of SnO₂ thin films BY Spray Pyrolysis. *ALJEST*, 8(1), 2285-2290.
- [2] Yates Heather, M., Evans, P., Sheel David, W., Nicolay, S., Ding, L., & Ballif, Ch. (2012). The development of high performance SnO₂:F as TCOs for thin film silicon solar cells. *Surface and Coatings Technology*, 213, 167-174.
- [3] Zebbar, N., Aida, M. A., Hafdallah, A. E. K., Daranf, O., Lekiket, H., & Kechouane. M. (2009). Properties of ZnO Thin Films Grown on Si Substrates by Ultrasonic Spray and ZnO/Si Heterojunctions. *Material Science Forum*, 609, 133-137.
- [4] Mondal, I., Kiruthika, S., Ganesha, M. K., Baral, M., Kumar, A., Vimala, S., ... & Kulkarni, G. U. (2021). ITO-free large area PDLC smart windows: a cost-effective fabrication using spray coated SnO₂ on an invisible Al mesh. *Journal of Materials Chemistry A*, 9(40), 23157-23168.
- [5] Amer, M. I., Moustafa, S. H. & El-Hagary, M. (2020). Enhanced band structure, optoelectronic and magnetic properties of spray pyrolysis Ni-doped SnO₂ nanostructured films. *Materials Chemistry and Physics*, 248, 122892.
- [6] Girtan, M., Cachet, H., & Rusu, G. I. (2003). On the physical properties of indium oxide thin films deposited by pyrosol in comparison with films deposited by pneumatic spray pyrolysis. *Thin Solid Films*, 427, 406.
- [7] Espindola-Rodriguez, M., Placidi, M., Vigil-Gala'n, O., Izquierdo-Roca, V., Fontane' X., Fairbrother, A. et al. (2013). Compositional optimization of photovoltaic grade Cu₂ZnSnS₄ films grown by pneumatic spray pyrolysis. *Thin Solid Films*, 535, 67.
- [8] Daranf, W., Aida, M. S., Attaf, N., Bougdira, J., & Rinnert. H.(2012). Cu₂ZnSnS₄ thin films deposition by ultrasonic spray pyrolysis. *Journal of Alloys and Compounds*, 542, 22-27.
- [9] Ajili, M., Castagne, M., & Kamoun Turki, N. (2015). Spray solution flow rate effect on growth, optoelectronic characteristics and photoluminescence of SnO₂:F thin films for photovoltaic application. *Optik*, 126, 708-714.
- [10] Ajili, M., Castagne, M., & Kamoun Turki. N. (2014). Characteristics of CuIn_{1-x}GaxS₂ thin films synthesized by chemical spray pyrolysis. *Journal of Luminescence*, 150, 1-7.
- [11] Burstein, E. (1954). Anomalous Optical Absorption Limit in InSb. *Physical Review*, 93, 632.
- [12] Chatelon, J. P., Terrier, C., & Roger, J. A. (1999). Electrical and optical property enhancement in multilayered sol-gel-deposited SnO₂ films. *Semiconductor Science and Technology*, 14, 642.
- [13] Edson, R., Leite, M., & Inset, B. (2004). Enhanced electrical property of nanostructured Sb-doped SnO₂ thin film processed by soft chemical method. *Thin Solid Films*, 449, 67-72.
- [14] Elangovan, E., Ramamurthi, K. (2003). Optoelectronic properties of spray deposited SnO₂:F thin films for window materials in solar cells. *Journal of Optoelectronics and Advanced Materials*, 5, 45-54.
- [15] Agashe, C., & Major, S. S., (1996). Effect of heavy doping in SnO₂:F films. *Journal of Materials Science*, 31, 2965-2969.

Copper Ferrites and Solar Radiation in the Removal of Rhodamine B: A Bibliometric Approach

Andrezza Pereira de Matos^{1*}, Ana Paula Freire de Araújo², Pollyana Caetano Ribeiro Fernandes³

^{1,2,3}Federal University of Paraíba (UFPB), João Pessoa, Brazil

¹andrezza.matos@cear.ufpb.br, ²ana.freire@cear.ufpb.br, ³pollyana@cear.ufpb.br

Abstract—This study conducted a comprehensive bibliometric analysis, focusing on the removal of the dye Rhodamine B from effluents, using copper ferrites (CuFe₂O₄) as a photocatalyst and solar radiation. The research encompasses a wide range of information sources on the Web of Science and Scopus databases, enabling an in-depth analysis of the research landscape in this field. Through the use of bibliometric tools, such as VOSviewer and RStudio, the study unveils significant research trends, including the identification of prominent countries, notable affiliations, renowned authors, relevant research sources, and the temporal evolution of the investigation. Keyword co-occurrence analysis provides a profound understanding of conceptual relationships in research, contributing to the identification of key thematic areas. Significant involvement from China and India was highlighted, reflecting the commitment of these nations to the research. Temporal analysis revealed a steady increase in the number of published articles, with a remarkable peak in 2022, indicating the growing relevance of the research. The findings underscore the increasing significance of research on the removal of Rhodamine B using CuFe₂O₄ and solar radiation, while offering a comprehensive view of the thematic structure in this field.

Keywords – ferrites, copper ferrites, solar photocatalysis, dyes, Rhodamine B

I. INTRODUCTION

Among the chemicals released by textile industries into wastewater, dyes are the most

significant pollutants. Untreated textile dyes can harm both terrestrial and aquatic life, causing long-term environmental impacts and health problems [1-4]. The waste from dye and pigment industries generates an excess of water contaminated with non-biodegradable organic dyes, making their treatment essential for environmental protection [1]. One of the most pressing challenges in this context is the efficient removal of organic dyes, widely used in textile, paper, and dyeing industries.

Among the most common dyes, Rhodamine B (RhB), widely employed due to its effectiveness, has garnered special attention due to its toxicity and resistance to degradation. (RhB) is water-soluble, serving as a fluorescent dye in biological contexts. Its use is common in various industrial processes, such as dye production, cosmetics, leather, textiles, food, pharmaceuticals, and cosmetics. Uncontrolled release of (RhB) into the environment poses substantial threats, directly affecting human health, flora, and fauna [5].

The exploration of solar energy as a clean and sustainable source to drive pollutant removal processes has gained prominence in recent decades. Solar energy offers the advantage of being abundant, accessible, and renewable, making it a highly attractive option for the development of environmentally friendly water treatment technologies.

*Supervisor: Joelda Dantas – Postgraduate Program in Alternative and Renewable/Federal University of Paraíba (UFPB), João Pessoa, Brazil.

In this context, copper ferrites (CuFe_2O_4), magnetic materials with remarkable properties, have attracted considerable attention due to their adsorption, photocatalysis, and effective pollutant removal capabilities. The uniqueness of photocatalysis lies in its dependency on solar energy and its low activation energy requirement, facilitated by a photocatalyst. It has become one of the most advanced and environmentally friendly methods for eliminating toxic substances from water under normal temperature and pressure conditions [6].

This article focuses on the intersection of these two technological domains, exploring the potential of solar energy in the effective removal of Rhodamine B (RhB) using copper ferrites as adsorbent and photocatalyst material. The synergy between solar energy and the magnetic properties of these ferrites presents a promising approach for water and effluent decontamination, offering the opportunity to mitigate the negative environmental impacts associated with the release of this dye into the environment.

This research aims to provide a comprehensive overview of the current landscape in the field of RhB removal based on copper ferrites and solar energy, highlighting its potential to address crucial environmental issues and pave the way for more sustainable applications in the water and effluent treatment industry.

In the context of this discussion, the objectives of this study included: (i) Conducting a comprehensive bibliometric analysis of publications related to the application of copper ferrites in RhB removal, with an emphasis on the use of solar energy as an activation source; (ii) Evaluating the current state of research in this area, identifying trends, advances, and knowledge gaps; (iii) Providing a critical and analytical insight into the results of related scientific publications, highlighting key challenges and opportunities for the development of more effective technologies for organic dye removal, thus contributing to the establishment of a solid foundation for future investigations.

II. METHODOLOGY

Bibliometric analysis is a quantitative approach that focuses on mapping knowledge and the relationships established among key elements such as authors, countries, keywords,

and articles [7]. In terms of relationships, three main types are identified: bibliometric coupling and direct citation, co-occurrence and co-keyword, co-author, and co-citation [8,9].

A set of crucial keywords was defined for this research, including “ferrites”, “copper ferrite”, “ CuFe_2O_4 ”, “photocatalysis”, “solar photocatalysis”, “dyes” and “rhodamine B”.

The Scopus and Web of Science databases were chosen due to their recognized breadth and quality in indexing academic and scientific articles. Scopus is a widely recognized multidisciplinary database known for its extensive global coverage. As noted by [10], Scopus provides a wide range of resources, including research metrics, trend analysis, and academic collaboration.

On the other hand, Web of Science, commonly acknowledged for its comprehensive indexing of academic journals, is praised for its quality and precision in covering high-impact journals.

Bibliometric research methodology relies on valuable tools that facilitate and enhance the scope of work in this focus. In this regard, VOSviewer is a widely recognized tool for co-occurrence analysis and term visualization in scientific texts. Similarly, [11] stated that VOSviewer offers an effective approach to create co-occurrence maps of terms and visualizations of co-authorship networks in bibliometric studies.

Bibliometric analysis plays a fundamental role in evaluating the productivity and impact of academic research. Moreover, in this context, R software has stood out as an essential tool for data analysis. As observed by [12], R is an open-source programming language that offers a wide range of packages and libraries for statistical analysis and data visualization, making it a popular choice among researchers and industry professionals.

However, the efficiency of using R is considerably enhanced by the integrated development environment (IDE) known as RStudio. As per the official RStudio website, the platform is designed to improve the productivity of R programmers, providing a user-friendly interface and powerful features for script creation, execution, management, and result visualization.

Furthermore, bibliometric analysis is often conducted with the assistance of specialized packages. A notable example is bibliometrix, an R package developed by [13]. Bibliometrix offers a wide range of functionalities for analyzing and visualizing bibliometric data, enabling the creation of co-authorship maps, co-keyword co-occurrence networks, and trend analyzes in scientific literature [13].

Based on this methodological approach, specific search strings were defined for each database. The search string for Scopus was formulated as TITLE-ABS-KEY (“ferrites” OR “copper ferrite” OR “CuFe₂O₄”) AND (“photocatalysis” OR “solar photocatalysis”) AND (“dyes” OR “rhodamine B”). The corresponding search string for Web of Science was TS ((“ferrites” OR “copper ferrite” OR “CuFe₂O₄”) AND (“photocatalysis” OR “solar photocatalysis”) AND (“dyes” OR “rhodamine B”).

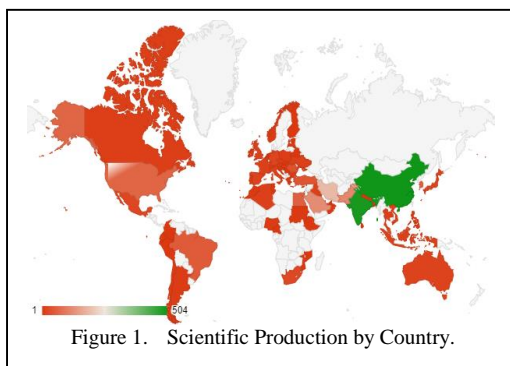
Furthermore, the publication period was defined between 2012 and 2023 to ensure the inclusion of recent and relevant studies, reflecting the most current practices and discoveries in the investigated research field.

III. RESULTS AND DISCUSSION

Bibliometric analysis has provided valuable insights into academic production, trends, and key players in this field of study. The results offer a comprehensive view of the current state of research and highlight prominent areas, significant collaborations, and major research themes.

From the search conducted in the Scopus database, a total of 1914 relevant records for the study were identified. Similarly, on the Web of Science, 64 records that fell within the study’s scope were detected. For a thorough and comprehensive data analysis, the RStudio platform allowed for a more refined screening and data preparation, including the cleansing and organization of the data. Twenty-nine duplicates were identified and removed, ensuring that only unique records were included in the analysis. Subsequently, biblioshiny was used to screen and further analyze the records.

Regarding production by countries, as illustrated in Fig. 1, a notably asymmetric distribution of research was revealed. Although China and India lead in terms of the quantity of publications, each representing approximately 25% of the total publications from the countries



involved, it is important to note that quantity does not always translate to the quality or relevance of research. The high research output from these countries may be related to a variety of factors, including the size of their populations and expansive higher education systems.

However, it is crucial to assess the depth and impact of these research works to better understand their real contribution to the advancement of the field.

Another aspect to consider is the notable presence of Iran and Saudi Arabia, which together have a significant number of widely disseminated works in the focused area, representing 9.37% and 6.14% of the total publications, respectively. These countries, despite their substantial presence in terms of publications, often face challenges related to limited resources and access to cutting-edge technologies. Therefore, it may be beneficial to explore the quality and applicability of research originating from these nations to determine their real impact on solving environmental problems.

Furthermore, it is necessary to observe the presence of countries such as the United States (with 66 works, representing 3.29% of total publications) and Brazil (with 50 works, representing 2.49% of total publications), which also contribute a substantial number of publications. These countries have the advantage of broader financial and technological resources, but it is crucial to ensure that their research translates into practical and applicable solutions to address the challenges of organic pollutant removal on a global scale.

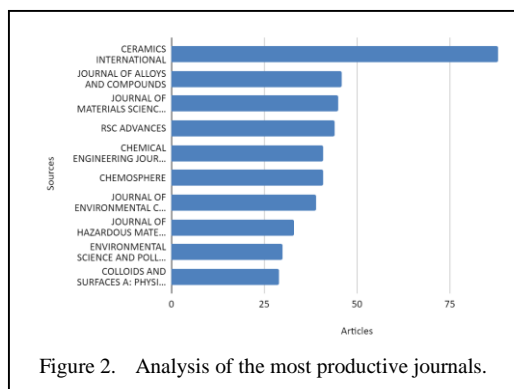
The analysis of the most productive journals, as presented in Fig. 2, reveals some interesting trends in the research field. The journal “Ceramics International” leads the list with an impressive number of 88 articles related to the topic. This suggests that this journal has played

a crucial role in publishing relevant research on the subject, which can be attributed to its wide acceptance among researchers in the field. However, the concentration in a single journal may indicate a need for diversification to ensure broader dissemination of research results.

Other notable journals, such as “Journal of Alloys and Compounds” with 2.29%, “Journal of Materials Science: Materials in Electronics” with 2.24%, “RSC Advances” with 2.19%, “Chemical Engineering Journal” with 2.04%, “Chemosphere” with 2.04%, and “Journal of Environmental Chemical Engineering” with 1.94%, also present significant numbers of published articles. This diversity of sources indicates the wide range of topics and research approaches covered by these publications.

It is essential to note that the choice of a journal for publication can affect the visibility and impact of research. Therefore, it is crucial for researchers to carefully consider their publication options to ensure that their findings reach the appropriate audience and have a significant impact within the scientific community and in addressing environmental issues.

The analysis of article production over the years, as illustrated in Fig. 3, reveals a notable trend of growth in the research field. The consistent increase in the number of published articles reflects a growing and sustained interest in this topic. In 2013, 38 articles related to the research in question were published, and since then, there has been a consistent year-over-year growth. The years 2022 and 2023 particularly showed significant increases, with 380 and 396 articles, respectively. This suggests substantial interest and engagement from the academic community in this field of study.

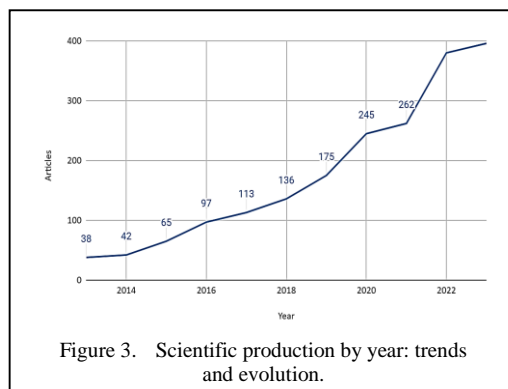


A remarkable increase in publications in 2022, as indicated by temporal analysis, is attributed to various significant factors. Likely drivers of this surge include the advent of innovative technologies related to RhB removal, as well as the development of more efficient and advanced methodologies in the domain of photocatalytic catalysis. Additionally, global events, such as conferences and initiatives focused on water treatment and environmental preservation, have been responsible for the dissemination of knowledge and collaboration among researchers. The growing recognition of global challenges associated with water pollution and the urgency to find sustainable solutions may have contributed to the intensification of research in this specific subject.

The increase in article production over the years can be attributed to several factors. The growing concern about water pollution and the need for effective solutions for the removal of organic pollutants, such as (RhB), may be driving this research. Furthermore, technological advancements and international collaboration may be contributing to the expansion of knowledge in this field.

The upward trend in article production over the years reflects the ongoing commitment to research in this field and the continued need for effective solutions to address environmental challenges related to (RhB) and similar pollutants.

The analysis of the most productive authors in research, as presented in Fig. 4, highlights the significant contributions of some prominent researchers. Authors Li X and Liu Y stand out with 37 articles each, demonstrating a notable dedication to research in this area. Their consistent contributions indicate a significant



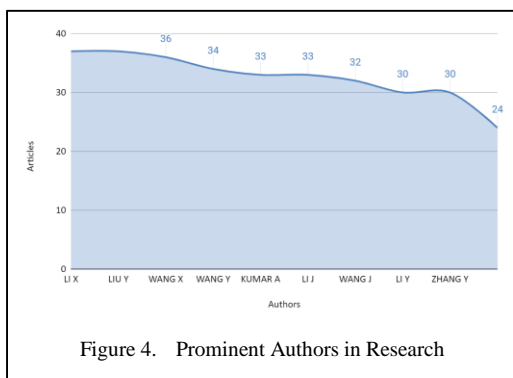


Figure 4. Prominent Authors in Research

specialization in the topic and a substantial impact on academic literature. Authors Wang X and Wang Y also show a high level of productivity, with 36 and 34 articles, respectively. The active presence of these authors in research indicates a comprehensive approach to the investigation of (RhB) removal.

Kumar A and Li J, with 33 articles each, make a substantial contribution to the field. Their research has been essential for expanding knowledge in this specific domain. Wang J, Li Y, Zhang Y, and Singhal S also deserve recognition, with significant numbers of 32 and 30 published articles, respectively.

The discovered authors have played a fundamental role in advancing knowledge about the removal of (RhB) and in the search for effective solutions. Their contributions have helped shape the field and guide research to address critical environmental challenges. It is important to note that collaboration among these researchers may lead to even more impactful results and innovations in the future.

Regarding the analysis of the most frequent terms found in publications related to research, as illustrated in Fig. 5, it highlights essential concepts and techniques for this field of study.

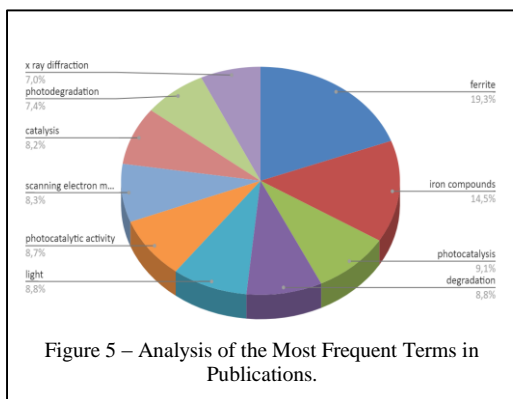


Figure 5 – Analysis of the Most Frequent Terms in Publications.

“Ferrites” is the most frequent term, with 985 occurrences. This reflects the central emphasis on the use of ferrites in research related to the removal of organic pollutants, such as (RhB). These materials have proven essential in catalysis and the degradation of organic compounds. Iron compounds also have a high frequency, with 738 occurrences. This is related to the chemical composition of copper ferrites, which includes iron compounds.

These compounds play a fundamental role in catalysis and the photodegradation of pollutants. “Photocatalysis” and “photocatalytic activity” are frequent terms, with 462 and 445 occurrences, respectively. These terms emphasize the importance of photocatalytic catalysis, where light plays a crucial role in the degradation of the compound. “Degradation”, “light”, “photodegradation” and “catalysis” are terms associated with the transformation of (RhB) into less toxic products and the catalysis of the removal process.

Scanning electron microscopy and X-ray diffraction indicate the importance of characterizing and analyzing materials and structures involved in the removal process. These techniques are essential for understanding the structure of copper ferrites and their properties.

Clusters play a fundamental role in bibliometric analysis, as they have the ability to reveal thematic structure and underlying patterns in complex datasets. In this study, the analysis of keyword co-occurrence resulted in the identification of four distinct clusters, each represented by a specific color. The importance of these clusters lies in their ability to categorize and group research items, allowing for a clear visualization of related trends and research areas.

In the context of Web of Science, the use of VOSviewer allowed for the creation of a keyword co-occurrence graph that featured 28 distinct items organized into four clusters, each identified by a specific color, as illustrated in Fig. 6.

Cluster 1, represented by the color red and composed of 11 items, stands out as the largest and most prominent. This coloring suggests that the keywords within this cluster share significant associations, forming a solid research topic or category.

for real-time monitoring of the effectiveness of these methods are potential avenues.

By addressing the elimination of (RhB) in aquatic environments, the research directly contributes to SDG 6 - Clean Water and Sanitation, aiming to ensure the availability and sustainable management of water for all. Additionally, by developing innovative and efficient methods for the removal of organic pollutants, the research aligns with SDG 12 - Responsible Consumption and Production, promoting sustainable practices in resource and chemical management. The reduction of environmental impact associated with the presence of (RhB) also aligns with SDG 13 - Climate Action, contributing to the mitigation of pollutants that directly affect water quality and climate balance. In conclusion, the removal of (RhB) transcends the realm of isolated research, aligning prominently with broader social and environmental goals outlined by the Sustainable Development Goals.

IV. CONCLUSION

When analyzing the data from two databases, patterns of keyword co-occurrence were identified, providing a comprehensive understanding of the research landscape.

It was observed that the main countries involved in this research are China and India, reflecting the interest and dedication of these nations in advancing knowledge about the removal of (RhB). Prominent institutional affiliations, such as King Saud University and The Islamia University of Bahawalpur, highlight the active contribution of these institutions to research in this field.

Authors who stand out in this area, such as Li X, Liu Y, and Wang X, demonstrate significant commitment to this research, contributing a considerable number of articles. Regarding the most relevant research sources, journals such as "Ceramics International", "Journal of Alloys and Compounds", and "Journal of Materials Science: Materials in Electronics" are highlighted, indicating the importance of these publications in disseminating knowledge in the area.

The temporal analysis revealed a steady growth in the number of articles published over the years, with a notable peak in 2022. This suggests that research on the removal of (RhB) using copper ferrites (CuFe_2O_4) and solar

radiation is on the rise and has become an increasingly relevant research field.

In the context of Web of Science, the analysis revealed 28 items arranged into four distinct clusters. In the Scopus database, the analysis covered a set of 1000 items, organized into six clusters, each with its own thematic relevance. The visual representation of these clusters, using different colors, allowed for a clear visualization of areas of interest, interactions between key concepts, and research trends.

As a result, this study provides a solid foundation for future research in this field, offering valuable guidance for identifying related research areas, emerging trends, and knowledge gaps. Bibliometric analysis, combined with cluster visualization, simplifies the understanding of the complex research landscape.

ACKNOWLEDGMENTS

The authors thank the Coordination for the Improvement of Higher Education Personnel (CAPES) for the master's scholarship and the Paraíba State Research Support Foundation (FAPESQ) for the master's scholarship and for the postdoctoral scholarship (No. 1990/2022, Notice No. 17 /2022).

REFERENCES

- [1] Zhu, X., et al. (2021). Carboxylcellulose hydrogel confined- Fe_3O_4 nanoparticles catalyst for Fenton-like degradation of Rhodamine B. *International journal of biological macromolecules*, 180, 792-803.
- [2] Merouani, S., Hamdaoui, O., Saoudi, F., & Chiha, M. (2010). Sonochemical degradation of Rhodamine B in aqueous phase: effects of additives. *Chemical Engineering Journal*, 158(3), 550-557.
- [3] Wilhelm, P., & Stephan, D. (2007). Photodegradation of rhodamine B in aqueous solution via $\text{SiO}_2@ \text{TiO}_2$ nano-spheres. *Journal of Photochemistry and Photobiology A: Chemistry*, 185(1), 19-25.
- [4] Zhang, Z., et al. (2016). Photocatalytic degradation of rhodamine B by using a nanocomposite of cuprous oxide, three-dimensional reduced graphene oxide, and nanochitosan prepared via one-pot synthesis. *Journal of Alloys and Compounds*, 659, 101-111.
- [5] Sukumar, M., et al. (2023). Synthesize and characterization of copper doped nickel ferrite nanoparticles effect on magnetic properties and visible light catalysis for rhodamine dye degradation mechanism. *Journal of Alloys and Compounds*, 953, 169902.
- [6] Heng, J. Z. X., Tang, K. Y., Regulacio, M. D., Lin, M., Loh, X. J., Li, Z., & Ye, E. (2021). Solar-powered photodegradation of pollutant dyes using silver-

- embedded porous TiO₂ nanofibers. *Nanomaterials*, 11(4), 856.
- [7] Zhang, X., Estoque, R. C., Xie, H., Murayama, Y., & Ranagalage, M. (2019). Bibliometric analysis of highly cited articles on ecosystem services. *PLoS one*, 14(2), e0210707.
- [8] Huang, Y., Ding, X. H., Liu, R., He, Y., & Wu, S. (2019). Reviewing the domain of technology and innovation management: A visualizing bibliometric analysis. *Sage Open*, 9(2), 2158244019854644.
- [9] Boyack, K. W., & Klavans, R. (2010). Co-citation analysis, bibliographic coupling, and direct citation: Which citation approach represents the research front most accurately? *Journal of the American Society for information Science and Technology*, 61(12), 2389-2404.
- [10] Falagas, M. E., Pitsouni, E. I., Malietzis, G. A., & Pappas, G. (2008). Comparison of PubMed, Scopus, web of science, and Google scholar: strengths and weaknesses. *The FASEB journal*, 22(2), 338-342.
- [11] Van Eck, N., & Waltman, L. (2010). Software survey: VOSviewer, a computer program for bibliometric mapping. *Scientometrics*, 84(2), 523-538.
- [12] Ihaka R., & Gentleman, R. (1996). *Interface Foundation of America R: A Language for Data Analysis and Graphics*. Available at: <http://www.jstor.org>URL:<http://www.jstor.org/stable/1390807>http://www.jstor.org/stable/1390807?seq=1&cid=pdf-reference#references_tab_contents
- [13] Aria, M., & Cuccurullo, C. (2017). bibliometrix: An R-tool for comprehensive science mapping analysis. *Journal of informetrics*, 11(4), 959-975.

Designing a Social Resilience Index for Electricity Power Systems

Amir Niroumandfam¹, Mohammad Hassan Bahmani², Amir Bairami Akhi Jahani³,
Masood Yahyaei⁴

^{1,2,4}Saba Power and Energy Group, Tehran, Iran

²Tarbiat Modares University, Tehran, Iran

³Faculty of Electrical Engineering, University of Zanjan, Zanjan, Iran

⁴Islamic Azad University Central Tehran Branch, Tehran, Iran

¹Niroumandfam@sabapeg.ir, ²Mh.Bahmani@Modares.ac.ir, ³mbairami65@gmail.com,

⁴M.Yahyaei.eng@iauctb.ac.ir

Abstract—Electricity power systems are the backbone of modern society, ensuring the functioning of essential services, industries, and households. Traditionally, resilience assessments of these systems have focused on technical aspects and infrastructure. However, as the world faces increasing risks from extreme weather events, cybersecurity threats, and other unexpected disruptions, it has become evident that the social aspect of resilience is equally crucial. Social resilience in power systems encompasses community engagement, equity, communication, and social support networks. Ensuring equitable access to resources and services, particularly for vulnerable populations, is a fundamental aspect of social resilience. In this paper, a social resilience index is proposed to measure the vulnerability of the power system. To this end, the concept of social welfare is borrowed from microeconomics to measure customers' satisfaction with electricity service curtailment. The risk aversion index is a crucial factor in the proposed resilience index, wherein customers with a high risk aversion derive greater welfare from electricity energy consumption. The numerical results demonstrate that the proposed social index can be controlled by applying different outage levels to different customers.

Keywords – resilience, social perspective, welfare, risk aversion index

I. INTRODUCTION

In an increasingly interconnected and electrified world, the resilience of power systems is paramount. The reliability of electricity supply underpins modern life, driving economic growth,

sustaining critical services, and ensuring the comfort and security of millions. However, this complex network of power generation, distribution, and consumption faces a variety of emerging challenges, including natural disasters and cyber threats, as well as changing climate patterns and societal shifts [1].

Traditionally, the assessment of power system resilience has focused on technical and engineering aspects. Engineers have meticulously crafted grids to minimize downtime by investing in redundant infrastructure, cutting-edge equipment, and proactive maintenance. While these efforts remain indispensable, they alone do not encompass the full range of challenges that the modern power grid faces. A new paradigm called social resilience is emerging in the study of power systems in response to this complexity. Social resilience in power systems is an interdisciplinary approach that goes beyond the scope of engineering. It recognizes the complex interaction between technology, policy, and human behavior in the pursuit of a more resilient grid. This shift is not just theoretical but also acknowledges the fact that the power grid is not an isolated entity; it is closely interconnected with the communities it serves [2].

This article explores the complex landscape of social resilience in power systems and the changing role of utility companies within this framework. To this end, this paper establishes a novel social resilience index of power systems that measures consumers' social perspectives due to electricity energy curtailment.

The main contributions of this paper are summarized as follows:

- Designing a novel social resilience index in the power system based on consumers' social welfare
- Measuring the social welfare of electricity consumers using the concept of risk aversion.
- Determining optimal demand curtailment for different customer types to maximize the social resilience index when an outage occurs.
- Determining optimal financial assistance to compensate different consumers' damage due to the outage.

The rest of this paper is organized as follows: Section II discusses the concept of social resilience. Section III provides a mathematical description of the proposed social resilience index. In this section, the welfare of electricity customers is modeled using various utility functions. Numerical results are discussed in Section IV and conclusions are drawn in Section V.

II. SOCIAL RESILIENSE CONCEPT

Resilience, in the context of electricity power systems, refers to the ability of these systems to withstand and recover from disturbances, ensuring uninterrupted electricity supply. While traditionally, the focus has been on physical infrastructure, such as power plants, transformers, and transmission lines, the modern understanding of resilience goes beyond hardware. It encompasses the social, economic, and environmental aspects that contribute to the robustness of a power system in the face of adversity. Incorporating these broader aspects of resilience into power system planning recognizes the interconnected and evolving nature of risks. It acknowledges that a resilient power system is not only about maintaining physical infrastructure but also about understanding and adapting to a complex and dynamic environment.

This paradigm shift is a response to the growing complexity of our interconnected world. The challenges and disruptions we face are not only technical but often rooted in social, behavioral, and cultural dimensions. By emphasizing the importance of integrating social and community factors into resilience assessments, we can model the complex

interconnections among individuals, systems, and their surroundings. This paradigm shift is a response to the increasing complexity of our interconnected world. The challenges and disruptions we face are not only technical but often rooted in social, behavioral, and cultural dimensions [3].

One of the primary reasons for incorporating social and community elements into resilience assessments is the acknowledgment that individuals and communities vary in their vulnerabilities and capacities when facing challenges. Vulnerability can be linked to socioeconomic status, geography, age, disability, or other factors that influence how individuals experience and respond to disruptions.

Incorporating social and community aspects into resilience assessments brings with it the crucial principles of community engagement and awareness. Engaging with local communities and involving them in resilience planning and response efforts are essential. Communities are not just passive recipients of aid during disasters; they are often the first responders, providing valuable local knowledge and resources that can significantly impact a community's ability to withstand and recover from adversity [4].

By emphasizing the importance of including social and community aspects in resilience assessments, several challenges can arise if these dimensions are ignored. Some of these challenges include:

- **Social Fragmentation:** Neglecting social and community factors can result in social fragmentation, where communities are not engaged and individuals are left to fend for themselves during crises.
- **Inequity:** Vulnerable populations may be disproportionately affected if resilience planning does not take into account social and economic disparities.
- **Misinformation:** Without clear communication and community engagement, misinformation can spread, leading to confusion and panic during crises.
- **Resistance to Change:** Communities may resist resilience efforts that do not take into account their unique cultural or behavioral preferences.

- **Resource Mismatch:** Allocating resources without understanding the social and community aspects can lead to ineffective resource utilization and a lack of community engagement.

Due to the mentioned aspects, this paper designs a social resilience index that measures consumers' resilience against electricity energy curtailment. This index will be described in the next sections.

III. SOCIAL RESILIENSE INDEX

In this article, the social resilience index (SRI_{total}) is defined as Eq. (1), where the total resilience is equal to the sum of the individual consumers' social resilience.

$$SRI_{total} = \sum_{i=1}^N SRI(i), \quad (1)$$

where i and N are the consumer index and number of consumers. Also, the social resilience of each consumer is related to his/her obtained welfare (W) regarding load consumption, as shown in Eq. (2).

$$SRI(i) = W(i). \quad (2)$$

The welfare of electricity customers can be determined by subtracting the cost of electricity from the satisfaction obtained by the customer from consumption, as shown in Eq. (3) [5]. To quantify the satisfaction obtained, this paper utilizes the concept of utility function (U), borrowed from microeconomics. The term "utility function" refers to the overall well-being and satisfaction that consumers derive from consuming electricity.

$$W(D(i), a(i)) = U(D(i), a(i)) - \pi D(i), \quad (3)$$

where $D(i)$, π and $a(i)$ represent the consumer's demand, electricity energy price, and risk aversion index, respectively. The risk aversion index relates to each consumer's individual preferences [3]. The consumers' welfare due to electricity energy consumption will increase as risk aversion increases.

A utility function is a function that is twice-differentiable and has the following properties:

Property 1: Marginal utility is positive, which means that utility increases with consumption. In

other words, more consumption is preferred to less consumption. This can be expressed as:

$$\frac{\partial U(D, \alpha)}{\partial D} \geq 0. \quad (4)$$

Property 2: Marginal utility is a non-increasing function, which means that the marginal utility of consumption decreases as consumption increases. This can be expressed as:

$$\frac{\partial^2 U(D, \alpha)}{\partial D^2} \leq 0. \quad (5)$$

Property 3: The customer utility function is non-decreasing in the risk aversion index. This means that a larger risk aversion indicates a greater degree of risk-aversion behavior. Mathematically, it can be expressed as:

$$\frac{\partial U(D, \alpha)}{\partial \alpha} > 0. \quad (6)$$

Property 4: It is assumed that without consumption, the utility will be zero, which means that no satisfaction is obtained when the customer does not consume any electric energy. Thus, we have:

$$U(0, \alpha) = 0. \quad (7)$$

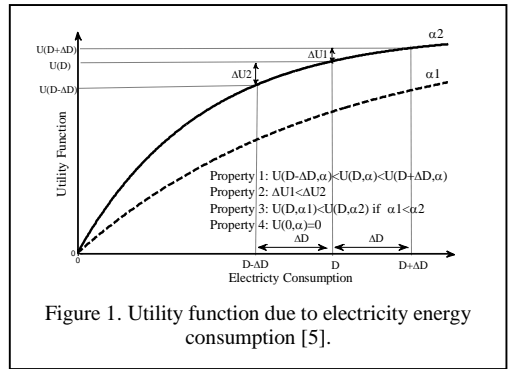


Figure 1. Utility function due to electricity energy consumption [5].

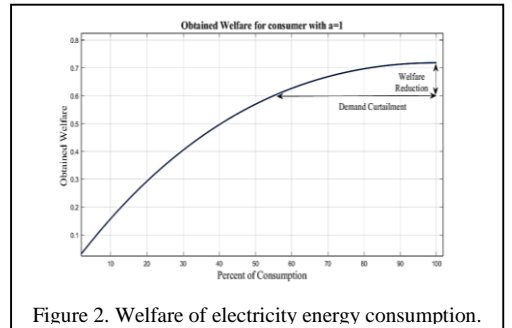
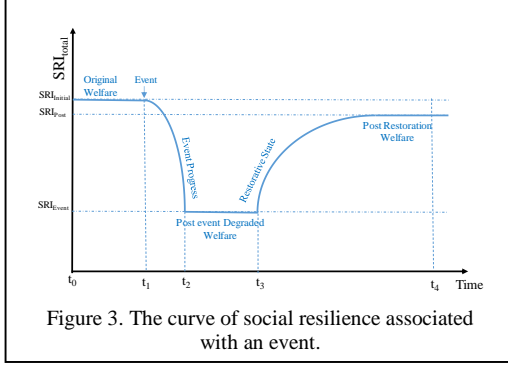


Figure 2. Welfare of electricity energy consumption.

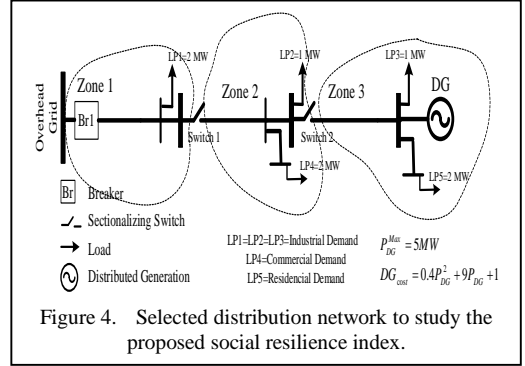


Based on the aforementioned properties, the utility function is an ascending and concave function that gradually saturates with consumption, as depicted in Figs. 1. and 2 illustrates the welfare obtained for different consumption levels for a customer with $a = 1$.

The proposed social resilience index is an indicator used to measure and enhance resilience, as depicted in Fig. 3. The welfare obtained by consumers during the event is divided into four phases accordingly. In the $[t_0, t_1]$ period, the system is in normal operation; therefore, the SRI is equal to the consumers' original welfare. After moment t_1 , system performance will be drastically degraded by unexpected events, causing the SRI to drop to the post-event welfare level. At time t_2 , the system starts to resist and absorb the negative consequences of the incident until time t_3 . In the $(t_3, t_{14}]$ period, the system gradually recovers and restores the power system performance to almost normal levels by implementing appropriate recovery strategies. Therefore, the SRI will be equal to the post-restoration welfare of the consumers.

Ensuring equity and addressing vulnerability are essential components of social resilience in electricity power systems. Resilience planning should aim to provide equitable access to resources and services during power outages. This includes ensuring that vulnerable populations have access to backup power, emergency shelters, and communication services. Also, efforts should be made to reduce disparities in the impact of power disruptions on various consumers. This may involve providing financial assistance, resources, or targeted outreach to vulnerable populations [6].

To ensure equity in electricity service provision, this paper proposes that financial assistance (R) is applied to the vulnerable consumers' based on their welfare reduction due



to demand curtailment, which can be expressed as:

$$R(\Delta D) = W(D, \pi, \alpha) - W(D - \Delta D(t), \pi, \alpha) \quad (8)$$

Through the proposed SRI, the utility company can manage outages among consumers to minimize financial assistance. The paid assistance is based on the reduction of customers' welfare, in which consumers with a low risk aversion index receive less reimbursement. Hence, to reduce financial assistance, more outages can be applied to consumers with a low risk aversion index. It should be mentioned that the assistance payment is fair and equal to the reduction in consumers' welfare due to demand curtailment.

To minimize the financial assistance, we have:

$$\min F = \sum_{i=1}^N R(\Delta D(i)) \quad (9)$$

Subject to:

$$\sum_{i=1}^N \Delta D(i) = P_{outage} \quad (10)$$

Different functions with the mentioned properties can be utilized as utility functions. As an example, in this paper, the exponential utility function, the popular form of the utility function that is frequently used to describe the risk preferences of consumers [6], is selected to survey the proposed SRI. It should be mentioned that utilizing any other form of utility function provides similar results.

The exponential utility function can be expressed as follows:

$$U(D, \alpha) = 1 - e^{-aD}, \quad a > 0. \quad (11)$$

For the exponential utility function, the welfare function and the calibration coefficient are determined as follows Eqs. (12) and (13).

$$W(D, \alpha) = A(1 - e^{-\alpha D}) - \pi D, \quad (12)$$

$$A = \frac{\pi_0}{\alpha} e^{\alpha D_0}. \quad (13)$$

This calibration coefficient (A) is used to calibrate the adjustment for the initial electricity price (π_0) and initial demand (D_0) [7].

Assuming that electricity consumers behave based on an exponential utility function, the optimal demand curtailment level of each consumer can be calculated as shown in Eq. (14) [8]:

$$\Delta D(i) = \frac{1/\alpha(i)}{\sum_{j=1}^N 1/\alpha(j)} P_{outage}, \quad (14)$$

where P_{outage} is the total outage due to the event.

IV. NUMERICAL RESULTS

The proposed social resilience index has been tested on a sample network, as depicted in Fig. 4. For the sake of simplicity, this study assumes that consumers are categorized into residential, commercial, and industrial sectors and that all consumers within each sector have the same risk aversion index. The indices for residential, commercial, and industrial are assumed to be 0.9, 0.7, and 0.5, respectively. Also, this paper assumes that the utility company is a non-profit company that buys electricity from the overhead network at a price equal to 10\$/MW and sells it to consumers at a price equal to 10 \$/MW.

To assess the efficiency of the proposed social resilience index in the selected electricity network, the index will be evaluated in five scenarios, as described below:

Sc. #1: The system is in a normal operational state, and all the demand is supplied with the overhead network (before the event).

Sc #2. An event occurred, and the overhead network has been disconnected. The installed DG generates 5 MW of electricity to supply the demands, and the energy price is the same after and before the event (10 \$/MW).

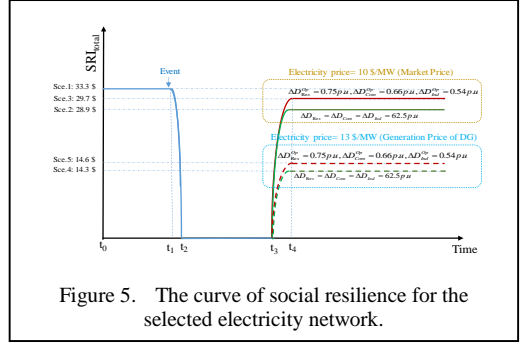


Figure 5. The curve of social resilience for the selected electricity network.

Sc. #3: All the situations are the same as in Sc. 2, except optimal demand curtailment is applied to the consumers based on Eq. (14).

Sc. #4: All the situations are the same as in Sc. 2, except the electricity price is equal to the DG generation price after the event happened (13 \$/MW).

Sc. #5: All the situations are the same as in Sc. 2, except the electricity price is equal to the DG generation price after the event happened (13 \$/MW) and optimal demand curtailment is applied to the consumers based on Eq. (14).

Fig. 5 illustrates the curve of the social resilience index for different scenarios. As depicted in this figure, the SRI level after the event is lower than its initial level due to the generation limit of the DG. Although only a few scenarios are surveyed as samples in this section, considering other scenarios for demand curtailment division among consumers, the highest SRI level and obtained welfare can be achieved by applying demand curtailment based on (14). As shown in Fig. 5, applying electricity energy with a high DG generation price reduces the welfare and SRI levels obtained.

Tables I and II demonstrate the energized demand and SRI for each load point under different scenarios. Sc. In scenario #1, the normal operational state is described, where all demand is supplied from the overhead network and the obtained welfare is equal to 33.3 \$. In all other scenarios, the overhead network is disrupted, and the DG generates its maximum capacity, 5MW, to energize different demands. In these scenarios, 3 MW of the demand will not be supplied due to the limited capacity of the DG. To ensure equality and compensate for consumers' dissatisfaction caused by demand curtailment, the utility company must provide compensation equal to the reduction in their welfare.

Table III illustrates the revenue and costs of the utility company. Considering Tables I-III, it is illustrated that the increase in financial assistance resulting from the application of the DG generation price to consumers is greater than its positive effect

TABLE I. DEMAND CURTAILMENT AND OBTAINED WELFARE LEVELS FOR SCE. 1, SCE. 2, AND SCE.3.

Load Point	Sce. #1		Sce. #2		Sce. #3	
	D (MW)	SRI (\$)	D (MW)	SRI (\$)	D (MW)	SRI (\$)
1	1	2.97	0.62	2.54	0.55	2.41
2	1	2.97	0.62	2.54	0.55	2.41
3	1	2.97	0.62	2.54	0.55	2.41
4	1	4.48	0.62	3.86	0.66	4.12
5	1	4.48	0.62	3.86	0.66	4.12
6	1	2.97	0.62	2.54	0.55	2.41
7	1	6.22	0.62	5.51	0.75	5.91
8	1	6.22	0.62	5.51	0.75	5.91
Tot.	8	33.3	5	28.9	5	29.7

TABLE II. DEMAND CURTAILMENT AND OBTAINED WELFARE LEVELS FOR SCE. 4 AND SCE.5.

Load Point	Sce. #4		Sce. #5	
	D (MW)	SRI (\$)	D (MW)	SRI (\$)
1	0.62	0.73	0.55	0.78
2	0.62	0.73	0.55	0.78
3	0.62	0.73	0.55	0.78
4	0.62	2.07	0.66	2.06
5	0.62	2.07	0.66	2.06
6	0.62	0.73	0.55	0.78
7	0.62	3.63	0.75	3.67
8	0.62	3.63	0.75	3.67
Tot.	5	14.3	5	14.6

TABLE III. UTILITY COMPANY'S LOSS FOR DIFFERENT SCENARIOS.

Scenario Number	Sce.#1	Sce.#2	Sce.#3	Sce.#4	Sce.#5
Revenue from Selling Energy to Consum.	80\$	50\$	50\$	65\$	65\$
Cost of Buying Energy from Network	80\$	0\$	0\$	0\$	0\$
Cost of Buying Energy from DG	0\$	65\$	65\$	65\$	65\$
Cost of Financial Assistance	0\$	4.4\$	3.6\$	19\$	18.7\$
Total Loss	0\$	19.4\$	18.6\$	19\$	18.7\$

on the utility company's cost reduction. The optimal scenario for the utility company is Scenario #3.

The main parameter of the propose social resilience index is the consumers' risk aversion coefficients. The proposed social resilience can be applied to any region or country by utilizing these coefficients. Authors in [8] has been proved that the risk aversion confidants are related to the price elasticity of electricity demand, hence by employing the elasticity data distribution companies can measure their customers' social resilience.

V. CONCLUSIONS

Current resilience models emphasize only technical and infrastructural aspects of power systems and do not consider consumers' social resilience. However, the consumption of electrical energy is closely related to today's life, and any power supply disruption has a significant impact on the social perspective of consumers. In this research, a social resilience index was designed for the power system. This index measures changes in the social welfare of consumers.

The concept of utility function from microeconomics was used to calculate consumers' welfare. The risk aversion index is a crucial variable in the utility function, and its value varies depending on the individual behavior and perspective of consumers. The results showed that individuals with a higher risk aversion index receive greater welfare from consuming electric energy. In the methodology section, an optimization model was developed to optimally divide load curtailment among consumers.

In the numerical results section, the social resilience index was tested on a sample network. Numerical results showed that the utilization of distributed generation after the event can enhance social resilience. On the other hand, it is essential to provide fair compensation to reimburse consumers for the reduction in their welfare caused by the curtailment of demand resulting from an event. Also, this section demonstrates that electricity price increments due to distributed generation utilization will also cause a decline in the social resilience index.

This study used concept of the utility function to measure consumers' perspective regards electricity energy consumption. This

measurement resulted in a simple and analyzable model for the social resilience index of electricity customers. However, in real-world applications, it is necessary to model the customers' point of view towards electricity energy consumption with more accurate and comprehensive models.

REFERENCES

- [1] Umunnakwe, A., Huang, H., Oikonomou, K., & Davis, K. R. (2021). Quantitative analysis of power systems resilience: Standardization, categorizations, and challenges. *Renewable and Sustainable Energy Reviews*, 149, 111252.
- [2] Bahmani, M. H., Haghifam, M. R., & Miri Larimi, S. M. (2019). Toward grid-scale microgrids; evaluating the capacity of financial structures. *IET Generation, Transmission & Distribution*, 13(7), 1057-1067.
- [3] Haavik, T. K. (2020). Societal resilience—Clarifying the concept and upscaling the scope. *Safety Science*, 132, 104964.
- [4] Hutter, G. É. R. A. R. D., & Lorenz, D. F. (2018). Social resilience. *Vulnerability and resilience to natural hazards*, 190-213.
- [5] Niromandfam, A., Yazdankhah, A. S., & Kazemzadeh, R. (2020). Modeling demand response based on utility function considering wind profit maximization in the day-ahead market. *Journal of Cleaner Production*, 251, 119317.
- [6] Bahmani, M. H., Haghifam, M. R., & Miri Larimi, M. (2018). Developing Policy Schemes Towards Grid-Scale Microgrids; Discussing The Iranian Case.
- [7] Niromandfam, A., Yazdankhah, A. S., & Kazemzadeh, R. (2020). Designing risk hedging mechanism based on the utility function to help customers manage electricity price risks. *Electric Power Systems Research*, 185, 106365.
- [8] Niromandfam, A., Pour, A. M., & Zarezadeh, E. (2020). Virtual energy storage modeling based on electricity customers' behavior to maximize wind profit. *Journal of Energy Storage*, 32, 101811.

Purification of Sewage and Pharmaceutical Wastewater in Urban Areas Using Renewable Dead Biomass

Esam Saleh¹, Touzout Ferial², Yous. R.³, Cherifi H.⁴, Salah Hanini⁵

^{1,2,3,4,5}Laboratory of Biomaterials and Transfer Phenomena LBMPT, University Dr. Yahia Fares, Medea, Algeria

¹Salehesam.ahmedali@univ-medea.dz, ²ferieltouzout@gmail.com

Abstract—The issue of water pollution in urban areas has become increasingly problematic, mainly due to the presence of sewage and pharmaceutical chemicals. This has developed as a significant concern that threatens urban ecosystems' overall health and stability. This study emphasises the significance of effectively tackling the escalating water pollution concerns in urban settings. The aim is to attain optimal and economical wastewater treatment, employing sustainable resources and inventive methodologies to address water contamination issues in metropolitan regions. The investigation also explores the experimental configuration and methods utilised to assess deceased biomass's efficacy in removing contaminants. Furthermore, this study investigates the feasibility of employing deceased biomass residues, frequently seen in Algeria, to remedy water pollution caused by dyes, specifically methylene blue, via adsorption. The procedure encompasses multiple sequential stages: washing, drying, grinding, and sieving. In addition, the study investigated the kinetics of methylene blue adsorption on biomass at varying concentrations of both the dye and the biomass. The research also aimed to determine the kinetic characteristics of this adsorption process. Three kinetic models, namely the pseudo-first-order and pseudo-second-order models, were formulated and investigated.

Keywords - dead biomass, methylene blue, kinetic model, adsorption

I. INTRODUCTION

Agriculture, responsible for nearly 70% of worldwide water usage, plays a vital role in fulfilling the nutritional requirements of the

growing global populace. However, the reliance on water challenges many countries, including Algeria. The quick pace of development has given rise to intricate ecological challenges that pose risks to public health, the conservation of delicate ecosystems, and future generations' access to essential resources for their socioeconomic welfare. Heavy metals are a significant challenge within the context of these difficulties. Certain metals, such as cadmium and iron, have been identified as carcinogens or cancer-causing agents capable of inducing various types of cancer. Furthermore, it should be noted that these compounds exhibit resistance to degradation through natural mechanisms, resulting in their prolonged presence in the environment and potential bioaccumulation throughout the food web. However, there has been a growing concern in recent years regarding developing organic contaminants, such as residues of sewage and pharmaceutical products in water bodies. This global worry has dramatically increased over time. This matter has emerged as a prominent environmental concern, exerting substantial influence on the natural ecosystem and the well-being of the general population. Therefore, it is imperative to identify and implement efficient and ecologically sustainable approaches to treat wastewater [1]. Currently, a diverse array of methods are available for treating home and industrial wastewater, each with distinct attributes. Several techniques are employed in this context, such as adsorption, electrolysis, flotation, precipitation, ion exchange, liquid-liquid extraction, and other ways [2]. Reference [3], argue that using natural

materials for adsorption is widely recognised as a highly efficient approach within the range of existing techniques. This is primarily attributed to its inherent simplicity and cost-effectiveness. Taking into account both economic and environmental viewpoints, it was imperative to investigate an adsorbent that is both cost-effective and environmentally sustainable. Numerous investigations have underscored the notable effectiveness of biomass in efficiently removing metallic cations [4]. This study intends to evaluate the possibilities of employing dead biomass residues widely found in Algeria for depolluting water tainted with eliminated methylene blue dye through adsorption.

II. MATERIALS AND METHODS

In this study, we employed deceased biomass derived from an agri-food sector, which consisted of grains and other particulate matter that underwent crushing as part of the production procedure.

A. Preparation of the Biomass

The methodology employed for the fabrication of the adsorption support is depicted in Fig. 1.

III. RESULTS AND DISCUSSION

The study employed deceased biomass derived from agricultural food remnants, encompassing pulverised grains and other particulates formed throughout the manufacturing procedure. The stock solutions were diluted in a stepwise manner using distilled water in order to attain the desired mineral concentration. No further purification of the compounds utilised was conducted. The ideal circumstances, such as the adsorbent dosage, the adsorbate's initial concentration, temperature, and pH, were determined in the initial phase. Subsequently, the combination underwent filtration utilising a RETSCH filter with a pore diameter of 0.45 μm . During the studies, a comprehensive stirring process was employed for all combinations of adsorbent and adsorbate. After achieving equilibrium, we identified the ideal period for contact and conducted all experiments accordingly. The metal concentration values were determined using a UV spectrophotometer (UV-mini 1240 SHIMADZU).

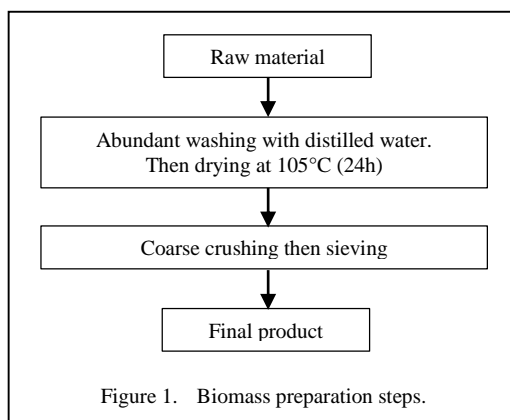


Figure 1. Biomass preparation steps.

A. Characterizations of Prepared Biomass

1) Particle size

The determination of the average diameter of the biomass particles obtained after grinding is based on the point of intersection between the cumulative reject and cumulative sieve curves. These results are visually presented in Fig. 2. The mean diameter of the particles collected is 220 μm .

2) Physical and chemical characterization of biomass

The physicochemical characterization results of the adsorbents utilised are succinctly presented in Table I. Based on the data depicted in Fig. 3, it can be deduced that the adsorbent demonstrates a negatively charged outer surface. The observed discrepancy between the pH_{zero} value and the measured pH level can be ascribed to the substantial difference in their respective magnitudes.

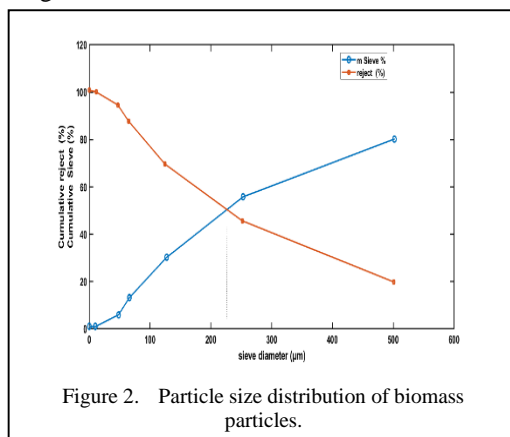


Figure 2. Particle size distribution of biomass particles.

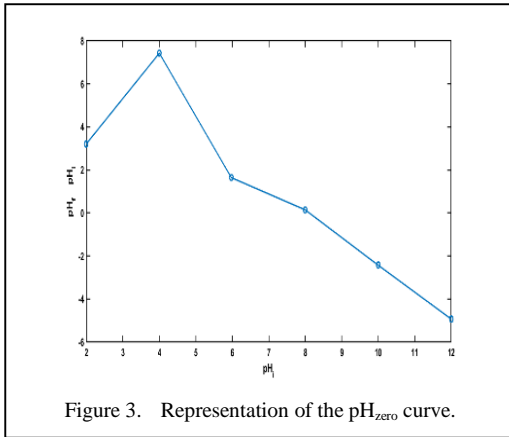


Figure 3. Representation of the pH_{zero} curve.

TABLE I. PHYSICAL AND CHEMICAL CHARACTERIZATION OF ADSORBENTS.

Biomass Parameters	The results
The equivalent diameter	220 μm
Specific surface per unit mass	0.0285
Humidity H%	1.5 %
Apparent volumetric mass	0.956 g/ml
Actual density	1.47 g/ml
Electrical conductivity	0.026 $\mu\text{s/cm}$
pH	8.42
pH_{zero}	8

B. Determination of Equilibrium Time

To assess the adsorption kinetics of the methylene blue under investigation, it is necessary to consider that adsorption involves the transfer of the pollutant from the liquid phase to the solid phase. In this context, the duration of contact between the two phases serves as a limiting factor, as depicted in Fig. 4.

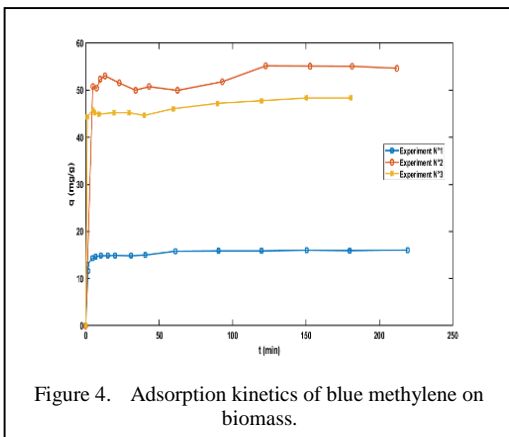


Figure 4. Adsorption kinetics of blue methylene on biomass.

C. Modeling of Adsorption Kinetics

The pseudo-first-order model and the pseudo-second-order model were taken into consideration, as presented in Table II.

1) Pseudo-first-order model

Based on the data presented in Fig. 5, it can be inferred that the Lagergren equation, namely the pseudo-first order model, is not suitable for describing the adsorption behaviour of methylene blue across the range of starting concentrations investigated in this study

2) Pseudo-second-order mode

In the diagram presented in Fig. 6. the pseudo-second order equation is frequently employed in accurately characterising the kinetics of pollutant fixation on the adsorbent. The utilisation of the pseudo-second order model enables the comprehensive analysis of adsorption kinetics, encompassing both scenarios of quick solute fixation on highly reactive sites and gradual fixation on energy sites.

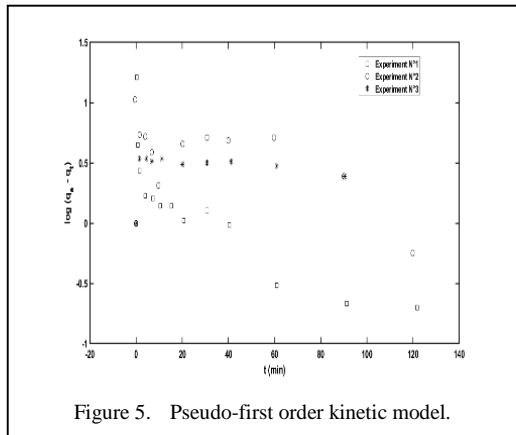


Figure 5. Pseudo-first order kinetic model.

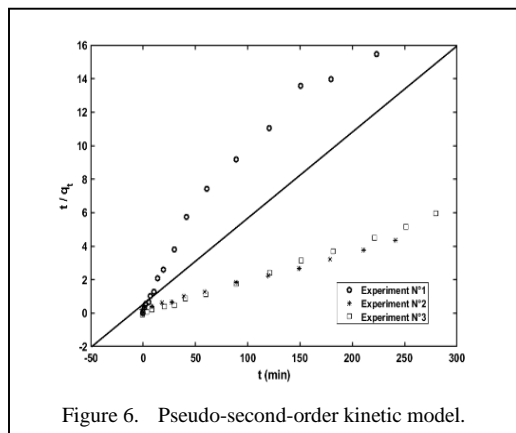


Figure 6. Pseudo-second-order kinetic model.

TABLE II. PSEUDO-FIRST-ORDER AND PSEUDO-SECOND-ORDER MODEL CONSTANTS.

	Pseudo-first order Parameters		Pseudo-second order Parameters	
	$C_0=50$ mg/l	K_1	0.0122	K_2
	R^2	0.828	R^2	0.958
	q_{exp}	16.1526	q_{exp}	16.1526
	q_{th}	1.256	q_{th}	13.21
$C_0=100$ mg/l	K_1	0.0059	K_2	0.01011
	R^2	0.5255	R^2	0.9995
	q_{exp}	57.6231	q_{exp}	57.6231
	q_{th}	5.5937	q_{th}	57.9034
$C_0=150$ mg/l	K_1	0.1264	K_2	0.04406
	R^2	0.736	R^2	0.9997
	q_{exp}	46.90325	q_{exp}	46.90325
	q_{th}	5.425	q_{th}	47.1698

IV. CONCLUSION

In this research, the adsorption method has been selected as a viable approach for eliminating contaminants. The specific objective is to purify water polluted with pharmaceutical compounds, emphasising utilising industrial dead biomass as the adsorbent material. The biomass is commonly disposed of in natural environments or utilised as agricultural fertiliser. Our analysis of this sorbent has regularly seen a notable abundance of negative charges within the biomass. The infrared spectroscopy analysis has facilitated identifying the precise chemical groups accountable for the adsorption process. In order to evaluate the efficacy of biomass in the remediation of water contaminated with methylene blue, a series of batch adsorption tests were conducted. The experimental findings presented herein provide evidence for biomass's effectiveness in removing pharmaceutical contaminants from water. It was observed that the equilibrium adsorption capacity increases with an increase in the starting concentration of methylene blue, ultimately reaching maximum adsorption of 57.80 mg/g after a contact time of 150 minutes. Furthermore, our study sought to determine the optimal kinetic model that portrays our empirical findings well. The pseudo-first-

order model and the pseudo-second-order model were taken into consideration. Upon conducting the necessary experiments and analyzing the data, it has been determined that the pseudo-second-order model provides the most accurate representation of the kinetics involved in the adsorption process.

ACKNOWLEDGEMENTS

University of Medea, LBMPT team and Hall Technology of University Dr. Yahia Fares.

REFERENCES

- [1] Visa, A., Maranescu, B., Lupa, L., Crisan, L., & Borota, A. (2020). New efficient adsorbent materials for the removal of Cd (II) from aqueous solutions. *Nanomaterials*, 10(5), 899.
- [2] Yous, R., Khalladi, R., & Cherifi, H. (2021). Simultaneous sorption of heavy metals on Algerian Bentonite: Mechanism study. *Water Science and Technology*, 84(12), 3676–3688.
- [3] Hou, D., et al. (2020). Simultaneous removal of iron and manganese from acid mine drainage by acclimated bacteria. *Journal of Hazardous Materials*, 396, 122631.
- [4] Alexander, J. A., Ahmad Zaini, M. A., Surajudeen, A., Aliyu, E.-N. U., & Omeiza, A. U. (2019). Surface modification of low-cost bentonite adsorbents—A review. *Particle Science and Technology*, 37(5), 538–549.

AC Current Measurement with ARM Microcontroller and Current Transformer CR8349-1500

Dorđe Lazarević¹, Uroš Ilić², Jovan Ćirić³, Aleksandar Veličković⁴

^{1,2}Faculty of Electronic Engineering, Niš, Serbia

^{3,4}Toplica Academy of Vocational Studies, Prokuplje, Serbia

¹djordje.lazarevic@elfak.ni.ac.rs, ²uros.ilic@elfak.ni.ac.rs, ³joca.ciric@gmail.com,

⁴avelickovic20@gmail.com

Abstract—This paper presents AC current measurement utilizing ARM microcontroller and the current transformer CR8349-1500. Also, this paper describes the method for measurement and using of the current transformer for determining the value of AC current. For this purpose was developed an experimental prototype system with a current transformer CR8349-1500 for PCB mounting and a STM32F401CCU6 microcontroller development board. Converting the signal from current to voltage is done using a resistor, by sampling the voltage signal on the resistor itself. First is used digital low-pass filter for the signal from the current transformer on the burden resistor. After that is done subtracting the sampling signal from the offset value and final calculation of the RMS current value. The final results of measurement are given in the tables with an appropriate comparison of errors in measuring on the microcontroller prototype system and high precision power analyzer Chauvin Arnoux C.A 8334B. This research describes prototyping and experimental work with AC current measurement system. This type of measurement is very useful for application in a device for power measurement such as power analyzers. In regulated electric drives, as well as in the diagnostics and monitoring of machines and transformers, current transformers can have significant applications.

Keywords - current transformer, ARM, microcontroller

I. INTRODUCTION

The method for current measurement in the electrical circuit using an ammeter is not efficient

in most industrial appliances. The Ampere meter has shunt resistance. The measured circuit is galvanically connected with a shunt and it can dissipate heat in the cases of large values of current. This implies that it is necessary to develop a system for current measurement in which there will be no significant affect of the sensor on the operation of the electric circuit [1]. A simple AC current measurement system can be realized using a new ARM microcontroller with CR8349-1500 current transformer. The utilizing this type of microcontroller and AD converter with a higher resolution, compared to the existing platforms with 8-bit controllers, a higher accuracy of alternating current measurement is achieved and a higher efficiency of the system itself. By using this type of measurement system, it is expected that the system will be able to obtain measurement results correctly and appropriately. The shunt can be used for the current measurement, but the main problem with it is heating. The heating of the shunt caused by high currents can lead to measurement errors. Achieving high measurement accuracy results in an increase in the price and dimensions of the shunt itself [2]. Also, for AC current measurement, Hall-effect sensors can be used. They are most often applied in measurement in power stations, electric motors, and power electronics [3]. Therefore, the using of current transformers in AC current measurement circuits has several advantages over Hall - Effect based sensors and shunts. Current transformers have a higher current capability without significant power losses and thermal limitations. Also, they

provide better electrical insulation, have better compatibility with standardized instrumentation, and offer better accuracy and linearity in comparison with Hall-effect sensors and shunts. The transformer current sensor consists of a toroid core, primary and secondary coils. The primary coil is a conductor which transmits an electric current to the load and it is pulled through the air gap of the toroid core. On the core is the secondary coil on which the current is induced. By processing the voltage induced on the coil, the value of the current flowing through the consumer is obtained. With this method, the current will be represented as a function of the voltage [4]. Typically, solutions that involve current measurement are usually part of research related to electricity consumption measurement systems. Often, this type of solution and research includes using or designing a prototype system that is based on 32-bit ARM or an 8-bit microcontroller, for example, Atmega328P or similar with external components such as EEPROM, RTC, LCD, Wi-Fi module, etc. [5].

II. CURRENT TRANSFORMERS

An instrumentation transformer, which is specially designed for transforming alternating current in its secondary coil is called a current transformer. The current in the primary coil is practically current which flows through the conductor. Indirect current measuring from the high voltage subsystem can be done by using this type of current transformer. This type of transformer is known as a window-type current transformer or as a core-balance transformer. The principle of working of the current transformer and voltage transformer is the same. A short circuit condition is a normal working mode for a current transformer with the use of a burden resistor. The current flowing on the primary coil affects the current flowing through

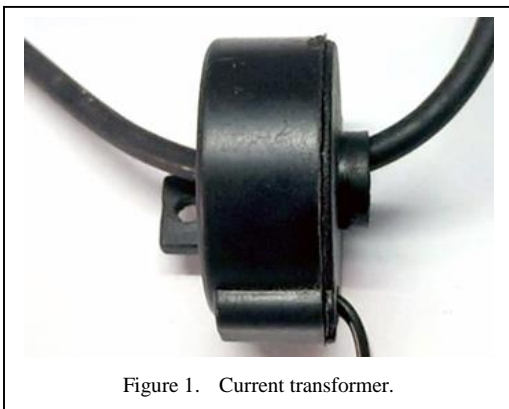


Figure 1. Current transformer.

the secondary coil. Fig. 1 is shown a current transformer.

Forming a single loop and the turns ratio 1:N is possible by placing a wire inside the window of the current transformer. A current transformer must satisfy the amp-turn ratio as well as any other transformer as shown in Eq. (1)

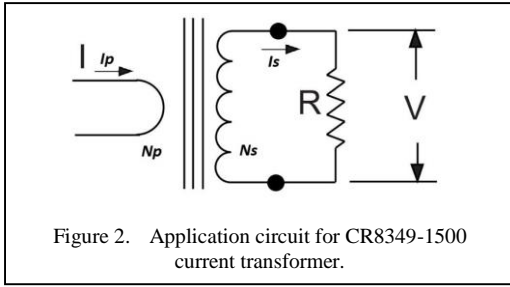
$$TR = \frac{N_p}{N_s} = \frac{I_s}{I_p}, \quad (1)$$

where, TR is ratio of the transformer, N_p is primary turns number, N_s is secondary turns number, I_p is primary coil current and I_s is Secondary coil current.

Secondary current can be expressed as in Eq. (2):

$$I_s = I_p \frac{N_p}{N_s}. \quad (2)$$

Theoretically, the primary current of the current transformer is exactly equal to the secondary current multiplied by the turns ratio, but in practice, it is not the case. To get it to an excitation state, the core of the transformer is consuming a part of the current. The primary and secondary current vector is zero for an ideal current transformer. In the real case, in a current transformer always exist a phase difference because the current from the primary coil has to excitability the core [6]. The values of uncertainty in current transformers are of order as a few parts in 10^3 [7]. A current measuring transformer manufactured by CR Magnetics of the CR8300 series was used for the preparation of this work. This current transformer is selected because of its small dimensions, availability on the market and ease of use in the circuit. The core of this type of current transformer is made of high-quality silicon and is intended for general use when measuring AC values. Also, this current-measuring transformer allows the measurement of alternating current in circuits with presents DC offset. Because of its small dimension, it is very convenient for using in electronic circuits. Also, making a prototype of a measuring system with this type of current transformer is relatively simple. The main application of this type of current transformer is in circuits for measuring motor current, power meters, and measuring electric current at high frequencies. Fig. 2 shows the application of a transformer in a circuit with a burden resistor in the secondary circuit. Equation (3) shows the

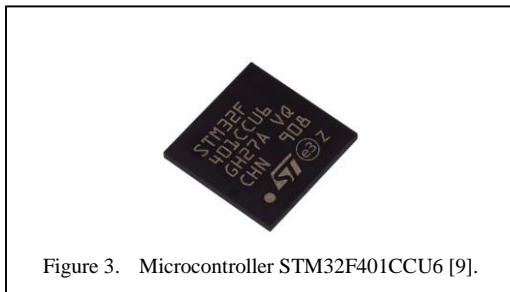


dependence of the voltage on the secondary on the applied current and resistance together with the coefficient provided by the manufacturer [8].

$$V = \frac{IR}{T_e} \quad (3)$$

III. ARM MICROCONTROLLERS

ARM microcontrollers are based on 32-bit processors depending on RISC (Reduced Instruction Set Computer) computer structure. This type of processor is contained in the STM32 series of microcontrollers and they are a product of ARM Holdings. Acorn Computers Limited named Acorn RISC Machine until the emergence of Advanced RISC Machines produced the first ARM processor in 1985 [9]. The successor of the ARM Cortex-M3 is the ARM Cortex-M4 microcontroller. All arithmetic and logical operations are performed in one clock cycle and it is a low cost small and energy-efficient ARM processor [10]. As opposed to the traditional device cost, engineers are increasingly looking at reducing the system cost. A single, more powerful device can potentially replace three or four traditional 8-bit devices which are implemented as it is by organizations. By improving the amount of code reuse across all systems other cost savings can be achieved. For programming Cortex-M processor-based microcontrollers can be used C programming language. These microcontrollers are based on a well-established architecture and that means the application code can be ported and reused easily. Also, this provides reducing development time and cost of testing [11]. Fig. 3 is shown the



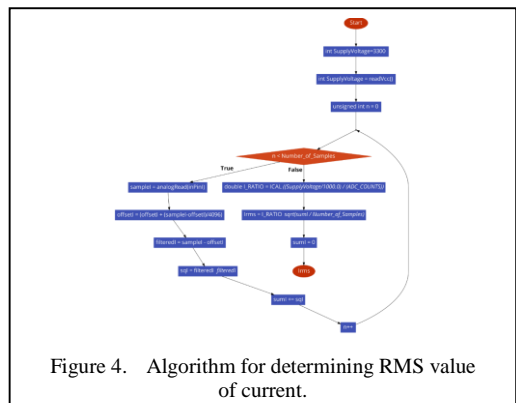
STM32F401CCU6 microcontroller, which is used for this research.

IV. MEASUREMENT METHOD

The method for current measurement in this research is based on the application of a current transformer and searching for the minimum and the maximum voltage value on the burden resistor and then finding the correct value of the current by using the formula for RMS value.

$$I_{rms} = \sqrt{\frac{1}{MN} \sum_{k=1}^{MN} i_k^2} \quad (4)$$

The current transformer in this case is used to sense the current by the secondary voltage which is present on the burden resistor. Converting the signal from current to voltage is done using a resistor, by sampling the voltage signal on the resistor itself. It is proportional to the current which flows through the conductor where the current is measured [12]. Then the voltage signal is scaled to 1.65V by a voltage divider and as such a signal is introduced to the input of the microcontroller. A digital low-pass filter is also used for the signal from a current transformer on the burden resistor. This digital low-pass filter is used for extracting a 1.65 V DC offset from the signal. After that subtracting the sampling signal forms an offset value and after that signal is centered on a 0 value. After that, the values of the voltage signal sampled on the resistor are summed and finally, the RMS value of the current is determined based on Eq. (4). After finishing the root-mean-square value calculation of the signal, accumulators are reset to 0. It must be noted that the main sources of potential errors in this circuit come from the components themselves, that is, from their tolerance values. This value of current is sent over UART to PC. Also, the measurement value is presented on an



LCD screen on the prototype. Fig. 4 shows the algorithm for determining the RMS value of the current.

V. EXPERIMENTAL WORK AND RESULTS

For the experimental purpose, it is developed a prototype measurement system based on a STM32F401CCU6 microcontroller [13]. The microcontroller is placed on the development board BlackPill and it is fully supported for programming in the STM32CubeIDE development environment and also in Arduino IDE. The prototype consists of a microcontroller development board, current transformer, voltage divider, LCD, buck regulator, and CAN Bus module based on MCP2515 [14] CAN bus controller with TJA1050 CAN transceiver [15]. The voltage divider consists of two 10K resistors and it forms an offset DC voltage of 1.6V from 3.3V. The output of the voltage divider is connected to channel 5 of the internal sigma-delta 12-bit AD convertor in a microcontroller. This experimental module can be supplied by an external power supply with a voltage range of 6-12V, thankfully to the buck regulator module. Also, the board has a 5V power supply over a micro USB type C connector which is on the development board with a microcontroller. For displaying information of measurement it is used an alphanumeric LCD 1602 display is connected to a microcontroller parallel operating mode. Also, measurement data is possible to read over UART protocol and USB on a PC or over CAN bus protocol over any other device which supports this type of interface for receiving data. Fig. 5 presents the experimental microcontroller board which is used for this research.

The results of the alternative current measurements are shown on the power analyzers display. These results are available for reading and comparison with the results shown on the display of the microcontroller system [16]. The connection of the system is shown in the block

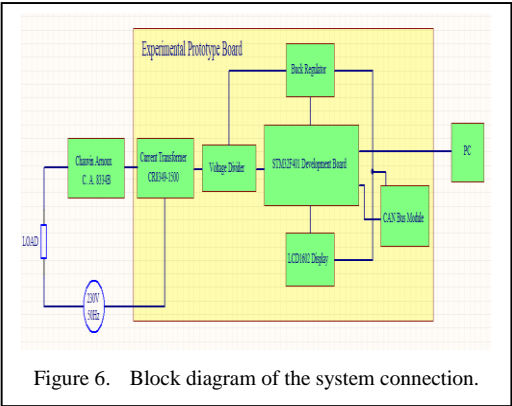
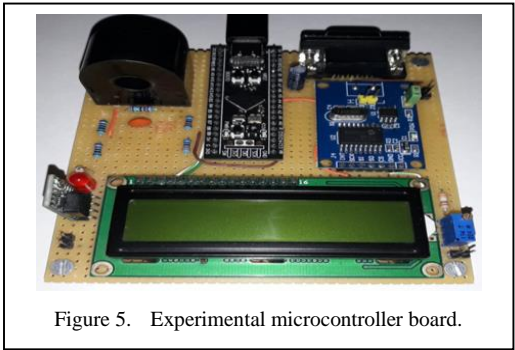
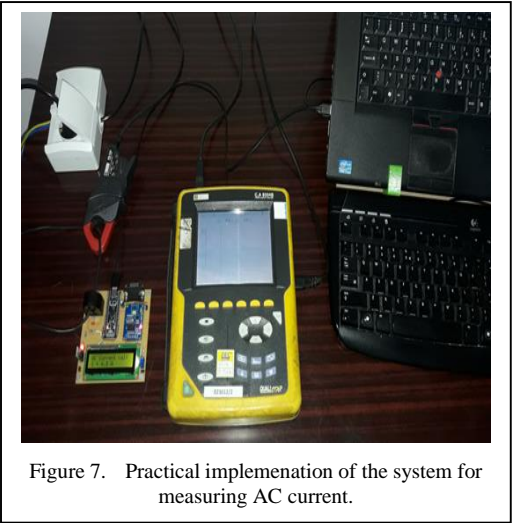


diagram of the connection of the system in Fig. 6. Also in the picture is presented a block diagram of the microcontroller board.

Power analyzer Chauvin Arnoux C. An 8334B [17] is used for measuring the current through the conductor which is drawn through the hole of the current transformer. This type of measuring instrument was used because it was calibrated and tested in the national laboratory before using in the experiment and it is used as a reference measuring device based on which measurement error was determined. The method for measuring alternating current with this type of instrument is indirect, using current clamps. The accuracy class of the C. A 8332B instrument is 0.5. For this measurement are used current clamps MN 93A [18] which have 100A and 5A measurement ranges. The range of measurement of the current clamp is set at 100A. The power supply for the experimental microcontroller board is used from the computer via a USB cable. The practical implementation of the system for measuring AC current is presented in Fig. 7.



As loads are used resistive, inductive, and mixed loads. For resistive loads are used iron with a power of 1000W and a heater of 750W. For inductive loads are used inductive cooker with a power of 2000W and a vacuum cleaner with a power of 1900W which represents non-linear loads with regulation. Higher values of current are got by turning on more devices at the same time and increasing the number of turns on the current transformer.

The results of measurements in this research are given in Tables I-V. Measurement is done in 3 steps. The first step presents the measuring of current without calibration of the experimental microcontroller system. As it is shown in Table I, these results are used for error calculation and calibration constant measuring which are integrated into the program for the microcontroller. Without any calibration of the sensor, an error that occurs during the process of measurement is very high so that means the results of the measurement in this way are unusable.

TABLE I. RESULTS OF THE CURRENT MEASUREMENT WITHOUT CALIBRATION.

Number of measurement	Experimental microcontroller board (A)	Power analyser Chavouin Arnoux C.A.8334B (A)	Relative Error (%)
1.	3.5	2.9	20.6
2.	6.2	5.3	16.9
3.	9.6	7.1	35.2
4.	10.3	9.4	9.6
5.	12.2	11	10.9
6.	16.1	14.9	8.1
7.	20.1	17.9	12.9
8.	23.2	21.4	8.4
9.	26.4	20.8	21.2
10.	33.6	30.7	9.4
11.	40.7	38.5	5.7
12.	43.9	41.2	6.5
13	47.5	45	5.5
14.	52.6	47.1	11.6

The calculated mean measurement error is 13.04%. From this mean measurement error is calculated as calibration constant and its value is 0.8696. With this value of calibration constant is obtained more precise measurement values for different types of loads are and this constant is used for all measurements for all types of loads.

The relative error for all measurements in this research can be expressed as in Eq. (5):

$$RE = \frac{|PM-PAM|}{PAM} \times 100\% . \quad (5)$$

The mean measurement error is calculated by the Eq. (6):

$$ME = \frac{1}{N} \sum_{i=1}^N \frac{|PM_i-PAM_i|}{PAM_i} \times 100\% , \quad (6)$$

where ME is mean error, N is number of measurement, PM is prototype measurement, PAM is power analyzer measurement. In addition to the relative error and the mean value of error for a larger number of measurements, for statistical data processing and increasing data reliability, it is important to define and use standard deviation. Standard deviation is calculated for cases with multiple results of measurements.

Equation (7) which is used for the calculation of standard deviation is defined as:

$$s = \sqrt{\frac{1}{n-1} \sum_{i=1}^n (X_i - \bar{X})^2} , \quad (7)$$

where S is standard deviation, N is number of measurement, \bar{X}_i is observed values of the AC current samples and \bar{X} is the mean value of observed values.

The second step presents current measurements with changing different types of loads. The first is a used heater with a power of 750W which is pure resistive load and current measurement results are given in Table II.

TABLE II. RESULTS OF THE CURRENT MEASUREMENT FOR THE HEATER WITH A POWER OF 750W.

Number of measurement	Experimental microcontroller board (A)	Power analyser Chavouin Arnoux C.A.8334B (A)	Relative Error (%)
1.	3.2	3.1	3.2

The third measurement was finished by using electrical iron with a power of 1000W and the current diagram through this type of load is presented in Fig. 8.

The results for these measurements are given in Table III.

TABLE III. RESULTS OF THE CURRENT MEASUREMENT FOR THE IRON WITH A POWER OF 1000W.

Number of measurement	Experimental microcontroller board (A)	Power analyser Chavouin Arnoux C.A.8334B (A)	Relative Error (%)
1.	4.6	4.8	4.1

The next measurement has done by using an induction cooker. This type of load has PWM regulation with an IGBT transistor. The shape of the current and voltage on this type of device is not pure sinusoidal and that is a particularly occasional device for checking the measuring performance of the microcontroller system. The mean measurement error is 3.47%, while the value of the standard deviation is approximately

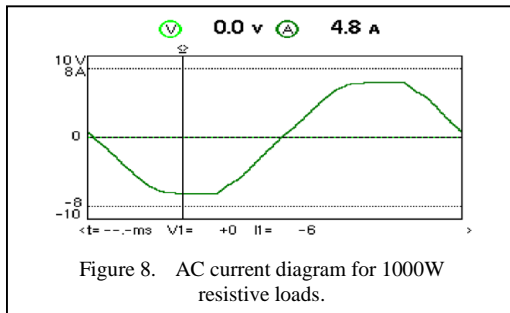


Figure 8. AC current diagram for 1000W resistive loads.

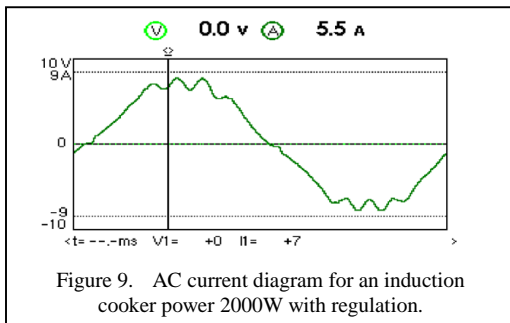


Figure 9. AC current diagram for an induction cooker power 2000W with regulation.

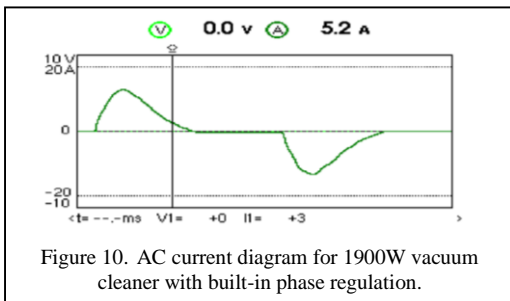


Figure 10. AC current diagram for 1900W vacuum cleaner with built-in phase regulation.

0.1885. The power is gradually increased and therefore current through the device. The AC current diagram for the induction cooker with regulation is presented in Fig. 9.

The results of measurement, in this case, are given in Table IV.

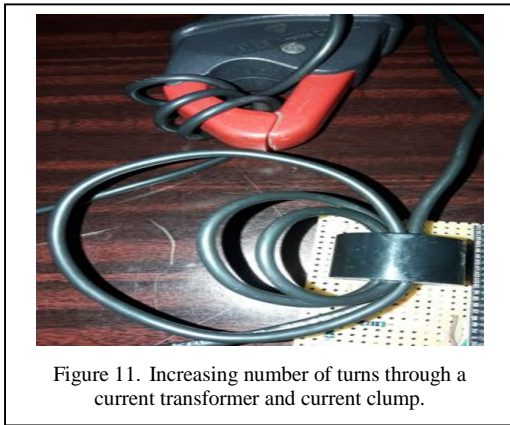
TABLE IV. RESULTS OF THE CURRENT MEASUREMENT FOR INDUCTION COOKER WITH POWER 2000W.

Number of measurement	Experimental microcontroller board (A)	Power analyser Chavouin Arnoux C.A.8334B (A)	Relative Error (%)
1.	4.2	4.4	4.5
2.	4.6	4.7	2.1
3.	5.2	4.9	6.1
4.	5.7	5.5	3.6
5.	6.0	5.8	3.4
6.	6.1	6.0	1.6
7.	6.8	6.6	3

As an inductive load with variable power is used a vacuum cleaner with a power of 1900W. As well as the induction cooker this device has also integrated regulation, but in this case, it is the circuit for phase regulation with Triac and it is also convenient for measurement of the current because it is a normal occurrence in practice. The mean measurement error for this case is 3.47%, while the value of the standard deviation is approximately 0.2047, and Fig. 10 is presented AC current diagram for this load.

TABLE V. RESULTS OF THE CURRENT MEASUREMENT FOR THE VACUUM CLEANER OF 1900W WITH CHANGING POWER.

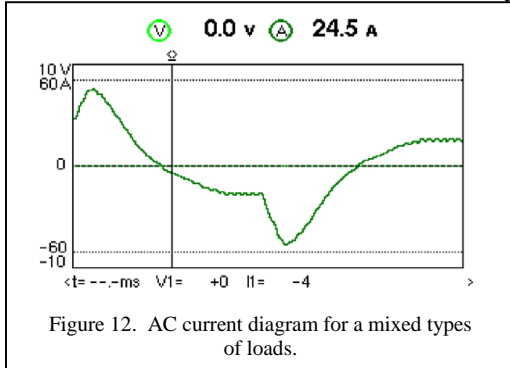
Number of measurement	Experimental microcontroller board (A)	Power analyser Chavouin Arnoux C.A.8334B (A)	Relative Error (%)
1.	3.3	3.2	3.1
2.	3.7	3.8	2.6
3.	4	3.9	2.6
4.	4.2	4.1	2.4
5.	4.4	4.5	2.2
6.	4.8	4.9	2
7.	5.0	5.2	3.8
8.	5.2	5.3	1.9
9.	5.4	5.8	7.4
10.	5.5	5.9	6.7



Results of the current measurement for a vacuum cleaner with 1900W power are given in Table V.

The final step in measurement is measuring AC current with high currents. The current transformer which is used in this research can measure current up to 75A. This current is not possible to provide, in the conditions in a classic single-phase electrical network, because the maximum value of current cannot exceed the value of 16A which is the max value of current of the fuse for every 230V electrical system. For providing a current higher than 16A it is possible to increase the turn number through the current transformer. This step allows making current with higher values. For this purpose are used different types of loads. This research used a conductor 2.5mm wide so it is possible to make 4 turns through the transformer and multiply readings of current. Also, this step is done on the side of the power analyzer where the current clamp is adjusted on the 100A range. Fig. 11 shows increasing turns on the current transformer on the side of the primary coil for getting higher values of current.

As expected increasing current through the current transformer also increases the accuracy



of measuring. Since the current transformer with 75A current capability is predicted for measuring higher values of current its accuracy is the highest between 10A and 60A. The calculated mean relative measurement error is 0.6%, while the value of the standard deviation is approximately 0.1091. The AC current diagram for mixed types of loads is presented in Fig. 12.

Table VI are given measurement results with mixed types of loads.

TABLE VI. MEASUREMENT RESULTS – MIXED TYPES OF LOADS.

Number of measurement	Experimental microcontroller board (A)	Power analyser Chavouin Arnoux C.A.8334B (A)	Relative Error (%)
1.	13.6	13.7	0.7
2.	15.2	15.1	0.6
3.	17.1	17.2	0.6
4.	19.6	19.5	0.5
5.	21.3	21.6	1.3
6.	24.6	24.5	0.4
7.	29.3	29.2	0.3
8.	30.1	30.2	0.3
9.	35.6	35.7	0.3
10.	39.7	40.6	2.2
11.	45.9	46	0.2
12.	52.3	52.2	0.2
13.	58.9	59.1	0.3

From this table, it can be concluded that the more precision measurement is obtained with higher values of current as aspected. There are great possibilities of expanding the proposed measuring system by adding other types of communication interfaces such as Ethernet and RS485, and it is also possible to expand by adding additional current measuring transformers, after which this system can be used to measure current in three-phase systems.

VI. CONCLUSION

This research describes prototyping and experimental work with AC current measurement system. This type of measurement is very useful for application in a device for power measurement such as power analyzers. In regulated electric drives, as well as in the diagnostics and monitoring of machines and transformers, current transformers can have significant applications. In addition to monitoring and testing machines, they can also be used in protection, control, and regulation

systems. This system could be particularly useful in the industry for measuring current through consumers of different types, and with the application of a current transformer for the current measurement range of up to 5A, with an external current transformer, it is also possible to use it in transformer stations and plants where measurements of higher values of the currents are required. Current measuring transformers are the basis for measuring power (active, reactive, and apparent). Using of ARM microcontroller with a 12-bit AD converter with this type of current transformer provides enough precision to get correct measurement results. After proper calibration of the system with high precision power analyzer can be seen that the measurements of a prototype are very close to the analyzer measurement with minimal error. Also utilizing a current transformer can be applied in the devices for AC motor protection together with electronics for relay or contactor control. The obtained results are at the expected level and are in agreement with the literature references of previous research and are certainly an inspiration for further work and continued research.

REFERENCES

- [1] Sari, M. B., Yuliantini, L., Prihadi, H., & Djamal, M. (2021). Easy monitoring and data record system of electric current detected by ACS712 affordable non-destructive electrical current sensor. *Pillar of Physics*, 13(2), 1-7.
- [2] Tan, X., Li, W., Xu, X., Ao, G., Zhou, F., Zhao, J., Tan, Q., & Zhang, W. (2023). Contactless AC/DC Wide-Bandwidth Current Sensor Based on Composite Measurement Principle. *Sensors*, 22(20), 7979-7998.
- [3] Lalwani, A. V., Yalamarthy, A. S., Alpert, H. S., Holiady, M. A., Eisner, S. R., Chapin, C. A., & Senesky, D. G. (2022). Hall-Effect Sensor Technique for No Induced Voltage in AC Magnetic Field Measurements Without Current Spinning. *IEEE Sensors Journal*, 22(2), 1245-1251.
- [4] Antara, M. A. S., Putra, I.G.E.W., Suteja, I. W. A., & Widja, I. B. P. (2022). Electricity Consumption Measurement System Using Current Transformer Sensor TA12-100. *E Protek Jurnal Ilmiah Teknik Elektro*, 9, 36-43.
- [5] Kishore, K. P. C., Antony, V. P. R. J., Ebenezer, A. B., Vishalakashi, S., & Vidhya, G. (2018). IOT Based Energy Meter Reading System with Automatic Billing. *International Journal of Engineering & Technology*, 7(3.27), 431-434.
- [6] Debashis, D. (2020). AC Current Measurement using Current Transformer and Arduino. Available at: <http://circuitdigest.com/electronic-circuits/ac-current-measurement-circuit-using-current-transformer-and-arduino>.
- [7] Timmons, R., & Barczyk, T. (2013). Precision AC Current Measurement Technique. *NCSLI Measure*, 8, 36-41.
- [8] CR Magnetics, datasheet. (2008). Available at: <https://www.crmagnetics.com/Assets/ProductPDFs/CR8300%20Series%20Specification%20Page.pdf>.
- [9] Kaplesh, P. (2020). Performance Evaluation of SHA-3(KECCAK) on ARM Cortex-A9 and Comparison with ARM 7TDMI and Cortex-M4. *International Journal of Computer Networks and Applications*, 7, 1-9.
- [10] Seo, H., & Azarderakhsh, R. (2021). Curve448 on 32-Bit ARM Cortex-M4. *Information Security and Cryptology – ICISC 2020*, 12593, 125-139.
- [11] Joseph, Y. (2010). The definitive guide to the ARM Cortex-M3. *Elsevier Inc., Kidlington, Oxford, UK*. Available at: http://http://centaur.sch.bme.hu/~holcsik_t/sem/The%20Definitive%20Guide%20to%20the%20ARM%20Cortex-M3.pdf.
- [12] Gupta, S. (2019). Current Sensing Techniques using Different Current Sensors. Available at: <https://circuitdigest.com/article/how-to-measure-current-in-a-circuit-with-different-current-sensing-techniques>.
- [13] STM32F401xB, datasheet. (2019). Available at: <https://www.st.com/resource/en/datasheet/stm32f401cb.pdf>.
- [14] MCP2515, Stand-Alone CAN Controller with SPI Interface. (2003). Available at: <https://ww1.microchip.com/downloads/en/DeviceDoc/MCP2515-Stand-Alone-CAN-Controller-with-SPI-20001801J.pdf>.
- [15] TJA1050, high-speed CAN transceiver. (2003). Available at: <https://www.nxp.com/docs/en/datasheet/TJA1050.pdf>.
- [16] Lazarević, Đ., Živković, M., Kocić, Đ., & Čirić, J. (2022). The Utilizing Hall Effect-Based Current Sensor ACS712 for TRUE RMS Current Measurement in Power Electronic Systems. *Systems, Scientific Technical Review*, 72, 27-32.
- [17] C.A 8332B, C.A. 8334B, Three Phase Power Quality Analyzer, users Manual. (2010). Available at: https://www.chauvin-arnoux.com/sites/default/files/download/nf-ca_8332_ca_8334.pdf.
- [18] MN93A, Current sensors. (2021) Available at: <https://www.chauvin-arnoux.co.uk/sites/default/files/hlhbwomd.pdf>

Characterization of Watermelon Rind for Energy Purposes

Mikaely Renaly Carlos da Silva^{1*}, Silvia Layara Floriani Andersen²

^{1,2}Graduate Program in Mechanical Engineering, Federal University of Paraíba, João Pessoa, Brazil

²Department of Renewable Energy Engineering, Federal University of Paraíba, João Pessoa, Brazil

¹mikaely.silva@alumni.cear.ufpb.br, ²silvia@cear.ufpb.br

Abstract—Due to the growth in energy demand, the search for renewable energy sources has increased. One of these energy sources is biomass, which is a resource with favorable physical, chemical, and economic characteristics for energy production. Agricultural residues are a suitable form of biomass for energy production. The objective of this study was to analyze the possibility of using agricultural waste, specifically watermelon (*Citrullus lanatus*) rind, as an alternative and renewable source of energy in thermochemical conversion processes. This is because its production is global, and the rind is a solid waste with limited utilization and often improperly disposed of in the environment. For characterization, proximate analysis, higher heating value, X-ray fluorescence of the ashes, and thermogravimetric analysis in an oxidizing atmosphere were performed to assess the thermal behavior of the waste. It was found that the analyzed watermelon rind has potential for use in thermal conversion processes, with a low ignition temperature of 120.52°C and a high content of volatile materials (73.76%), indicating rapid biomass combustion. As for the analysis of its ashes, it was possible to observe an ash content of 12.08%, with a higher quantity of the chemical compounds P₂O₅, K₂O, and Cl in its composition, and an Alkali index of 14.25. Among the results obtained, a high moisture content of 95.18% and a heating value of 3620 kcal/kg were confirmed, indicating its energy potential.

Keywords – *Citrullus lanatus*, biomass, bioenergy, solid waste

I. INTRODUCTION

Energy influences life and all aspects related to it, with a connection to the development of countries and civilization. Additionally, it is of great importance for the ecosystem. The demand for energy has been surpassing the available supply, and factors such as the scarcity of fossil fuels and climate change have increased the pursuit of sustainability and renewable energy sources. Due to the high energy demand, renewable energy sources are desirable, and one of these sources is biomass, which is a renewable resource derived from organic matter such as plants, wood, and various waste materials [1].

Brazil is one of the countries where renewable energies are widely used. In 2022, approximately 47.4% of the energy generated in Brazil came from renewable sources, accounting for 14.1% of global energy production and 11.5% concerning the countries in the Organisation for Economic Co-operation and Development. The most commonly used renewable energy source in Brazil is biomass, which encompasses all renewable resources derived from organic matter with the capacity to be used as an energy source [2].

One consequence of urban development is the increase in solid waste. In the case of waste from fruit pulp production, which is characterized by high moisture and a rich content of organic matter, companies are seeking alternative methods for utilizing this waste to

*Supervisor: Monica Carvalho - Renewable Energy Engineering Department/Federal University of Paraíba (UFPB), João Pessoa, Brazil

prevent groundwater contamination and soil damage [3].

As an agricultural country, watermelon is a popular fruit in Brazil due to its accessibility, good taste, and the presence of essential fibers, minerals, and vitamins [4]. However, the entire fruit is not consumed, and its rind and seeds are discarded. As a result, a significant amount of agricultural waste, specifically watermelon waste, is produced. While watermelon is consumed as fresh fruit, most of the watermelon rind is discarded, resulting in a large amount of waste (about one-third of the total watermelon mass) [5].

Watermelon rind can become an environmental problem due to the quantity of waste generated in association with their consumption [6]. Finding an energy use for watermelon rinds will not only reduce environmental pollution but also have an impact on human health (pathogens can rapidly develop in watermelon waste – [7]). In this context, considering the ongoing energy crisis, studying the potential of watermelon rinds for energy purposes aligns with the goals of energy transition.

With the aim of using watermelon rinds as a raw material in conversion processes, it is essential to study their physicochemical properties to aid in understanding the selection of the most compatible conversion processes for a specific biomass. Lignocellulosic biomass varies based on species, plants, age, climate, and location of origin, leading to variations in the physical and chemical properties of biomass species.

The use of solid watermelon rind waste for energy production would reduce improper waste disposal and could also replace other energy sources, emphasizing the importance of developing studies in this area. The objective of this work was to characterize watermelon rind waste for energy purposes. The characterization analyses conducted indicated the potential for use in thermal conversion processes.

II. MATERIAL AND METHODS

The solid waste selected for this study was watermelon rind, obtained from a restaurant located in the municipality of João Pessoa, Paraíba.

The moisture content was determined as the first step, using a Moisture analyzer AND MF-

50. After measuring the moisture content, the samples were dried in an air-circulating oven at $100 \pm 5^\circ\text{C}$, then ground in an industrial blender and sieved through a 100-mesh screen (< 0.149 mm) for compatibility with the analysis methodologies. Following these procedures, the physical-chemical characterization of the waste was performed using proximate analysis, higher heating value analysis, thermogravimetric analysis, and X-ray fluorescence of the ashes.

The proximate analysis is divided into percentages of moisture (% U), volatile matter (% MV), fixed carbon (% CF), and ash content (% Z). The volatile matter content expresses the material's combustion ease and is determined as the mass fraction of the fuel that volatilizes during the heating of a standardized sample [8].

The higher heating value (HHV) refers to the amount of energy contained in a given substance, measured through complete combustion at constant pressure and temperature. Thermogravimetry (TG or TGA) monitors the mass loss and/or gain of the sample over time/temperature, while derivative thermogravimetry (DTG) is the mathematical treatment where the first derivative of mass variation over time/temperature is recorded [9]. X-ray fluorescence allows for the identification of the composition and concentration of elements present in a sample [10].

The volatile matter content (% MV) was determined following ASTM E872 [11] standards, and the ash content (% Z) followed ASTM E1755 [12] standards. For these analyses, a muffle furnace was used. The fixed carbon content of the sample was determined on a dry basis as the difference between 100 and the sum of the ash content and volatile matter. The tests were conducted at least in duplicate, and the results represent the arithmetic mean of these.

For the analysis of higher heating value (HHV), an IKA C200 calorimetric bomb was used, following ASTM D5865 – 13 [13] standards. In the combustion chamber, a high-pressure reaction between oxygen and the sample being analyzed occurs. The sample is heated by an electric current, and the temperature change over time is measured by a precision thermometer.

The thermogravimetric analysis (TGA) and its derivative (DTG) were conducted using the TA instrument, model TGA Q50, under an oxidizing atmosphere at a constant flow rate of

50 mL/min, with approximately 10 mg of the sample. The analysis was performed starting from room temperature up to a temperature of 900°C, with a heating rate of 10°C/min.

X-ray fluorescence analysis (XRF) was carried out following ASTM E1621-13 [14] standards. In this analysis, watermelon rind ashes, produced using a muffle furnace at 575°C, were used. Hard pellets of the samples were prepared by pressing the ashes in a hydraulic press, with the addition of boric acid as a binder. Subsequently, these pellets were dried in oven at 100°C for 24 hours to remove residual moisture. The pellets were analyzed using the Shimadzu X-ray diffractometer, model FRX 1800, using the elemental method, with a 10 mm mask aperture diameter.

The Alkali Index, AI, is a parameter used in the context of thermochemical conversion processes, particularly in the combustion and gasification of biomass. AI is defined as the ratio of the basic to the acidic compounds in the ash [15] (i.e., a measure of the alkali metal content in biomass feedstock, primarily referring to sodium and potassium). AI is significant because these alkali metals (Na, K) can have substantial impacts on the efficiency and operation of thermochemical conversion processes.

III. RESULTS AND DISCUSSION

Regarding the physicochemical characterization of the biomass, Table I shows the results obtained in the proximate analysis and the higher heating value.

The watermelon rind exhibited a moisture content of 95.18%, which is an important parameter to consider. This result has an impact on pyrolysis and combustion processes, necessitating prior drying. Thus, the higher the moisture content in the biomass, the more energy is required to initiate the burning process. In other words, more energy is needed to vaporize the water, and less energy is available for the endothermic reactions.

A study conducted by [16] suggests that the presence of moisture in biomass hinders combustion due to reduced calorific value, leading to increased fuel consumption. According to [17], high moisture content results in environmental pollution due to an increase in particulate matter and products from incomplete combustion.

TABLE I. PROXIMATE ANALYSIS AND HIGHER HEATING VALUE.

Moisture content	95.18 (\pm 0.32)
Fixed Carbon*	26.11 (\pm 1.82)
Volatile Material*	73.76 (\pm 1.82)
Ashes*	12.08 (\pm 0.0014)
HHV measured (kcal/kg)*	3620.22 (\pm 27.72)

* On dry basis

Reference [18] notes that in the gasification process, high moisture content does not create technical difficulties but rather reduces process efficiency. This is because energy is used for water evaporation and to maintain the operating temperature, requiring additional fuel and oxidants.

The high volatile matter content of 73.76% indicates significant amount of combustible gases that can be released after heating the dry biomass. This value is also related to the ease of ignition and the speed of biomass combustion [15]. Moreover, a higher volatile matter content increases the capacity to produce oil from biomass subjected to pyrolysis [19].

The ash content is an important parameter for the combustion process, and the result found in this analysis was 12.08%. When utilizing the ashes resulting from watermelon rind combustion, it is important to predict that many of the elements found in the samples will be volatilized. Therefore, before proposing their use as fuel in boilers, it is important to ensure that this application does not represent a source of air pollution and does not cause damage to equipment [20]. Despite each residue having distinct composition characteristics, even when a material has a high ash content, it may still have favorable conditions for thermal processes [21].

According to [18], ashes can reduce efficiency because an excess of ash can decrease the heat involved in the process and lead to problems with deposition in the reactor. Therefore, it is fundamentally important to analyze the ash content.

The fixed carbon content is related to the amount of ash and volatiles. It represents the remaining mass after the volatile compounds have been removed, excluding ash and moisture content [22]. The fixed carbon content percentage of 26.11% determines the amount of

heat generated. The higher the fixed carbon content, the slower the combustion, and the longer the residence time.

The higher heating value (HHV) of the watermelon rind sample measured using a calorimetric bomb was 3620.22 kcal/kg. When calculated using Equation 1 with data obtained from the proximate analysis, the result of the HHV was 4651.91 kcal/kg.

Table II presents the HHV of various biomasses for comparison with the watermelon rind results from this study. It can be observed that practically all of the biomasses exhibit a high HHV when co [23], is 4274.15 kcal/kg for *Eucalyptus grandis*.

Regarding the thermogravimetric analysis, Fig. 1 displays the results of TGA and DTG analysis for watermelon rind in a synthetic air atmosphere. The TGA curve is represented by the black line, starting at 100°C, showing the sample's mass loss as the temperature increases under controlled atmosphere. The DTG curve is illustrated in blue and represented by temperature peaks, highlighting the rates of mass loss with increasing temperature.

Table III provides the results of temperatures and mass losses for the watermelon rind sample in an oxidizing atmosphere. The first event in the TG analysis is the 3.35% mass loss related to the material's moisture loss. The second event is associated with the decomposition of organic matter in the biomass, including the degradation of hemicellulose, cellulose, and lignin. Analyzing the results, it is evident that the mass loss occurs between temperatures of 220 to 290 °C, which is where the main hemicellulose degradation fractions take place [27]. According to the literature, lignin degradation begins at a temperature close to 200°C and ends near 800°C [28].

Analyzing the DTG curve, it was possible to determine that the ignition temperature was around 120 °C, coinciding with the beginning of the first volatile peak in the TGA curve. It was also observed that there was an increase in the rate of mass loss in the DTG curve.

The volatile matter content starts to be released at approximately 120 °C, initiating the combustion process. In this analysis, the volatile matter content was found to be 70.43%, the fixed

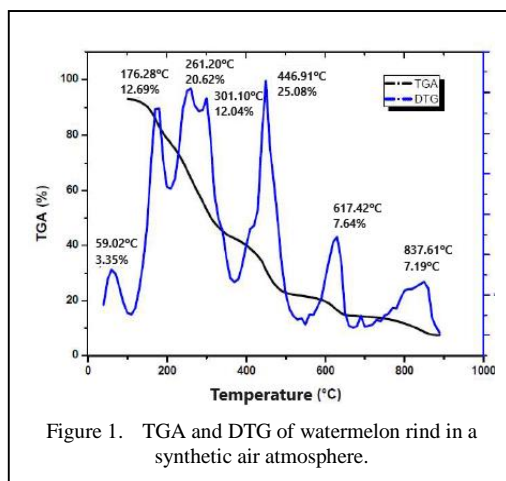


Figure 1. TGA and DTG of watermelon rind in a synthetic air atmosphere.

TABLE II. HIGHER HEATING VALUE OF DIFFERENT TYPES OF BIOMASS (KCAL/KG).

Watermelon rind	3620.22 (this study)
Poplar Residues	3943.50 ¹
Wood Chips	2222.75 ³
Wheat Straw	4851.81 ²
Açaí	4445.50 ²
Banana Stem	3895.79 ²
Rice Husk	3907.74 ²
Soybean Husk	4278.20 ²
Coffee	4445.50 ²
Grass	4008.12 ²
Eucalyptus Residues	6042.06 ³

¹Tabakaev [24], ²Rambo [25], ³Cai et al. [26].

TABLE III. TEMPERATURES AND MASS LOSSES FOR THE WATERMELON RIND SAMPLE IN A SYNTHETIC AIR ATMOSPHERE.

Temperature intervals (°C)	Peak temperature (°C)	Mass loss rate (mg.min ⁻¹)	Mass loss (%)
40 – 110	59.02	0.08	3.35
110 – 220	176.28	2.61	12.69
220 – 290	261.20	3.20	20.62
290 – 350	301.10	2.82	12.04
350 – 550	446.91	3.40	25.08
550 – 680	617.42	1.25	7.64
680 – 900	837.61	0.70	7.19

carbon content was 14.83%, and at the end of combustion, the residue generated is the ashes.

However, the ash composition varies depending on the analyzed biomass, with an ash content of approximately 8.5%. Comparing the

TABLE IV. X-RAY FLUORESCENCE SPECTROMETRY (XRF) RESULTS FOR WATERMELON RIND ASHES.

XRF	(% m/m)
P ₂ O ₅	27.03
K ₂ O	26.86
Cl	19.96
Na ₂ O	8.55
MgO	4.84
SO ₃	4.27
SiO ₂	3.79
Al ₂ O ₃	1.04
Fe ₂ O ₃	0.86
ZrO ₂	0.76
CaO	0.69
Cr ₂ O ₃	0.49
Br	0.40
ZnO	0.20
SrO	0.19
Al	14.25

*Calculated with XRF data.

results obtained from thermogravimetric analysis with those obtained from proximate analysis, differences can be observed, which may be attributed to the operational conditions under which the analyses were conducted.

As for XRF analysis, Table IV presents the composition of watermelon rind ashes, as well as the ash fusion values calculated.

The chemical composition of watermelon rind ashes primarily consists of compounds such as P₂O₅, K₂O, and Cl. The high Cl content found in watermelon rind could be result from the irrigation process during its cultivation or the soil where it was grown. Also, Cl can be associated with the use of pesticides and herbicides [29].

Different incineration temperatures and rates lead to varying ash compositions, affecting the ash fusion characteristics [30]. When the furnace temperature approaches the calcination temperature, some of the ashes volatilize, resulting in mass loss, particularly when the ashes have a high K₂O content [31].

The ash fusion, obtained from XRF analysis, was determined to be 14.25, indicating an Alkali index higher than 0.75. According to Pronobis [32], base/acid ratio results above 0.75 and rich in Na₂O and K₂O compounds suggest the formation of deposits in equipment.

The sodium (Na), potassium (K), and phosphorus (P) contents in the ashes can lower the ash fusion point. Therefore, the content in the biomass used as fuel in boilers should be reduced [33].

The presence of potassium (K) in the ashes can lead to the formation of compounds with lower fusion temperatures, potentially causing ash deposition in boilers or thermal conversion reactors. This ash deposition can reduce mass transfer, thereby decreasing equipment efficiency [34].

Utilizing watermelon rind as a biomass source can have broader environmental and economic implications beyond its energy potential. Environmental implications include the reduction of waste and decrease in greenhouse gas emissions, as the use of watermelon rind for energy production can help mitigate greenhouse gas emissions associated with organic waste as well as contribute to the principles of a circular economy. However, the economic viability depends on the logistics of collection, transportation, and processing.

Finally, the production of energy from watermelon rind and other food waste can be a promising approach to reduce food waste while offering a cleaner and more sustainable energy source. Utilizing watermelon rind for energy production in regions where watermelon production is prevalent holds potential feasibility and benefits for local communities. Additionally, these studies can contribute to meeting the growing energy demands and reducing dependence on fossil fuels, aligning with sustainability goals and greenhouse gas emissions reduction.

IV. CONCLUSIONS

Through the analysis of the results obtained from the experiment, the potential for using watermelon rind for energy generation has become evident. This potential is justified by its ease of acquisition and the amount of energy it can produce, making it suitable for thermal processes, provided its characteristics (moisture content, volatile matter, ash content, and fixed carbon) are considered, along with appropriate conversion technology.

The high moisture content in the sample can influence the Higher Heating Value, so this biomass needs to undergo a drying process before being used for energy generation.

The high volatile matter content of 73.76% indicates that the combustion of this biomass should occur rapidly, as confirmed by the Thermogravimetric Analysis, where it was

observed that the ignition point occurred at a low temperature of 120°C.

The ash content found in the analysis is relatively high, which is an important parameter when selecting biomass for combustion processes, as it can negatively affect the HHV and process efficiency. In the X-ray Fluorescence analysis, the Alkali index was 14.25 (> 0.75), suggesting the possibility of equipment fouling.

Watermelon rind exhibits a high fixed carbon content, which is one of the key properties to consider, as it generates a significant amount of heat, indicating the formation of char (solid carbonaceous material). This indicates the amount of fuel that can be oxidized through combustion or gasification processes.

Watermelon rind has a high calorific value of 3620.22 kcal/kg, which is a crucial factor in selecting biomass for use as a fuel. Using watermelon rinds for energy purposes not only helps reduce waste but also contributes to a more sustainable and environmentally friendly energy mix. It must be highlighted that the efficiency of these processes can vary based on the composition of watermelon rinds and the technology and conditions used. Therefore, research and development efforts can optimize and expand these methods for energy production from watermelon rinds and other agricultural residues.

Future research directions related to the use of agricultural waste, including watermelon rind, in thermochemical conversion processes could focus on advancing efficiency, sustainability, and the broader application of such biomass resources. Economic and environmental assessments can be developed to evaluate the life cycle impacts of utilizing agricultural waste in thermochemical conversion processes.

ACKNOWLEDGMENT

The authors wish to acknowledge the support of the National Council for Scientific and Technological Development (CNPq Productivity Grant 309452/2021-0).

REFERENCES

[1] Perea-Moreno, M. A., Samerón-Manzano, E., & Perea-Moreno, A. J. (2019). Biomass as renewable energy: Worldwide research trends. *Sustainability*, 11(3), 863.

[2] Empresa de Pesquisa Energética, EPE. Balanço energético nacional 2023: ano base 2022 [National

Energy Balance 2023: base year 2022]. EPE. Rio de Janeiro, 2023.

- [3] Esparza, I., Jiménez-Moreno, N., Bimbela, F., Ancín-Azpilicueta, C., & Gandía, L. M. (2020). Fruit and vegetable waste management: Conventional and emerging approaches. *Journal of environmental management*, 265, 110510.
- [4] Du, X., & Ramirez, J. (2022). Watermelon rind and flesh volatile profiles and cultivar difference. *Horticulturae*, 8(2), 99.
- [5] Chen, X., Lin, Q., He, R., Zhao, X., & Li, G. (2017). Hydrochar production from watermelon peel by hydrothermal carbonization. *Bioresour. Technol.*, 241, 236-243.
- [6] Ali, I., Idrees, N., Siddique, A., Shah, K. H., Ahmad, R., Ali, A., & Fateh, A. (2021). Microbial composition of processed foods. *Biological and Clinical Sciences Research Journal*, 2021(1).
- [7] Yaseen, F., Siddique, A., Idrees, N., Fateh, A., Ahmad, R., Ali, A., & Ali, I. (2021). Enzyme biocatalysis in organic synthesis. *Biological and Clinical Sciences Research Journal*, 2021(1).
- [8] Kumar, R. M. D., & Anand, R. (2019). Production of biofuel from biomass downdraft gasification and its applications. In *Advanced biofuels* (pp. 129-151). Woodhead Publishing.
- [9] Saadatkhan, N., Carillo Garcia, A., Ackermann, S., Leclerc, P., Latifi, M., Samih, S., ..., & Chaouki, J. (2020). Experimental methods in chemical engineering: Thermogravimetric analysis—TGA. *The Canadian Journal of Chemical Engineering*, 98(1), 34-43.
- [10] Lindon, J. C., Tranter, G. E., & Koppenaal, D. (2016). *Encyclopedia of spectroscopy and spectrometry*. Academic Press.
- [11] ASTM E872-82. (2019) Standard Test Method for Volatile Matter in the Analysis of Particulate Wood Fuels.
- [12] ASTM E1755. (2010). Standard Test Method for Ash in Biomass.
- [13] ASTM D5865-13. (2019) Standard Test Method for Gross Calorific Value of Coal and Coke.
- [14] ASTM E1621-13. (2021). Standard Guide for Elemental Analysis by Wavelength Dispersive X-Ray Fluorescence Spectrometry.
- [15] Ozer, M., Basha, O. M., Stiegel, G., & Morsi, B. (2017). Effect of coal nature on the gasification process. In *Integrated gasification combined cycle (IGCC) technologies*, 257-304.
- [16] Klautau, J. V. P. (2008). Análise Experimental de uma Forno a lenha de Fluxo Cocorrente Para Secagem de Grãos. [Experimental Analysis of a Cocurrent Flow Wood Furnace for Grain Drying]. MSc. Thesis. PPGERHA, UFPR. Curitiba, 2008.
- [17] Vieira, A. C. (2012) Caracterização da biomassa proveniente de resíduos agrícolas. Dissertação de mestrado em Energia na agricultura [Characterization of biomass from agricultural residues]. MSc. Thesis. Unioeste. Paraná, 2012.
- [18] Hoffmann, B. S. (2010). O ciclo Combinado com Gaseificação Integrada e a Captura de CO₂: Uma Solução para mitigar as emissões de CO₂ em Termelétricas a carvão em larga escala no curto prazo?

- [Combined Cycle with Integrated Gasification and CO₂ Capture: A Solution to Mitigate CO₂ Emissions in Large-Scale Coal Power Plants in the Short Term?]
MSc. Thesis. PPGPE, UFRJ, Rio de Janeiro.
- [19] Corton, J. (2016). Expanding the biomass resource: sustainable oil production via fast pyrolysis of low input high diversity biomass and the potential integration of thermochemical and biological conversion routes. *Applied Energy*, v.177, 852-862.
- [20] Leobet, J. (2016) Casca de banana (*Musa cavendishii*) como fonte de energia e caracterização do resíduo mineral fixo. [Banana (*Musa cavendishii*) peel as an energy source – characterization of the fixed mineral residue]. MSc. Thesis. UFSC. Florianópolis. *In Portuguese*.
- [21] Vale, A. T., Brasil, M. A. M., de Carvalho, C. M., & de Arruda Veiga, R. A. (2000). Produção de energia do fuste de *Eucalyptus grandis* Hill ex-Maiden e *Acácia mangium* Willd em diferentes níveis de adubação. [Energy Production from *Eucalyptus grandis* Hill Ex-Maiden and *Acacia mangium* Willd Stems at Different Fertilization Levels]. *Cerne*, 6(1), 83-88. *In Portuguese*.
- [22] Gómez, Y. R., Hernández, R. C., Guerrero, J. E., & Mejía-Ospino, E. (2018). FTIR-PAS coupled to partial least squares for prediction of ash content, volatile matter, fixed carbon, and calorific value of coal. *Fuel*, 226, 536–554.
- [23] Müzel, S. D., Oliveira, K., Hansted, F. A. S., & Pratez, G. A. (2014). HHV for *Eucalyptus grandis* and *Hevea brasiliensis*. *Revista Brasileira de Engenharia de Biosistemas*, 8(2), 166.
- [24] Tabakaev, R., Shanenkov, I., Kazakov, A., & Zavorin, A. (2017). Thermal processing of biomass into high-calorific solid composite fuel. *Journal of analytical and applied pyrolysis*, 124, 94-102.
- [25] Rambo, M. K. D., Schmidt, F. L., & Ferreira, M. M. C. (2015). Analysis of the lignocellulosic components of biomass residues for biorefinery opportunities. *Talanta*, 696–703.
- [26] Cai, Z., Ma, X., Fang, S., Yu, Z., & Lin, Y. (2016). Thermogravimetric analysis of the co-combustion of eucalyptus residues and paper mill sludge. *Applied Thermal Engineering*, 106, 938-943.
- [27] Dhyani, V., Kumar, J., & Bhaskar, T. (2017). Thermal decomposition kinetics of sorghum straw via thermogravimetric analysis. *Bioresource Technology*, 245, 1122-1129.
- [28] Martin, A. R., Martins, M. A., Silva, O. R. R. F., & Mattoso, L. H. C. (2010). Studies on the thermal properties of sisal fiber and its constituents. *Thermochimica Acta*, 506, 14-19.
- [29] Osborn, R. A. (1943). Chlorine in ash of fruit products. *Journal of the Association of Official Agricultural Chemists*, 28, 437-440.
- [30] Zajac, G., Szyszlak-Bargłowicz, J., & Szczepanik, M. (2019). Influence of biomass incineration temperature on the content of selected heavy metals in the ash used for fertilizing purposes. *Applied Sciences*, 9(9), 1790.
- [31] Niu, Y. Q., Tan, H. Z., Wang, X. B., Liu, Z. N., Liu, H. Y., & Liu, Y. (2010). Study on fusion characteristics of biomass ash. *Bioresource Technology*, 101, 9373-9381.
- [32] Pronobis, M. (2005). Evaluation of the influence of biomass co-combustion on boiler furnace slagging by means of fusibility correlations. *Biomass & Bioenergy*, 28, 375-383.
- [33] Du, S., Yang, H., Qian, K., Wang, X., & Chen, H. (2014). Fusion and transformation properties of the inorganic components in biomass ash. *Fuel*, 117, 1281–1287.
- [34] Xing, P., Mason, P. E., Chilton, S., Lloyd, S., Jones, J. M., Williams, A., Nimmo, W., & Pourkashanian, M. (2016). A comparative assessment of biomass ash preparation methods using X-ray fluorescence and wet chemical analysis. *Fuel*, 182, 161–165.

Tube Geometry Influence on Heat Exchanger Efficiency: Part B - Comparative Analysis

Abdulmuttalib A. Muhsen¹, Natalya Kizilova², Bashar Hassan Attiya³

^{1,2}Warsaw University of Technology, Warsaw, Poland

^{1,3}Haditha Hydropower Station, Ministry of Electricity, Haditha, Iraq

¹abdulmuttalib.muhsen.dokt@pw.edu.pl

Abstract—The objective of this study is to examine the influence of tube geometries on the thermal efficiency of shell and tube heat exchangers utilized in hydropower facilities. This study centers on the examination of a particular heat exchanger, namely the Koncar shell and tube model that has been implemented in the Haditha power plant. In this study, four distinct tube geometries were investigated utilizing Computational Fluid Dynamics (CFD) through the ANSYS Fluent software. These geometries encompassed circular, T-shaped fractal, Y-shaped fractal, and irregular fractal configurations. The findings indicate that the T-shaped fractal tube demonstrates superior heat transfer efficiency, resulting in a decrease in oil temperature from 95°C to 93.88°C and an increase in water temperature from 25°C to 31.82°C. The Y-shaped tube demonstrates a high level of effectiveness, as evidenced by the reduction in oil temperature from 95°C to 93.93°C and the corresponding increase in water temperature from 25°C to 31.61°C. On the other hand, the circular tube exhibits reduced efficiency, resulting in a decrease in oil temperature from 95°C to 94.16°C and an increase in water temperature from 25°C to 30.04°C. The irregular fractal tube demonstrates the least efficient heat transfer, resulting in a decrease in oil temperature from 95°C to 94.64°C and an increase in water temperature from 25°C to 38.99°C. The aforementioned findings offer valuable perspectives on how to optimize the design of heat exchangers in hydropower facilities, improve cooling effectiveness, and promote energy conservation.

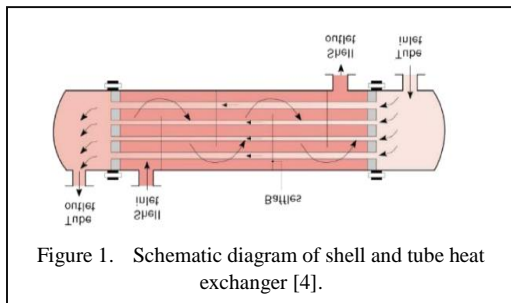
Keywords - computational fluid dynamics (CFD), heat exchanger performance, thermal efficiency

I. INTRODUCTION

Hydropower plants are electrical generation power plants, which uses the kinetic energy of flowing water passing through gates and making impact on water turbine blades which in turn rotates the blades to rotate an electrical generator to produce electricity in the process. Haditha hydropower plant (HPP) is one of principal hydropower plants in Iraq, the plant has 6 units of Kaplan turbines capable generating of 110 MW of power each which generates a total capacity of 660MW [1,2]. Friction is generated due to the rotation of the rotary components of the generators and fluid friction generates massive amounts of heat as well as the fluid friction also causes heat on the generator components and the electrical transformers. The need for the cooling system in hydropower generators is required.

In plants where a sufficient quantity of cooling water is available, water coolers heat exchangers are used for cooling transformers. They are constructed as traverse heat exchangers, where water flows through tubes and oil vertically to them (cooling type OFWF). Their main features are small dimensions and large cooling capacity.

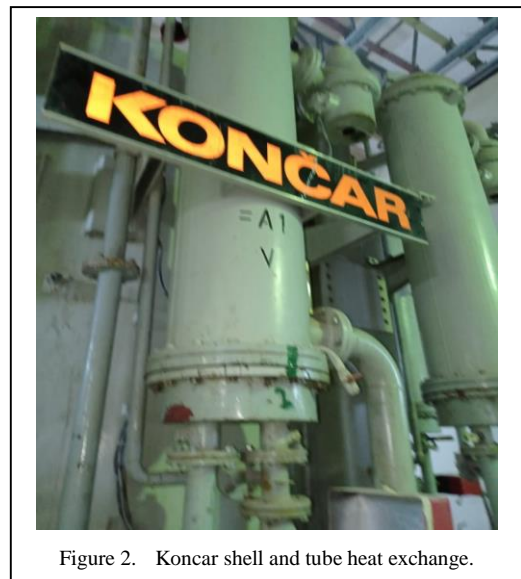
Heat exchangers are devices used for transferring heat energy between two or more media, where one of the mediums serves as the source and the other media serves as the working fluid in order to transfer heat from one of the media to the other. Heat exchangers are widely used in sewage treatment, petrochemical



processes, heat, ventilation & air conditioning, refrigeration, natural gas processing, power generation plants as well as chemical industries, food industries, etc. The shell and tube heat exchanger are a class of heat exchangers which is the most common heat exchanger type used in industries for cooling or heating processes. The study, design and analysis of shell and tube heat exchanger is very essential in engineering in order to achieve effective performance when it comes to cooling and heating processes in industries. The shell and tube heat exchanger configurational shape and robustness make shell and tube heat exchanger ideal for high pressure applications [3].

The shell and tube heat exchanger consist of a tube bundle which are enclosed in a cylindrical casing called a shell (Fig. 1). Fluid (liquid or gas) flows through the tubes, and another fluid flows through the shell over the tubes in order to exchange heat between the fluids. The heat transfer occurs between the two fluids when the fluid flows into the heat exchanger with different starting temperatures, where one fluid flows from the inlet of the tubes to the outlet while the other fluid flows from the inlet of the shell to the outlet. The heat is transferred when there is contact between the fluid flowing in the shell and the tubes while there is fluid flowing in the tubes. The heat transfer area of the shell and tube heat exchanger should be large in order to achieve efficient heat transfer in the shell and tube heat exchanger, most times many tubes are used in the system to achieve more efficient results. In this way, waste heat can be put to use. This is a great way to conserve energy. Typically, the ends of each tube are connected to plenums through holes in tube sheets. The tubes may be straight or bent in the shape of a U, called U-tubes. Most tubular heat exchangers are 1, 2, or 4 pass designs on the tube side [5,6].

In this paper, different cross-sectional shapes of tubes are analyzed using Ansys Fluent in order to compare the thermal performance &



properties of the shell and the tube heat exchanger and determine which of the tube is more efficient and has better heat transfer properties. This study focused on one heat exchanger tube, not the entire system. The main reason is the high cost of the computational resources needed to conduct the simulations based on the entire system. Future work will cover the entire heat exchanger body.

A. Heat Exchanger Modeling and Geometry

The shell and tube heat exchanger in focus is the Koncar shell and tube heat exchanger which was installed in in Haditha powerplant as shown in Fig. 2, it is the primary heat exchanger used for cooling the transformer. The shell of the heat exchanger was made of steel and the tubes were made of copper. The length of the shell which the heat transfer takes place is 1900mm and has 450mm diameter. There are 160 tubes in the heat exchanger which are 17mm diameter in size.

For simplicity, a single tube shell and tube heat exchanger was modeled for the purpose of the analysis of thermal performance of irregular and fractal types of tubes. The model of the tube is shown in Fig. 3.

The shell and tube heat exchanger were modeled in SolidWorks as parts which consist of the shell, the tube and shell fluid and the tube fluid then assembled to make the unit.

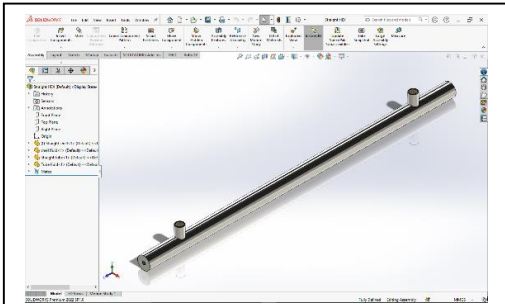


Figure 3. Shell and tube heat exchanger model in SolidWorks.

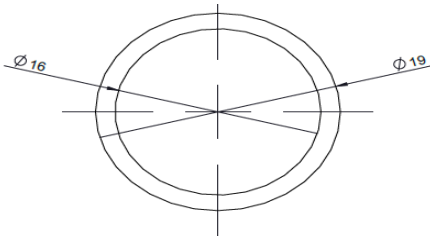


Figure 4. Circular tube geometry.

Four types of tubes were modeled for the purpose of analysis in order to obtain the thermal performance of the irregular and fractal geometries of the tubes in the heat exchanger. The types of tubes are:

- Circular tube (Fig. 4)
- T-Shaped fractal tube (Fig. 5)
- Y-Shaped fractal tube (Fig. 6)
- Irregular Shaped fractal tube (Fig. 7)

The tubes were modeled 1900mm long which is the length for the heat transfer between the shell fluid and the tube fluid. The circular tube has 16mm internal diameter and it is 3mm thick which is shown in the figure below.

The T and the Y fractal shaped tubes have 16mm internal diameter with 4mm thickness, the T shaped fractal tube have 12 T shaped extruded fins around the tube which are dimensioned in order to achieve a certain cross-sectional area which is shown below.

The irregular shaped fractal tube was also modeled with irregular star shape pattern with a specified dimension in order to achieve a certain cross-sectional area as well for the shell and tube heat exchanger which is shown in Fig. 7. The T, Y and the irregular shaped fractal tubes have a cross-sectional area of 154.3mm^2

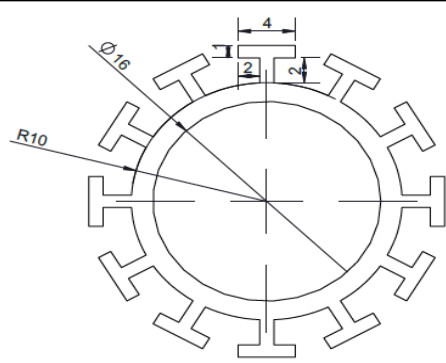


Figure 5. T-shaped fractal tube geometry.

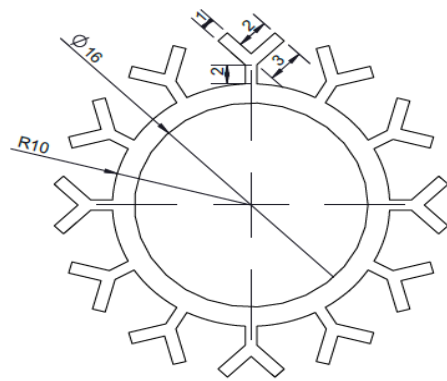


Figure 6. Y-shaped fractal tube geometry.

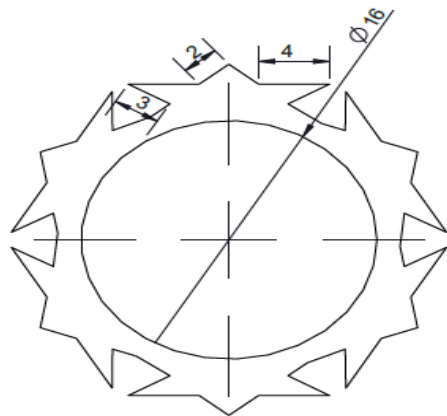


Figure 7. Irregular shaped fractal tube geometry.

II. PRE-PROCESSING

The pre-processing setup of the sets of shell and tube heat exchangers with different types of fractal tubes were converted to STEP files in order to use the files in ANSYS workbench. Ansys tool called Fluent was used as Computational Fluid Dynamics (CFD) tool in

order to compute, obtain and visualize the thermal performance of all the fractal tubes of heat exchangers. The shell and tube heat exchangers are prepared by discretizing the model by dividing the model into smaller components called meshing. Meshing was done in the mechanical window inside Ansys, using 60mm element sizing which is smaller than the default size (150mm) with smoothing quality set to high as shown in Fig. 8. Tetrahedron method type of meshing was used on the model to achieve patch conformity between the interfaces of the shell and tube heat exchanger model.

After the meshing was done, the shell and tube heat exchangers were set up for CFD computations by defining some parameters and boundary conditions.

The materials to be used for the analysis were defined first; these materials are divided into fluid and solid. The solids are steel for the shell and copper for the tube while the fluids are oil as the working fluid which flows in and out of the shell in order to be cooled and the second fluid is water serving as the coolant for the oil which flows through the tube. Table I shows the properties of the materials used in the shell and tube heat exchanger.

The Realizable k-epsilon with two turbulent equations was used as viscous model and scalable wall functions for the near wall treatment with following model constants in Table II.

The cell zone conditions for the shell and tube heat exchanger were also defined where water is applied to the geometry in the tube, the tube as copper, the shell fluid as oil and steel applied to the shell of the heat exchanger.

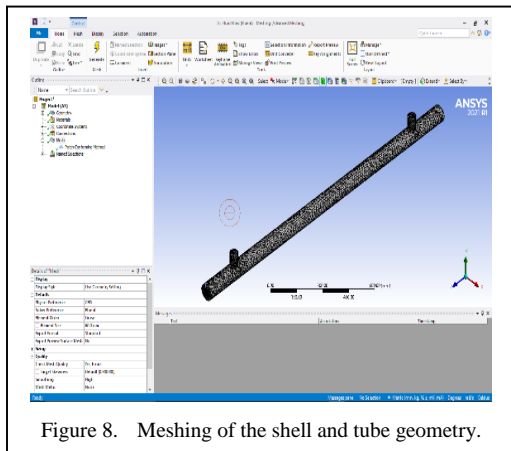


Figure 8. Meshing of the shell and tube geometry.

III. NUMERICAL SETTINGS

Boundary conditions were applied to the inlets and outlets of the heat exchangers in order to compute the thermal performance and behavior of the heat exchangers. The inlet of the shell where the oil enters flows into the shell at mass flow rate of 20.43kg/s and temperature of 95°C into the heat exchanger is set as mass flow

TABLE I. PROPERTIES OF MATERIALS USED IN SHELL AND TUBE HEAT EXCHANGER.

Properties	Oil	Water	Steel	Copper
Density (kg/m ³)	681	998.2	8030	8978
Specific heat (J/kg.k)	3048	4182	502.48	381
Thermal Conductivity (W/m.k)	0.111	0.6	16.27	387.6
Viscosity (kg/m.s)	6.0735x 10 ⁻⁵	0.001003	-	-

TABLE II. K-EPSILON MODEL CONSTANTS.

Model constants	Values
C2-epsilon	1.9
TKE Prandtl number	1
TDR Prandtl Number	1.2
Energy Prandtl Number	0.85
Wall Prandtl Number	0.85

inlet. The tube inlet where the water enters the heat exchanger as coolant is set as pressure inlet which the water enters the system with pressure of 25bar and temperature of 25°C. The computation of the individual heat exchanger system of different fractal tubes was done using pressure-velocity coupling solutions methods called coupled setting the pressure, momentum,

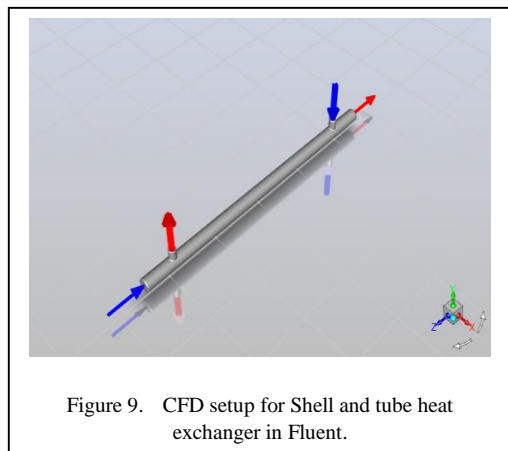


Figure 9. CFD setup for Shell and tube heat exchanger in Fluent.

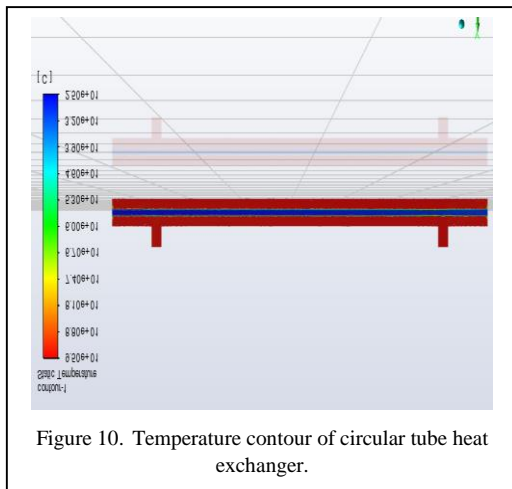


Figure 10. Temperature contour of circular tube heat exchanger.

turbulent kinetic energy, turbulent dissipation rate and energy as second order upwind in the spatial discretization scheme to achieve optimal values. Hybrid initialization was used, and the number of iterations was set to 3000 number of iterations.

IV. RESULTS

From the CFD analysis carried out in Ansys Fluent software to compare the cooling effect of the four various types of tubes in the heat exchanger the power plant generator with the variations in tubes, the temperature, velocity, and pressure of both the oil and water outlet are observed.

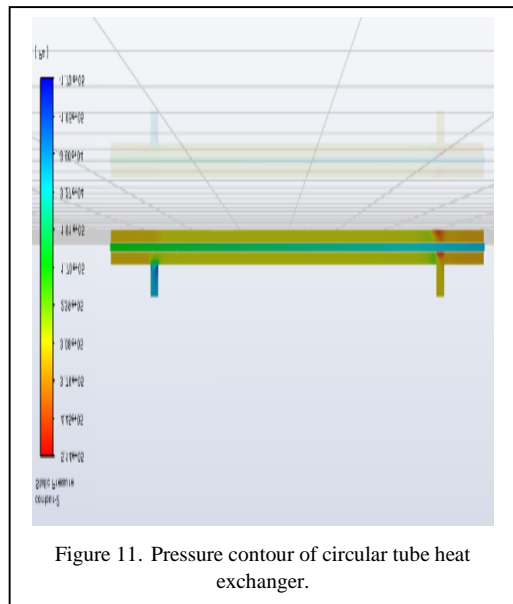


Figure 11. Pressure contour of circular tube heat exchanger.

A. The Circular Tube Heat Exchanger

The flow of fluid in the circular heat exchanger was observed to examine the thermal performance of the circular tube where oil and water flows in the heat exchanger. It was found that the temperature of the oil leaving the heat exchanger is 94.16°C which shows a decrease of 0.84°C from 95°C as it made contact with the water in the circular tube and water temperature increases from 25°C to 30.04°C. The Table III shows the thermal properties of the circular tube heat exchanger.

B. The T-tube Heat Exchanger

The flow of fluid in the T-shaped tube heat exchanger was observed to examine the thermal performance of the T tube where oil and water flow in the heat exchanger. It was found that the

TABLE III. THERMAL PROPERTIES OF THE MODEL COMPONENTS.

	Oil inlet	Oil outlet	Water inlet	Water outlet
Mass flow rate (kg/s)	20.43	-20.43	2.49	-2.49
Pressure (Pa)	324357.58	0	170927.66	0
Temp. (°C)	95	94.16	25	30.04
Velocity (m/s)	24.27	25.56	12.58	12.65
Turbulent kinetic energy (m ² /s ²)	2.21	11.86	0.59	0.69
Turbulent viscosity (kg/ms)	0.069	2.035	0.037	0.282
Thermal conductivity (W/mk)	246.77	7235.17	184.37	1430.50

temperature of the oil leaving the heat exchanger is 93.88°C which shows decrease of 1.12°C from 95°C as it made contact with the water in

the T-shaped tube and water temperature increases from 25°C to 31.824°C. The Table IV

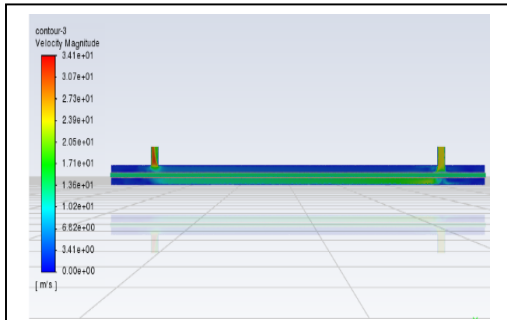


Figure 12. Velocity contour of circular tube heat exchanger.

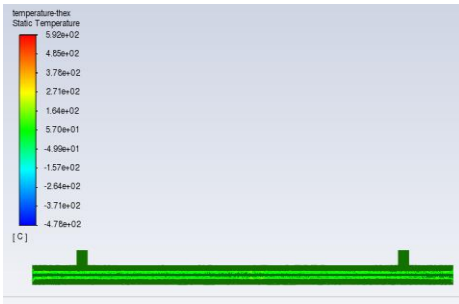


Figure 13. Temperature contour of T-Shaped tube heat exchanger.

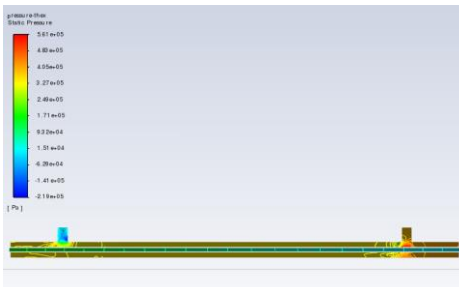


Figure 14. Pressure contour of T-Shaped tube heat exchanger.

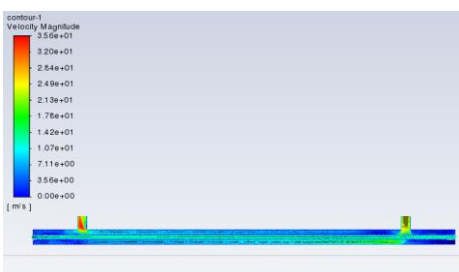


Figure 15. Velocity contour of T-Shaped tube heat exchanger.

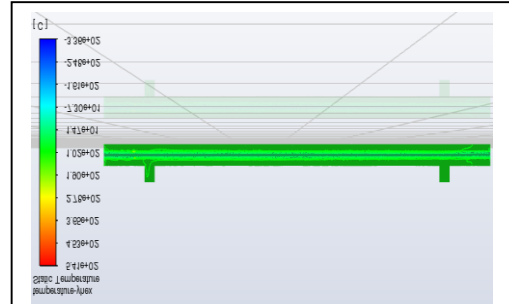


Figure 16. Temperature contour of Y-Shaped tube heat exchanger.

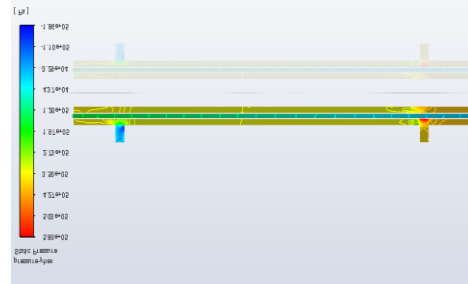


Figure 17. Pressure contour of Y-Shaped tube heat exchanger.

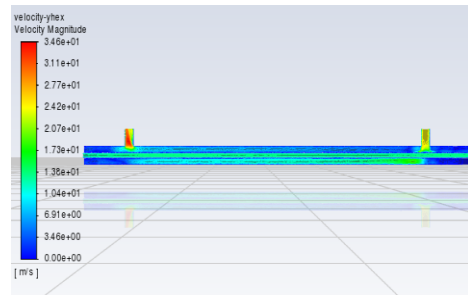


Figure 18. Velocity contour of Y-Shaped tube heat exchanger.



Figure 19. Temperature contour of irregular-Shaped tube heat exchanger.

shows the thermal properties of the T-shaped tube heat exchanger.

The flow of fluid in the Y-shaped tube heat exchanger was observed to examine the thermal performance of the tube where oil and water flows in the heat exchanger. It was found that the temperature of the oil leaving the heat exchanger is 93.93°C which shows decrease of 1.07°C from 95°C as it made contact with the water in the Y-shaped tube and water temperature increases from 25°C to 31.61°C. The Table V shows the thermal properties of the Y-shaped tube heat exchanger.

C. The Irregular Shaped Tube Heat Exchanger

The flow of fluid in the irregular shaped heat exchanger was observed to examine the thermal performance of the irregular shaped tube where oil and water flows in the heat exchanger. It was found that the temperature of the oil leaving the heat exchanger is 94.64°C which shows decrease of 0.36°C from 95°C as it made contact with the water in the irregular shaped tube and water temperature increases from 25°C to

TABLE IV. THERMAL PROPERTIES OF THE T-TUBE MODEL.

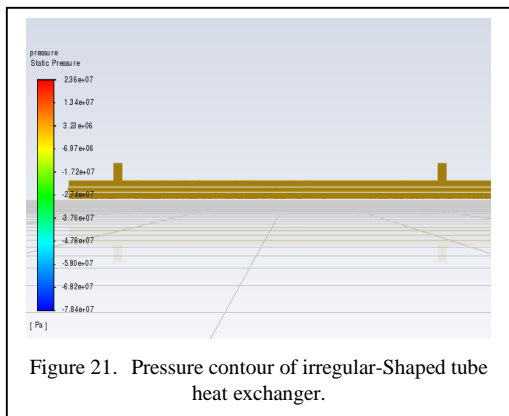
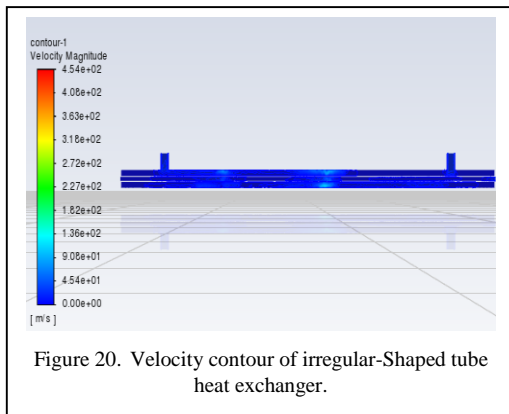
	Oil inlet	Oil outlet	Water inlet	Water outlet
Mass flow rate (kg/s)	20.43	-20.43	2.48	-2.48
Pressure (Pa)	383844.13	0	170923.13	0
Temperature (°C)	95	93.88	25	31.82
Velocity (m/s)	24.27	25.35	12.587	12.582
Turbulent kinetic energy (m ² /s ²)	2.21	18.50	0.59	0.70
Turbulent viscosity (kg/ms)	0.072	2.55	0.037	0.28
Thermal conductivity (W/mk)	258.52	9147.87	184.56	1375.021

TABLE V. THERMAL PROPERTIES OF THE Y-TUBE MODEL.

	Oil inlet	Oil outlet	Water inlet	Water outlet
Mass flow rate (kg/s)	20.43	-20.43	2.48	-2.48
Pressure (Pa)	38645.36	0	170932.27	0
Temperature (°C)	95	93.93	25	31.61
Velocity (m/s)	24.27	25.45	12.59	12.58
Turbulent kinetic energy (m ² /s ²)	2.21	17.47	0.59	0.71
Turbulent viscosity (kg/ms)	0.05	2.5	0.037	0.28
Thermal conductivity (W/mk)	246.77	7235.17	184.37	1430.50

TABLE VI. THERMAL PROPERTIES OF THE IRREGULAR MODEL.

	Oil inlet	Oil outlet	Water inlet	Water outlet
Mass flow rate (kg/s)	20.43	-20.43	2.49	-2.49
Pressure (Pa)	346348.29	0	170926.45	0
Temperature (°C)	95	94.64	25	38.99
Velocity (m/s)	24.27	20.38	2.35	15.62
Turbulent kinetic energy (m ² /s ²)	2.20	21.53	0.55	0.77
Turbulent viscosity (kg/ms)	0.07	2.5	0.05	0.56
Thermal conductivity (W/mk)	270.02	18897.74	7722.35	2769.42



38.99°C. The Table VI shows the thermal properties of the irregular tube heat exchanger.

V. CONCLUSION

This study presents a comprehensive examination of the flow and heat transfer properties of shell and tube heat exchangers through the utilization of Computational Fluid Dynamics (CFD). The primary objective of this investigation is to determine the optimal tube geometry for enhancing heat transfer between oil and water. The study examined four different tube configurations, namely the circular tube, T-shaped fractal tube, Y-shaped fractal tube, and irregular fractal tube. The selection of copper as the material for the tubes and steel for the shell reflects the practical considerations observed in real-world hydropower installations. Within these systems, water functions as the cooling medium that circulates through the tubes, while oil serves as the hot working fluid contained within the shell. As a result, effective cooling by the water is necessary to maintain optimal performance. The results of our study provide valuable insights into the comparative performance of these tube geometries. The T-

shaped fractal tube exhibited higher efficiency by reducing the temperature of the oil from an initial value of 95°C to a final temperature of 93.88°C. Concurrently, the water exhibited efficient heat absorption, resulting in an increase in temperature from 25°C to 31.82°C. The Y-shaped fractal tube shows good heat transfer capabilities, leading to a reduction in the temperature of the oil from 95°C to 93.93°C and an elevation in the temperature of the water from 25°C to 31.61°C. In contrast, the circular tube demonstrated lower efficiency in terms of heat transfer when compared to the T- and Y-shaped counterpart. The oil temperature experienced a decrease from an initial value of 95°C to a final value of 94.16°C, whereas the water temperature underwent an increase from an initial value of 25°C to a final value of 30.04°C. Ultimately, the irregular fractal tube exhibited the least optimal heat transfer efficiency. Although there was a certain amount of heat transfer from the oil to the water, the observed geometric configuration resulted in a reduction of the oil temperature from 95°C to 94.64°C. Consequently, the water temperature experienced a more significant rise, increasing from 25°C to 38.99°C. These findings hold significant implications for the design and optimization of heat exchangers in hydropower facilities. By comprehending the optimal tube geometry that facilitates efficient heat transfer, it is possible to augment the effectiveness of cooling mechanisms and promote energy conservation. This, in turn, can significantly enhance the performance of vital components utilized in hydropower generation systems.

REFERENCES

- [1] Muhsen, A. A., & Kizilova, N. (2022). The Advanced Cooling System of Generator for Hydropower Plant. *Changes*, 8, 10.
- [2] Muhsen, A. A., et al. (2021, June). Modal analysis of Kaplan turbine in Haditha hydropower plant using ANSYS and SolidWorks. In *IOP Conference Series: Materials Science and Engineering* (Vol. 1105, No. 1, p. 012056). IOP Publishing.
- [3] Muhsen, A. A., & Attiya, B. H. CFD Based Optimization of Different Types of Fractal Systems.
- [4] Olaiya, K. A., Alabi, I. O., Okediji, A. P., & Alonge, O. I. (2018). Parametric and quantitative analysis on the development of shell and tube heat exchanger.
- [5] Muhsen, A. A., & Attiya, B. H. Comparative Analysis of Energy Loss and Flow Uniformity of Different Fractals.
- [6] Muhsen, A. A., Attiya, B. H., & Algburi, H. A. Theoretical Analysis of Different Fractal-Type Pipelines

Urban Waste as an Energy Source: Dumps Change in Paraíba's Landfills

Sahyonara Estrela de Lacerda Hussein Mélo¹, Kelly Cristiane Gomes²,
Joelda Dantas³

^{1,2,3}Federal University of Paraíba, Postgraduate Program in Mechanical Engineering
(PPGEM), João Pessoa/PB, Brazil

¹sahyonarahussein@gmail.com, ²gomes@cear.ufpb.br, ³joelda.dantas@cear.ufpb.br

Abstract—This work addressed inadequate urban waste management practices in Brazil and the challenge of closing open dumps. The generation of urban waste during the pandemic was 82.5 million tons in 2020, with the Northeast region responsible for 16.5 million. Faced with this problem, thermal conversion through pyrolysis is seen as a potential solution for mitigating negative impacts on the environment, at high temperatures it produces renewable energy and reduces CO₂. In this present work, we sought to contribute to the area of renewable energy, focusing on the thermal conversion of two samples of waste from landfills in Paraíba into sustainable energy, which were named dry waste (RS) and organic waste (RO). The samples received drying and grinding pre-treatment, passing through a 200 mesh ABNT mesh for characterization by UV-Vis, FTIR, FRX and TG/DSC. FT-IR and UV-visible analyzes revealed organic and inorganic compounds such as carboxylic acids, starch carbonyls, aromatic compounds and groups of CH₂, CH₃ and aromatic and unsaturated compounds with absorption bonds C=C, C=O and N=N. The XRF analysis showed inorganic elements such as potassium, sodium, calcium and magnesium. In TG/DSC, the thermal decomposition process was demonstrated by increasing the temperature from 100°C to 600°C for RS, obtaining a mass loss of 55% and for RO from 100 °C to 900 °C, a mass loss of 60% was obtained. From the results obtained, it is possible to indicate that the thermal conversion of MSW promotes energy recovery and contributes to sustainability.

Keywords – waste from landfills, state of Paraíba, energy recovery, characterizations, sustainability

I. INTRODUCTION

Brazil faces a significant challenge in closing open dumps and finding environmentally appropriate destinations for solid waste. Solid waste management has become a globally complex issue in recent decades, with the main form of disposal in Brazil being landfills. However, many municipalities still dispose of their waste inappropriately in landfills, causing environmental and public health problems, such as the proliferation of vectors, pollution and lack of control [1].

The COVID-19 pandemic impacted the generation of urban solid waste in Brazil, leading to a significant increase in the amount of waste generated. This was influenced by changes in social dynamics. The search for alternatives to minimize waste production becomes urgent, with several studies aiming to improve management and explore new forms of treatment, including energy reuse [2].

According to the United Nations (UN, 2023), the Sustainable Development Goals (SDGs) are a set of 17 global goals that were established by the United Nations General Assembly in 2015. The thermochemical treatment of urban waste for energy generation is aligned with the SDG, highlighting its contribution to SDG 7 - Clean and Affordable Energy, SDG 11 - Sustainable Cities and Communities and SDG 12 - Sustainable Consumption and Production by promoting sustainable energy sources, efficient management of urban waste and reducing dependence on landfills. Furthermore, thermochemical treatment acts to mitigate climate change (SDG 13) by reducing

greenhouse gas emissions associated with inadequate disposal. In the context of SDG 15 - Life on Earth, it positively influences waste management and the preservation of terrestrial ecosystems [3].

A promising method for achieving these goals is pyrolysis, which converts solid waste into renewable energy, reducing dependence on fossil fuels. Pyrolysis occurs at relatively low temperatures and does not contribute to the greenhouse effect, making it an environmentally friendly option [4].

To combat the construction of landfills and the impacts of landfills, energy recovery through pyrolysis is an appropriate solution, generating energy from mixed waste. The objective of the work is to study the thermal conversion of solid waste from landfills through laboratory experiments, using spectroscopic techniques to evaluate the maturity of the compound and its potential for generating renewable energy.

II. MATERIAL AND METHODS

A. Preparation of Raw Materials

Both residues passed through a knife mill with a 5 mm sieve and crushed in an industrial blender, sieving through a 100 mesh in accordance with ABNT, aiming to achieve adequate particle size for the characterizations. The RO required only one unequal stage, which was drying in an oven at a controlled temperature of 105°C for three hours.

B. UV-VIS Spectrophotometry Analysis

The equipment used to measure the absorption of the residues obtained was through the Spectrophotometer in the Ultraviolet and Visible region (UV-Vis), model UV-2600, operating in the region of 220 to 1400 nm in absorbance mode.

C. Analysis of Fourier Transform Infrared Spectrophotometry (FTIR)

The FTIR spectra were measured in equipment with full scanning range, based on the preparation of spectroscopic grade KBr (potassium bromide) pellets, in a proportion of approximately 1 mg of the RS and RO sample for 100 mg of KBr, separately.

D. Analysis of the Elemental Composition of Ash by X-ray Fluorescence (FRX)

The inorganic compounds present in ash samples from RS and RO solid waste were analyzed and quantified using the XRF technique. Ash is generated through the burning of organic residues and the oxidation of inorganic components. In a muffle furnace, a temperature of 250°C was used for 30 minutes, then increased to 550°C for approximately 2 hours to obtain the ash.

E. Analysis Thermogravimetric (TG/DSC)

To verify the behavior of dry and wet solid waste when subjected to increased temperature, TG/DSC analyzes were carried out. An inert atmosphere, with nitrogen, was used, with programming starting from room temperature to 910°C, carried out at heating rate ratios of 20°C/min and gas flow of 50 mL/min. The mass of the sample was approximately 5 mg in an alumina crucible.

III. RESULTS AND DISCUSSION

A. UV-VIS Spectrophotometry

Spectroscopic analyzes showed peaks in several bands, highlighting the presence of aromatic, phenolic, peptide, aliphatic and polysaccharide compounds in organic residues (Fig. 2). Predominant peaks around 3700-3000cm⁻¹ indicate the stretching vibration of hydroxyl groups in cellulose, hemicelluloses and lignin.

According to the authors Biyada et al., (2020) the wavelength ranges that appear in RS (Fig. 1) and RO (Fig. 2) between 220 and 800 nm are analyzed to detect aromatic and unsaturated compounds with bonds absorption of C=C, C=O and N=N. Three key regions can be identified in the UV-Visible spectra around 280 nm, 400-500 nm and beyond 600 nm. Absorbance at 260-280 nm is associated with lignin and quinone, indicating early stages of transformation. Absorbance values at 460-480 nm reflect the humification of organic matter, while 600-670 nm indicates the presence of highly humified materials with condensed aromatic groups [5].

B. Espectrofotometria de Infravermelho por Transformada de Fourier (FTIR)

The infrared spectra of the RS and RO samples are presented in Fig. 3. The first bands begin to appear in the band range from 1250cm^{-1} to 500cm^{-1} in both residues, initially belonging to the silicate group, coming to have more pronounced peaks after 1000cm^{-1} due to the effect of the coupling of angular deformation in the O – H bond plane and C – O deformation, present in carboxylic acids [6].

It is observed that in relation to the broad band that occurs in the range of 1750cm^{-1} to 1500cm^{-1} , it is clear that the RO organic waste sample presented a more expressive event band in the range of 1500cm^{-1} when compared to RS sample in which the event was less significant. These occurrences are caused by different functional groups, such as starch carbonyls, aromatic compounds and groups of CH_2 and CH_3 and hydrocarbons and cellulose [6].

After the range of 3000cm^{-1} to 2750cm^{-1} , light bands appeared that could be the result of axial C–H deformation of aliphatic structures, occurring more predominantly near the range of 3000cm^{-1} , with RO having a higher concentration than the RS, in which it appears slightly.

The stretching vibrations of the O – H (water, alcohols, phenols and carboxylic acids) and N–H (amines and amides) groups occur in the band range from 4000cm^{-1} to 3250cm^{-1} .

C. Analysis of the Elemental Composition of Ash by X-ray Fluorescence (XRF)

X-ray fluorescence analysis demonstrated the main chemical elements identified in the RS and RO samples. Inorganic compounds were found in the composition of the waste, including elements such as potassium (K), sodium (Na), calcium (Ca) and magnesium (Mg). These elements can manifest themselves in the form of different compounds, such as oxides, silicates, carbonates, sulfates, chlorides and phosphates, the presence of these inorganic compounds can influence the behavior of chemical reactions during processes such as gasification and pyrolysis. Some of these inorganic compounds can act as catalysts, accelerating reactions, while others can act as retarders, therefore, the specific composition of elements and inorganic compounds present in waste has implications for the overall performance of the operating system,

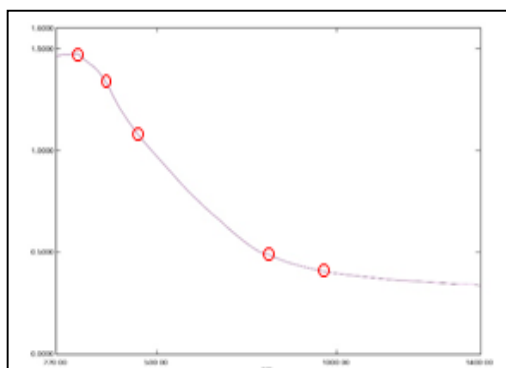


Figure 1. UV-Vis absorbance for the RS sample.

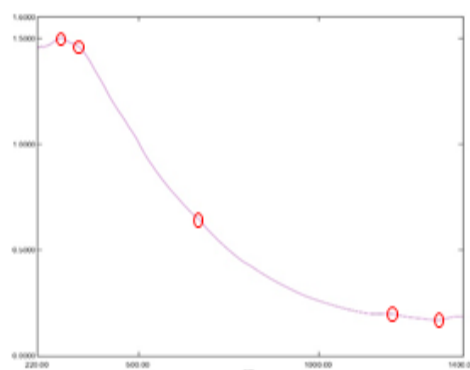


Figure 2. UV-Vis in absorbance for the RO sample.

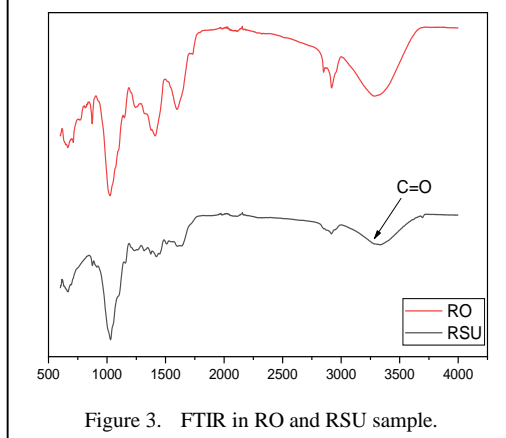


Figure 3. FTIR in RO and RSU sample.

affecting the effectiveness and efficiency of processes [7].

The results obtained from the XRF analysis are detailed in Table I, allowing visualization of the elemental composition and the temperature range in which they are found. These results express a summarized representation of the mass changes in relation to temperature for each compound.

TABLE I. CHEMICAL COMPOSITION FOR RS AND RO SAMPLES GIVEN BY FRX.

Inorganic Elements	Chemical composition		
	Elemental Composition Gray RS (%)	Composition Elementary Ashes RO (%)	Thermogravimetric Temperature Range
SiO ₂	31.77	2.51	Stable
CaO	24.63	59.31	800°C – 1200°C
Al ₂ O ₃	11.46	1.10	Stable
Fe ₂ O ₃	8.49	0.18	600°C – 800°C
K ₂ O	5.80	23.46	Stable
MgO	5.2	2.9	Stable
Na ₂ O	2.9	0.8	Stable
SO ₃	2.6	0.81	Reactive, not typical
P ₂ O ₅	2.49	2.73	300°C – 500°C
Cl	2.30	5.97	Variable volatilization
TiO ₂	1.57	-	Stable
Cr ₂ O ₃	0.28	-	Stable
ZnO	0.23	0.02	Stable
MnO	0.08	0.07	Stable
ZrO ₂	0.06	-	Stable
SrO	0.06	0.11	Stable
NiO	0.04	-	Stable
CuO	0.04	-	Stable
PbO	0.02	-	Stable
SnO ₂	0.01	0.01	700°C – 800°C
Br	0.01	0.01	Stable

It is noted that silicon oxide (SiO₂), with a prevalence of 31.77%, is the most abundant component for the RS sample, in contrast, for RO, its presence decreases to 2.51%.

After SiO₂, it is observed that the most prevalent oxides found for the RS sample were CaO, with 24.63% and Al₂O₃, with 11.46%. In relation to the RO sample, the predominant oxides were CaO, with 59.31%, K₂O, with 23.46% and MgO, with 2.9%. These oxides have the ability to act as melting agents when exposed to temperatures around 1000°C, potentially contributing to optimizing the technological characteristics of the material during the burning stage. This effect manifests itself through the reduction of porosity, a beneficial phenomenon that can improve the overall performance of the material in the burning process [8].

D. Thermogravimetric Analysis (TG/DSC)

The thermogravimetric analysis of the RS and RO samples represented in Fig. 4 and Fig. 5, showing the profile of the heat flow (blue line) and mass (red line) curves, showing the loss of mass of the samples as the temperature increases, given by controlled atmosphere using N₂ gas.

In this analysis of waste samples, variations in mass loss peaks can be observed depending on temperature, due to different decomposition processes. However, the composition of these residues varies between samples due to local and management factors, resulting in variations in temperatures and peaks.

As illustrated in Fig. 4, for the RS sample, the first event and temperature occurred up to 100°C, referring to the removal of moisture or dehydration, enabling a reduction in the sample mass of almost 10%. It is important to highlight that moisture removal is an initial and fundamental step in thermogravimetric analysis, since the presence of water can mask or interfere with subsequent decomposition processes or thermal reactions that occur as the temperature increases, the water present can come from different sources, such as atmospheric humidity, absorbed into porous materials and adsorbed on surfaces [9].

The second peak, which appears between 200°C and around 400°C, represents a fundamental stage in which the volatile elements in the sample are broken down at high temperatures, causing a considerable mass loss of approximately 45%. This peak corresponds to the decomposition of low-complexity organic

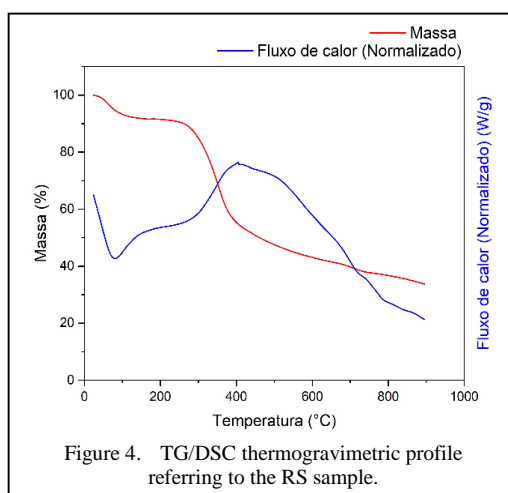


Figure 4. TG/DSC thermogravimetric profile referring to the RS sample.

matter, where chemical bonds break in simple organic compounds. As the temperature increases, these compounds gradually release volatile components, with the induction of thermal energy facilitating decomposition into gases such as CO₂, H₂O and NH₃, thus resulting in a reduction in sample mass [10].

The third peak is the carbon residue cracking stage, which covers the temperature range from 400°C to 600°C. This peak is linked to the degradation of more complex organic materials, such as polymers, lignin and paper waste, characterized by the gradual degradation of more complex organic compounds as the temperature increases, resulting in a continuous decrease in the mass of the RS sample with a discrepancy of just 10% in relation to the second peak. As the temperature rises, there is a stabilization in the amount of mass loss, since most of the components have already been converted, with the final stage being ash [11].

In relation to the RO sample presented in Fig. 5, the mass loss events presented can often be associated with the thermal decomposition of different organic components present in the sample. The temperature range up to 100°C refers to the evaporation of moisture from the sample, at around 160 °C the lignin begins to be degraded and can reach the end of the process. The second observed event frequently varied between approximately 200°C and 450°C, referring to light organic components, such as sugars and organic acids, which begin to decompose, releasing volatile gases such as CO₂ and H₂O [11].

Another observed event occurred at 600°C, where the most complex organic components, such as polymers and lignin, begin to

decompose, releasing volatile products. Above 600°C, the oxidation and combustion process of the remaining residues is triggered, resulting in the release of carbon dioxide. In the temperature range of 700°C, the RO organic waste sample shows a relevant mass loss of approximately 60%. As the temperature rises, residual carbon is generated. Around the range of 750°C to 800°C, the last increase in temperature is observed, associated with inorganic components, such as minerals and ash, marking the completion of the process at around 900°C [9].

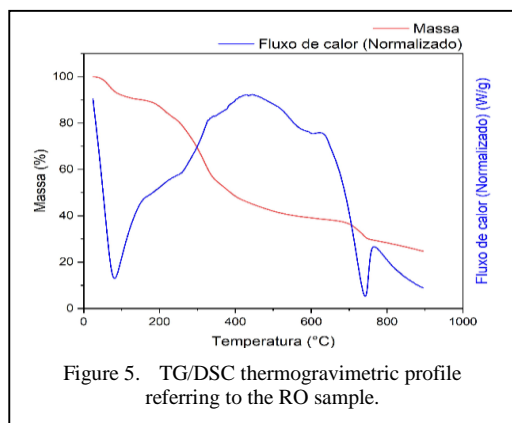
IV. CONCLUSIONS

The generation of urban solid waste increased significantly during the pandemic, increasing the challenges of managing and disposing of these materials. Thermal conversion by pyrolysis appears as a promising alternative to reduce dependence on non-renewable energy sources by mitigating CO₂ emissions, reducing the volume of waste by up to 90% and recovering valuable materials. Compared to other technologies, it presents advantages such as its efficiency, flexibility in using a wide variety of urban waste and the high quality of the products purchased.

This study sought to contribute to research in renewable energy, focusing on the analysis of the thermal conversion of landfill waste to energy generation. Two spectroscopic techniques were used, such as FT-IR and UV-Vis, to evaluate the composition of the residues and their behavior during thermal conversion. X-ray fluorescence analysis identified inorganic elements present in the waste samples, which can potentially influence reactions during pyrolysis.

The results revealed the prevalence of inorganic compounds, such as silicon oxide, calcium and aluminum, in samples of urban solid and organic waste. Thermogravimetric analyzes demonstrated the processes of mass loss in the samples as the temperature increases, indicating stages of dehydration, decomposition of volatile components and breakdown of more complex organic materials.

Spectroscopic and thermogravimetric analyzes have provided valuable insights into the composition and behavior of waste during thermal conversion, contributing to the advancement of research in renewable energy and waste management.



Therefore, there is great importance in the use of landfill waste and its management, and initiatives of this type can promote energy recovery and application according to the desired need. Thus, based on the set of results achieved, thermal conversion by pyrolysis stands out as a promising solution for the production of renewable energy from this waste, contributing to sustainability and reducing environmental impacts in the region.

ACKNOWLEDGMENT

The authors would like to thank CAPES for the financial support, the Postgraduate Program in Mechanical Engineering (PPGEM) and the Thin Film Synthesis and Characterization Laboratory (LabFilm).

REFERENCES

- [1] Souza, R. G. (2020). E-waste situation and current practices in Brazil. In *Handbook of electronic waste management* (pp. 377-396). Butterworth-Heinemann.
- [2] Leme, G. R., Fernandes, D. M., & Lopes, C. L. (2017). Utilização da pirólise para o tratamento de resíduos no Brasil. *Fórum Internacional de Resíduos Sólidos*, 8.
- [3] United Nations Organization. (2023). *Sustainable Development Goals*. Available at: <https://www.un.org/sustainabledevelopment/sustainable-development-goals/>.
- [4] Chhabra, V., Bambery, K., Bhattacharya, S., & Shastri, Y. (2020). Thermal and in situ infrared analysis to characterise the slow pyrolysis of mixed municipal solid waste (MSW) and its components. *Renewable Energy*, 148, 388-401.
- [5] Biyada, S., Merzouki, M., Elkarrach, K., & Benlemlih, M. (2020). Spectroscopic characterization of organic matter transformation during composting of textile solid waste using UV-Visible spectroscopy, Infrared spectroscopy and X-ray diffraction (XRD). *Microchemical Journal*, 159, 105314.
- [6] Pedrosa, M. M. (2011). Bio-óleo e Biogás da degradação termoquímica de lodo de esgoto doméstico em cilindro rotativo.
- [7] Pavia, D. L., Lampman, G. M., Kriz, G. S., & Vyvyan, J. R. (2010). *Introdução à espectroscopia*. Cengage Learning.
- [8] Yildiz, G., Ronsse, F., Venderbosch, R., van Duren, R., Kersten, S. R., & Prins, W. (2015). Effect of biomass ash in catalytic fast pyrolysis of pine wood. *Applied Catalysis B: Environmental*, 168, 203-211.
- [9] Passos, C. A. Artefatos cerâmicos a partir de cinzas de gaseificador de resíduos sólidos urbanos. Dissertação Universidade Federal do Paraná, Setor de Tecnologia, Programa de Pós-Graduação em Engenharia Química. Curitiba, 2019.
- [10] Ma, W., Rajput, G., Pan, M., Lin, F., Zhong, L., & Chen, G. (2019). Pyrolysis of typical MSW components by Py-GC/MS and TG-FTIR. *Fuel*, 251, 693-708.
- [11] Orfão, J. J., Antunes, F. J., & Figueiredo, J. L. (1999). Pyrolysis kinetics of lignocellulosic materials—three independent reactions model. *Fuel*, 78(3), 349-358..

Utilization of the Probabilistic Robust Design in Concurrent Optimization of Machinability and Tool Life in Machining Process

Maosheng Zheng¹, Jie Yu²

¹School of Chem. Eng., Northwest University, Xi'an, 710069, China

²School of Life Sci. & Tech., Northwest University, Xi'an, 710069, China

¹mszhengok@aliyun.com, ²yujie@nwu.edu.cn

Abstract—This article presents a concurrent optimization of machinability and tool life of machining process of Ferrite – Bainite dual-phase steel by means of probabilistic robust design. The arithmetic mean value and standard error of each performance utility indicator of alternative are usually the representatives of a group of tests, which are taken as the twin independent responses to perform the robust design; each response contributes one part of the partial preferable probability to the performance indicator. The arithmetic mean value of each performance utility indicator is assessed as a representative of the performance indicator according to its role or preference in the assessment, and the standard error is the unbeneficial type of response in evaluation; the product of the above two parts of partial preferable probability results in the actual preferable probability of the corresponding performance indicator; the product of the whole partial preferable probabilities of all possible performance indicators gives the total preferable probability of an alternative, which is the unique index of each alternative in robust optimum competitively. The optimal parameters of the dual-phase steel are 1297.3333s with standard error of 2.0817s for tool life, and 2.22μm with standard error of 0.02μm for surface roughness at heating temperature of 790°C, cutting speed of 150m/min, feed rate of 0.15mm/rev, and cutting depth of 0.2 mm.

Keywords - multi-objective optimization, concurrent optimization, preferable probability, integral optimization, robust design

I. INTRODUCTION

It is very important to improve quality of product by reducing the effect of uncertain or uncontrollable factors on response, which was recognized by Taguchi in 1950s [1,2], an approach entitled Taguchi's method was then proposed thereafter. Designed experiments could be conducted to investigate the effects of both controllable and uncontrollable factors on response. Taguchi called the uncontrollable factors as noise factors [1,2]. The aim of robust design is to seek a set of controllable factors which makes the quality of product insensitive to the uncontrollable factors (noise) or with minimum sensitivity to the noise [1,2].

Moreover, Taguchi introduced a term "signal-to-noise" ratio (*SNR*) to characterize the robust design. He further assumed that the optimized set of controllable factors guarantees the *SNR* maximum. Thereafter, three types of standard types of *SNR* were proposed [1,2]:

- Nominal the best:

$$SNR_T = 10 \log \left(\frac{y^{-2}}{s^2} \right). \quad (1)$$

- Smaller the better:

$$SNR_s = -10 \log \left(\frac{1}{m} \sum_{i=1}^m y_i^2 \right). \quad (2)$$

- Smaller the better:

$$SNR_L = -10 \log \left(\frac{1}{m} \sum_{i=1}^m \frac{1}{y_i^2} \right). \quad (3)$$

In above Eqs. (1)-(3), m indicates the repeated number in each experimental test, and \bar{y} the arithmetic mean value of the m data of experimental tests, s the standard error.

In general, the mean value \bar{y} and the standard error s of the test points are inherently independent responses for a set of actual experiments or processes [3-7].

However, the Eq. (1) of SNR solids the two responses \bar{y} and s into one response SNR_T , the optimization of the maximum of the SNR_T does not equal to the concurrent optimization of the both minima of s and \bar{y} closing to its target reasonably. What is more serious is that the Eqs. (2) and (3) of the “smaller the better” and “larger the better” cases even exclude the role of the standard error s . Statisticians criticized this point strikingly, and they advised to consider both responses of mean value and standard error with twin independent models individually [3-7].

Therefore, the optimization of the both minima of s and \bar{y} closing to its target should be treated with separate models concurrently so as to ensure the robust optimization with rationality.

Recently, the probabilistic method for multi-objective optimization (PMOO) was proposed from viewpoint of system theory to solve the intrinsic problems of “additive algorithm” with subjective factors in the traditional (previous) multi-objective optimizations [8-11]. The novel concept of preferable probability was introduced to reflect the preferable degree of performance utility indicator of the candidate schemes in optimization. In this new methodology, all performance utility indicators of alternative schemes could be preliminarily divided into two types, i.e., beneficial or unbeneficial types according to their roles or pre-required preferences in the optimization; every performance utility indicator of the alternative scheme could contribute to a partial preferable probability quantitatively. Moreover, the product of all partial preferable probabilities results in the total preferable probability of a alternative scheme in the spirit of probability theory, which is the unique decisive index of the candidate scheme in the optimization process,

and thus transfers the multi-objective optimization problem into a single-objective optimization one.

In this paper, the concurrent optimization of robust design of tool life and surface roughness of Ferrite-Bainite dual-phase steel in cutting process is conducted in detail to illuminate the probabilistic robust design; the optimal input parameters include heating temperature, cutting speed, feed rate, and depth of cutting.

II. PROCESS OF ROBUST DESIGN BY MEANS OF PROBABILISTIC MULTI-OBJECTIVE OPTIMIZATION

A. Fundamental of Probabilistic Multi-objective Optimization

In the probabilistic method for multi-objective optimization [8-11], a novel concept of preferable probability was introduced to represent the preferable degree of a performance utility indicator in the optimization, all performance utility indicators of alternative schemes could be classified into two types preliminarily, i.e., beneficial or unbeneficial types according to their roles or pre-required preferences in the optimization; every performance utility indicator of the alternative contributes to a partial preferable probability quantitatively; moreover, the product of all possible partial preferable probabilities leads to the total preferable probability of a alternative scheme in the respect of probability theory, which reflects the essence of their simultaneous optimization. The total preferable probability is the uniquely decisive index in the optimization process, which could thus transfer the multi-objective optimization problem into a single-objective optimization one. The procedure of the assessment of probabilistic multi-objective optimization is as following:

As to beneficial type of objective $P_{ij} = \eta_j Y_{ij}$,
 $i = 1, 2, \dots, n, j = 1, 2, \dots, m$;

$$P_{ij} = \eta_j Y_{ij}, i = 1, \dots, n; j = 1, \dots, m, \quad \eta_j = 1 / (n \bar{Y}_j) \quad (4)$$

For unbeneficial type of objective

$$P_{ij} = \lambda_j (Y_{jmin} + Y_{jmax} - Y_{ij}), \quad i = 1, 2, \dots, n; j = 1, 2, \dots, m, \quad \lambda_j = 1 / [n(Y_{jmin} + Y_{jmax}) - n \bar{Y}_j] \quad (5)$$

The meanings of the quantities and factors in Eqs. (4) and (5) are as followings:

- P_{ij} expresses the partial preferable probability of the j -th performance utility indicator Y_{ij} of the i -th alternative scheme; n indicates the total number of the alternative scenario; m reflects the total number of the performance (objective); \bar{Y}_j represents the arithmetic value of the j -th performance utility indicator; Y_{jmax} and Y_{jmin} show the maximum and minimum values of the j -th performance utility indicator, respectively; η_j and λ_j express the normalized factors of the j -th performance utility indicator Y_{ij} of beneficial type or unbeneficial type, individually; the beneficial type or unbeneficial type of the j -th performance utility indicator Y_{ij} is determined according to its specific rule or preset preference in the instant problem; P_i represents the total (overall) preferable scheme [8-11].

B. Process of the Robust Design by Means of Probabilistic Multi-objective Optimization

In the light of probabilistic multi-objective optimization (PMOO) and the advice of statisticians that both responses of mean value and standard error could be into taken account by using two individual models [8-10], the process of the robust design by means of probabilistic multi - objective optimization (PMOORD) is as follows.

A) Since the arithmetic mean value of the performance utility indicator is the main representative of the performance indicator in general, and the standard error of the performance indicator is an index to present the uncertainty of the corresponding performance indicator in the study, the arithmetic mean value and the standard error of the performance indicator are reasonably the twin responses of an actual performance indicator in quantification, respectively. The standard error of the performance indicator belongs to unbeneficial type in the evaluation usually, which has the characteristic of “smaller the better” in common cognition, while the arithmetic mean value of the performance indicator is the general indicator of the corresponding response, which is assessed according to its role and pre-required preference.

B) The arithmetic mean value and the standard error of the performance indicator of the alternatives are taken as twin independent responses of the alternatives, each of above twin responses contributes one part of the partial preferable probabilities to the performance utility indicator of the alternatives to perform the robust design, respectively;

C) The product of above two parts of partial preferable probabilities of both arithmetic mean value and the standard error of the performance utility indicator forms the actual partial preferable probability of the performance indicator;

D) The product of the entire partial preferable probabilities of all possible performance utility indicators forms the total preferable probability of each alternative, which is the overall and unique index of each alternative in the robust optimum;

E) The total preferable probability of alternatives is used as the decisive index of every alternative scheme to complete the robust optimum with competition;

F) In addition, in the case of “nominal the best”, the standard error of the performance indicator is specified by the actual standard error of the performance indicator from its desirable (target) value, and the departure of the arithmetic mean value from its target value of the performance utility indicator is employed in the evaluation as another index, which is an unbeneficial type of index [11].

The main innovation of the PMOORD is that it takes both arithmetic mean value and standard error of each performance utility indicator of alternative as the twin independent responses in the robust study concurrently.

III. UTILIZATION OF PMOORD IN CONCURRENT OPTIMIZATION OF MACHINABILITY AND TOOL LIFE OF DUAL-PHASE STEEL MACHINING

In this paper, the robust design of dual-phase steel machining is given in detail to illustrate the approach.

Reference [12] conducted the robust design to optimize the input parameters of Ferrite-Bainite dual-phase steel (AISI1040 F-B) machining by taking the tool life and surface roughness of sample as the concurrent optimization objectives experimentally.

There are four controllable input variables in their experiments, which includes heating temperature (Factor *A*), cutting speed (Factor *B*), feed rate (Factor *C*), and depth of cutting (Factor *D*), each factor is with three levels, and three specimens were used to conduct the experiments in each test condition with Taguchi $L_9(3^4)$ design [12]. The arithmetic value and standard error of their experiments are shown in Table I. The quantities $T_{LA}(E)$ and $\delta T_L(F)$ indicate the arithmetic value and standard error of tool life, while the quantities $S_{RA}(G)$ and $\delta S_R(H)$ reflect the arithmetic value and standard error of surface roughness of sample.

The aim of the robust design is to seek a set of input parameters which guarantee tool life and surface roughness with robustness concurrently.

TABLE I. ARITHMETIC VALUE AND STANDARD DEVIATION OF CUTTING PARAMETERS OF DUAL-PHASE STEEL (AISI1040 F-B) WITH $L_9(3^4)$.

No.	Input variable			
	A, (°C)	B, (m/min)	C, (mm/rev)	D, (mm)
1	750	80	0.13	0.2
2	750	115	0.15	0.4
3	750	150	0.18	0.6
4	770	80	0.15	0.6
5	770	115	0.18	0.2
6	770	150	0.13	0.4
7	790	80	0.18	0.4
8	790	115	0.13	0.6
9	790	150	0.15	0.2
No.	Result			
	$T_{LA}, E,$ (s)	$S_{RA}, G,$ (μm)	$\delta T_L, F,$ (s)	$\delta S_R, H,$ (μm)
1	2646	4.2633	24.0555	0.0340
2	1907	4.0833	1.4143	0.1297
3	994	2.6233	2.9440	0.0450
4	1464	4.07	5.6569	0.0374
5	2168.333	3.11	13.1234	0.0697
6	1172	2.5567	15.5134	0.0450
7	1528.333	3.1067	1.6997	0.0736
8	700	2.42	3.5590	0.0726
9	1297.333	2.22	1.6997	0.0163

TABLE II. ASSESSED RESULTS OF PREFERABLE PROBABILITY AND RANK OF CUTTING PARAMETERS OF DUAL-PHASE STEEL (AISI1040 F-B) WITH $L_9(3^4)$.

No.	Partial preferable probability				Total	
	P_E	P_F	P_G	P_H	$P_i \times 10^4$	Rank
1	0.1907	0.0089	0.0743	0.1417	0.1778	9
2	0.1374	0.1508	0.0803	0.0206	0.3432	8
3	0.0716	0.1412	0.1291	0.1277	1.6679	3
4	0.1055	0.1242	0.0807	0.1373	1.4523	4
5	0.1563	0.0774	0.1128	0.0965	1.3162	5
6	0.0845	0.0624	0.1313	0.1277	0.8842	6
7	0.1101	0.1490	0.1129	0.0915	1.6961	2
8	0.0504	0.1373	0.1359	0.0929	0.8743	7
9	0.0935	0.1490	0.1426	0.1640	3.2564	1

The assessed results in Table II indicate that the test No. 9 is with the highest value of total preferable probability P_i . So, the robust configuration is around the tests No. 9.

Moreover, Table III shows the result of range analysis for the total preferable probability P_i shown in Table II, the order of the impact of input variables is $A > B > C > D$, which also shows that the optimal configuration is $A_3B_3C_2D_1$, it is exactly the experiment No. 9.

TABLE III. RANGE ANALYSIS FOR TOTAL PREFERABLE PROBABILITY OF DUAL-PHASE STEEL (AISI1040 F-B) WITH $L_9(3^4)$.

Level	Input variable			
	A	B	C	D
1	0.7296	1.1087	0.6454	1.5835
2	1.2176	0.8446	1.6840	0.9745
3	1.9423	1.9362	1.5600	1.3315
Range	1.2126	1.0916	1.0386	0.6090
Order	1	2	3	4
Optimal conf.	A_3	B_3	C_2	D_1

However, Hegde et al used ANOVA technique to conduct statistical analysis of the relative contribution of each factor on T_L and S_R individually, their optimal result is close to the test No. 2 [12]. Obviously, the responses of the test No. 2 are worse than those of the test No. 9 in the respect of probability theory comparatively.

IV. CONCLUSION

Above discussion indicates that the new robust design by means of probabilistic multi-objective optimization is reasonable; the arithmetic mean values of the performance utility indicators of the alternatives and their standard errors are taken as twin independent responses of the alternatives in the treatment, which contribute two parts of their partial preferable probabilities to the alternative respectively; the arithmetic mean value of the performance indicator is assessed as a representative of the performance indicator according to its role and pre-required preference, and the standard error is index of unbeneficial type of performance indicator; the total preferable probability of each alternative is the overall and unique index of each alternative in the robust optimum.

REFERENCES

- [1] Teruo, M. (2011). Taguchi Methods Benefits, Impacts, Mathematics. *Statistics, and Applications*. New York, USA.
- [2] Roy, R. K. (2010). *A primer on the Taguchi method*. Society of Manufacturing Engineers.
- [3] Box, G. (1988). Signal-to-noise ratios, performance criteria, and transformations. *Technometrics*, 30(1), 1-17.
- [4] Box, G. E., & Meyer, R. D. (1986). Dispersion effects from fractional designs. *Technometrics*, 28(1), 19-27.
- [5] Welch, W. J., Yu, T. K., Kang, S. M., & Sacks, J. (1990). Computer experiments for quality control by parameter design. *Journal of quality technology*, 22(1), 15-22.
- [6] Welch, W. J., Buck, R. J., Sacks, J., Wynn, H. P., Mitchell, T. J., & Morris, M. D. (1992). Screening, predicting, and computer experiments. *Technometrics*, 34(1), 15-25.
- [7] Nair, V. N., Abraham, B., MacKay, J., Box, G., Kacker, R. N., Lorenzen, T. J., ... & Jeff Wu, C. F. (1992). Taguchi's parameter design: a panel discussion. *Technometrics*, 34(2), 127-161.
- [8] Zheng, M., Wang, Y., & Teng, H. (2022). A novel method based on probability theory for simultaneous optimization of multi-object orthogonal test design in material engineering. *Metallic Materials/Kovové Materiály*, 60(1).
- [9] Zheng, M., Wang, Y., & Teng, H. (2022). A novel approach based on probability theory for material selection. *Materialwissenschaft und Werkstofftechnik*, 53(6), 666-674.
- [10] Zheng, M., Teng, H., Yu, J., Cui, Y., & Wang, Y. (2022). *Probability-based multi-objective optimization for material selection*. Springer.
- [11] Zheng, M., & Yu, J. (2023). Probabilistic approach for robust design with orthogonal experimental methodology in case of target the best. *Journal of Umm Al-Qura University for Engineering and Architecture*, 1-5.
- [12] Hegde, A., Hindi, J., Gurumurthy, B. M., Sharma, S., & Kini, A. (2022). Machinability study and optimization of tool life and surface roughness of ferrite-bainite dual phase steel. *Journal of Applied Engineering Science*, 20(2), 358-364.

Fuzzy Logic Control of 5MW Grid Connected Wind Turbine

Ali Berboucha¹, Kamel Djermouni², Kaci Ghedamsi³, Djamel Aouzellag⁴

^{1,2,3,4}Laboratoire de Maitrise des Energies Renouvelables, Faculté de Technologie, Université de Bejaia, Bejaia, Algérie

¹ali.berboucha@univ-bejaia.dz

Abstract—In this paper, we introduce a configuration of a three-phase wind turbine system based on permanent magnet synchronous generator connected to the electrical grid using a three-level inverter. The objectives of this system is ensuring unity power factor operation and optimizing power extraction from the wind source. To achieve these objectives, a control strategy based on the fuzzy logic theory is developed. The control algorithm proposed is based on fuzzy logic to tracks and extract the maximum wind power by controlling the rotational speed of wind turbine, which is most appropriate when there is a lack of information on the characteristic $C_p(\lambda, \beta)$ of the turbine. The inverter is controlled by simplified space vector modulation which allows us to reduce the computational time and reduce the algorithm complexity compared to the conventional three-level space vector modulation. The regulation of the d - q axis grid currents is achieved through the use of fuzzy logic-based regulators. To evaluate the performance of the proposed control strategy, simulations were conducted using the Matlab/Simulink platform while considering varying levels of wind speed.

Keywords - wind turbine generator, FUZZY logic MPPT, 5MW Permanent Magnet Synchronous Generator (PMSG), Three-level Neutral Point Clamped (NPC) inverter, Simplified Space Vector Pulse Width Modulation (SSVPWM)

I. INTRODUCTION

In 2019, electricity accounted for approximately 19.7% of global final energy consumption, exhibiting a substantial increase from 9.5% recorded in 1973. During the same year, in 2019, the worldwide production of wind electricity estimated to around 1427 TWh compared to 104 TWh in 2005 [1]. Over the past

few decades, the use of wind energy conversion system has significantly increased. The installed wind turbines can be divided into two categories: fixed-speed and variable-speed wind turbines, authors in [2] listed several advantages of the latter type of wind turbine over the fixed-speed model. Numerous controllers have been developed in the literature [2-4] to track the maximum power available from the wind. The authors in [3] provided advantages and disadvantages for each technique; in the situation where the turbine parameters and the climate conditions are unknown, MPPT-based fuzzy logic is the most appropriate approach.

Multilevel inverters have gained significant attention and application in medium and high voltage/power since their introduction. They have undergone extensive research and find utility in various sectors of the power industry, encompassing industrial drives, renewable energy applications, power system applications such as flexible AC transmission systems (FACTS) and high voltage DC transmission (HVDC), among others. In the context of high power and large-scale grid-connected renewable energy systems, multilevel inverters emerge as one of the best choice due to their numerous advantages. These advantages include a reduction in harmonic distortion (THD), resulting in lower filter requirements, modularity, decreased voltage stress experienced by power semiconductor devices, and increased overall efficiency [2]. The use of multilevel inverters in such systems enhances their performance and reliability, making them a preferred option within the power industry. In this paper a three-level Neutral Point Clamped inverter topology is used with its simplified

space vector modulation control taking into account the balancing of the capacitor voltage.

II. MATERIALS AND METHODS

A typical grid-connected wind turbine system is shown in Fig. 1, the proposed system consists of a 60m wind turbine coupled to a 5MW *PMSG* which is connected to a *AC-DC* converter. The *MPPT* method used in this paper, as indicate previously is based on fuzzy logic theory, the *AC-DC* converter is connected to a three-phase three-level *NPC* inverter, this late is controlled using a simplified space vector modulation with voltage capacitor balancing, a filter which is typically used at the output of the inverter to attenuate high-frequency harmonics, and step-up transformers, it is used to raise the output voltage of the inverter and adapt it to the distribution grid voltage.

A. Modeling of the Wind Turbine

The aerodynamics of wind turbine may be characterized by its $C_p(\lambda, \beta)$ curve, which is usually provided by manufacturers. C_p is the power coefficient; it matches to maximum mechanical power recovered from wind at its maximum value and it depends of tip-speed ratio λ and pitch angle β . For a given C_p , mechanical power P_m and mechanical torque T_{pm} extracted from wind by the wind turbine may be given by [4]:

$$P_m = 0.5\rho SC_p(\lambda, \beta)V_w^3, \quad (1)$$

$$T_{em} = \frac{P_m}{\Omega_m}. \quad (2)$$

Power coefficient is a function of blade pitch angle, and linear relation between wind speed and the speed of blade tip, this coefficient indicates the efficiency that wind turbine transforms kinetic energy contained in wind into mechanical energy. According to the BETZ limit, for horizontal axis turbines with three blades, maximum possible value is approximately 0.593.

In Fig. 2 is presented some power coefficient curves for different pitch angles; the best result is with angle in zero degrees.

B. Modeling of the Wind Turbine

The generator selected for conversion of wind energy is *PMSG*; dynamic model of *PMSG* in $d-q$ frame can be represented by following equations [4]:

$$\begin{pmatrix} V_{sd} \\ V_{sq} \end{pmatrix} = R_s \begin{pmatrix} i_{sd} \\ i_{sq} \end{pmatrix} + \frac{d}{dt} \begin{pmatrix} \lambda_{sd} \\ \lambda_{sq} \end{pmatrix} + \omega_s \begin{pmatrix} -1 & 0 \\ 0 & 1 \end{pmatrix} \begin{pmatrix} \lambda_{sq} \\ \lambda_{sd} \end{pmatrix}, \quad (3)$$

where $V_{sd}, V_{sq}, i_{sd}, i_{sq}, \lambda_{sd},$ and λ_{sq} , are d, q axis stator voltages, currents, and flux linkages. R_s is stator resistance; equations for these values without damper circuits can be expressed in terms of stator currents and magnetic flux as following:

$$\begin{pmatrix} \lambda_{sd} \\ \lambda_{sq} \end{pmatrix} = \begin{pmatrix} L_{sd} & 0 \\ 0 & L_{sq} \end{pmatrix} \begin{pmatrix} i_{sd} \\ i_{sq} \end{pmatrix} + \begin{pmatrix} \Psi_f \\ 0 \end{pmatrix}, \quad (4)$$

$$\omega_s = P\Omega_r. \quad (5)$$

$L_{ds},$ and $L_{qs},$ are d, q axis stator inductances; ψ_f is magnetic flux; ω_s is generator electrical angular speed; Ω_r mechanical angular speed and P is pair number of poles. Electromagnetic torque is given as [4]:

$$T_{em} = \frac{3}{2}P(\lambda_{sd}i_{sq} - \lambda_{sq}i_{sd}). \quad (6)$$

C. Modeling of Multilevel Inverter

The multilevel inverter is a structure designed to generate a sinusoidal voltage by combining multiple levels of voltages, typically

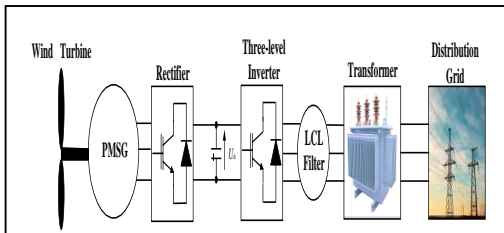


Figure 1. Global diagram of the studied system.

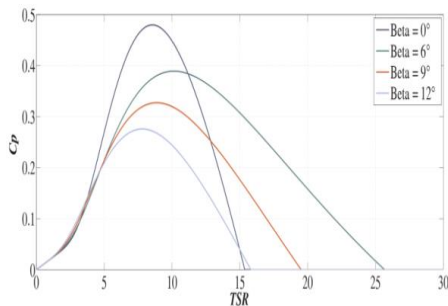


Figure 2. C_p - λ curves for different pitch angles.

derived from capacitor voltage sources. Among various multilevel inverter topologies, the three-level Neutral Point Clamped (*NPC*) inverter, depicted in Fig. 3 is widely used for motor drive applications. However, as the number of voltage levels exceeds three, the complexity and the requirement for clamping diodes in the *NPC* inverter become limiting factors [2].

In the three-phase three-level *NPC* inverter circuit, each phase of the inverter shares a common *DC* bus. This bus is divided into three levels using two capacitors. Each capacitor maintains a voltage of $E/2$, ensuring that the voltage stress across each switching device is limited to $E/2$.

By employing complementary control between the upper switches and lower switches, we can write:

$$\begin{cases} S_{k1} = 1 - S_{k3} \\ S_{k2} = 1 - S_{k4} \end{cases}, \quad (7)$$

where $k=(a,b,c)$ is the leg index. Assuming ideal switches, connection functions are defined as:

$$\begin{cases} G_{k1}^a = S_{k1}S_{k2} \\ G_{k2}^a = S_{k3}S_{k4} \end{cases}. \quad (8)$$

Voltage of leg k ($k=a,b,c$) of three-level inverter is given by the this equation:

$$V_{k0} = [(G_{k1}^a - G_{k2}^a)] \frac{E}{2}. \quad (9)$$

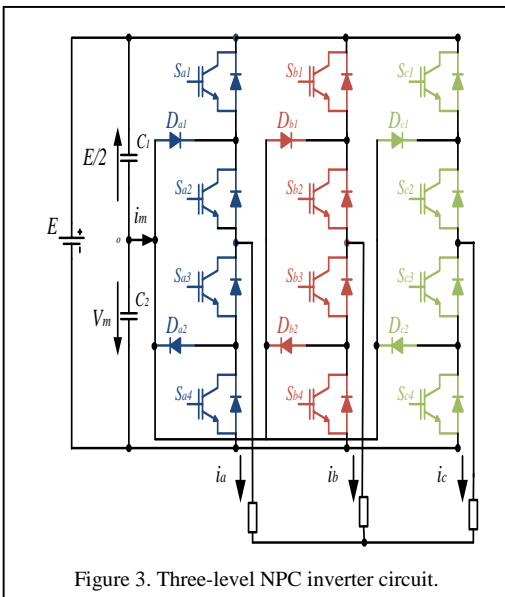


Figure 3. Three-level NPC inverter circuit.

Output voltage of the three levels inverter is given by:

$$\begin{pmatrix} V_a \\ V_b \\ V_c \end{pmatrix} = \frac{1}{3} \begin{pmatrix} 2 & -1 & -1 \\ -1 & 2 & -1 \\ -1 & -1 & 2 \end{pmatrix} \begin{pmatrix} V_{10} \\ V_{20} \\ V_{30} \end{pmatrix}. \quad (10)$$

D. MPPT With Fuzzy Logic Control

The goal of the *MPPT* is to pick up the maximum power from the wind given by:

$$P_m = 0.5\rho S C_p^{opt}(\lambda_{opt}) V_w^3. \quad (11)$$

The *MPPT* controls speed of rotor by controlling torque generator according to the optimal tip speed ratio λ_{opt} by requiring on electromagnetic motor torque to be the same as its optimal reference value:

$$T_{em} = T_{em-ref}. \quad (12)$$

Usually wind turbine characteristic is stranger, a research based on fuzzy logic is provided, rules of behavior to keep in order converging to the optimal point, are relatively easy to establish. These rules are based on variation of electrical power (ΔP) and the rotation speed of turbine ($\Delta\Omega$). Composition of a fuzzy control system is made up of following blocs:

- Fuzzification;
- Knowledge base (Rules);
- Inference engine;
- Defuzzification.

Fig. 4 shows structure of a fuzzy logic controller.

To each wind speed, system has to find the maximal torque, this corresponds in search of optimal rotation speed, from the existence of linguistic rules, controller by fuzzy logic (*FLC*) works in same way as the classic regulator. Block diagram for power optimization by fuzzy logic is shown in Fig. 5. *MPPT* device based on measurement of electrical power variation (ΔP) and rotation speed ($\Delta\Omega$) as input of *FLC* and proposes a change ($\Delta\Omega^*$) of rotational speed reference of wind turbine (Ω^*) as output of *FLC*. The block diagram of fuzzy logic *MPPT* is shown in Fig. 5.

The rotational speed of wind turbine is regulated so as to follow the reference speed (Ω^*) obtained at the output of fuzzy *MPPT*

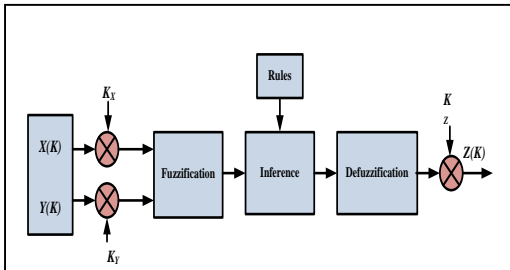


Figure 4. General diagram of a fuzzy controller.

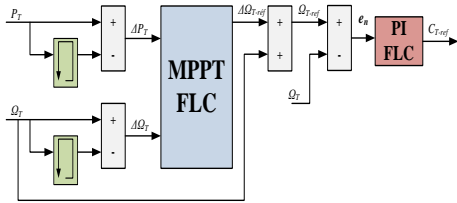


Figure 5. Structure of controller fuzzy MPPT.

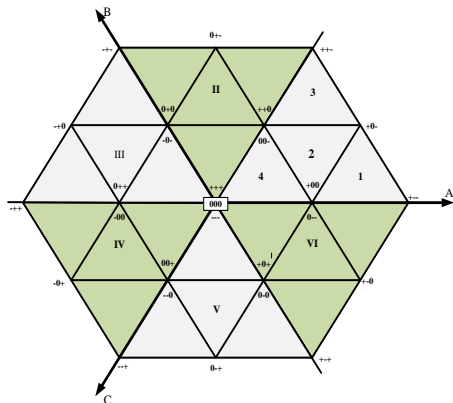


Figure 6. Three-level space vector diagram.

controller; the output of regulator defines the reference of electromagnetic torque of machine. Each of both linguistic inputs of fuzzy *MPPT* controller possesses seven fuzzy sets, which gives a set of forty-nine rules, these ones can be mentioned on Table I.

Each of both linguistic inputs of fuzzy *PI* controller possesses five fuzzy sets, which gives a set of twenty five rules. These ones can be represented by the inference matrix (Table II). Inputs are error and error variation of reference speed and the output of our regulator is torque reference.

E. Control of Three-level Inverter

Space Vector Pulse Width Modulation is a widely used control method for multilevel inverters that takes variables provided by the

control system to represent each switching vector as a point in the complex (α, β) space. *SVPWM* schemes offer improved performance in terms of harmonic elimination and fundamental voltage ratios compared to Sinusoidal Pulse Width Modulation (*PWM*) schemes [5]. The three-level *NPC* inverter, as depicted in Fig. 6, has 27 different switching states; each phase leg of the inverter consists of four switching devices, which can be in one of three distinct switching states denoted as +, 0, and - to represent positive, zero, and negative switching sequences.

The zero voltage vectors has three switching states as [(0 0 0), (+ + +), (- - -)].

As per the *SVPWM* technique described in [6], the external three-level hexagon is subdivided into six smaller two-level hexagons, as depicted in Fig. 7.

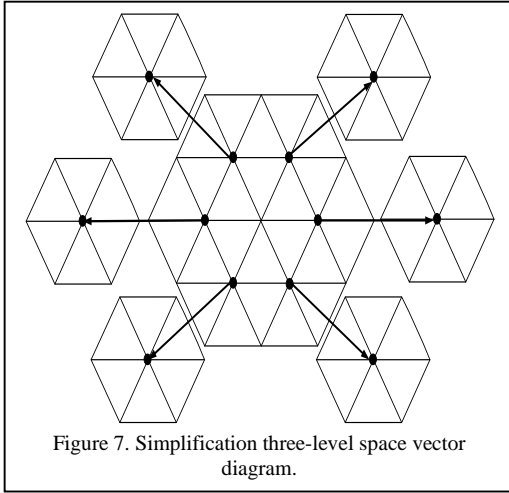
The objective is to determine the location of the reference voltage vector within one of these two-level hexagons based on the given reference voltage.

TABLE I. RULES GENERATED FOR THE FUZZY MPPT.

$\Delta\Omega / \Delta P$	NB	NM	NS	Z	PS	PM	PB
NB	PB	PB	PM	Z	NM	NB	NB
NM	PB	PM	PS	Z	NS	NM	NB
NS	PM	PS	PS	Z	NS	NS	NM
Z	NB	NM	NS	Z	PS	PM	PB
PS	NM	NS	NS	Z	PS	PS	PM
PM	NB	NM	NS	Z	PS	PM	PB
PB	NB	NB	NS	Z	PM	PB	PB

TABLE II. RULES GENERATED FOR THE FUZZY MPPT.

$\Delta e_n / e_n$	NB	NS	Z	PS	PB
NB	NB	NS	NS	ZE	ZE
NS	NB	NS	NS	ZE	PS
Z	NS	NS	Z	PS	PS
PS	NS	Z	PS	PS	PB
PB	Z	Z	PS	PS	PB



For this, the knowledge of the reference voltage is required, by performing a vector subtraction between the reference voltage vector and the center vector connecting the center of the external hexagon to the center of the respective two-level hexagon, a new two-level reference vector is deduced, then, triggering the three-level inverter is as simple as in a conventional two-level inverter.

The selection of a specific two-level hexagon is determined based on the known position of a reference voltage vector. Every hexagon is recognized by the angle θ such as:

$$H = \begin{cases} 1 & \text{if } \frac{11\pi}{6} \leq \theta < \frac{\pi}{6} \\ 2 & \text{if } \frac{\pi}{6} \leq \theta < \frac{\pi}{2} \\ 3 & \text{if } \frac{\pi}{2} \leq \theta < \frac{5\pi}{6} \\ 4 & \text{if } \frac{5\pi}{6} \leq \theta < \frac{7\pi}{6} \\ 5 & \text{if } \frac{7\pi}{6} \leq \theta < \frac{3\pi}{2} \\ 6 & \text{if } \frac{3\pi}{2} \leq \theta < \frac{11\pi}{6} \end{cases} \quad (13)$$

After having selected a hexagon, the new reference vector $V_s^{*'}$ is calculated as follows:

$$\left\{ \begin{array}{l} \text{if } H = 1 \rightarrow V_{\alpha}^{*'} = V_{\alpha}^* - \frac{1}{2}, V_{\beta}^{*'} = V_{\beta}^* \\ \text{if } H = 2 \rightarrow V_{\alpha}^{*'} = V_{\alpha}^* - \frac{1}{4}, V_{\beta}^{*'} = V_{\beta}^* - \frac{\sqrt{3}}{4} \\ \text{if } H = 3 \rightarrow V_{\alpha}^{*'} = V_{\alpha}^* + \frac{1}{4}, V_{\beta}^{*'} = V_{\beta}^* - \frac{\sqrt{3}}{4} \\ \text{if } H = 4 \rightarrow V_{\alpha}^{*'} = V_{\alpha}^* + \frac{1}{2}, V_{\beta}^{*'} = V_{\beta}^* \\ \text{if } H = 5 \rightarrow V_{\alpha}^{*'} = V_{\alpha}^* - \frac{1}{4}, V_{\beta}^{*'} = V_{\beta}^* + \frac{\sqrt{3}}{4} \\ \text{if } H = 6 \rightarrow V_{\alpha}^{*'} = V_{\alpha}^* + \frac{1}{4}, V_{\beta}^{*'} = V_{\beta}^* + \frac{\sqrt{3}}{4} \end{array} \right. \quad (14)$$

In this study, the balancing of two capacitors, C_1 and C_2 , is achieved using redundant states. Redundant states, such as $(+ 0 0)$ and $(0 - -)$, are employed to balance the capacitors. In the state $(+ 0 0)$, capacitor C_1 discharges while C_2 charges, whereas in the state $(0 - -)$, capacitor C_1 charges and C_2 discharges.

The technique for neutral point balancing varies depending on the operation of the converter. Table III provides an overview of how the utilization of redundant states can impact the neutral point in both an inverter and a rectifier.

TABLE III. EFFECT OF REDUNDANT STATES ON THE CAPACITORS VOLTAGE.

Redundant states	Capacitor's voltage	
	Inverter	Inverter
$(0 - -) (0 0 -)$ $(- 0 -) (- 0 0)$ $(- - 0) (0 - 0)$	$V_{c1} \uparrow$ and $V_{c2} \downarrow$	$V_{c1} \downarrow$ and $V_{c2} \uparrow$
$(+ 0 0) (+ + 0)$ $(0 + 0) (0 + +)$ $(0 0 +) (+ 0 +)$	$V_{c1} \downarrow$ and $V_{c2} \uparrow$	$V_{c1} \uparrow$ and $V_{c2} \downarrow$

F. Grid Side Control

Fig. 8 shows us the diagram of the grid side control. The conventional PI controllers are replaced by fuzzy PI and rules used for this part are given in Table II. The inputs are error and error variation of i_{gd} and i_{gq} current, and outputs are V_{gd} and V_{gq} respectively.

III. RESULTS AND DISCUSSION

Global wind turbine grid-connected system of Fig. 1 is simulated using *MATLAB-*

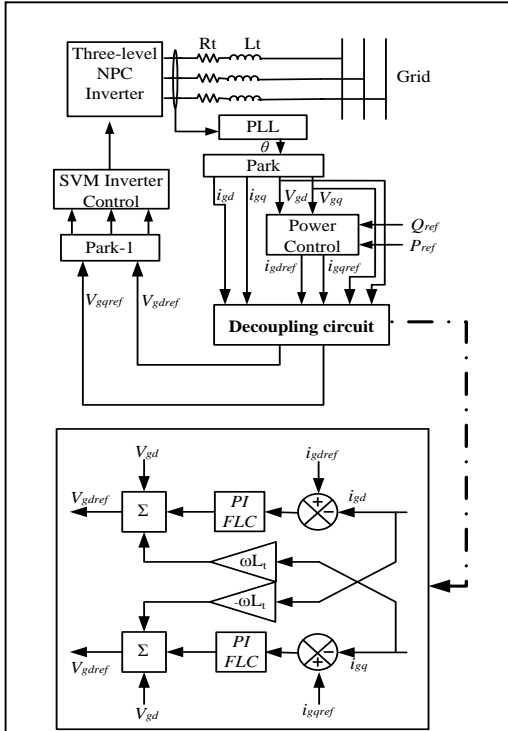


Figure 8. Diagram of the grid side control.

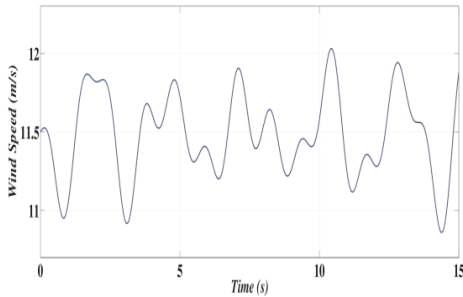


Figure 9. Wind speed profile.

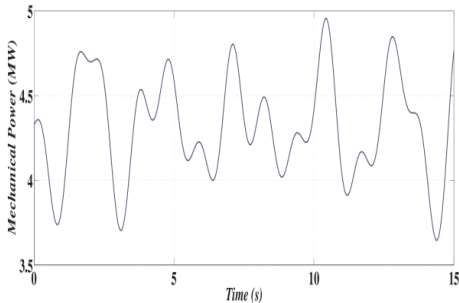


Figure 10. Mechanical power generated by the wind turbine.

SIMULINK, variable wind speed is taken as shown in Fig. 9.

Fig. 10 shows the mechanical power generated by the wind turbine it has the same look as wind profile taken which demonstrates the effectiveness of our *MPPT* controller.

Fig. 11 shows us the *DC* bus Voltage, It is maintained at a value of 5000V which corresponds to the input voltage of our three-level *NPC* inverter.

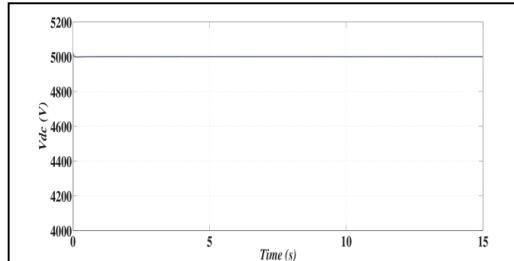


Figure 11. DC bus voltage.

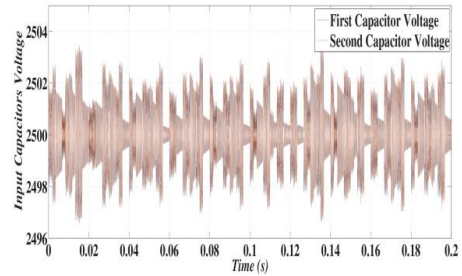


Figure 12. Input inverter capacitors voltage.

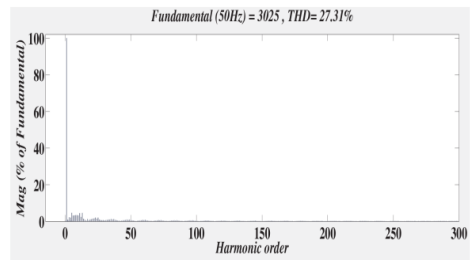
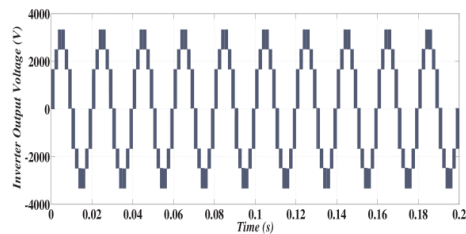


Figure 13. Output voltage of the NPC inverter and its spectral analysis.

Fig. 12 shows us the voltage of the two capacitors which split the *DC* bus, its value oscillates between $2500V \pm 0.12\%$ which shows the effectiveness of our capacitor voltage balancing algorithm.

Fig. 13 shows the output voltage of the *NPC* inverter and its spectral analysis; the output voltage has a staircase shape with several levels which relates to a sinusoid compared to a classic two-level inverter and the *THD* of our signal is 27.31%, value which is acceptable.

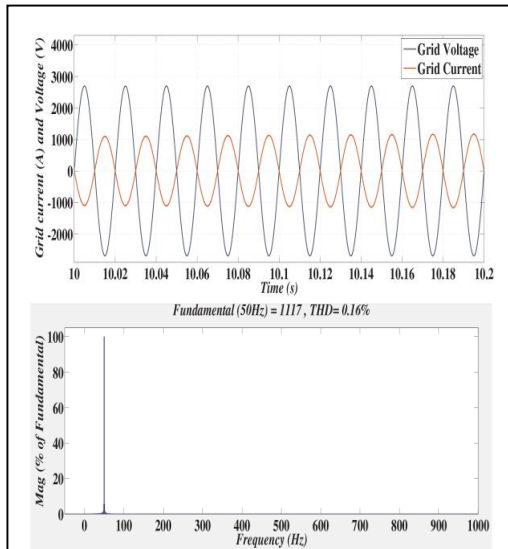


Figure 14. Current injected to the grid and its spectral analysis.

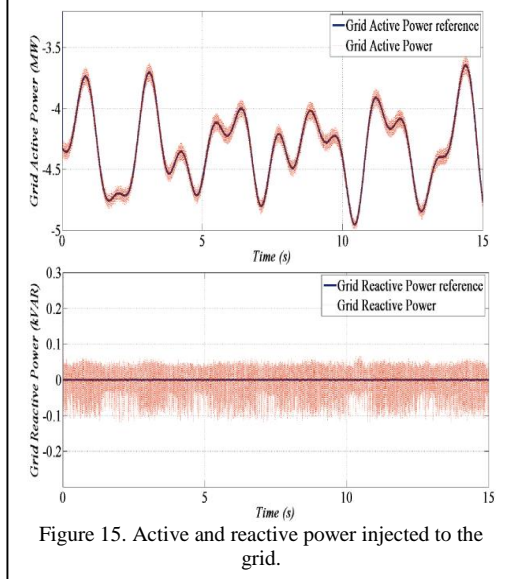


Figure 15. Active and reactive power injected to the grid.

Fig. 14 shows a zoom of current injected to the grid and its spectral analysis; the *THD* of our signal is 0.36% , value which is very acceptable.

Fig. 15 shows us the active and reactive power injected to the grid, we note that the active and reactive power injected to the grid follow well their reference which shows the robustness of our grid side control.

IV. CONCLUSION

This paper presents a fuzzy logic control of a 5MW grid connected wind turbine system using three phases three-level *NPC* inverter. The configuration for the proposed system was designed first and simulated using *MATLAB/simulink*, the results of simulation shows the robustness and the effectiveness of the control algorithms proposed.

- The proposed control scheme features several advantages such as the generation of high-quality voltage, the capacity to operate at a lower switching frequency than a two-level.
- The *FLC* can provide more efficient than the conventional controller for nonlinear systems.
- The inverter can be easily expanded by increasing the levels. Thus, number of the output levels is increased and the inverter generates higher-quality output voltage.

The proposed system ensure unity power factor operation by controlling and maintaining the reactive power injected to the grid equals to zero, the advantage of this action is that the power extracted from the wind is provided to the grid but the disadvantages is that the system proposed didn't participate in voltage regulation.

The advantages of using simplified space vector modulation for inverter control compared to conventional three-level space vector modulation are reducing the complexity algorithm given that in the end we end up with the algorithm of a two-level converter instead that of three-level, and reducing computational time given that before choosing a vector only two conditions must be verified unlike the conventional technique where we must verify three conditions.

Under different wind speed conditions, below wind speed cut-out, our MPPT control extract well the maximum power available given that the rotation speed follows its reference very well.

As a perspective and continuation of this work other non-linear control techniques such as Sliding Mode Control and H^∞ control will be used and a comparison will be made by simulations and implementation.

REFERENCES

- [1] Key World Energy Statistics (2021).
- [2] Berboucha, A., & Ghedamsi, K. (2018). Control of Wind-Battery Energy Systems connected to Grid using Nine-Level Inverter. *Electrotehnica, Electronica, Automatica (EEA)*, 66(1), 17-24.
- [3] Abdullaha, M.A., Yatima, A.H.M., Tana, C.W., & R, Saidurb. (2012). A review of maximum power point tracking algorithms for wind energy systems. *Renewable and Sustainable Energy Reviews*, 16, 3220–3227.
- [4] Berboucha, A., Djermouni, K., Ghedamsi, K., & Aouzellag, D. (2017). Fuzzy logic control of wind turbine storage system connected to the grid using multilevel inverter. *International Journal of Energetica*, 2(1), 15-23.
- [5] Colak, I., Kabalcib, E., & Bayindira, R. (2011). Review of multilevel voltage source inverter topologies and control schemes. *Energy Conversion and Management*, 52(2), 1114–1128.
- [6] Seo, J.H., Choi, C.H., & Hyum, D.S. (2001). A new simplified space-vector PWM method for three-level inverters. *IEEE Transactions on Power Electronics*, 16(4), 545–550.

Self-excited Induction Generator for Supporting Grid-isolated Loads in Microgrid with its Techno-economic Analysis

Arunava Chatterjee¹

¹Department of Electrical Engineering, Raghunathpur Government Polytechnic, Purulia, India

¹arunava7.ju@mail.com

Abstract—This paper provides a technical and financial analysis of integrating a microgrid structure for power generation with a wind energy conversion system. This study's primary objective is to identify solutions to issues that arise when isolated induction generators are employed in microgrids. A closed loop electronic load connection is used to control the loads of the induction generator-based systems. Using HOMER software, an economic study of the proposed wind-based microgrid structure is presented. Additionally, by employing a straightforward variable capacitor design to inject reactive power during voltage dips, it provides a way to sustain the voltage profile. The suggested approach and its control are investigated with the aid of a lab experimental setup. The outcomes demonstrate that the suggested plan to be implemented in grid-isolated areas.

Keywords - electronic load connector, induction generator; microgrid, voltage regulation, wind power

I. INTRODUCTION

These days, burning fossil fuels like coal, oil, and natural gas produces the bulk of the energy needed to produce electricity. The supply of these fossil fuels is limited, and their combustion results in the emission of a sizable amount of poisonous gases into the environment. Finding sustainable and clean sources of energy is thus constantly required. A clean, unlimited renewable energy source is wind. A wind turbine is by far the most popular technique to convert wind energy into electrical energy, while there

are other alternatives as well [1]. Theoretically, any generator may be mounted on top of a wind turbine to generate power. Even if the generator only produces direct current or alternating current with variable amplitude and frequency, the requirement for grid-compatible electric current may currently be satisfied by connecting the appropriate inverters.

The induction generator (IG) appears to be a great choice for these applications because to its reliability, low maintenance needs, and simple controls [2]. Because of its simplicity of use, durability, and small size per generated kilowatt, IG is recommended for producing wind energy. Additionally, IGs may generate the excitation magnetic field on their own without the aid of an outside power source. As a result, they may be used in remote and desolate areas [3-5]. Although the development of static power converters has made it simpler to manage the output voltage of IGs, reactive power consumption and poor voltage regulation at variable speeds continue to be the primary drawbacks of IGs [6]. The self-excited induction generator (SEIG), especially in locations with variable wind speed and isolation, is a great option for wind-driven electric production applications since it does not require an additional power source to create the magnetic field. Despite the fact that the SEIG scheme was developed more than 80 years ago, a sizable number of research articles have just lately begun to concentrate more on the analysis of and

applications for SEIGs [7,8]. This is due to improved voltage and frequency management methods as well as the recent thirty years' significant worldwide attention paid to the development of renewable energy sources. The main operational problem with the SEIG system is its inability to control voltage and frequency under fluctuating load conditions. A change in the load impedance has an instantaneous effect on the machine excitation. This is due to the fact that the reactive power of the excitation capacitors is shared by the induction machine serving as the generator and the load impedance. The generator's voltage therefore decreases as the load impedance rises, resulting in poor voltage management. The slip of the induction generator, on the other hand, increases with increasing load despite the fact that the speed of the prime mover remains constant, leading to a frequency that is dependent on the load. To control the voltage and frequency of a SEIG system working with fluctuating loads, several research have been done in the past. A traditional SEIG controller is a high-priced speed governor. According to [9], a sliding mode controller was presented, demonstrating regulated dynamic response and behavior of the system in response to changes in generator characteristics and load. A SEIG's voltage and frequency regulation under different load circumstances was investigated using an electronic load controller [10]. The voltage control issue is partially handled with the use of static converters; however, the system cost is significantly raised [11,12]. Control methods based on maximum power point tracking (MPPT) are often used. Grid-connected generation may be operated more easily with the help of MPPT techniques [13]; nevertheless, standalone grid-secluded generating is usually managed without MPPT to lessen system complexity [14]. However, as independent generations are regularly used to carry out significant tasks, keeping a steady generation becomes essential [15]. However, the regulation of speed and voltage does not always result in a performance level that is always adequate due to the machine's severe dynamic slip changes and the difficulties of developing a smooth variable reactive power supply at an affordable price.

In order to help with the resolution of the aforementioned operational challenges, this research comprises a technical and economic analysis of the IG system when feeding varied home loads. The intended study suggests a

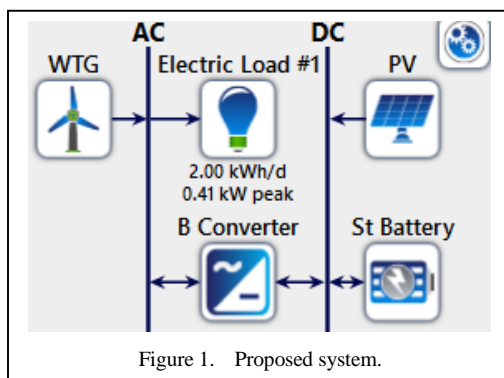


Figure 1. Proposed system.

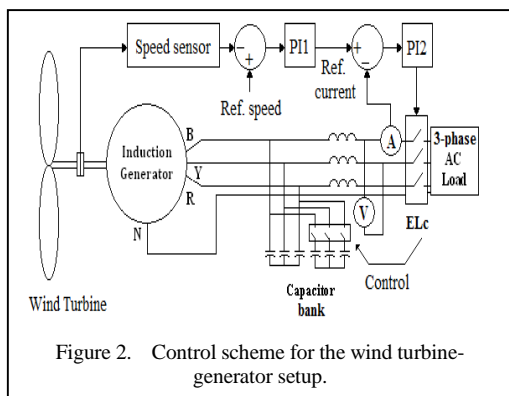
dynamic capacitor-based voltage regulation method that has the potential to deliver changeable reactive power for the IG powering grid-isolated loads during load and speed transients. A suggested capacitor switching system based on a microcontroller is also demonstrated to improve the transient responsiveness. To continuously power grid-isolated loads, the IG-based structure may subsequently be linked to other renewable energy generators.

II. DESCRIPTION OF THE PROPOSED SYSTEM

The suggested generating system comprises of a three-phase induction machine which is coupled to wind turbine for generation purpose. The IG is linked to a bus where system loads can also be attached for supply. The induction machine's stator windings are connected to a capacitor bank to provide the initial reactive power. Reactive power balancing is used to determine the initial excitation [16]. The IG system may also be coupled to a standby PV panel for boosting and sustaining generation. Additionally linked through a charge controller is a storage battery that will supply the loads during times of low power production. Fig. 1 depicts the integrated system as a whole. The suggested system is designed for usage in an onshore, eastern Indian site that is grid-isolated. Since there is no grid connection at the location, the usefulness of the proposed generating plan is crucial in providing electricity to the loads that are linked remotely.

III. PROPOSED SYSTEM CONTROL

The IG is used to offer the suggested system generation. A photovoltaic (PV) panel may also be connected to the IG. The microgrid structure with PV panels is not considered for the control. With varying wind speeds and varied loads, the



control is primarily concentrated on the IG side control of the electronic load connection (ELC) and the capacitor bank control. In Fig. 2, the control system is displayed. The shaft speed of the IG linked to the prime mover is noted for the proposed control, and the data is passed to a comparator circuit.

A proportional-integral controller (PI) receives the set error after comparing the reference and comparing it to it. The output from the PI1 is used as the reference current, and the system load current is contrasted with it. Following that, the same method is used to create pulses to control the ELC. The well-known Ziegler-Nichols tuning method is used to adjust the PI controllers. The benefit of speed reference is that it can manage and make use of the lower ranges of wind speeds, which are frequently disregarded for wind generating. Depending on the situation, additional capacitors are regulated by load and speed factors.

IV. MICROGRID SETUP

It will also be necessary to assess the cost of connecting the IG-based power system to a microgrid. The “HOMER” program is used for cost estimation and optimization [17]. In all industries, from village electricity and island utilities to grid-connected campuses and military locations, HOMER Energy is the industry standard for maximizing microgrid architecture. HOMER (Hybrid Optimization Model for Multiple Energy Resources), which was initially created at the National Renewable Energy Laboratory and improved and made available by HOMER Energy, combines three potent tools into a single software program to enable the coexistence of engineering and economics.

Some components are utilized in the creation of the online microgrid simulation. An IG-based wind generator, a primary load, a converter, a

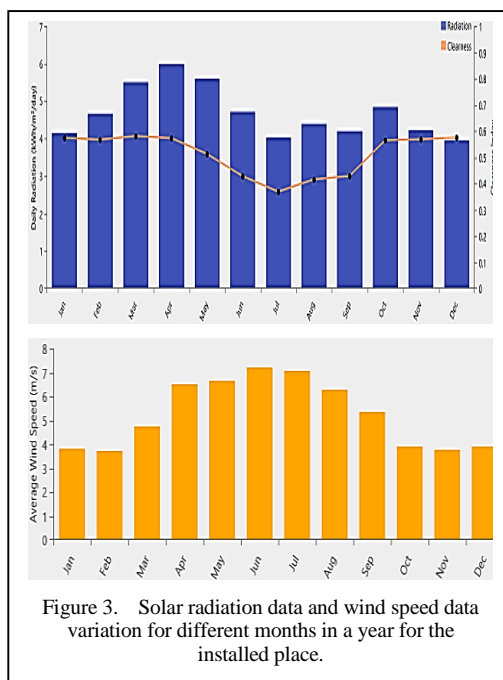


Figure 3. Solar radiation data and wind speed data variation for different months in a year for the installed place.

battery, and a PV cell are the components. Two buses are in operation. Only a DC bus should be used to connect PV cells. It is only utilized when there is insufficient wind power to start the generator.

There, in addition to the DC bus serving as a backup power supply, a battery is also employed. Since the generator is an IG, it is solely linked to the AC bus. The AC bus is connected to a main load. The converter in this instance is linked to both an AC and a DC bus. The outcomes of the connection can be computed and optimized after a variety of iterations. NREL’s laboratory was used to gather the solar and wind data for the setup location that was suggested, as shown in Fig. 3. Although it is always linked to the system and stores any excess energy in a battery, the PV module is used when wind power is scarce. Thus, loads may be supplied at that time utilizing the PV module. According to Fig. 3, whenever the wind power is low, the PV module supplies the electricity, and whenever the power from the PV module is low. The two powers are determined to be complementary for the suggested setup location. The HOMER is mostly used to offer economic analysis and examination of technology assistance. Fig. 4 in the program displays the tabulated output. The initial capital required, the system’s net present cost, and the annual operating costs are the parameters considered for the study and all are included in the table. As can be seen, operational costs are

Architecture						Cost				System	
PV (kW)	WTG	St Battery	B Converter (kW)	NPC (\$)	COE (\$)	Operating cost (\$/yr)	Initial capital (\$)	Ren Frac (%)	Total Fuel (L/yr)		
1.80		8	0.428	\$4,059	\$0.430	\$89.06	\$2,907	100	0		
1.75	1	4	0.583	\$6,619	\$0.701	\$76.90	\$5,625	100	0		
	1	12	0.292	\$8,187	\$0.868	\$162.41	\$6,088	100	0		

Figure 4. Optimized result.

the modest, and it is anticipated that the system will be in use for 25 years. The cost of fossil fuel generation ranges from \$0.20 to \$0.40 per kWh and is therefore almost equivalent to the current case's 100% renewable energy generation [18]. Also, since the project lifetime is 25 years, it is expected that the system cost will be recovered within that period of operation

A clear benefit of grid connection is the cost of producing a single unit of electricity with 100% renewable fraction obtained meaning loads are fully supplied from renewable sources. The proposed scheme is thus advantageous when implemented in grid secluded onshore area considering the cost and generation ease. Although, through proper generation and storage sizing, some more optimization can be made and this can be seen as a future scope of study. This research is also scalable to be implemented for grid connection.

V. RESULTS AND DISCUSSION

The scheme's hardware implementation is split into two phases. First, a lab prototype is used to validate the simulation findings against a hardware implementation. Second, for the suggested IG, an electronic load connector and variable excitation connector were created.

The three-phase induction generator has a rating of 2.2 kW at 415V, 50Hz, and is coiled for four stator poles. Without the suggested regulation, the voltage generation starts at 1150 rpm with no load (Fig. 2). Despite the low generation speed, the capacitor in use lowers the IG's working point, allowing for lower generation speed. However, at this pace, the frequency of the produced voltage is less than 50Hz. Terminal loads can be connected across the generator's primary windings once it has reached a steady condition.

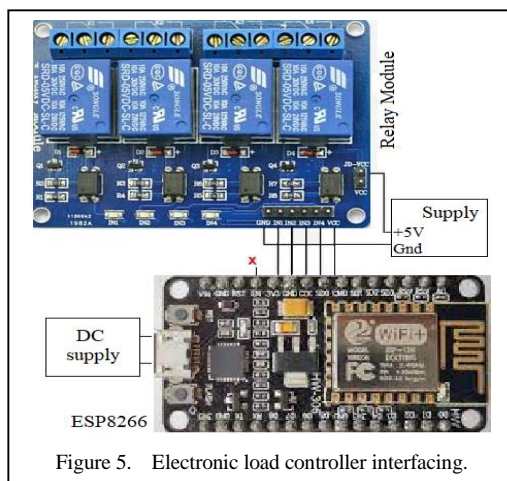
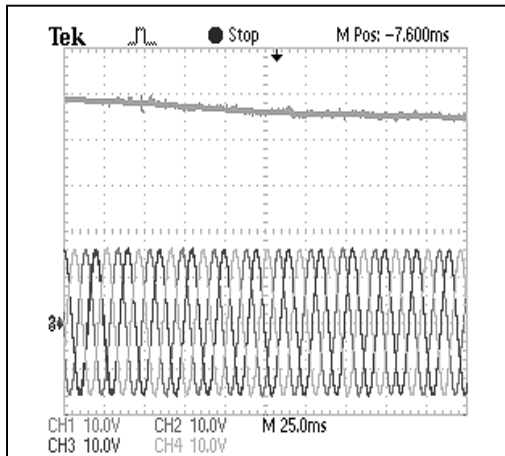


Figure 5. Electronic load controller interfacing.

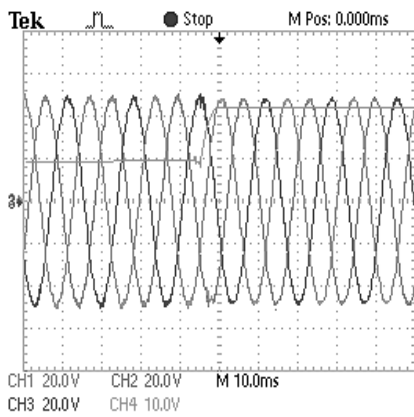
However, given that various gears may be employed in actual operation with the wind turbine to generate at rated speed for the IG, it is assumed that the turbine drives the generator at rated speed. The mechanical contacts of the laboratory-based experimental IG were shown to be capable of repeated usage. A digital contactor switch was required because of mechanical wear and tear. The variable capacitors and loads were connected with an ESP8266 (Wi-Fi enabled controller)-based switch. Relay switches are used for operation.

The circuit is more effective when used for various loading circumstances and wind speed conditions thanks to the connection of the relay coil for switching loads and capacitances.

The electronic load connector is shown in Fig. 5. The controller uses ESP8266 Wi-Fi enabled board which is also capable of controlling the loads remotely using internet enabling smart control. Furthermore, experimental waveforms for the suggested generation method are shown. Fig. 6(a) and



(a)



(b)

Figure 6. Experimental IG generated voltage with change in (a) speed (CH1: Y-axis: 300 r/min/div., CH2, 3 and 4: Y-axis: 200V/div.) and (b) load (CH1,2 and 3: Y-axis 200V/div., CH4: Y-axis: 1A/div.).

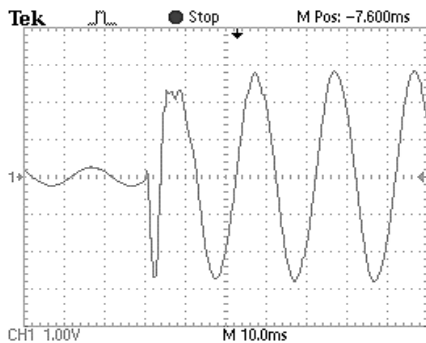


Figure 7. Experimental waveform for change in load in ELc (CH1: Y-axis 100V/div.).

Fig.6 (b), which demonstrate the produced voltage profile and corresponding changes in load and wind speed, respectively.

The fluctuation in IG voltage caused by the suggested regulation is then observed. With a load shift from half rated to rated load current (rms value), it is seen that the produced voltage varies very little. With only a little voltage shift when the shaft speed changes, the resulting voltage control is demonstrated to be effective. The biggest problem of isolated IG when used in a microgrid is its poor load voltage regulation and it can be controlled effectively using the proposed control. Additionally, voltage can also be maintained with change in wind speeds as observed from the results.

Experimental observations of the electronic load connection switching transients are made. Fig. 7 displays the measured waveform with a change in load. The connection transients are evidently quite low. Fig. 6(b) depicts the voltage regulation for the same. The observed voltage regulation is superior than the majority of traditional control strategies. Also improved are the load and speed transients. The method is also rather simple and inexpensive, which are additional benefits.

VI. CONCLUSION

This study provides a technical and financial examination of the integration of wind energy conversion with microgrid architecture for power production. The HOMER modeling tool offers a platform for simulating the scheme's economic feasibility. With less sophisticated systems, the cost of generation is equivalent to traditional generation. This study's primary objective is to identify solutions to issues that arise when isolated IG is utilized in a microgrid. By supplying reactive power during voltage dips utilizing an electronic load connection with capacitive control, it also provides a way to sustain the voltage profile.

Using an experimental prototype, the characteristics of IG and its suggested control are explored. Analyses of IG control strategies have been conducted. Future improvements to the induction generator's design processes and more optimizations can be made to enhance its performance.

REFERENCES

- [1] Patel, M. R., & Beik, O. (2021). *Wind and solar power systems*. CRC Press, UK, 3rd Ed.
- [2] Chojaa, H., et al. (2023). A novel DPC approach for DFIG-based variable speed wind power systems using dspace. *IEEE Access*, 11, 9493-9510.
- [3] Faisal Khan, M., Khan, M., & Iqbal, A. (2022). Effects of induction machine parameters on its performance as a standalone self-excited induction generator. *Energy Reports*, 8, 2302.
- [4] Grgić, I., Bašić, M., Vukadinović, D., & Bubalo, M. (2020). Optimal control of a standalone wind-solar-battery power system with a quasi-z-source inverter. In *Proceedings 2020 9th International Conference. Renewable Energy Research and Application (ICRERA)*, Glasgow, UK, (pp. 61-66).
- [5] Islam, M., & Chatterjee, A. (2019). Analysis of a hybrid energy system for supplying a remote critical load in onshore coastal India. In *Proceedings 5th Jubilee Virtual International Conference on Science, Technology and Management in Energy*, Nis, Serbia, (pp. 1-5).
- [6] Hamid, B., Hussain, I., Iqbal, S., Singh, B., Das, S., & Kumar, N. (2022). Optimal MPPT and BES control for grid-tied DFIG-based wind energy conversion system. *IEEE Transactions on Industry Applications*, 58(6), 7966-7977.
- [7] Ion, C. (2020). A comprehensive overview of single-phase self-excited induction generators. *IEEE Access*, 8, 197420-197430.
- [8] Chatterjee, A., & Chatterjee, D. (2017). PV- assisted microgeneration scheme with single- phase induction generator suitable for wide speed range application. *IET Power Electronics*, 10(14), 1859-1869.
- [9] Mi, Y., Song, Y., Fu, Y., & Wang, C. (2020). The adaptive sliding mode reactive power control strategy for wind-diesel power system based on sliding mode observer. *IEEE Transactions on Sustainable Energy*, 11(4), 2241-2251.
- [10] Murali, V., & Sandeep, V. (2020). Design and simulation of current sensor based electronic load controller for small scale three phase self-excited induction generator system. *International Journal of Renewable Energy Research*, 10(4), 1638-1644.
- [11] Chatterjee, A. (2022). Analysis of a Wind-PV hybrid system with smart control for grid-secluded critical loads in onshore Indian area. In *Proceedings of International Conference Ind. Instr. Control. Lecture Notes in Electrical Engineering*, 815, Springer, Singapore.
- [12] Chatterjee, A., Ghosh, S., & Mitra, A. (2022). Wind-PV based isolated hybrid generation for smart irrigation management and supplying other critical loads. In *Proceedings IEEE Sustainable Energy and Future Electric Transportation (SeFeT)*, Hyderabad, India, (pp. 1-6).
- [13] Huynh, P., Tungare, S., & Banerjee, A. (2021). Maximum power point tracking for wind turbine using integrated generator-rectifier systems. *IEEE Transactions on Power Electronic*, 36(1), 504-512.
- [14] Roy, K., Chatterjee, A., Chatterjee, D., & Ganguli, A. (2015). A photovoltaic-based improved excitation control strategy of three-phase self-excited induction generator suitable for wind power generation. *Electric Power Components and Systems*, 43(17), 1912-1920.
- [15] Chatterjee, A. (2022). Wind-PV based generation with smart control suitable for grid-isolated critical loads in onshore India. *Journal of The Institution of Engineers (India): Series B*, 52, 1-11.
- [16] Trzynadlowski, A. (2001). *Control of induction motors*. Academic Press, USA, 1st Edn.
- [17] Homer Energy. (2023). Available at: <https://www.homerenergy.com/>
- [18] Global Petrol Prices. (2023). Available at: https://www.globalpetrolprices.com/India/electricity_prices/

Environmental Payback of a Solar Photovoltaic System Installed in the Brazilian Northeast

Luiz Felipe Souza Fonseca¹, Italo Roger Ferreira Moreno Pinheiro da Silva², Luiz Moreira Coelho Junior³, Raphael Abrahão⁴, Monica Carvalho⁵

^{1,2,3,4,5}Department of Renewable Energy Engineering, Federal University of Paraíba, João Pessoa, Brazil

¹luiz.fonseca@cear.ufpb.br, ²italo@cear.ufpb.br, ³luiz@cear.ufpb.br,
⁴raphael@cear.ufpb.br, ⁵monica@cear.ufpb.br

Abstract—The planning and feasibility study for the installation of power plants has gradually been incorporating environmental criteria, in addition to the traditional technical and financial criteria. A widely used parameter to verify the financial viability of an energy project is the payback time, which can be adapted to environmental metrics. This study uses the Life Cycle Assessment methodology to quantify the environmental impacts associated with a photovoltaic solar system. From technical data relating to photovoltaic panels and meteorological information (irradiation and temperature) from João Pessoa (Northeast Brazil), the electricity production is estimated. Subsequently the environmental payback time of the system is calculated, which is the time (in years) that the system takes to generate electricity (with low greenhouse gas emissions) equivalent to the energy consumed in its manufacture, use and final disposal. The software SimaPro is used with ecoinvent database and IPCC 2021 GWP 100y environmental impact assessment method. The environmental impact of the photovoltaic solar system is 22.535kg CO₂-eq, which includes extraction of raw materials, component manufacturing, transport, assembly and use, and decommissioning. Considering João Pessoa, the average electricity production is 30.361 MWh/year. The environmental payback is slightly under three years, highlighting the ability of the system to reduce greenhouse gas emissions.

Keywords – photovoltaic energy, environmental impacts, greenhouse gas emissions, life cycle assessment

I. INTRODUCTION

According to the United Nations Development Program (UNDP) [1], the global amount of greenhouse gases (GHG) released into the atmosphere was approximately 24×10^6 t in 2000 with a significant share referring to electricity generation. In Brazil, according to the Energy Research Company (ERC), emissions related to electricity generation were 445.4 Mt CO₂-eq in 2021 and 398.3 Mt CO₂-eq in 2020 [2]. In 2021, Brazil increased by 25.7 TWh (or +3.9%) its internal energy supply (IES) in relation to 2020, with photovoltaic solar generation presenting an increase of +55.9% compared to 2020 [2]. This shows that there is a positive vision for the use of renewable sources and the generation of electricity from solar sources, specifically photovoltaics.

However, generating electricity through photovoltaic panels is not completely free from environmental impacts. Panels need energy and raw materials for manufacture, transportation, installation and final disposal. Each of these stages needs to be evaluated so that the quantitative environmental impact generated by photovoltaic systems can be estimated throughout the life cycle [3]. The advancement of technologies in manufacturing processes and machinery helps to reduce emissions, consequently reducing the overall impact associated with production. This increases the potential for using photovoltaics to generate

electricity with fewer associated environmental impacts [4].

Low-carbon electricity, with lower GHG emissions has been increasingly encouraged and international agreements have been enforced to this end. Brazil presents the majority of its energy matrix based on low-carbon technologies [2]. Low-carbon energy contributes to achieving goals established in the Paris Agreement signed in 2015, as well as national plans for reducing emissions and adapting to climate change as established in the Ten-Year Energy Expansion Plan 2032 (TEP 2032), released in 2022 [5].

Achieving low-carbon energy requires knowledge on the steps, procedures and components that constitute the electricity generation system. The Life Cycle Assessment (LCA) methodology can be used for this purpose, enabling the entire lifetime of the photovoltaic system to be analyzed (“from cradle to grave”). Furthermore, LCA also allows comparison with other electricity generation systems and can lead to the elaboration of strategic actions to further reduce environmental impacts and support for the creation of public policies aimed at sustainable actions [6].

The objective of this study is to calculate the environmental payback of a 16.4 MW monocrystalline photovoltaic panel system installed in the municipality of João Pessoa, Brazil. The environmental payback is the time required to amortize the emissions generated in the construction of the system.

II. METHODOLOGY

LCA is a powerful environmental management tool, used to examine, throughout the lifetime of a system or product, the impacts it can cause when some environmental issues are pre-determined [7]. During the production of a certain product, there are different ways that the production process can end up emitting greenhouse gases. The LCA ranges from these emissions in the production process, to other forms of subsequent emissions in other stages of the lifetime of that product or service.

In this context, LCA is used here to examine the environmental impacts (in terms of GHG emissions) caused from the extraction of raw materials for the production of the photovoltaic panel, through manufacturing, transportation, installation and decommissioning phase at the end of its life. Photovoltaic panels are a way of

generating renewable electricity, but they are not completely free of GHG emissions. These emissions occur mainly during the manufacturing and decommissioning phases, making it necessary to use LCA in these stages to assess the impact on the environment [8].

LCA is standardized by ISO 14040 [9] and ISO 14044 [10], which in Brazil are equivalent to standards of the Brazilian Association of Technical Standards (ABNT), NBR 14040 [11] and NBR 14044 [12]. There are basically four phases for a LCA [9,10]: definition of the objective and scope, inventory analysis, assessment of environmental impacts, and interpretation of results.

The assessment of environmental impacts and interpretation of results were carried out with the help of SimaPro software [12]. SimaPro is the world’s leading sustainability and life cycle assessment software that helps policymakers make informed choices and minimizes the environmental impact of products and services [13]. The database used to develop the life cycle assessment was Ecoinvent v3.9.1 [14]. The ecoinvent database is a repository encompassing diverse global and regional sectors. It models various human activities and processes, providing information on industrial or agricultural processes, including resources consumption, emissions and product generation [14]. The environmental impact assessment method used was the IPCC 2021 GWP 100y [15]. The method considers the lifetime in the atmosphere for different substances, taking into account their contributions to global warming (GWP – Global Warming Potential) [16], and groups emissions of greenhouse gases in terms of CO₂-eq, over a time horizon of 100 years, with CO₂ being the reference gas.

Regarding the photovoltaic energy system, the work of [17] is used. Not only the photovoltaic panels are included, but also the inverters, installation area, cabling, cleaning of the installation site, transportation, maintenance throughout its lifetime (which includes necessary equipment changes), and some other considerations. Therefore, the following characteristics and parameters were used herein: 59248 panels; 8 inverters; 112 junction boxes; 8 medium voltage and 2 high voltage transformers. The lifetime of the panels was considered as 25 years.

Table I present the material composition of the photovoltaic system. Table II presents fuel

consumption and replacements during the operation and maintenance phase of the entire system.

Finally, regarding the decommissioning (or final disposal) phase of the entire photovoltaic system, the realistic scenario of sending all decommissioned material to landfill was adopted.

To calculate the average monthly production of electricity, Eqs. (1)-(4) are employed [18,19]:

$$P = NIP \times A \times eff \times \frac{G}{1000} \times f_{temp} , \quad (1)$$

$$B = \gamma \times \log \left(\frac{G_{\beta}}{G_{\beta,ref}} \right) , \quad (2)$$

$$f_{temp} = 1 - \beta' (\theta_{cell} - \theta_{cell,ref}) + B , \quad (3)$$

$$\theta_{cell} = \theta_a + (NOCT - 20) \times \left(\frac{G_{\beta}}{800} \right) , \quad (4)$$

where NIP is the number of installed panels, A is the area of a single photovoltaic panel, eff is the panel efficiency, G is irradiation and f_{temp} is the operational loss factor as a function of module temperature. f_{temp} is calculated according to Eq. (3), where β' is the temperature power coefficient, θ_{cell} is the module operating temperature, $\theta_{cell,ref}$ is the module operating temperature under standard test conditions, G_{β} in Eq. (2) is the solar radiation reaching the surface of the module, $G_{\beta,ref}$ is the solar radiation under standard test conditions, NOCT is the nominal operating temperature of the module and θ_a is the ambient temperature. Finally, the γ factor is the solar radiation coefficient defined as $\gamma = 0.12$ [20].

Eqs. (1)-(4) depend on parameters that are acquired empirically, through the panel datasheet and meteorological database. For this paper, meteorological data were obtained from the Meteorological Database (BDMEP) [21] of

TABLE I. MATERIAL COMPOSITION OF THE PHOTOVOLTAIC ENERGY SYSTEM.

Material	Mass (kg)
Steel	626.737
Aluminum	3.550
Concrete	304.427
Copper	86.882
Plastic	65.331

Source: [17].

TABLE II. OPERATION AND MANAGEMENT PARAMETERS OF THE PHOTOVOLTAIC ENERGY SYSTEM.

Maintenance	Consumption
Vegetation management	252 liters of diesel/year
Panels washing	287 liters of diesel/year
Inverters replacement	0.08/year
Panels replacement	37.5/year

Source: [17].

the National Institute of Meteorology (INMET) and by the Prediction of Worldwide Energy Resource (POWER) [22] Project - Data Access Viewer. The variables obtained from these two databases were ambient temperature (°C), using BDMEP, and Irradiation (kWh/m²day), using POWER.

The location of the study is João Pessoa, a city in Northeast Brazil. The coordinates of João Pessoa are: 7° 5' 43" S 34° 50' 55" W. The remaining parameters of the solar panels were obtained from the manufacturer datasheet [23].

The environmental payback was based on [17], using Eqs. (5)-(7).

$$GPBT_n = GPBT_{n-1} - E_{y,n-1} \times EF_T , \quad (5)$$

$$EF_T = 1000 \times (EF_{mix} - EF_{PV}) , \quad (6)$$

$$EF_{PV} = \frac{Emissions_{PV25}}{E_{plant,tot25}} , \quad (7)$$

where GPBT is the environmental payback time in years; E_y is the annual energy generated by the panels, and this value varies annually due to the degradation of the panels, where the percentage of annual degradation is provided by the manufacturer and is equal to 3% after the first year, 0.7% between the second and sixth year and 0.5% from the seventh to the last year of the panel's lifetime; EF_{mix} is the emission factor of the national energy mix, in kg of CO₂-eq/kWh; EF_{PV} is the emission factor of the photovoltaic system, also in kg of CO₂-eq/kWh; the factor 1000 converts the calculated annual energy from MWh to kWh; the index "n" is the current year analyzed, which varies from 2 to 25 years, with 25 years being the lifetime established in this paper; $E_{plant,tot25}$ is the sum of the energy generated by the photovoltaic system over the 25 years of useful life, considering its annual degradation; and Emissions_{PV25} value is obtained from the LCA result, considering the

installation's emissions and emissions during the operation and maintenance (O&M) phases.

For a more recent and adequate representation of the Brazilian electrical mix, the Ecoinvent database was adapted following the methodology proposed by [24]. The most recent Brazilian electricity mix was considered (National System Operator, 2022): 63.35% hydroelectric, 11.97% wind, 11.49% natural gas, 4.37% biomass, 2.77% coal, 2.17% fuel oil, and 1.29% solar.

III. RESULTS AND DISCUSSION

Fig. 1 presents a diagram with the LCA results, in kg CO₂-eq., for each part of the photovoltaic system, as well as the percentage of participation of each part.

As can be seen in Fig. 1, the installation accounted for the highest percentage of emissions from the photovoltaic system, with approximately 89% referring to the panels alone. The part of the frame, cables, etc. (which refers to the structure, cabling and landfill) accounted for 4.65%, which shows us that the decision to send the materials to landfill, during the decommissioning phase, could have an influence

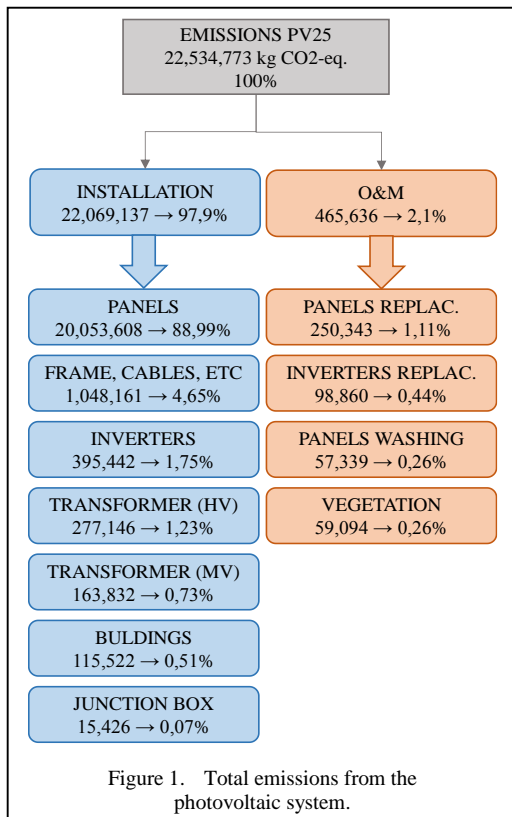


Figure 1. Total emissions from the photovoltaic system.

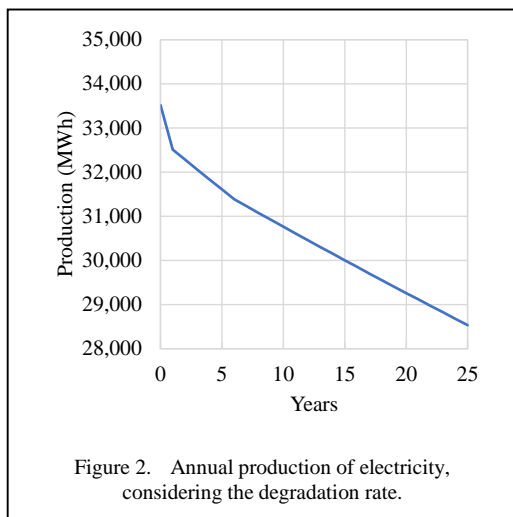
on greater emissions. Therefore, as an idea for future work, it is recommended that materials be recycled in the disposal part, in order to verify the possible reduction in the total emissions. Table III presents the participation of some materials in the stages showed in Fig. 1. It is observed that only the metals would contain approximately 85% of material that can be recycled, leading to reductions in GHG emissions and also in the system's environmental payback.

As for the O&M part, it has 2.1% of total emissions, a very low value. However, 1.11% refers to the replacement of panels during the 25 years of operation of the photovoltaic system. Therefore, adding this percentage to the value related to the installation of the panels, it appears that approximately 90.1% of all emissions from the photovoltaic system refer only to the panels. According to Table III, silicon is the main responsible for emissions, with a total amount of 66.92%, followed by aluminum with a total of 10.47%.

Regarding the calculations of electricity, based on Eqs. (1) to (4), using ambient temperature and irradiation, and considering the location of João Pessoa, the result is 759.039,86MWh in 25 years. The calculations take into account the monthly averages (for each climatological variable), calculated based on daily data from the

TABLE III. PARTICIPATION OF SOME MATERIALS IN THE STAGES OF THE PHOTOVOLTAIC SYSTEM.

Phase	Part	Material	Emission kg CO ₂ -eq.	% of total
Installation	Panels	Silicon	14.894,039	66.09
		Aluminum	2.329,451	10.34
		Glass	1.047,469	4.65
		Others	1.782,649	7.91
	Frame, cables, etc	Copper	478.111	2.12
		Steel	411.598	1.83
		PVC	69.716	0.31
		Other	88.736	0.39
O&M	Panels replac.	Silicon	185.933	0.83
		Aluminum	29.080	0.13
		Glass	13.076	0.06
		Other	22.254	0.10



entire period of data available and considering the annual degradation, mentioned previously. Fig. 2 shows the energy production results.

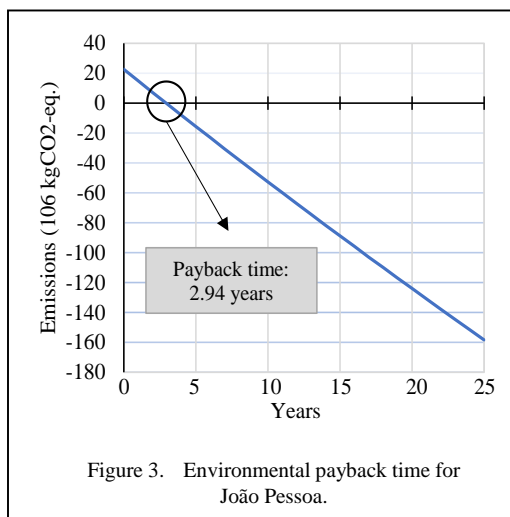
Furthermore, there is a greater decrease in production between year 0 (zero) and year 1, since the degradation rate for the first year is higher, unlike the other years that appear to show an almost linear decline.

Considering the Brazilian electricity mix and applying the method of [24], the value for GHG emissions associated with electricity consumption from the Brazilian electrical grid is obtained (0.268kg CO₂-eq/kWh consumed). With the calculated values of electrical energy production and the result of the LCA, it is possible to calculate the environmental payback time, the GPBT. The $E_{plant,tot25}$ is 759.039,86 MWh, as mentioned earlier. Emissions_{pv25} are obtained from Fig. 1, in a total of 22.534.773kg CO₂-eq. Thus, using (7), it is possible to calculate the EF_{pv} and obtain the environmental payback time.

Fig. 3 shows the payback time for João Pessoa. The point at which the line cuts the horizontal axis is the point that represents the system's payback value for that city.

The payback time was approximately 2 years 11 months and 11 days for João Pessoa.

According to [17], the calculated payback was 5 years, 8 months and 1 day, slightly higher than the value obtained herein. Although the same photovoltaic system is considered, a different location is used. Also, the Ecoinvent database used by [17] was an earlier version. The



IPCC method used by [17] was the version from 2013, while this study used the 2021 version. The energy equations used by [17] were also slightly different than those employed herein (based on the adaptation of [19] by [18]).

Reference [4] showed the environmental payback of Monocrystalline silicon photovoltaic panels in the United States. The authors evaluated predictions for the use of panels in energy production to reduce the country's environmental impacts. They used the TRACI tool (Tool for the Reduction and Assessment of Chemicals and other Environmental Impacts), which presents impact categories for Life Cycle Impact Assessment (LCIA) studies [25]. As a result, considering the Global Warming category, from all states in the United States, an average payback was 8 years. This value is almost triple the payback time calculated here, but some cities had lower values, and the payback values were between 0.3 and 113 years. Reference [4] concludes by saying that not all categories presented by TRACI are relevant in the context of renewable energies, therefore, considering the average 8 years of payback, most states contain a net environmental benefit in reducing greenhouse gas emissions, within the lifetime of the panels, considered in the work to be 30 years.

In the study developed by [26], the authors present the payback of a photovoltaic system integrated on the roof of a building (BIPV - Building Integrated Photovoltaics) in Hong Kong, in addition to also presenting the energy payback of the system. As for GPBT, the calculated value was 5.2 years, considering the lifetime of the system between 20-30 years.

Reference [26] also explain that the payback time can vary considerably according to the orientation of the system in relation to the geographic north and also according to the inclination of the panels in relation to the ground, reaching a value of up to 20 years. The payback time of 5.2 years is close to that calculated in this paper and to that calculated by [17], showing that even a system integrated into a building can present very attractive payback values.

A sensitivity analysis was performed by [27] and the environmental payback time was calculated for a 3 MWp photovoltaic plant installed in Brazil, in the state of Minas Gerais. The lifetime of the panels was taken as 25 years and the payback time obtained was 11.8 years, and the sensitivity analysis demonstrated that this period could vary between 8.3-15.6 years. Reference [27] concludes that installing panels in regions with a high incidence of solar radiation is extremely beneficial for the Brazilian energy mix, as it contributes to reducing the emission of greenhouse gases for the production of electrical energy. This payback time found by [27] is higher than that found here. However, some considerations made by the authors may explain this difference, for example, the import of panels from China, which increases the amount of CO₂-eq emitted by sea transport and road transport from the port to the system installation site, thus increasing the system's payback time. However, the authors make it clear that panel manufacturing is the main contributor to the system's emissions, with 97% coming from this sector alone.

The studies presented previously show that there are differences in the results obtained for the payback time compared to the value calculated in this paper. The factors that could cause these differences, in comparison with works that address the same topic, could be: different radiation levels in the different regions analyzed, energy mix of the electrical matrix of the country where installation of the system was suggested, methods used in the analysis, individual characteristics of the panels, size of the photovoltaic system studied, and many others. Even so, when the results obtained in the studies are analyzed, it is possible to see that the payback time is shorter, in most cases, than the lifetime of the system and, therefore, for most systems the investment becomes advantageous.

Therefore, the use of photovoltaic systems to mitigate GHG emissions and generate cleaner

electrical energy is extremely important. The country, at COP27 (Conference of Parties 27) [28], which took place in Egypt in 2022, confirmed through its National Determined Contribution, or NDC, sent to the United Nations Framework Convention on Climate Change [29], which commits to reducing greenhouse gas emissions by 37% by 2025 and 50% by 2030, with reference to the year 2005. Furthermore, in the NDC, the country commits to achieving the objective of climate neutrality by the year 2050. To achieve this, it is important to adopt energy generation technologies from renewable sources and continuous investment in these technologies.

As mentioned in the NDC, in 2020, Brazil had a total of 48.4% of its internal energy supply corresponding to renewable sources, which is more than triple the world average. In 2021, the IES was 44.7% renewable, still 3 times higher than the world average and, in relation to 2020, the country showed an increase of 55.9% in the internal energy supply from photovoltaic solar sources, specifically [2].

Finally, according to objective 7 of the Sustainable Development Goals, "access to energy must be ensured for all, in a clean, safe, sustainable way and at fair prices". Furthermore, it is also stipulated that "by the year 2030, the participation of renewable energies in the global energy matrix must be substantially increased, reinforcing international cooperation in clean energy research and technologies, including renewable energies" [30], which corroborates the growing increase in investment in renewable technologies in Brazil and the way the country is moving towards achieving all these objectives.

IV. CONCLUSIONS

Life Cycle Assessment can play a fundamental role in decision-making regarding the use of energy generation systems using renewable sources, as it can present the impact of using these sources to mitigate greenhouse gas emissions. In this paper, specifically, LCA made it possible to verify the quantity regarding the GHG mitigation capacity that a photovoltaic system has.

It was found that the photovoltaic system presented 759,04 GWh of electricity generation throughout its lifetime (25 years), and that it was able to present an environmental payback in less than 3 years for the city of João Pessoa.

In Brazil, there are still few studies that address LCA and environmental payback of photovoltaic systems. The growth in investments in the area of energy generation from renewable sources, specifically in the photovoltaic area as shown by data from the National Energy Balance, encourages more analyzes focused on the viability of these systems for generating electrical energy and mitigating GHG emissions.

This paper demonstrated that photovoltaic energy has great potential for mitigating climate change and can be used in strategies to reduce environmental impacts.

ACKNOWLEDGMENT

The authors wish to acknowledge the support of the Paraíba State Research Foundation (FAPESQ) (call n° 09/2021), National Council for Scientific and Technological Development (CNPq Productivity Grants 309452/2021-0, 308753/2021-6, 310871/2021-2), and Scientific Initiation Scholarship (PIBIC) within the Federal University of Paraíba (UFPB).

REFERENCES

- [1] United Nations Development Programme. (2023). *Don't choose extinction*. Available at: <https://dontchooseseextinction.com/en/>
- [2] Brazil. Ministry of Mines and Energy. (2022). *National Energy Balance 2022: Summary Report/Base Year 2021*. Available at: https://www.epe.gov.br/sites-pt/publicacoes-dados-abertos/publicacoes/PublicacoesArquivos/publicacao-675/topico-631/BEN_S%C3%A Dntese_2022_PT.pdf
- [3] Nishimura, A., Hayashi, Y., Tanaka, K., Hirota, M., Kato, S., Ito, M., Araki, K., & Hu, E. J. (2010). Life cycle assessment and evaluation of energy payback time on high-concentration photovoltaic power generation system. *Applied Energy*, 87, 2797-2807.
- [4] Grant, C., Garcia, J., & Hicks, A. (2020). Environmental payback periods of multi-crystalline silicon photovoltaics in the United States - How prioritizing based on environmental impact compares to solar intensity. *Sustainable Energy Technologies and Assessments*, 39(100723).
- [5] Brazil. Ministry of Mines and Energy. (2022). *Ten-Year Energy Expansion Plan 2032: NT Energy and Environment*. Available at: <https://www.epe.gov.br/sites-pt/publicacoes-dados-abertos/publicacoes/PublicacoesArquivos/publicacao-689/topico-639/NT%20Energia%20e%20Meio%20Ambiente%20-%20PDE%202032.pdf>
- [6] Brazil. Ministry of Science, Technology and Innovation. (2023). *LCA: Life Cycle Assessment*. Available at: <https://www.gov.br/ibict/pt-br/assuntos/informacao-cientifica/avaliacao-do-ciclo-de-vida-acv>
- [7] Mcmanus, M. C., & Taylor, C. M. (2018). Greenhouse Gas Balances of Bioenergy Systems: The Role of Life Cycle Assessment. *Greenhouse Gases Balances of Bioenergy Systems*, 29-41.
- [8] Muteri, V., Cellura, M., Curto, D., Franzitta, V., Longo, S., Mistretta, M., & Parisi, M. L. (2020). Review on life cycle assessment of solar photovoltaic panels. *Energies*, 13(1), 252.
- [9] International Organization for Standardization. (2022). *ISO14040:2006 – Environmental management – Life cycle assessment – Principles and framework*. Available at: <https://www.iso.org/standard/37456.html>
- [10] International Organization for Standardization. (2022). *ISO14044:2006 – Environmental management – Life cycle assessment – Requirements and guidelines*. Available at: <https://www.iso.org/standard/38498.html>
- [11] Brazilian Association Of Technical Standards. (2014). *Environmental Management – Life cycle assessment – Requirements and guidelines. NBR ISO 14044:2009*. Available at: <https://www.abntcatalogo.com.br/pnm.aspx?Q=T3loZHEzRU5MbklATDZWSjJ6L2pZdSt6a1dKRWFpTRha1NiTodsVUR5dz0=>
- [12] Brazilian Association Of Technical Standards. (2014). *Environmental Management – Life cycle assessment – Principles and structure. NBR ISO 14040:2009*. Available at: <https://www.abntcatalogo.com.br/pnm.aspx?Q=SEJPWW0wYXVhcG5tWllZVVlb0pjVF MwUDVNTHA1ME1xL0J3c1RtNmF2az0=>
- [13] Pré Sustainability. (2022). *Sustainability software for fact-based decisions*. Available at: <https://pre-sustainability.com/solutions/tools/simapro/>
- [14] Ecoinvent. (2023). *Ecoinvent Database*. Available at: <https://ecoinvent.org/the-ecoinvent-database/#/!releases>
- [15] Intergovernmental Panel On Climate Change. (2021). *Climate Change 2021: The Physical Science Basis*. Available at: <https://www.ipcc.ch/assessment-report/ar6/>
- [16] Neves, T. I., Uyeda, C. A., Carvalho, M., & Abrahão, R. (2018). Environmental evaluation of the life cycle of elephant grass fertilization – *Cenchrus purpureus* (Schumach.) Morrone – using chemical fertilization and biosolids. *Environmental Monitoring and Assessment*, 190(30).
- [17] Schultz, H. S., & Carvalho, M. (2022). Design, Greenhouse Emissions, and Environmental Payback of a Photovoltaic Solar Energy System. *Energies*, 15(16), 6098.
- [18] Medeiros, S. E. L., Nilo, P. F., Silva, L. P., Santos, C. A. C., Carvalho, M., & Abrahão, R. (2021). Influence of climatic variability on the electricity regeneration potential by renewable sources in the Brazilian semi-arid region. *Journal of Arid Environments*, 184(104331).
- [19] Notton, G., Cristofari, C., Mattei, M., & Poggi, P. (2005). Modelling of a double-glass photovoltaic module using finite differences. *Applied Thermal Engineering*, 24, 2854-2877.
- [20] Evans, D. L. (1981). Simplified method for predicting photovoltaic array output. *Solar Energy*, 27(6), 555-560.
- [21] National Institute of Meteorology. (2023). *INMET Meteorological Database*. Available at: <https://bdmep.inmet.gov.br/>
- [22] United States of America. (2023). *National Aeronautics and Space Administration. POWER Data Access Viewer*. Available at: <https://power.larc.nasa.gov/data-access-viewer/>

- [23] CanadianSolar. (2023). *Downloads: modules*. Available at: <https://www.csisolar.com/downloads/>
- [24] Carvalho, M., & Delgado, D. (2017). Potential of photovoltaic solar energy to reduce the carbon footprint of the Brazilian electricity matrix. *LALCA - Revista Latino-Americana em Avaliação do Ciclo de Vida*, 1(1), 64-85.
- [25] United States Environmental Protection Agency. (2012). *Tool for the Reduction and Assessment of Chemical and other Environmental Impacts (TRACI) TRACI version 2.1: User's Guide*. Available at: <https://www.epa.gov/chemical-research/tool-reduction-and-assessment-chemicals-and-other-environmental-impacts-traci#:~:text=TRACI%20is%20an%20environmental%20impact,categories%20in%20common%20equivalence%20units>
- [26] Lu, L., & Yang, H. X. (2010). Environmental payback time analysis of a roof-mounted building-integrated photovoltaic (BIPV) system in Hong Kong. *Applied Energy*, 87, 3625-3631.
- [27] Pinto, M. A., Frate, C. A., Rodrigues, T. O., & Pires, A. C. (2020). Sensitivity analysis of the carbon payback time for a Brazilian photovoltaic power plant. *Utilities Policy*, 63(101014).
- [28] United Nations Framework Convention on Climate Change. (2022). *COP 27*. Available at: <https://unfccc.int/event/cop-27>
- [29] United Nations Framework Convention on Climate Change. (2022). *Party-authored reports*. Available at: https://unfccc.int/reports?f%5B0%5D=corporate_author%3A128
- [30] United Nations. (2023). *Os Objetivos de Desenvolvimento Sustentável no Brasil*. Available at: <https://brasil.un.org/pt-br/sdgs/7>

Neural Networks in Pellet Combustion Control - an Overview of the Group's Research Work in 2022/2023

Stefan Popović¹, Dejan Djukić², Sonja Djukić Popović³, Milan Gligorijević⁴

^{1,2,4}Alfa BK University - Faculty of Information Technologies, Belgrade, Serbia

³University of Belgrade, Faculty of Mathematics, Belgrade, Serbia

¹stefan.popovic@alfa.edu.rs, ²dejan.djukic@alfa.edu.rs, ³sonjica27@yahoo.com,

⁴milan.gligorijevic@alfa.edu.rs

Abstract—The problems of pollution and global warming have plagued the planet for more than a century, and are the result of excessive consumption of fossil fuels. The last decades have brought innovations in the heating of smaller buildings, heating fuel oil and coal are being shut down, and boilers with automatic gas and biomass heating are being introduced. This significantly reduces pollution, but not enough. Hence the need for greater application of artificial intelligence and machine learning in combustion control in boilers with automatic firing. This paper presents a description of the experimental application of artificial intelligence, machine learning and neural networks to the ATI Terming Ozone 55 boiler and a brief summary of the results obtained.

Keywords - boilers with automatic firing, neural networks, environmental protection

I. INTRODUCTION

Neural networks have a very wide application, both in complex security systems, improving the quality of life through applications used in everyday life, and in industrial plants [1]. Today, when we are faced with uncontrolled pollution, and at the same time, the sale of boilers with automatic firing is expanding, we must take care of saving the fuel that the boiler consumes. By increasing the degree of fuel utilization, we reduce the emission of harmful gases into the atmosphere, reduce the consumption of biomass or fossil fuels that are used, and therefore have a positive effect on the environment and increase the quality of living conditions. Neural networks, although they were presented as a mathematical

model in the middle of the twentieth century, are experiencing their full expansion only today, at the end of the first quarter of the twenty-first century. The application of neural networks is very broad, there is almost no area in which they have not played a key role in the functioning of automatic control systems, object recognition, decision systems and many other areas that we are surrounded by [2]. The group to which the authors of this paper belong started preliminary research on software solutions for controlling the automation of combustion when one of the members saw that changing the type of pellets on the ATI Terming 50 boiler led to inexplicable stoppages. The jam was solved by simply resetting the system or manually recalibrating the firing parameters. This solution did not give the desired effect for the end user, as it impairs comfort and leads to unpleasant situations when the heating system stops working for no reason or does not start at the given time.

II. ASSUMPTION OF THE CAUSE OF THE PROBLEM

By monitoring the operation of the boiler during the 2019/2020 heating season, it was established that whenever pellets from another manufacturer are introduced, there is a stoppage in operation. Then the reason for the uncontrolled shutdown of the boiler and the impossibility of automatic ignition is sought. It is recognized that the automation system that works according to the already defined parameters on the quality of wood pellets cannot work with pellets of lower quality. When pre-calibration is performed in

order to burn pellets with higher humidity or lower calorific value, the problem of uncontrolled overheating occurs in case of encountering pellets of better quality. Here comes the idea of introducing a recalibration system during burning.

There was a need for a system that would be able to assume the quality of incoming pellets and perform independent recalibration during operation in order to eliminate the main problem of downtime.

In parallel with trying to find a quick solution to the problem that is becoming more and more frequent with the arrival of pellets of lower quality on the market, research is being carried out on the application of neural networks and machine learning in this sphere of industry. By reading the papers published in the relevant journals for this field, we came to the conclusion that the application of neural networks in this field is quite rare [1].

Undeniably, the boiler is one of the three main arrangements of the thermal power plant. A single capacity of boilers in power plants is constantly growing, and boilers are developing towards large capacity and high parameters [3,4]. Searching for examples of the use of neural networks yielded data that for large or large coal-fired boilers (supercritical units), if combustion instability occurs during combustion, establishing direct improvement, establishing direct improvement. there will be a large number of pollution by-products, even some extreme situations may occur, such as furnace cavity shutdown and major safety accidents in the furnace [5,6]. One of the applications of neural networks in boilers with automatic firing is given in the work of Zhang in 2020, where thermal energy diagnostics of boilers is done using computer recognition of objects and neural networks. The computer image processing and neural network technology are applied to diagnose the thermal energy of boiler plants, i. e., the flame combustion diagnosis, to verify their effectiveness and superiority [7]. Another example of the application of neural networks in boilers with automatic firing is given in the work of Chen Ji in 2022. There is described a random spectral attenuation method proposed to reduce moisture content disturbances. The calibration spectra were replicated and multiplied by random attenuation coefficients to introduce information about the possible interference. All of the simulated attenuated spectra were used to train

the artificial neural network (ANN) quantitative model. Compared with direct modeling without random spectral attenuation, the coefficient of determination (R^2) was improved from -3.4291 to 0.7102 , and the root-mean-square error (RMSE) was reduced from 1.8709% to 0.4786% in the analysis of volatile matter content interfered by moisture. The results showed sufficient ability of the method to detect samples disturbed by moisture without additional sample pretreatment and improve the speed of LIBS analysis [8].

One of the most significant and extensive works describing the application of neural networks in boiler control is Hang Ta Wen's work from 2021. The purpose of his study is to utilize two artificial intelligence (AI) models to predict the syngas composition of a fixed bed updraft gasifier for the gasification of rice husks. Air and steam-air mixtures are the gasifying agents. In the present work, the feeding rate of rice husks is kept constant, while the air and steam flow rates vary in each case. The consideration of various operating conditions provides a clear comparison between air and steam-air gasification. The effects of the reactor temperature, steam-air flow rate, and the ratio of steam to biomass are investigated here. The concentrations of combustible gases such as hydrogen, carbon monoxide, and methane in syngas are increased when using the steam-air mixture. Two AI models, namely artificial neural network (ANN) and gradient boosting regression (GBR), are applied to predict the syngas compositions using the experimental data. The coefficients of determination (R^2) range from 0.80 to 0.89 for the ANN model, while the value of R^2 ranges from 0.81 to 0.93 for GBR model. In this study, the GBR model outperforms the ANNs model based on its ensemble technique that uses multiple weak learners. As a result, the GBR model is more convincing in the prediction of syngas composition than the ANN model considered in this research [9]. Reading the literature leads to the conclusion that the safe and stable operation of boilers often determines the safe and environmentally friendly operation of the entire unit. The most direct indicator of combustion stability is the combustion flame. Therefore, it is necessary to monitor the state of flame combustion in the furnace chamber in real time in order to ensure the safe and economical operation of the boilers. How to establish a safe and reliable coal burning system in an energy saving furnace has become a critical

issue [10,11]. Although there are systems with better results (GBR model), the use of knowledge from the field of neural networks for application in combustion control in boilers with automatic ignition would greatly improve the degree of fuel utilization, ensure more stable operation of boilers, which would lead to significant energy savings, and therefore would help preserve the environment, reduce the emission of harmful gases, reduce the amount of ash and reduce the consumption of biomass and fossil fuels, which are becoming less and less every day on planet Earth [1].

III. BUILDING A MONITORING SYSTEM

In order to adequately approach the finding of causes and possible solutions, the issue of monitoring the operation of the boiler was imposed. The possibility of using one of the existing data logging systems was analyzed. After a comprehensive overview of the complexity, it was decided to implement a special purpose system that will collect data from sensors that are built into the boiler system in such a way that they do not disturb the system and have no points of contact with the combustion management system. For the experimental data collection, which has been carried out since March 2022 and is still ongoing, an Arduino Uno was used to which K-type temperature probes, humidity meters and gas meters are connected. Temperature probes are placed at the probe points that control the operation of the boiler, but also directly under the firebox, in the smoke channel one meter above the smoke exit from the boiler, as well as for measuring the external and internal air temperature. Humidity sensors monitor the relative humidity of air and pellets. Gas sensors are placed in the flue to measure the amount and type of gases that are a product of combustion. Until May 2022, the system underwent a series of both hardware and software changes in order to adapt it for more accurate and purposeful measurements. The experimental measurements taken for the research part are measurements from October 2022.

IV. METHODOLOGICAL APPROACH

Experimental measurements were made in real time every 3 seconds and the following parameters were measured: temperature immediately below the combustion chamber, smoke temperature at the exit from the boiler, smoke temperature one meter after exiting the boiler, return water temperature, pressure water

temperature, air temperature in boiler rooms, outside temperature, air humidity and pellet humidity and the amount of unburned gases in the smoke and the amount of soot. After the measurements, the data were passed through a three-layer neural network in series as follows. First, the neural network is trained with 70 percent of the data, after that it is allowed to predict new measurements and then the actual values are compared with the values obtained by the prediction.

V. RESULTS OBTAINED

A recurrent neural network was used for data processing. Recurrent neural networks represent a network architecture specialized for processing sequential data, such as natural language sentences and time series. Convolutional networks can also be used for sequential data. The current trend is to reduce the use of recurrent networks and to insist more and more on the use of convolutional networks even in situations for which recurrent networks seem like a natural solution because they are not easy to train [12]. Nevertheless, in the paper, the recurrent neural network was trained in order to check its effect on the operating parameters of boilers with automatic firing.

Note that a recurrent neural network determines one sequence element at a time (Fig. 1). We bring a set of measured values to the input and after that we start the calculation. The next mesh is fed only after the calculation for the previous mesh has already been performed. A recurrent network maintains a so-called hidden state (vector h) and has a current hidden state at each step. For the given input, based on that input and the current hidden state (e.g. h_0 and x_1) it calculates a new hidden state as a linear combination of the matrices U and W with the vectors of the current hidden state and the current input. An activation function is applied to the obtained result and thus a new hidden state is obtained. An activation function is applied to the obtained result and thus a new hidden state is obtained. After that, it is the turn of a new set of measurements (x_2), based on the current state (h_1) and the representation of the set, with the help of the same matrices U and W , linear transformations are performed, an activation function is applied and a new state (h_2) is obtained, and so on for all sets measurements. In each step, some output can be generated from the hidden state.

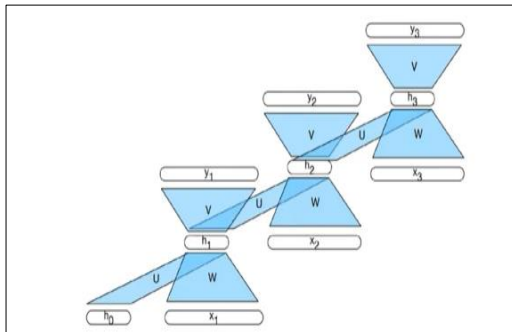


Figure 1. Scheme of a recurrent neural network.

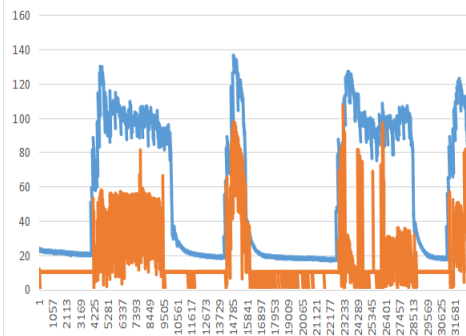


Figure 2. Comparison of measured values and values obtained by calculation.

By using this model, and after comparing the results, deviations between the computationally obtained hidden states and the actual measured values were seen (Fig. 2). By increasing the number of measurement points, the error decreased.

The graphic above shows the relationship between measured values and values obtained by calculation, it can be seen that the calculated value generally follows the measured value, but there is an error. In this research, the neural network obtained an approximate value to the measured value. The error decreased with the number of measurements. And in some cases, the neural network of this type gave results that are not in agreement with the measured results.

VI. CONCLUSION

The development of a model of neural networks that will be applied to optimize the control parameters of boilers with automatic firing can lead to a significant reduction in fuel consumption and an increase in the degree of fuel utilization. The prediction of the temperatures of the combustion chamber, the energy power of the pellets, the amount of oxygen in the air mixture

can significantly improve the operation of the heating system, thereby increasing the comfort of the population and contributing to the protection of the environment. In 2022 and the first three months of 2023, the first conclusions were reached, and after determining that the recurrent type neural network can predict future firing parameters with some accuracy, the development of the firing parameter recalibration system was started. A big problem in the development of this model is the short period of operation of the boiler, which is contributed by the uneven weather conditions of the last two winters. This leads to the need to develop a model in which, in addition to the parameters necessary for fire maintenance and pellet quality, parameters related to the climatic conditions of the microregions where the measurements are made will be included.

REFERENCES

- [1] Popović, S., Đukić, D., Đukić Popović S., & Lazar Kopanja, L. (2022). Preliminary Research on the Application of Neural Networks to the Combustion Control of Boilers with Automatic Firing, In *Proceedings of the 8 the Virtual International Conference on Science Technology and Management in Energy* (pp. 299-303).
- [2] Popovic, S., Kopanja, L., Djukic Popovic, S., & Djukic, D. (2022). Neural networks and their application in object recognition. In *12th International Conference on Applied Internet and Information Technologies (AIIT 2022)*, Zrenjanin, Serbia.
- [3] Zhu, Y. (2018). Research on the architecture and behavior model of high-speed channel for thermal image processing. *Wireless Personal Communications*, 102(4), 3869-3877.
- [4] Rajah, T. T. R., Chiam, Y. K., & Azizul, Z. (2018). Fuzzy-based framework for the selection of image processing software for diagnosis and outcome prediction of cardiac diseases. *Advanced Science Letters*, 24(2), 1109-1113.
- [5] Lazić, V., Arsić, D., Nikolić, R. R., Rakić, D., Aleksandrović, S., Djordjević, M., & Hadzima, B. (2016). Selection and analysis of material for boiler pipes in a steam plant. *Procedia Engineering*, 149, 216-223.
- [6] Wu, S. (2015). A traffic motion object extraction algorithm. *International Journal of Bifurcation and Chaos*, 25(14), 1540039.
- [7] Zhang, J. (2020). Computer image processing and neural network technology for thermal energy diagnosis of boiler plants. *Thermal Science*, 24(5 Part B), 3221-3228.
- [8] Chen, J., Li, Q., Liu, K., Li, X., Lu, B., & Li, G. (2022). Correction of moisture interference in laser-induced breakdown spectroscopy detection of coal by combining neural networks and random spectral attenuation. *Journal of Analytical Atomic Spectrometry*, 37(8), 1658-1664.

- [9] Wen, H. T., Lu, J. H., & Phuc, M. X. (2021). Applying artificial intelligence to predict the composition of syngas using rice husks: A comparison of artificial neural networks and gradient boosting regression. *Energies*, 14(10), 2932.
- [10] Fernández-Alemán, J. L., López-González, L., González-Sequeros, O., Jayne, C., López-Jiménez, J. J., Carrillo-de-Gea, J. M., & Toval, A. (2016). An empirical study of neural network-based audience response technology in a human anatomy course for pharmacy students. *Journal of medical systems*, 40(4), 1-12.
- [11] Soltani, A., Battikh, T., Jabri, I., & Lakhoua, N. (2018). A new expert system based on fuzzy logic and image processing algorithms for early glaucoma diagnosis. *Biomedical Signal Processing and Control*, 40, 366-377.
- [12] Orvieto, A., Smith, S. L., Gu, A., Fernando, A., Gulcehre, C., Pascanu, R., & De, S. (2023). Resurrecting recurrent neural networks for long sequences. *arXiv preprint arXiv:2303.06349*

Effect of Temperature on the Absorption of Chrome and Silica-based Solar Absorbing Surfaces

Mikaely Renaly Carlos da Silva^{1*}, Kelly Cristiane Gomes²

¹Graduate Program in Mechanical Engineering/Federal University of Paraíba (UFPB), João Pessoa, Brazil

²Renewable Energy Engineering Department/Federal University of Paraíba (UFPB), João Pessoa, Brazil

¹mikaely.silva@cear.ufpb.br, ²gomes@cear.ufpb.br

Abstract—The significant increase in energy demand, the dominance of fossil fuels in electricity generation, and the need to reduce the impacts associated with the rapid growth of carbon dioxide emissions into the atmosphere favors the development of research on renewable energy sources. In this sense, this work aims to produce absorbing solar surfaces obtained via Magnetron Sputtering and to evaluate the effect of the working temperature on the absorption efficiency of the surfaces. For this purpose, a layer of metallic chromium and chromium oxide or silica was deposited on AISI 304 stainless steel substrates electropolishing. The surfaces were subjected to four different working temperatures (25°C, 100°C, 150°C and 200°C) and characterized via UV-Vis-NIR and Infrared with Fourier Transform Spectroscopy and Optical Profiling. The results indicate that the Magnetron Sputtering technique presented a high potential for use in the manufacture of selective surfaces due to the high reproducibility and homogeneity of the coatings produced. For temperatures up to 100°C, Cr/Cr₂O₃ based surfaces are the most efficient, while at 200 °C the Cr/SiO₂ are the most promising in terms of absorptivity, as the anti-reflective SiO₂ layer minimizes the thermal losses of the selective solar surface.

Keywords - absorber surface, sputtering, temperature, layer antireflexive

I. INTRODUCTION

A country's socio-economic development involves using natural materials, energy consumption, and local impacts on habitats. The inherent environmental impacts are cumulative and will become apparent to future generations. Therefore, it is necessary to understand which dynamics and mechanisms must be modified to make the built environment more sustainable [1,2].

In this context, the energy dimension becomes challenging as energy supply is strongly intertwined with factors such as national security, the ability to meet basic human needs, drive economic growth, and complex environmental problems such as global climate change [3]. The significant increase in energy demand and the dominance of fossil fuels in its generation requires a transformation in current energy systems to reduce the impacts associated with the rapid growth of carbon dioxide emissions into the atmosphere [4].

Replacing energy sources based on fossil fuels with renewable energy sources is one of the ways to achieve more sustainable development, in addition to playing a central role in offering competitiveness and ensuring energy security [5,6].

*Supervisor: Monica Carvalho - Renewable Energy Engineering Department/Federal University of Paraíba (UFPB), João Pessoa, Brazil

Brazil is prominent in developing and using renewable energy sources because of its geographic location, territorial extension, and climate. However, solar resources have a timid participation in the Brazilian internal energy supply (0.32% in 2020) compared to the high levels of solar radiation in Brazil throughout the year [7,8].

Solar energy can be used for heating water, drying crops, and generating electricity through solar collectors and solar cells [9,10]. Solar thermal energy can heat residential water and swimming pools, generate steam for processes, and power cycles for electricity generation [11].

However, this use has limitations when trying to heat fluids between 100°C and 400°C (medium-temperature collectors) or above 400°C (high-temperature collectors). These limitations are associated with radiation's high emission of heat and the materials' low thermal and optical stability in the mentioned temperature ranges [12,13]. The surface of the solar absorber is the most critical part of these systems. For an efficient photothermal conversion to occur, it must have high solar absorbance (>90%) in the solar spectrum region (0.25–2.5µm) and low emittance thermal (<15%) in the infrared region (2.5–25 µm). Coatings that have these characteristics are called selective surfaces and make it possible to increase the photothermal conversion efficiency of solar collectors, enabling them to operate at a higher temperature [14,15].

Several authors [14,16,17] have sought to optimize the structural and optical properties of these surfaces by combining different types of materials, surface modification and composition settings adopted, in addition to the use of anti-reflective layers that protect the absorber film (composed of metallic material) from degradation by oxidation in the environment.

In addition to the type of coating on selective solar surfaces, which directly influences the cost-effectiveness of the equipment, the degradation of coatings at high working temperatures due to thermal load, high humidity, or water condensation on the surface of the absorber is highly relevant [13]. In this sense, the present work aims to evaluate the effect of temperature on the absorptivity of chromium and silica-based absorber surfaces obtained via Magnetron Sputtering.

II. EXPERIMENTAL TECHNIQUES

A. Preparation of Solar Absorbing Surfaces

The coatings were deposited on AISI 304 stainless steel substrate (25x25x1 mm). Before deposition, the substrates were treated with an electropolishing process to ensure a polished surface, clean of impurities. For the surface treatment, a solution was prepared to contain phosphoric acid (H₃PO₄), sulfuric acid (H₂SO₄), and glycerol (C₃H₈O₃) in the proportion of 2:1:1, using a source (Agilent, model E3631A), operating with a voltage of 6V and current of 1.35 A for 10 minutes. After the process, the substrates were subjected to an ultrasonic bath (Cienlab model CE-160/30 MAG) with isopropyl alcohol for 20 minutes at 25°C, then washed in distilled water, dried, and stored.

For the deposition of the coatings, a Magnetron Sputtering Orion 5 system from AJA International Inc. was used, using metallic chromium targets and chromium and silicon oxides with a high degree of purity. The Cr target is 2" (50.8 mm) in diameter and 0.125" (3.175 mm) in thickness with a purity of 99.95% and supplied by the company Kurt J. Lesker. The Cr₂O₃ targets have a diameter of 2" (50.8 mm) and 0.118" (3 mm) thickness with a purity of 99.99%, and the SiO₂ target has a diameter of 2" (50.8 mm) and a thickness of 0.125" (3.175 mm) with 99.995% purity, both supplied by Macashew Tecnologias LTDA.

For the formation of the plasma, a pressure of 1×10^{-5} Torr was used using Argon 5.0 gas with a flow of 10 sccm until the establishment of the equilibrium pressure of 5.0×10^{-3} Torr (0.7 Pa) that was used during the entire process of deposition of Cr, Cr₂O₃ layers. and SiO₂. For the deposition of the absorber layer (Cr), 60 W was applied for 40 minutes, while for the oxide layers (Cr₂O₃ and SiO₂), 200W was used for 60 minutes). In both depositions, a working distance of 106 mm was used.

B. Characterization of Solar Absorbing Surfaces

To evaluate the effect of the working temperature, the surfaces produced were subjected to 4 different temperatures (T₁ = 25°C, T₂ = 100°C, T₃ = 150°C and T₄ = 200°C), totaling 8 samples (4 samples of Cr/Cr₂O₃ and 4 of Cr/SiO₂ samples) performed in triplicates. The heat treatment was carried out in a Lucadema muffle furnace, model 2000F/DI, where they remained for 220 hours (time established in the

first step of the process to evaluate the thermal stability by ISO 22975-3:2014 [18].

To evaluate the absorption efficiency of the absorbing surfaces produced, a spectrophotometer in the ultraviolet, visible and near-infrared regions, manufactured by Shimadzu, model UV-2600, operating in the wavelength range between 220 to 1.400 nm, with reflectivity measurements was used. using the integration ball accessory.

Knowing that it is an opaque sample, and that, therefore, does not transmit light, as well as that the total hemispherical absorptivity of solid materials is defined as the ratio between the amount of radiation absorbed and the amount of radiation incident on it, the absorptivity of the produced surfaces were obtained according to Eqs. (1) and (2).

$$\alpha = 1 - \rho, \quad (1)$$

$$\alpha = \frac{\int_{250}^{2500} \alpha_{\lambda} I_{solar} d\lambda}{\int_{250}^{2500} \alpha_{\lambda} d\lambda}. \quad (2)$$

In which α is the total hemispherical absorptivity, ρ is the total hemispherical reflectivity, α_{λ} is the spectral absorptivity of the solid, and I_{solar} is the spectral distribution of solar radiation.

Considering that the solid is opaque and substituting from Eqs. (1)-(3) is obtained:

$$\alpha = \frac{\int_{250}^{2500} (1-\rho_{\lambda}) I_{solar} d\lambda}{\int_{250}^{2500} (1-\rho_{\lambda}) d\lambda}. \quad (3)$$

In which ρ_{λ} is the spectral reflectivity of the solid.

Fourier Transform Infrared Spectroscopy (FTIR) was used to evaluate the composition of the surfaces, as it has high resolution and sensitivity and makes it possible to assess the vibration frequency of atoms when subjected to radiation. From it, the amount of absorbed radiation is determined as a function of the corresponding energy. This analysis was performed in the spectral range from 4,000 to 600 cm^{-1} , in transmittance mode, to detect the vibrational frequencies of the molecules present in the films. These analyses were performed on the IR-Tracer-100 spectrophotometer, manufactured by Shimadzu, with an attenuated total reflectance (ATR) accessory.

Optical profilometry was used to evaluate the influence of surface roughness on the absorptivity of the surfaces produced, as well as the effect of thickness of the selective coatings.

Analyses were performed using a non-contact optical profilometer CCI MP, manufactured by Taylor Hobson, connected to a computerized unit containing the Talysurf CCI software (Taylor Hobson, England). The “stop” methodology was used to measure thickness, which consists of fixing a tape on the substrate before deposition so there is no deposition in this area. After the coating deposition process, the tape is removed, and then the films were subjected to an ultrasonic bath to remove impurities from the tape and then the profilometry analysis.

III. RESULTS AND DISCUSSION

A. Effect of Temperature on the Absorptivity of Coatings

Fig. 1 shows the spectra of absorbance of the surfaces produced and submitted to different working temperature conditions, power and deposition time, four different samples were used for each temperature variation, subjected to radiation with wavelengths in the range of 220 nm to 1400 nm, thus determining the total spectral reflectance of these films.

The conversion of these results to absorbance, as well as the calculation of the average absorbance of each sample, were carried out as detailed in section 2.1.

It can be seen from the spectra (Fig. 1) of the absorbing surfaces based on Cr/Cr₂O₃ and Cr/SiO₂ that the coatings produced allowed a gain of 13% in the percentage of absorption compared to the stainless steel substrate. The coating that showed the highest percentage of

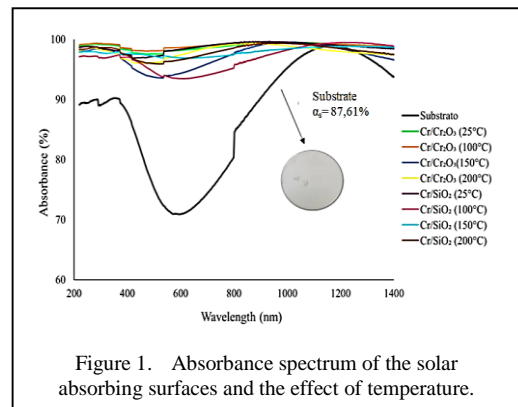


Figure 1. Absorbance spectrum of the solar absorbing surfaces and the effect of temperature.

absorption was Cr/Cr₂O₃ under working conditions at 100°C (99.13%), while the one with the lowest percentage was Cr/SiO₂ operating at 100°C with 97.13% absorption.

Observing the general behavior of Cr₂O₃-based coatings, there is a slight decrease in absorption with increasing temperature, while the opposite effect is observed for SiO₂-based coatings. Possibly, this may be due to the transformation process of the less stable phases of Cr₂O₃ at temperatures above 150°C [19,20], while in the silica based, be stable at the temperatures evaluated in the present study, that is, 25 to 200°C [21].

Table I presents the averages of solar absorptivities calculated according to Eq. (3), standard deviations, and thicknesses of the coatings produced.

TABLE I. AVERAGE SOLAR ABSORBANCE, STANDARD DEVIATION AND THICKNESSES OF THE COATINGS PRODUCED.

Sample	Temp. (C°)	$\bar{\alpha}_s$ (%)	Stand. Devi. (%)	Thickness (μm)
Cr/Cr ₂ O ₃	25°C	99.01	0.55	0.221
Cr/Cr ₂ O ₃	100°C	99.13	0.39	0.087
Cr/Cr ₂ O ₃	150°C	97.86	1.83	0.234
Cr/Cr ₂ O ₃	200°C	98.15	0.94	0.143
Cr/SiO ₂	25°C	97.39	1.45	0.123
Cr/SiO ₂	100°C	97.13	2.03	0.205
Cr/SiO ₂	150°C	97.91	0.67	0.082
Cr/SiO ₂	200°C	98.33	1.01	0.198

Table I shows that the coatings produced by the *Magnetron Sputtering* deposition technique present reproducibility, as can be seen by the values of standard deviations, ranging from 0.39 to 2.03 (%).

It is observed that at room temperature (25°C), the thickness of chromium oxide-based coatings is greater than that of silica based coatings. This is due both to the binding energy of the respective oxides and to the size of their rays. Such conditions change as a result of the increase in temperature and changes in phases

related to these variations, as well as a result of the deposition rate associated with the working temperature [22].

B. Effect of Temperature on the Chemical Composition of Coatings

The coatings produced were subjected to FTIR analysis and the spectra obtained can be seen in Fig. 2.

It can be observed that all coatings suffered variations with the increase in temperature. For the Cr/Cr₂O₃ coatings, it was observed that the bands became more evident with increasing temperature, especially for coatings subjected to temperatures of 200°C.

The bands around 680 cm⁻¹ correspond to Cr₂O₃ [23]. The presence of silica can be observed through the band 1.200 cm⁻¹, which is attributed to the vibration of asymmetric stretching of the Si-O-Si bonds [14,24]. The bands of 1.980, 2.035, and 2.165 cm⁻¹ are characteristic of the diamond crystal of the ATR accessory [25].

C. Effect of Temperature on the Morphology of the Surfaces

Fig. 3 shows the morphological profiles obtained for the Cr/Cr₂O₃ and Cr/SiO₂-based coatings using the optical profilometry technique, where the color scale represents the depths of the measured points concerning the highest point on the surface. Table II summarizes the roughness data measured for each sample, such as R_a (arithmetic mean deviation), R_p (maximum peak height), R_v (maximum valley depth), and S_a (arithmetic mean height

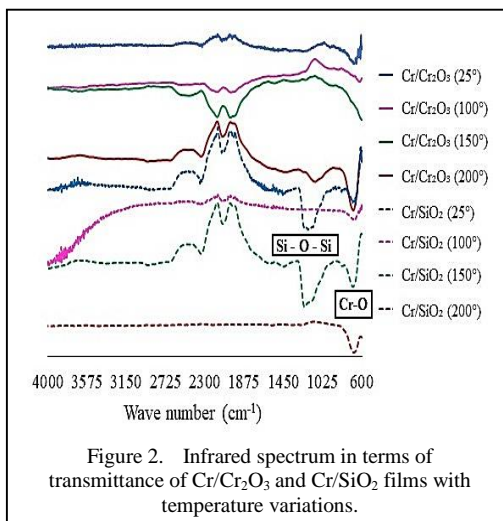


Figure 2. Infrared spectrum in terms of transmittance of Cr/Cr₂O₃ and Cr/SiO₂ films with temperature variations.

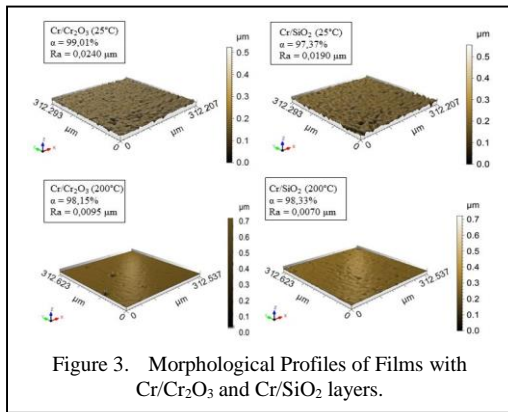


Figure 3. Morphological Profiles of Films with Cr/Cr₂O₃ and Cr/SiO₂ layers.

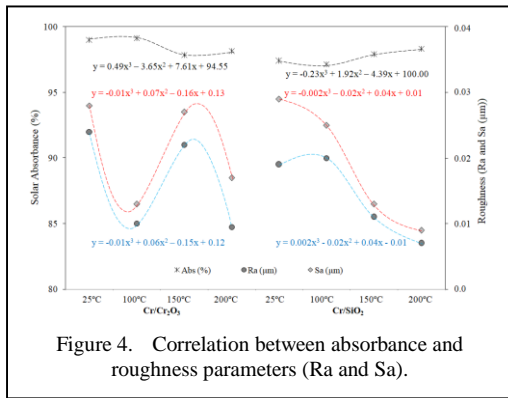


Figure 4. Correlation between absorbance and roughness parameters (Ra and Sa).

for a surface), as well as the average solar absorbance corresponding to each coating.

Fig. 3 and Table II show that the type of material and the working temperature influence the morphology (roughness) of the coatings produced. This was expected because Cr₂O₃ and SiO₂ have different deposition rates associated with working temperatures, as seen in Table I, resulting in different amounts and sizes of deposited materials [26].

Comparing the coatings produced at a temperature of 25°C, it is observed that those

TABLE II. PARAMETER RA, SA, RV, AND RP OF HEAT-TREATED FILM.

Sample Temp (°C)	Ra (μm)	Rv (μm)	Rp (μm)	Sa (μm)	$\bar{\alpha}_s$ (%)
Cr/Cr ₂ O ₃ 25°C	0.024	0.061	0.110	0.028	99.01
Cr/Cr ₂ O ₃ 200°C	0.009	0.021	0.041	0.017	98.15
Cr/SiO ₂ 25°C	0.019	0.056	0.075	0.029	97.39
Cr/SiO ₂ 200°C	0.007	0.018	0.028	0.009	98.33

produced based on Cr₂O₃ obtained a morphology that favored an increase in solar absorption. However, with increasing temperature, SiO₂ based coatings proved to be more efficient, since the silica layer is not transparent to infrared radiation, which influences the reduction of emissivity with gains in the efficiency of the coatings accessory [25].

Fig. 4 shows the correlation between solar absorption and roughness parameters (R_a and S_a) observed for the coatings produced. For Cr/Cr₂O₃-based coatings, the higher the roughness, medium, and surface, the lower the percentages of absorptivity that are directly influenced by the morphology presented by the coatings at different working temperatures. For SiO₂-based coatings, it is observed that with increasing temperature, the roughness decreases, and the absorption percentages increase slightly.

IV. CONCLUSIONS

Obtaining absorbing surfaces based on Cr/Cr₂O₃ and Cr/SiO₂ by the *Magnetron Sputtering* process is possible with a high potential for application as all the coatings produced present absorptivity greater than 97%. For ambient temperatures, the solar surfaces of Cr/Cr₂O₃ are the most efficient, and for temperatures of 200°C the surfaces with the layer of SiO₂ present the same potential.

Coatings based on Cr₂O₃ obtained the highest absorptivity up to 100 °C, but with the increase in temperature, the coatings suffered a slight drop in this percentage, which may have been influenced by the transformation processes of the chromium phases. On the other hand, SiO₂-based coatings had an increase in absorption percentages with increasing temperature due to the thermal stability of silica and the oxidation of chromium in the absorber layer, which turns into Cr₂O₃.

The FTIR confirmed the presence of chromium bands in the Cr/Cr₂O₃ coatings, which became more evident with increasing temperature, as well as the presence of silica in the Cr/SiO₂-based coatings.

Profilometry confirms that the type of material and the working temperature influence the deposition rate of materials and, consequently, the morphology and the percentages of absorption of solar surfaces. Comparing the coatings produced, it is observed that the SiO₂ layer favors the increase in

absorptivity at higher temperatures, since the silica is not transparent to infrared radiation, reducing the emissivity of the coatings.

ACKNOWLEDGEMENT

Mikaely Silva acknowledges the financial support of grant 046/2021 from the Paraíba State Research Foundation (FAPESQ) during her MSc.

REFERENCES

- [1] Dovers, S., & Hussey, K. (2013). *Environment and Sustainability: A Policy Handbook*. 2. Sydney: Federation Press. 256.
- [2] Twidell, J. (2021). *Renewable Energy Resources*. Oxfordshire: Taylor & Francis Group, 774(4).
- [3] Holdren, J. P. (2007). Energy and sustainability. *Science*, 315(5813), 737-737.
- [4] Owusu, P.A., & Asumadu-Sarkodie, S.A. (2016). Review of renewable energy sources, sustainability issues and climate change mitigation. *Cogent Engineering*, 3(1), 1167990.
- [5] Frass-Ehrfeld, C. (2009). *Renewable energy sources: a chance to combat climate change*. Alphen aan den Rijn: Kluwer Law International BV
- [6] Hossin K.; Mahkamov, K.; & Belgasim, B. (2020). Thermodynamic Analysis and Sizing of a Small Scale Solar Thermal Power System Based on Organic Rankine Cycle. *Journal of Sustainable Development of Energy, Water and Environment Systems*, 8, 493-506.
- [7] Calca, M.V.C., Raniero, M. R., Anacleto, K. B., Franco, J. R., Pai, A. D., & Caneppele, F. L. (2021). Uma perspectiva sobre o aproveitamento térmico e a conversão direta da energia solar em áreas rurais no Brasil [A perspective on the thermal use and direct conversion of solar energy in rural Brazilian areas]. *Research, Society and Development*, 10(6), 9810615610.
- [8] Empresa de Pesquisa Energética (EPE). (2020). *Balanco energético nacional 2020: ano base 2019*. EPE. Rio de Janeiro.
- [9] Lakatos, L., Hevessy, G., & Kovács, J. (2020). Advantages and disadvantages of solar energy and wind-power utilization. *World Futures*, 67(6), 395-408.
- [10] Ampuno G., Garcia, J.L., & Jurado, F. (2020). Evaluation of Energy Efficiency and the Reduction of Atmospheric Emissions by Generating Electricity from a Solar Thermal Power Generation Plant. *Energies*, 13(645), online.
- [11] Struckmann, F. (2008). Analysis of a flat-plate solar collector. Heat and Mass Transport, *Project Report*, 2008MVK160.
- [12] Carlin, J. (2004). Renewable Energy in the United States. Separata de: CLEVELAND, C. J. *Encyclopedia of Energy*. Amsterdã: Elsevier, 347-363.
- [13] Silva N.J.F., Torres, S.M., Gomes, K.C., Filho, M.R.F.L., & Gomes, R.M. (2019). Chromium silica co-sputtered graded Cermet for solar thermal collectors. *Solar Energy*, 193, 212-219.
- [14] Khoza, N., Kuru, Z. Y., Sackey, J., Kotsedy, L., Matinise, N., Ndlangamandla, C., & Maaza, M. (2019). Structural and optical properties of ZrOx/Zr/ZrOx/AlxOy multilayered coatings as selective solar absorbers. *Journal of Alloys and Compounds*, 773, 975-979.
- [15] Lovegrove, K., & Stein, W. (2020). Concentrating solar power technology. *Oxford*.
- [16] Tabor, H. (1961). Selective radiation. I. Wavelength discrimination. II. Wavefront discrimination. *The Bulletin of the Research Council of Israel*, 5A(2), 119-134.
- [17] Sousa, G. C. P., Gomes, K.C., Junior., W.F.A & Duarte, R.N.C. (2021). Selective Surfaces of Ilmenite for Use in Solar Absorbers. *Materials Research*, 24, e20200359.
- [18] Internacional Organization For Standardization – ISO (2014) ISO 22975-3: Solar Energy – Collector Components and Materials– Part 3: Absorber Surface Durability. Suíça.
- [19] Daí, J., Tang, J., Xu, H., Spinu, H., Wang, W., Wng, K., Kumbhar, W., Li, M., & Diebold, U. (2000). Characterization of the natural barriers of intergranular tunnel junctions: Cr₂O₃ surface layers on CrO₂ nanoparticles. *Applied Physics Letters*, 77(18), 2840-2842.
- [20] Medeiros, J.V.F.F., Oliveira, A.S., Galvão, G.O., Medeiros, I.D.M., & Gomes, K.C. (2022). Effect of Electrodeposition Time on Absorptance, Roughness and Thermal Stability of Black Chromium Absorbing Surfaces. *Materials Research-Ibero-american Journal of Materials*, 25, 1-5.
- [21] Gomes, L.S., Furtado, A.C.R., & Souza, M.C. (2018). A sílica e suas particularidades [Silica and its particularities]. *Virtual Quim.*, 10 (4), 1018-1038.
- [22] Medeiros, I.D.M., Gomes, K.C., Gonçalves, R.P.N., & Galvão, G.O. (2019). Solar Surface Solar Based on Black Chromium: Influence of Electrodeposition Parameters in the Absorption of Surfaces. *Materials Research*. 22(2), e20180625.
- [23] Khelifa, A. B., Khamlich, S., Nuru, Z.Y., Kotsedi, L., Mebrahtu, A., Balgouthi, M., Guizani, A.A., Dimassi, W., & Maaza, M. (2018). Growth and characterization of spectrally selective Cr₂O₃/Cr/Cr₂O₃ multilayered solar absorber by e-beam evaporation. *Journal of Alloys and Compounds*, 734, 204-209.
- [24] Joni, I. M., Nulhakim, L., Vanitha M., & Panatarani, C. (2018). Characteristics of crystalline silica (SiO₂) particles prepared by simple solution method using sodium silicate (Na₂SiO₃) precursor. *Journal of Physics: Conference Series*, online.
- [25] Fang, C., Zhang, Y., Zhang, Z., Shan, C., Shen, W., & Jia, X. (2018). Preparation of “natural” Diamonds by HPHT an nealing of synthetic diamonds. *Cryst. Eng. Comm.*, 20(4), 505-511.
- [26] Gonçalves, R. P. N., Medeiros, I. D., Gomes, K. C., Oliveira, A., & Galvão, G. (2019). Efeitos do pós-tratamento térmico em superfícies seletivas à base de óxidos de cromo obtidas pelo processo de eletrodeposição [Effects of thermal post-treatment on selective surfaces based on chromium oxide obtained from electrodeposition processes]. *Enciclopédia Biosfera*, 16(29).

Exploiting Renewable Energy in Iraq to Conquer the Problem of Electricity Shortage and Mitigate Greenhouse Gas Emissions

Muthanna M. Al-Hadeethi¹, Mohd Wazir Bin Mustafa², Abdulmuttalib A. Muhsen³

^{1,3}Haditha Hydropower Station, Ministry of Electricity, Haditha, Iraq

²Faculty of Electrical Engineering, University Teknologi Malaysia, Skudai, Johor Bahru, Malaysia

³Warsaw University of Technology, Warsaw, Poland

¹muthanna.alhadeethi@gmail.com

Abstract—The use of renewable energy sources is increasing rapidly to obtain clean energy and avoid environmental crises. This work is to examine the reality of electricity and the state of renewable energy in Iraq, as well as the possibility of using renewable technology to enhance the country's power generation and mitigate greenhouse gas emissions. The study found that Iraq has an abundance of renewable energy sources (water, solar, wind, biomass and geothermal energy) and nuclear energy as a source for clean power generation. However, all of these resources are unexploited in the production of electrical energy, except for the use of hydroelectric energy, which is a small percentage 7.41% of the total production where the dependence on fossil fuels by 92.59% in the production of electrical energy. The report presented recommendations that represent a vision for the use of various renewable energy sources in Iraq to conquer the electricity crisis and reduce dependence on fossil fuels, which is not an eternal resource, and subject to depletion and price increases, as well as a cause of pollution and global warming.

Keywords - renewable energy, pollution, power generation and global warming

I. INTRODUCTION

The global demand for energy continues and gradually increasing, including electric power. Reliance on clean energy has also increased

rapidly to preserve the environment from pollution resulting from burning fossil fuels. In addition to rising prices of fossil fuels as well as non-renewable energy is not eternal [1,2]. Energy plays a vital role in the global economy as well as the political and security stability of a country. Electric power is the main driver of many fields such as industry and agriculture. Therefore, it is considered a measure of a country's strength and development [3]. The use of renewable energy as an alternative to fossil fuels in electric power generation plays an important role in reducing the emission of harmful gases such as carbon dioxide and slowing down global warming [4]. In Iraq, the electrical system suffers from a significant lack of power supply, the electrical system before 1991 was one of the best systems in the region. However, 90% of the production stations were destroyed in the war 1991, more than 50% were not rehabilitated because of the international embargo on Iraq until the occupation of Iraq in 2003 and the subsequent acts of sabotage, so that the electrical system has become unreliable and unable to meet the increasing demand. Iraqi household receives on average less than 10 hours of supply from the national grid per day [5]. After 2003, the required electrical energy was not provided in Iraq despite the diversity of renewable energy sources, which were not invested as a result of the abundance of large quantities of oil, which made decision-makers

lose interest in renewable energy sources, except for the use of hydroelectric power for dams originally intended for agriculture [6]. Most Iraqis rely heavily on private power generators (small diesel generators or medium-sized private generators shared in the streets) to compensate for the lack of energy supply from the national grid [5,7]. Iraq's electricity demand has risen from 11000 megawatts in 2007 to 16000 megawatts in 2013, to 24500 megawatts in summer 2018, and it is predicted to rise to more than 30000 megawatts in 2020 [7,11]. The reason for the increased demand for electricity is the increase in the population growth rate and the relative growth rates gross domestic production GDP, as well as the rise in temperatures to 50 degrees Celsius in the summer [1,4,6]. Thus, the shortage in the production reached (6000) megawatts in 2018 [7] Although Iraq imports 914 MW from the neighboring countries such as Iran [10]. Iraq relies heavily on fossil fuels to generate electric power, the largest part is gas turbine stations, steam stations that depend on crude oil, hydroelectric power, and diesel engine stations [6,8]. The severe shortage of electrical energy production in Iraq needs short and long-term plans to overcome this crisis, and among these plans is the diversity in the use of energy sources, especially renewable energy water, wind, and solar (WWS) as well as nuclear energy, this is due to the abundance of these sources in Iraq.

II. ELECTRICAL POWER SYSTEM IN IRAQ

The electrical power system in Iraq, like any system in the world, consists of:

- (1) Power Generating Plants.
- (2) Transmission stations and lines.
- (3) Distribution stations and lines. As shown if Fig. 1.

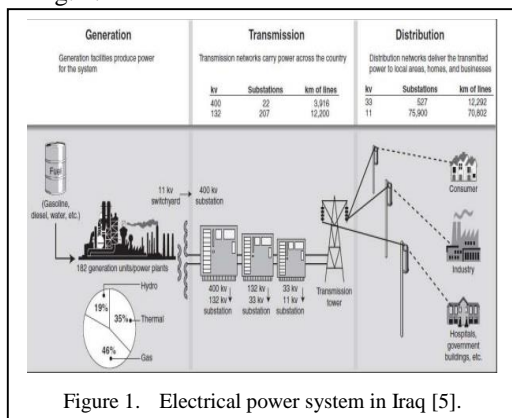


Figure 1. Electrical power system in Iraq [5].

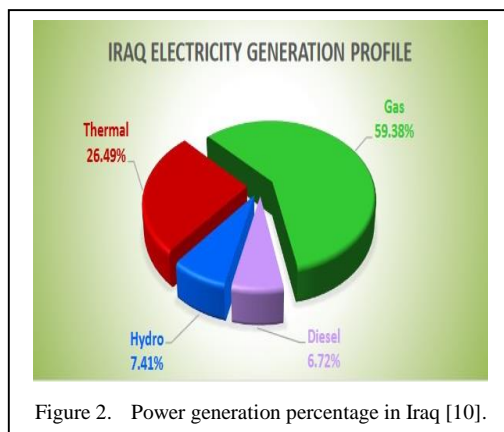


Figure 2. Power generation percentage in Iraq [10].

A. Power Generating Plants

There are different types of generating stations. Thermal plants that depend on crude oil, gas, diesel and hydroelectric plants, the largest production was from the share of gas, thermal, hydroelectric plants, and diesel engine stations respectively [8,10] as shown in Fig. 2.

The first type of power plants is gas turbine power plants, which represents the largest proportion of production in Iraq at 59.38% of the total production through 33 plants with total design capacity of 13414 megawatts [10].

The second type of power plants is thermal plants, which represents 26.49% of the total production, as Iraq owns eight thermal plants with total design capacity of 5985 megawatts [10].

The third type is hydropower plans, which represent 7.41% of the total production through eight hydropower plants with total design capacity of 2456 megawatts [6,10]. Table I shows the active dams and their design capacity, and Table II shows the dams under construction [6].

TABLE I. ACTIVE DAMS WITH THEIR DESIGN CAPACITY [6].

Name	Location	Capacity MW	Status
Bekhme	Erbil	1500	Under Constr.
Mandawa	Erbil	620	Under Constr.
Taq Taq	Erbil	300	Under Constr.
Al Baghdadi	Anbaar	300	Under Constr.
Badush	Ninawa	171	Under Constr.
Bakerman	Ninawa	24	Under Constr.
Total		2615	Under Constr.

TABLE II. UNDER CONSTRUCTION DAMS WITH THEIR DESIGN CAPACITY [6].

Type	Plant	No of Units	Installed Unit Size (MW)	Installed Storage Capacity (MW)
With Storage Reser-voir	Mosul Main	4	187.5	750
	Haditha	6	110	660
	Dukan	5	80	400
	Darbandikhan	3	83	249
	Himreen	2	25	50
With Limited Storage	Mosul Regulat	4	15	60
	Samarra barr.	3	28	84
	Hindiya- barr.	4	3.75	15
	Kufa barrage	4	1.25	5

TABLE III. TYPE OF DAMS WITH THEIR DESIGN CAPACITY [2].

Name	Location	Capacity/MW	Status
Mosul	Ninawa	1010	Active
Haditha	Anbar	660	Active
Dokan	Sulaimaniyah	400	Active
Darbandikhan	Hexagonal	240	Active
Samara	Salahuddin	75	Active
Hamrin	Dyala	50	Active
Hindiya	Karbala	15	Active
Kufa	Karbala	6	Active
Total		2456	

The hydroelectric plants are classified into two types. The first type covers hydropower stations with storage reservoirs, whereas the second type includes those with barrages with limited storage [2] as shown in Table III. However, the percentage of energy production from hydropower plants is gradually decreasing because of the increase in energy production from thermal and gas stations, as shown in Fig. 3.

The fourth type is diesel engine stations, which represents 6.72% of the total production

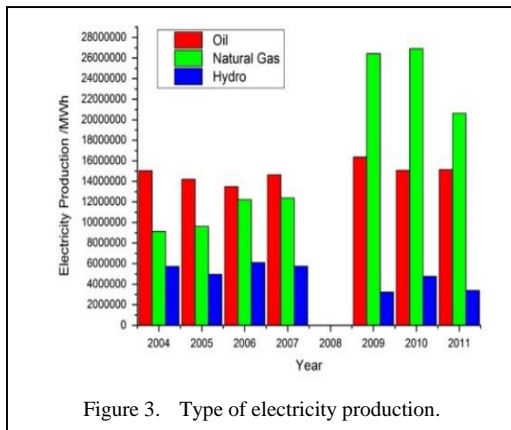


Figure 3. Type of electricity production.

by 12 diesel stations with total design capacity of 1549 megawatts [10].

B. Transmission Stations and Lines

The power transmission system transfers power from generating stations to the load centers [11]. The electrical power transmission system in Iraq consists of 400 and 132 KV, the 400 KV system consists of 22 substations and 3916 km of lines, and the 132 KV system consists of 207 substations and 12.200 km of lines [5].

C. Distribution Stations and Lines

The distribution system supplies electrical power to homes, industry and service facilities [11]. The electrical power distribution system in Iraq consists of 33 KV and 11 KV, the 33 KV system consists of 527 substations and 12292 km of lines, and the 11 KV system consists of 75900 substations and 70802 km of lines [5]. Like the generation system, the transmission and distribution system are unstable and suffers from many problems where network equipment are outdated, poor management and planning. The electrical energy losses are very high in generating stations, transmission and distribution lines as follows: 4.4%, 6.8% and 25%

respectively [9]. About 90% of the losses are in the distribution network, divided into technical, commercial, and administrative losses, as 79% of the losses are not technical (thefts from the network, unpaid and not collected bills) [11]. The poor situation in the Iraqi electrical power system in all parts of generation, transmission, distribution led to the instability of the network and the occurrence of frequent power cuts and energy losses, in addition to increasing the gap between the demand and the actual product of energy as shown in Fig. 4.

The electric power sector in Iraq needs many measures and plans to overcome the problem of the deficit between production and demand. The use of renewable energy sources contributes to supplying production and reducing harmful gas emissions as well. In addition to the use of nuclear energy greatly helps to increase production in the long term. Moreover, the use of distributed energy resources and smart grid system for transmission of energy contribute to reducing energy losses [9].

III. RENEWABLE ENERGY RESOURCES IN IRAQ

There are many types of renewable energy (water, solar, wind, biomass, and geothermal energy) as shown in the Fig. 5. In Iraq, the percentages of their availability and exploitation vary from one type to another. Several studies have clarified these sources and indicated their abundance and the possibility of using them in the production of electrical energy in Iraq where it will be discussed briefly.

A. Water Energy

Iraq has two large rivers, the Tigris, and the Euphrates, extending from northern Iraq to its south. Despite that, the percentage of hydropower utilization in the production of

electrical energy through dams is very low (7.41% of the total production) [10,12].

To make the best use of the hydropower from these two rivers, the decision maker can follow the steps below:

1. Completion of the construction of dams that are under construction and suspended since 2003 due to the occupation and subsequent events [6]. This will add 2,615 megawatts to the national grid, and this means an increase in the hydroelectric production rate of 100% of the current production. In addition to increasing the water storage that can be used in the dry seasons.
2. Micro-Hydrokinetic River: It is a turbine installed on the course of rivers or streams. It converts the kinetic energy of water into electrical energy. These turbines do not need to build dams as in traditional hydroelectric stations, but only need to be fixed in the river stream [12,13] as shown in Fig. 6. The two most frequent small-scale hydrokinetic turbine concepts are axial-flow turbine and cross flow turbine. The turbine type chosen is determined by the flow type, velocity, and required output of the system, which can reach 100 KW [12]. Micro-Hydrokinetic River turbine is an economically suitable option as well as in terms of reliability in generating power for remote and rural areas near the river. In addition, it is considered a compensator for the non-continuous energy generated from other renewable



Figure 4. Capacity and demand of energy in Iraq [9].

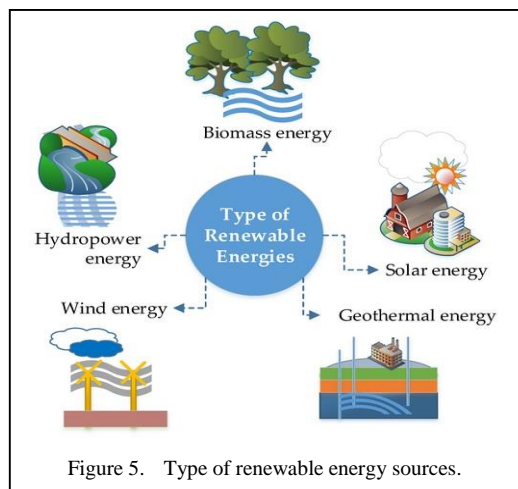


Figure 5. Type of renewable energy sources.

energy sources (wind, solar) [12]. The use of this type of turbine is a good exploitation of hydropower, as it helps isolate remote areas from the national grid, thus reducing energy losses and maintenance losses.

3. Tidal wave turbine: It converts the kinetic energy of marine tidal waves into electrical energy. Tidal energy is a type of renewable energy that has multiple advantages such as operating at low speeds, predictable, environmentally friendly, long life and not much affected by the climate. The construction of large plants of this type of turbine can produce high capacities of energy up to 254 MW, as is the case with the largest production plant in the world that relies on tidal waves in South Korea [14]. Iraq has a 58 km long beach on the Arabian Gulf, where it can be used to install tidal wave turbines to generate electric power.

B. Solar Energy

Iraq is famous for its long days and long hours of sunshine in the summer [1]. Iraq collects more than 3000hours/year of solar radiation in Baghdad only [1,2]. In comparison to the yearly worldwide average horizontal surface radiance of 170W/m², the western desert of Iraq has the greatest sun irradiation for electric power generation. According to the German Aerospace Center, the deserts of Iraq produce a mean power density of 270W/m² to 290W/m², with a peak power density of 2310kWh/m²/year [2]. Iraq can produce electricity in large quantities from solar energy, as the sunny hours exceed 12 hours in the summer and reached 14 hours on June 21 [6]. Solar field construction does not take as long as other types of power plants, where a 500MW station may be built in a year [7]. It is separated into two systems: photovoltaic (PV) energy

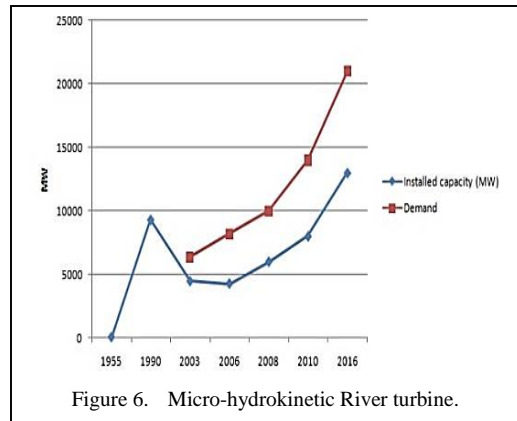


Figure 6. Micro-hydrokinetic River turbine.

systems, which directly convert solar energy into electrical energy, and solar thermal power systems or concentrated solar power (CSP), which convert solar energy into thermal energy, which is then used to generate electrical energy [7,8]. Photovoltaic can be used to generate electricity in remote and rural areas when grid connections are not available. It can be used for outdoor street lighting, as well as supplying homes with light electrical loads and communication towers [4]. While CSP can be connected to the grid because of its high energy output. Reference [2], suggested some areas in Iraq in which CSP stations can be established, depending on the amount of available solar radiation, the nature of the area and the availability of water, as shown in Table IV in addition to the possibility of merging solar energy stations with gas and thermal stations to increase their productivity [2,11], as shown in Fig. 7. for the Kuraymat combined power plant in Egypt, where it is noted that production increases by 25% during the period of solar radiation in the day.

Solar energy is not exploited well in Iraq to produce electrical energy except in some small attempts, such as street lighting, despite its

TABLE IV. CSP PLANT POTENTIAL IN IRAQ [2].

Region	Resource (kWh/m ²)	Area for Plant (ha)	Possible No. CPS Plant	Installed Power (MW)
Centar Iraq (Babylon, Diyala, Baghdad)	2100-2200	318	28	1400
South Iraq (Missan, Thi-Qar, Basrah)	2100-2200	203	18	900
Govemorate of Al-Anbar	2200-2300	504	44	2900

availability in all seasons of the year, especially in summer, when demand for electricity increases and peak load is reached. The use of photovoltaic cells to feed remote areas, as well as CSP stations to produce high capacities, has become a necessity to increase energy production on the one hand, and to exploit clean renewable energy and reduce pollution on the other hand. In addition to using solar energy to produce electrical energy, solar water heating systems can be used in the winter to reduce electrical energy consumption [15].

C. Wind Energy

The use of wind-generated energy is not a new concept. It spans thousands of years of human existence on the planet. Wind energy was used by ships and windmills [6]. Wind turbines are used to convert the kinetic energy of the wind into electrical energy. As a result of the wind movement on the wind turbine blades, a rotating movement of the turbine is produced which is used to generate electric power [4]. In Iraq, 8% of its regions have a relatively high wind speed exceeding 5 meters per second and 35% have wind speeds ranging between (3.1 - 4.9) meters per second at 10 meters high and it increases with increasing height [1,2]. Iraq is one of the countries with high wind potential in the Middle East [3]. The wind speed is active in the summer and is faster than it is in the winter, so it can be used well with the great demand for electrical energy in the summer [1]. Many areas of Anbar and the southern regions can be exploited, as they have a relatively good wind speed, for example, the wind speed in Nasiriya is 7.7 m/s at 34 meters height. Wind-mill turbines can be used with the wind speed available in Iraq [6]. Wind energy in Iraq is less abundant compared to solar energy in Iraq [16]. However, it can be exploited well in rural and remote areas as well as on the shore of the Arabian Gulf in southern Iraq because the

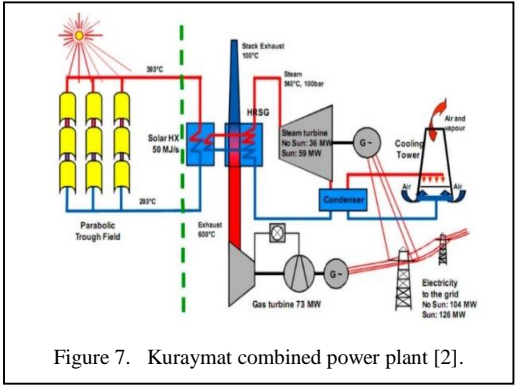


Figure 7. Kuraymat combined power plant [2].

wind speed is higher despite the short length of the Iraqi coast. In addition, wind and solar energy can be used together as a hybrid system [4] as shown in Fig. 8 that compensates for each other when one of the sources is absent due to low wind speed or during the night as well as the presence of clouds that block the sun rays.

D. Biomass Energy

Iraq is wealthy in biomass resource. Unfortunately, the abundance of oil and gas as a fuel source has a detrimental effect on biomass research and investigations. Iraqi researchers have conducted a small number of investigations into the use of bioethanol and methanol in mixed fuels. However, no attempt in Iraq to convert biomass into electricity has been documented [1,2].

E. Geothermal Energy

Geothermal energy can be benefited from in two ways. The first is the use of geothermal energy to generate electric power. The second is the direct use of geothermal energy in heating and cooling households as well as industrial purposes [15,17,18]. Many countries of the world have exploited geothermal energy in the production of electrical energy, for example the Philippines, where 22% of its electrical energy is produced by geothermal energy. The use of surface geothermal energy through the exploitation of groundwater for air conditioning purposes helps to significantly reduce electrical energy consumption [17]. Geothermal energy is another type of unexploited energy in Iraq that can be used as a source of clean, renewable energy to support the production of electrical energy.

IV. NUCLEAR SOURCES

Electricity can be produced with high capacities from nuclear energy with low carbon emissions. The percentage of electricity production in the world using nuclear energy

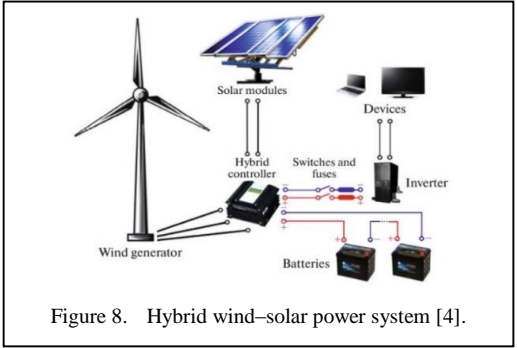


Figure 8. Hybrid wind-solar power system [4].

reaches 20% [17]. Iraq is one of the pioneers in the Middle East in the field of atomic energy. The Iraqi Atomic Energy Commission was established in 1958, and Iraq joined the International Atomic Energy Agency in 1959 [6]. Iraq possessed the first nuclear reactor for research purposes in 1967 with a capacity of 2 megawatts. In 1981, the construction of the second reactor with a capacity of 40 megawatts was completed in the Al-Tuwaitaha area, located 15 km south of Baghdad. Unfortunately, in the same year, this reactor was attacked and destroyed by Israel. After that, Iraq contracted with the former Soviet Union to construct two nuclear reactors for the purposes of producing electric power with a capacity of 2GW. It was planned to be completed in 2000, but this was not done due to the embargo imposed on Iraq [16]. Iraq possesses large quantities of uranium ore in the form of rocks and compounds in northern and western Iraq [6], which can be used in the production of clean electric energy with high capabilities to reduce the gap between demand and actual production and reduce the emission of harmful gases from the use of fossil fuels.

V. CONCLUSION

In this work, the electricity system in Iraq and the problems in the sectors of production, transmission and distribution that hinder the achievement of production that meets the increasing demand are discussed. The sources of renewable energy in Iraq and the possibility of using them in the production of electrical energy were also discussed. Iraq needs some measures and plans to overcome the electricity crisis; these are some recommendations that we think may help solve this crisis:

1. Completing the construction of dams whose construction stopped after 2003 to exploit the wasted water energy. In addition to the use of Micro-Hydrokinetic River turbines on the course of the Tigris and Euphrates rivers as well as the use of tidal wave turbines on the shore of the Arabian Gulf.
2. Building solar power stations (CSP) with high capacities because Iraq possesses very high amounts of solar radiation. In addition to the use of combined stations to improve the production of fossil fuel stations by integrating them with solar energy. Moreover, the use of photovoltaic cells (PV) to produce electrical energy, as well as the use of solar water heating techniques that helps reduce electricity consumption.
3. The use of wind energy to produce electrical energy in areas where winds are active, especially in remote and rural areas. In addition to the use of hybrid systems to combine wind and solar energy.
4. The use of biomass energy in the production of electrical energy as well as geothermal energy for air conditioning purposes to reduce energy consumption.
5. The use of nuclear energy in the production of electrical energy has become a necessity because of the high capabilities that can be provided by nuclear energy.
6. The use of smart grid system and distributed power source system helps reduce electrical power transmission losses.

This research may contribute to developing future plans to solve the electricity problem in Iraq, as well as reduce the emission of harmful gases and global warming resulting from the combustion of fossil fuels.

REFERENCES

- [1] Kazem, H. A., & Chaichan, M. T. (2012). Status and future prospects of renewable energy in Iraq. *Renewable and Sustainable Energy Reviews*, 16(8), 6007-6012.
- [2] Al-Kayiem, H. H., & Mohammad, S. T. (2019). Potential of renewable energy resources with an emphasis on solar power in Iraq: An outlook. *Resources*, 8(1), 42.
- [3] Nematollahi, O., Hoghooghi, H., Rasti, M., & Sedaghat, A. (2016). Energy demands and renewable energy resources in the Middle East. *Renewable and Sustainable Energy Reviews*, 54, 1172-1181.
- [4] Abd Ali, L. M., Al-Rufae, F. M., Kuvshinov, V. V., Krit, B. L., Al-Antaki, A. M., & Morozova, N. V. (2020). Study of hybrid wind-solar systems for the Iraq energy complex. *Applied Solar Energy*, 56, 284-290.
- [5] Rashid, S., Peters, I., Wickel, M., & Magazowski, C. (2012). *Electricity problem in Iraq*. Hamburg.
- [6] Saeed, I. M., Ramli, A. T., & Saleh, M. A. (2016). Assessment of sustainability in energy of Iraq, and achievable opportunities in the long run. *Renewable and Sustainable Energy Reviews*, 58, 1207-1215.
- [7] Abass, A. Z., & Pavlyuchenko, D. A. (2019). The exploitation of western and southern deserts in Iraq for the production of solar energy. *International Journal of Electrical and Computer Engineering*, 9(6), 4617.

- [8] Al-Juboori, S. S., Abduljabbar, R. H., & Abdulmajeed, N. M. Using Concentrated Solar Power Techniques to Generate Electric Power in Iraq, a Review on Present Status and Future Directions.
- [9] Abed, F. T., ALRikabi, H. T. S., & Ibrahim, I. A. (2020, June). Efficient Energy of Smart Grid Education Models for Modern Electric Power System Engineering in Iraq. In *IOP Conference Series: Materials Science and Engineering* (Vol. 870, No. 1, p. 012049). IOP Publishing.
- [10] Nadhum, A. A., & Erzaij, K. R. (2020, August). Evaluating implementation of electric power generation projects in Iraq. In *IOP Conference Series: Materials Science and Engineering* (Vol. 901, No. 1, p. 012034). IOP Publishing.
- [11] Abass, A. Z., Pavlyuchenko, D. A., & Hussain, Z. S. (2021). Survey about impact voltage instability and transient stability for a power system with an integrated solar combined cycle plant in Iraq by using ETAP. *Journal of Robotics and Control (JRC)*, 2(3), 134-139.
- [12] Muhsen, A. A., Al-Malik, A. A. R., Attiya, B. H., Al-Hardane, O. F., & Abdalazize, K. A. (2021, June). Modal analysis of Kaplan turbine in Haditha hydropower plant using ANSYS and SolidWorks. In *IOP Conference Series: Materials Science and Engineering* (Vol. 1105, No. 1, p. 012056). IOP Publishing.
- [13] Attiya, B., Altimemy, M., Daskiran, C., Liu, I. H., & Oztekin, A. (2019, November). Micro-Hydrokinetic Turbine Operating in the Vicinity of a Free Surface: Multiphase Large Eddy Simulations. In *ASME International Mechanical Engineering Congress and Exposition* (Vol. 59445, p. V007T08A040). American Society of Mechanical Engineers.
- [14] Vermaak, H. J., Kusakana, K., & Koko, S. P. (2014). Status of micro-hydrokinetic river technology in rural applications: A review of literature. *Renewable and Sustainable Energy Reviews*, 29, 625-633.
- [15] Hamdan, A. N. A., Abbas, A. A., & Al-Asadi, K. (2019). Perspective and Prospect of Tidal Electricity Generation in Iraq. *Perspective*.
- [16] Jacobson, M. Z., Howarth, R. W., Delucchi, M. A., Scobie, S. R., Barth, J. M., Dvorak, M. J., ... & Ingraffea, A. R. (2013). Examining the feasibility of converting New York State's all-purpose energy infrastructure to one using wind, water, and sunlight. *Energy Policy*, 57, 585-601.
- [17] Al-Hamadani, S. (2020). Solar energy as a potential contributor to help bridge the gap between electricity supply and growing demand in Iraq: A review. *Int J Adv Appl Sci ISSN, 2252(8814)*, 8814
- [18] Al-Samari, A. S., & Ali, S. D. (2018). Experimental evaluation of surface geothermal energy for air conditioning applications in Iraq. *Journal of Mechanical Engineering Research and Developments*, 41(1), 38-43.
- [19] Fridleifsson, I. B. (2001). Geothermal energy for the benefit of the people. *Renewable and sustainable energy reviews*, 5(3), 299-312.

MHD Mixed Convection and Pressure Drop in an Open Cavity with a Solid-porous Fin

Brahim Fersadou¹, Walid Nessab², Khaled Mouaici³, Nawal Guerroudj⁴,
Henda Kahalerras⁵

^{1,2,3,4,5}University of Science and Technology Houari Boumedien USTHB, Algiers, Algeria

¹brahim04@live.fr, ²nessabwalid@gmail.com, ³khaledmouaici7@gmail.com,
⁴nawguer@yahoo.fr, ⁵kahalerrashenda@yahoo.fr

Abstract—The current numerical study examines the MHD mixed convection and pressure drop occurring in an open cavity. The enclosure contains a nanofluid (Cu/Water) flowing through it and is equipped with a solid-porous fin placed at the mid-length. Each right and left wall alternately includes heated or cooled sources kept at constant and different heat flux densities along with adiabatic regions. The Darcy-Brinkman-Forchheimer model is used to describe the fluid flow in the porous zone, and the conservation equations are solved by the finite volume method using the SIMPLE algorithm. The principal purpose of this work is to analyze the impact of control parameters on the flow structure, the heat transfer characteristics, and the pressure drop. These control parameters include the fin width, the position of the porous portion, and the Hartmann number Ha . The outcomes reveal that the heat transfer rate decreases at small Ha but improves with the magnetic field intensification. Its evolution with the fin size and location of the porous region depends on the heated source being considered and the value of the Hartmann number. Regarding the pressure drop, it reduces as the magnetic field strength decreases and the fin width diminishes. It is almost independent of the location of the porous part.

Keywords – MHD, solid-porous fin, open cavity, mixed convection, pressure drop

I. INTRODUCTION

Nanofluids are colloidal suspensions of nanoparticles in a base fluid engineered for more suitable suspension stability than larger particle sizes. This new class of fluids has unique

properties that make it useful for various applications. It has higher thermal conductivity and convective heat transfer coefficient compared to common fluids, which means that it can transfer heat at a more heightened rate. This translates into more efficient heating or cooling while lessening energy consumption.

Nanofluid flow and heat transfer in open cavities with magnetic field effects have various applications, including cooling electronic apparatuses, heat exchangers, solar energy collectors, and chemical processing equipment. As a result, this subject has attracted significant interest from engineers and scientists for decades. Reference [1] scrutinized the (Cu-Water) convective flow within a T-shaped cavity under a uniformly applied magnetic field. The study analyzes the influence of control parameters such as the Reynolds, Richardson, and Hartmann numbers, nanoparticle volume fraction, and cavity aspect ratio on thermal efficiency. Reference [2] analyzed MHD mixed convection and entropy production of a nanofluid in a ventilated cavity. Growing the Richardson number, heat flux ratio, nanoparticle volume fraction, and reducing the opening ratio enhance the heat transfer rate. Similarly, they found that thermal irreversibility brings the most thermodynamic disorder to the system. Reference [3] analyzed the effect of a magnetic field on the convective flow of a hybrid nanofluid inside an open cavity with a heated obstacle. The researchers discovered that the Lorentz force gradually reduces the buoyancy effect. Additionally, they found that increasing the

concentration of suspended nanoparticles results in an improvement in the heat exchange. Reference [4] conducted numerical simulations to investigate the effects of uniformly and partially magnetic fields with water-MWCNT nanofluid as heat transfer fluid. The study revealed that a partial magnetic field applied to the center of the left wall diminished thermal exchange more effectively than the base-centered and top fields. Reference [5] performed a numerical investigation to evaluate the effects of a hybrid nanofluid and a spatial sinusoidal magnetic field on phase transition dynamics. The study is carried out on a phase change material partially located in a ventilated enclosure with a triangular cross-section. In a specific setup consisting of two enclosures joined by a conductive plate with perforations, study [6] performed numerical simulations on forced convection under the influence of a magnetic field. The perforated separation improves the heat transfer under particular circumstances while simultaneously lessening the system's material, weight, and cost. Reference [7] operated permeable and permeable-perforated plates to control nanofluid convective flow within an open cavity equipped with an inclined flexible wall under the action of a magnetic field. The findings revealed that without a magnetic field, the maximum thermal efficiency is achieved without a plate and elastic wall. Nevertheless, when the Lorentz force is present, the configuration with the porous plate and flexible wall becomes the most appropriate.

Although much research has been carried out on the simultaneous use of nanofluid, magnetic field, and porous medium in open cavities, operating a solid-porous fin can bring something new to existing studies. To this end, the present work aims to examine numerically the mixed convective heat transfer and pressure drop of copper-water nanofluid in an open cavity with a solid-porous fin under the influence of a magnetic field. The effects of parameters such as the Hartmann number, the position of the porous portion, and the fin width are analyzed.

II. MATHEMATICAL FORMULATION

A. Physical Domain

The physical configuration being studied is a rectangular cavity with an aspect ratio of $\ell/H = 5$. A solid-porous fin divides the enclosure into two compartments, each with an opening width d and having on the right and left walls cooled or heated sources of width s , kept at heat flux

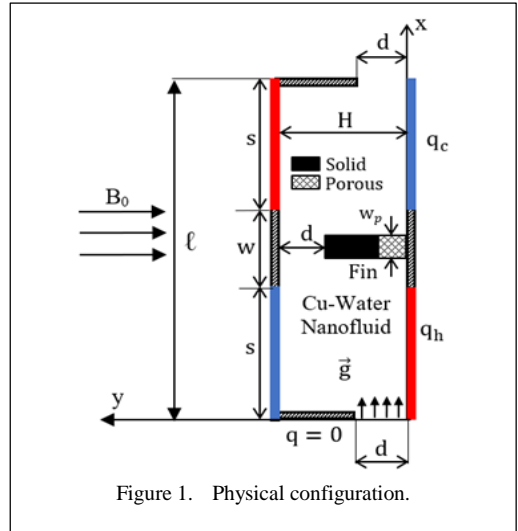


Figure 1. Physical configuration.

densities q_h and q_c , respectively and alternated by adiabatic regions of width $w/2$ Fig. 1 illustrates the arrangement of these zones, with the upper and lower sides of the cavity being thermally insulated. A nanofluid consisting of a mixture of copper nanoparticles and water enters the system with uniform velocity U_i and constant temperature T_i under an external magnetic field applied uniformly in the transverse direction. The fin of width w_p is positioned at the mid-length of the cavity and holds a porous portion of height $H/4$, whose location changes. It is in contact with the right wall in position 1, whereas in positions 2 and 3, it is located in the center and on the left.

B. Governing Equations

The fluid flow is two-dimensional, steady-state, and laminar. The nanofluid is Newtonian, electrically conductive, incompressible, and viewed as a homogeneous mixture in which no chemical reaction happens. The nanoparticles are mixed into the base fluid along with surfactants to prevent any aggregation and settling issues. It is assumed that the porous medium is isotropic and homogeneous. The base fluid, nanoparticles, and porous matrix are all in thermal equilibrium, and any energy loss due to friction is neglected.

The Tiwari and Das model [8], along with the Darcy-Brinkman-Forchheimer model, is employed to describe nanofluid MHD mixed convection. The equations of continuity, motion, and energy in their dimensionless form are written as follows:

$$\frac{\partial u}{\partial x} + \frac{\partial v}{\partial y} = 0, \quad (1)$$

$$\frac{1}{\varepsilon^2} \left[U \frac{\partial U}{\partial X} + V \frac{\partial U}{\partial Y} \right] = -\frac{\partial P}{\partial X} + \frac{\rho_{bf}}{\rho_{nf}} \frac{1}{Re} \times \left[\frac{\partial}{\partial X} \left(\frac{\mu_{nf}}{\mu} \frac{\partial U}{\partial X} \right) + \frac{\partial}{\partial Y} \left(\frac{\mu_{nf}}{\mu} \frac{\partial U}{\partial Y} \right) \right] - \frac{\rho_{bf}}{\rho_{nf}} \frac{\mu_{nf}}{\mu} \frac{1}{Re Da} U - \frac{C}{\sqrt{Da}} |\vec{V}| U + Ri \frac{(\rho\beta)_{nf} \rho_{bf}}{(\rho\beta)_{bf} \rho_{nf}} \theta - \frac{Ha^2}{Re} \frac{\sigma_{nf} \rho_{bf}}{\sigma_{bf} \rho_{nf}} U \quad (2)$$

$$\frac{1}{\varepsilon^2} \left[U \frac{\partial V}{\partial X} + V \frac{\partial V}{\partial Y} \right] - \frac{\partial P}{\partial Y} + \frac{\rho_{bf}}{\rho_{nf}} \frac{1}{Re} \times \left[\frac{\partial}{\partial X} \left(\frac{\mu_{nf}}{\mu} \frac{\partial V}{\partial X} \right) + \frac{\partial}{\partial Y} \left(\frac{\mu_{nf}}{\mu} \frac{\partial V}{\partial Y} \right) \right] - \frac{\rho_{bf}}{\rho_{nf}} \frac{\mu_{nf}}{\mu} \frac{1}{Re Da} V - \frac{C}{\sqrt{Da}} |\vec{V}| V \quad (3)$$

$$U \frac{\partial \theta}{\partial X} + V \frac{\partial \theta}{\partial Y} = \frac{(\rho C_p)_{bf}}{(\rho C_p)_{nf}} \frac{1}{Re Pr} \times \left[\frac{\partial}{\partial X} \left(\frac{k_{nf}}{k_{bf}} \frac{\partial \theta}{\partial X} \right) + \frac{\partial}{\partial Y} \left(\frac{k_{nf}}{k_{bf}} \frac{\partial \theta}{\partial Y} \right) \right] + EC \frac{Ha^2}{Re} \frac{\sigma_{nf} (\rho C_p)_{bf}}{\sigma_{bf} (\rho C_p)_{nf}} U^2 \quad (4)$$

Outside the porous region, these equations remain valid by taking $\varepsilon = 1$ and $D_a \rightarrow \infty$.

R_e , D_a , R_i , H_a , E_c , and P_r are the Reynolds, Darcy, Richardson, Hartmann, Eckert, and Prandtl numbers. C is the inertial coefficient representing the inertia effect in the porous material.

The subscripts bf and nf indicate the base fluid and nanofluid, respectively.

C. Boundary Conditions

The associated boundary conditions are:

Inlet

$$\begin{cases} U = V = 0, \frac{\partial \theta}{\partial X} = 0 & \text{Wall} \\ U = 1, V = 0, \theta = 0 & \text{Elsewhere} \end{cases} \quad (5)$$

Right wall

$$\begin{cases} U = V = 0, \frac{\partial \theta}{\partial Y} = -\frac{k_{bf}}{k_{nf}} & \text{Heated source} \\ U = V = 0, \frac{\partial \theta}{\partial Y} = 0 & \text{Elsewhere} \\ U = V = 0, \frac{\partial \theta}{\partial Y} = \frac{q_c k_{bf}}{q_h k_{nf}} & \text{Cooled source} \end{cases} \quad (6)$$

Left wall

$$\begin{cases} U = V = 0, \frac{\partial \theta}{\partial Y} = -\frac{q_c k_{bf}}{q_h k_{nf}} & \text{Cooled source} \\ U = V = 0, \frac{\partial \theta}{\partial Y} = 0 & \text{Elsewhere} \\ U = V = 0, \frac{\partial \theta}{\partial Y} = \frac{k_{bf}}{k_{nf}} & \text{Heated source} \end{cases} \quad (7)$$

Exit

$$\begin{cases} U = V = 0, \frac{\partial \theta}{\partial X} = 0 & \text{Wall} \\ \frac{\partial U}{\partial X} = V = \frac{\partial \theta}{\partial X} = 0 & \text{Elsewhere} \end{cases} \quad (8)$$

The subscripts h and c stand for the hot and cold sources, respectively.

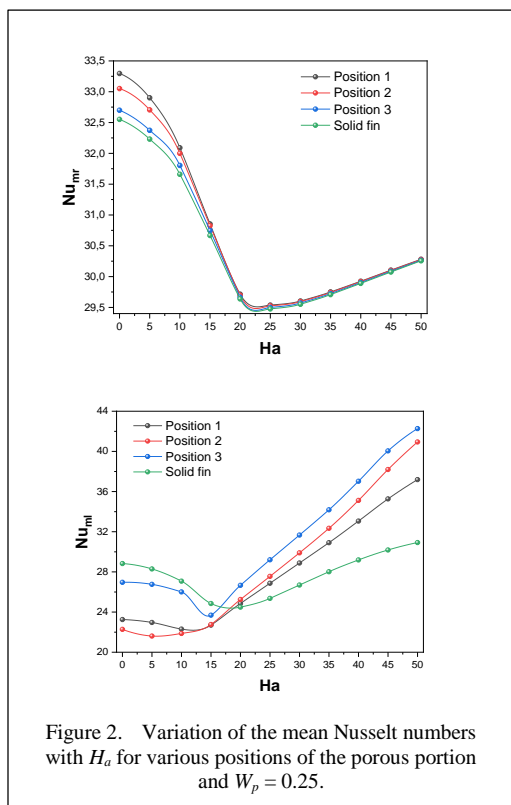
III. NUMERICAL MODELING

The system comprised of the equations and boundary conditions is solved numerically using the finite volume approach and SIMPLE algorithm [9]. The diffusive and convective terms are discretized using the power-law scheme, and the obtained algebraic equations are then solved using the line-by-line method. The mesh distribution is not uniform in both directions, becoming narrower at the fin interfaces and solid walls. After conducting numerous tests, an optimal number of nodes of 300×50 (in the X and Y directions, respectively) has been selected to ensure an accurate numerical solution and a reasonable calculation time. The chosen convergence condition for the iterative process to end is for the highest relative error between two successive iterations of the velocity components and temperature to be smaller than 10^{-6} .

IV. RESULTS

Many control parameters govern the current problem, so some have been fixed, while others have been varied. For this purpose, we set the porosity of the porous medium ($\varepsilon = 0.9$), the width ($S = 2$) and spacing ($W = 1$) of the sources, the Reynolds number ($R_e = 100$), the Darcy number ($D_a = 10^{-3}$), and the Richardson number ($R_i = 10$). On the other hand, we varied the Hartmann number ($0 \leq H_a \leq 50$), the fin width ($0.25 \leq W_p \leq 1$) and the position of the porous portion.

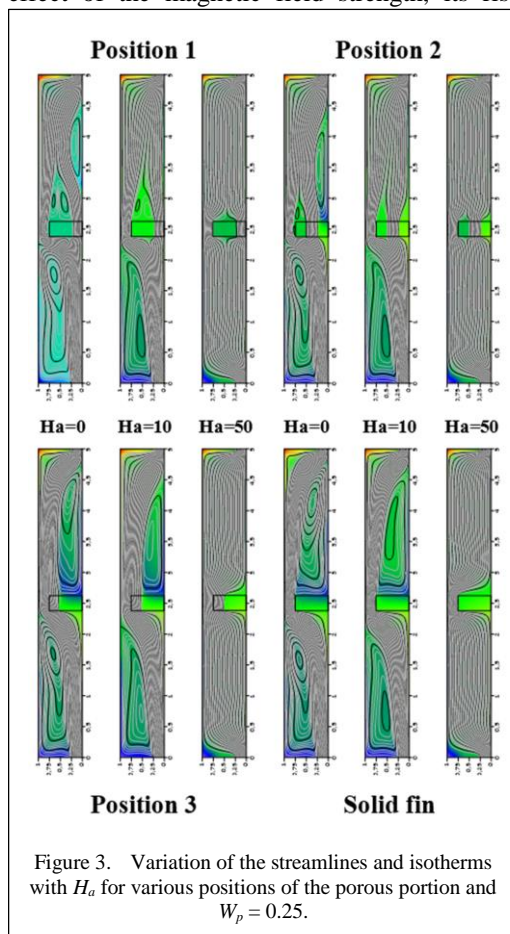
Fig. 2 illustrates the evolution of the streamlines and isotherms for different Hartmann number values and three positions of the porous

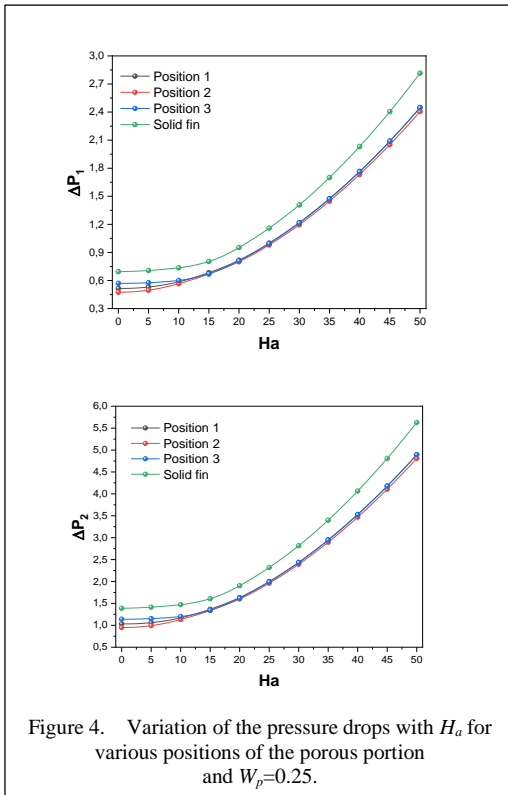


portion, as well as the case of a solid fin. Without a magnetic field, the nanofluid in both compartments exhibits an upward primary flow controlled by the fluid entering each compartment and a secondary flow that operates in the same direction near the hot sources and the opposing direction around the cold sources. This secondary flow accelerates the nanofluid flow in the first region. In contrast, in the second region, it causes a deceleration or even a flow reversal characterized by two extensive recirculation zones. The arrangement of the porous portion of the separating fin determines the flow in the second compartment. The dynamic distribution of the nanofluid in position 3 and the solid fin is similar to that of the first compartment. On the other hand, in position 1 and position 2, the nanofluid goes through multiple outlets, attenuating the reverse flow's magnitude. When a magnetic field is applied, it alters the streamline patterns. This creates a competition between the ascending flow and eddies. The size of the eddies reduces as the Hartmann number increases until they vanish entirely at $Ha = 50$. This phenomenon is because the magnetic field creates supplemental opposition to the flow given by the Lorentz force, which performs vertically and in the opposing direction of the

nanofluid main movement and the buoyancy force. When the magnetic field becomes more substantial, the upward flow produced by the Lorentz force at the cold sources overpowers the downward flow caused by the buoyancy force, leading to the complete disappearance of the flow reversal.

The evolution of the mean Nusselt numbers per compartment with the number of Hartmann and for various porous portion arrangements is depicted in Fig. 3. Position 1 is thermally the most efficient in the first compartment because of the heat released from the hot source to the second compartment through the porous portion. As the porous portion is shifted to the left, the cooling capability decreases due to poor heat evacuation. Finally, when the fin is entirely solid, the mean Nusselt number reaches its lowest value. The position effect becomes negligible at high Hartmann numbers as the magnetic field dominates the flow, giving rise to identical structures, as shown in Fig. 2. Concerning the effect of the magnetic field strength, its rise





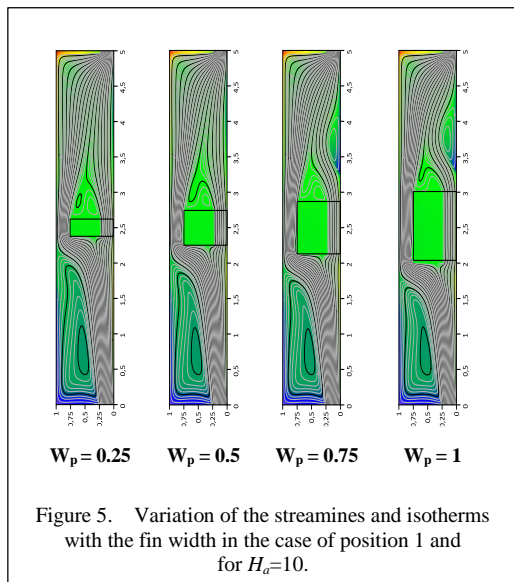
results in two trends; the first is characterized by the reduction in heat exchange up to a critical Hartmann number between 20 and 25. This behavior arises due to the slowing down of the nanofluid motion near the hot source and the compaction of the recirculation cell close to the cold one. Above the Ha critical value, a second tendency arises where the mean Nusselt number increases due to the Lorentz force's advantage over the fluid, whose distribution is uniformed, as shown in Fig. 2. Based on the Nu_{ml} curves analysis, the same evolutionary pattern is observed, but with a change happening at a critical Hartmann number, approximately at a value of 15. Before the critical Ha value, the solid fin is the most effective because due to the large recirculation zone located at the level of the cold source of the first compartment, the main flow is injected into the second compartment at a high velocity, thus effectively evacuating the heat released by the second hot source. However, beyond this value, position 3 is identified as the most efficient for maximum heat exchange at the hot source in the second compartment. The increase in the Hartmann number causes a reduction in the size of the vortices inside the cavity. This decrease leads to an expansion of the uniform flow zone, allowing more fluid to come

in contact with the second hot source. This phenomenon becomes increasingly significant and reaches its maximum at position 3 of the porous portion.

The pressure drops in the first compartment's ΔP_1 and the second compartment's ΔP_2 are illustrated in Fig. 4. Due to the retarding effect of the Lorentz force, the hydrodynamic performance of the system is reduced with increasing Ha under all conditions. However, an interesting result appears when examining the impact of the porous portion position. Indeed, changing the location of the permeable part does not affect the pressure drops in the cavity. Still, its presence reduces ΔP compared to a solid fin, which exhibits the highest values.

In the second part of the results, the effect of the fin width is discussed for position 1 of the porous portion. Fig. 5 displays the changes in streamlines and isotherms for different W_p values. Expanding the width of the fins has a significant impact on the flow structure, primarily near the cold sources. In the first compartment, the size of the vortex is reduced due to the narrower space created by wider fins, while in the second compartment, a recirculation zone emerges near the right wall and grows as W_p increases. The isotherms indicate that a thicker fin positively affects the heat exchange occurring on the hot source of the left wall.

In Fig. 6, it can be observed that the mean Nusselts numbers at the hot sources evolve similarly to Fig. 3. A decrease in W_p leads to an



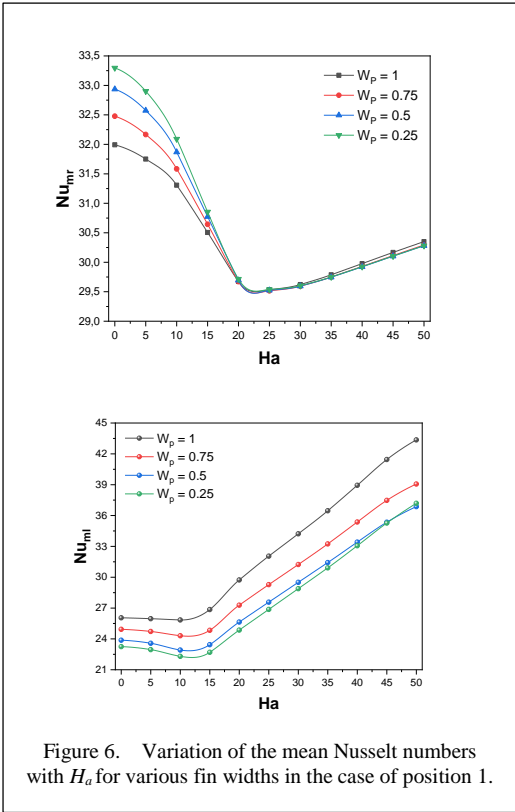


Figure 6. Variation of the mean Nusselt numbers with H_a for various fin widths in the case of position 1.

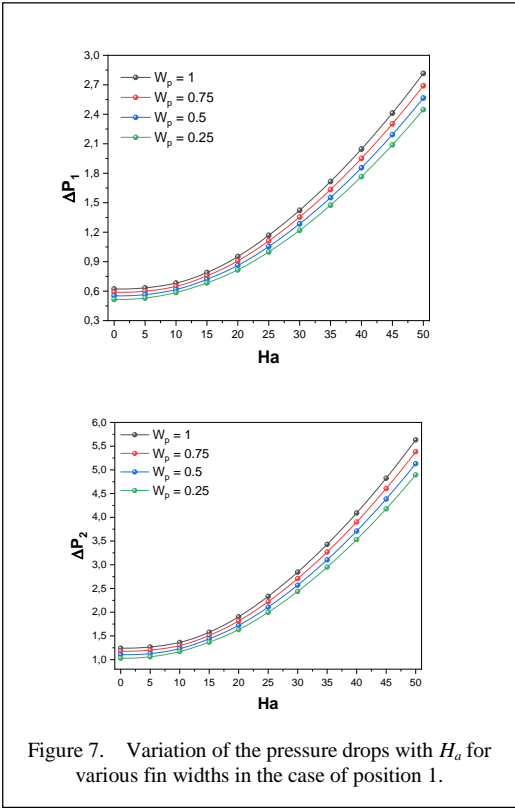


Figure 7. Variation of the pressure drops with H_a for various fin widths in the case of position 1.

improved heat transfer at the right wall until a Hartman number value of approximately 20 is reached. Beyond this value, the effect of H_a becomes more significant than that of the fin width. Increasing the W_p reduces the distance between the fin and the first hot source until it vanishes at $W_p = 1$. The nanofluid can then no longer effectively transport the heat released away from the source, decreasing the heat transfer rate. In contrast, Nu_{ml} evolves oppositely, where the highest heat transfer rates are obtained when $W_p = 1$. This behavior can be explained by the fact that increasing W_p forces the fluid flowing over the fin to contact the left-hand heated source over a long length, resulting in greater heat release.

It is expected to notice an increase in ΔP_1 and ΔP_2 with the rise in H_a and W_p , as displayed in Fig. 7. This is because strengthening the Lorentz force results in slower nanofluid flow and raising the width of the fin leads to a higher resistance against fluid motion due to the larger volume.

V. CONCLUSION

This study investigates the impact of a magnetic field and a solid-porous fin on heat transfer and pressure drop in an open cavity. Based on the analysis, the following are the primary outcomes:

The heat transfer rate declines at low Hartmann numbers but grows with higher magnetic field intensity.

In the first compartment, Position 1 is the most thermally efficient. In the second compartment, the solid fin is the most effective before $H_a = 15$. Beyond this value, Position 3 leads to a maximum heat exchange rate.

Concerning the effect of the fin width, a decrease in W_p leads to an improved heat transfer at the right wall and, oppositely, at the left wall.

The pressure drop is increased with H_a and W_p and is nearly independent of the position of the porous portion in the fin. Nevertheless, its presence lowers ΔP compared to a solid fin.

Using a compact and straightforward geometrical configuration such that in the current study, it is possible to absorb high heat densities generated by electronic power modules while achieving energy savings for the entire system.

Further research can be conducted to explore the entropy generation analysis and the impact of other variables, such as the permeability,

dimensions, number, and inclination of the solid-porous fin and the mixed convection parameter. These additions will enhance the numerical findings of the present investigation and strengthen their prospective applicability.

REFERENCES

- [1] Kasaeipoor, A., Ghasemi, B., & Aminossadati, S. M. (2015). Convection of Cu-water nanofluid in a vented T-shaped cavity in the presence of magnetic field. *International Journal of Thermal Sciences*, 94, 50-60.
- [2] Fersadou, B., Kahalerras, H., Nessab, W., & Hammoudi, D. (2019). Effect of magnetohydrodynamics on heat transfer intensification and entropy generation of nanofluid flow inside two interacting open rectangular cavities. *Journal of Thermal Analysis and Calorimetry*, 138, 3089-3108.
- [3] Du, R., Gokulavani, P., Muthamilselvan, M., Al-Amri, F., & Abdalla, B. (2020). Influence of the Lorentz force on the ventilation cavity having a centrally placed heated baffle filled with the Cu-Al₂O₃-H₂O hybrid nanofluid. *International Communications in Heat and Mass Transfer*, 116, 104676.
- [4] Geridönmez, B. P., & Öztıp, H. F. (2021). Effects of partial magnetic field in a vented square cavity with aiding and opposing of MWCNT-water nanofluid flows. *Engineering Analysis with Boundary Elements*, 133, 84-94.
- [5] Selimefendigil, F., Öztıp, H. F., & Izadi, F. (2022). Non-uniform magnetic field effects on the phase transition dynamics for PCM-installed 3D conic cavity having ventilation ports under hybrid nanofluid convection. *Journal of Building Engineering*, 49, 104074.
- [6] Selimefendigil, F., & Öztıp, H. F. (2023). Forced convection of nanofluid in double vented cavity system separated by perforated conductive plate under magnetic field. *Engineering Analysis with Boundary Elements*, 149, 18-26.
- [7] Kolsi, L., Selimefendigil, F., Omri, M., Rmili, H., Ayadi, B., Maatki, C., & Alshammari, B. M. (2023). CFD study of MHD and elastic wall effects on the nanofluid convection inside a ventilated cavity including perforated porous object. *Mathematics*, 11, 695.
- [8] Tiwari, R. K., & Das, M. K. (2007). Heat transfer augmentation in a two-sided lid-driven differentially heated square cavity utilizing nanofluids. *International Journal of Heat and Mass Transfer*, 50, 2002-2018.
- [9] Patankar, S. V. (1980). *Numerical heat transfer and fluid flow*. Mc Graw-Hill, New York.

Developing Policy Schemes for Grid-scale Microgrids - A Case Study of the USA

Mohammad Hassan Bahmani¹, Amir Niroomandfam², Masood Yahyaei³

¹Tarbiat Modares University, Tehran, Iran

²Sahand University of Technology

³Islamic Azad University Central Tehran Branch, Tehran, Iran

^{1,2,3}Saba Power and Energy Group, Tehran, Iran

¹Mh.Bahmani@Modares.ac.ir, ²Niroomandfam@sabapeg.ir, ³M.Yahyaei.eng@iauctb.ac.ir

Abstract—Microgrids face significant obstacles in three crucial areas: technical, financial, and regulatory, which hinder their ability to achieve optimal integration. Extensive research indicates that these challenges necessitate a coordinated approach for effective resolution. This research delves into the financial flows associated with microgrid investment and employs an economic viability analysis to assess the financial dimensions of microgrid investment as potential business opportunities in the United States. The paper quantifies the costs and revenues involved in a microgrid investment, with a particular emphasis on assessing the impact of fluctuations in interest rates over the past decade on the feasibility of microgrid investment as a viable business option in the US economic landscape. Furthermore, as the capacity of financial platforms is evaluated concerning their ability to tackle the development challenges of microgrids, the imperative of formulating novel policy schemes and regulatory platforms to augment the grid-scale penetration of microgrids is deliberated.

Keywords – microgrids, policy schemes, financial analysis

I. INTRODUCTION

Microgrids are recognized as clusters of distributed energy resources that rely on integrated control systems to effectively coordinate various forms of distributed generation, including intermittent renewables, demand response, and energy storage units [1]. The development of microgrids offers a multitude of benefits for diverse stakeholders,

such as investors and grid operators. Extensive research and academic literature have extensively investigated these advantages [2,3].

Microgrids are positioned as fundamental components for enhancing the flexibility and resilience of future power networks [4,5]. They have the potential to enhance grid reliability, facilitate local active and reactive power generation, and enable island operation capabilities [6]. Additionally, microgrids play a crucial role in mitigating global environmental challenges by facilitating the integration of higher levels of renewable energy generation [7,8]. However, the integration of microgrids into power grids on a large scale is hindered by various challenges, particularly financial and regulatory barriers [9,10]. These challenges must be addressed to achieve a satisfactory level of integration for microgrids.

In this regard, grid-scale microgrids have garnered significant attention in recent years as a promising solution for enhancing energy resilience [4], reducing carbon emissions [7], and promoting distributed energy generation [11]. To support the successful deployment of grid-scale microgrids, it is crucial to develop effective policy schemes that address technical, economic, regulatory, and social aspects.

Several countries and regions have recognized the potential of grid-scale microgrids and have implemented policy frameworks to facilitate their development [12]. In the United States, various federal, state, and local initiatives

have been introduced to promote the deployment of grid-scale microgrids [12]. These initiatives include financial incentives, regulatory reforms, and research and development programs. For instance, the Federal Energy Regulatory Commission (FERC) Order 2222 enables the participation of aggregated distributed energy resources, including microgrids, in wholesale electricity markets [13].

Interconnection standards play a crucial role in enabling the integration of grid-scale microgrids into existing power systems [14]. In recent years, regulatory reforms have been initiated to streamline the interconnection process and ensure grid compatibility. The Institute of Electrical and Electronics Engineers (IEEE) has developed standards such as IEEE 1547 and IEEE 2030.7, which provide guidelines for the interconnection of microgrids and ensure their safe and reliable operation [15].

To incentivize the development of grid-scale microgrids, financial mechanisms, and business models have been introduced. These include feed-in tariffs, tax credits, grants, and performance-based incentives. In the United States, the Investment Tax Credit (ITC) and Production Tax Credit (PTC) have played a significant role in encouraging investment in renewable energy projects, including microgrids [16,17]. The successful deployment of grid-scale microgrids also relies on community engagement and social acceptance. Policies encouraging community participation, such as community-owned microgrids or shared savings programs, can enhance acceptance and promote local benefits. Additionally, policies that consider the social and environmental impacts of microgrid projects can ensure equitable distribution of benefits and address potential concerns [18].

Despite the progress made in developing policy schemes for grid-scale microgrids, several challenges remain. These challenges include regulatory complexities, technical integration issues, market barriers, and financing constraints.

The development of effective policy schemes is crucial for the successful deployment of grid-scale microgrids. This paper considering the highlights in the advancements of policy frameworks, regulatory reforms, financial incentives, and community engagement efforts, discusses the capacity of financial structures to

help the promotion of grid-scale microgrids in the United States.

As part of a comprehensive effort to improve the United States electrical grid, this paper focuses on the role of financial structures in identifying and addressing the challenges faced by microgrid developments. The paper introduces a platform that thoroughly examines the financial aspects influencing the revenue and cost cycle of microgrid development. By employing a net present value (NPV) based economic analysis, the paper explores various business models and assesses the impact of fluctuating interest rates in the United States on the financial viability of microgrid investments. This research aims to provide authorities with a better understanding of the financial considerations involved in microgrid development and their implications for decision-making.

In this context, section two of the paper provides an initial definition of the cost and revenue parameters that constitute the financial cycle of microgrid investment. It also introduces the framework employed to evaluate the feasibility of microgrid investment as a viable business option. Moving forward, section three examines the presented framework through a case study and conducts a sensitivity analysis to validate the reliability of the framework's outcomes. Finally, section four concludes the paper by summarizing the key findings and implications.

II. MICROGRID AS BUSINESS INVESTMENT

To assess microgrids as business models the financial flow of microgrids considering the characteristics of the US economy is investigated. Fig. 1, shows the platform in which the investigations are carried out for this purpose [10]. In this platform in section A, the parameters of revenue and cost flow are investigated and quantified. In section B, five conceptual business models are presented and discussed and in section C, an economic viability analysis using a simple Net Present Value (NPV) method is performed to financially assess the models.

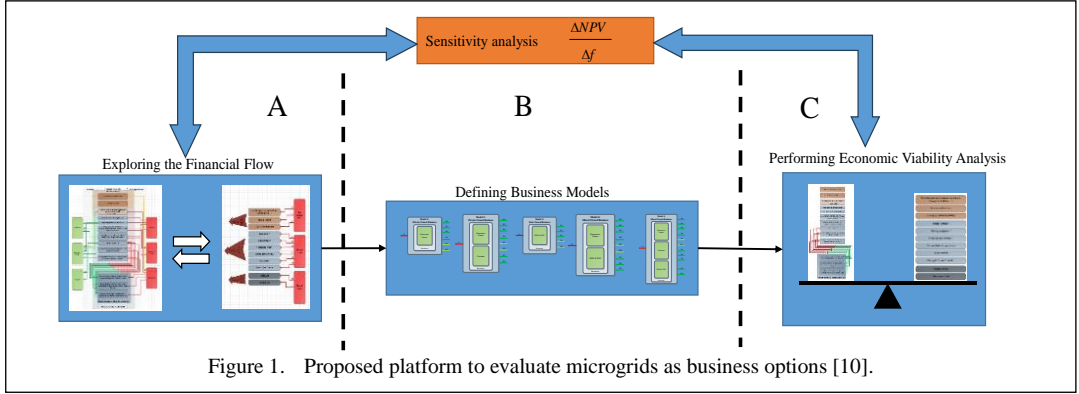


Figure 1. Proposed platform to evaluate microgrids as business options [10].

A. Quantifying the Financial Terms

As shown in Fig. 1, revenue and cost flows in the financial assessment of microgrid development consist of various terms, which is discussed in detail in [10]. To be able to formalize the economic evaluation of microgrid investment as a business option, these terms are quantified in the following. as shown in Eq. (1) is taken into account for the cost flow:

$$C_T = C_{DER_Inv} + C_{\mu Grid_Inv} + C_{\mu Grid_Op} \cdot (1)$$

In this equation, the terms are respectively, cost of Distributed Energy Resource (DER) investment, additional costs to enable microgrid capabilities for a DER, and costs of microgrid operation which are discussed and quantified later in this section.

Accordingly, microgrid operation cost as presented in Eq. (2), is calculated as projected costs of DERs operation, the cost of energy purchase from the main grid, and finally the customers interruption costs. Generation costs for nondispatchable units and energy storage systems are assumed, zero.

$$C_{Mgrid-Op}: \sum_{n=1}^{N_p} \alpha_{Interest-rate} \sum_{D=1}^{365} \sum_{t=1}^3 \alpha_{Operation-Cost} \times P_{G-D_{tD}} \times T + \sum_{n=1}^{N_p} \alpha_{Interest-rate} \sum_{D=1}^{365} \sum_{t=1}^3 \left[L_{tD}^{MG} - \left(P_{G-D_{tD}} + a \times P_{G-ND_{tD}} \right) \right] \times \rho_{price_{tD}} \times T + , (2) + \sum_{n=1}^{N_p} \alpha_{Interest-rate} \times CIC^{microgrid}$$

$$CIC = P_{av} SAIFI c_{ref}^C(0^+) + P_{av} SAIDI \left. \frac{dc_{ref}}{dr} \right|_{r=r_a}, (3)$$

$$C_{DER-Inv}: \sum_{n=1}^{N_p} \alpha_{Interest-rate} \times (CC_{Dis} \times P_{G-Dis}^{Max} + CC_{NDis} \times P_{G-NDis}^{Max} + (CP_{Storage} \times P_{Storage}^{Max} + CE_{Storage} \times C_{Storage}^{Max})) . (4)$$

In Eq. (2), three load levels are considered for each day as, peak, shoulder, and off-peak with equal duration, T . $P_{G-D_{tD}}$ is the dispatchable unit output at time t , and day D , $a \times P_{G-ND_{tD}}$ is the average output considered for non-dispatchable unit during period T and day D . $\alpha_{Interest-rate}$ is the considered interest rate while $CIC^{Microgrid}$ and L_{tD}^{MG} are respectively the micro-grid customer interruption cost and micro-grid load at time t and the day D of the year. Also N_p is the number of the years of the planning horizon. CIC is calculated using Eq. (3).

Generation facility and sitting plant investment costs are calculated in Eq. (4). In Eq. (4), P_{G-Dis}^{Max} , P_{G-NDis}^{Max} , $P_{Storage}^{Max}$ and $C_{Storage}^{Max}$ are respectively the rated powers of dispatchable, non-dispatchable, and storage units and the rated capacity of the storage system.

Equation (5), calculates the revenue obtained due to the deferred investment, regarding the microgrid establishment effect on peak shading.

where, $DP^{Microgrid}$ as is calculated in (6), is the deferred investment period resulting from microgrid establishment.

$$R_3: DP^{Microgrid} \times \left(CC_{Dis} \times (P_{G-D_{t_D}} + a \times P_{G-ND_{t_D}}) \right) \times \alpha_{Interest-Rate} , \quad (5)$$

$$DP^{Microgrid} = \frac{1}{\alpha_{Annual-Load-Growth}} \times \left[\left(\frac{L_{Annual-Peak-Network}}{L_{Annual-Peak-Network} - (P_{G-D_{t_D}} + a \times P_{G-ND_{t_D}})_{t=Annual-Peak-Network}} \right) - 1 \right] , \quad (6)$$

In Eq. (6) $L_{Annual-Peak-Network}$ is the annual peak of the network where the microgrid is established, and $\alpha_{Annual-Load-Growth}$ is the estimated annual demand growth for the study network.

In Eq. (7), revenue regarding the increased reliability for microgrid participants is presented.

$$R_5: ECOST^{Micro-Grid} = CIC^{ref-Micro-Grid} - CIC^{Microgrid} . \quad (7)$$

Reliability increase benefits are calculated as the enhancement in customer interruption costs. In Eq. (7), $CIC^{ref-Micro-Grid}$ is the customer interruption cost of the microgrid participants when the microgrid is not yet installed, and $CIC^{Microgrid}$ is the interruption cost for microgrid participants when it is installed.

Network utilization quality enhancement benefits, regarding microgrid presence calculated based on customer interruption, cost as the following:

$$R_6 + R_7 + R_{11}: ECOST = CIC^{ref-Grid} - CIC^{Grid+Microgrid} , \quad (8)$$

where $CIC^{ref-Grid}$ is the customer interruption cost for the grid and $CIC^{Grid+Microgrid}$ is the customer interruption cost for the grid when the microgrid is installed. Equation (9) calculates the benefits of microgrids regarding their impact on

loss reduction. For this purpose, grid loss costs are compared with and without microgrid presence.

In Eq. (9), $COST(Loss^{Grid})$ is the cost of grid loss when no microgrid is established, and $COST(Loss^{Grid+Microgrid})$ is the cost of grid loss in the presence of the microgrid. Equation (10), shows microgrid income regarding energy sales. The first part calculates the benefit equal to the cost of purchasing energy from the main grid in case the microgrid is unavailable, and the second part calculates the income regarding the sale of the excess energy to the main grid, at the K_{MES} times the price of energy purchase from the grid. Where K_{MES} is supposed to represent the interconnection tariff policy. It is assumed in this paper, that the grid operator is obligated to purchase all the microgrid surplus energy.

B. Conceptual Business Models

In this paper, five different investment models allow the investors access to different revenue systems, under three main categories, namely Private investment, State-owned, and mixed investment (three mixed investment models contain, Customer-State investment, private investor - State investment, and costumer-private Investor-State investment), are discussed. Five business models presented in this paper are carefully set to contain each possible form of microgrid ownership. Microgrids are either, invested and operated by private investors or they are owned and utilized by state-owned

$$R_1 + R_4: COST(Loss^{Grid}) - COST(Loss^{Grid+Microgrid}) . \quad (9)$$

$$R_8 + R_9: \left[\sum_{n=1}^{N_p} \alpha_{Interest-rate} \sum_{D=1}^{365} \sum_{(P_{G-D_{t_D}} + a \times P_{G-ND_{t_D}}) \leq L_{t_D}^{MG}} (P_{G-D_{t_D}} + a \times P_{G-ND_{t_D}}) \times \rho_{price_{t_D}} \times T \right] + \left[\sum_{n=1}^{N_p} \alpha_{Interest-rate} \sum_{D=1}^{365} \sum_{(P_{G-D_{t_D}} + a \times P_{G-ND_{t_D}}) \geq L_{t_D}^{MG}} \left[(L_{t_D}^{MG} \times \rho_{price_{t_D}} \times T) + \left((P_{G-D_{t_D}} + a \times P_{G-ND_{t_D}}) - L_{t_D}^{MG} \right) \times \rho_{price_{t_D}} \times K_{MES} \times T \right] \right] . \quad (10)$$

$$NPV = \sum_{t=0}^n (B_t - C_t) / (1 + i)^t = \frac{\sum_{t=0}^n (B_t - C_t)}{P_{f,i,t}}, \quad (11)$$

where: $C_t = \sum^t C_T$,
 $B_t = \sum^t \sum_{j=1}^{11} R_j$.

entities, or a mixture of these forms could be considered. To ensure the comprehensiveness of the introduced models, private investment is assumed to contain forms of microgrid participants' investment and a third-party private investor, to make possible the assessment of various structures of revenue flow.

C. Economic Viability Analysis

There are various aspects to the economic evaluation of an investment project. The NPV analysis method is used in this study because, in addition to being comprehensive, it is also simple. The minimum acceptable rate of return (MARR) value can be considered equal to the interest rate, and as the funding resources are presumed unlimited, then any project rejected by this method can decisively be considered a no option. Net present value (NPV) is calculated as in Eq. (11).

Where, n shows the number of years for the planning horizon. B_t and C_t in Eq. (11) are respectively the income and expense value for the year t and i is the interest rate which is considered equal to the minimum acceptable rate of return (MARR) value for the sake of analysis.

III. DISCUSSING THE RESULTS

In this paper, US national power grid data containing hourly electricity prices, reliability indices, investment costs, and demand growth data are utilized for the case study [19]. Fig. 2, shows the results of NPV analysis of the discussed microgrid business models for the case study. The current contribution tries to explore the potential and capacity of financial frameworks to address the challenge by evaluating microgrids as business models. As shown in Fig. 2, the level of economic attractiveness for business models increases, as more entities are involved in microgrid foundation. That is because the financial structure in the current microgrid financial flow has deficiencies in the appropriate allocation of financial interests as discussed earlier. Rather than that, the results suggest a state investment over private investment, as the current state of financial structure enables state entities to enjoy the advantages of microgrid establishment more

than private investors. For the sake of simplicity, analyses are done using per-unit values, where numbers are measured as a portion of the cost for generation plant installation.

Fig. 3 illustrates the US 90-day annual average interest rate for financial commercial paper over the past 10 years [20]. The data reveals a range of interest rates experienced in the US during this period, spanning from approximately 0.1 percent to 5.5 percent in 2023. In Fig. 2, the results of the Net Present Value (NPV) analysis for the five examined business models are presented across different interest rate ranges. The findings demonstrate that microgrid investment, as a viable business option, is deemed unfeasible for interest rates around 1 percent or higher. For interest rates around 1.5 percent, the analysis indicates that an external resource injection of approximately 0.2 Pu (equivalent to 20 percent of the cost of the generation plant installation) is necessary to render the investment economically viable. At a 5 percent interest rate, a minimum of 0.6 Pu in

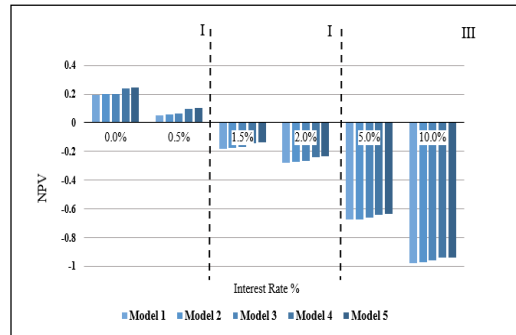


Figure 2. Results of NPV evaluation.

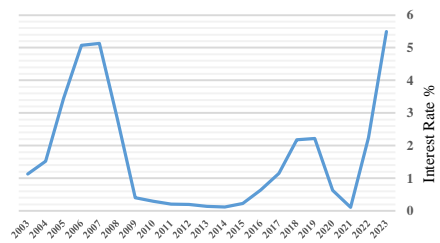


Figure 3. US 90-Day Annual Average Financial Commercial Paper Interest Rate.

subsidies is required, and for interest rates around 10 percent, subsidies of approximately 0.9 Pu are needed to make the microgrid investment in the case study financially acceptable. These findings highlight the fluctuating nature of microgrid investment as a financially justifiable business option in the US over the past decade, necessitating regulatory interventions in certain cases.

Model 5 represents a scenario where all entities participate in the establishment of the microgrid, without considering their contribution share. This ensures a fair allocation of revenue sources, as all the benefits derived from the microgrid are assigned to its investors. This is comparable to the outcomes of a revised allocation structure, where the benefits of microgrid establishment are directed toward the appropriate entities. Table I, presents the results of the sensitivity analysis conducted for NPV evaluation, considering various parameters. Specifically, sensitivity analysis was performed for models 1, 3, and 5 at a 2% interest rate. Selected parameters were chosen due to the possible adoption of different supportive policies regarding microgrids or the fact that they may vary significantly from one grid to the other [21]. The results of the analysis confirm that the NPV results are more dependent on adopted policies (ρ_{price}) as energy price and a supportive interconnection tariff policy) than the inherent technical grid specifications and features (like the cost-of-service interruption). Economic analysis results from high sensitivity to interconnection tariff strategies ($\frac{\Delta NPV}{\Delta K_{MES}}$) as suggested by Table I, confirm the efficiency of defining tariff policy as a functional government-

tal supportive strategy to help increase microgrid penetration.

The negligible effect of pollution costs on the NPV results ($\frac{\Delta NPV}{\Delta \rho_{Mit-Pollu-Price}}$) shows the need for supportive policies to invigorate the financial incentives of microgrid establishment in promoting renewable penetration, as a solution to global pollution challenges. The comparison of the NPV results for different business models also reveals the limited capacity of the financial mechanisms to engage the microgrid development challenges. It also confirms that an attempt solely based on modification of the current structure of microgrid financial flow to make microgrid investment an economically competitive option, wouldn't be sufficient, and an exploration of untapped microgrid potentials is also needed.

IV. CONCLUSIONS

The current financial flow of microgrids exhibits deficiencies and resource misallocation that require proper attention. The economic viability of microgrid investment as a business option depends on various factors, including regional characteristics, power network conditions, and the characteristics of microgrid participants. However, the findings of a case study using a net present value (NPV) economic analysis indicate that solely modifying the existing financial structure will not significantly improve the viability of microgrid systems in all regions. Therefore, it is necessary to explore additional revenue sources and investigate supportive governmental policies and regulatory platforms to address the challenges of microgrid development. Furthermore, there are untapped potentials in leveraging microgrids to establish more resilient and flexible power systems, which are key priorities for governments. These potentials should be translated into new incentives to encourage increased participation in microgrid investments. These regulatory interventions play a pivotal role in addressing the financial obstacles that hinder the advancement of microgrids. Such interventions are crucial in creating a supportive framework that encourages investment and fosters the growth of microgrid projects. By establishing clear and favorable regulations, policymakers can provide incentives for private sector participation and attract capital for microgrid development. Additionally, regulatory interventions can help streamline the

TABLE I. NPV SENSITIVITY ANALYSIS.

Parameter	Description	$\Delta NPV/\Delta f$		
		Model 1	Model 3	Model 5
ρ_{price}	Energy Price	3.7721	4.3872	5.1097
K_{MES}	The ratio of the price of energy purchased from the microgrid to the main grid energy price	1.5228	1.5821	1.8292
CI	Cost of Service Interruption	0.0367	0	0.0441
$\rho_{Mit-Pollu-Price}$	Pollution Price	0	0.0861	0.0990

process of obtaining permits and approvals, reducing the administrative burden and associated costs. Furthermore, well-designed regulations can facilitate fair and transparent pricing mechanisms, ensuring that microgrid operators can generate sufficient revenue to sustain their operations.

To expand the future directions of this study, additional aspects can be explored. These may include investigating the potential impact of various financial incentive policies in facilitating microgrid investments as a business option. Such policies could encompass supportive measures like defining interconnection tariffs, establishing carbon cost regulations, and offering initial investment subsidies. Furthermore, the future researches can delve deeper into examining the role of different regulations in promoting the implementation of grid-scale microgrids. By exploring these areas, the future studies can provide a more comprehensive understanding of the factors influencing the success of microgrid investments and offer valuable insights for future regulatory and policy developments.

REFERENCES

- [1] Shi, J., Ma, L., Li, C., Liu, N., & Zhang, J. (2022). A comprehensive review of standards for distributed energy resource grid-integration and microgrid. *Renewable and Sustainable Energy Reviews*, 170, 112957.
- [2] Boche, A., Foucher, C., & Villa, L. F. L. (2022). Understanding microgrid sustainability: A systemic and comprehensive review. *Energies*, 15(8), 2906.
- [3] Trivedi, R., Patra, S., Sidqi, Y., Bowler, B., Zimmermann, F., Deconinck, G., ... & Khadem, S. (2022). Community-based microgrids: Literature review and pathways to decarbonise the local electricity network. *Energies*, 15(3), 918.
- [4] Hamidieh, M., & Ghassemi, M. (2022). Microgrids and resilience: A review. *IEEE Access*.
- [5] Debouza, M., Al-Durra, A., EL-Fouly, T. H., & Zeineldin, H. H. (2022). Survey on microgrids with flexible boundaries: Strategies, applications, and future trends. *Electric Power Systems Research*, 205, 107765.
- [6] Kostenko, G., & Zaporozhets, A. (2023). Enhancing of the power system resilience through the application of micro power systems (microgrid) with renewable distributed generation. *System Research in Energy*, 3 (74), 25-38.
- [7] Shahzad, S., Abbasi, M. A., Ali, H., Iqbal, M., Munir, R., & Kilic, H. (2023). Possibilities, Challenges, and Future Opportunities of Microgrids: A Review. *Sustainability*, 15(8), 6366.
- [8] Kiehadrouinezhad, M., Hosseinzadeh-Bandbafha, H., Rosen, M. A., Gupta, V. K., Peng, W., Tabatabaei, M., & Aghbashlo, M. (2023). The role of energy security and resilience in the sustainability of green microgrids: Paving the way to sustainable and clean production. *Sustainable Energy Technologies and Assessments*, 60, 103485.
- [9] Norouzi, F., Hoppe, T., Elizondo, L. R., & Bauer, P. (2022). A review of socio-technical barriers to Smart Microgrid development. *Renewable and Sustainable Energy Reviews*, 167, 112674.
- [10] Bahmani, M. H., Haghifam, M. R., & Miri Larimi, S. M. (2019). Toward grid- scale microgrids; evaluating the capacity of financial structures. *IET Generation, Transmission & Distribution*, 13(7), 1057-1067.
- [11] Twaisan, K., & Barışçı, N. (2022). Integrated Distributed Energy Resources (DER) and Microgrids: Modeling and Optimization of DERs. *Electronics*, 11(18), 2816.
- [12] Chartier, S. L., Venkiteswaran, V. K., Rangarajan, S. S., Collins, E. R., & Senjyu, T. (2022). Microgrid emergence, integration, and influence on the future energy generation equilibrium—A Review. *Electronics*, 11(5), 791.
- [13] Cartwright, E. D. (2020). FERC order 2222 gives boost to DERs. *Climate and Energy*, 37(5), 22-22.
- [14] Rebolal, D., Carpiñero-Rentería, M., Santos-Martín, D., & Chinchilla, M. (2021). Microgrid and distributed energy resources standards and guidelines review: Grid connection and operation technical requirements. *Energies*, 14(3), 523.
- [15] Danley, D. R. (2019). Defining a Microgrid Using IEEE 2030.7. *Business & Technology Surveillance*.
- [16] Liu, J., Ou, M., Sun, X., Chen, J., Mi, C., & Bo, R. (2022). Implication of production tax credit on economic dispatch for electricity merchants with storage and wind farms. *Applied Energy*, 308, 118318.
- [17] Keightley, M. P., Marples, D. J., & Sherlock, M. F. (2019). Tax Equity Financing: An Introduction and Policy Considerations. *Congressional Research Service Report*, 45693.
- [18] Parag, Y., & Ainspan, M. (2019). Sustainable microgrids: Economic, environmental and social costs and benefits of microgrid deployment. *Energy for Sustainable Development*, 52, 72-81.
- [19] Barrows, C., Bloom, A., Ehlen, A., Ikäheimo, J., Jorgenson, J., Krishnamurthy, D., ... & Watson, J. P. (2019). The IEEE reliability test system: A proposed 2019 update. *IEEE Transactions on Power Systems*, 35(1), 119-127.
- [20] Board of Governors of the Federal Reserve System (2023). *Selected Interest Rates*. Available at: <https://www.federalreserve.gov/releases/h15/>
- [21] Niromandfam, A., & Niromandfam, R. Distribution Grid Reliability Improvement Considering Electricity Customers' Satisfaction based on the Kano Model. *eNergetics 2022*, 131.

Lab-scale Assessment of Biogas Generation using Seaweed in Northeast Brazil

Mikaely Renaly Carlos da Silva^{1*}, Sayonara A. Eliziario², João Marcelo Dias Ferreira³

¹Graduate Program in Mechanical Engineering, Federal University of Paraíba, João Pessoa, Brazil

^{2,3}Department of Renewable Energy Engineering, Federal University of Paraíba, João Pessoa, Brazil

¹mikaely.silva@alumni.cear.ufpb.br, ²sayonara@cear.ufpb.br, ³ferreira@cear.ufpb.br

Abstract—The need to reduce the consumption of fossil fuels has led to increased incentives and the use of technologies that utilize renewable, clean, and sustainable resources to diversify the national and global energy matrix. In this context, the energy conversion of biomass and the production of energy from organic waste represent important contributions. Anaerobic digestion is a natural biological process in which anaerobic microorganisms generate biogas, which can be used as an energy source in three ways: thermal (utilizing heat), electrical (by converting gas into electrical energy through generators), and as a biofuel (bio methane CH₄ > 96%). The objective of the study was to evaluate biogas production using marine algae as the raw material. To this end, concentrations of Total Volatile Solids (a parameter related to the biodegradable fraction of the substrate - organic matter) were analyzed. Three bench-scale digesters were produced: one containing only marine algae as a substrate, another containing marine algae and sugarcane juice inoculum, and the third containing marine algae and tapioca starch inoculum. These digesters were observed for 22 days. From the analysis of the total solid content, fixed and volatile, it was possible to observe a significant volatile content, an important factor for the biogas production potential of a substrate. It is demonstrated that biogas production from marine algae represents a promising and sustainable avenue for addressing some of the most pressing global challenges. The potential of this renewable energy source is

multifaceted, with far-reaching implications for our environment, economy, and society.

Keywords – anaerobic digestion, bioenergy, total fixed solids, total volatile solids, total solids, seaweed, macroalgae

I. INTRODUCTION

Due to the increasing energy demand, the generation of energy from alternative and renewable sources aims to reduce the environmental impact generated by polluting sources such as oil and its derivatives. In order to improve the quality of life, the search for the development of technologies to reduce environmental impacts through primary and renewable sources has grown. However, these technologies are expensive, and in order to lower costs and achieve better results, research is of fundamental importance to make the system favorable for use [1].

Biomass is one of the most commonly used sources for energy generation, as its resource is abundant, renewable, and sustainable, not posing a risk of carbon dioxide accumulation in the Earth's atmosphere, unlike energy produced from fossil fuels [2]. Bioenergy production from decomposing organic matter can be obtained through the utilization of plant residues, such as marine algae, plants, waste from agricultural activities, including animal waste, and other

*Supervisor: Monica Carvalho - Renewable Energy Engineering Department/Federal University of Paraíba (UFPB), João Pessoa, Brazil

residues from industrial and urban effluents [3,4].

The anaerobic digestion process, as an option for waste treatment, presents an excellent alternative that can be applied in the agro-industrial sector, especially in properties with confined or semi-confined animal farming, residential wastewater treatment plants, and the management of urban organic waste [5-7].

For non-woody plants, which include aquatic residues such as marine algae, the anaerobic digestion process can lead to biogas production. The main resulting products of this treatment process are biogas, primarily composed of methane (CH_4) and carbon dioxide (CO_2), also containing small quantities of hydrogen (H_2), ammonia (NH_3), other gases, and sludge [8]. Methane obtained as a result, if properly filtered, represents a renewable source of energy, in addition to its sanitary and environmental functions. Therefore, the production of energy from biogas is gaining importance, and its use for energy purposes represents a saving of environmental resources, as well as the reduction of sewage pollutants and the elimination of methane released into the biosphere [4,7].

Seaweed, also known as marine algae, holds significant importance for biogas production [9]. Marine algae is a renewable resource that grows abundantly in the oceans. Its cultivation does not require arable land, freshwater, or the use of fertilizers, making it a sustainable biomass source. Also, high biomass production rates are obtained compared to land-based crops, and algae has a rapid growth rate [10].

As marine algae is grown in the ocean, it does not compete with other land uses or require substantial amounts of freshwater for irrigation. Usually, its cultivation has a low environmental impact, as it can help absorb excess nutrients from the water and provide habitat for marine life [11].

Marine algae captures and stores carbon dioxide during its growth [12], which can contribute to carbon sequestration and help mitigate climate change. There is also a high potential for biogas production, as algae is rich in organic matter, and its anaerobic digestion can produce biogas, mainly methane which is a valuable source of renewable energy. Besides these clear environmental benefits, biogas production from marine algae can also realize economic benefits, associated with the creation

of jobs and energy independence. Social benefits can also be observed, such as community development and health benefits associated with the use of biogas instead of fossil fuels. Therefore biogas production from marine algae can contribute to sustainability goals in various ways, offering environmental, economic, and social benefits.

However, it is essential to consider the specific characteristics and challenges of seaweed-based biogas production [13], such as optimizing the digestion process, addressing variability in seaweed composition, and minimizing environmental impacts associated with cultivation and harvesting. Additionally, research and development efforts are ongoing to improve the efficiency and scalability of seaweed-based biogas production technologies [14].

The motivation for this work was to analyze the potential use of marine algae biomass for energy purposes, where it was possible to verify the feasibility of use in the biogas production process.

II. METHODOLOGY

The organic material chosen for this work was marine algae, obtained at the Seixas Beach (7.1548°S, 34.7932°W), located in the municipality of João Pessoa, Paraíba (Northeast Brazil). The experiment was conducted at the Laboratory of Materials and Environmental Chemistry (LabMaQ) at the Center for Alternative and Renewable Energy (CEAR) of UFPB (Federal University of Paraíba).

Three bioreactors were built using three 600ml glass containers, where three valves were used to block and release the gas produced for analysis when necessary. A manometer was used to measure pressure.

The laboratory-scale tests were conducted with different materials: one biodigester was filled with marine algae biomass and tapioca starch inoculum, the second digester was filled with marine algae biomass and sugarcane juice inoculum, and third was filled with marine algae biomass. The inoculants were used to activate the reactor and accelerate gas production.

Initially, the substrates were homogenized and crushed in an industrial blender, and then placed in the bio digesters. Rapid fermentation of the substrates was observed. A limitation of the substrate was that leaks were verified in the bio

digester valves, leading to the impossibility of measuring adequately biogas production and its components.

Fig. 1 shows the three bioreactors. The leftmost bioreactor contains only marine algae, the middle one contains sugarcane juice inoculum, and the right one contains tapioca starch inoculum. The accumulation time was 22 days, with daily monitoring of biogas production. This was the available period for the experimental tests, due to personnel and administrative constraints. The tests were carried out at environmental conditions, to establish a reference for future studies.

Sample preparation: Initially, the natural biomass underwent a cleaning process to remove solid materials such as small leaves and small solid residues before being subjected to analysis. Fig. 2 shows the algae used in this research. The tests were conducted in triplicate, and the results represent the arithmetic average of these. Before the entire analysis procedure was carried out, the samples were weighed on a precision scale.

With the biomass dried after removing all the moisture, it was possible to determine the solids content. To carry out the analysis of solids



Figure 1. Biodigesters used in the study.



Figure 2. *In Natura* biomass.



Figure 3. AND MF-50 moisture scale.

content, a muffle furnace (Zezimaq 2000 F) was used, where the analyzed sample was placed in the muffle furnace at a temperature of 550°C, with each sample left for one hour.

Determination of solids content: The determination of solids content was performed following the NBR 10664 standard [15]. To calculate the solids content, it was necessary to remove the moisture from the sample, using a digital moisture balance (Fig. 3), with three samples, each containing approximately 25g of the natural biomass. The process is straightforward, requiring proper handling of the moisture scale.

For this stage, 600 mL bio digesters were used, and the amount of inoculum was equivalent to 20% of the total biomass mass used. Data are presented in Table I. Due to the availability of raw material, tests were conducted in triplicate.

TABLE I. BIODIGESTER VOLUME, AMOUNT OF BIOMASS, AND INOCULUM IN EACH REACTOR.

Biodigester (mL)	Biomass (g)	Inoculum (g)
600	89.6334	17.9267
600	87.7379	17.5476
600	89.2037	0

III. RESULTS AND DISCUSSION

With the analyzed samples, it was possible to determine the moisture content of 41.90% in the algae. It is essential to know the moisture content because moisture contributes to a more efficient fermentation and, consequently, a higher biogas production [16].

It is important to understand that these results are obtained in laboratory settings, where the

environment for bacterial development is controlled. In practice, biogas production can vary due to factors such as temperature, pH, and the type of bioreactor used.

The production of biogas can vary depending on the bioreactor employed, so it is essential to understand the parameters of the substrate used. Table II shows the results obtained for total solids (TS), fixed solids (FS), and volatile solids (VS).

For comparison purposes, Table III presents some parameters for other substrates.

Comparing the results of Tables II and III, the fixed solids content of marine algae is similar to that of chicken manure, municipal waste, and organic waste.

TABLE II. SOLID CONTENT: TOTAL, FIXED, AND VOLATILE.

	Concentration (%)
Total Solid Content	58.1000
Fixed solid content	34.6880
Volatile solid content	65.6522

TABLE III. TOTAL AND VOLATILE CONTENT OF OTHER SUBSTRATES [17].

Substrate	Total solid content %	Total volatile content %
Chicken manure	32	63-80
Municipal residues	30-40	50-60
Organic residues	30-40	70-80
Food waste	15-10	85-95
Sugarcane vinasse	3-5	75-85

The volatile solids content of algae is equivalent to that of chicken manure and municipal waste, which is a favorable outcome for biogas production according to this parameter. Food waste and sugarcane vinasse have a high volatile solids content, which is a fundamental characteristic for biogas production.

All organic materials contain water in their composition and a solid fraction. The percentage of solids in the biomass used in the bioreactor is

important and should be considered to achieve better degradation [18].

According to [19], the determination of volatile solids is an essential parameter to determine if the biomass undergoes good organic matter degradation and, consequently, good biogas production.

The volatile solids content obtained herein for marine algae is favorable for biogas production because the higher this parameter, the higher the biogas production.

Finally, it is important to consider marine algae-based biogas for the diversification of the energy mix, by providing a clean and renewable energy source, thus reducing reliance on fossil fuels. Seaweed cultivation and biogas production can be conducted in coastal areas, contributing to localized energy production and rural economic development.

The relationship between algae biogas and the United Nations Sustainable Development Goals (SDGs) is significant, as algae biogas contributes to several key goals and targets within the SDGs [20], specifically SDG 7 (Affordable and Clean Energy). Marine algae biogas supports SDG 7 by promoting the use of sustainable energy sources, which helps reduce greenhouse gas emissions and combat climate change.

Also, there is alignment with SDG 9 (Industry, Innovation, and Infrastructure). The development and implementation of marine algae biogas technologies involve innovation in the field of renewable energy and sustainable infrastructure. Regarding climate action (SDG 13), there are reductions in the emission of methane, a potent greenhouse gas, while also sequestering carbon during the growth of algae. In addition, marine algae biogas contributes to more sustainable consumption and production patterns (SDG 12) by providing an eco-friendly energy source and promoting efficient use of resources.

A laboratory-scale biogas production was presented herein, but when considering marine algae for large-scale biogas production, several important considerations should be taken into account to ensure the sustainability, efficiency, and environmental responsibility of the process. Algae species selection and cultivation methods are key factors, as native species should be preferred to minimize the risk of invasiveness and ecological disruptions and scalability,

productivity, and resource efficiency should also be accounted for.

In summary, marine algae biogas can play a key role in advancing multiple SDG by providing clean energy, mitigating climate change, promoting sustainable land and marine practices, and fostering innovation and partnerships.

IV. CONCLUSION

Based on the conducted experiment, it was possible to observe biogas production from marine algae, understand its potential and chemical composition. A simple analysis was conducted herein, to establish a starting point for future optimization studies.

The total solid content demonstrated that the characteristics of marine algae, as well as the use of anaerobic digestion, make algae a promising system for biogas production. This is especially relevant in areas with effluent discharge, where they may pose environmental pollution potential. The yield in converting the organic matter present in the biomass into biogas was satisfactory, confirming the efficiency of its use.

A bioreactor was successfully developed, which will be useful for upcoming laboratory experiments. In addition to the personal knowledge gained, this work has left a result that will also assist other students. Future work is directed to designing a prototype of a full-scale biogas digester.

ACKNOWLEDGEMENT

The authors wish to acknowledge the support of the National Council for Scientific and Technological Development (CNPq Productivity Grant 309452/2021-0).

REFERENCES

- [1] Stram, B. N. (2016). Key challenges to expanding renewable energy. *Energy Policy*, 96, 728-734.
- [2] Stančin, H., Mikulčić, H., Wang, X., & Duić, N. (2020). A review on alternative fuels in future energy system. *Renewable and sustainable energy reviews*, 128, 109927.
- [3] Nanda, S., & Berruti, F. (2021). A technical review of bioenergy and resource recovery from municipal solid waste. *Journal of hazardous materials*, 403, 123970.
- [4] Chacartegui, R., Carvalho, M., Abrahão, R., & Becerra, J. (2015). Analysis of a CHP plant in a municipal solid waste landfill in the South of Spain. *Applied Thermal Engineering*, 91, 706-717.
- [5] Li, Y., Chen, Y., & Wu, J. (2019). Enhancement of methane production in anaerobic digestion process: A review. *Applied energy*, 240, 120-137.
- [6] Pramanik, S. K., Suja, F. B., Zain, S. M., & Pramanik, B. K. (2019). The anaerobic digestion process of biogas production from food waste: Prospects and constraints. *Bioresource Technology Reports*, 8, 100310.
- [7] Pereira Nascimento, D., Menezes, V. L., Carvalho, M., & Chacartegui, R. (2019). Energy analysis of products and processes in a sanitary landfill. *IET Renewable Power Generation*, 13(7), 1063-1075.
- [8] Milledge, J. J., Nielsen, B. V., Maneein, S., & Harvey, P. J. (2019). A brief review of anaerobic digestion of algae for bioenergy. *Energies*, 12(6), 1166.
- [9] Faisal, S., Zaky, A., Wang, Q., Huang, J., & Abomohra, A. (2022). Integrated marine biogas: a promising approach towards sustainability. *Fermentation*, 8(10), 520.
- [10] Pardilhó, S., Boaventura, R., Almeida, M., & Dias, J. M. (2022). Marine macroalgae waste: A potential feedstock for biogas production. *Journal of environmental management*, 304, 114309.
- [11] Abusweireh, R. S., Rajamohan, N., Sonne, C., & Vasseghian, Y. (2023). Algae biogas production focusing on operating conditions and conversion mechanisms—A review. *Heliyon*.
- [12] Iglina, T., Iglin, P., & Pashchenko, D. (2022). Industrial CO₂ capture by algae: a review and recent advances. *Sustainability*, 14(7), 3801.
- [13] Thakur, N., Salama, E. S., Sharma, M., Sharma, P., Sharma, D., & Li, X. (2022). Efficient utilization and management of seaweed biomass for biogas production. *Materials Today Sustainability*, 18, 100120.
- [14] Laurens, L. M., & Nelson, R. S. (2020). Sustainable technologies for seaweed conversion to biofuels and bioproducts. In *Sustainable Seaweed Technologies* (pp. 643-661). Elsevier.
- [15] Brazilian Association of Technical Standards. (1989). *NBR10664 DE 04/1989 Determination of solid residues – Gravimetric method – Test method*.
- [16] Avinash, L. S., & Mishra, A. (2023). Enhancing biogas production in anaerobic digestion of MSW with addition of bio-solids and various moisture sources. *Fuel*, 354, 129414.
- [17] CIBIOGÁS. Conceitos básicos e digestão anaeróbia. Curso de Biogás: fundamentos e aplicações do CIBiogás [Basic concepts and anaerobic digestion. Biogas course: foundations and applications]. Brazil, Foz do Iguaçu, 2018.
- [18] Induchoodan, T. G., Haq, I., & Kalamdhad, A. S. (2022). Factors affecting anaerobic digestion for biogas production: A review. *Advanced Organic Waste Management*, 223-233.
- [19] Lisý, M., Lisá, H., Jecha, D., Baláš, M., & Křižan, P. (2020). Characteristic properties of alternative biomass fuels. *Energies*, 13(6), 1448.
- [20] Carlsen, L., & Bruggemann, R. (2022). The 17 United Nations' sustainable development goals: A status by 2020. *International Journal of Sustainable Development & World Ecology*, 29(3), 219-229.

Activation Function Effects on the Power Forecasting of a Photovoltaic Plant

Antonio Rivero-Cacho¹, Alejandro Pulido-Guerra², Víctor Collar-Serradilla³, Manuel Botejara-Antúnez⁴, Gonzalo Sánchez-Barroso⁵, Justo García-Sanz-Calcedo⁶

^{1,2,3,4,5,6}University of Extremadura, Engineering Project Department, Badajoz, Spain

¹antoniorc@unex.es, ²alejandropulido@unex.es, ³victorcs@unex.es, ⁴manuelba@unex.es, ⁵gsm@unex.es, ⁶jgsanz@unex.es

Abstract—There is currently a strong interest in improving the performance of artificial neural networks in forecasting the behaviour of complex systems through activation functions. Photovoltaic plants are a type of installation made up of a large amount of equipment, and systems affected by operation and maintenance processes, which makes it difficult to predict the electrical energy generated. This work aims to test the activation function that provides the best results in the energy prediction of photovoltaic plants using an artificial neural network of the multilayer perceptron type. The most commonly used activation functions in artificial neural networks for predicting the energy performance of a photovoltaic plant were compiled. Then, the feasibility of applying each activation function to the problem under study was tested. Finally, a multilayer perceptron network with five layers was designed to determine the performance of the network for each activation function used. For each network, the performance was evaluated using metric functions such as Mean Absolute Percentage Error, Root Mean Square Error, Mean Absolute Error, Mean Square Error and Correlation Coefficient. It was concluded that the highest performance was presented by the hyperbolic tangent activation function for forecasting the electricity generation of a photovoltaic plant. This work will reduce the uncertainty in the configuration of the basic design parameters of artificial neural networks.

Keywords – activation function, ANN, forecasting, PV plant

I. INTRODUCTION

Global energy consumption has been increasing steadily over the years. In addition, the heavy dependence on fossil fuels forces the search for alternatives to generate renewable energy. Moreover, the price of fossil fuels is also constantly increasing, aggravated by the evidence that their consumption hurts the environment [1].

Current energy policies promote energy generation in a safe, environmentally sustainable, and affordable way. Therefore, the use of energy from the sun is a cost-effective alternative. Among the existing technologies for this purpose, one of the most prominent is photovoltaics (PV). Due to the huge increase in the number of PV plants, technological developments have led to a significant reduction in the cost of manufacturing and installing [2,3].

This boom in the installation of PV systems is because they do not have the price fluctuations of fossil fuel energy, have no environmental impact through the generation of greenhouse gases, and, in addition, are an inexpensive technology [4]. As a result, the contribution of PV technology to the global energy mix has enlarged. Moreover, this technology is increasingly boosted by national governments through financial incentives granted to investors in this technology [5].

However, as the energy source of PV systems can be considered unpredictable, PV is a technology that suffers uncertainty in its operation and maintenance (O&M). PV performance is influenced by weather conditions such as solar irradiation, ambient temperature and relative humidity, cloud cover, rainfall, snow and deposition or fouling of animal faeces on PV panels. Consequently, this causes the surface area of the panel to capture the solar energy to decrease and, therefore, its electrical efficiency [6,7].

Consequently, it is a crucial challenge that the PV panel conditions are always under control and monitored to ensure the productivity of energy. Thus, it is also possible to anticipate low PV panel productivity situations resulting from inadequate O&M performance. This supervision makes it possible to enhance the energy production of the PV panels and reduce O&M costs [8].

Prediction of energy production is achieved through forecasting techniques. Prediction allows PV systems to improve their reliability, increasing the quality of the supply energy, and reducing the uncertainty of energy production. In recent years, research has focused on developing predictive models to foresee the performance of PV technology.

However, the nature of the problem of predicting PV energy production is influenced by meteorological and other parameters, which became in a non-linear problem. Diverse factors are involved in electricity production, such as meteorological, human, and the effectiveness of O&M plans [9].

Many researchers have applied Artificial Neural Networks (ANN) to solve problems of a non-linear nature, such as system optimisation, function fitting, pattern identification, system control, system prediction, etc. All these applications have become ANN a very powerful tool for solving complex problems. ANN build relationships between input and output variable data so that they use the information provided to understand the operation of the system under study, improve its performance and save incomplete data [10].

To design an ANN properly, it is necessary to configure the parameters of its architecture. First, the optimiser must be defined, as it is the algorithm used to make the ANN converge to a solution by reducing errors. Secondly, the

number of hidden layers in the ANN and, in turn, the number of neurons in each layer must be defined. The selection of the number of hidden layers and their neurons is done by a heuristic trial-and-error procedure. The last step in defining the ANN architecture is to select the activation function. This aspect is decisive in making the ANN perform well and preventing the ANN from common learning problems, such as gradient leakage [11].

In this sense, a debate has emerged in the literature about which activation function can achieve the best performance for an ANN in the problem of predicting the energy production of a PV plant.

As in [12] developed a multilayer perceptron (MP) ANN in which they selected as input variables: relative humidity, temperature, wind speed and wind direction to predict the electrical production of a PV plant. They used ReLU as the activation function. They obtained errors of 1.98 p.u. for the Mean Square Error (MSE) and 1.02 p.u. for the Mean Absolute Error (MAE).

As in [13] developed an ANN of the MP type again to predict the electrical energy produced in a PV plant. To do this, they used ambient temperature and solar irradiance monitored for one year as input variables. The activation function used was the Sigmoid. They obtained a correlation coefficient R^2 ranging from 0.96 to 0.99.

As in [14] compared the performance of two ANNs (MP and Long Short-Term Memory (LSTM)) to predict the power generation of a PV plant. To do so, they implemented Sigmoid and ReLU as activation functions in the hidden layers of both the MP and LSTM networks. The LSTM model obtained a Root Mean Square Error (RMSE) performance of 2.987 p.u. and a 2.365 p.u. MAE. In the case of the MP model, they obtained a 5.65 p.u. RMSE and a 4.38 p.u. MAE.

As in [15] employed the LSTM model to predict the electricity production of a PV plant one day in advance. They used data from different variables such as ambient temperature, irradiance, wind direction, wind speed, luminosity, precipitation, relative humidity, and global radiation. They compared the performance of LSTM when the Tanh and ReLU activation function was applied through the RMSE metric. They concluded that by applying the Tanh activation function, they achieved an

RMSE value of 0.494 p.u., while applying ReLU achieved an RMSE of 0.828 p.u.

However, according to reference [16], in recent years, new activation functions such as Leaky ReLU, SeLU or Swish have been proposed that consider parameters to improve the performance of ANNs applied to predict PV energy.

This paper aims to contribute to the debate on which activation functions perform best in predicting PV electrical power using an ANN that simulates the behaviour of a plant. The large number of available ANN types makes the controversy in this aspect grow.

Thus, the main objective of this work is to analyse which activation function shows the best performance in an ANN to predict the electricity production of a PV plant. The criterion to be used to select the best ANN will be based on the lowest error produced in the prediction, which can be measured through the following functions: MSE, MAE, RMSE, Mean Absolute Percentage Error (MAPE), etc. [17]. Thus, this work intends to reduce uncertainty in the development of ANNs to predict the production of a PV plant.

II. MATERIAL AND METHODS

A. Overview

To carry out this study, the activation functions of the most recent major research papers related to the problem under study were compiled. Next, the controversy between the selection of activation functions used in this research field was analysed. In this way, the activation functions were related to the types of ANNs best suited to their nature. Subsequently, the new trend of developing activation functions whose functionality is beginning to be tested was explored.

The characteristics of the most commonly used activation functions were then extracted from the literature to discover their merits concerning the prediction of PV energy in this case study.

With all this in mind, the case study of this work was proposed, for which an MP network was selected due to its wide validation in the literature, even though each author used different activation functions.

B. Multi – Layer Perceptron Neural Network.

To test the performance of each selected activation function, an MP-type ANN was developed to predict the response of a PV plant. Solar irradiance, ambient temperature, and cell temperature were selected as input variables and electrical power was chosen as output variable.

This ML network was trained by a dataset consisting of 5.184.000 data for each variable used. These data have been taken every second for two months by monitoring. Therefore, the ANN was trained with 20.736.000 data. This dataset was divided into 70% for training and 30% for predictions. For the ANN to train a large amount of data, it was necessary to use deep learning, i.e. the application of two or more hidden layers in the ANN.

Deep learning avoids overtraining the artificial neurons and produces optimal results. The configuration of the number of hidden layers and the neurons in each layer was determined by a heuristic process involving a multitude of tests until the ANN's error rates were reduced.

Consequently, the developed PM was divided into five layers as shown in Fig. 1. The three neurons in the initial layer are due to the existence of three input variables in the network and the neuron in the output layer corresponds to the output variable of the ANN.

Once MP was trained with each activation function, the performance of each case was evaluated according to the activation function used. With the results of this analysis, the capacity of each activation function to predict electricity generation in a PV plant was assessed. Also, the impact that a proper selection of the activation function has on the goodness of the provided solution was then analysed.

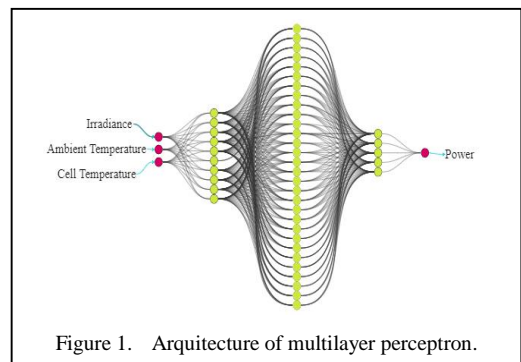


Figure 1. Architecture of multilayer perceptron.

C. Activation Function

There is a great variety of activation functions, such as Linear, Sigmoid, Tanh, ReLU, Leaky ReLU, SeLU, Softmax and Swish. These activation functions were implemented in ANN to predict the power generation of a PV plant.

1) Sigmoid

Sigmoid is a well-accepted activation function by the scientific community. It is capable of transforming values from an infinite range to values within the range of 0 to 1. Its tendency to bring the values calculated in backpropagation algorithms to zero during the training phase is the main disadvantage. Eq. (1) represents the mathematical expression of Sigmoid.

$$f(x) = \frac{1}{1+e^{-x}}. \quad (1)$$

2) ReLU

ReLU has two advantages: i) it avoids the leakage gradient problem and ii) it facilitates the simultaneous activation of layered neurons [18]. This makes ANN better able to size the problem for which it was developed. However, ReLU suffers from disadvantages such as zero differentiability. This implies that the output of the neuron tends to be zero when there is a large weight of negative values. ReLU is defined by Eq. (2).

$$f(x) = \max(0, x). \quad (2)$$

3) Leaky ReLU

This is a rectification of the ReLU activation function described above. Therefore, it attempts to solve the ReLU problem previously discussed. Leaky ReLU allows the neuron to supply a small gradient when it is inactive and saturated. The authors showed that Leaky ReLU and a standard rectifier have a similar impact on network performance. Leaky ReLU was defined using Eq. (3).

$$f(x) = \max(0.1x, x). \quad (3)$$

4) Tanh

The Tanh activation function is like the Sigmoid, however, Tanh is symmetric about the origin. Tanh is a non-linear function that is continuous and derivable. It can take values in the interval between -1 and 1. The advantage of Tanh is that its gradient is steeper, which means

that it is not restricted to vary in a given direction [19]. Tanh was defined by Eq. (4).

$$f(x) = \frac{e^x - e^{-x}}{e^x + e^{-x}}. \quad (4)$$

5) SeLU

SeLU is another modification of the ReLU activation function. The difference is that SeLU can reach negative values. This modification allows the ANN to have an output close to zero as it helps the model to converge quickly to the solution. SeLU was expressed by Eq. (5).

$$f(x) = \gamma \begin{cases} \alpha(e^x - 1) & \text{para } x < 0 \\ x & \text{para } x \geq 0 \end{cases}. \quad (5)$$

6) Swish

Swish is a relatively recently discovered activation feature. Swish has the advantage that it is a non-monotonic activation function, i.e. the value of Swish can decrease even though the values at the inputs increase. In addition, Swish does not suffer from the gradient fading problem. Depending on the application for which the ANN is designed, Swish even outperforms ReLU [20]. Its higher computational cost is its biggest disadvantage. Swish was stated by Eq. (6).

$$f(x) = \frac{x}{1+e^{-\beta x}}. \quad (6)$$

III. RESULTS AND DISCUSSION

All activation functions have been applied in the same ML shown in Fig. 1 to measure the impact of the activation functions concerning the prediction results obtained. This is reasonable since modifying the composition of the layers and neurons of the ANNs would not identify the improvement of using one or another activation function.

Once the activation functions shown were implemented in the MP network described in the Multilayer Perceptron Neural Network, the tests were performed. After that, the results in PV energy prediction are obtained and shown in Table I.

The results of the MP network predictions are shown for the different cases proposed. Each case corresponds to a different activation function for the same MP architecture design. Table I shows in blue the power production values that MP should predict and in red the values that MP predicts. It can be seen that the

results obtained by applying the ReLU and Tanh activation functions are more accurate than those obtained by applying SeLU, Leaky ReLU and Swish because these activation functions produce negative electricity values. Table II shows how well-behaved the MP network is for each case in which a different activation function is applied. Firstly, the MSE values were very similar for all case studies. The lowest value was Tanh, and the highest was Tanh.

Secondly, based on the MAPE, the error was lowest when the ReLU activation function was applied (1399.32), followed by the Tanh function (1557.59), then SeLU (3693.45), Leaky ReLU (2347.94) and Swish (2685.68), respectively.

Then, evaluating with which activation function the lowest RMSE is obtained, it is observed that it occurs when the Tanh activation function is applied. On the other hand, when applying the activation functions ReLU, SeLU, Leaky ReLU, and Swish, the error increased by 2.53%, 13.04%, 20.99%, and 12.59% respectively. It can be seen that the RMSE error reached a similar value when SeLU and Swish were applied.

Hereafter, the MAE metric was evaluated with a minimum value of 0.0507 when Tanh was applied, followed by the ReLU activation function (0.0514). With higher values were SeLU and Leaky ReLU. The highest MAE value was obtained when the Swish activation function was applied.

Finally, the performance of the ANN was evaluated with the correlation coefficient (R^2), in this aspect, the best result was 0.8745 corresponding to the application of the Tanh activation function, followed very closely by the value of 0.8705 obtained when applying the ReLU activation function.

In the literature, some works mention improvements in the activation functions concerning the traditional ones (Tanh or ReLU), these improvements are the development of modifications in their application (Leaky ReLU, SeLU and Swish). However, it can be seen that

the results of the emerging activation functions are not better than the results of the traditional ones. Leaky ReLU solves the leakage gradient problem of ReLU, but its performance is worse than ReLU. Its explanation could be that during training there are no leakage gradient problems.

SeLU can output negative values, a virtue that ReLU does not have. However, the performance of SeLU is worse than ReLU. If the explanation may be that the temperature and irradiance data supplied to ANN is mostly positive the major virtue of SeLU is lost. In the case of Swish, whose origin is different from Tanh and ReLU, it performs worse than the two activation functions mentioned, possibly because the application used does not benefit from the virtues of Swish.

In the configuration of the basic parameters of an ANN a large number of factors have to be defined, such as the division of the dataset used, the number of hidden layers and their neurons, activation functions, optimiser, and metrics to evaluate the performance of the ANN. Defining all the factors is complex and also requires a large amount of time to develop the ANN. Therefore, this research tries to reduce the uncertainty of designing ML for energy produced by PV plants. In this way, this research is useful for PV plant managers who intend to anticipate the state of the plant through the application of this technology, reducing the uncertainty in the injection of electricity into the grid.

Future lines of research should be aimed at determining the most influential variables in the energy production of a photovoltaic plant. These variables can be meteorological or related to the installation itself. The variables used in this work have been exclusively meteorological.

Another future work would be to investigate the impact on the selection of activation functions by applying other types of ANNs. Depending on the type of ANN, their training is different, so the impact of the activation functions could be different.

TABLE I. COMPARISON OF RESULTS WHEN ACTIVATION FUNCTIONS ARE APPLIED.

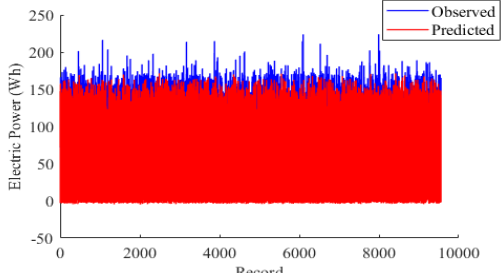
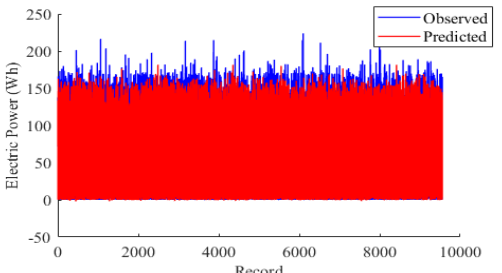
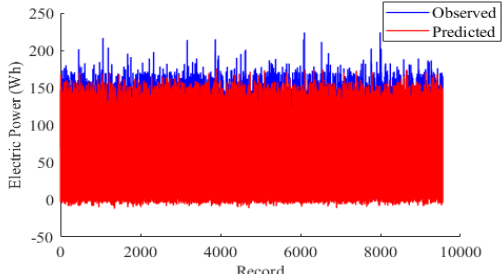
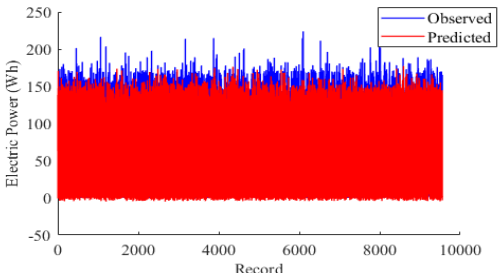
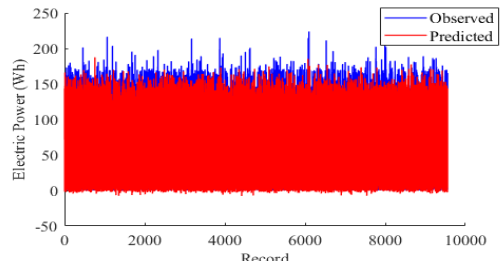
ANN	Forecast Results
Tahn	
ReLU	
SeLU	
Leaky ReLU	
Swish	

TABLE II. SUMMARY OF RESULTS.

Activation Function	MSE	MAPE	RMSE	MAE	R ²
<i>Tanh</i>	0.0072	1557.59	0.0847	0.0507	0.8745
<i>ReLU</i>	0.0074	1399.32	0.0869	0.0514	0.8705
<i>SeLU</i>	0.0076	3693.45	0.0974	0.0638	0.8674
<i>Leaky ReLU</i>	0.0074	2347.94	0.1072	0.0589	0.8589
<i>Swish</i>	0.0075	2685.68	0.0969	0.0720	0.8488

IV. CONCLUSIONS

The methodology proposed in this work was adequate to generate non-existent knowledge due to the debate produced by several authors on the use of activation functions in ML-type ANNs.

This analysis of the activation functions employed for the electrical energy prediction in a PV plant highlights the importance of a suitable selection in the construction phase of an ANN. Even though each activation function has a series of advantages and disadvantages in its application, all of them still have an important application in the resolution of problems of an equivalent nature to the one proposed in this work.

Research continues on the development of activation functions that avoid the problems associated with traditional activation functions without increasing the computational cost of the ANN to solve this problem. This work tested five activation functions to predict the energy generated by a photovoltaic plant using an ANN of the MP type. The activation function that gave the best results was Tahn because it achieved the highest R², with the lowest MSE, MAE and RMSE errors for each case study.

This research shows the importance of the application of an activation function suitable for its particular application, allowing the application of this research to effectively define ML-type ANNs used for problems of a similar nature to the one shown.

ACKNOWLEDGEMENT

This research was supported by the Government of Extremadura (grant GR21098) through the VI Regional Plan for Research, Technological Development & Innovation of the Autonomous Community of Extremadura cofinanced by the European Regional Development Fund.

REFERENCES

- [1] Teo, T. T., Logenthiran, T., & Woo, W. L. (2015). Forecasting of photovoltaic power using extreme learning machine. 2015 IEEE Innovative Smart Grid Technologies - Asia (ISGT ASIA), 1–6.
- [2] Candelise, C., Winskel, M., & Gross, R. J. (2013). The dynamics of solar PV costs and prices as a challenge for technology forecasting. *Renewable and Sustainable Energy Reviews*, 26, 96-107.
- [3] Raugei, M., & Frankl, P. (2009). Life cycle impacts and costs of photovoltaic systems: current state of the art and future outlooks. *Energy*, 34(3), 392-399.
- [4] Muhammad Ehsan, R., Simon, S. P., & Venkateswaran, P. R. (2017). Day-ahead forecasting of solar photovoltaic output power using multilayer perceptron. *Neural Computing and Applications*, 28, 3981-3992.
- [5] Ministerio de Industria, E. y T. (2015). Real Decreto 900/2015, de 9 de octubre, por el que se regulan las condiciones administrativas, técnicas y económicas de las modalidades de suministro de energía eléctrica con autoconsumo y de producción con autoconsumo. (pp. 94874-94917).
- [6] Lim, S. C., Huh, J. H., Hong, S. H., Park, C. Y., & Kim, J. C. (2022). Solar Power Forecasting Using CNN-LSTM Hybrid Model. *Energies*, 15(21), 8233.
- [7] Sánchez-Barroso, G., González-Domínguez, J., García-Sanz-Calcedo, J., & Sanz, J. G. (2021). Markov chains estimation of the optimal periodicity for cleaning photovoltaic panels installed in the dehesa. *Renewable Energy*, 179, 537-549.
- [8] Succetti, F., Rosato, A., Araneo, R., & Panella, M. (2020). Deep neural networks for multivariate prediction of photovoltaic power time series. *IEEE Access*, 8, 211490-211505.
- [9] Pei, T., Li, L., Zhang, J., & Hao, X. (2020). Module block fault locating strategy for large-scale photovoltaic arrays. *Energy Conversion and Management*, 214, 112898.
- [10] Reddy, K. S., & Ranjan, M. (2003). Solar resource estimation using artificial neural networks and comparison with other correlation models. *Energy conversion and management*, 44(15), 2519-2530.
- [11] Braga-Neto, U. (2020). *Fundamentals of pattern recognition and machine learning* (pp. 1-286). Berlin/Heidelberg, Germany: Springer.
- [12] Jogunuri, S., & Josh, F. T. (2022, June). Deep Neural Network based Forecasting of Short-Term Solar Photovoltaic Power output. In *2022 2nd International Conference on Intelligent Technologies (CONIT)* (pp. 1-5). IEEE.

- [13] Elamim, A., Hartiti, B., Haibaoui, A., Lfakir, A., & Thevenin, P. (2020). Generation of photovoltaic output power forecast using artificial neural networks. In *Advanced Intelligent Systems for Sustainable Development (AI2SD'2019) Volume 7-Advanced Intelligent Systems for Sustainable Development Applied in Energy and Electrical Engineering* (pp. 127-134). Springer International Publishing.
- [14] Wen, L., Zhou, K., Yang, S., & Lu, X. (2019). Optimal load dispatch of community microgrid with deep learning based solar power and load forecasting. *Energy*, *171*, 1053-1065.
- [15] Liu, C. H., Gu, J. C., & Yang, M. T. (2021). A simplified LSTM neural networks for one day-ahead solar power forecasting. *Ieee Access*, *9*, 17174-17195.
- [16] Apicella, A., Donnarumma, F., Isgrò, F., & Prevete, R. (2021). A survey on modern trainable activation functions. *Neural Networks*, *138*, 14-32.
- [17] Adelekan, D. S., Ohunakin, O. S., & Paul, B. S. (2022). Artificial intelligence models for refrigeration, air conditioning and heat pump systems. *Energy Reports*, *8*, 8451-8466.
- [18] Montalto, A., Tessitore, G., & Prevete, R. (2015). A linear approach for sparse coding by a two-layer neural network. *Neurocomputing*, *149*, 1315-1323.
- [19] Kiliçarslan, S., Kemal, A. D. E. M., & Çelik, M. (2021). An overview of the activation functions used in deep learning algorithms. *Journal of New Results in Science*, *10*(3), 75-88.
- [20] Ding, B., Qian, H., & Zhou, J. (2018, June). Activation functions and their characteristics in deep neural networks. In *2018 Chinese control and decision conference (CCDC)* (pp. 1836-1841). IEEE.

Ejector Stack Design and Fan Selection for Efficient Flue Gas Discharge: A Computational Fluid Dynamics Study

Masoud Darbandi¹, Masoud Fazeli², Behnam Basiriani³, Seyyed Mohsen Hosseinian⁴,
Masoud Allah Dadi⁵

¹Sharif University of Technology, Tehran, Iran
^{2,3,4,5}Esfahan's Mobarakeh Steel Company, Esfahan, Iran

¹darbandi@sharif.edu, ²mdotfazeli@gmail.com, ³behnam.behnambasiriani@gmail.com,
⁴sm_hoseinian1372@yahoo.com, ⁵Allahdadi.m.67@gmail.com

Abstract—This study focuses on the design, analysis, and performance evaluation of an ejector stack for the discharge of flue gas into the atmosphere. The research combines detailed design considerations with computational fluid dynamics (CFD) simulations to optimize the performance of the ejector stack. Emphasis is placed on the selection of an appropriate motive air fan, operated at a 50% damper opening angle, to ensure flexibility in adapting to fluctuations in flue gas flow rates. The CFD analysis provides valuable insights into the flow dynamics within the ejector stack. Additionally, the performance curve of the selected fan and velocity field contours are presented, offering critical information for the design and operation of ejector stacks in industrial applications. This study contributes to the understanding of ejector stack design and optimization, with potential applications in diverse industrial sectors. The knowledge gained from this research can enhance the efficiency and reliability of similar ejector stack systems, making it a valuable resource for engineers and professionals working in fluid transportation and related fields.

Keywords – ejector stack, flue gas, computational fluid dynamics, fan

I. INTRODUCTION

Fluid transport is gaining prominence in industrial applications. Past observations highlight the pivotal role played by the appropriate design and selection of the feeding

mechanism in achieving a successful positive-pressure fluid conveying system, particularly in transitioning materials from high to atmospheric pressure environments. Consequently, extensive numerical investigations have been undertaken to identify optimal feeding devices capable of accommodating a growing array of applications. This has led to the ongoing development of various types of feeding devices. In recent times, the jet pump, also referred to as an ejector, has seen a surge in popularity as an alternative feeding device for pneumatic transportation systems. This heightened interest is attributed to the following advantages offered by ejectors: 1- Simplicity and Reliability: Ejectors are characterized by their straightforward design and remarkable reliability, primarily owing to the absence of moving parts; 2- Zero Air Leakage: Ejectors excel in maintaining airtight integrity, minimizing air leakage concerns, and ensuring efficient operation; 3- Cost-Effectiveness: Ejectors come with a distinct advantage in terms of their low capital cost, making them an economically viable choice with little to no maintenance requirements; 4- Suitability for High-Temperature Applications: Ejectors are well-suited for applications involving high temperatures, making them a preferred choice in such scenarios. The focus of the current work lies in the design of an ejector stack with the purpose of expelling the hot flue gas emanating from a DRI (Direct Reduced Iron) unit into the

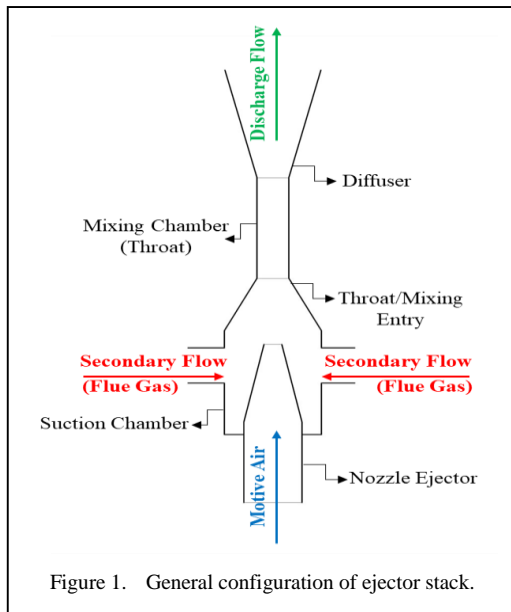


Figure 1. General configuration of ejector stack.

atmosphere. Consequently, it becomes imperative to gain an understanding of how the geometrical parameters of the ejector stack impact its performance and efficiency. For a clearer understanding of the general configuration of the ejector stack, Fig. 1 is provided. As depicted in this figure, the motive air flows into the nozzle to discharge the secondary flow, which, in this particular case, is the flue gas. Additionally, the stack comprises four other components: a suction chamber, a throat or mixing entry, a mixing chamber, and a diffuser.

Numerous studies have been conducted to explore the influence of nozzle geometry on ejector stack performance, employing both experimental and numerical methods. For example, a methodology for predicting the optimal dimensions of the throat section, nozzle positioning, and intake shape for jet pumps based on the principles of energy and momentum conservation is introduced [1]. An investigation on the impact of various geometric parameters and nozzle quantities on the performance of a subsonic air-air ejector, relying on experimental measurements, has been carried out [2]. The optimization of throat section dimensions, nozzle placement, and divergence angle has been explored [3]. An experimental research study has been conducted to evaluate the effects of ejector geometry, including nozzle shape and nozzle exit position, on ejector performance [4]. Furthermore, a CFD model was developed, and experiments were performed on an ejector

refrigeration system using R134a as the working fluid to investigate the impact of operating conditions and ejector geometry on the system's performance [5]. An experimental investigation was conducted into the impact of nozzle exit position on the performance of an air ejector, identifying an optimal nozzle exit position resulting in the maximum entrainment ratio and compression ratio [6]. The effect of nozzle position on the performance of jet ejectors in both constant pressure and constant-area designs was examined, revealing a significant influence of nozzle position on the jet ejector's performance [7]. In a separate study, an analysis was performed on the impact of various configurations on the ability of gas-gas and gas-liquid ejectors to induce fluid flow, offering insights and explanations regarding the distinct entrainment behaviors observed in gas-gas and gas-liquid ejectors, which hold significance for ejector design and operation [8]. The dependency of mass transfer characteristics in gas-liquid ejectors on fluid properties, ejector geometry, and process parameters was examined, aiming to establish design and scale-up guidelines for gas-liquid ejectors [9]. In a related study, the flow characteristics within steam ejectors with various nozzle structures were analyzed, while the impact of nozzle position on ejector performance was explored, revealing that the ejector coefficient was optimized at a specific nozzle position [10]. The influence of the nozzle exit position and the mixing section angle on ejector performance was investigated, identifying optimal values for these parameters and offering insights on their adaptation for achieving optimal performance under different operational conditions [11]. The impact of ejector geometry on the performance of natural gas ejectors was explored, determining optimal angles and ratios of ejector components that maximize entrainment ratios [12].

The present research has been conducted to increase the production capacity of one of the Direct Reduction Iron (DRI) units of Esfahan's Mobarakeh Steel Company. In this study, the goal is to discharge 327.190 Nm³/h of flue gas at a temperature of 272°C into the atmosphere by designing an ejector stack using Computational Fluid Dynamics. Additionally, the appropriate motive fan will be chosen.

II. METHODOLOGY AND EQUATIONS

As mentioned in the previous section, the goal of the current study is to release 327190

Nm³/h of flue gas from two distinct units into the atmosphere. The design of the stack, encompassing the determination of dimensions, lengths, diameters, and angles for all stack components, has been completed but is not presented in this section. On the other hand, the assessment of the designed stack's performance in discharging the flue gas is conducted using computational fluid dynamics. The underlying assumption is that the flow within the ejector stack is steady, incompressible, viscous, and turbulent. In the current study, a pressure-based solver was utilized, employing a steady-state formulation and including the energy equation along with the species transport equation to model the mixture of H₂O, O₂, N₂, and CO₂ with varying volume fractions in different sections of the ejector stack. Furthermore, the Semi-Implicit Method for Pressure-Linked Equations scheme served as the pressure-velocity coupling method, which is widely adopted for steady-state solver algorithms. The corresponding continuity, momentum, and energy conservation equations (Navier-Stokes equations) applicable to a fixed control volume are as follows:

$$\frac{\partial \rho}{\partial t} + \nabla(\rho V) = 0, \quad (1)$$

$$\rho \frac{dV}{dt} + \rho(V\nabla)V = -\nabla p + \mu \nabla^2 V + \beta, \quad (2)$$

$$\begin{aligned} & \frac{\partial}{\partial t} \left(\frac{\rho |V|^2}{2} + \rho \varepsilon \right) + \nabla \times \\ & \times \left(\frac{\rho |V|^2 V}{2} + \rho \varepsilon V + pV - \tau V - q \right) = 0. \quad (3) \end{aligned}$$

Here, ρ represents density, t stands for time, ∇ is the vector differential operator, V is the velocity vector, P is static pressure, μ is fluid viscosity, B is body force, e is specific internal energy, τ represents the viscous stress tensor, and q is the heat flux vector. In this study, the standard k - ε turbulence model is employed to simulate the flow within the ejector stack. In this context, an extensive investigation is conducted [13,14]. The standard k -epsilon model encompasses two transport equations: one for turbulent kinetic energy (k) and another for turbulent dissipation rate (ε). The equations for turbulent kinetic energy (k) and dissipation rate (ε) in the k - ε model are as follows:

$$\begin{aligned} \frac{\partial(\rho k)}{\partial t} + \frac{\partial(\rho k u_i)}{\partial x_i} &= \frac{\partial}{\partial x} \left[\frac{\mu_t}{\sigma_k} \frac{\partial k}{\partial x_i} \right] + \\ &+ 2\mu_t E_{ij} E_{ij} - \rho \varepsilon \end{aligned} \quad (4)$$

$$\begin{aligned} \frac{\partial(\rho \varepsilon)}{\partial t} + \frac{\partial(\rho \varepsilon u_i)}{\partial x_i} &= \frac{\partial}{\partial x_j} \left[\frac{\mu_t}{\sigma_\varepsilon} \frac{\partial \varepsilon}{\partial x_j} \right] + \\ &+ C_{1\varepsilon} \frac{\varepsilon}{k} 2\mu_t E_{ij} E_{ij} - C_{2\varepsilon} \rho \frac{\varepsilon^2}{k} \end{aligned} \quad (5)$$

Here, u_i represents the velocity component in the respective direction, E_{ij} is the deformation rate component, μ_t represents the eddy viscosity, and the constants C_μ , σ_k , σ_ε , $\sigma_{1\varepsilon}$ and $\sigma_{2\varepsilon}$ were determined through comprehensive data fitting across various turbulent flow scenarios.

III. GEOMETRY, MESHING AND BOUNDARY CONDITIONS

As mentioned previously, the detailed component design of the ejector stack is not presented here. However, Fig. 2 illustrates the geometry of the designed ejector stack. In this figure, the red surfaces represent the entrances for flue gas at a temperature of 272°C, with a gauge pressure of -9 millibar and a volumetric flow rate of 327.190 Nm³/h. Additionally, the blue surface signifies the designed nozzle ejector, with inlet and outlet diameters of 2600 and 1250 millimeters, respectively. The distance between the outlet of the nozzle ejector and the inlet of the mixing chamber is approximately 2890 millimeters. Furthermore, the gray surfaces represent the stack's geometry, including the circular suction chamber with an internal diameter of 5730 millimeters, the mixing chamber with a length and diameter of 7700 and 3300 millimeters, respectively, and finally, the diffuser with a length and an angle of nearly 19.000 millimeters and 2.7 degrees.

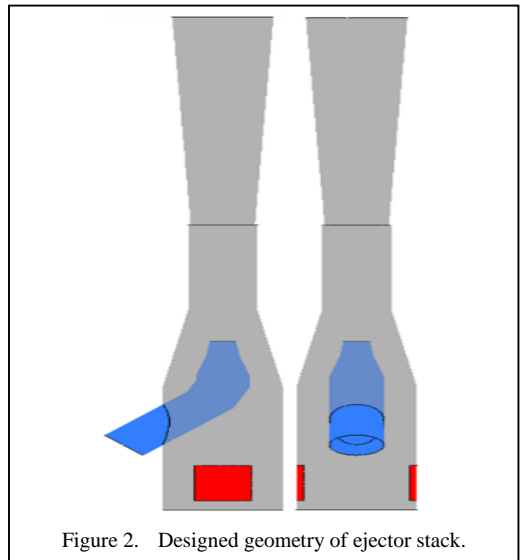
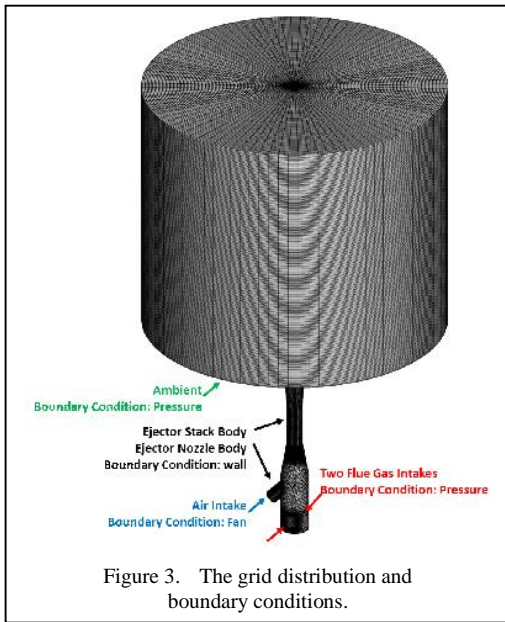


Figure 2. Designed geometry of ejector stack.

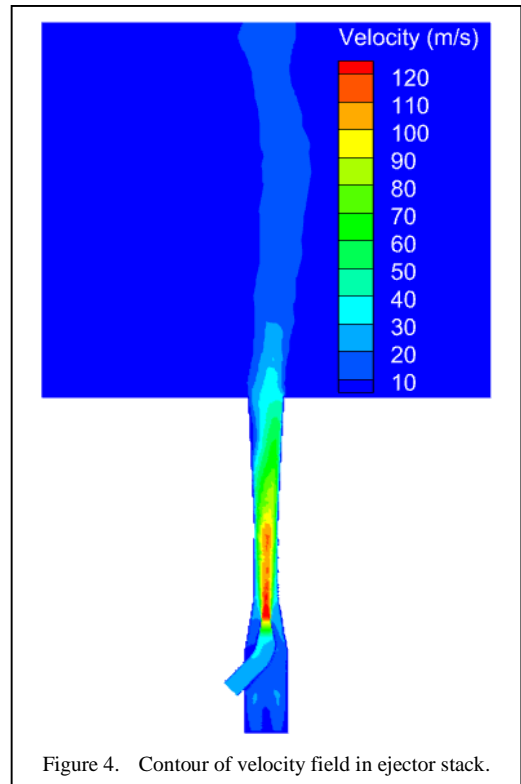


A high-quality mesh has been generated for the geometric model of the ejector stack, and boundary conditions have been defined to address the computational fluid dynamics problem. In Fig. 3, it's evident that the mesh has been refined in regions with narrow geometry, high curvature, proximity to the walls, and areas with significant flow parameter gradients. Notably, greater mesh refinement is observed at locations where the cross-section of the stack ejector and the ejector nozzle undergo transitions. Moreover, a grid-independent analysis has been conducted by monitoring the volumetric flow rate of flue gas, and the near-wall spacing satisfies the condition $y^+ < 1$. Consequently, the total number of mesh elements created is approximately 4.2 million, all of which are tetrahedrons. Four boundary conditions have been applied to define the computational fluid dynamics problem. The first boundary condition pertains to the air passing through the ejector stack fan, where an intake fan boundary condition is assumed. The second boundary condition is related to the flue gas flow, and in this case, a pressure boundary condition is used. The third boundary condition serves to observe the exit jet from the stack and the phenomena occurring beyond the design point at the stack exit, and it employs a pressure boundary condition set to the ambient pressure value for the domain representing the ambient. Finally, a wall boundary condition is used for the ejector stack and ejector nozzle walls.

IV. RESULTS AND DISCUSSION

In this section, we present the results of the computational fluid dynamics analysis and the selection of the motive air fan. To determine the most suitable intake fan, our objective is to operate the fan at a 50% opening angle of its damper. In this configuration, if the performance of the ejector stack deteriorates over time, the damper of the intake fan can be further opened to compensate for the reduction in the flue gas flow rate. To achieve this goal, we have considered various industrial fan performance curves as boundary conditions to identify the most appropriate one. The results indicate that with the selected fan and a 50% opening angle of its damper, the motive flow reaches $387446 \text{ Nm}^3/\text{h}$ at a temperature of 35°C and a pressure of 77 millibar. Fig. 4 displays the contour of the velocity field. In this figure, it is evident that the maximum velocity, reaching approximately 120 m/s, occurs at the outlet of the nozzle ejector.

Fig. 5 illustrates the performance curve of the selected fan. The red circle on the graph represents the design point of the fan during normal operation. The x-values on the graph are the volumetric flow rates normalized with respect to the design value, while the y-values



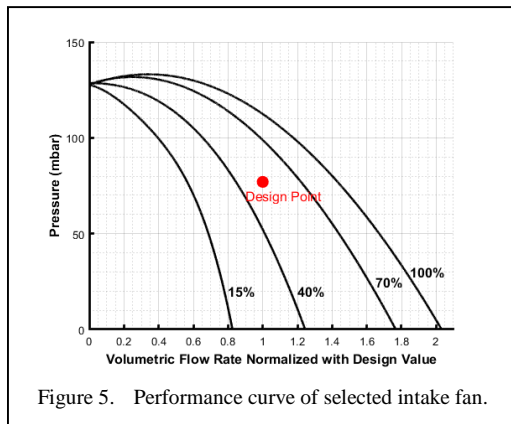


Figure 5. Performance curve of selected intake fan.

represent the pressure of the motive air after passing through the fan. Additionally, there are four black lines on the graph, each representing the performance curve of the intake fan at different opening angles.

V. CONCLUSION

In summary, the comprehensive design of the ejector stack and the utilization of computational fluid dynamics have provided valuable insights into its performance. The selection of an appropriate motive air fan, operated at a 50% damper opening angle, has demonstrated the system's adaptability to fluctuations in flue gas flow rates. The findings, including the field contours and the performance curve of the selected fan, offer essential information for the design and operation of ejector stacks in similar industrial applications. This study contributes to the understanding of ejector stack design and optimization, with potential applications in various industries. In industries where there is a requirement to release flue gas into the atmosphere at a pressure lower than atmospheric pressure, this research can be beneficial. In conclusion, the meticulous design, computational analysis, and fan selection have collectively contributed to achieving the desired performance in discharging flue gas. The knowledge obtained from this study can be applied to enhance the efficiency and reliability of similar ejector stack systems in industrial settings.

ACKNOWLEDGMENT

The authors would like to acknowledge the financial support received from the Esfahan's Mobarakeh Steel Company.

REFERENCES

- [1] Kroll, A. E. (1947). The design of jet pumps. *Chemical Engineering Progress*, 43(1), B21-B24.
- [2] Meakhail, T. A., Zien, Y., Elsallak, M., & AbdelHady, S. (2008). Experimental study of the effect of some geometric variables and number of nozzles on the performance of a subsonic air—Air ejector. *Proceedings of the Institution of Mechanical Engineers, Part A: Journal of Power and Energy*, 222(8), 809-818.
- [3] Croft, D. (1976). Jet pump design and performance analysis. In *14th Aerospace Sciences Meeting* (p. 183).
- [4] Eames, I. W. (2002). A new prescription for the design of supersonic jet-pumps: the constant rate of momentum change method. *Applied thermal engineering*, 22(2), 121-131.
- [5] Riffat, S. B., & Omer, S. A. (2001). CFD modelling and experimental investigation of an ejector refrigeration system using methanol as the working fluid. *International Journal of Energy Research*, 25(2), 115-128.
- [6] Yadav, R. L., & Patwardhan, A. W. (2008). Design aspects of ejectors: Effects of suction chamber geometry. *Chemical Engineering Science*, 63(15), 3886-3897.
- [7] DW, S., & IW, E. (1995). Recent developments in the design theories and applications of ejectors—a review. *Journal of the Institute of Energy*, 68(475), 65-79.
- [8] Li, C., Li, Y., & Wang, L. (2012). Configuration dependence and optimization of the entrainment performance for gas–gas and gas–liquid ejectors. *Applied Thermal Engineering*, 48, 237-248.
- [9] Cramers, P. H. M. R., & Beenackers, A. A. C. M. (2001). Influence of the ejector configuration, scale and the gas density on the mass transfer characteristics of gas–liquid ejectors. *Chemical Engineering Journal*, 82(1-3), 131-141.
- [10] Yang, X., Long, X., & Yao, X. (2012). Numerical investigation on the mixing process in a steam ejector with different nozzle structures. *International journal of thermal sciences*, 56, 95-106.
- [11] Zhang, X., Jin, S., Huang, S., & Tian, G. (2009). Experimental and CFD analysis of nozzle position of subsonic ejector. *Frontiers of Energy and Power Engineering in China*, 3, 167-174.
- [12] Zhu, Y., Cai, W., Wen, C., & Li, Y. (2009). Numerical investigation of geometry parameters for design of high performance ejectors. *Applied Thermal Engineering*, 29(5-6), 898-905.
- [13] Darbandi, M., & Jalali, R. (2023). A cost-effective approach to generate accurate correlations via analyzing a minimum number of data points; Case study on the convection heat transfer problem. *The Canadian Journal of Chemical Engineering*, 101(6), 3634-3647.
- [14] Darbandi, M., & Jalali, R. (2023). Internal cooling sensitivity analysis to improve the thermal performance of gas turbine blade using a developed robust conjugate heat transfer method. *International Journal of Engine Research*, 24(3), 949-964.

Calorific Value and Thermogravimetry of Bio-oil from Pyrolysis of Paraíba and Paraná

Philip Alexandre Araújo Ventura dos Santos¹, Joelda Dantas², Elvia Leal³, Alisson Marcos Fogaça⁴, Flávia de Medeiros Aquino⁵, Andrya Lays Freire Alves⁶

^{1,3,4,5,6}Federal University of Paraíba, João Pessoa - PB, Brazil

²Federal University of Campina Grande, Campina Grande - PB, Brazil

¹philip.santos@cear.ufpb.br, ⁶joelda.dantas@cear.ufpb.br

Abstract—Sludge contains harmful and toxic substances, so inadequate treatment poses a serious threat to the environment. In this sense, pyrolysis stands out as an efficient sanitization process, as well as being able to transform sewage sludge into valuable bioproducts that are simple to store, transport and use. Bio-oil is the most common bioproduct of high-temperature pyrolysis, and can be used as a fuel or converted into a chemical product. Bio-oil derived from pyrolysis is typically composed of multiple organic compounds, the composition and quantity of which vary depending on the source of the pyrolyzed waste and the process employed. In this work, we studied the calorific value and thermogravimetry of 3 samples of bio-oil from 2 representative Brazilian states (PB and PR) in order to begin to understand their properties. The results obtained in the calorific value analysis were 39.336 J/g, which is very close to fossil diesel (42.286 J/g) and higher than biodiesel (37.681 J/g), demonstrating that the Brazilian bio-oil studied is a promising biofuel. In terms of its thermal behaviour, upon exposure to heating rates of 5°C/min, 10°C/min and 20°C/min, synthetic air flow of 30 mL/min, with a temperature of 27 °C up to 800°C, it was found that the increase in temperature led to a higher content of volatile compounds, showing the importance of characterizing bio-oil to determine its best applications.

Keywords - sewage sludge, pyrolysis, bio-oil, characterization, biofuel

I. INTRODUCTION

With a view to the more sustainable production of biofuels in general, waste materials must be taken into account. Sewage sludge, for example, is a waste product from the sewage treatment process, its composition is complex and growing, and it has been considered a significant environmental concern. The proper disposal of sewage sludge is vital due to the presence of microorganisms and pathogens, high levels of metals, which are harmful to the environment, plants, animals and humans. However, sewage sludge has been considered a promising resource due to its high content of organic matter, nitrogen and phosphorus, and has generated great interest in the areas that study it [1].

As population and urbanization increase, sewage treatment plants (STPs) generate large volumes of sewage sludge, which must be processed and subsequently disposed of [2]. In this way, the flow of hazardous waste needs to be managed in such a way that it does not exceed the limited properties in terms of stock and rate of its receiving ecosystems [3]. The treatment methods for sewage sludge, incineration and landfill, release unwanted emissions into the soil and water, this pollution can build up and cause harm to humans and wildlife [4]. The cost of treating and disposing of sludge is extremely high and usually represents more than half of the operating costs of STPs [5].

Pyrolysis is a promising method for treating sewage sludge, with the potential to replace other

methods. It can have a direct and effective effect on reducing the volume of sewage sludge, eliminating parasites, pathogens, harmful and toxic substances, through the high temperatures present in the process [6].

Bio-oil generated from the pyrolysis process is a significant substitute for liquid fuel. It has high energy density and potential to replace fossil fuels. The bio-oil derived from pyrolysis is typically composed of multiple organic compounds, the composition and quantity of which vary depending on the source of the pyrolyzed residue and the process used. The organic phase components of the phase are aromatic and aliphatic compounds, including alkanes, alkenes, benzene derivatives, phenols, ketones, aldehydes and nitriles. The ability to understand the generation, structure and composition characteristics during pyrolysis is crucial for its future application in industry [7–9].

This work is aligned with the Sustainable Development Goals (SDGs), which are global targets set by the United Nations to address environmental, social and economic issues by 2030.

With the results of this work, we hope to contribute to research in the area and help decision-makers define more appropriate and sustainable renewable energy policies in Brazil and around the world.

II. MATERIAL AND METHODS

A. Characterization of Bio-Oil Samples

Three samples of bio-oils obtained by pyrolysis at temperatures of 500°C, named BO1, BO2 and BO3, from the cities of João Pessoa/PB, Campina Grande/PB and Ponta Grossa/PR, respectively, were characterized. The samples were provided by PyroCompany, a micro-company from the state of Paraíba, which has in-house technology for the process of sanitizing sewage sludge via pyrolysis and converting it into high value-added bioproducts, and which also aims to make a social contribution by training qualified human resources.

1) Calorific value

The calorific value of the 3 bio-oil samples (BO1, BO2 and BO3) was analyzed at the Federal University of Paraíba (UFPB) in the Materials and Environmental Chemistry Laboratory (LaBMaQ) of the Center for

Alternative and Renewable Energies (CEAR), using the PCs - IKA C200 calorimetric balance. Combustion was carried out in excess O₂ and at a pressure of 30bar. Samples weighing 1g were placed in a quartz crucible mounted inside a metal container and run for 15 minutes.

2) Thermogravimetric analysis

Taking into account what was reported by [10], that increasing the pyrolysis temperature significantly increases the yield in bio-oil, up to a temperature of 650°C, so, on this basis, one of the three bio-oil samples, BO1, was selected and thermogravimetric analysis (TGA/DTG) was carried out on a TA Instruments apparatus, model SDT650, at LaBMaQ/CEAR/UFPB.

The sample was tested using 13.048 mg, which was placed on an alumina support. The support was then heated at a rate of 5°C/min, varying the temperature up to 800°C, in an atmosphere of synthetic air with a flow rate of 30 mL/min. The aim was to identify the temperature at which the organic and inorganic components of the sample were eliminated, and the possible phase transitions that occurred at higher temperatures.

A maximum heating temperature of 800°C was set, since the degradation of bio-oil occurs close to this temperature [11].

III. RESULTS AND DISCUSSION

A. Calorific Value

Table I shows the calorific value results of the bio-oil samples generated from the conversion of sewage sludge (BO1, BO2 and BO3), produced by pyrolysis at 500°C.

In general, the bio-oil samples studied had excellent calorific values, and these were very close to each other, varying only 7.5% from the lowest to the highest value. The highest calorific value found was 39.336,00 J·g⁻¹, obtained for sample BO1, and the lowest value was 36.386,00 J·g⁻¹, obtained for sample BO3.

Thus, it can be said that the results obtained for all the samples studied are potential, since they are higher than the ANP reference value [12] for the calorific value of biodiesel, which is 37.681,00 J·g⁻¹, which is an important biofuel already consolidated in Brazil and worldwide.

TABLE I. CALORIFIC VALUE OF CRUDE BIO-OIL SAMPLES COMPARED TO VALUES FOR BIODIESEL AND FOSSIL DIESEL.

Bio-oil samples	Calorific value (J·g ⁻¹)	References
BO1 sample at 500°C	39.336,00	(Authors, 2023)
BO2 sample at 500°C	38.423,00	(Authors, 2023)
Sample BO3 at 500°C	36.386,00	(Authors, 2023)
Biodiesel	37.681,00	[12]
Fossil diesel	42.286,00	[12]

In addition, the calorific value of the crude bio-oil samples was close to that of fossil diesel, which is 42.286,00J·g⁻¹, which suggests a high content of hydrogen and carbon in the samples, implying that Brazilian sewage sludge bio-oil has great potential as a biofuel.

The results obtained are superior to those reported by [13], in which the calorific value of sewage sludge bio-oil from China was 22.000 - 34.000J·g⁻¹, possibly due to the characteristics of the sludge at each site.

By analyzing the calorific value, the amount of energy released in the form of heat during thermochemical processes can be confirmed, thus verifying the energy potential of bio-oil. Research has shown that pyrolyzed oil usually has a high calorific value, which makes it a potential alternative to fossil fuels [14].

According to [15], increasing the content of high calorific value components increases the

fuel's energy potential. Therefore, selecting the optimum final pyrolysis temperature is vital for increasing the yield and calorific value of bio-oil.

According to [16] the higher the calorific value of bio-oil, the greater its potential for use as a fuel. According to [17] the energy content of bio-oil can increase with lower oxygen and higher calorific value.

In this way, it can be said that the pyrolysis process successfully produces a bio-oil from sewage sludge, and that this bioproduct has good properties in relation to the expected calorific value.

B. Thermogravimetric Analysis

The crude bio-oil was analyzed to observe the thermogravimetric profile as a function of atmosphere, with the BO1 sample being heated from room temperature to 800°C.

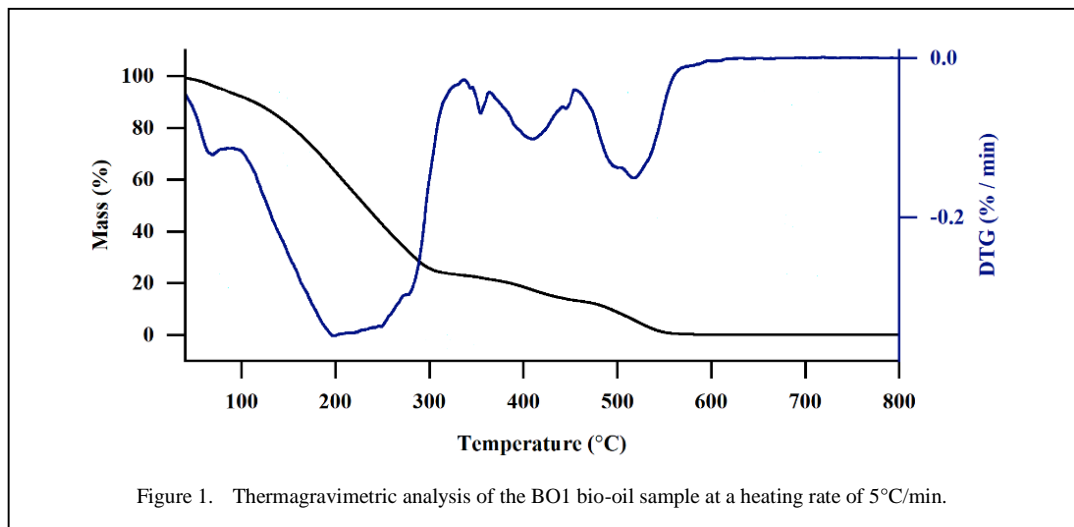


Figure 1. Thermogravimetric analysis of the BO1 bio-oil sample at a heating rate of 5°C/min.

Fig. 1 shows the curve obtained for a heating rate of 5°C/min, under a synthetic air atmosphere.

In general, the TGA and DTG events of the bio-oil analyzed can be divided into 4 stages of mass loss, described as follows.

- In the temperature range from 40°C to 100°C, the loss of mass is probably attributable to the evaporation of free water.
- From 100 to 300°C, hydrocarbons and carboxylic acids are reduced.
- From 300 to 400°C, which suggests the decomposition of larger molecular groups such as phenols and carbonyls.
- Possibly the decomposition of inorganic groups occurs at temperatures above 450°C.

According to [18] at temperatures up to 150°C there is a characteristic peak in the loss of free water, followed by the loss of structural water.

According to [19] at 200°C there is a peak characteristic of the combustion and volatilization of organic compounds, such as the carbonyl group, and between 400 and 650°C there is the decomposition of inorganic groups such as heavy hydrocarbons and aromatics.

Other authors who have studied bio-oil from sewage sludge obtained by pyrolysis in other parts of the world have also observed the presence of the events mentioned and obtained in this work. For example, the study by [11] in which the last thermal decomposition of the bio-oil occurred between 400 and 600°C, leading to the breakdown of heavy compounds, stability and lignin degradation.

There are also widespread studies involving bio-oil from the pyrolysis of different raw materials, such as Reutealis trisperma, in which a significant decrease in weight of 82.5% was observed between 378 and 486°C due to the decomposition of triglycerides [20].

The good thermal stability of the Brazilian bio-oil obtained from the pyrolysis of sewage sludge stands out, signaling a promising application as a more sustainable biofuel.

IV. CONCLUSION

The pyrolysis process is a thermal process for degrading materials with little impact on the environment, which has advantages in reducing urban and rural waste.

In relation to the analyses carried out on pyrolysis bio-oil samples from the states of Paraíba and Paraná, the preliminary results obtained were very promising, since the calorific value of the raw bio-oil reached the mark of 41.051,00J·g⁻¹. This value is close to that of fossil diesel and higher than that of biodiesel, which demonstrates its potential to replace non-renewable energy sources. The characterization of bio-oil by thermogravimetry was of great importance in assessing the pyrolysis potential of this bioproduct, showing that combustion and volatilization of organic compounds occur at temperatures above 200°C. It also helped to define important process variables, such as the experimental rate and time intervals.

From the results achieved so far, it can be said that pyrolysis is a potential process for producing bio-oil from sewage sludge and is very attractive due to the enormous economic value of this product.

The next steps of the research will be focused on methods of refining and purifying bio-oil, with the aim of reducing viscosity, removing the characteristic odor, in addition to increasing the calorific value, finally, applying bio-oil as fuel and fertilizer.

V. ACKNOWLEDGEMENTS

The authors thank PNPd/CAPES/CNPq, process number (88882.317968/2019-01), and PNPd/FAPESQ/PB (N°1990/2022, Edital N°17/2022), beneficiary program (24001015072P9-Renewable Energy), for the financial support for financial support.

The authors acknowledge the financial support of the Postgraduate Research Grant, grant 16/2022, Paraíba State Research Foundation (FAPESQ), Program 22210.12.573.5011.1998, line 3390.18 of the Source 500.

REFERENCES

- [1] Hu, W., Tong, W., Li, Y., Xie, Y., Chen, Y., Wen, Z., et al. (2020). Hydrothermal route-enabled synthesis of sludge-derived carbon with oxygen functional groups for bisphenol A degradation through activation of peroxymonosulfate. *Journal of Hazardous Materials*. 388 121801.

- [2] Liu, H., Basar, I.A., Lyczko, N., Nzihou, A., & Eskicioglu, C. (2022). Incorporating hydrothermal liquefaction into wastewater treatment – Part I: Process optimization for energy recovery and evaluation of product distribution. *Chemical Engineering Journal*, 449, 137838.
- [3] Zhang, G. (2024). Energetic, bio-oil, biochar, and ash performances of co-pyrolysis-gasification of textile dyeing sludge and Chinese medicine residues in response to K₂CO₃, atmosphere type, blend ratio, and temperature. *Journal of Environmental Sciences*.
- [4] Hu, Y., Xia, Y., Di Maio, F., Yu, F., & Yu, W. (2020). Investigation of polycyclic aromatic hydrocarbons (PAHs) formed in three-phase products from the pyrolysis of various wastewater sewage sludge. *Journal of Hazardous Materials*, 389, 122045.
- [5] Yang, T., Liu, X., Li, R., Li, B., & Kai, X. (2019). Hydrothermal liquefaction of sewage sludge to produce bio-oil: Effect of co-pretreatment with subcritical water and mixed surfactants. *The Journal of Supercritical Fluids*, 144, 28–38.
- [6] Wang, G., Dai, Y., Yang, H., Xiong, Q., Wang, K., Zhou, J., et al. (2020). A Review of Recent Advances in Biomass Pyrolysis. *Energy & Fuels*, 34 (12), 15557–15578.
- [7] Andreides, D., Fliegerova, K.O., Pokorna, D., & Zabranska, J. (2022). Biological conversion of carbon monoxide and hydrogen by anaerobic culture: Prospect of anaerobic digestion and thermochemical processes combination. *Biotechnology Advances*, 58, 107886.
- [8] Leng, L., Yang, L., Chen, J., Leng, S., Li, H., Li, H., et al. (2020). A review on pyrolysis of protein-rich biomass: Nitrogen transformation. *Bioresource Technology*, 315, 123801.
- [9] Qing, M., Long, Y., Liu, L., Yi, Y., Li, W., He, R., et al. (2022). Pyrolysis of the food waste collected from catering and households under different temperatures: Assessing the evolution of char structure and bio-oil composition. *Journal of Analytical and Applied Pyrolysis*, 164, 105543.
- [10] Huang, Z., Qin, L., Xu, Z., Chen, W., Xing, F., & Han, J. (2019). The effects of Fe₂O₃ catalyst on the conversion of organic matter and bio-fuel production during pyrolysis of sewage sludge. *Journal of the Energy Institute*, 92(4), 835–842.
- [11] Allende, S., Brodie, G., & Jacob, M.V. (2022). Energy recovery from sugarcane bagasse under varying microwave-assisted pyrolysis conditions. *Bioresource Technology Reports*, 20, 101283.
- [12] ANP (2023). Publicações. Agência Nacional do Petróleo, Gás Natural e Biocombustíveis.
- [13] Liu, Y., Ran, C., Siyal, A.A., Song, Y., Jiang, Z., Dai, J., et al. (2020). Comparative study for fluidized bed pyrolysis of textile dyeing sludge and municipal sewage sludge. *Journal of Hazardous Materials*, 396, 122619.
- [14] Djandja, O.S., Wang, Z.-C., Wang, F., Xu, Y.-P., & Duan, P.-G. (2020). Pyrolysis of Municipal Sewage Sludge for Biofuel Production: A Review. *Industrial & Engineering Chemistry Research*, 59(39), 16939–16956.
- [15] Lin, J., Sun, S., Ma, R., Fang, L., Zhang, P., Qu, J., et al. (2018). Characteristics and reaction mechanisms of sludge-derived bio-oil produced through microwave pyrolysis at different temperatures. *Energy Conversion and Management*, 160, 403–410.
- [16] Zaker, A., Chen, Z., Wang, X., & Zhang, Q. (2019). Microwave-assisted pyrolysis of sewage sludge: A review. *Fuel Processing Technology*, 187, 84–104.
- [17] Gao, N., Kamran, K., Quan, C., & Williams, P.T. (2020). Thermochemical conversion of sewage sludge: A critical review. *Progress in Energy and Combustion Science*, 79, 100843.
- [18] Erdogdu, A.E., Polat, R., & Ozbay, G. (2019). Pyrolysis of goat manure to produce bio-oil. *Engineering Science and Technology, an International Journal*, 22(2), 452–457.
- [19] Chen, G.-B., Li, J.-W., Lin, H.-T., Wu, F.-H., & Chao, Y.-C. (2018). A Study of the Production and Combustion Characteristics of Pyrolytic Oil from Sewage Sludge Using the Taguchi Method. *Energies*, 11(9), 2260.
- [20] Buyang, Y., Suprpto, S., Nugraha, R.E., Holilah, H., Bahruji, H., Hantoro, R., et al. (2023). Catalytic pyrolysis of Reutealis trisperma oil using raw dolomite for bio-oil production. *Journal of Analytical and Applied Pyrolysis*, 169, 105852.

Numerical Model for Computation of Induced Voltages along Double-circuit Overhead Transmission Lines

Ivica Jurić-Grgić¹, Dino Lovrić², Ivan Krolo³

^{1,2,3}University of Split, Faculty of Electrical Engineering, Mechanical Engineering and Naval Architecture, R. Boskovicica 32, HR-21000 Split, Croatia

¹ijuricgr@fesb.hr, ²dlovric@fesb.hr, ³ikrolo@fesb.hr

Abstract—This paper presents a simple and reliable algorithm for the harmonic analysis of both current and voltage conditions along double-circuit system overhead transmission lines. The developed numerical model is based on the finite element technique which is essential in the process of reducing the problem of solving a complicated system to the problem of solving a subsystem, for which we can easily define a local system of equations based on a mathematical model. To calculate the short-circuit current distribution along the considered double-circuit system overhead transmission lines, it is necessary to divide the entire transmission line into as many finite elements as there are spans between power line towers. It is also necessary to model the grounding of each tower as a separate finite element. An assumed hydroelectric power plant with associated generators and incident network are also shown as separate finite elements with associated parameters. The safety of the maintenance worker on the disconnected and passive circuit of double-circuit overhead transmission line system is directly related to the induced voltages at the worksite. As a worst-case scenario from the standpoint of induced voltages, we considered the case of a single-phase earth fault on the active circuit of a double-circuit overhead transmission line system, where the highest possible single-phase earth fault current value has been taken into account. During this fault, the passive circuit of the double-circuit overhead transmission line system is grounded on both ends of the line. Induced voltages were analyzed in the case of a grounded worksite tower and two adjacent towers along the entire double-circuit system overhead transmission lines system.

Keywords - single-phase earth fault, induced voltages, finite element technique, double circuit overhead transmission lines

I. INTRODUCTION

It is widely acknowledged that when conducting maintenance work on double-circuit overhead transmission lines, standard procedures can be applied to the de-energized or a passive overhead line triplet while the active triplet of the double-circuit overhead transmission line remains in normal operation. Standard procedures for working on the passive triplet of the double-circuit overhead transmission lines involve grounding the passive triplet and short-circuiting it on the transmission line tower in the vicinity of the worksite as well as grounding the passive triplet on two adjacent towers.

During the maintenance on the passive triplet, induced voltages can be detected on the passive phase conductors due to capacitive and inductive coupling. The magnitude of these induced voltages is primarily dependent upon the geometry of conductors, voltage and current conditions of the active phase conductors. The most critical scenario is the occurrence of a single-phase ground fault on the active triplet, which can lead to extremely high induced voltages along the passive triplet, as well as on the shielding wire and grounded towers of the transmission line.

The finite element technique (FET) is a well-established method used to solve a wide range of engineering problems, including structural analysis and continuum issues [1-2], numerical

problem-solving related to transmission lines [3,4], power system short-circuit analysis [5], and angular stability analysis of power systems [6]. This technique's core concept involves simplifying complex systems by dividing them into subsystems, for which we can readily define local sets of equations based.

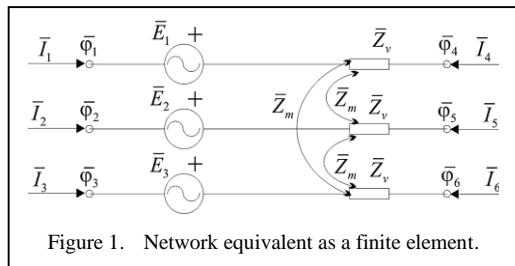
This paper introduces a straightforward and reliable algorithm for conducting harmonic analysis of both current and voltage conditions along double-circuit overhead transmission lines. The developed numerical model for analyzing induced voltages along these transmission lines is based upon the FET.

To assess induced voltages from the standpoint of the most critical scenario, we focused on a single-phase short circuit on an active triplet of the double-circuit transmission line, taking into account the highest possible current value that can arise. During this situation, the de-energized or passive triplet is grounded on both sides. Induced voltages were analyzed in the case of a grounded work site with two adjacent transmission line towers being grounded also.

II. ANALYSIS OF INDUCED VOLTAGES ALONG DOUBLE-CIRCUIT OVERHEAD TRANSMISSION LINES USING THE FINITE ELEMENT TECHNIQUE

In [5], a generalized finite-element-technique-based procedure for deriving the local system of equations for the case of harmonic analysis of various short-circuit scenarios within an electric power system is described. In this paper however, we build upon the algorithm introduced in [5] and adapt it specifically for analyzing induced voltages along double-circuit overhead transmission lines.

Our objective in this paper is to perform a thorough harmonic analysis, encompassing both current and voltage conditions along double-circuit overhead transmission lines. This will also involve simultaneous computations of short-circuit current distribution and induced voltages along the passive system of the double-circuit overhead transmission line. In order to achieve this goal, it is necessary to divide the entire double-circuit transmission line into as many finite elements as there are overhead transmission line spans between towers. It is also essential to represent each tower grounding grid as a separate finite element.



In the scenario considered in this paper a hydroelectric power plant along with its associated generators is assumed to be connected to a double-circuit system which is connected on the other side to an assumed incident network. The power plant and the incident network are also depicted as separate finite elements described by a corresponding set of parameters.

A. Hydroelectric Power Plant and the Incident Network as Finite Elements

According to [5], the finite element representing the hydroelectric power plant and the incident network (Fig. 1), can be modified as to represent a network equivalent using six local nodes. This finite element consists of a serial connection of impedances (with mutual inductances between them taken into account) with corresponding electromotive forces.

In order to define the local system of equations, necessary in one of the steps of the FET, for this specific case branch currents must be mathematically linked to the currents associated with local nodes. Consequently, the following local system of equations for the finite element of the network equivalent is obtained:

$$\begin{aligned} \{\bar{I}\} = & \begin{bmatrix} [\bar{Y}^{abc}] & -[\bar{Y}^{abc}] \\ -[\bar{Y}^{abc}] & [\bar{Y}^{abc}] \end{bmatrix} \cdot \{\bar{\varphi}\} \\ & - \begin{bmatrix} [\bar{Y}^{abc}] & 0 \\ 0 & -[\bar{Y}^{abc}] \end{bmatrix} \cdot \begin{Bmatrix} \{\bar{E}\} \\ \{\bar{E}\} \end{Bmatrix}, \quad (1) \end{aligned}$$

where:

$[\bar{Y}^{abc}] = [\bar{Z}^{abc}]^{-1}$ – matrix containing phasors of admittances,

$[\bar{Z}^{abc}]$ – equivalent matrix of the hydroelectric power plant or the incident network in the a, b, c system containing phasors of impedances,

$\{\bar{E}\} = \{\bar{E}_1 \bar{E}_2 \bar{E}_3\}^T$ – vector containing phasors of electromotive forces,

$\{\bar{I}\} = \{\bar{I}_1 \bar{I}_2 \bar{I}_3 \bar{I}_4 \bar{I}_5 \bar{I}_6\}^T$ – vector containing phasors of currents associated with local nodes,

$\{\bar{\varphi}\} = \{\bar{\varphi}_1 \bar{\varphi}_2 \bar{\varphi}_3 \bar{\varphi}_4 \bar{\varphi}_5 \bar{\varphi}_6\}^T$ – vector containing phasors of scalar electric potentials of local nodes.

In summary, the finite element of the hydroelectric power plant or the incident network contains six local nodes. The local system of equations for this finite element is defined by the system of algebraic equations given in Eq. (1) which is pivotal in seamlessly assembling the hydroelectric power plant or the incident network finite element into the broader model of the electric power system under consideration.

B. Span of the Double-circuit Overhead Transmission Line as a Finite Element

In most cases, double-circuit overhead transmission line is composed of two sets of triplets (three phases) and one shielding wire, i.e., six phase conductors and one shielding wire. Hence, it is necessary to define a finite element with 14 local nodes, each node corresponding to one end of either a phase conductor or a shielding wire. According to [5], the finite element of the double-circuit overhead transmission line can be modified to represent this exact case (Fig. 2). As can be seen, the finite element is modelled as a serial connection of six phase conductors and one shielding wire with mutual inductance taken into account.

In order to define the local system of equations for this finite element we must mathematically link the branch currents with the corresponding local nodes. Consequently, the following local system of equations is obtained:

$$\{\bar{I}\} = \begin{bmatrix} [\bar{Y}] & -[\bar{Y}] \\ -[\bar{Y}] & [\bar{Y}] \end{bmatrix} \{\bar{\varphi}\}, \quad (2)$$

where:

$[\bar{Y}] = [\bar{Z}]^{-1}$ – matrix containing phasors of admittances,

$[\bar{Z}]$ – matrix containing phasors of impedances of the seven conductors over a finite element in the a, b, c system,

$\{\bar{I}\} = \{\bar{I}_1 \bar{I}_2 \bar{I}_3 \bar{I}_4 \bar{I}_5 \bar{I}_6 \bar{I}_7 \bar{I}_8 \bar{I}_9 \bar{I}_{10} \bar{I}_{11} \bar{I}_{12} \bar{I}_{13} \bar{I}_{14}\}^T$ – vector containing phasors of current joined to local nodes,

$\{\bar{\varphi}\} = \{\bar{\varphi}_1 \bar{\varphi}_2 \bar{\varphi}_3 \bar{\varphi}_4 \bar{\varphi}_5 \bar{\varphi}_6 \dots \bar{\varphi}_{12} \bar{\varphi}_{13} \bar{\varphi}_{14}\}^T$ – vector containing scalar electric potentials of local nodes.

To summarize, the finite element of the double-circuit overhead transmission line span is defined using 14 local nodes. The local system of equations is mathematically described using a system of algebraic equations given in (2) which is used to assemble the transmission line span with the rest of the considered part of the electric power system.

C. Grounding Grids of Transmission Line Towers, Hydroelectric Power Plant and the Incident Network as Finite Elements

According to [5], the finite element of the grounding grid depicted in Fig. 3 can be modified to a finite element which only has one local node. In the considered model, the finite element of the grounding system only utilizes resistances.

According to Fig. 3, a simple algebraic equation can be written which represents the mathematical model of the grounding grid as a finite element:

$$\bar{I}_1 = \frac{1}{R} \bar{\varphi}_1, \quad (3)$$

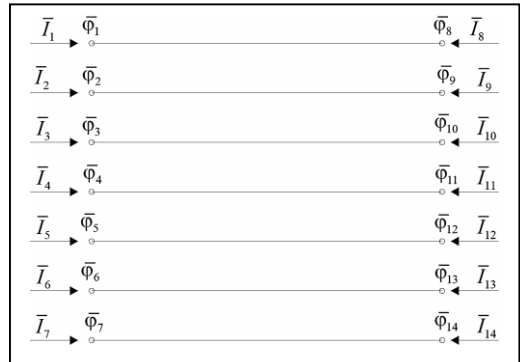


Figure 2. Span of a double-circuit overhead transmission line as a finite element.

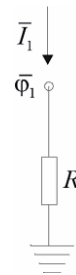


Figure 3. Grounding grid as a finite element.

III. NUMERICAL EXAMPLE

On the basis of the presented theoretical background, a numerical algorithm was developed in MATLAB for the analysis of induced voltages along double-circuit overhead transmission lines. The considered part of the electric power system is depicted in Fig. 4. As can be seen from this figure, the system is composed of an assumed hydroelectric power plant connected via transformer to the 220 kV Bus A and the equivalent network connected to the 220kV Bus B.

The hydroelectric power plant is connected to the equivalent network via a 220kV double-system overhead transmission line. In the assumed hydroelectric power plant three generators are connected to corresponding transformers. In order to perform the short circuit analysis along the observed transmission line as well as the induced voltages on the passive part of the double-circuit it is necessary to subdivide the entire double-circuit transmission line into as many parts as there are line spans between towers.

Fig. 5 depicts the hydroelectric power plant, i.e., the equivalent Transformer station A (TS A), the 220kV double-circuit overhead transmission

line and the incident 220kV network via the Transformer station B (TS B). The transmission line is considered to contain 81 towers which corresponds to 82 line spans. Resistances R_1 and R_{83} represent the grounding resistances of Transformer stations A and B, respectively. Resistances R_2 to R_{82} represent grounding resistances of towers. Single-phase short circuit is simulated on the first tower counting from side A of the considered system.

A. Calculation of Parameters of the Hydroelectric Power Plant

Three synchronous generators are considered to be installed in the assumed hydroelectric power plant with the following input parameters: $S_n = 83$ MVA, $U_n = 10.5$ kV, $x_d'' = 18.25\%$. The adjoining transformers have the following input data: $S_n = 83$ MVA, $U_{n1}/U_{n2} = 10.5/220$ kV, $u_k = 12.06\%$, $P_k = 270$ kW. It's assumed that the transformers are connected using Yd5, where the star-connected 220kV side of the transformer is grounded. Reducing these parameters to the 220 kV voltage level, the following equivalent matrix of impedance phasors (in Ω) is obtained in the a, b, c system for the hydroelectric power plant:

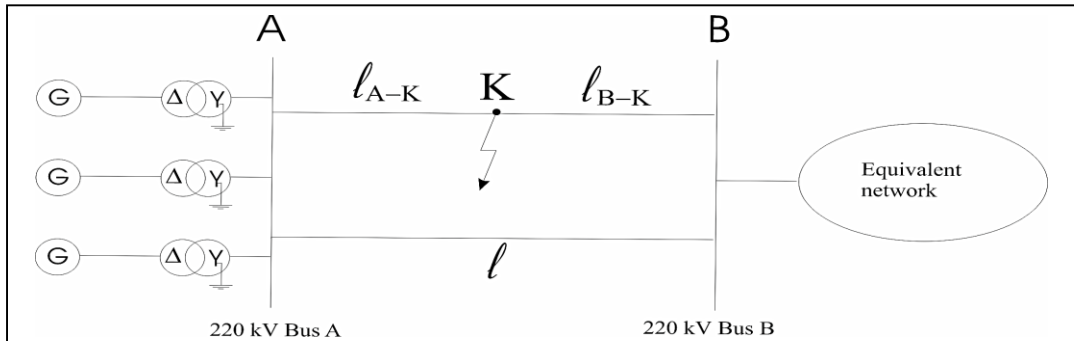


Figure 4. Schematic of the considered electric power system.

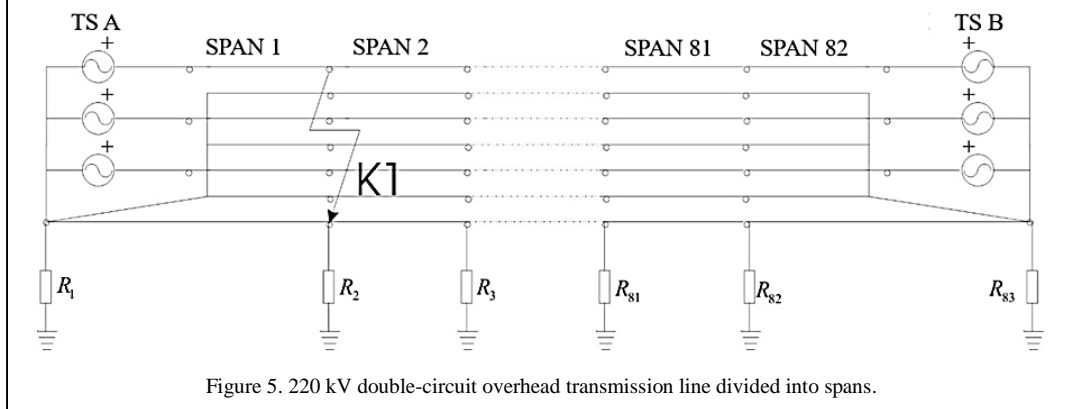


Figure 5. 220 kV double-circuit overhead transmission line divided into spans.

$$[\bar{Z}^{abc}] = \begin{bmatrix} 0.632 + j46.11 & -j11.34 & -j11.34 \\ -j11.34 & 0.632 + j46.11 & -j11.34 \\ -j11.34 & -j11.34 & 0.632 + j46.11 \end{bmatrix}, \quad (4)$$

B. Calculation of Parameters of the Equivalent 220 kV Incident Network

By calculating the three-phase and single-phase short circuit on Bus B without taking into consideration $\bar{I}_{k3} = 18.14e^{-j48^\circ}$ the contribution of the hydroelectric power plant the following values are obtained: $\bar{I}_{k1} = 18.14e^{-j48^\circ} \text{ kA}$ Reducing these parameters to the 220 kV voltage level, the following equivalent matrix of impedance phasors (in Ω) of the incident network in the a, b, c system is obtained:

$$[\bar{Z}^{abc}] = \begin{bmatrix} 0.74 + j8.46 & -0.06 - j0.73 & -0.06 - j0.73 \\ -0.06 - j0.73 & 0.74 + j8.46 & -0.06 - j0.73 \\ -0.06 - j0.73 & -0.06 - j0.73 & 0.74 + j8.46 \end{bmatrix}, \quad (5)$$

C. Calculation of Parameters of the 220 kV Double-circuit Overhead Transmission Line

Using the usual tower and overhead line geometry, one can simply calculate the per-unit matrix of impedance phasors of the transmission line conductors (given in Table I in Ω/km).

The considered 220 kV double-circuit transmission line is comprised of phase conductors made of aluminum-steel material (ACSR) with a cross-section area of $360/57 \text{ mm}^2$. The shielding wire is made of AWG with a cross-section area of 117 mm^2 . The transmission line contains 81 towers with corresponding 82 line spans. The lengths of line spans are randomly taken to be Eq. (6).

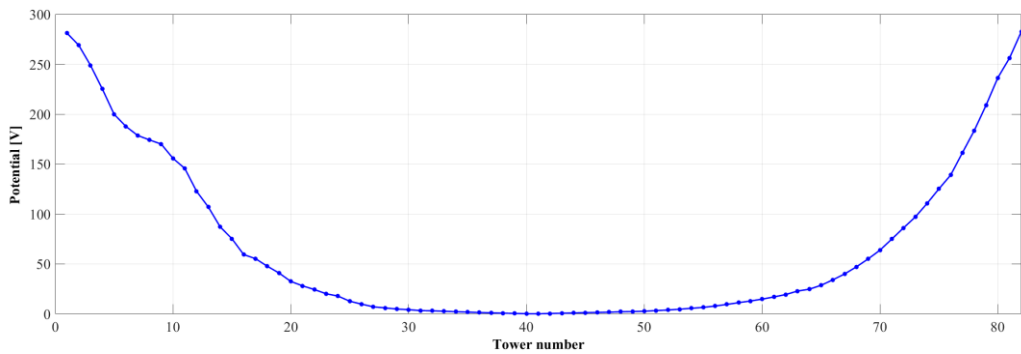
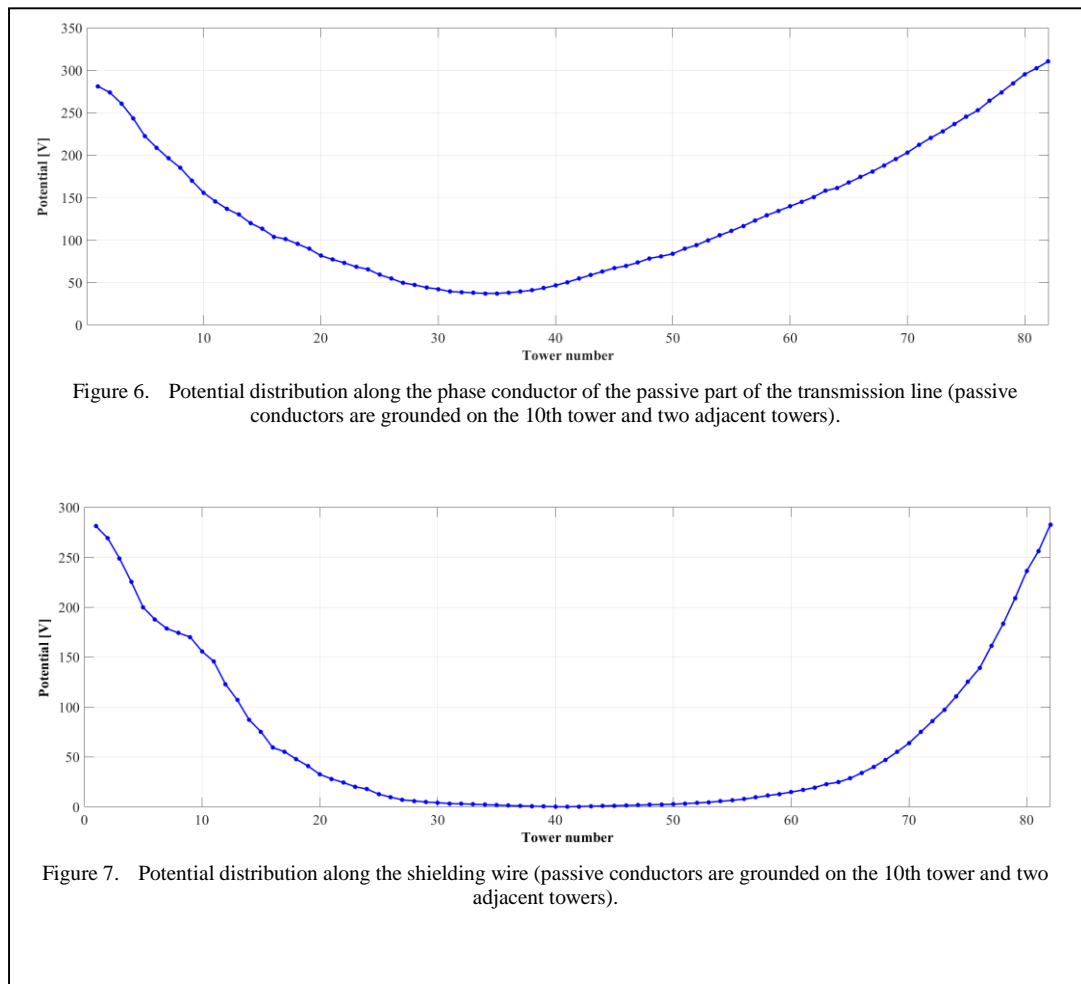
Grounding resistances of Transformer station A, all towers and Transformer station B are considered to be equal to Eq. (7).

$$l \text{ (km)} = \begin{bmatrix} 0.132 & 0.247 & 0.341 & 0.442 & 0.308 & 0.300 & 0.283 \\ 0.422 & 0.440 & 0.334 & 0.373 & 0.284 & 0.471 & 0.325 \\ 0.475 & 0.151 & 0.318 & 0.323 & 0.499 & 0.286 & 0.259 \\ 0.321 & 0.197 & 0.477 & 0.365 & 0.474 & 0.242 & 0.369 \\ 0.236 & 0.518 & 0.134 & 0.273 & 0.337 & 0.307 & 0.436 \\ 0.328 & 0.295 & 0.405 & 0.389 & 0.424 & 0.432 & 0.404 \\ 0.368 & 0.352 & 0.218 & 0.326 & 0.405 & 0.190 & 0.245 \\ 0.453 & 0.317 & 0.446 & 0.416 & 0.386 & 0.411 & 0.439 \\ 0.419 & 0.358 & 0.358 & 0.352 & 0.355 & 0.455 & 0.198 \\ 0.381 & 0.356 & 0.342 & 0.372 & 0.386 & 0.380 & 0.439 \\ 0.391 & 0.345 & 0.384 & 0.371 & 0.320 & 0.460 & 0.396 \\ 0.403 & 0.390 & 0.253 & 0.263 & 0.297 & & \end{bmatrix}, \quad (6)$$

$$R \text{ } (\Omega) = \begin{bmatrix} 0.45 & 24 & 22 & 22 & 11 & 20 & 10.5 \\ 25.5 & 25 & 25 & 16 & 25 & 6.8 & 16.5 \\ 26 & 8.5 & 16 & 17 & 8.5 & 23 & 24 \\ 22 & 14 & 24 & 4.5 & 4.3 & 5 & 5 \\ 7 & 5 & 25 & 20 & 19 & 9 & 20 \\ 15 & 16 & 5.5 & 6 & 10 & 10.5 & 7 \\ 9 & 10 & 28 & 33 & 15 & 17 & 23 \\ 7 & 20 & 18 & 16 & 20 & 7 & 18 \\ 20 & 22 & 21 & 15 & 28 & 21 & 13 \\ 23 & 5 & 22 & 25 & 32 & 27 & 25 \\ 21 & 27 & 26 & 27 & 29 & 24 & 22 \\ 24 & 26 & 28 & 10 & 25 & 0.5 & \end{bmatrix}. \quad (7)$$

TABLE I. PER-UNIT MATRIX OF IMPEDANCE PHASORS OF THE TRANSMISSION LINE CONDUCTORS (Ω/KM).

	a	b	c	a	b	c	p
a	$0.13 + j0.76$	$0.05 + j0.36$	$0.05 + j0.32$	$0.05 + j0.34$	$0.05 + j0.32$	$0.05 + j0.30$	$0.05 + j0.33$
b	$0.05 + j0.36$	$0.13 + j0.76$	$0.05 + j0.36$	$0.05 + j0.32$	$0.05 + j0.31$	$0.05 + j0.31$	$0.05 + j0.30$
c	$0.05 + j0.32$	$0.05 + j0.36$	$0.13 + j0.76$	$0.05 + j0.30$	$0.05 + j0.31$	$0.05 + j0.33$	$0.05 + j0.28$
a	$0.05 + j0.34$	$0.05 + j0.32$	$0.05 + j0.30$	$0.13 + j0.76$	$0.05 + j0.36$	$0.05 + j0.32$	$0.05 + j0.33$
b	$0.05 + j0.32$	$0.05 + j0.31$	$0.05 + j0.31$	$0.05 + j0.36$	$0.13 + j0.76$	$0.05 + j0.36$	$0.05 + j0.30$
c	$0.05 + j0.30$	$0.05 + j0.31$	$0.05 + j0.33$	$0.05 + j0.32$	$0.05 + j0.36$	$0.13 + j0.76$	$0.05 + j0.28$
p	$0.05 + j0.33$	$0.05 + j0.30$	$0.05 + j0.28$	$0.05 + j0.33$	$0.05 + j0.30$	$0.05 + j0.28$	$0.79 + j0.80$



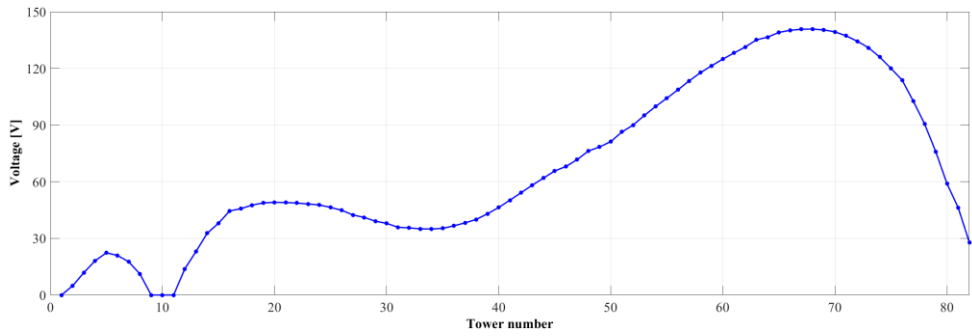


Figure 8. Voltage distribution between passive phase conductors and the shielding wire (passive conductors are grounded on the 10th tower and two adjacent towers).

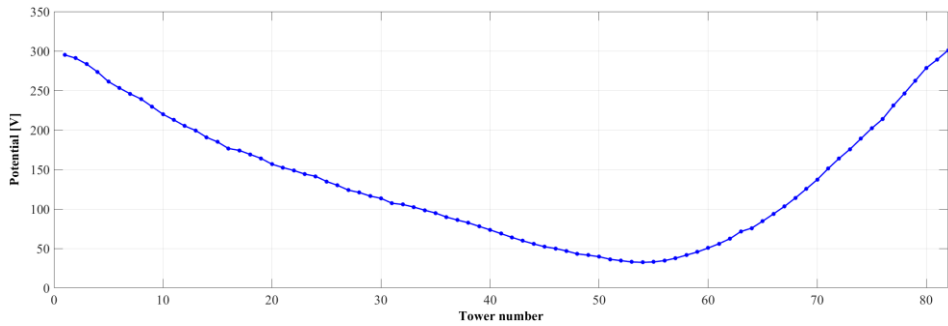


Figure 9. Potential distribution along the phase conductor of the passive part of the transmission line (passive conductors are grounded on the 60th tower and two adjacent towers).

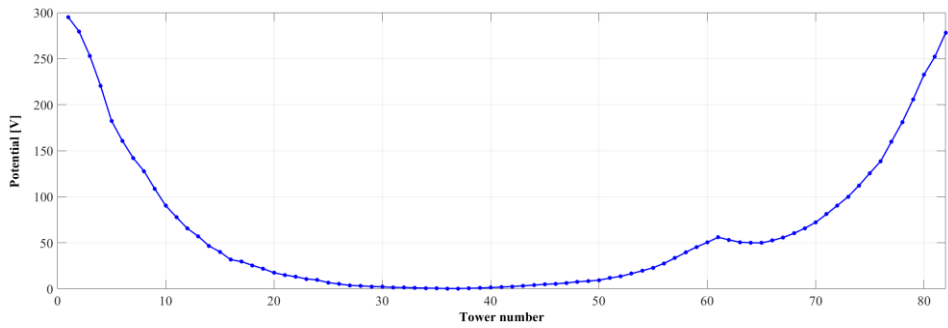


Figure 10. Potential distribution along the shielding wire (passive conductors are grounded on the 60th tower and two adjacent towers).

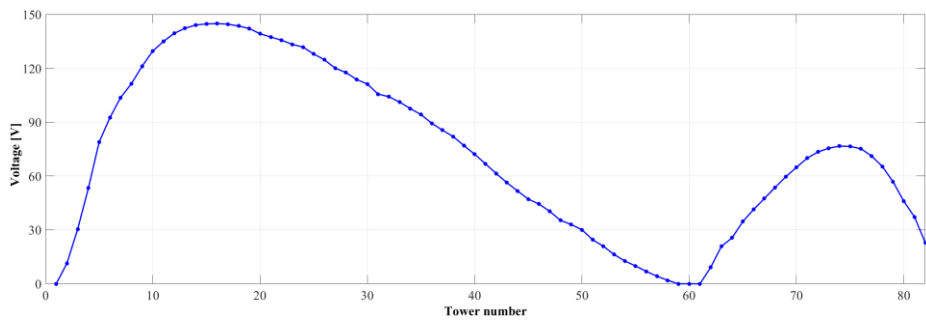


Figure 11. Voltage distribution between passive phase conductors and the shielding wire (passive conductors are grounded on the 60th tower and two adjacent towers).

D. Computation Results

In this analysis, we evaluated the worst-case scenario from the standpoint of induced voltages, focusing on single-phase short circuit occurrence on the active triplet of the double-circuit transmission line, considering the highest achievable short-circuit current magnitudes (Figs. 6-11). Consequently, we analyzed a nearby failure scenario, specifically a single-phase short circuit incident on the first tower counting from side A. In the analysis the passive part of the double-circuit transmission line is disconnected and grounded at both ends (side A and B).

Induced voltages were analyzed in the case of a grounded work site as well as two grounded adjacent towers along the double-circuit transmission. As a result of the computation, we obtained the potential distribution along the phase conductors of the passive part of the transmission line, the potential distribution along the shielding wire, and the voltage distribution between the phase conductors of the passive conductors and the shielding wire.

IV. CONCLUSION

This paper presents a straightforward and reliable algorithm for harmonic analysis of both current and voltage conditions along a double-circuit overhead transmission line. The developed numerical model for evaluating induced voltages along these transmission lines is based on the finite element technique. To conduct a comprehensive harmonic analysis, encompassing both current and voltage conditions on double-circuit overhead transmission lines, the entire line is divided into as many finite elements as there are spans between transmission line towers. This is of particular importance to the simultaneous computation of single-phase short-circuit current distribution and induced voltages on the passive triplet along the observed double-circuit overhead transmission line. Additionally, each grounding grid of a transmission line tower is treated as a separate finite element, as is the

hydroelectric power plant, its associated generators, and the incident network.

Based on this theoretical foundation, a numerical algorithm for induced voltage analysis along double-circuit overhead transmission line was developed using the MATLAB software package. We considered the most severe scenario regarding induced voltages, which involved a single-phase short circuit on an active triplet of the transmission line, taken into account the highest possible current values.

We analyzed induced voltages in two scenarios, both with a grounded worksite at a particular tower with two adjacent towers being grounded also. Potential distribution along the phase conductors of the passive triplet was obtained, as well as the potential distribution along the shielding wire and the voltage distribution between the phase conductors of the passive triplet and the shielding wire.

Based on the performed analyses it can be concluded that working on a passive triplet of a double-circuit overhead transmission line is possible under the fundamental condition that this passive triplet is properly grounded.

REFERENCES

- [1] Zienkiewicz, O. C., Taylor, R. L. (1989). *The finite element method Vol.1. McGraw-Hill.*
- [2] Zienkiewicz, O. C., Taylor, R. L. (1991). *The finite element method Vol.2. McGraw-Hill.*
- [3] Lucic, R., Juric-Grgic, I., & Kurtovic, M. (2010). Time domain finite element method analysis of multi-conductor transmission lines. *European transactions on electrical power*, 20(6), 822-832.
- [4] Lee, S. Y., Konrad, A., & Saldanha, R. (1993). Lossy transmission line transient analysis by the finite element method. *IEEE Transactions on Magnetics*, 29(2), 1730-1732.
- [5] Jurić-Grgić, I., Lucić, R., & Kurtović, M. (2009). *Power system fault studies using finite element technique*. International Review on Modelling and Simulations, 2(1), 12-17.
- [6] Jurić-Grgić, I., Grulović-Plavljančić, N., & Dabro, M. (2019). *An Analysis of Power System Transient Stability Using Finite Element Technique*. International Transactions on Electrical Energy Systems, 29(1), e2694.

Dynamic Influence of Shapes inside Reformer of Methanol Steam Reaction

Abaidi Abou Houraira¹, Madani Brahim²

^{1,2}LTPMP/FGM&GP/USTHB, Algiers, Algeria

¹abaidiadel70@gmail.com

Abstract—This work is simulation study by using COMSOL software, which treats the dynamics influence of fins and blocs shapes inside the reformer of hydrogen production from methanol steam reforming process. The purpose of the current simulations is to study the dynamic influence of fins and blocs on phenomena of hydrogen production, methanol consumption and reactor efficiency. The primary numerical results show that: the insertion of fins and blocs inside the reformer will increase the hydrogen consumption and methanol consumption by the value 5%, but we need to make more propositions and technics to increase the last percentage.

Keywords - fins and blocs shape, dynamic influence, heat and mass transfer, hydrogen production, methanol steam reforming

I. INTRODUCTION

Delivering hydrogen for fuel cells safely and efficiently is the premise and guarantee of distributed power generation. A methanol and methane steam reforming reformer process was considered like industry source of hydrogen to fuel cells. Many studies were intersected to how increase the hydrogen recuperation form MSR process, it can cite some work on increasing hydrogen production. Firstly, the segmentation of the catalyst layer [1] in similar parts increases the reformer of methanol steam reforming efficiency (Hydrogen production) by 2.11%, 4.23%, 6.77%, and 8.6% for 2, 4, 8, and 16 identical parts, respectively. As well as, the metal foam as catalyst support is more efficient compared to the other configurations, the efficiency is equal to 64% at $T=495K$. Secondly, the results of [2] show that the Methane Steam Reforming efficiency can be improved by extending the catalytic zone and discretizing the catalyst coating. Comparing to conventional

MSR with continuous catalytic layers, enhancement of 28.71% in CH_4 conversion and 88.574% in H_2 production is realized by using discretized catalytic layers.

The efficiency can be increased by different technics; like the diffuser [3], a proton exchange membrane fuel cells (PEMFC) connected with a methanol steam reformer designed to enhance its performance. In comparison with a traditional reformer, the reformer with a diffuser of $\theta_d = 6$ and $L_d = 75$ mm obtains the maximum enhancement of 22.96% in methanol conversion, 44.62% in hydrogen production, and 24.59% in estimated net power of fuel cell at wall temperature of $250^\circ C$. In addition, the novel reformer with a diffuser of $\theta_d = 6$ and $L_d = 100$ mm generates the maximum reduction of 44.17% in CO production at $T_w = 250^\circ C$. Another study [4], a micro-channel heat exchanger reactor with different micro-baffle shapes has been studied numerically. In addition to the straight micro-channel, other types of micro-channel with different micro-baffle shapes on both sides of the solid section were studied. The results show that; the hydrogen yield obtained by a rectangular micro-baffle is 17% higher, on average, than that obtained with by a straight configuration. The methanol conversion can be increased by $\sim 25\%$ by using segmented catalyst layer configurations with less catalyst in the reforming and combustion sides [5]. In addition, the cascading metal foams were used as catalyst supports for constructing a new type of cylindrical laminated methanol steam reforming microreactor for hydrogen production [6]. Furthermore, the effect of the type of catalyst placement, pores per inch (PPI) and foam type on the performance of methanol steam reforming microreactor was studied. Compared with two

other types of catalyst placement studied, the microreactor containing catalyst-loaded metal foams without clearance cascading (3 x 2) showed the highest hydrogen production performance. When the PPI of the metal foam was increased from 50 to 100, both the methanol conversion and the H₂ flow rate gradually increased.

Optimal design of the flow pattern can enhance the hydrogen production effectively [7]. An A-type microchannel reactor with a flow pattern design of one inlet and two outlets was applied to conduct methanol steam reforming for hydrogen production. The results showed that the species distributions in the A-type microchannel were more homogeneous. In addition, the A-type microchannel reactor was shown to effectively increase the methanol conversion rate by up to around 8% and decrease the pressure drop by about 20%. Likewise, a novel porous copper fiber sintered felt (PCFSF) [8] as catalyst support is fabricated to construct the methanol steam reforming microreactor for hydrogen production. The results show that the PCFSF with different porosities exhibits good uniform heat transfer. The thermal conductivity is decreased with increasing porosity in the porosity range of 70–90%. The PCFSF with 80% porosity as catalyst support presents better reaction performance because of the enhancement of heat and mass transfer resulting from the unique porous structure.

The porous copper fiber sintered felts (PCFSFs) [9] with surface microchannels as catalyst supports were used to construct a new type of laminated methanol steam reforming microreactor for hydrogen production. The results show that the PCFSF with rectangular microchannels demonstrated a lower pressure drop, higher average velocity and higher permeability compared to the stepped and polyline microchannel. Furthermore, the PCFSF with rectangular microchannels also exhibited the highest methanol conversion and H₂ flow rate. The best reaction performance of methanol steam reforming microreactor for hydrogen production was obtained using PCFSF with rectangular microchannels when 0.5g catalyst was loaded.

The aim of the current study is how to increase the hydrogen production from methanol steam reformer. Such that the path used to solve this problem is a numerical path, besides the numerical simulation by COMSOL Multiphasic

software is done and the numerical results will be elaborated and treated in the discussion part of the results in this present work.

II. METHANOL STEAM REFORMING PROCESS

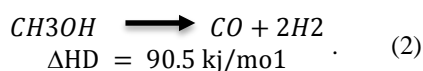
A. Reaction of Methanol Steam reforming

The Methanol Steam Reforming reaction demands an external heater source. According to the flowing studies [1,10-13] three reactions would take place in the MSR reformer with most widely used CuO/ZnO/Al₂O₃ catalysts, which are bellow:

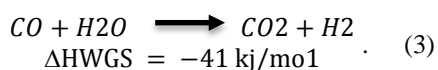
- Steam Reforming reaction:



- Decomposition reaction:



- Water gas Shift reaction:



III. PHYSICS MODEL

Before you begin to format your paper, first This reactor is a two-dimension rectangle Height * Length (10mm *100 mm) Fig. 1, then it defines by the inlet, outlet for fluid flow and top and bottom walls, and the lower wall is supposed the supports of catalysts layers, and upper wall of reactor contains the shapes in the inner side, such us each catalyst layer length is 90mm. For the boundary conditions: the velocity Inlet is equal to 0.1m/s. temperature at the T_{inlet}, T_{wall} is equal to 393K and 500K, respectively.

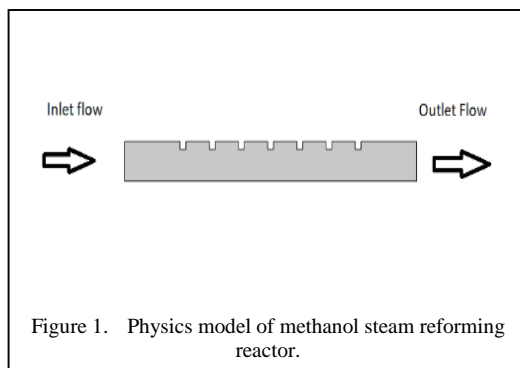


Figure 1. Physics model of methanol steam reforming reactor.

The numerical simulation is subjected to the following assumptions [10,14-16]:

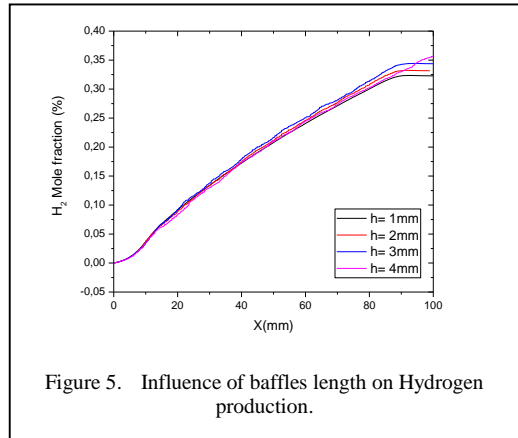
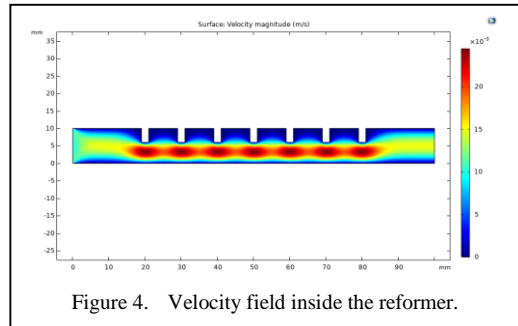
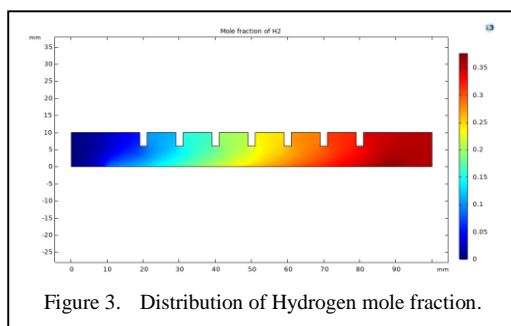
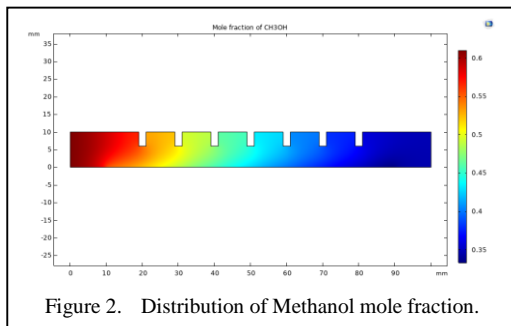
- Mixture of CH_3OH and H_2O is vaporized before entering the reformer;
- Species in the reactor are in gas phase;
- Gas flow in the reactor is incompressible and laminar in the steady state;
- Effect of gravity on the flow is neglected;
- Catalyst layer domain is treated as porous medium which is homogenous and isotropic;
- Effect of thermal radiation is neglected.

IV. RESULTS AND DISCUSSION

A. Case 1: Baffles

Figs. 2-3 present the distribution of Methanol and Hydrogen respectively. Note that; the diminution of methanol refer to the chemical reaction that have been occurred, in other hand the production of hydrogen mole. At the outlet, it remarked also the mole fraction of methanol and hydrogen are nearly 34% and 35%, respectively.

Fig. 4 displays the fluid flow inside the reformer. Noticed that; at the inlet the velocity is equal 0.1m/s after that there is acceleration of fluid flow near the baffles and it will be 0.2m/s.



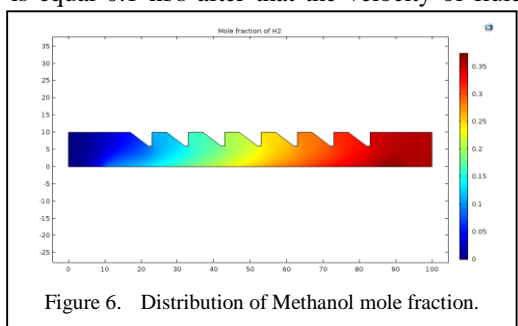
Moreover, it observed that almost no reacting fluid flow between the baffles.

Fig. 5 shows the influence of baffles high on hydrogen production. Remarked that; there is no large change between the high baffles ($h=1, 2, 3$ and 4 mm), a little gain for $H=0,4$ mm.

B. Case 2: Triangles

Figs. 6 and 7 illustrate the distribution of Methanol and Hydrogen respectively. Note that; this case is like the pervious case, there are methanol composition and hydrogen production near the active wall (catalyst layer).

Fig. 8 displays the fluid flow inside the reformer. Remarked that; at the inlet the velocity is equal 0.1 m/s after that the velocity of fluid



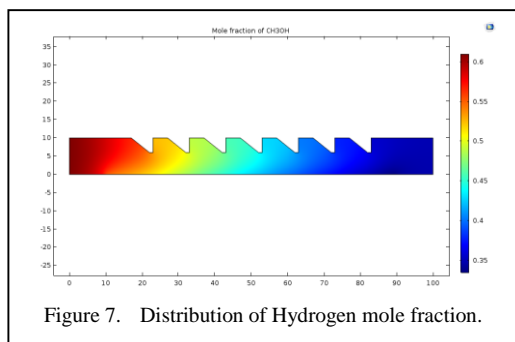


Figure 7. Distribution of Hydrogen mole fraction.

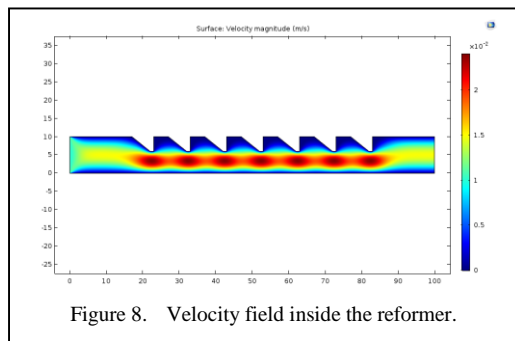


Figure 8. Velocity field inside the reformer.

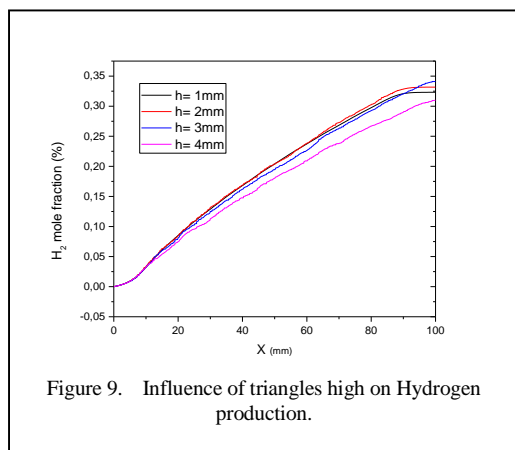


Figure 9. Influence of triangles high on Hydrogen production.

flow increase to 0.2 m/s near the triangles and. Besides, it observed that nearly no reacting fluid flow between the triangles shapes.

Fig. 9 shows the influence of baffles high on hydrogen production. Also observed that; there is no important variation comparing the four high baffles ($h=1, 2, 3$ and 4 mm), it can see a small gain for baffle $h=0.3$ mm.

V. CONCLUSION

Conversion of green methanol into hydrogen by external heating is an industrial way to power fuel cells and subsequently produce clean electrical energy. The methanol steam reforming procedure is the combination reaction of steam

and methanol in gas form inside the reactor with the presence of $\text{CuO}/\text{ZnO}/\text{Al}_2\text{O}_3$ catalyst. The numerical results of COMSOL show that; the two cases (baffles and triangles shapes) have the same effect on hydrogen production from methanol steam reforming. At the outlet, nearly the same quantity of hydrogen production and methanol consumption also the augmentation of flow velocity in the middle of reformer. However, there is no significant effect of the blocks inside the reformer in the upper wall, or in other words a small effect on the hydrogen production, for this reason it is necessary to continue the simulation and find a dynamic effect to increase hydrogen production. Anyway, the continuity of numerical simulation by COMSOL to increase reactor efficiency by a dynamic effect on the methanol steam reforming process for the production of hydrogen is under studding.

REFERENCES

- [1] Madani, B. (2021). Intensification of hydrogen production from methanol steam reforming by catalyst segmentation and metallic foam insert. *International Journal of Hydrogen Energy*, 46(75), 37583-37598.
- [2] Settar, A., Mansouri, Z., Nebbali, R., Madani, B., & Abboudi, S. (2019). Impact of Ni-based catalyst patterning on hydrogen production from MSR: External steam reformer modelling. *International journal of hydrogen energy*, 44(22), 11346-11354.
- [3] Perng, S. W., Horng, R. F., & Wu, H. W. (2017). Effect of a diffuser on performance enhancement of a cylindrical methanol steam reformer by computational fluid dynamic analysis. *Applied Energy*, 206, 312-328.
- [4] Omidbakhsh Amiri, E. (2015). Steam reforming integrated with oxidation of methanol in a micro-channel reactor with different micro-baffle shapes. *Hydrogen, Fuel Cell & Energy Storage*, 2(2), 75-83.
- [5] Herdem, M. S., Mundhwa, M., Farhad, S., & Hamdullahpur, F. (2019). Catalyst layer design and arrangement to improve the performance of a microchannel methanol steam reformer. *Energy Conversion and Management*, 180, 149-161.
- [6] Zhou, W., Ke, Y., Wang, Q., Wan, S., Lin, J., Zhang, J., & Hui, K. S. (2017). Development of cylindrical laminated methanol steam reforming microreactor with cascading metal foams as catalyst support. *Fuel*, 191, 46-53.
- [7] Mei, D., Liang, L., Qian, M., & Feng, Y. (2014). A performance study of methanol steam reforming in an A-type microchannel reactor. *International journal of hydrogen energy*, 39(31), 17690-17701.
- [8] Zhou, W., Wang, Q., Qiu, Q., Tang, Y., Tu, J., Hui, K. S., & Hui, K. N. (2015). Heat and mass transfer characterization of porous copper fiber sintered felt as catalyst support for methanol steam reforming. *Fuel*, 145, 136-142.
- [9] Ke, Y., Zhou, W., Chu, X., Yuan, D., Wan, S., Yu, W., & Liu, Y. (2019). Porous copper fiber sintered felts with surface microchannels for methanol steam reforming microreactor for hydrogen production.

- International Journal of Hydrogen Energy*, 44(12), 5755-5765.
- [10] Zhuang, X., Xu, X., Li, L., & Deng, D. (2020). Numerical investigation of a multichannel reactor for syngas production by methanol steam reforming at various operating conditions. *International Journal of Hydrogen Energy*, 45(29), 14790-14805.
- [11] Peppley, B. A., Amphlett, J. C., Kearns, L. M., & Mann, R. F. (1999). Methanol–steam reforming on Cu/ZnO/Al₂O₃. Part 1: the reaction network. *Applied Catalysis A: General*, 179(1-2), 21-29.
- [12] Jiang, C. J., Trimm, D. L., Wainwright, M. S., & Cant, N. W. (1993). Kinetic study of steam reforming of methanol over copper-based catalysts. *Applied Catalysis A: General*, 93(2), 245-255.
- [13] Jiang, C. J., Trimm, D. L., Wainwright, M. S., & Cant, N. W. (1993). Kinetic mechanism for the reaction between methanol and water over a Cu-ZnO-Al₂O₃ catalyst. *Applied Catalysis A: General*, 97(2), 145-158.
- [14] Nehe, P., Reddy, V. M., & Kumar, S. (2015). Investigations on a new internally-heated tubular packed-bed methanol–steam reformer. *International Journal of Hydrogen Energy*, 40(16), 5715-5725.
- [15] Huang, Y. X., Jang, J. Y., & Cheng, C. H. (2014). Fractal channel design in a micro methanol steam reformer. *International journal of hydrogen energy*, 39(5), 1998-2007.
- [16] Perng, S. W., Horng, R. F., & Ku, H. W. (2013). Effects of reaction chamber geometry on the performance and heat/mass transport phenomenon for a cylindrical methanol steam reformer. *Applied Energy*, 103, 317-327.

Exergetic Evaluation and Life Cycle Assessment as Strategies for Sustainability Analysis: Application for Industrial Refrigeration Systems

Marcos Antônio Oliveira Lima^{1*}, Alexandre Magno Vieira Gonçalves de Brito², Daniel de Paula Diniz³, Fazal Um Min Allah⁴, Raphael Abrahão⁵

^{1,2,3,4}Graduate Program in Mechanical Engineering, João Pessoa, Brazil

⁵Department of Renewable Energy Engineering, João Pessoa, Brazil

¹marcosoliveiralima0@gmail.com, ²alexandreh_magno@hotmail.com, ³danieldiniz@alumni.cear.ufpb.br, ⁴fazaluminallah@hotmail.com, ⁵raphael@cear.ufpb.br

Abstract—The need for sustainability analysis arises as the technological advancement of refrigeration systems has progressed. The processes involved in industrial refrigeration systems are highly energy intensive. The rationalization of energy consumption for these systems poses a sustainability challenge. Therefore, there are numerous studies carried out to minimize energy consumption and environmental impact of these systems. The present study involves a Systematic Literature Review of the studies encompassing exergetic analyses and life cycle assessments (LCA) of industrial refrigeration systems. The review resulted in affirming the efficacy of employing exergetic analysis and life cycle assessment methods for the optimization of energy consumption and emission mitigation. Finally, combining exergy analysis with LCA is important for a more comprehensive and holistic evaluation of the environmental and resource impacts of products, processes, and systems.

Keywords – industrial refrigeration, exergy, LCA, SLR

I. INTRODUCTION

The modern life is unthinkable without the existence of refrigeration as it provides cooling effect for various necessary applications, which

are needed for the sustenance of life itself [1,2]. The cold chain process provides ensures the safety and maintains better quality of the product that needs to preserve under controlled temperature from the origin to its final consumption [3].

The demand in refrigeration for air conditioning systems has been increasing, whereas the global warming has been on the rise as well [4]. This increase in demand could be attributed to the increase in requirements for thermal comfort, access to the technology, however, at the expense of environmental impacts [5]. The industrial refrigeration systems refer to thermal systems which are designed to remove heat to maintain desired temperature on an industrial scale.

Industrial refrigeration systems have evolved in accordance with the technological developments and due to the increased demand for more robust systems to meet the demands that arise over time. Accordingly, the systems could be designed to meet the demands for a wide variety of applications [6].

In the wake of the technological evolution of refrigeration systems, there is a need to evaluate the energy, economic and environmental impacts

*Supervisor: Monica Carvalho - Renewable Energy Engineering Department/Federal University of Paraíba (UFPB), João Pessoa, Brazil

associated with the production, operation, and disposal of such systems [7]. As industrial refrigeration processes are large energy consumers, continuous technological development is essential as a strategy to rationalize consumption associated with their operation, increase their energy efficiency, and make them more sustainable [8].

The exergy analysis allows to comprehensively identify and quantify system inefficiencies which in turns provides an opportunity for optimization of energy consumption [9,10]. The exergy analysis itself offers an opportunity for the improvement of the thermal system design by revealing the system losses. Therefore, its purpose is to promote optimization, providing a reduction in energy losses, as a basic tool for thermoeconomic and environmental analyses [11].

In this context, there are numerous studies published involving exergy analysis of different thermal systems encompassing vast number of applications such as electricity production, air conditioning, etc. [12].

The studies related to these systems have been recurrent, as there are plausible reasons that make it necessary to adopt thermo-environmental assessment methodologies, such as the sustainable use of energy, the reduction of emissions associated with the operation of refrigeration systems, the use of renewable energy sources, increased thermal efficiency, in addition to the assessment of economic impact related to energy conversion processes [13]. The topic is extremely important due to the dynamics of energy consumption, environmental impact associated with greenhouse gas emissions and economic costs related to industrial refrigeration systems [14].

Thus, the objective of this study is to carry out a Systematic Literature Review (SLR) to understand the state-of-the-art methodologies and discussions regarding exergetical analysis and life cycle assessment for industrial refrigeration. The scope of the SLR was to map the primary studies that were related to the following research question: What is the current scenario regarding studies applied to exergetical analysis and life cycle assessment for industrial refrigeration considering the period from 2018 to 2022?

The SLR is focused on highlighting the discourse in the literature regarding the topic

under study. Subsequently, the procedures used in this SLR are outlined, containing a synthesis of the primary studies previously identified. Finally, based on the results obtained by SLR, the final considerations are accentuated by presenting main findings and discussions found in the literature.

II. MATERIALS AND METHODS

Clearly, through systematic review, it is possible to evaluate and understand the research relevant to a specific research question, area or specificity of relevance. Thus, systematic reviews, when based on a delimited search strategy, are directed to the location of as many relevant studies as possible [15].

It is highlighted why the definition of the protocol in the systematic review minimizes bias in the study and that it is necessary to specify the processes that will be followed [16]. Similarly, the importance of the systematic review is highlighted by describing in detail along with transparent methodological procedures, so that other researchers can reproduce the defined protocol [17].

In this study, the guidelines proposed by [15] were used to construct this systematic review. The systematic review process covers the following phases: i) planning the review, ii) conducting the review and iii) reporting the review.

After defining the protocol, the studies, carried out from 2018 to 2022, were established as an analysis overview in order to highlight the main discussions on exergy analysis and life cycle assessment for industrial refrigeration.

To search for articles related to the research objective, the inclusion criteria for the SLR were defined, with the step-by-step instructions described below. Initially, three databases were used: Scopus, Web of Science and Science Direct. It is worth noting that to identify the articles in the databases, the search was carried out manually using the following keywords: "Refrigeration", "Exergy", "Cold rooms", "Life cycle assessment", "Carbon footprint", "Greenhouse gases" accompanied by the Boolean operators AND or OR. It is noteworthy that the collection in these databases took place between the months of May and June 2023.

In this study, only articles that had open access and were available for download were

considered and works that did not meet the criteria were eliminated from the analysis.

To select the studies, the databases *Scopus*, *Web of Science* and *Science Direct* were used, and the articles were searched through keywords to identify the works related to “Industrial refrigeration”, “Exergy”, “Cold chambers”, “Life Cycle Assessment”, “carbon footprint” and “greenhouse gases”. Particularly, the articles that encompassed exegetical analyses and Life Cycle Assessments (LCA) for industrial refrigeration were included.

In order to carry out a survey of the recent studies published regarding discussions on exegetical analysis and Life Cycle Assessment (LCA) for industrial refrigeration, It should be noted that the gray literature was not included in this review and therefore only scientific articles were analyzed.

During the process of excluding articles, the study is realized by considering only those that are not written in English language. The choice to limit the time to the last five years in the article searches is because the methods planned in the articles evolve very quickly [17], so it is important to define a time for analyzing the state of the art and report the latest discussions on the topic at hand.

To assess the quality of articles, journals that had an Impact Factor (JCR) lower than 1 are excluded. Furthermore, the articles with duplicate results are also eliminated.

Therefore, searches in the databases occurred as follows : TS= (“Refrigeration” OR “cooling” OR “cold room” OR “cold chain”) AND (“exergy”) AND (“life cycle assessment” OR “carbon footprint” OR “greenhouse gases” OR “GHG”). These searches are being conducted in English language, the time frame of 5 years (2018 to 2022), the type of study selected was “research article” and only works with open access were considered.

III. RESULTS AND DISCUSSION

The searches carried out in the databases for the time frame from 2018 to 2022 and, from then on, it was verified whether the results presented were only articles with open access, so that 290 documents were identified, of which a total of 116 studies in *Scopus*, 96 articles in *Web of Science* and 78 articles in *Science Direct*.

Then, the titles of the articles are considered, to analyze whether they are aligned with the research question and therefore the unrelated are excluded, thus eliminating 239 articles, totaling 51 articles for application of the next criterion are considered. It is noteworthy that articles that are unavailable for download are therefore excluded, resulting in 49 studies. It is worth highlighting that the filtering by reading the titles and abstracts of the works aimed to identify the primary studies that are related to the research question delimited in this systematic review.

Articles with an impact factor lower than 1 and/or that were secondary studies were also used as an exclusion criteria, totaling 28 primary articles. Therefore, after reading the abstracts of the works, 9 studies that are not related to the objective of the research are therefore excluded, indicating 19 articles.

After this screening stage, articles that are not relate exergy analysis and industrial refrigeration are excluded, with 9 studies being eliminated. Finally, in the last stage, the 10 articles are analyzed in detail as they fit the criteria established in this SLR.

Through the articles identified in this systematic review, it is observed that the works focused on the use of exergetic and environmental analyses using both established thermoeconomic and environmental assessment methodologies, and proposing new methods of combining these tools, as a diagnostic measure for applied thermal systems, energy conversion processes, cooling, and heating processes. Once the 10 works are screened, 9 of them deal directly with thermoeconomic and environmental analyses in thermal plants.

Among the main subjects covered in the articles identified during SLR, specifically, there is a preponderance for assessment of exergetic and environmental performance.

For the following themes: Exergetic analysis, life cycle assessment (LCA) and Refrigeration, and greenhouse gas emissions, respectively, containing the works well aligned with the objective defined for this review.

In relation to the objectives of this study of the selected researches, the concentration of discussions is identified in percentage terms,

thermoeconomic and environmental assessments applied to refrigeration and air-conditioning systems (50%), trigeneration (40%) and refrigerant fluids used in equipment (10%), are preferred for analysis by using these methodologies or combinations thereof, the efficiencies of the systems by keeping in view the energy, economic and environmental aspects, in addition to proposing sustainable alternatives through evaluations of specific scenarios for each objective of the study.

Among the authors of the studies identified in the RSL, only one author published more than one work on the same theme of thermoeconomic and environmental assessment, using exergy analysis and LCA tools to study thermal systems by [19] and [20]. Thus, it is understood that the analysis regarding the subject has been evidenced in the literature, but that the discussions have not yet been exhausted and deserve further investigation, considering that potential for further developments is expected.

This observation is justified when considering the time span of the SLR, where the works have been regularly published throughout the years of the time frame defined in this research, with the year 2022 presenting more published work, three articles by [18,19] and [21].

According to the evaluation of the identified works, it is observed that the authors use established methodologies for thermoeconomic and environmental assessment of thermal systems for various applications, from trigeneration plants to equipment analysis.

From the analysis of the 10 articles identified with the SLR, greater discussions were observed focused on the following topics: Exergy Analysis, Life Cycle Assessment, Refrigeration, Cooling and Energy Efficiency, Exergoeconomic and Exergoenvironmental Assessment.

A word cloud is constructed (see Fig. 1) and the keywords contained in the 10 articles that are analyzed. It is noteworthy that, in the cloud, the repetition of words in articles is related to size, so that the larger the size of the word in the cloud means that it appears more times among the 10 selected articles. In this way, the words highlighted emphasize a greater understanding of the main issues raised in the screened articles.

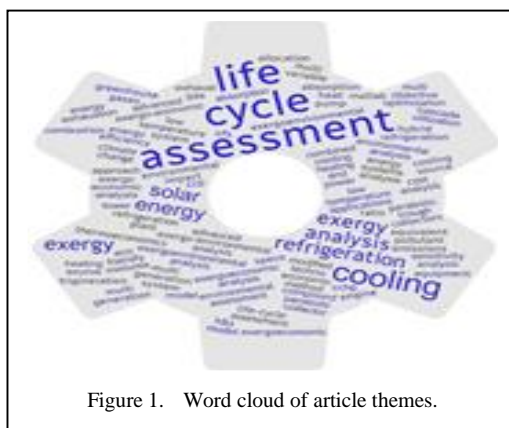


Figure 1. Word cloud of article themes.

It is also observed by the formation of word, the recurrence of terms for: Life cycle assessment, Cooling, exergy analysis, exergy, and solar energy. Other keywords such as: emissions, refrigeration plants, trigeneration, exergoeconomics and exergoenvironmental are also recurrent in the cloud and in the works, thus demonstrating the alignment of studies with the theme of SLR.

Henceforth, the ten studies identified from the preparation of this systematic review are presented in temporal order, with the results and main contributions of each of the ten studies.

A comparative Life Cycle Assessment (LCA) and exergoenvironmental study of a natural gas microtrigeneration system was carried out by [13]. To evaluate LCA, two methodologies were used, Eco-indicator 99 and ReCiPe. The environmental data was estimated by surveying the energy flows of the system's equipment, which served as the basis for the detailed exergy analysis used in the exergoenvironmental assessment. As a result, the study developed an exergo-environmental assessment model for the microtrigeneration system, in addition to a comparative study between the methodologies used at LCA stage. It is noteworthy that, despite presenting different results in magnitude relative to the quantification of environmental impact associated with the system, it showed similar behavior, where the improvements of the system as a whole are focused on equipment with the greatest potential for exergy destruction, such as the internal combustion engine (ICE) and the steam generator, which also exhibited higher energy and exergy costs as a result of the exergoenvironmental assessment.

The study carried out by [22] developed an integrated study based on the TEC-LCA evaluation method, applied to a water-cooled chiller for air conditioning purposes. The study was aimed to apply the life cycle assessment (LCA) methodology combined with thermoeconomics as a tool to analyze the exergo-environmental profile of energy systems, using the capabilities of both techniques to simultaneously evaluate the thermodynamic aspects of energy conversion processes and the environmental impacts associated with the equipment's life cycle. The methodology outlined by the authors focused on accounting for exergy costs after carrying out an exergy balance of the energy flows of the system. The LCA stage was based on the ISO 14040 series to evaluate and quantify the environmental impacts generated by the Chiller throughout its life cycle. The study resulted in evaluations of operating scenarios with the chiller in modified thermal plants, considering different technology and maintenance plans, where they concluded that the TEC-LCA integrated approach method provides a comprehensive view of environmental impacts through LCA and thermoeconomic costs analysis for energy conversion systems.

In another work, [23] carried out a comprehensive study on a new cascade absorption-compression refrigeration system, where they evaluated, the refrigeration process from end to end by using exergy analysis, in which they were able to estimate the total exergy efficiency, global exergy destruction rate and System performance coefficient and Ecoindicator 99 by considering the System's useful life period for environmental assessment. The exergo-environmental assessment was carried out by estimating the purchasing and operating costs of the equipment. As a result, they identified sources of irreversibilities associated with the system due to the compressor and heat exchangers, as well as optimization points. Furthermore, the authors proved the feasibility of using parametric analyzes as an advanced tool to evaluate cascade absorption-compression systems for refrigeration purposes.

A new CCHP system was proposed by [24] by using solar energy that combines cooling, heating, and electricity production. Thereafter, an analysis was carried out from a thermodynamic and thermoeconomic point of view. The authors carried out exergy, exergoeconomic and exergoenvironmental

assessments by the creation of codes in the Engineering Equation Solver (EES) software. It was identified that the "storage tank has the highest exergy destruction rate and the highest exergy destruction cost.

An environmental impact assessment of heating and cooling sources in office buildings was developed by [25]. The authors chose a commercial building in Tianjin, China, which was equipped with an air conditioning system. Therefore, they selected 7 energy sources to evaluate and compare the environmental impacts associated with each source in different combinations of usage, to verify the most economically viable and environmentally sustainable for its application in the building. The results of the study, involving exergy analyses of the selected heating and cooling sources, showed that the efficiency rates for heating are significantly higher in relation to those of cooling, due to the differences in the calorific value of the energy sources (oil, gas and coal) and the differences between the amounts of energy consumed to meet the thermal demands of the building. In relation to environmental impacts, the study brought important results, as it indicates the best combinations between available sources and systems, demonstrating that gas cogeneration systems and heat pumps with geothermal sources combined with conventional refrigeration systems resulted in the best options in relation to the thermal, economic efficiencies and associated environmental impacts.

The study carried out by [20] showed that the system presents lower energy efficiency and maximum exergy efficiency operating in cooling mode – refrigeration demand. While operating in heating mode, it exhibited maximum energy efficiency. On the other hand, operating in a hybrid form, it presents low energy and exergy efficiencies. The results of the study showed that the AHP unit, that employed the trigeneration system, had improved efficiency while using the heat from solar and geothermal sources, with COP between 1.38 and 2, depending on the mode of operation. It was also concluded that the specific exergy cost of the system as a whole was around 0.31 \$/kWh, in addition to having a payback period of 3.5 years.

A comparative study was carried out by [26] for the evaluation of energy performance and greenhouse gas emissions potential of different

ecological refrigerant mixtures with low GWP (Global Warming Potential) as an alternative to the usage of R134a. The study aimed at investigating, through simulations and experimental tests, the different mixtures of refrigerant fluids, equivalent to R134a with lower GWP. From the simulations and experimental investigation, the results obtained showed that the R1234ze/R134a mixtures, a COP reduction of up to 20% was observed compared to that of R134a, meanwhile noticing an improvement in exergy efficiency of up to 16% and a drop in the general irreversibility of the system by 12.4%. Furthermore, in relation to TEWI (Total Equivalent Warming Impact) indices, R1234ze/R134a performed better than R134a, being able to be a good substitute for it in low temperature applications and being able to meet the expectations of the Montreal and Kyoto Protocols regarding GWP emissions [26].

An evaluation of a Chiller system for producing chilled water in a Shopping Center, combining thermo-economic and thermo-environmental assessment to estimate the energy, financial and environmental costs related to the processes of air conditioning purposes was carried out by [15]. To evaluate the building's chilled water plant, they used the plant's operational data during the data collection stage, as well as based on the technical data of the system's equipment, where they were able to carry out exergy analysis as well as exergoeconomic and environmental assessments associated with the production of chilled water. Through the life cycle assessment (LCA) methodology, based on the ISO 14040 standard and using the SimaPro® software while adopting the Ecoinvent database, they estimated the environmental impact associated with the production of the system equipment until its disposal. The study evaluated, because of the quantitative analysis related to the energy, financial and environmental costs due to the processes, as well as presenting the feasibility of the combined application of thermoeconomic and environmental assessment focused on the analysis of greenhouse gas (GHG) emissions.

Through the criteria related to LCA, [21] developed a more suitable method for energy and environmental assessment for cooling towers in their study, where it was observed that the application area, life cycle perspective physical quantities of inventory analysis, impact categories, efficiency analysis are the main factors that strongly influence the application of

energy and environmental assessment methodologies. As a main result, the study concluded that multi-criteria assessment, systematically combining energy and environmental assessment methods, considering the specific objectives of each case can be used. Consequently, for the case study in question, the methods that comprise the assessment of energy flows through exergy analysis, are the most appropriate.

A modified technical-economic method combined with life cycle assessment (LCA) was proposed by [19], by involving a trigeneration system driven by an internal combustion engine coupled to a Rankine Cycle unit which was equipped with a heat exchanger by absorption. To carry out the analysis, they used evaluation criteria and indicators related to energy/exergy, environment, and economy, since the proposed method takes into account all of these results. The equivalent emissions method was used to quantify the environmental impact related to pollutant emissions during the operation of the system for each type of the fuel analyzed. For the techno-economic assessment, they used the conventional methodology by combining the equivalent emission cost resulted from the LCA. The results showed, through detailed analysis of the system, that the operating stage of this system is responsible for the highest fuel consumption.

Finally, from the analysis of the articles, it was found that discussions focused on exergy evaluation as an initial analysis led to more detailed investigations from a thermodynamic point of view. Recognizing that sustainability is a term that encompasses social, economic, and environmental aspects, and that most tools for quantifying sustainability involve indicators based on energy flows. Therefore, there is enormous potential to combine exergy and life cycle analyzes in the search for solutions to environmental problems, with direct applications both in industrial refrigeration systems and in any energy-demanding process.

IV. CONCLUSIONS

From the analysis of the articles, the trends in current discussions were observed with the systematic review, focused on exergy analysis as a starting tool for exergo-environmental and exergoeconomic investigations of thermal power, heating, and cooling systems. The works identified in the RSL addressed the use of established thermo-economic and

environmental assessment methods through exergy analysis, combination of assessment methodologies and even the development of methods derived from traditional methods, contributing to greater assertiveness in assessments compared to traditional methods, thus showing the versatility and importance of combining/modifying assessment methodologies as a means of obtaining more accurate thermal, economic and environmental efficiency results.

The contribution of this work was to demonstrate, through the identified studies, the developments of current research related to the application of exergy analysis and LCA as a basic tool for thermo-environmental and thermo-economic assessments in thermal systems, with direct implications in the industrial refrigeration sector. Thus, demonstrating the importance of the topic as part of efforts to rationally use energy, increase thermal efficiency, mitigate and/or rationalize environmental and economic impacts associated with the operation of these systems, as well as how to directly influence other processes that make intense use of energy.

ACKNOWLEDGEMENT

The authors acknowledge the support from the National Council for Scientific and Technological Development (CNPq) through a PhD scholarship and research productivity grants (309452/2021-0 and 308753/2021-6), and the financial support of grants 77/2022 and 08/2023 from the Paraíba State Research Foundation (FAPESQ).

REFERENCES

- [1] Antoine, P., Maxime, P. M., Pascal, O., & Driss, S. (2022). Thermodynamic performance's analysis of a cold production by hybrid compressor-based thermochemical sorption processes using ammoniated salts. *Energy Conversion and Management*, 267, 115931.
- [2] Wu, W., Beretta, C., Cronje, P., Hellweg, S., & Defraeye, T. (2019). Environmental trade-offs in fresh-fruit cold chains by combining virtual cold chains with life cycle assessment. *Applied Energy*, 254, 113586.
- [3] Sadi, M., & Arabkoohsar, A. (2020). Techno-economic analysis of off-grid solar-driven cold storage systems for preventing the waste of agricultural products in hot and humid climates. *Journal of Cleaner Production*, 275, 124143.
- [4] Randazzo, T., De Cian, E., & Mistry, M. N. (2020). Air conditioning and electricity expenditure: The role of climate in temperate countries. *Economic Modelling*, 90, 273-287.
- [5] Alrobaian, A. A. (2023). Impact of optimal sizing and integration of thermal energy storage in solar assisted energy systems. *Renewable Energy*, 211, 761-771.
- [6] Zhu, Y. D., Peng, Z. R., Wang, G. B., & Zhang, X. R. (2021). Thermodynamic analysis of a novel multi-target-temperature cascade cycle for refrigeration. *Energy conversion and management*, 243, 114380.
- [7] Liu, X., Yang, X., Yu, M., Zhang, W., Wang, Y., Cui, P., ... & Gao, J. (2020). Energy, exergy, economic and environmental (4E) analysis of an integrated process combining CO₂ capture and storage, an organic Rankine cycle and an absorption refrigeration cycle. *Energy Conversion and Management*, 210, 112738.
- [8] Terehovics, E., Soloha, R., Veidenbergs, I., & Blumberga, D. (2018). Analysis of fish refrigeration electricity consumption. *Energy Procedia*, 147, 649-653
- [9] Colakoglu, M., & Durmayaz, A. (2022). Energy, exergy, economic and emission saving analysis and multiobjective optimization of a new multi-generation system based on a solar tower with triple combined power cycle. *Sustainable Energy Technologies and Assessments*, 52, 102289.
- [10] Ibrahim, T. K., Mohammed, M. K., Awad, O. I., Abdalla, A. N., Basrawi, F., Mohammed, M. N., ... & Mamat, R. (2018). A comprehensive review on the exergy analysis of combined cycle power plants. *Renewable and Sustainable Energy Reviews*, 90, 835-850.
- [11] Saini, S. K., Dasgupta, M. S., Widdel, K. N., & Bhattacharyya, S. (2021). Comparative study of exergetic and economic analysis of multi-evaporator NH₃ and NH₃-CO₂ CRS for a seafood processing plant.
- [12] Fu, C., Shen, Q., & Wu, T. (2022). Exergo-economic comparisons of solar cooling systems coupled to series/parallel absorption chiller types considering the lowest heat transfer area. *Case Studies in Thermal Engineering*, 39, 102456.
- [13] Marques, A. S., Carvalho, M., Ochoa, A. A., Abrahão, R., & Santos, C. A. (2021). Life cycle assessment and comparative exergoenvironmental evaluation of a micro-trigeneration system. *Energy*, 216, 119310.
- [14] Alsaman, A. S., Hassan, A. A., Ali, E. S., Mohammed, R. H., Zohir, A. E., Farid, A. M., ... & Askalany, A. A. (2022). Hybrid solar-driven desalination/cooling systems: Current situation and future trend. *Energies*, 15(21), 8099.
- [15] Kitchenham, B. (2004). Procedure for undertaking systematic reviews. *Computer Science Department, Keele University (TRISE-0401) and National ICT Australia Ltd (040001IT. 1), Joint Technical Report*, 33.
- [16] Brereton, P., Kitchenham, B. A., Budgen, D., Turner, M., & Khalil, M. (2007). Lessons from applying the systematic literature review process within the software engineering domain. *Journal of systems and software*, 80(4), 571-583.
- [17] Aguinis, H., Ramani, R. S., & Alabduljader, N. (2018). What you see is what you get? Enhancing methodological transparency in management research. *Academy of Management Annals*, 12(1), 83-110.
- [18] Chen, Y., Hua, H., Xu, J., Yun, Z., Wang, J., & Lund, P. D. (2022). Techno-economic cost assessment of a

- combined cooling heating and power system coupled to organic Rankine cycle with life cycle method. *Energy*, 239, 121939.
- [19] Abreu, R. P., Correia, V. H. L., Lourenço, A. B., da Silva Marques, A., & Carvalho, M. (2022). Thermo-economic and thermo-environmental analysis of the chilled water system in a shopping mall. *International Journal of Refrigeration*, 134, 304-311.
- [20] Chen, Y., Xu, J., Zhao, D., Wang, J., & Lund, P. D. (2021). Exergo-economic assessment and sensitivity analysis of a solar-driven combined cooling, heating and power system with organic Rankine cycle and absorption heat pump. *Energy*, 230, 120717.
- [21] Wenzel, P. M., & Radgen, P. (2022). Multi-criteria comparison of energy and environmental assessment approaches for the example of cooling towers. *Applied System Innovation*, 5(5), 89.
- [22] Catrini, P., Cellura, M., Guarino, F., Panno, D., & Piacentino, A. (2018). An integrated approach based on Life Cycle Assessment and Thermo-economics: Application to a water-cooled chiller for an air conditioning plant. *Energy*, 160, 72-86.
- [23] Mousavi, S. A., & Mehrpooya, M. (2020). A comprehensive exergy-based evaluation on cascade absorption-compression refrigeration system for low temperature applications-exergy, exergoeconomic, and exergoenvironmental assessments. *Journal of Cleaner Production*, 246, 119005.
- [24] Montazerinejad, H., Ahmadi, P., & Montazerinejad, Z. (2019). Advanced exergy, exergo-economic and exergo-environmental analyses of a solar based trigeneration energy system. *Applied Thermal Engineering*, 152, 666-685.
- [25] Wang, C., Xu, A., Jiao, S., Zhou, Z., Zhang, D., Liu, J., & Zuo, J. (2020). Environmental impact assessment of office building heating and cooling sources: A life cycle approach. *Journal of Cleaner Production*, 261, 121140.
- [26] Padmavathy, S. R., Chockalingam, M. P., Kamaraj, N., Glivin, G., Thangaraj, V., & Moorthy, B. (2022). Performance studies of low GWP refrigerants as environmental alternatives for R134a in low-temperature applications. *Environmental Science and Pollution Research*, 29(57), 85945-85954.

Comparative Study on the Impact of the Nature of Fluids Used in CPV/T-TEG Systems

Khaled Mouaici¹, Brahim Fersadou², Walid Nessab³, Nawal Guerroudj⁴, Henda Kahalerras⁵

^{1,2,3,4,5}USTHB, Algiers, Algeria

¹kmouaici@usthb.dz, ²brahim04@live.fr, ³nessabwalid@gmail.com, ⁴nawguer@yahoo.fr, ⁵kahalerrashenda@yahoo.fr

Abstract—The present study aims to investigate numerically the impact of the nature of fluids on thermoelectric performance of hybrid solar collector (PV/T) equipped with a compound parabolic concentrator (CPC) and thermoelectric generator (TEG). The used heat transfer fluids (Water, Water-Cu nanofluid, Water/Cu-Al₂O₃ hybrid nanofluid) are conveyed in a metallic tube on the rear side of the electrical system and in forced convection mode. The nodal approach and the Runge Kutta fourth-order algorithm are used to solve the energy balance equations in each system component. The parametric study is founded on the influence of the solar concentration ratio (CR) and mass flow rate (\dot{m}). The findings showed that growing these parameters promotes the production of electrical and thermal powers. The results also reveal that limit values of the concentration ratio, to ensure normal functioning of photovoltaic cells, are improved while using more performant HTF and with rising mass flow rate.

Keywords - hybrid photovoltaic thermal solar collector, hybrid nanofluid, parabolic concentrator, thermoelectric generator

I. INTRODUCTION

The global energy consumption is constantly increasing and the alarm bells have already been pulled to manifest the climate and ecological emergencies, the energy situation in the world is worsening. Renewable energy represented by solar energy may be the key in this challenge that facing humanity, it's noteworthy that this kind of energy still considered unreliable but it

can reduce the dependence of humanity on fossil fuel. Solar energy is clean, environmentally friendly and freely available over the planet, also it's one of the most promising renewable resources which can be used to promote both thermal and electrical energies. To supply the energy demand two different mechanisms were used to generate electrical energy and thermal energy independently of each other. Further, a novel technology developed in order to join these two types of systems in one mechanism leading to produce electrical and thermal powers simultaneously. It consists of the hybrid photovoltaic-thermal collectors (PV/T), maintaining at high amounts the electrical efficiency of cooled photovoltaic (PV) modules during daytime.

The combination of TEG thermoelectric generators with CPV/T systems is an innovative way to improve the conversion of solar energy and develop an extra electrical power. This has led researchers to increase studies in this direction in recent years. In Da et al. [1] paper. Comprehensive photon and heat management approaches are proposed to increase the use of full-spectrum solar energy in a hybrid PV-TEG system. Bio-inspired nanostructured butterfly eye shaped surface is adopted to remove photon reflection from the full solar spectrum, while the enhanced transmission film is used to improve the transmission of photons whose energy is below the band gap of photovoltaic cells, which allows a reasonable use of the energy of the solar spectrum. The results showed that the new

system has better performance than pure photovoltaic cells. It also appears that a concentration ratio lower is more suitable for PV-TEG hybrid systems in terrestrial and space applications, unless more important temperature management measures are taken. The study by Riahi et al. [2] focused on CPV/T and CPV/T-TEG hybrid solar systems. Prototypes of these sensors were designed and manufactured, and experimental tests were carried out. Mathematical models have also been established to analyze the electrical and thermal performances of these two systems. The results showed that the electrical power of the CPV/T-TEG is higher than that of the CPV/T and the integration of thermoelectric generators allows to improve the electrical efficiency by a rate of 7.46%. In addition, the analysis showed that this new system was capable of producing considerable annual electrical and thermal energy and saving fossil energy and equivalent emissions of CO₂. A new bifacial CPV-TEG system combined with a flat plate heat pipe (FPHP) was proposed by Gao et al. [3]. 3D numerical simulations were conducted to analyze the performance of the newly designed sensor and those of a traditional sensor (monofacial). The effects of solar concentration ratio, convective transfer coefficient, and external load resistance, different working fluids on output power and conversion efficiency were examined. The results indicated that the overall performance of the bifacial system is higher than that of the conventional system. Increases of 20.98% and 14.05% in overall energy production and energy conversion efficiency were achieved. A hybrid photovoltaic-thermoelectric system (PV-TEG) using a new solar concentrator was designed and built by Alnajidee and Min [4] to demonstrate the feasibility of improving the overall efficiency of converting light into electricity based on a spectral division strategy. The concentrator consists of four rectangular dichroic mirrors arranged in cross V that reflect and concentrate the visible spectrum on a photovoltaic cell located in the center, while the infrared spectrum is transmitted to a heat absorber that produces heat for the thermoelectric generator. The experimental results noted that the overall efficiency of the PV-TEG hybrid system is 16.9% compared to 15.9% for the same configuration, except for the use of aluminum specular mirrors. A 6.3% increase in the overall efficiency was achieved thanks to the thermoelectric harvesting of light energy in the

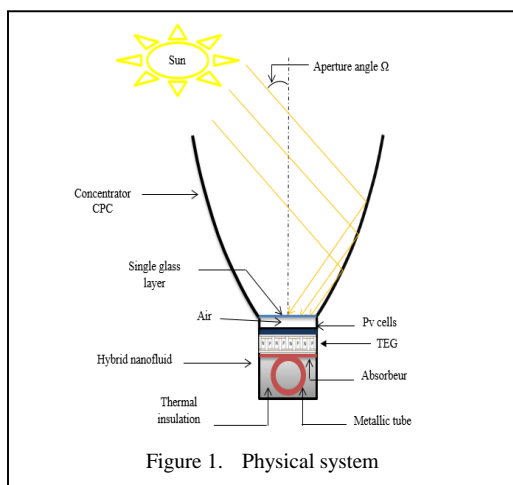
infrared spectrum. The results also showed a significant increase in output power from 12.41mW in the bare cell to 62.04 mW of the same cell in the concentrated system. In the study of Indira et al. [5], a new hybrid system prototype Concentration photovoltaic/thermal combined with a thermoelectric generator was designed and built for the simultaneous production of heat and electricity. In the developed hybrid system, solar cells and thermoelectric modules, which share the same heat transfer fluid, are exposed to concentrated irradiation via a compound parabolic concentrator and a parabolic cylindrical concentrator, respectively. The tests resulted in a maximum electrical efficiency of 4.86% and a thermal efficiency of 40% when solar irradiation is greater than or equal to 1000W/m². The overall efficiency of the developed prototype is three times higher than that of an autonomous photovoltaic system. The hybrid system has reduced carbon emissions by 0.5 kg/h, with an associated environmental cost of 0.025 €/h.

II. MATHEMATICAL MODELING

A. System Description

The physical system considered and illustrated in Fig. 1 is a hybrid photovoltaic thermal collector (PV/T) equipped with a compound parabolic concentrator (CPC). The hybrid collector, which combines the mechanism of solar thermal absorbers and PV modules, is made essentially of: PV module covered by single glass layer separated by an air gap, an absorber plate and metallic tube in which the HTF is conveyed are attached to the back the PV module through an adhesive layer, a thermal insulation material placed at the bottom and the sides of the collector to minimize heat losses, and finally an enclosure which carry all collector components for mainly protection purpose and ensure correct placement.

The incident concentrated solar irradiance by the CPC is partially absorbed by the photovoltaic module. Losses occur at the cover glass due to reflection and at the inner PV module. The PV module absorbs and converts the solar irradiance into electrical power, while its cell temperature begins to rise due to losses and heat of surrounding atmosphere. Some of this heat is transferred back onto the surrounding atmosphere via convection, while the remaining is transferred to the thermal absorber via conduction. The heat transfer fluid (HTF), enters from a fluid source into the PV/T collector and



flow within the tube. It will absorb the heat from the walls of the tubes and carry them into the outlet connection

B. Assumptions

The thermo-electric behavior of the CPV/T system is defined by means of explicit dynamic analysis through solving transient energy balance equations for the various collector components. It must be noted that such a work is extremely difficult due to the presence of the three processes of heat transfer and non-continuity of the studied domain. So, in order to get over these difficulties the sky is supposed as a black body, Employing one dimensional heat transfer, and the thermophysical properties of all components are supposed constant. Each component of the hybrid collector is considered at uniform temperature and it will be represented by node. And finally, the transport delay will be not invoked.

C. Mathematical Formulation

As mentioned earlier in this section, the nodal approach appears appropriate for this study. With mentioned assumptions, the energy equation for each component will be reduced as follows in Table I.

III. RESULTS AND DISCUSSION

In this section we'll exhibit the main results obtained while studying the effect of concentration ration (CR) and mass flow rate (\dot{m}) of each HTF on the performance of the CPV/T-TE system. The performances of studied device are predicted over a typical day of Ain Salah city and by keeping fixed the concentration of nanoparticles at 5% and for wind velocity which assumed to be constant at

1m/s. It is noteworthy that the maximal value of contraction ratio that could be reached depend strongly on solar cell temperature. So, also in this section we will define the technological limitations obtained when changing the nature of the HTF, and by adopting a stop criterion which consist that the system should be shut down immediately if the instantaneous temperature of a PV module is equal at 350 K.

In order to extract the nature of interactions between different parameters such as interaction mass flow rate and concentration ratio on CPV/T-TE performance we have plotted the curves shown in Figs. 2(a)-(c). It displays the variations of mean electro-thermal and TEG mean electric outputs with respect to concentration ratio for different levels of mass flow rate. This figure reveals that all energies evolve in the same way with concentration ratio. This variation is described by a sharp increase. In fact, the increasing mass flow rate of heat transfer fluid (in this case water) inside tube improves the absorption of heat provided by PV module which lead to diminish its temperature, and by consequence allows the system to develop more thermal and electrical power.

Figs. 3(a)-(c) Depict the variation of electro-thermal and TEG mean electrical efficiencies with concentration ratio for large range of mass flow rate. From the figure it's clear that increasing concentration ratio affect negatively both of efficiencies of CPV/T system with more apparent effect for electrical efficiency than thermal one, unlike that of the thermoelectric generator, the electrical efficiency increases significantly as a function of CR because of the temperature gradients raised at the level of the ceramic layers. This unwanted behavior is related to conversion performance of CPV/T system. Admitting that the efficiency is only a relationship between what the system receives and what it produces, and referring to the results shown in Figs. 2(a)-(c), we can explicitly say that the increase of CR allows to have a greater gain in terms of electrical and thermal power but with a lower conversion rate. Also, it's remarkable that increasing mass flow rate is beneficial for the performance of CPV/T system whether electrical or thermal efficiency. This figure also shows an important result concerning the interaction between the mass flow rate and concentration ratio. The increase in the flow rate stops the undesired effect of the concentration ratio on the thermal performance of the system

TABLE I. ENERGY EQUATION OF EACH COMPONENT OF CPV/T-TE SYSTEM.

	Energy Equation	Description
Glass cover	$M_g C_{pg} \frac{dT_g}{dt} = \alpha_g G \rho_{con} C R \gamma_t - (h_{c,g-a} + h_{r,g-s}) \times (T_g - T_a) - (h_{c,g-pv} + h_{r,g-pv})(T_g - T_{pv})$	Where G is the global solar irradiation received. ρ , γ_t and α symbolize reflectivity, interception factor and absorptivity respectively. h_r , h_c and T represent the radiation and convection heat transfer coefficients and the temperature respectively. Besides, the subscripts con , g , a , pv and s refer to the concentrator, glazing, ambient, photovoltaic and sky respectively. M and C_p are respectively mass and calorific capacity. CR is the concentration ratio.
PV Panel	$M_{pv} C_{ppv} \frac{dT_{pv}}{dt} = \alpha_{pv} G \rho_{con} C R \gamma_t \tau_g - E - (h_{c,g-pv} + h_{r,g-pv})(T_{pv} - T_g) - h_{cond,pv-cr}(T_{pv} - T_h)$	Where τ denotes transmittance; h_{cond} represent the conduction heat transfer coefficient; the subscripts cr and h indicate the ceramic layer and TEG hot layer respectively. $E(W/m^2)$ is the electrical power produced by the photovoltaic module
TEG hot layer	$M_{cr} C_{p,cr} \frac{dT_h}{dt} = h_{cond,pv-cr} A_{te} (T_{pv} - T_h) - N_{te} (S I_{te} T_h + k_{te} (T_h - T_c) - 0.5 R_i I_{te}^2)$	N_{te} - number of TEG items I_{te} - TEG output current intensity R_i - TEG internal electrical resistance T_h - TEG hot ceramic layer temperature T_c - Temperature of the cold ceramic layer of the TEG k_{te} - TEG thermal conductance S - Seebeck coefficient
TEG cold layer	$M_{cr} C_{p,cr} \frac{dT_c}{dt} = N_{te} (S I_{te} T_c + k_{te} (T_h - T_c) + 0.5 R_i I_{te}^2) - h_{cond,cr-abs}(T_c - T_{abs}) - h_{cond,cr-t}(T_c - T_t)$	The subscripts abs and t indicate the absorber and tube respectively
Thermal absorber plate	$M_{abs} C_{pabs} \frac{dT_{abs}}{dt} = h_{cond,cr-abs}(T_c - T_{abs}) - h_{cond,abs-t}(T_{abs} - T_t) - h_{abs-i}(T_{abs} - T_i)$	The subscript i refer to the thermal insulation.
Tube	$M_t C_{pt} \frac{dT_t}{dt} = h_{cond,abs-t}(T_{abs} - T_t) + h_{cond,cr-t}(T_c - T_t) - h_{nf-t}(T_t - T_{nfm}) - h_{cond,t-i}(T_t - T_i)$	h_{nf} is the convective heat transfer coefficient inside the tube.
Thermal insulation	$M_i C_{pi} \frac{dT_i}{dt} = h_{cond,abs-i}(T_{abs} - T_i) + h_{cond,t-i}(T_t - T_i) - h_{air-i}(T_i - T_a)$	h_{ai} is the coefficient that reflects the overall thermal losses between the thermal insulation and the ambient environment.
Nanofluid	$M_{nf} C_{pnf} \frac{dT_{nfm}}{dt} = A_{nf-t} h_{nf} (T_t - T_{nfm}) - \dot{m} C_{pnf} (T_{nfo} - T_{nfi})$	Mass flow rate and averaged temperature of nanofluid are \dot{m} and T_{nfm} respectively.

The use of high-performance nanofluids does not directly affect the physical behavior of the performance of CPV/T-TEG systems, but allows to expand the field of use of this technology. Fig. 4. shows the interaction of the technological limit of CPV/T-TEG CRLimit systems with the fluid mass flow rate. The figure states that in laminar regime the contribution of nanofluids on CRLimit is timid and sometimes less important than that of the classical fluid on the other hand in turbulent flow regime the effect

of nanofluids becomes more and more apparent and allows to increase the CRLimit value and consequently widen the technological limit of CPV/T-systemsTEG. The valorization of the use of the nano suspension technique makes it possible to achieve attractive results in terms of performance optimization of hybrid CPV/T-TEG systems. It should be noted that from an improvement point of view the use of the nanofluid Water-Cu and the nanofluid Hybrid Water/Cu-Al2O3 for a turbulent flow led to an improvement rate of (8.69%; 9.16%) thermal

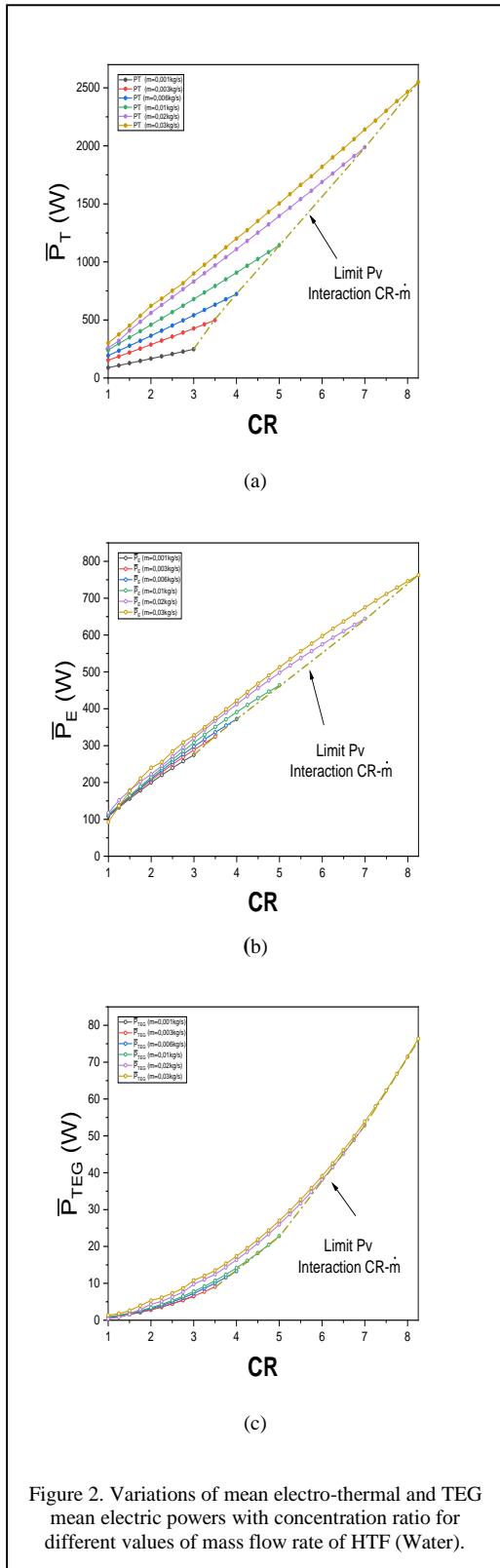


Figure 2. Variations of mean electro-thermal and TEG mean electric powers with concentration ratio for different values of mass flow rate of HTF (Water).

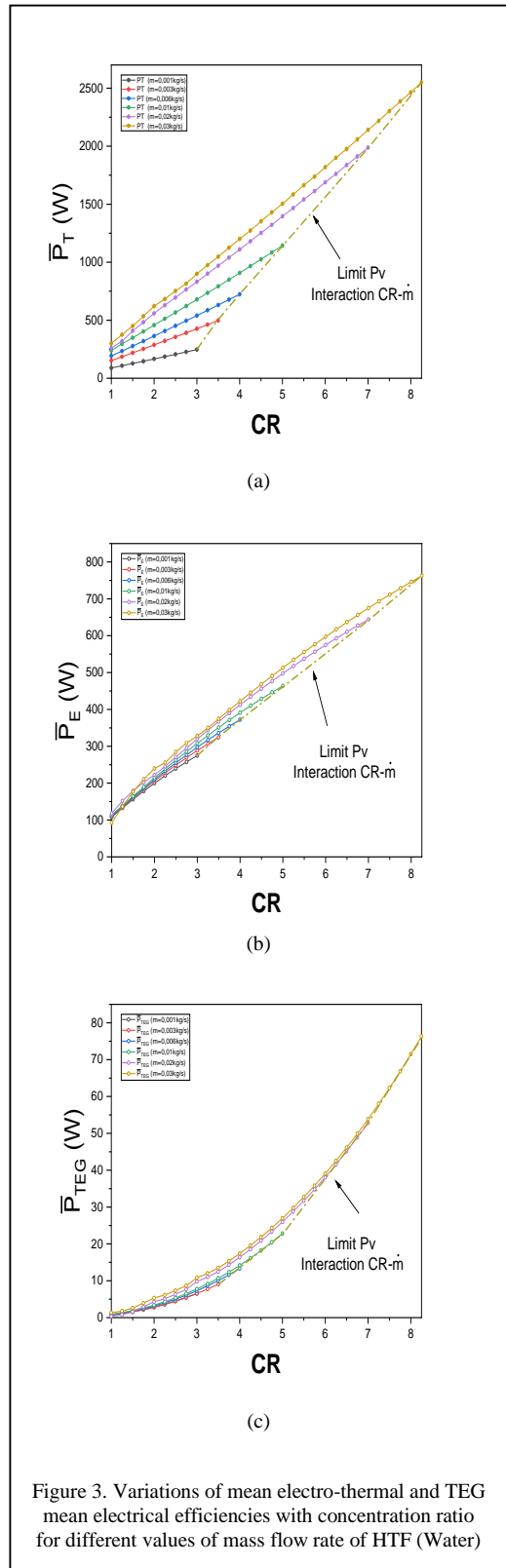
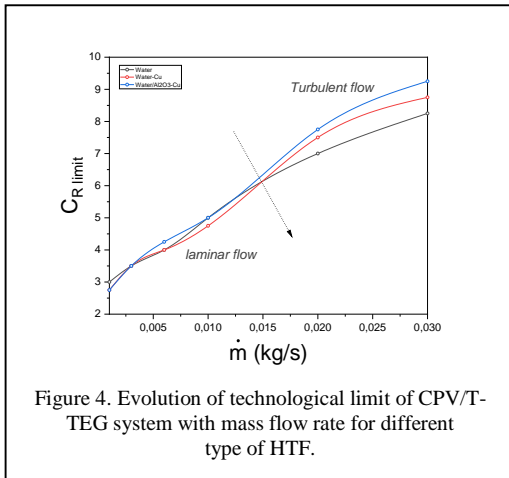


Figure 3. Variations of mean electro-thermal and TEG mean electrical efficiencies with concentration ratio for different values of mass flow rate of HTF (Water)



production, (6.8%; 12.60%) electrical production, and (14%; 29.26%) of thermoelectric production respectively.

The technological challenge in the use of nanofluid in CPV/T-TEG systems is to maximize the thermal production by recovering the maximum amount of heat and stabilize the temperature of the PV module around its optimal value. The solar concentration technique which means the concentration of solar irradiation on a focal point, this method is represented by a CR concentration ratio that improves the performance of CPV/T-TEG systems. The increase of the CR amplifies the energy received at the sensor so that the system will produce more electricity to the photovoltaic cells, this large amount of energy concentrated on the sensor increases the heat of the component of the studied system, and therefore, a considerable part of this thermal energy will be collected by HTF.

According to the present study, it is concluded that the optimal value of CR is the maximum value if only if the temperature of the PV module is checked, in the wake of this conclusion a second conclusion can be drawn concerning the choice of HTF, the correct choice of the latter makes it possible to achieve higher concentration rates with a normal operating temperature of the PV module.

The functionnmet of CPVT-TEG systems is directly related to exogenous parameters describing the meteorological state of the chosen geographical site. The dimensioning of the systems covered by this technology should be subject to utilization and process requirements. The effectiveness of this technology depends strongly on the solar irradiation which differs

from one zone to another, this leads us to say that the performance cannot be generalized because it risks to sweep the scales by changing the geographical site. But what is general that the interactions between the different techniques will undergo the same evolutions as that which is the studied area.

IV. CONCLUSION

The present work is a scrutiny study which aimed to investigate numerically the impact of the nature of fluids on thermoelectric performance of hybrid solar collector (PV/T) equipped with a compound parabolic concentrator (CPC) and thermoelectric generator (TEG).

The performance of the CPV/T system is affected by control parameters such as concentration ratio and mass flow rate as follows:

- The study of the effect of the compound parabolic concentrator, and translated by the concentration ratio, shows that the increase in the value of CR is favorable to the power produced either electrical or thermal. However, the increase in this parameter is harmful to the different yields characterizing the rate of electrical and thermal conversion.
- The increase in the concentration rate is benefic for the operation of thermoelectric generators.
- The use of nanotechnology increases the technological limits of CPV/T-TEG systems and expands their scope of application.
- For technical and economic reasons it is recommended to use a conventional fluid as a coolant when it is a flow in laminar regime in the system CPV/T-TEG, on the other hand, it is preferable to opt for a suitable nanofluid in the case of a tutbulent flow within the thermal part of the studied system.
- The limit concentration ratio, characteristic of a maximum instantaneous temperature T_{pvmax} not exceeding 350 K in order to ensure normal operation conditions of the PV cells, is improved with the increase of mass flow rate.

REFERENCES

- [1] Da, Y., Xuan, Y., & Li, Q. (2016). From light trapping to solar energy utilization: A novel photovoltaic-thermoelectric hybrid system to fully utilize solar spectrum. *Energy*, 95, 200-210.
- [2] Riahi, A., Ali, A. B. H., Fadhel, A., Guizani, A., & Balghouthi, M. (2020). Performance investigation of a concentrating photovoltaic thermal hybrid solar system combined with thermoelectric generators. *Energy Conversion and Management*, 205, 112377.
- [3] Gao, Y., Wu, D., Dai, Z., Wang, C., Chen, B., & Zhang, X. (2021). Performance analysis of a hybrid photovoltaic-thermoelectric generator system using heat pipe as heat sink for synergistic production of electricity. *Energy Conversion and Management*, 249, 114830.
- [4] Alnajideen, M., & Min, G. (2022). Hybrid photovoltaic-thermoelectric system using a novel spectral splitting solar concentrator. *Energy Conversion and Management*, 251, 114981.
- [5] Indira, S. S., Vaithilingam, C. A., Sivasubramanian, R., Chong, K. K., Narasingamurthi, K., & Saidur, R. (2022). Prototype of a novel hybrid concentrator photovoltaic/thermal and solar thermoelectric generator system for outdoor study. *Renewable Energy*, 201, 224-239.
- [6] Wen, X., Ji, J., Li, Z., & Song, Z. (2022). Performance analysis of a concentrated system with series photovoltaic/thermal module and solar thermal collector integrated with PCM and TEG. *Energy*, 249, 123777.

